NPL REPORT CETM 13

REPORT

Electric Field Probe Measurements in the *NPL* Untuned Stadium Reverberation Chamber

L R ARNAUT, P D WEST

SEPTEMBER 1999



NPL
National Physical Laboratory

The National Physical Laboratory is operated on behalf of the DTI by NPL Management Limited, a wholly owned subsidiary of Serco Group plc

NPL Report CETM 13

Electric Field Probe Measurements in the *NPL* Untuned Stadium Reverberation Chamber

L R Arnaut, P D West

Center for Electromagnetic and Time Metrology
National Physical Laboratory
Queens Road
Teddington
Middlesex TW11 0LW
United Kingdom

September 1999

Abstract

Measurements results and chamber characteristics are reported for the *NPL* stadium reverberation chamber in mode-tuned operation, using a miniature 3-axis electric field sensor. Results are based on the analysis of the measured stirrer data for the magnitude of the electric field, for mechanical wall stirring, at 2.5GHz and 8.2GHz. The measured probability distributions and various associated sample statistics are compared with theoretical results for ideal chambers, showing excellent agreement. The present study confirms and extends earlier results which were based on the measurement of power density. In addition, total field anisotropy and field inhomogeneity levels are obtained from the field probe data, quantifying the reverberation performance. Some new theoretical results are also derived.

Keywords: reverberation chamber, mode-stirred cavity, chamber calibration, EMC test environments, electromagnetic immunity and vulnerability testing, electric field probe, numerical modelling, random fields, statistical analysis, spectral analysis.

© Crown Copyright 1999
Reproduced by permission of the Controller of HMSO

ISSN 1467–3932

National Physical Laboratory
Teddington, Middlesex TW11 0LW, United Kingdom

Extracts of this report may be reproduced provided that the source is acknowledged and the extract is not taken out of context

Approved on behalf of the Managing Director of NPL by
Stuart Pollitt, Head of the Center for Electromagnetic and Time Metrology

Contents

1 Introduction 19

2 Three-axis electric field probe 21
2.1 Probe description and operation 21
2.2 Probe calibration and measurement uncertainty 22

3 Measurement results 23
3.1 Measurements at 2.5GHz 23
3.1.1 Rationale 23
3.1.2 Measurement set-up and procedure 25
3.1.3 Probe noise performance 25
3.1.4 Stirrer sweep data 26
3.1.5 Correlation functions 27
3.1.6 Distribution functions of field magnitude 29
3.1.7 Distribution functions of maximum-to-mean ratio for field magnitude . . . 31
3.1.8 Field anisotropy 32
3.1.9 Field inhomogeneity 33
3.1.10 Spectral analysis 36
3.2 Measurements at 8.2GHz 36
3.2.1 Rationale 36
3.2.2 Measurement set-up and procedure 36
3.2.3 Probe performance 37
3.2.4 Stirrer sweep data 37
3.2.5 Correlation functions 37
3.2.6 Distribution functions of field magnitude 38
3.2.7 Distribution functions of maximum-to-mean ratio for field magnitude . . . 39
3.2.8 Field anisotropy 41
3.2.9 Field inhomogeneity 42
3.2.10 Spatial correlation 42
3.2.11 Spectral analysis 43
3.2.12 Upward threshold crossings and mean excursion lengths 43

4 Miscellaneous results 44
4.1 Distribution and statistics of input power 44
4.1.1 Averaging of insertion loss 44
4.1.2 Distribution of input power 46
4.2 Effect of antenna aperture size on characterization of reverberation chamber 46

4.2.1 Introduction 46
4.2.2 Method 47
4.2.3 Results 47
4.3 Peak restoration and estimation of true maximum field strength 49
4.3.1 Cubic spline interpolation 49
4.3.2 Digital Laplace filtering 50

5 Summary 51

6 Conclusions 54

7 Acknowledgements 54

A Distributions, statistics and extreme values of field and energy density distribution functions 58
A.1 Energy density for single field component 58
A.2 Energy density for total field 59
A.3 Field strength for single field component 60
A.4 Field strength for total field 60

B Low-cost conversion of anechoic chambers into reverberation chambers 62

C On increasing mode density at low frequencies 64

D Use of nonreciprocal loading for enhanced reverberation performance 66

E Autofiltering 68

F Numerical eigenmode analysis of the stadium reverberation chamber 70
F.1 Cavity spectrum using MAFIA^{TM} electromagnetic simulator 70
F.2 Optimization of stadium parameter for maximum Kholmogorov entropy . 71

G Local averaging 72
G.1 Introduction 72
G.2 Measures of local averaging in spatial and stir domain 73
G.2.1 Variance function 73
G.2.2 Scale of fluctuation 77
G.2.3 Point–interval correlation functions for local averaging 79
G.3 Spectral measures for stirring performance under local averaging 80
G.3.1 First normalized spectral bandwidth 80
G.3.2 Second normalized spectral bandwidth 82

G.4 Upward threshold crossing frequency under local averaging 84
G.4.1 General local averaging 84
G.4.2 Upward threshold crossing frequency for specific underlying distributions under extreme local averaging 88
G.4.3 Upward threshold crossing frequency for stirrer step averaging 90
G.4.4 Upward threshold crossing frequency for sensor aperture averaging 91
G.5 Time to first passage 92
G.6 Mean excursion lengths 93
G.7 Conclusion 95

H Distribution of some goodness-of-fit statistics for measured field magnitude and energy density **96**
H.1 Introduction 96
H.2 Kholmogorov–Smirnov (K–S) statistic 96
H.3 Squared Kholmogorov–Smirnov statistic 98
H.4 Cramér–von Mises statistic 98

I Tables **100**
I.1 Field statistics 100
I.2 Theoretical vs. measured mean-normalized field 107
I.3 Theoretical vs. measured mean-normalized maximum field 107

J Figures **113**

List of Tables

1 Field statistics @ $f = 2.5$GHz, $r = 91$mm ($m_\alpha = 2$). 101
2 Field statistics @ $f = 2.5$GHz, $r = 91$mm ($m_\alpha = 1$). 102
3 Field statistics @ $f = 2.5$GHz, $r = 345$mm ($m_\alpha = 2$). 103
4 Field statistics @ $f = 2.5$GHz, $r = 345$mm ($m_\alpha = 1$). 104
5 Field statistics @ $f = 8.2$GHz, $r = 91$mm ($m_\alpha = 3$). 105
6 Field statistics @ $f = 8.2$GHz, $r = 91$mm ($m_\alpha = 1$). 106
7 Theoretical vs. measured coefficients of variation for mean-normalized field @ $f = 2.5$GHz, $r = 91$mm: decimated data set ($m_\alpha = 2$). 107
8 Theoretical vs. measured coefficients of variation for mean-normalized field @ $f = 2.5$GHz, $r = 91$mm: full data set ($m_\alpha = 1$). 107
9 Theoretical vs. measured coefficients of variation for mean-normalized field @ $f = 2.5$GHz, $r = 345$mm: decimated data set ($m_\alpha = 2$). 107
10 Theoretical vs. measured coefficients of variation for mean-normalized field @ $f = 2.5$GHz, $r = 345$mm: full data set ($m_\alpha = 1$). 108
11 Theoretical vs. measured coefficients of variation for mean-normalized field @ $f = 8.2$GHz, $r = 91$mm: decimated data set ($m_\alpha = 3$). 108
12 Theoretical vs. measured coefficients of variation for mean-normalized field @ $f = 8.2$GHz, $r = 91$mm: full data set ($m_\alpha = 1$). 108
13 Theoretical vs. measured max-to-mean field W with 95% confidence interval @ $f = 2.5$GHz, $r = 91$mm: decimated data ($M = 137$, $N = 275/1.5 = 183$). 109
14 Theoretical vs. measured max-to-mean field W with 95% confidence interval @ $f = 2.5$GHz, $r = 91$mm: full data ($M = 275$, $N = 275/1.5 = 183$). 109
15 Theoretical vs. measured max-to-mean field W with 95% confidence interval @ $f = 2.5$GHz, $r = 345$mm: decimated data ($M = 137$, $N = 275/1.5 = 183$). 109
16 Theoretical vs. measured max-to-mean field W with 95% confidence interval @ $f = 2.5$GHz, $r = 345$mm: full data ($M = 275$, $N = 275/1.5 = 183$). 110
17 Theoretical vs. measured max-to-mean field W with 95% confidence interval @ $f = 8.2$GHz, $r = 91$mm: decimated data ($M = 400$, $N = 1200/3 = 400$). 110
18 Theoretical vs. measured max-to-mean field W with 95% confidence interval @ $f = 8.2$GHz, $r = 91$mm: full data ($M = 1200$, $N = 1200/3 = 400$). 110
19 Spectral parameters and spectral bandwidths @ 2.5GHz, $r = 91$mm, 345mm and 8.2GHz, $r = 91$mm. 111
20 Numerical simulation results (MAFIA™) for first few resonances of stadium cavity. 112

List of Figures

(a) 3-axis electric field probe (Schmid & Partner ER3Dxxx family); (b) connector plan and front view; (c) local near-field distortions [Poković, 1999]. 114

Spread as a function of average field strength for S&P probe measurements @ $f = 2.5$GHz, $r = 91$mm for 40 readings per sample and sample size $M = 275$. . . . 115

Sweep data @ $f = 2.5$GHz, $r = 91$mm. 116

Sweep data @ $f = 2.5$GHz, $r = 345$mm. 117

Autocorrelation functions $|\rho_\alpha|$ for power and field magnitude for $|E_\alpha|$ $(\alpha = x, y, z, t)$ as a function of wall position $\tau/\Delta\tau$ @ $f = 2.5$GHz, $r = 91$mm. 118

Single-sample and ensemble decimation factors m_α for $|E_\alpha|^2$ $(\alpha = x, y, z, t)$ as a function of sample size M @ $f = 2.5$GHz, $r = 91$mm. 119

Single-sample and ensemble power autocorrelation functions ρ_α for $|E_\alpha|$ $(\alpha = x, y, z, t)$ as a function of wall position $\tau/\Delta\tau$ @ $f = 2.5$GHz, $r = 91$mm. 120

Single-sample and ensemble power autospectral density functions g_α for $|E_\alpha|$ $(\alpha = x, y, z, t)$ as a function of spectral wall position $\omega/\Delta\omega$ @ $f = 2.5$GHz, $r = 91$mm, with Bartlett estimates of spectral parameters β_α for smoothed density function (1st-order exponential model). 121

Field and power variance functions for $|E_\alpha|$ $(\alpha = x, y, z, t)$ as a function of stirrer averaging length $\mathcal{T}/\Delta\tau$ @ $f = 2.5$GHz, $r = 91$mm. 122

Autocorrelation functions $|\rho_\alpha|$ for power and field magnitude for $|E_\alpha|$ $(\alpha = x, y, z, t)$ as a function of wall position $\tau/\Delta\tau$ @ $f = 2.5$GHz, $r = 345$mm. 123

Single-sample and ensemble decimation factors m_α for $|E_\alpha|^2$ $(\alpha = x, y, z, t)$ as a function of sample size M @ $f = 2.5$GHz, $r = 345$mm. 124

Single-sample and ensemble power autocorrelation functions ρ_α for $|E_\alpha|$ $(\alpha = x, y, z, t)$ as a function of wall position $\tau/\Delta\tau$ @ $f = 2.5$GHz, $r = 345$mm. 125

Single-sample and ensemble power autospectral density functions g_α for $|E_\alpha|$ $(\alpha = x, y, z, t)$ as a function of spectral wall position $\omega/\Delta\omega$ @ $f = 2.5$GHz, $r = 345$mm. 126

Power crosscorrelation functions $\rho_{\alpha\beta}$ for $|E_\alpha|$, $|E_\beta|$ $(\alpha, \beta = x, y, z)$ as a function of wall position $\tau/\Delta\tau$ @ $f = 2.5$GHz, $r = 91$mm. 127

Power crosscorrelation functions $\rho_{\alpha\beta}$ for $|E_\alpha|$, $|E_\beta|$ $(\alpha, \beta = x, y, z)$ as a function of wall position $\tau/\Delta\tau$ @ $f = 2.5$GHz, $r = 345$mm. 128

Coefficients of variation ν_α for $|E_\alpha|$ $(\alpha = x, y, z, t)$ as a function of sample size M @ $f = 2.5$GHz, $r = 91$mm. 129

Coefficients of variation ν_α for $|E_\alpha|$ $(\alpha = x, y, z, t)$ as a function of sample size M @ $f = 2.5$GHz, $r = 345$mm. 130

18 Probability density functions f_α of $|E_\alpha|/\langle|E_\alpha|\rangle$ ($\alpha = x, y, z, t$) @ $f = 2.5$GHz, $r = 91$mm for decimated data set ($m_\alpha = 2$). (See text for correct interpretation of Figure.) 131

19 Probability density functions f_α of $|E_\alpha|/\langle|E_\alpha|\rangle$ ($\alpha = x, y, z, t$) @ $f = 2.5$GHz, $r = 91$mm for full data set. (See text for correct interpretation of Figure.) 132

20 Probability density functions f_α of $|E_\alpha|/\langle|E_\alpha|\rangle$ ($\alpha = x, y, z, t$) @ $f = 2.5$GHz, $r = 345$mm for decimated data set ($m_\alpha = 2$). (See text for correct interpretation of Figure.) 133

21 Probability density functions f_α of $|E_\alpha|/\langle|E_\alpha|\rangle$ ($\alpha = x, y, z, t$) @ $f = 2.5$GHz, $r = 345$mm for full data set. (See text for correct interpretation of Figure.) . . . 134

22 Cumulative distribution functions F_α of $|E_\alpha|/\langle|E_\alpha|\rangle$ ($\alpha = x, y, z, t$) @ $f = 2.5$GHz, $r = 91$mm for decimated data set ($m_\alpha = 2$). 135

23 Cumulative distribution functions F_α of $|E_\alpha|/\langle|E_\alpha|\rangle$ ($\alpha = x, y, z, t$) @ $f = 2.5$GHz, $r = 91$mm for full data set. 136

24 Cumulative distribution functions of standardized deviations $|E_\alpha|_{theo} - |E_\alpha|_{meas}$ ($\alpha = x, y, z$) @ $f = 2.5$GHz, $r = 91$mm for full data set. 137

25 Kholmogorov–Smirnov test statistic between measured and theoretical cumulative distribution functions of $|E_\alpha|/\langle|E_\alpha|\rangle$ ($\alpha = x, y, z$) as a function of sample size M @ $f = 2.5$GHz, $r = 91$mm for full data set. . . . . .

26 Cramér–von Mises test statistic between measured and theoretical cumulative distribution functions of $|E_\alpha|/\langle|E_\alpha|\rangle$ ($\alpha = x, y, z$) as a function of sample size M@ $f = 2.5$GHz, $r = 91$mm for full data set. 139

27 Crosscorrelation coefficients $\varrho_{\alpha\beta}$ between measured and theoretical cumulative distribution functions of $|E_\alpha|/\langle|E_\alpha|\rangle$, $|E_\beta|/\langle|E_\beta|\rangle$ ($\alpha, \beta = x, y, z$) as a function of sample size M@ $f = 2.5$GHz, $r = 91$mm for full data set. . . . . .

28 Cumulative distribution functions F_α of $|E_\alpha|/\langle|E_\alpha|\rangle$ ($\alpha = x, y, z, t$) @ $f = 2.5$GHz, $r = 345$mm for decimated data set ($m_\alpha = 2$). 141

29 Cumulative distribution functions F_α of $|E_\alpha|/\langle|E_\alpha|\rangle$ ($\alpha = x, y, z, t$) @ $f = 2.5$GHz, $r = 345$mm for full data set. 142

30 Distribution functions, theoretical median, theoretical mean, measured values, and 95% and 99% confidence intervals of max-to-mean field for $|E_\alpha|/\langle|E_\alpha|\rangle$ ($\alpha = x, y, z, t$) @ $f = 2.5$GHz, $r = 91$mm for decimated data set ($m_\alpha = 2$). 143

31 Distribution functions, theoretical median, theoretical mean, measured values, and 95% and 99% confidence intervals of max-to-mean field for $|E_\alpha|/\langle|E_\alpha|\rangle$ ($\alpha = x, y, z, t$) @ $f = 2.5$GHz, $r = 91$mm for full data set. 144

32 Distribution functions, theoretical median, theoretical mean, measured values, and 95% and 99% confidence intervals of max-to-mean field for $|E_\alpha|/\langle|E_\alpha|\rangle$ ($\alpha = x, y, z, t$) @ $f = 2.5$GHz, $r = 345$mm for decimated data set ($m_\alpha = 2$). 145

33 Distribution functions, theoretical median, theoretical mean, measured values, and 95% and 99% confidence intervals of max-to-mean field for $|E_\alpha|/\langle|E_\alpha|\rangle$ ($\alpha = x, y, z, t$) @ $f = 2.5$GHz, $r = 345$mm for full data set. 146

34 Theoretical and measured max-to-mean field for $|E_\alpha|/\langle|E_\alpha|\rangle$ ($\alpha = x, y, z, t$) as a function of sample size M @ $f = 2.5$GHz, $r = 91$mm. 147

35 Theoretical and measured max-to-mean field for $|E_\alpha|/\langle|E_\alpha|\rangle$ ($\alpha = x, y, z, t$) as a function of sample size M @ $f = 2.5$GHz, $r = 345$mm. 148

36 Theoretical (simulated) field anisotropy coefficients $A_{\alpha\beta}$ and A_{tot} for sample of size $M = 275$ taken from a perfectly reverberant field. 149

37 Measured field anisotropy coefficients $A_{\alpha\beta}$ and A_{tot} @ $f = 2.5$GHz, $r = 91$mm for full data set. 150

38 Single-sample average of measured field anisotropy coefficients $A_{\alpha\beta}$ and A_{tot} as a function of sample size M @ $f = 2.5$GHz, $r = 91$mm for full data set (linear scale). 151

39 Magnitude of single-sample average of measured field anisotropy coefficients $A_{\alpha\beta}$ and A_{tot} as a function of sample size M @ $f = 2.5$GHz, $r = 91$mm for full data set (dB scale). 152

40 Magnitude of bootstrap average of measured field anisotropy coefficients $A_{\alpha\beta}$ and A_{tot} as a function of sample size M @ $f = 2.5$GHz, $r = 91$mm for full data set (dB scale). 153

41 Theoretical and measured cumulative distribution functions of field anisotropy coefficients $A_{\alpha\beta}$ and A_{tot} @ $f = 2.5$GHz, $r = 91$mm for decimated data set ($m_\alpha = 2$). 154

42 Theoretical and measured cumulative distributions of field anisotropy coefficients $A_{\alpha\beta}$ and A_{tot} @ $f = 2.5$GHz, $r = 91$mm for full data set. 155

43 Measured field anisotropy coefficients $A_{\alpha\beta}$ and A_{tot} @ $f = 2.5$GHz, $r = 345$mm for full data set. 156

44 Single-sample average of measured field anisotropy coefficients $A_{\alpha\beta}$ and A_{tot} as a function of sample size M @ $f = 2.5$GHz, $r = 345$mm for full data set (linear scale).157

45 Magnitude of single-sample average of measured field anisotropy coefficients $A_{\alpha\beta}$ and A_{tot} as a function of sample size M @ $f = 2.5$GHz, $r = 345$mm for full data set (dB scale). 158

46 Magnitude of bootstrap average of measured field anisotropy coefficients $A_{\alpha\beta}$ and A_{tot} as a function of sample size M @ $f = 2.5$GHz, $r = 345$mm for full data set (dB scale). 159

47 Theoretical and measured cumulative distribution functions of field anisotropy coefficients $A_{\alpha\beta}$ and A_{tot} @ $f = 2.5$GHz, $r = 345$mm for decimated data set ($m_\alpha = 2$).160

48 Measured field inhomogeneity coefficients $I_{\alpha\alpha}$ ($\alpha = x, y, z, t$) @ $f = 2.5$GHz, $r_0 = 91$mm, $r_1 = 101$mm for full data set. 161

49 Total measured field inhomogeneity coefficient I_{tot} @ $f = 2.5$GHz, $r_0 = 91$mm, $r_1 = 101$mm for full data set. 162

50 Single-sample average of measured field inhomogeneity coefficients $I_{\alpha\alpha}$ ($\alpha = x, y, z, t$) as a function of sample size M @ $f = 2.5$GHz, $r_0 = 91$mm, $r_1 = 101$mm for full data set (linear scale). 163

51 Single-sample average of total measured field inhomogeneity coefficient I_{tot} as a function of sample size M @ $f = 2.5$GHz, $r_0 = 91$mm, $r_1 = 101$mm for full data set (linear scale). 164

52 Magnitude of single-sample average of measured field inhomogeneity coefficients $I_{\alpha\alpha}$ ($\alpha = x, y, z, t$) as a function of sample size M @ $f = 2.5$GHz, $r_0 = 91$mm, $r_1 = 101$mm for full data set (dB scale). 165

53 Magnitude of single-sample average of total measured field inhomogeneity coefficient I_{tot} as a function of sample size M @ $f = 2.5$GHz, $r_0 = 91$mm, $r_1 = 101$mm for full data set (dB scale). 166

54 Magnitude of bootstrap average of measured field inhomogeneity coefficients $I_{\alpha\alpha}$ ($\alpha = x, y, z, t$) as a function of sample size M @ $f = 2.5$GHz, $r_0 = 91$mm, $r_1 = 101$mm for full data set (dB scale). 167

55 Magnitude of bootstrap average of total measured field inhomogeneity coefficient I_{tot} as a function of sample size M @ $f = 2.5$GHz, $r_0 = 91$mm, $r_1 = 101$mm for full data set (dB scale). 168

56 Spatial correlation coefficients between $|E_\alpha(r_0)|^2$ and $|E_\alpha(r_1)|^2$ as a function of sample size M @ $f = 2.5$GHz, $r_0 = 91$mm, $r_1 = 101$mm for full data set. 169

57 Theoretical and measured cumulative distribution functions of field inhomogeneity coefficients @ $f = 2.5$GHz, $r_0 = 91$mm, $r_1 = 101$mm for decimated data set ($m_\alpha = 2$). 170

58 Radial dependence of field inhomogeneity coefficients $I_{\alpha\alpha}$ ($\alpha = x, y, z, t$) @ $f = 2.5$GHz, $r_0 = 91$mm, $r_1 = 101 \ldots 349$mm. 171

59 Radial dependence of magnitude of bootstrap averaged field anisotropy coefficients $A_{\alpha\beta}$ and A_{tot} @ $f = 2.5$GHz. 172

60 Radial dependence of bootstrap averaged crosscorrelation coefficients $\varrho_{\alpha\beta}$ @ $f = 2.5$GHz for full data set. 173

61 Radial dependence of bootstrap averaged transmission loss @ $f = 2.5$GHz. 174

62 Mean of ratio of power densities vs. ratio of mean of power densities as a function of sample size M @ $f = 2.5$GHz, $r = 91$mm for full data set. 175

63 Theoretical composite quality factors computed for mean of ratio of total power densities vs. ratio of mean of total power densities as a function of sample size M @ $f = 2.5$GHz, $r = 91$mm for full data set (assuming free space wave impedance). 176

64 Theoretical composite quality factors computed for mean of ratio of individual power densities vs. ratio of mean of individual power densities as a function of sample size M @ $f = 2.5$GHz, $r = 91$mm for full data set (assuming free space wave impedance). . . . . .

65 Cumulative distribution functions of measured input power P_i, received rectilinear power P_α and received total power P_t @ $f = 2.5$GHz, $r = 91$mm for full data set. 178

66 Normalized power autospectral density functions g_α and 3rd order exponential fits as a function of normalized spectral wall position $\omega/\Delta\omega$ @ $f = 2.5$GHz, $r = 91$mm for full data set. 179

67 Normalized power crossspectral density functions $g_{\alpha\beta}$ and 3rd order exponential fits as a function of normalized spectral wall position $\omega/\Delta\omega$ @ $f = 2.5$GHz, $r = 91$mm for full data set. . . . . .

68 Normalized spectral bandwidths δ_α and ϵ_α as a function of radial distance @ $f = 2.5$GHz. 181

69 Spread as a function of average field strength for S&P probe measurements @ $f = 8.2$GHz, $r = 91$mm for 40 readings per sample and sample size $M = 1200$. .

70 Sweep data @ $f = 8.2$GHz, $r = 91$mm. 183

71 Average normalized squared field strength as a function of sample size M @ $f = 8.2$GHz, $r = 91$mm for full data set. . . . . .

72 Average normalized squared field strength as a function of sample size N @ $f = 8.2$GHz, $r = 91$mm for decimated data set ($m_\alpha = 4$). 185

73 Autocorrelation functions $|\rho_\alpha|$ for power and field magnitude for $|E_\alpha|$ ($\alpha = x, y, z, t$) as a function of wall position $\tau/\Delta\tau$ @ $f = 8.2$GHz, $r = 91$mm. 186

74 Field and power variance functions for $|E_\alpha|$ ($\alpha = x, y, z, t$) as a function of stirrer averaging length $\mathcal{T}/\Delta\tau$ @ $f = 8.2$GHz, $r = 91$mm. . . . . .

75 Single-sample and ensemble decimation factors m_α for $|E_\alpha|^2$ ($\alpha = x, y, z, t$) as a function of sample size M @ $f = 8.2$GHz, $r = 91$mm. 188

76 Single-sample and ensemble power autocorrelation functions ρ_α for $|E_\alpha|^2$ ($\alpha = x, y, z, t$) as a function of wall position $\tau/\Delta\tau$ @ $f = 8.2$GHz, $r = 91$mm. 189

77 Single-sample and ensemble power autospectral density functions g_α for $|E_\alpha|$ ($\alpha = x, y, z, t$) as a function of spectral wall position $\omega/\Delta\omega$ @ $f = 8.2$GHz, $r = 91$mm, with Bartlett estimates of spectral parameters β_α for smoothed density function (1st-order exponential model). 190

78 Power crosscorrelation functions $\rho_{\alpha\beta}$ for $|E_\alpha|$, $|E_\beta|$ ($\alpha, \beta = x, y, z$) as a function of wall position $\tau/\Delta\tau$ @ $f = 8.2$GHz, $r = 91$mm for full data set. 191

79 Power crosscorrelation coefficients $\varrho_{\alpha\beta}$ for $|E_\alpha|$, $|E_\beta|$ ($\alpha, \beta = x, y, z$) as a function of sample size M @ $f = 8.2$GHz, $r = 91$mm for full data set. 192

80 Coefficients of variation ν_α for $|E_\alpha|$ ($\alpha = x, y, z, t$) as a function of sample size M @ $f = 8.2$GHz, $r = 91$mm. 193

81 Probability density functions f_α of $|E_\alpha|/\langle|E_\alpha|\rangle$ ($\alpha = x, y, z, t$) @ $f = 8.2$GHz, $r = 91$mm for decimated data set ($m_\alpha = 3$). (See text for correct interpretation of Figure.) 194

82 Probability density functions f_α of $|E_\alpha|/\langle|E_\alpha|\rangle$ ($\alpha = x, y, z, t$) @ $f = 8.2$GHz, $r = 91$mm for full data set ($m_\alpha = 1$) (for demonstration only). (See text for correct interpretation of Figure.) 195

83 Cumulative distribution functions F_α of $|E_\alpha|/\langle|E_\alpha|\rangle$ ($\alpha = x, y, z, t$) @ $f = 8.2$GHz, $r = 91$mm for decimated data set ($m_\alpha = 3$). 196

84 Cumulative distribution functions F_α of $|E_\alpha|/\langle|E_\alpha|\rangle$ ($\alpha = x, y, z, t$) @ $f = 8.2$GHz, $r = 91$mm for full data set ($m_\alpha = 1$) (for demonstration only). 197

85 Cumulative distribution functions of standardized deviations $|E_\alpha|_{theo} - |E_\alpha|_{meas}$ ($\alpha = x, y, z$) @ $f = 8.2$GHz, $r = 91$mm for decimated data set ($m_\alpha = 3$). 198

86 Cumulative distribution functions of standardized absolute deviations $||E_\alpha|_{theo} - |E_\alpha|_{meas}|$ ($\alpha = x, y, z$) @ $f = 8.2$GHz, $r = 91$mm for decimated data set ($m_\alpha = 3$). 199

87 Cumulative distribution functions of standardized squared deviations $||E_\alpha|_{theo} - |E_\alpha|_{meas}|^2$ ($\alpha = x, y, z$) @ $f = 8.2$GHz, $r = 91$ mm for decimated data set ($m_\alpha = 3$). 200

88 Cumulative distribution functions of standardized deviations $|E_\alpha|_{theo} - |E_\alpha|_{meas}$ ($\alpha = x, y, z$) @ $f = 8.2$GHz, $r = 91$mm for full data set. 201

89 Kholmogorov–Smirnov test statistic between measured and theoretical cumulative distribution functions of $|E_\alpha|/\langle|E_\alpha|\rangle$ ($\alpha = x, y, z$) as a function of sample size M@ $f = 8.2$GHz, $r = 91$mm for full data set. 202

90 Cramér–von Mises test statistic between measured and theoretical cumulative distribution functions of $|E_\alpha|/\langle|E_\alpha|\rangle$ ($\alpha = x, y, z$) as a function of sample size M@ $f = 8.2$GHz, $r = 91$mm for full dataset. 203

91 Crosscorrelation coefficients $\varrho_{\alpha\beta}$ between measured and theoretical cumulative distribution functions of $|E_\alpha|/\langle|E_\alpha|\rangle$, $|E_\beta|/\langle|E_\beta|\rangle$ ($\alpha, \beta = x, y, z$) as a function of sample size M @ $f = 8.2$GHz, $r = 91$mm for full data set. 204

92 Distribution functions, theoretical median, theoretical mean, measured values, and 95% and 99% confidence intervals of max-to-mean field for $|E_\alpha|/\langle|E_\alpha|\rangle$ ($\alpha = x, y, z, t$) @ $f = 8.2$GHz, $r = 91$mm for decimated data set ($m_\alpha = 3$). 205

93 Distribution functions, theoretical median, theoretical mean, measured values, and 95% and 99% confidence intervals of max-to-mean field for $|E_\alpha|/\langle|E_\alpha|\rangle$ ($\alpha = x, y, z, t$) @ $f = 8.2$GHz, $r = 91$mm for full data set (for demonstration only). . . . 206

94 Theoretical and measured max-to-mean field for $|E_\alpha|/\langle|E_\alpha|\rangle$ ($\alpha = x, y, z, t$) as a function of sample size N @ $f = 8.2$GHz, $r = 91$mm. 207

95 Comparison between measured max-to-mean field for $|E_\alpha|/\langle|E_\alpha|\rangle$ ($\alpha = x, y, z$) and various estimates a function of sample size N @ $f = 8.2$GHz, $r = 91$mm. 208

96 Theoretical (simulated) field anisotropy coefficients $A_{\alpha\beta}$ and A_{tot} for sample of size $M = 1200$ taken from a perfectly reverberant field. 209

97 Measured field anisotropy coefficients $A_{\alpha\beta}$ and A_{tot} @ $f = 8.2$GHz, $r = 91$mm for full data set. 210

98 Single-sample average of measured field anisotropy coefficients $A_{\alpha\beta}$ and A_{tot} as a function of sample size M @ $f = 8.2$GHz, $r = 91$mm for full data set (linear scale). 211

99 Magnitude of single-sample average of measured field anisotropy coefficients $A_{\alpha\beta}$ and A_{tot} as a function of sample size M @ $f = 8.2$GHz, $r = 91$mm for full data set (dB scale). 212

100 Magnitude of bootstrap average of measured field anisotropy coefficients $A_{\alpha\beta}$ and A_{tot} as a function of sample size M @ $f = 8.2$GHz, $r = 91$mm for full data set (dB scale). 213

101 Magnitude of bootstrap average of measured field anisotropy coefficients $A_{\alpha\beta}$ and A_{tot} @ $f = 8.2$GHz, $r = 91$mm for decimated data set ($m_\alpha = 4$) (dB scale). 214

102 Theoretical and measured cumulative distribution functions of field anisotropy coefficients $A_{\alpha\beta}$ and A_{tot} @ $f = 8.2$GHz, $r = 91$mm for decimated data set ($m_\alpha = 3$). 215

103 Theoretical and measured cumulative distribution functions of field anisotropy coefficients $A_{\alpha\beta}$ and A_{tot} @ $f = 8.2$GHz, $r = 91$mm for full data set (for demonstration only). 216

104 Measured field inhomogeneity coefficients $I_{\alpha\alpha}$ ($\alpha = x, y, z, t$) @ $f = 8.2$GHz, $r_0 = 91$mm, $r_1 = 94$mm for full data set. 217

105 Total measured field inhomogeneity coefficients I_{tot} @ $f = 8.2$GHz, $r_0 = 91$mm, $r_1 = 94$mm for full data set. 218

106 Single-sample average of measured field inhomogeneity coefficients $I_{\alpha\alpha}$ ($\alpha = x, y, z, t$) as a function of sample size M @ $f = 8.2$GHz, $r_0 = 91$mm, $r_1 = 94$mm for full data set (linear scale). 219

107 Single-sample average of total measured field inhomogeneity coefficients I_{tot} as a function of sample size M @ $f = 8.2$GHz, $r_0 = 91$mm, $r_1 = 94$mm for full data set (linear scale). 2:

108 Magnitude of single-sample average of measured field inhomogeneity coefficients $I_{\alpha\alpha}$ ($\alpha = x, y, z, t$) as a function of sample size M @ $f = 8.2$GHz, $r_0 = 91$mm, $r_1 = 94$mm for full data set (dB scale). 221

109 Magnitude of single-sample average of total measured field inhomogeneity coefficient I_{tot} as a function of sample size M @ $f = 8.2$GHz, $r_0 = 91$mm, $r_1 = 94$mm for full data set (dB scale). 22

110 Magnitude of bootstrap average of measured field inhomogeneity coefficients $I_{\alpha\alpha}$ ($\alpha = x, y, z, t$) as a function of sample size M @ $f = 8.2$GHz, $r_0 = 91$mm, $r_1 = 94$mm for full data set (dB scale). 22:

111 Magnitude of bootstrap average of total measured field inhomogeneity coefficient I_{tot} as a function of sample size M @ $f = 8.2$GHz, $r_0 = 91$mm, $r_1 = 94$mm for full data set (dB scale). 224

112 Spatial correlation coefficients between $|E_\alpha(r_0)|^2$ and $|E_\alpha(r_1)|^2$ as a function of sample size M @ $f = 8.2$GHz, $r_0 = 91$mm, $r_1 = 94$mm for full data set. 225

113 Theoretical and measured cumulative distribution functions of field inhomogeneity coefficients @ $f = 8.2$GHz, $r_0 = 91$mm, $r_1 = 94$mm for decimated data set ($m_\alpha = 3$).226

114 Mean of ratio of power densities vs. ratio of mean of power densities as a function of sample size M @ $f = 8.2$GHz, $r = 91$mm for full data set. 227

115 Theoretical composite quality factors computed for mean of ratio of total power densities vs. ratio of mean of total power densities as a function of sample size M @ $f = 8.2$GHz, $r = 91$mm for full data set (assuming free space wave impedance). 228

116 Theoretical composite quality factors computed for mean of ratio of individual power densities vs. ratio of mean of individual power densities as a function of sample size M @ $f = 8.2$GHz, $r = 91$mm for full data set (assuming free space wave impedance). 229

117 Cumulative distribution functions of measured input power P_i, received rectilinear power P_α and received total power P_t @ $f = 8.2$GHz, $r = 91$mm for full data set. . 230

118 Normalized power autospectral density functions g_α and 3rd order exponential fits as a function of normalized spectral wall position $\omega/\Delta\omega$ @ $f = 8.2$GHz, $r = 91$mm for full data set. 231

119 Normalized power cross-spectral density functions $g_{\alpha\beta}$ and 3rd order exponential fits as a function of normalized spectral wall position $\omega/\Delta\omega$ @ $f = 8.2$GHz, $r =$ 91mm for full data set. 232

120 Theoretical and measured upward threshold crossing rate ν_T^+ for field magnitudes as a function of threshold level b/σ_0 @ $f = 8.2$GHz, $r = 91$mm for full data set. . . 233
121 Theoretical and measured mean excursion length $\mathrm{E}[\mathcal{L}_T]$ for field magnitudes as a function of threshold level b/σ_0 @ $f = 8.2$GHz, $r = 91$mm for full data set. 234
122 Sweep data for synthetic Rx apertures of minimum and maximum width L @ $f = 2.5$GHz. 235
123 Coefficients of variation ν_α for $|E_\alpha|$ ($\alpha = x, y, z$) as a function of width L of synthetic Rx aperture @ $f = 2.5$GHz. 236
124 Theoretical and measured cumulative distribution functions of $|E_\alpha|/\langle|E_\alpha|\rangle$ ($\alpha = x, y, z, t$) for synthetic Rx apertures of various widths L @ $f = 2.5$GHz. 237
125 Crosscorrelation coefficients $\varrho_{\alpha\beta}$ between theoretical and measured cumulative distribution functions of $|E_\alpha|/\langle|E_\alpha|\rangle$, $|E_\beta|/\langle|E_\beta|\rangle$ ($\alpha, \beta = x, y, z, t$) as a function of aperture width L @ $f = 2.5$GHz. 238
126 Measured field anisotropy coefficients $A_{\alpha\beta}$ and A_{tot} for synthetic Rx aperture of maximum width ($L = 243$mm) @ $f = 2.5$GHz. 239
127 Single-sample average of measured field anisotropy coefficients $A_{\alpha\beta}$ and A_{tot} as a function of width L of synthetic Rx aperture @ $f = 2.5$GHz for full data set. . . . 240
128 Bootstrap averaged insertion loss $\langle P_\alpha/P_i\rangle$ ($\alpha = x, y, z, t$) as a function of width L of synthetic Rx aperture @ $f = 2.5$GHz. 241
129 Normalized spectral bandwidths δ_α, ϵ_α ($\alpha = x, y, z, t$) as a function of width L of synthetic Rx aperture @ $f = 2.5$GHz. 242
130 Peak restoration for stirrer data using cubic spline interpolation and digital Laplace filtering with $\zeta = 0.08$ @ $f = 2.5$GHz, $r = 91$mm (first 40 data points only). 243
131 Integrand of edge line integral (edge length contribution to mode density) as a function of dihedral opening angle ϕ. 244
132 Ground plan of a 4-segment 'bow-tie' room. 245
133 Spectrum (incomplete) of 3D stadium cavity with $R = 0.35$m, $a = 0.175$m obtained with eigenmode solver of MAFIA™. 246
134 Comparison between cumulative mode count for 3D stadium cavity obtained with MAFIA™, classical Weyl formula and extended Weyl formula. 247
135 Distribution of $\underline{\mathrm{E}}_t$ for 1st eigenmode of 3D stadium ($R = 0.35$m, $a = 0.175$m). . . 248
136 Distribution of $\underline{\mathrm{B}}_t$ for 1st eigenmode of 3D stadium ($R = 0.35$m, $a = 0.175$m). . . 249
137 Distribution of $\underline{\mathrm{E}}_t$ for 2nd eigenmode of 3D stadium ($R = 0.35$m, $a = 0.175$m). . . 250
138 Distribution of $\underline{\mathrm{B}}_t$ for 2nd eigenmode of 3D stadium ($R = 0.35$m, $a = 0.175$m). . . 251
139 Distribution of $\underline{\mathrm{E}}_t$ for 3rd eigenmode of 3D stadium ($R = 0.35$m, $a = 0.175$m). . . 252
140 Distribution of $\underline{\mathrm{B}}_t$ for 3rd eigenmode of 3D stadium ($R = 0.35$m, $a = 0.175$m). . . 253
141 Distribution of $\underline{\mathrm{E}}_t$ for 4th eigenmode of 3D stadium ($R = 0.35$m, $a = 0.175$m). . . 254

142 Distribution of $\underline{B}_t$ for 4th eigenmode of 3D stadium ($R = 0.35$m, $a = 0.175$m). . . 255
143 Distribution of $\underline{E}_t$ for 5th eigenmode of 3D stadium ($R = 0.35$m, $a = 0.175$m). . . 256
144 Distribution of $\underline{B}_t$ for 5th eigenmode of 3D stadium ($R = 0.35$m, $a = 0.175$m). . . 257
145 Distribution of $\underline{E}_t$ for 6th eigenmode of 3D stadium ($R = 0.35$m, $a = 0.175$m). . . 258
146 Distribution of $\underline{B}_t$ for 6th eigenmode of 3D stadium ($R = 0.35$m, $a = 0.175$m). . . 259
147 Distribution of $|\underline{E}_t|$ (V/m) in 3D stadium ($R = 0.35$m, $a = 0.175$m) @ $f =$ 2.53GHz. 260
148 Distribution of $\underline{E}_t/|\underline{E}_t|$ in 3D stadium ($R = 0.35$m, $a = 0.175$m) @ $f = 2.53$GHz. . 261
149 Distribution of $|\underline{B}_t|$ (Vs/m^2) in 3D stadium ($R = 0.35$m, $a = 0.175$m) @ $f =$ 2.53GHz. 262
150 Distribution of $|\underline{E}_t|$ (V/m) in 3D stadium ($R = 0.35$m, $a = 0.175$m) @ $f =$ 8.26GHz. 263
151 Distribution of $\underline{E}_t/|\underline{E}_t|$ in 3D stadium ($R = 0.35$m, $a = 0.175$m) @ $f = 8.26$GHz. . 264
152 Distribution of $|\underline{B}_t|$ (Vs/m^2) in 3D stadium ($R = 0.35$m, $a = 0.175$m) @ $f =$ 8.26GHz. 265
153 Variance function $\gamma_\mathcal{T}$ for power density of total field as a function of normalized interval width $\mathcal{T}/\beta$ for local stir averaging. 266
154 Variance function $\gamma_\mathcal{T}$ for power density of total field as a function of normalized interval width $k\mathcal{T}$ for local spatial averaging. 267
155 Variance function $\gamma_\mathcal{T}$ for magnitude of total field as a function of normalized interval width $k\mathcal{T}$ for local stir averaging. 268
156 Variance function $\gamma_\mathcal{T}$ for magnitude of total field as a function of normalized interval width $k\mathcal{T}$ for local spatial averaging. 269
157 Point-interval correlation function $\varrho_{\mathcal{T}0}$ for power density and field magnitude as a function of normalized interval width $\mathcal{T}/\beta$ or $k\mathcal{T}$ for local spatial or stir averaging. 270
158 Normalized spectral bandwidths $\delta_\mathcal{T}$ and $\epsilon_\mathcal{T}$ as a function of normalized interval width $\mathcal{T}/\beta$ for local stir averaging. 271
159 Normalized spectral bandwidths $\delta_\mathcal{T}$ and $\epsilon_\mathcal{T}$ as a function of normalized interval width $k\mathcal{T}$ for local spatial averaging. 272
160 Cumulative distribution function of first-order difference of normalized measured $|E_\alpha(\tau)|$ and $|E_t(\tau)|$. 273
161 Crosscorrelation function between normalized measured $|E_\alpha(\tau)|$ or $|E_t(\tau)|$ and their first-order difference. 274
162 Cumulative distribution function of crosscorrelation function between normalized measured $|E_\alpha(\tau)|$ or $|E_t(\tau)|$ and their first-order difference. 275
163 Cumulative distribution function of first-order difference of normalized measured $|E_\alpha(\tau)|^2$ and $|E_t(\tau)|^2$. 276

164 Crosscorrelation function between normalized measured $|E_\alpha(\tau)|^2$ or $|E_t(\tau)|^2$ and their first-order difference. 277
165 Cumulative distribution function of crosscorrelation function between normalized measured $|E_\alpha(\tau)|^2$ or $|E_t(\tau)|^2$ and their first-order difference. 278
166 Cumulative distribution function of second-order difference of normalized measured $|E_\alpha(\tau)|$ and $|E_t(\tau)|$. 279
167 Cumulative distribution function of second-order difference of normalized measured $|E_\alpha(\tau)|^2$ and $|E_t(\tau)|^2$. 280
168 Upward threshold crossing frequency $\nu_T^+(b/\sigma_0)$ for magnitude of total field upon local stir averaging. 281
169 Upward threshold crossing frequency $\nu_T^+(b/\sigma_0)$ for total power density upon local stir averaging. 282
170 Upward threshold crossing frequency $\nu_T^+(b/\sigma_0)$ for magnitude of total field upon local spatial averaging. 283
171 Upward threshold crossing frequency $\nu_{b/\sigma_0}^+(\mathcal{T})$ for magnitude of total field upon local spatial averaging. 284
172 Upward threshold crossing frequency $\nu_T^+(b/\sigma_0)$ for total power density upon local spatial averaging. 285
173 Upward threshold crossing frequency $\nu_{b/\sigma_0}^+(\mathcal{T})$ for total power density upon local spatial averaging. 286
174 First-passage probability $\mathcal{P}_{b/\sigma_0}(\tau_0)$ for magnitude of total field upon local spatial averaging. 287
175 First-passage probability $\mathcal{P}_T(\tau_0)$ for magnitude of total field upon local spatial averaging. 288
176 First-passage probability $\mathcal{P}_{b/\sigma_0}(\tau_0)$ for total power density upon local spatial averaging. 289
177 First-passage probability $\mathcal{P}_T(\tau_0)$ for total power density upon local spatial averaging. 290
178 First-passage probability $\mathcal{P}_{b/\sigma_0}(\tau_0)$ for magnitude of total field upon local stir averaging. 291
179 First-passage probability $\mathcal{P}_T(\tau_0)$ for magnitude of total field upon local stir averaging. 292
180 First-passage probability $\mathcal{P}_{b/\sigma_0}(\tau_0)$ for total power density upon local stir averaging. 293
181 First-passage probability $\mathcal{P}_T(\tau_0)$ for total power density upon local stir averaging. 294
182 Mean excursion length $\mathrm{E}[\mathcal{L}_T(b)]$ for magnitude of total field upon local spatial averaging. 295
183 Mean excursion length $\mathrm{E}[\mathcal{L}_T(b)]$ for total power density upon local spatial averaging. 296
184 Mean excursion length $\mathrm{E}[\mathcal{L}_T(b)]$ for magnitude of total field upon local stir averaging. 297
185 Mean excursion length $\mathrm{E}[\mathcal{L}_T(b)]$ for total power density upon local stir averaging. . 298

186 Asymptotic probability density function $f_{\chi_1(N)}(w_D)$ of max-to-mean ratio of sampled values of $f_{\chi_1}(x)$ for Kholmogorov–Smirnov statistic. 299
187 Asymptotic cumulative distribution function $F_{\chi_1(N)}(w_D)$ of max-to-mean ratio of sampled values of $f_{\chi_1}(x)$ for Kholmogorov–Smirnov statistic. 300
188 Mean and standard deviation for asymptotic distribution of max-to-mean ratio of sampled values of $f_{\chi_1}(x)$ for Kholmogorov–Smirnov statistic. 301
189 Asymptotic probability density function $f_{\chi_1^2(N)}(w_D)$ of max-to-mean ratio of sampled values of $f_{\chi_1^2}(x)$ for squared Kholmogorov–Smirnov statistic. 302
190 Asymptotic cumulative distribution function $F_{\chi_1^2(N)}(w_D)$ of max-to-mean ratio of sampled values of $f_{\chi_1^2}(x)$ for squared Kholmogorov–Smirnov statistic. 303
191 Mean and standard deviation for asymptotic distribution of max-to-mean ratio of sampled values of $f_{\chi^2}(x)$ for squared Kholmogorov–Smirnov statistic. 304

1 Introduction

So far, the majority of theoretical analyses and experimental characterizations of reverberation chambers have been performed by starting from the assumptions of perfect statistical field uniformity, i.e. field isotropy (polarization uniformity) and field homogeneity (spatial uniformity) to hold or to be required. One then proceeds by making mainly qualitative comparisons between the experimental statistical data collected on the basis of one or more 'point' measurement(s) in the actual chamber on the one hand, and the statistics of an ideal chamber on the other hand. Such is done by judging the similarity of field or power density distributions and their statistics between the real and ideal reverberation conditions. To this end, *statistical* metrics, e.g. using tests of hypotheses and goodness-of-fit tests, are often used to decide between a 'good' or 'bad' correspondence between theory and experiment. In this way, the final result is still based on a nonobservable, nonphysical and often obscure uncertainty parameter (confidence level for acceptance/rejection of the hypothesis).

Our theoretical and experimental study of electromagnetic reverberation environments arose from the lack of, and need for quantification of the performance of good but imperfect reverberation chambers using good but imperfect measurement techniques and equipment. In this respect, it was felt that the absence of proper *deterministic* metrics to assess and quantify imperfect reverberation performance, which allow for smaller uncertainties, may become of increasing concern in the design, optimization and use of reverberation chambers. It may also be an issue in the interpretation, certification and uncertainty analysis of test results for equipment under test (EUT) and their characterization in such chambers. Furthermore, deterministic metrics are useful in intercomparisons of test results obtained in a reverberation chamber on one hand and an open-area test site, anechoic chamber, (G)TEM cell, etc. on the other hand, or among different reverberation chambers themselves.

In a reverberation chamber without EUT or containing an EUT in an arbitrary but fixed position, a deterministic pseudo-random field is observed during the stirring process. In interpreting measured data, it is of crucial importance to distinguish between imperfections in the *physical* reverberant field and imperfections in the *measurement* of this field[1], more so than in other electromagnetic compatibility (EMC) test environments. As will be explained, both effects normally mask one another in the observed data. Without a detailed understanding and quantification of both effects individually, it is difficult if not impossible to interpret reverberation data correctly. Good but imperfect reverberation is caused by the 'high' but finite mode density in practical overmoded enclosures, resulting from operation at 'high' but finite frequencies and causing im-

[1] in addition to the usual measurement uncertainties encountered in measurement of deterministic fields

perfections in the mode stirring process. Its proper assessment is important in its own right, for certain EUT test specifications may not require (very) high levels of field uniformity. If the level of imperfection is acceptable for the test specification in actual fact but not accurately calculable, then this usually leads to overspecification and expensive test environments in terms of chamber dimensions and/or power amplification requirements.
Imperfections in the measurement of reverberation are caused by local spatial or temporal averaging effects that occur when measuring or numerically simulating over nonzero widths of spatial or temporal intervals. This local averaging has its own uncertainty on the measurand associated with it, which directly interferes with the standard deviation on the physical reverberant field. This statistical measurement uncertainty due to local averaging is thus of *fundamental* importance in reverberation measurements. While physically inevitable, averaging should be properly quantified and, if necessary, accounted for either by data post-processing or by limiting the scale so that its effect on the measurement becomes negligible or insignificant.

A theory for characterization of field anisotropy and field inhomogeneity in imperfect reverberation environments was developed in [33]. First test results, based on well-established theory and techniques thereby using the proposed new metrics given in [33], were obtained in the *NPL* untuned stadium reverberation chamber and reported in [34]. In this initial study, the characterization was based on power density measurement. The measurements were carried out for mechanical and electronic stirring at 2.5, 8.2 and 18GHz, using horn antennas and open-ended waveguides. For a description of the chamber specifications and the measurement set-up we refer to [34, Sec 2].

In [34], various energy density statistics and distribution functions were calculated for a single direction of polarization, as governed by the orientation of the antenna or waveguide aperture. The degree of planar field isotropy was quantified on the basis of comparing the statistics of the measured energy densities for two mutually perpendicular directions of polarization in a locally transverse plane (i.e. perpendicular to the local radial direction, in the azimuthal plane) to the theoretical statistics for an ideal statistically reverberant field in that plane, i.e. for perfect planar field isotropy. The thus obtained level of planar field anisotropy was found to decrease rapidly, in the mean, as the number of stirrer positions is increased.
Measurement of the statistics of the third, i.e. radial field component was found to be difficult in this set-up. Consequently the total statistical field anisotropy, defined as a weighted average of the planar anisotropies for the three mutually perpendicular measurement planes, could not be assessed. However, a full 3D field characterization is required to assess the degree of isotropy for the total field. Moreover, the locally transverse plane is of special importance because it is parallel to the rotation axis of the chamber, coinciding with a direction of statistical symmetry.

Measurements in such a plane only may hide important deficiencies or suggest an unrealistic overall chamber performance. Therefore, we made a full characterization of all three local field components by using an electric field probe. Details of the measurements are given in this report, and the results are summarized in Sec 5.

2 Three-axis electric field probe

2.1 Probe description and operation

For the present measurements we used a three-axis electric-field probe manufactured by Schmid & Partner Engineering AG, Zürich, CH (S&P model ER3DV4R (SN:2218)) (Fig 1). The probe comes with a PC plug-in card with 66MHz digital signal processor and 96k×24-bit 12ns memory, for full and OS-independent control of the probe operation and data management. The probe measures the magnitude of the local electric field components along three (nominally) mutually orthogonal directions, individually, by means of three linear dipoles. One dipole is directed along the probe axis; the remaining two form a (nominally) orthogonal triplet with it. For every position of the stirrer, the local field is read in 16-bit format and stored 40 times[2] at regular intervals within a 4s time frame, starting after an initial and user-specified 4s settling time interval. The control software returns the sample mean, spread and standard deviation for each one of the three field components, as well as the values of the 120 individual readings per cycle (optional). The mean value of the 40 vector readings constitutes one sample point. An auto-zero (short-circuiting of input terminals) can be invoked periodically, e.g. between stirrer positions, to compensate for offset and drift.

The probe essentially consists of three mutually perpendicular 'short' rectilinear dipoles, each of length 3mm, whose centers are offset[3] by about 2.5mm. The impinging RF field is rectified at the terminals of each dipole, using detector diodes in the sensor gap, to yield three DC voltages. These levels are then transmitted, unperturbed, across the RF environment via three miniature high-loss transmission lines (2MΩ) to the signal processing box (DAE3). The amplitude of the electric field, $|E_\alpha|$, is calculated by the signal processor from the measured diode voltage, V_α (in

[2]This is only a fraction of the total 3×2604=7812 readings per second made by the probe, because the data are transferred at a slower rate to the DASY3 control program. The full set of readings can be accessed only at the expense of excluding the notch filter for the line frequency.

[3]Hence the measurements are strictly speaking *distributed* in contrast to true *local* measurements. This may become a significant issue at high frequencies. The wider spacing between the dipole elements, compared to the more recent compact probe heads with interleaved dipole designs by S&P, do have the advantage of causing less mutual coupling between elements, making the software calibration correction factors which account for local near-field field distortions to be more accurate than for more compact probe heads [52].

μV), at the connector and the associated power[4] P_α as:

$$|E_\alpha| = \sqrt{\frac{V_\alpha + V_\alpha^2[\max(P_\alpha)/\mathrm{avg}(P_\alpha)]/C}{S_\alpha}} \qquad \text{(V/m)}, \qquad (\alpha = x, y, z) \qquad (1)$$

in air, where C is the diode compression point (in μV) and S_α is the sensitivity of the element (in $\mu\mathrm{V}/(\mathrm{V/m})^2$). The data are passed through a notch filter tuned to the line frequency. All data are referenced to the input voltage of DAE3 which is compared internally with the probe calibration data. The electronics box is kept outside of the cavity at all times, as also recommended in [42], because of its unknown EMC/EMI characteristics when placed within the cavity field. The probe and electronics box are powered by a rechargeable battery. The resulting limitation on the maximum duration of a single scan (approximately 8hrs) poses no problem for our purposes at present.

It is clear that only scalar measurements can thus be made, i.e. no phase information can be retrieved as would be required, for example, to detect the state and degree of wave polarization [35] or complex scattering parameters. The probe can be used as an alternative or supplement to waveguide and horn antenna measurements. It has the added advantage of a much smaller aperture compared to horns. Although this reduces the sensitivity, a smaller aperture has the advantage of reducing local spatial averaging, thus decreasing its effect on the measured statistical field anisotropy (see App G). Note further that, unlike waveguide or horn antenna measurements, the measured response is wide-band because no radio-frequency (RF) filtering is applied between reception and rectification. This makes the readings sensitive to noise. The short lengths of the dipoles result in less directionality of the receiver than in the case of a receiving (Rx) horn ($\pm 0.3 \ldots 0.4$dB [37]), hence greater precautions must be taken to avoid direct illumination of the probe.

This type of miniature probe was selected on the basis of its anticipated superior performance for typical reverberation chamber data, which is characterized by a large dynamic range, rapid spatial variations in magnitude, orientation and polarization. Such stringent requirements make larger commercial probes less suitable [42].

2.2 Probe calibration and measurement uncertainty

The probe has been found to operate satisfactorily in an *NPL* TEM cell for frequencies at least as high as 1.8GHz [48] (as covered by the manufacturer's specification using R22/R26 waveguide calibration up to 2.5GHz [41]), but remains unknown at 8.2GHz. This uncertainty makes the assessment of field isotropy using calibration-independent field anisotropy factors and the use of

[4] It is unclear if and how the correct maximum-to-mean P_α is deduced from the sampled V_α. Presumably, a Gauss normal density function is assumed to hold or a sample estimate is taken.

mean-normalized field quantities attractive and important. The free-space characterization of the probe at the frequencies of interest is the subject of ongoing work. The probe is quoted by the manufacturer to have a calibration uncertainty of ±5% on the field strength in air for frequencies between 100MHz and 3GHz, a ±0.2dB linearity uncertainty across the same frequency range, a ±0.3dB spherical isotropy uncertainty, a minimum field strength threshold of 1...2V/m and a boundary effect error of 5% at a distance of 2.5mm, decreasing to less than 0.1dB at 6mm distance from an electromagnetic boundary in proximity [52].

Electric field probes are notoriously difficult to calibrate by conventional methods at higher frequencies (> 1GHz). Furthermore, the differences – however small – between the three constituent dipoles give rise to increasing differences between their radiation patterns as frequency increases. Therefore, we chose a self-normalized quantity $A_{\alpha\beta}$ to characterize the individual planar field anisotropies [33]. This makes their values largely independent of the differences between the probe dipole elements and their tolerances. Assuming the probe readings to exhibit a small but systematic uncertainty $\mathrm{d}|E_\alpha|$ between measured (read) and 'true' values at a constant input power, it follows that the uncertainty on $A_{\alpha\beta}$ is:

$$\Delta A_{\alpha\beta} = \Delta\left(\frac{|E_\alpha|^2 - |E_\beta|^2}{|E_\alpha|^2 + |E_\beta|^2}\right) = \frac{|E_\beta|\,\mathrm{d}|E_\alpha| \;-\; |E_\alpha|\,\mathrm{d}|E_\beta|}{(|E_\alpha|^2 + |E_\beta|^2)^2/(4|E_\alpha||E_\beta|)} \tag{2}$$

where $\Delta = (\partial/\partial\alpha)\mathrm{d}\alpha + (\partial/\partial\beta)\mathrm{d}\beta$ represents a total differential. This uncertainty is relatively small if $\mathrm{d}|E_{\alpha,\beta}| \ll |E_{\alpha,\beta}|$ or, generally, if the uncertainties are proportional to their true values:

$$\frac{\mathrm{d}|E_\alpha|}{\mathrm{d}|E_\beta|} = \frac{|E_\alpha|}{|E_\beta|} \tag{3}$$

3 Measurement results

Measurements at 2.5GHz

Rationale

In [34, Sec 5.1], we initiated measurements at 2.5GHz using two open-ended waveguides for the excitation and detection. Even without using horns, these measurements suffer from exhibiting relatively large apertures for the excitation source in comparison with the chamber dimensions.

Nonzero antenna or waveguide apertures have two major effects on reverberation measurements. First, their nonzero size increases the degree of *local spatial averaging* of the stochastic field, such averaging being inevitable when making practical measurements. Therefore, the measured degree

of (deterministic) wave chaos increases, in comparison with the zero apertures of idealized point (dot) sources/receivers. As a result, an extended antenna ($\lambda/2$-dipole, log-periodic, horn, etc.) may not be able to measure the reverberation quality with sufficient accuracy and may, in fact, mask an actual poor reverberation performance! Therefore, an inverse local averaging technique is suggested in App G to refer all measurements to reference point values, thus decoupling the effect of the measurement from the chamber (cavity) performance.
Secondly, the aperture of a receiving antenna, whether it is located inside the chamber or in or on the wall, causes *nonuniform absorption* inside the chamber. A perfectly matched antenna or waveguide acts as a localized sink (black body) for electromagnetic energy, even if it were ideally lossless. Also, the transmitting antenna loads the chamber because of its nonideal antenna efficiency (ohmic losses). Hence the measured chamber characteristics are those for a 'loaded' chamber, even if it were perfectly conducting and would contain only transmitter and receiver antennas. It has been demonstrated, numerically [26] and experimentally [34, Sec 10.2.2], that *non*uniform chamber absorption has a profound effect on the characteristic temporal decay of reverberant energy in that it gives rise to a t^{-1}- time dependence for the late decay of a pulsed signal, i.e. after the familiar average exponential decay for early and intermediate times. The nonuniformity of the absorption is believed to be one of the prime reasons behind the major discrepancies found between predicted and measured chamber quality factors. The absorption nonuniformity, of course, increases with increasing aperture size.
In summary, the use of a small-aperture field sensor should reduce the effect of inevitable absorption and local spatial averaging and, hence, yield, morely measured accurate chamber characteristics.

From a practical point of view, the direct measurement of field anisotropy and field inhomogeneity coefficients using an open-ended Rx waveguide is cumbersome and inaccurate, because of its bulkiness and large aperture. Also, the limited height of the coupling plates of our chamber did not allow for cross-polar orientations at 2.5GHz. In spite of this, stirrer data were collected for a single direction of polarization and a single position of the Rx waveguide [34]. For this frequency, the cumulative distribution function of the mean-normalized received power suggested a begin of deterioration of the stirring performance, when compared to the measured performance at 8.2GHz. To investigate this further, field probe measurements were now carried out. Generally, knowing the 'lowest' usable frequency is important for the efficient use and economical design of a reverberation chamber [34, Sec A.4]. However, this frequency is never clear cut as it depends on the tolerable levels of statistical field uniformity (anisotropy/inhomogeneity). As a result, measurements and operation below this 'lowest' frequency remain meaningful.

3.1.2 Measurement set-up and procedure

As in our previous study, open-ended waveguide excitation (Tx) was used for reasons of excitation and radiation efficiency. At 2.5GHz, a horn is bulky and would load our chamber significantly, mainly through ohmic losses. It would also decrease the stirring performance because of the large conductor (wall) area this introduces. The waveguide aperture is placed as close as possible to the stirring wall and its normal direction is pointing away from the probe. The field probe, whose housing of the signal processor and battery isbeing kept outside the cavity at all times (cfr. Sec 2.1), is slid along an external pedestal which is mounted onto one of the cavity coupling plates. Aluminium foil on this plate is used to minimize the aperture introduced by the glass housing for the transmission lines of the probe. It is important to remember that the air line surrounding the transmission lines of the probe extends through the cavity to the outside world. Hence, measurements with the probe head close to the cavity wall exhibit a (small) aperture behind the probe head, rather than a conducting wall.

The chamber is operated in mode-tuned operation in all measurements, taking $M = 275$ sample points per scan. At 2.5GHz, the unit wall step size as measured along the cavity rim, is chosen as $\Delta s = 8.48$mm, corresponding to a unit angular step size $\Delta\tau = 24.3$mrad. The field is evaluated at various cavity locations, from well inside the cavity (probe tip at a distance $r = 91$mm from the cavity center, corresponding to the maximum penetration depth of the field probe) down to a distance close to the cavity wall ($r = 349$mm, i.e. probe tip at only 1mm ($=\lambda/120$) off the wall). We concentrate particularly on the data for two extreme probe locations, viz. at $r = 91$mm and $r = 345$mm.

3.1.3 Probe noise performance

As mentioned in Sec 2.1, the DASY3 probe software returns the mean and spread (the latter being defined as the sample range, i.e. the difference between linear-scale maximum and linear-scale minimum reading), as calculated from 40 readings per sample point. Fig 2 shows the spread, s, as a function of the mean, avg, for the field strength readings of the S&P probe per dipole for each one of the $M = 275$ sample points.

Interestingly, the spreads show a split into two distinct groups of data points. Both uncertainties differ by a proportionality factor, as they form parallel curves in the logarithmic plot. The origin of this degeneracy is believed to be due to gain switching by the pre-amplifier of the probe, between two different amplification stages, during measurement. The noise on the electric field is larger for lower field levels. The probe amplifier toggles, automatically, between low and high amplification factors depending on its first few measurements. This amplification range affects all channels [51]. It is possible, however, to disable this automatic switching. Such technical reasons

are of practical importance, e.g. when estimating the uncertainty on the maximum-to-mean and minimum-to-mean field strength of the reverberation chamber, for which the lower and upper uncertainties should be used, respectively.
Furthermore, the spread is seen to decrease inversely proportional with increasing mean values: from the Figure, $\log[s(E_\alpha)] = c_\alpha - (1-\epsilon_\alpha)\log[\mathrm{avg}(E_\alpha)]$, i.e.:

$$s(E_\alpha) \propto [\mathrm{avg}(E_\alpha)]^{-(1-\epsilon_\alpha)} \qquad (0 < \epsilon_\alpha \ll 1) \tag{4}$$

Thus, the probe noise could be labelled as 'logarithmic divisional' or 'logarithmic reciprocal multiplicative', in analogy with the notions of additive (channel) noise and multiplicative noise. The regression lines are seen to 'thicken' with increasing mean field strengths. For such fields, the signal-to-noise ratio of the detector is large and the effect of source noise becomes noticeable. At low field strengths, the source noise becomes negligible compared to the large detector noise. More importantly, however, it is found that the probe sensitivity and noise figure are different for $|E_z|$ as compared to $|E_x|$ and $|E_y|$, which is possibly a result of differences in the quality of the diode contacts or transmission-line imperfections between the three channels: for $|E_x|$ and $|E_y|$:

$$\approx 4.03|E_{x,y}|^{-0.86} \quad \text{(high amplification setting)} \tag{5}$$
$$\approx 1.74|E_{x,y}|^{-0.94} \quad \text{(low amplification setting)} \tag{6}$$

whereas for $|E_z|$

$$s_z \approx 2.24|E_z|^{-0.87} \quad \text{(high amplification setting)} \tag{7}$$
$$s_z \approx |E_z|^{-1} \quad \text{(low amplification setting)} \tag{8}$$

Thus, whereas the *averaged* readings by the probe may show good isotropy, such is not the case for the *spread* on the values read.

We finally mention that DASY3 occasionally returns (small) negative values, even after averaging and auto-zeroing, which were discarded on physical grounds. In the remaining we will only make use of the mean values per sample point.

3.1.4 Stirrer sweep data

Fig 3 shows sweep data as a function of wall position, $\tau/\Delta\tau$, for the probe tip positioned at $r = 91$mm. The magnitudes of all field components, $|E_\alpha|$, show a fair degree of structure, i.e. the stirring quality appears to be reasonable in all three directions of measurement (wave polarization), and exhibit a comparable dynamic range. The variations in the input power P_i were

measured with a directional coupler on the input waveguide. Note the variation of P_i with wall position. This is due to the small distance between the aperture of the Tx waveguide and the corrugated stirring wall. The variation of the distance between the waveguide aperture and wall surface during the stirring process causes a substantial variation in the output impedance of the waveguide with stirrer position. Thus, the forward (incident) power remains reasonably constant (as verified using a power meter), but the reflected power changes significantly. The mean periodicity in the data for P_i is caused by the change in distance and provides an 'image' of the structure of the inner wall. It demonstrates the need for pointwise normalization of the field strength, which enables a correct analysis of the data [34, Sec 3]: changes in the chamber geometry cause corresponding changes in the wave impedance for the Tx and Rx antennas.

For the sweep data at $r = 345$mm, it is seen that $|E_x|$, $|E_y| \ll |E_z| \equiv |E_r|$ due to the EM boundary conditions (Fig 4). The input power shows similar variations to those in Fig 3, demonstrating the deterministic nature of the average periodicity of P_i.

3.1.5 Correlation functions

3.1.5.1 Autocorrelation functions Fig 5 shows the autocorrelation functions[5] (acfs), viz. $|\rho_x(\tau/\Delta\tau)|$, $|\rho_y(\tau/\Delta\tau)|$, $|\rho_z(\tau/\Delta\tau)|$ and $|\rho_t(\tau/\Delta\tau)|$, for the field magnitude and for the power density associated with the three measured field components and with the total field, with reference to an arbitrary stirrer position $\tau = 0$ and measured at $r = 91$mm (see [40] for an overview and properties of various definitions of acfs for stirrer data). All acfs have a comparable dynamic range and demonstrate small linear dependence between stirrer positions. This is due to the relatively large unit wall step being chosen.

The decimation factors m_α for the full data set, as obtained on the basis of the '$|\rho_\alpha(\tau/\Delta\tau)| < \exp(-1)$'-criterion[6] are found to be about 1.5 in all cases. We also studied the dependence of m_α

[5] Since the sample acfs are symmetric with respect to the midway point, only the first half of the series is plotted.

[6] No real justification appears to exist for the choice of such a threshold level for reverberation processes, and its origin remains unclear. Possibly, its choice is modelled after the definition of decay time as the time needed for the initial energy to be reduced by a factor $1/e$. However, a correlation function does not represent a physical decay. Another possible origin arises from other application areas of statistical analysis in physics and engineering, where the acf can often be modelled as a single or multidimensional exponential function (e.g. in image coding [13]), where the level $\exp(-1)$ corresponds to the autocorrelation after one 'time' constant. For Gauss normal distributions, this is known as the Ornstein–Uhlenbeck process. In our case, the (power) acf appears to closely follow a $[1+(\tau/\beta)^2]^{-1}$ dependence [40], where β is defined by the power spectral density function (psdf), $g(\omega) \sim \exp(-\beta\omega)$. Hence a better choice for the correlation length in mode-stirring and reverberation applications could be based on the analysis of the psdf, viz. selecting ω_o for which $g_\alpha(\omega_o/\Delta\omega)/g_\alpha(0) = 1/e$, from which the decimation factor for the acf would follow as proportional to $\tau_o/\Delta\tau = 2\pi/(\omega_o/\Delta\omega)$, on the basis of the Wiener–Khinchine theorem [34, Sec 4.1]. The (fixed) proportionality factor is to be determined empirically. For the stirring process with

on the record length M for fixed $\Delta\tau$, based on the same criterion, using interpolation[7]. It may be expected that for sufficiently large M, the values of m_α reach an asymptotic limit because $\Delta\tau$ remains constant throughout. The result, shown in Fig 6 and marked 'single sample', reveals that some variation of $m_\alpha(M)$ occurs for $M > 75$ and that at least $M \geq 50$ is required in order to obtain realistic 'stable' values for the m_α (not shown).
The thus obtained values for m_α are strongly dependent on the chosen threshold level $\exp(-1)$. The main result of this analysis is the requirement for a minimum number of data points that are needed to obtain a reliable decimation factor. Consequently, too low a value of M gives rise to too large an uncertainty on the equivalent number of independent samples, $N_\alpha = M/m_\alpha$, for statistical analysis of reverberation chambers to be practical: the uncertainty on N_α adds to the uncertainty on the statistic of interest (e.g. maximum-to-mean ratio), giving rise to an extended uncertainty.
Results obtained using the *ensemble* acfs [40] are also shown in Fig 6, marked 'ensemble'. These are based on the calculated power spectral density functions (psdfs) (Fig 8, resulting in the acfs of Fig 7 on application of the Wiener–Khinchine theorem. Also shown in Fig 8 are Bartlett estimates for the 1st order spectral parameters β_α (see Sec 3.1.10)). The ensemble acfs yield marginally larger decimation factors. The irregular variations in $m_\alpha(M)$ are an artefact of the large bias in the estimated psdf, as a consequence of a reduction in the variance of the estimation. This affects the estimated acf and, hence, m_α. Fig 9 shows the variance functions $\gamma_{\alpha,\mathcal{T}}$ for $|E_\alpha|$ and $|E_\alpha|^2$ upon local stir averaging. A small but consistent bias towards lower values of $\gamma_{\alpha,\mathcal{T}}$ is found for the power densities as compared to those for the corresponding field magnitudes, confirming a small but consistent difference between the correlations between power densities on one hand and the those for the corresponding field magnitudes on the other hand, at this frequency.

The acfs for the probe located at 5mm off the wall show similar characteristics (Figs 10–13). Note the quasi-periodicity in ρ_y. The same decimation factors are observed (Fig 11).

3.1.5.2 Crosscorrelation functions Fig 14 shows the pairwise crosscorrelation functions $\rho_{\alpha\beta}(\tau/\Delta\tau)$ for the field magnitudes at $r = 91$mm. It is seen that $|\rho_{\alpha\beta}(\tau/\Delta\tau)| < 0.36$ for all $\tau/\Delta\tau$, i.e. a small crosscorrelation, signifying small linear dependence between the individual field components.
A similar behaviour is found at $r = 345$mm (Fig 15), although the levels for crosscorrelation are somewhat larger in this case, on average.

$\rho(\tau/\Delta\tau) = [1 + (\tau/\beta)^2]^{-1}$, an alternative expression of the correlation length was derived, in the stirrer domain, in [40, Eqn (7)].

[7] No difference in results were found in using cubic spline interpolation compared to more elementary linear interpolation.

3.1.6 Distribution functions of field magnitude

3.1.6.1 Field statistics Tbls 7 and 8 compare the measured coefficient of variation $n_X = s_X/m_X$ with the theoretical values $\nu_X = \sigma_X/\mu_X$ for the magnitudes of the ideal, mean-normalized reverberant field components $X = |E_\alpha|$ at $r = 91$mm. The agreement appears to be reasonable. Fig 16 shows that the n_X approach some limit values as M increases. However, these values remain substantially different from the theoretical values for χ_2 and χ_6 distributions, shown by dotted lines in the Figure, suggesting modest stirring performance.

At 5mm away from the cavity wall, the coefficient of variation for the total field shows further discrepancies in comparison with the values for the previous case, as expected (Tbls 9 and 10). Comparison of Fig 17 with Fig 16 confirms that the differences between measured and ideal values for χ_2 and χ_6 distributions have further increased.

3.1.6.2 Probability density functions Fig 18 shows the probability density functions[8] for the mean-normalized field magnitudes at $r = 91$mm. The correspondence between the theoretical[9] χ_2 resp. χ_6 pdf and the measured pdf for the individual field components resp. total field is reasonable: the coverage of the theoretical curve by the measured values is fairly uniform, although some occasional 'bold patches' are apparent. As can be expected, very small and very large values were not observed in the measured data. The absence of small values is due to the limited sensitivity[10] of the probe. Very large values do not appear because of the limited number of stirrer positions and limited quality factor. Clearly, the differences in local densities are being obscured as the number of sample points increases, e.g. compare Fig 18 for decimated data ($m_\alpha = 2$) with Fig 19 for the full data set ($m_\alpha = 1$).

At $r = 345$mm, the coverage for small field magnitudes worsens, because of the lower limit on probe sensitivity (Figs 20 and 21). This is because of the fact that lower *mean-normalized*

[8] Unlike more conventional representations which use bar charts, we chose to plot measured values directly onto the theoretical pdf, with each circle representing one of the M/m measured and decimated values. Therefore, ideally, the local density of circles should be proportional to the local height of the theoretical curve, i.e. the experimental curve should show a 'dark dense top', gradually changing to a 'light scant base'. In this way, the problem of data 'binning' is circumvented and the probability 'density' is more apparent. To minimize binning errors when using conventional histogram or frequency polygon pdfs, theoretical arguments have been given for choosing uniform bin sizes as $0.6M^{-1/3}(x_{max} - x_{min})$ [19] or $0.35M^{-1/5}(x_{max} - x_{min})$ [22], respectively. Smoothing of measured pdfs can be achieved, a posteriori, based on moving an averaging window of optimum (finite) width across the measured cdfs (see e.g. [18]).

[9] In this and subsequent Figures, the label 'theory' refers to the case of *ideal* reverberant field (infinite mode density), not to the characteristic for the actual but theoretical imperfect field (finite mode density).

[10] To verify this, the minimum $|E_x|$ for the sweep data was measured to be 1.48V/m, corresponding to $|E_x|/\langle|E_x|\rangle = 0.048$. This minimum field strength is of the order of the value specified by the manufacturer (1...2V/m).

field strengths appear less frequently when the mean field amplitude decreases. The relative absence of lower values suggests that, in this case, the pdf for a single field component resembles more closely a higher-order gamma pdf as the stirring deteriorates, i.e. the curve taking off slower from zero for small mean-normalized values than does a curve for a χ_2 pdf.

3.1.6.3 Cumulative distribution functions Figs 22 and 23 show the cumulative distribution function (cdf) for the mean-normalized field magnitudes for $m_\alpha = 2$ and $m_\alpha = 1$ at $r = 91$mm, respectively. Both graphs show substantial deviations between theoretical and measured cdfs, typically with low amplitudes being over-represented and high amplitudes being underrepresented. Fig 24 shows the cdf of the standardized deviations between the theoretical and measured cdfs, $F_{theo}(x) - F_{meas}(x)$. The deviations from Gauss normality (see App H) are seen to be substantial.

The mismatch between measured and theoretical cdfs is usually expressed by defining one or other metric between both curves to quantify the goodness of fit. For example, the Kholmogorov–Smirnov (K–S) test statistic D_M for a sample of size M measures their maximum absolute difference across all measured mean-normalized field strengths x as [34, Sec 5], [49]:

$$D_M = \frac{\sqrt{M}\ \sup_x |F_{theo}(x) - F_{meas}(x)| \quad \max_{j=1,\ldots,M} [M\ F_{theo}(x_j) - (j-1),\ j - M\ F_{theo}(x_j)]}{\sqrt{M}} \tag{9}$$

An alternative test statistic is the Cramér–von Mises (C–vM) statistic W_N^2, which is defined as a Stieltjes integral of the pointwise difference between both cdfs:

$$W_M^2 = M \int_0^\infty [F_{theo}(x) - F_{meas}(x)]^2\, \mathrm{d}[F_{theo}(x)] \quad 12M)^{-1} + \sum_{j=1}^{M} \left[F_{theo}(x_j) - \frac{2j-1}{2M} \right]^2 \tag{10}$$

where the x_j are the measured values ranked in ascending order. A yet more robust measure, akin to the Cramér–von Mises test statistic, is the cross-correlation coefficient $\varrho_{\alpha\beta}$ between both curves ($\alpha, \beta = x, y, z$), which integrates *and* normalizes the overall curve mismatch. Such a measure is possible because both the sampled (i.e. measured) and continuous (i.e. theoretical) cdfs are stochastic. This measure minimizes the effect of accidental and isolated large curve mismatches having a small overall weight. Moreover, it enables the mismatch to be weighted differently for values of the mean-normalized field, e.g. to attach greater importance to mismatches occurring at higher mean-normalized field strengths than at lower field strengths. For now, we apply simple

uniform weighting.

Figs 25, 26 and 27 show the K–S statistic, C–vM statistic and sample crosscorrelation coefficients $\varrho_{\alpha\beta}$ between the theoretical and measured cdfs of all three field components as a function of sample size M at $f = 2.5$GHz, $r = 91$mm, respectively. The deviation/crosscorrelation of the cdfs is seen to decrease/increase with sample size, in the mean, respectively, if the data decimation is decreased. This suggests an improving match (i.e. better stirring). However, proper decimation criteria and factors must clearly be observed whn comparing with F_{theo} (based on independent and identically distributed data). It thus follows that these crosscorrelation coefficients are in general high[11]. To appreciate the associated mismatch between the curve pairs, the values of the sample crosscorrelation coefficients should be compared to those for 8.2GHz, for which reverberation quality is known to be much better (see Sec 3.2.6.3).

Interestingly, the mismatch of the cdfs near the cavity wall ($r = 345$mm) (Figs 28 and 29) appears to be not appreciably worse than at $r = 91$mm. In other words, each *mean-normalized* field component remains reasonably well stirred close to the wall, but of course with markedly different normalizing mean values between normal (z- $\equiv r$-) and tangential (x-, y-) components. Hence, the often cited minimum-distance criterion requiring a distance of at least $\lambda/4$ away from the wall to achieve adequate stirring is a criterion for (statistical) field isotropy, not for field stochasticity (reverberation). The latter exists down to very small distances from the cavity wall. This result will be confirmed by the results for the field anisotropy factors (cfr. Sec 3.1.8).

3.1.7 Distribution functions of maximum-to-mean ratio for field magnitude

For the field components at $r = 91$mm, Tbls 13 and 14 compare the measured max-to-mean ratios W_M for $M = 275$ and $M = 137$ with the theoretical mean values μ_{W_N} for $N = M/m = 275/1.5 = 183$, respectively[12]. The Tables also list 95% confidence intervals, taken symmetrically with respect to the median[13], $F^{-1}_{W_N}(1/2)$, i.e. between the $\eta = 2.5\%$ and $\eta = 97.5\%$ percentiles. The limits for these percentiles are defined by $F^{-1}_{W_N}(\eta) = \sqrt{(4/\pi)\ln[1-\eta^{1/N}]^{-1}}$ for the individual max-to-mean field components and calculated numerically from the numerical cdf for the max-

[11]It is not straightforward to determine baseline values for the $\varrho_{\alpha\beta}$ as to what constitutes a 'good' or 'bad' match. The situation is comparable with the choice of e^{-1}-threshold level for uncorrelatedness for the acf, and depends not in the least on the required level of uncertainty for the cavity fields. Based on the present study, we suggest a threshold working value for $\varrho_{\alpha_{meas}\alpha_{theo}}$ of 0.99 for each individual field component.

[12]The ensemble decimation factors m_α were used to estimate N.

[13]The median is marginally lower than the mean, e.g. $(F^{-1}_{W_N}(1/2) = 2.6650) < (\mu_{W_N} = 2.6987)$ for χ_2 with $N = 275/1.5$. Thus, using the mean instead of the median for the center point of the confidence interval would shift the interval marginally upwards.

to-mean total field[14]. Theoretical and measured values, together with 95% and 99% confidence intervals, are also depicted in Figs 30 and 31 for $m_\alpha = 2$ and $m_\alpha = 1$, respectively. The measured max-to-mean ratios are seen to be near the boundaries of the 95% confidence interval, indicating moderate stirring performance that may be only just acceptable. Fig 34 compares the theoretical mean μ_W and standard deviation σ_W for the max-to-mean field strength with the measured and bootstrapped[15] mean m_W and standard error se_W as a function of total sample size M, decimated to N values. For the mean values, a small but consistent underestimation by the theory is found, indicating that the stirring is inadequate or that the estimated equivalent number of independent samples N may be too low, or both. The bootstrap standard error reflects the predicted uncertainty fairly well.

For $r = 345$mm, we find the values listed in Tbls 15 and 16. The measured max-to-mean ratio for $|E_t|$ is now well outside its 95% confidence interval (Figs 32 and 33). Similar conclusions hold for the dependence on sample size M, with N selected, as for the case $r = 91$mm (Fig 35).

3.1.8 Field anisotropy

Figs 36 and 37 show simulated and measured planar and total field anisotropy coefficients as a function of wall position for one realization of the stirring process with $M = 275$ data points, respectively. The measured single-sample averages, $avg(A_{\alpha\beta})$, are shown in Figs 38 and 39[16]. A markedly lower degree of field anisotropy in the oxz-plane compared to oxy and oyz is noted. This result is confirmed by the measured cdf of A_{zx} (Fig 41), showing a substantially smaller deviation from the theoretical uniform distribution $F_{A_{zx}} = (1 + a_{zx})/2$ as compared to A_{xy} and A_{yz}. For $M = 275$ and $r = 91$mm, we found for the bootstrapped averages:

[14]Unlike the standard deviation or the coefficient of variation, the interpercentile range is a robust statistic, i.e. less sensitive to extreme sample values (outliers). For example, the Pearson–Tukey range $r_{W_N} = [F^{-1}_{W_N}(0.95) - F^{-1}_{W_N}(0.05)]/3.25$ is a robust estimate for σ_{W_N} [11]. Likewise, the median $F^{-1}_{W_N}(0.5)$ yields a robust estimate for the mean i.e. location. Robust measures are of particular relevance to estimation for small sample sizes M, say $M \leq 20$.

[15]Obviously, for the maximum sample size one never finds a larger maximum from bootstrapping than the largest observed value, as there is only one measured sample vector available. For small subsamples, however, one may get a larger bootstrap maximum than that for one arbitrary subsample. Bootstrapping is used here mainly to smoothen fluctuations as a function of sample size. The measured and then bootstrapped value is *not* an unbiased estimator for the theoretical max-to-mean. Thus, the significance of the bootstrapping diminishes with increasing sample size.

[16]The large 'spikes' in the logarithmic plot (Fig 39) [47] are caused by zero crossings of $avg(A_{\alpha\beta})$ for certain sample sizes. Such is confirmed when $avg(A_{\alpha\beta})$ rather than $|avg(A_{\alpha\beta})|$ is plotted (Fig 38). Zero crossings of $\langle A_{\alpha\beta} \rangle$ correspond to the average transmission scattering coefficient $\langle S_{21} \rangle$ for the (complex) partial field $E_\alpha \underline{1}_\alpha + E_\beta \underline{1}_\beta$ passing through the origin in a scatter plot of the field, although magnitudes of $\langle S_{21} \rangle$ and $avg(A_{\alpha\beta})$ or $avg(A_{tot})$ are generally not comparable. The 'spikes' can be suppressed by applying a running local average of the $avg(A_{\alpha\beta})$.

- $|\langle A_{xy}\rangle| = -10.73$dB (standard error $= -15.2$dB);

  $|\langle A_{yz}\rangle| = -12.16$dB (standard error $= -15.3$dB);
- $|\langle A_{zx}\rangle| = -19.77$dB (standard error $= -15.1$dB);
- $|\langle A_{tot}\rangle| = -12.58$dB (standard error $= -14.8$dB).

Parenthetically, note that for the dependency of the mean on the sample size, a decorrelated sample is not required, i.e. one can investigate the dependence of $\langle A_{\alpha\beta}\rangle$ on N as well as on M. For the comparison with the theoretical cdf, however, the data must be decorrelated. Hence Fig 42 should *not* be used to compare between theory and measurement.

For the probe close to the cavity wall ($r = 345$mm), Figs 43–46 confirm that in this case the measured field isotropy is poor, particularly in the oyz- and oxz-planes. For $M = 275$ and $r = 345$mm, we obtain:

- $|\langle A_{xy}\rangle| = -6.92$dB (standard error $= -14.9$dB);
- $|\langle A_{yz}\rangle| = -0.87$dB (standard error $= -17.6$dB);
- $|\langle A_{zx}\rangle| = -1.43$dB (standard error $= -16.2$dB);
- $|\langle A_{tot}\rangle| = -4.48$dB (standard error $= -15.5$dB).

It may appear as if the field in the oxy-plane is better stirred ($|\langle A_{xy}\rangle| \ll |\langle A_{yz}\rangle|, |\langle A_{zx}\rangle|$). However, this discrepancey in values is at least partially due to the fact that both $|E_x|$ and $|E_y|$ only take very small values here, hence the denominator in the definition of A_{xy}, i.e. $|E_x|^2+|E_y|^2$, is small. The large discrepancy between the stirring performance for $|E_z|$ and either $|E_x|$ or $|E_y|$ also follows from the cdfs for A_{yz} and A_{zx} at $r = 345$mm (Fig 47). The experimental cdfs deviate substantially from the theoretical[17] characteristics: for all three cdfs, a consistent bias with respect to the theoretical $F_{A_{\alpha\beta}} = (1+a_{\alpha\beta})/2$ is noted. This can be explained by differences in standard deviation for the pdf of the three field components, i.e. *anisotropic stirring*. Typical field anisotropy distributions predicted in [33] for such case correspond well with the here measured characteristics. The results furthermore confirm the conclusions stated in Sec 3.1.6.3.

3.1.9 Field inhomogeneity

3.1.9.1 Measurement procedure The probe was moved in discrete steps along a radial direction in the azimuthal plane, from very close to the cavity wall ($r = 349$mm) to the maximum possible penetration depth of the probe ($r = 91$mm). As before, $M = 275$ stirrer positions were generated at each probe location, with stirrer step $\Delta s = 8.5$mm.

[17]The theoretical characteristic which applies to an ideal RC refers to a chamber where one can stir *all* field components *equally* well, *arbitrarily close* to the cavity walls.

3.1.9.2 Field inhomogeneity coefficients The spatial inhomogeneity can be quantified using field inhomogeneity coefficients for the field components and total field, as observed along an arbitrary direction $\underline{1}_i$ [33], [34, Sec 6.1]. In the present case, $\underline{1}_i \equiv \underline{1}_r \equiv \underline{1}_z$. In order not to overload the notation, as inevitable when allowing for general directions of observation of the field inhomogeneity for different directions of polarizations, we here denote

$$I_{\alpha\alpha} = \frac{|E_\alpha(r_0)|^2/P_i - |E_\alpha(r_1)|^2/P_i}{|E_\alpha(r_0)|^2/P_i + |E_\alpha(r_1)|^2/P_i} \qquad (\alpha = x,\ y,\ z,\ t) \tag{11}$$

as the field inhomogeneity coefficient between $|E_\alpha(r_0)|$ and $|E_\alpha(r_1)|$ in the direction $\underline{1}_r = (\underline{r}_1 - \underline{r}_0)/|\underline{r}_1 - \underline{r}_0|$. Fig 48 shows the measured field inhomogeneity coefficients for two locations spaced a radial distance 10mm ($\sim 0.083\lambda$) apart, viz. $r_0 = 91$mm, $r_1 = 101$mm. In perfect reverberation conditions, the theoretical distribution of $I_{\alpha\alpha}$ is similar to that of $A_{\alpha\beta}$ because of ergodicity: perfect statistical field isotropy exists if and only if perfect field homogeneity holds, because of the equivalence of spatial and ensemble averages apart from a subset of zero weight [14]. Hence the distribution of the measured values for $I_{\alpha\alpha}$ ($\alpha = x, y, z$) in Fig 48 should be compared to the one for the simulated values for $A_{\alpha\beta}$ in Fig 36. This comparison shows that the radial field component, $|E_z|$, is particularly understirred and, on average, too similar at both locations (I_{zz} near zero). This causes the total statistical field inhomogeneity[18], defined in analogy with A_{tot} as:

$$I_{tot} = \sqrt{(I_{xx}^2 + I_{yy}^2 + I_{zz}^2)/3} \tag{12}$$

to take values that are too small, in the mean (compare I_{tot} in Fig 49 with the theoretical distribution of A_{tot} in Fig 37). The single-sample averages of the $I_{\alpha\alpha}$ and I_{tot} are shown as a function of M in Figs 50–53; bootstrap averages are shown in Figs 54–55. All average coefficients tend to zero, in the mean, except $avg(I_{tt})$ which approaches 1/3 (~ -4.77dB) for large samples. The theoretical and measured distributions of the $I_{\alpha\alpha}$ and I_{tot} are shown in Fig 57.

Fig 58 shows the radial variation of the average field inhomogeneity coefficients. To this end, the field was repeatedly stirred and measured at 27 locations along a radius in the azimuthal plane, i.e. $r_n = (91 + 10n)$mm ($n = 0, \ldots, 25$) and $r_{26} = 349$mm. The $I_{\alpha\alpha}(r_0, r_n)$ were computed for the full data sets ($M_n = 275$), all with reference to the first location, $r_0 = 91$mm. Note also the qualitative differences in radial variation for the respective field components. Interestingly, the value of I_{tt} for the statistical total field is largely constant and appears to characterize the inhomogeneity of the cavity at the operating frequency, in the radial direction.

[18]The total statistical field inhomogeneity, I_{tot}, is an rms average obtained from individual field components, not to be confused with the statistical inhomogeneity of the total field, I_{tt}, as defined above.

3.1.9.3 Inhomogeneity of the field anisotropy The planar and total field anisotropy coefficients were computed for each location r_n using Efron bootstrapping of the measured data and are shown as a function of radial distance in Fig 59. As expected, all $|\langle A_{\alpha\beta}\rangle|$ tend to unity (0dB) as the wall is being approached, although somewhat slower for $|\langle A_{xy}\rangle|$ as compared to the other coefficients. As the probe moves deeper inside the cavity, the field anisotropy coefficients decrease approximately exponentially with distance, initially (i.e. linearly on the logarithmic scale). Further away from the cavity wall, an oscillatory variation with distance sets in, with the spatial mean lowering steadily. The $|\langle A_{\alpha\beta}\rangle|$ typically vary between -22dB and -4dB with distance; $|\langle A_{tot}\rangle|$ varies between about -13dB and -6dB. These figures clearly indicate a rather modest field homogeneity at 2.5GHz compared to 8.2GHz (compare with [34, Fig 6.4]). However, such stirring performance may still be acceptable in certain cases, depending on the test specifications. The field appears somewhat more homogeneous in the oxy-plane as compared to the oyz- and oxz-planes.

3.1.9.4 Inhomogeneity of the planar correlation coefficients Similar results are obtained for the planar correlation coefficients, $\varrho_{\alpha\beta}$, as may be expected. Fig 60 shows that $\langle \varrho_{yz}\rangle$ and $\langle \varrho_{zx}\rangle$ approach unity near the cavity wall, but fall off rapidly as the distance from the wall increases. The radial variation of $\langle \varrho_{xy}\rangle$ is substantially smaller than for the other two coefficients and its absolute value remains low, down to very small distances from the wall, confirming the previous results for $|\langle A_{xy}\rangle|$ near the wall. Thus, the cavity wall does not significantly affect the field correlation in the plane that is locally tangent to the wall, unlike the field correlation in planes normal to the wall.

3.1.9.5 Inhomogeneity of the insertion loss The variation of the estimated insertion loss $\langle p_\alpha\rangle \propto \langle |E_\alpha|^2/P_i\rangle$ as a function of radial distance is shown in Fig 61. The estimation is based on an assumed free space value for the wave impedance, but this is only an approximation at this frequency: the fact that the estimated insertion loss is similar the value at 8.2GHz (cfr. [34, Sec 6.1]) suggests that this value is only approximate for the insertion loss is known to increase with frequency. The variations with radial distance are somewhat larger than at 8.2GHz. The radial variation of $|E_z|$ is significantly smoother and smaller (about 2dB) than for the other two field components (more than 5dB) and the total field (about 4.5dB), for distances Δr up to 300mm. The insertion loss for the average received total power, i.e. associated with the total field $|E_t|$, is a factor 3 ($\sim$ 4.77dB) larger than for the average of the Cartesian components, because the excitation is itself linearly polarized. Near the conducting wall, the insertion loss is verified to diverge.

3.1.10 Spectral analysis

The psdf was already shown in Fig 8 as a basis for calculation of the ensemble autocorrelation functions and decimation factors. A 1st order exponential fit showed approximate exponential decay, to good approximation, i.e. $g_\alpha(\omega) \approx \beta_\alpha \exp(-\beta_\alpha \omega)$. The estimates $\langle \beta_\alpha \rangle$ for the spectral parameter β_α, obtained using the Bartlett procedure for smooting the psdf [15, Ch 11], are also shown in the Figure as a function of subsample (partition) length M. Fig 66 shows again these autospectral densities, now with 3rd order exponential fits $\sum_{i=0}^{3} b_i(\omega/\Delta\omega)^{3-i}$, to account for possible deviations from the exponential law. Similarly, Fig 67 shows the (complex) cross-spectral densities and their 3rd order fits. Although the bias on such fittings is known to be considerable in view of the large standard deviation, a decay slower than exponential at low frequencies appears to be characteristic for nearly all psdfs.
The normalized spectral bandwidths δ_α and ϵ_α are shown as a function of radial distance in Fig 68, and numerical values at selected points are tabulated in Tbl 19. As for the power density measurements at 8.2GHz [34, Sec 12.4], the minimum bounds for 3D field isotropy:

$$\delta_{\alpha,min} = \epsilon_{\alpha,min} = \sqrt{2/3} \approx 0.816 \tag{13}$$

are not met for the δ_α, but are exceeded for the ϵ_α over a large radial span.

Measurements at 8.2GHz

Rationale

The reasons for making field probe measurements at 8.2GHz are much the same as those at 2.5GHz (see Sec 3.1.1), even though the horn antenna measurements in [34] suggested a good stirring quality at 8.2GHz. Furthermore, the total field anisotropy could not be assessed from the X-band open-ended waveguide measurements in [34], as only a single planar field anisotropy coefficient could be assessed. The electric field probe now enables the easy evaluation of all three $A_{\alpha\beta}$ and, hence, A_{tot}.

3.2.2 Measurement set-up and procedure

We performed a similar, though larger series of measurements of field anisotropy as for the antenna measurements in [34, Sec 5.2]. A set of $M = 1200$ data points was collected for each of the three probe elements at a distance $r = 91\text{mm} \sim 2.49\lambda$ from the cavity center (i.e. at $259\text{mm} \sim 7.08\lambda$ from the cavity wall) for a unit wall step $\Delta s = 1.515\text{mm}$ between sample points as measured along the outer circumference of the chamber, corresponding to an angular wall step $\Delta\tau = 4.33\text{mrad}$. The set-up is the same as for 2.5GHz (Sec 3.1.2), except that now a Tx horn was being used with

an extra 90deg waveguide bend inserted. The latter causes the horn aperture to face the stirring wall, thus minimizing the effects of direct illumination for the probe.

3.2.3 Probe performance

At 8.2GHz, the spread for 40 probe readings as a function of mean value (Fig 69) is comparable to the probe performance at 2.5GHz (Fig 2), viz. a regression curve with the same slope and degeneracy for each dipole elemnt. Hence the probe uncertainty appears to be similar at 8.2GHz compared to 2.5GHz, and may possibly be frequency independent.

3.2.4 Stirrer sweep data

Fig 70 shows a fair degree of structure in the stirrer data. The stirrer data appear very similar for all three probe elements and all have approximately the same dynamic range. Note the absence of a noticeable quasi-periodicity in P_i, as apposed to Figs 3 and 4, because the Tx horn was not as close to the cavity wall as the open-ended waveguide in the measurements at 2.5GHz. The bootstrap averaged squared field components are shown in Fig 71 as a function of sample size M, assuming a free space wave impedance. The values are seen to converge to about the same limit, within the standard error *se*, when the sample size M is increased from 5 to 1200, suggesting a high degree of statistical field isotropy for large M. Interestingly, when this averaging is performed for a decimated (subsampled) data set ($N = 1 \ldots 300$), as shown in Fig 72, one finds that the values and isotropy of the three components are hardly affected and have almost identical limit values. This suggests that the full data series are correlated and that this autocorrelation does not improve the statistical field isotropy, provided M is sufficiently large.

3.2.5 Correlation functions

3.2.5.1 Autocorrelation function The absolute value of the acfs for the power density and magnitude of the field components and the total field, $|\rho_x(\tau/\Delta\tau)|$, $|\rho_y(\tau/\Delta\tau)|$, $|\rho_z(\tau/\Delta\tau)|$ and $|\rho_t(\tau/\Delta\tau)|$, are shown in Fig 73 (only first 100 points of the acfs are shown). Interestingly, the similarity between the field and power acfs is now even greater than at 2.5GHz (compare with Figs 5 and 10), suggesting that their match may serve as an indicator of mode stirring performance. The Figure further shows that all acfs yield comparable sample decimation factors for the full sample, viz. $m_\alpha \approx 4$ for the '$|\rho_\alpha| < \exp(-1)$'-criterion. Fig 74 shows the corresponding variance functions. Compared to Fig 9, the differences between power and field magnitude characteristics are now almost indistinguishable with no consistent bias between them, although a small bias exists the between different Cartesian components. The dependence of m_α on M for the power acfs, shown in Fig 75, exhibits several discontinuities. A rising or falling edge indicates that at these values of M the next few stirrer positions are little correlated with the previous positions.

It demonstrates that stirring as a process of generating uncorrelated field components is not a totally smooth process. In general, plots of $m_\alpha(M)$ may help in deciding on suitable sample lengths (and, possibly, stirrer starting positions), minimum record length for a chosen stirrer step, etc. The ensemble decimation factors ($m_\alpha \approx 3$) are seen to be somewhat smaller than the sample decimation factors. The former were again obtained based on the ensemble power acfs (Fig 76) which in turn are obtained from the ensemble psdfs (Fig 77). The latter also shows Bartlett estimates for the spectral parameters β_α, as obtained from smoothed psdfs based on sample partitioning and averaging, which are seen to show little variation between field components as well as for the total field.

3.2.5.2 Crosscorrelation functions The values of the pairwise crosscorrelation functions $\rho_{\alpha\beta}(\tau/\Delta\tau)$ (Fig 78) are relatively small compared to the results for 2.5GHz: $|\rho_{\alpha\beta}(\tau/\Delta\tau)| < 0.19$. Furthermore, $\max(\rho_{\alpha\beta})$ was found to decrease to very small values as M increases (not shown in Figure), signifying a diminishing linear dependence between the individual field components with increasing sample size.
The crosscorrelation *coefficients* for the data series decrease, in mean absolute value, as the sample size increases (Fig 79). For decimated sets, the crosscorrelation coefficients are lower in the mean, because of the reduced autocorrelation compared to the full data set, but the standard error is on average larger.

3.2.6 Distribution functions of field magnitude

3.2.6.1 Field statistics Tbl 11 compares the measured coefficient of variation $n_X = s_X/m_X$ with the theoretical values $\nu_X = \sigma_X/\mu_X$ for ideal mean-normalized reverberant field components $X = E_\alpha$. The agreement is in general very good. Fig 80 shows that the n_α now closely approach the theoretical values ν_α as M increases.

3.2.6.2 Probability density functions Figs 81 and 82 show the theoretical and measured pdfs for $m_\alpha = 3$ and $m_\alpha = 1$, respectively, indicating a uniform spread of the mean-normalized measured field in accordance with height across the plotted range. Due to the larger composite quality factor at 8.2GHz, the mean field strengths are higher, hence the proportion of small mean-normalized field amplitudes has decreased, in comparison with 2.5GHz. Consequently, the measured pdf now better covers the region near the origin.

3.2.6.3 Cumulative distribution functions Fig 83 shows the corresponding cdfs for $m_\alpha = 3$. Overall, the match between measured and theoretical characteristics is good and conforms with what was expected on the basis of the cdf of the power density for antenna measurements [34, Fig 5.3]. The match further improves if correlated data would be considered which, however,

does not have a mathematical justification (Fig 84) In the present case the distributions of the cdf deviations between the theoretical and the sorted measured data, their magnitude and their squared magnitude as shown in Figs 85, 86 and 87, respectively, all conform with the expected Gauss normal, error function and incomplete gamma function, respectively (see App H). As the decimation is reduced[19], i.e. allowing for increased data autocorrelation, a nearly perfect match is found for all curve pairs (Fig 84 for $m_\alpha = 1$). This could give the impression, falsely, that further subsampling of the data leads to improved reverberation characteristics. Interestingly, however, the cdf of the deviations for the full data set now deviates more from Gauss normality than for the decimated set (Fig 88). Thus, proper decimation must always be observed for comparison with the theoretical χ_2 and χ_6 statistics (i.e. rms of sum of squares of independent Gauss normal random variables) to remain applicable.

Figs 89, 90 and 91 show the K–S and C–vM test statistics and the crosscorrelation coefficients between the measured and theoretical cdfs as a function of sample size, respectively. For the latter, note the comparable values at $M = 275$ with Fig 27, in spite of the larger data autocorrelation at 8.2GHz. This demonstrates that the match is better at the higher frequency end.

3.2.7 Distribution functions of maximum-to-mean ratio for field magnitude

For the field components, Tbls 17 and 18 compare the measured max-to-mean ratios W_M for $M = 1200$ and $M = 400$ with the theoretical mean values μ_{W_N} for $N = M/m = 1200/3 = 400$, respectively. The Tables also list the boundaries of the 95% confidence intervals, again taken symmetrically with respect to the theoretical median. Fig 92 shows the pdf, the cdf, the theoretical mean, mode and median[20], and the 95% and 99% confidence intervals, as well as the measured max-to-mean ratios of all field components for the decimated data set. Additional confidence intervals, symmetric or not, for arbitrary η% confidence levels can be deduced from the Figures for the cdfs. The measured ratios for the field components show considerable deviations from the theoretical mean (although all within the 95% confidence interval). The ratio for the total field is better behaved, i.e. closer to its mean value. This confirms the fact that the total field can be characterized with smaller uncertainty than the individual field components. Comparing the measured values to those for the full data set in Fig 93 ($m_\alpha = 1$), one witnesses marginal increases of the measured values for $|E_x|$ and $|E_z|$ (less than 0.03dB), but a larger increases for $|E_y|$ (0.52dB) and $|E_t|$ (0.34dB). These increases can be expected qualitatively, as the sample maximum is more sensitive to changes in sample size than is the sample mean. In fact, comparison of the Figures for $m_\alpha = 3$ to those for $m_\alpha = 1$ may serve in indirectly estimating the 'true' value of the dec-

[19]Strictly, this is not permitted as the sample points are then no longer 'un'correlated. It is only done here for demonstrative purposes.

[20]The mode is not marked explicitly in the Figures, but follows immediately as the maximum of the pdf.

imation factors for the field components and for the total field, if the 'true' value is defined as the value for which the measured max-to-mean value of $|E_t|$ exactly coincides with its theoretical mean value, after bootstrapping for a large number of decimated sets. The sample mean of a large number of max-to-mean measurements is then expected to yield the ensemble decimation factor. Of course, such a method is only justified if the chamber is known to reverberate properly.

A concern could arise about the large discrepancy found for $|E_z|$ (viz. measured max-to-mean value only marginally inside the 95% confidence interval). Therefore, the stirring process was repeated but for the radial position of the field probe increased by 3mm. The result (not shown) demonstrates that indeed the measured max-to-mean ratio is now better behaved, i.e. closer to the predicted mean. Hence the previously measured unusually high value for $|E_z|$ was probably accidental.

Fig 94 shows the theoretical mean, μ_W, and standard deviation, σ_W, as well as the measured and bootstrapped mean, m_W, with associated standard error, se_W, for the max-to-mean ratios $W_\alpha = \max(|E_\alpha|)/\langle|E_\alpha|\rangle$ for the decimated set as a function of $N = M/m$. It is seen that for W_x and W_y the predicted and measured values agree fairly well, but that the measured W_z is significantly smaller than the estimated value. Note furthermore that the standard deviation on W_t is only about half the value for the standard deviation on the W_α for the field components ($\alpha = x, y, z$), and that the estimated uncertainties are rather conservative compared to the standard errors, especially for W_t. It is confirmed that the total maximum field strength can be characterized with lower uncertainty than the maximum for the individual field components. Likewise, the theoretical mean max-to-mean value μ_W of the mean-normalized total field is considerably smaller than the corresponding values for field components: from 1.19 compared to 1.41 (difference 15.6%) at $N = 3$, to 2.04 compared to 3.08 at $N = 400$ (difference 51%).

Fig 95 compares the measured max-to-mean ratio (average of max-to-mean ratios for the three individual Cartesian components), as a function of sample size N, with a number of theoretical estimates obtained using different approaches. An analytical closed-form expression for the mean max-to-mean ratio of field strength is difficult to obtain. Therefore, the mode [34, Sec C.1] and median [50] of the max-to-mean distribution have been suggested as approximations which approach the mean as $N \to \infty$, as a consequence of the central limit theorem. Both statistics are shown in the Figure as w_1 and w_3, respectively. Alternatively, one can use the expression for the mean max-to-mean energy density, after correction for the difference between the mean of the square root of a random variable as compared to the square root of the mean of the variable, according to [36, Sec 3.2.3]:

$$\langle\sqrt{|E_\alpha|^2}\rangle = \frac{\sqrt{\pi}}{2}\sqrt{\langle|E_\alpha|^2\rangle} \tag{14}$$

(which satisfies the Schwarz inequality, viz. $\langle\sqrt{|E_\alpha|^2}\rangle \leq \sqrt{\langle|E_\alpha|^2\rangle}$), from which an expression for the estimate[21] w_2 follows (see inset to Figure). The respective estimates w_1, w_2 and w_3 each appear to have their merit for predicting the measured max-to-mean accurately for a particular range of values for N. Finally, an estimate w_4 can be formulated based on the spectral bandwidth ϵ_α, but because of the computational inaccuracies and presumptions regarding underlying statistics [34, Sec 12.4] this estimate w_4 is found to give less agreement. Making ϵ_α dependent on N is expected to improve the accuracy of the estimate.

3.2.8 Field anisotropy

Simulated and measured planar[22] and total field anisotropy coefficients are shown in Figs 96 and 97 as a function of wall position for $M = 1200$, respectively. Compared to the results for 2.5GHz, one now notices closer agreement between measured field isotropy and ideal (statistical) field isotropy; only the spread of the values of the measured A_{tot} appears to be somewhat larger than for the simulated A_{tot}. The measured sample average values, $avg(A_{\alpha\beta})$, are shown in Figs 98 and 99; the absolute values of the bootstrap averaged coefficients, $|\langle A_{\alpha\beta}\rangle|$, are given in Fig 100. The mean and standard deviation plotted as a function of the number of wall steps show the familiar decrease with N, in the mean. For $M = 1200$, we obtain the bootstrap estimates:

$|\langle A_{xy}\rangle| = -18.58$dB;

- $|\langle A_{yz}\rangle| = -17.10$dB;
- $|\langle A_{zx}\rangle| = -15.82$dB;
- $|\langle A_{tot}\rangle| = -16.27$dB.

3.2.8.1 Effect of subsampling on field anisotropy coefficients Subsampled sweep data were extracted from the full data set in such a way that the subsampled data are uncorrelated using a decimation factor $m_\alpha = 4$, i.e. $N = 300$. On this basis a very similar stirring performance is obtained when compared to the one for the full data set. For example, comparing $|\langle A_{\alpha\beta}\rangle|$ and $|\langle A_{tot}\rangle|$ in Fig 100 with Fig 101, the curves for $N = 5 \ldots 300$ appear as almost scaled replicas

[21] Note that this correction is only partial because the factor $\sqrt{\pi}/2$ applies to the mean field, not to the max-to-mean ratio.

[22] The planes spanned by the transversely directed probe dipole elements and the transverse plane in [34, Sec 3] for the open-ended waveguide for two directions are obviously parallel. Therefore, the present field probe results should be compared to interpolated values for file 135 ($r = 88$mm) and file 136 ($r = 98$mm) in [34].

of those for $M = 5 \ldots 1200$, with only marginally larger[23] average field anisotropies. The finer structure of the latter, in comparison with the former, is a demonstration of the data autocorrelation. However, the former show considerably larger uncertainties (standard errors), to such an extent that all $|\langle A_{\alpha\beta}\rangle|$ and $|\langle A_{tot}\rangle|$ are almost entirely within one standard error. Thus, the economy gained through subsampling of a data set, i.e. choice of a larger stirrer step size, comes at the expense of a significant increase in the uncertainty for the derived parameters, but does not cause any significant decrease in the stirring performance.

The values of $|\langle A_{\alpha\beta}\rangle|$ are markedly higher than in the case of open-ended waveguide measurements [34, Fig 5.5]. This confirms the fact that reducing the aperture size of the receiver *decreases* the degree of apparent field isotropy and, hence, of the perceived level of electromagnetic wave chaos.

From the measured $A_{\alpha\beta}$ the corresponding cdfs $F_{A_{\alpha\beta}}$ are computed, shown in Fig 102. The cdfs for the planar anisotropies are equally close to the theoretical characteristics $F_{A_{\alpha\beta}} = (1 + a_{\alpha\beta})/2$, as shown in the Figure. The measured total field anisotropy shows somewhat larger discrepancies with the theoretical $F_{A_{tot}}$, confirming the conclusions of Sec 3.2.6.2. Again, reducing the data decimation is seen to improve the match (Fig 103).

3.2.9 Field inhomogeneity

Figs 104 and 105 show the measured field inhomogeneity coefficients $I_{\alpha\alpha}$, as defined in Sec 3.1.9.2, as a function of wall position. One notices a poorer coverage during the early part of the sequence ($\tau/\Delta\tau < 400$) for all three field components but particularly for $|E_z|$. This results in values for I_{tt} and I_{tot} below average in this part of the sample. The running averages are shown in Figs 106–109; the bootstrap averages are given in Figs 110–111. The good reverberation is further confirmed by comparing the theoretical cdf with the measured sigmoidal cdf. The latter appears centered around the theoretical cdf (Fig 113), but the swing is now considerably smaller than at 2.5GHz.

3.2.10 Spatial correlation

The probe was withdrawn from its original position by 3mm to $r_1 = 94$mm, and the same $M = 1200$ stirrer positions were generated. The crosscorrelation coefficients $\varrho_{\alpha\beta}$ between $|E_\alpha(r_0)|^2$ and $|E_\alpha(r_1)|^2$ were then computed and bootstrapped for the full data set. They are shown in Fig 112. The theoretically expected spatial data correlation between both locations for the total field is $\mathrm{sinc}(k\Delta r) \approx 0.956$. It was found that the measured correlations are now considerably smaller.

[23] Deviations are partly due to the limited number of replicas being generated in the bootstrapping process, here set to be 50.

3.2.11 Spectral analysis

File 77 showed the estimates $\langle\beta_\alpha\rangle$ of the spectral parameter as a function of the subsample (partition) length M, using Bartlett smoothing of the psdf. Fig 118 and Fig 119 show the same autospectral densities and the cross-spectral densities, together with 3rd-order exponential fits $\sum_{i=0}^{3}\exp[b_i(\omega/\Delta\omega)^{3-i}]$, respectively. As for 2.5GHz, the decay is somewhat slower than exponential at low frequencies. The associated normalized spectral bandwidths δ_α and ϵ_α at this distance are tabulated in Tbl 19.

3.2.12 Upward threshold crossings and mean excursion lengths

Upward threshold crossing rates were calculated in [34, Sec 12.6, App C.2] for the pointwise power density. In App G, the analysis is extended to allow for local averaging due to finite-sized antenna apertures and finite stirrer steps (see also Sec 4.2). Here we compare the theoretical results with measured data.

Fig 120 compares the measured upward threshold frequency $\nu_T^+(b/\sigma_0)$ for the magnitudes of the total field and the Cartesian field components to the theoretical[24] dependencies given by (142) and (145), respectively. A correct analysis would incorporate both local stir and local spatial averaging simultaneously, but for simplicity we consider only type, viz. local stir averaging. The theoretical ν_T^+ for the total field is seen to match the measured crossing rate closely, particularly for large values for b/σ_0. This can be expected on the basis of the asymptotic validity for b/σ_0. The slight but consistent bias in the model towards overestimating the measured crossing rate for large b/σ_0 is due to the fact that the (small) spatial averaging across the spatial averaging length (dipole length) was not included. This would have shifted the theoretical curve marginally to the left.

Fig 121 compares the measured and the theoretical mean excursion lengths for the total field magnitude, now incorporating local spatial averaging, as well as for the Cartesian components, assuming no local averaging. In both cases, the agreement is good. Note in particular that the change in slope of $\mathrm{E}[\mathcal{L}_T(b/\sigma_0)]$ for $|E_t|$ is being accurately predicted by (162).

[24]No correct expression for the spatial correlation function of Cartesian field components is currently known. Hence, no expression for ν_T^+ has been derived at present. For comparison for the Cartesian components we therefore assumed no local averaging $[\nu_0^+(b/\sigma_0)]$.

4 Miscellaneous results

4.1 Distribution and statistics of input power

4.1.1 Averaging of insertion loss

In the analysis above, the measured field strengths were normalized by the square root of the mean-normalized input power:

$$E_\alpha(\tau/\Delta\tau)| \triangleq \frac{|E_{\alpha,meas}(\tau/\Delta\tau)|}{\sqrt{P_i(\tau/\Delta\tau)/\langle P_i\rangle}} \tag{15}$$

prior to mean-normalization by the average field strengths, $\langle E_\alpha\rangle$. In this way, the stirrer data is corrected for fluctuations in the incident power with stirrer position (Figs 3 and 70). The reference incident power is the source output power less the external losses, the reflection from the cavity due to impedance mismatch at the cavity input port, random fluctuations (measurement uncertainty) and possible drift of the power source. Since the source output power is held constant (and has been verified to remain so within about 5%) throughout the stirring process, variations of P_i with stirrer position are mainly due to the variations in cavity input impedance and the inevitable random measurement uncertainty. As stated before, the changes in input impedance and, hence, in insertion loss are due to the rotating wall. These cause amplitude modulation of the excitation, which may be considered as an elementary[25] form of 'electronic source stirring'.

Our interest is naturally in statistical, not deterministic, changes of the input power. Usually, these changes are neglected by assuming that the input power is constant throughout the stirring process. When antennas are positioned so as to illuminate a (mechanically static) corner of a prismatic room, the statistical changes of the input impedance induced by the paddle wheel rotating behind the antennas are relatively small so that this assumption is probably sufficiently accurate. In our case of wall stirring, the Tx horn or waveguide face a rotating wall, hence, changes in the wave impedance as a function of $(\tau/\Delta\tau)$ are likely to be significant.

In general, $\langle P_{\alpha,rec}/P_i\rangle \neq \langle P_{\alpha,rec}\rangle/\langle P_i\rangle$ [29, Sec 3.1], [34, Sec 3]. To investigate the significance of this difference for practical measurements, we calculated running averages of $\langle P_{\alpha,rec}/P_i\rangle$ and $\langle P_{\alpha,rec}\rangle/\langle P_i\rangle$ across the interval $[0,\tau]$ with τ = 91mm, for f = 2.5GHz and f = 8.2GHz, which are shown in Figs 62 and 114, respectively. Fig 114 shows that at 8.2GHz, both quantities are in effect almost indistinguishable. It was found that their absolute differences are less than 5% of the standard deviation on $P_{\alpha,rec}/P_i$, i.e.

[25] In the linear regime, these amplitude variations only result in the scaling of modal or wave amplitudes, i.e. they do not give rise to a *qualitative* change in the field configuration or distribution.

$$\frac{|\langle P_{\alpha,rec}/P_i\rangle - (\langle P_{\alpha,rec}\rangle/\langle P_i\rangle)|}{\sigma_{(P_{\alpha,rec}/P_i)}} < 0.05$$

Thus, for this experiment, one can replace the mean of the ratio of power densities by the ratio of their mean values. Whereas this simplifies the measurement in one manner in that there is no need to track the input power for each stirrer position, the problem of finding an accurate estimate for $\langle P_i\rangle$ from a single measurement of P_i or even from a selected number of stirrer positions remains. If P_i is Gauss normal distributed (see Sec 4.1.2) this means that $\langle P_i\rangle$ is only known within $\pm 32.2\%$, at the 95% confidence level, for a single measurement. This may or may not be acceptable for the required accuracy of the measurement. Consequently, the uncertainty for parameters which depend on the average insertion loss (e.g. the composite cavity quality factor) is large if the input power is not monitored constantly as will be illustrated below.
At 2.5GHz, however, the differences between the mean of the power ratio[26] and the ratio of the power means becomes more distinct (Fig 62). Hence, the error caused by replacing the former by the latter increases. This indicates that the fluctuation of $P_i(\tau)$ is for the greater part determined by the input impedance, which exhibits larger fluctuations for electrically smaller cavities.

Figs 63 and 115 show the composite quality factors[27] $\langle Q^{(\prime)}\rangle$ at $f = 2.5$GHz and $f = 8.2$GHz, respectively, as calculated using both approaches, i.e.:

$$\langle Q\rangle \triangleq \frac{16V\pi^2}{\lambda^3}\left\langle\frac{P_t}{P_i}\right\rangle$$

and

$$\langle Q'\rangle \triangleq \frac{16V\pi^2}{\lambda^3}\frac{\langle P_t\rangle}{\langle P_i\rangle}$$

together with the standard deviations σ_Q and $\sigma_{\langle Q\rangle} \equiv \sigma_Q/\sqrt{M}$. One notices that for large M, the deviations $|\langle Q'\rangle - \langle Q\rangle|$ are of the order of $\sigma_{\langle Q\rangle}$, at both frequencies. The differences are mainly due to the difference in the loading of the Tx antenna, the effect of which is more masked by higher wall losses if the frequency increases [45].

[26]Comparing Figs 62 and Fig 114, it might seem as if the average insertion loss *decreases* with increasing frequency, which is clearly unphysical. The reason for the higher values at 2.5GHz is that a free space wave impedance was assumed in calculating the $\langle P_\alpha\rangle$, which is inaccurate for the relatively electrically small size of the chamber at this frequency. The emphasis is here on the differences between the mean of power ratios and the ratio of power means, rather than on their actual values which are only indicative per frequency.

[27]The same remark regarding the actual values of the Qs applies as in the case for the insertion loss, i.e. a frequency-dependent scaling factor applies in both cases to get to the true Q factors, as a result of the inaccuracies in the estimated effective wave impedance. Hence the Q values are expresses in arbitrary units (a.u.).

The quality factor can also be computed from the power density for the individual rectangular field components, P_α ($\alpha = x, y, z$). Because the effective antenna aperture is largely independent[28] of the radiation pattern in an isotropic environment, (17) and (18) can be used for all components α. The results, shown in Figs 64 and 116, show comparable values for $\langle Q_\alpha \rangle$ and $\langle Q'_\alpha \rangle$, but with larger uncertainties as compared to those for $\langle Q \rangle \equiv \langle Q_t \rangle$.

4.1.2 Distribution of input power

Monitoring P_i enables the statistics of the cavity reflection (return loss) $|S_{11}|$ to be determined, supplementary to the conventional chamber characterization which only considers the transmission, $|S_{21}|$. Fig 117 shows the cdf of the standardized P_i at 8.2GHz. For comparison, the cdf for a standard Gauss normal random variable and for the received powers $P_{x,y,z}$ and P_t are also shown. One notices close similarity with a Gauss normal cdf, but extreme values of the standardized P_i appear underrepresented at the expense of values closer to the mean. Recall that the input power is completely and linearly polarized along a *fixed* direction, hence the distribution of P_i should be compared to the cdf for P_x rather than P_t.

Effect of antenna aperture size on characterization of reverberation chamber

Introduction

Testing and characterization of reverberation chambers is generally performed using waveguides and dipole, horn, log-periodic, ...antennas having standard dimensions. Current EMC standards [43, 44] do not specify or recommend Tx/Rx antenna size and its effect on measured chamber performance. This might, wrongly, suggest that antenna size is not significant.

As mentioned before, the effect of increasing the Rx aperture size is the increase of the degree of local spatial averaging of the stochastic field. An increase in the extent of local averaging gives rise to an *increase* in the perceived level of reverberation, i.e. in the randomness and uniformity of the statistical field. It is thus concluded that, as a result, if EUTs are being measured in the chamber using antennas that are significantly smaller or larger than the antennas used for chamber calibration then undertesting or overtesting of the EUT will result, respectively.

It is important to realize that the effects of local averaging protrude for perfect statistical field homogeneity as well. In the latter case, the cavity field can be modelled as pink noise integrated over a nonzero length, area or volume i.e. as a 'summation' of various noise time series. This 'sum' will then tend to a constant average value as the area of integration is increased, i.e. a

[28] This feature has recently been investigated in more detail in [39].

decrease in the standard deviation on the measured value. Strictly, when investigating the effects of spatial averaging for the synthetic aperture, the complex fields at arbitrary spatial locations for corresponding stirrer positions should be measured and superimposed. However, when the unstirred chamber itself is sufficiently well reverberating (i.e. electrically large and intrinsically ergodic, e.g. a 2D or 3D stadium [14, 20]), then the scalar field magnitudes in such a chamber can be considered as spatially random variables. Consequently, one is then justified in averaging the energy densities at these locations for each stirrer position. The intrinsic ergodic properties are only reached asymptotically, i.e. for sufficiently high frequencies, in nonintegrable cavity geometries. Therefore, some error is inevitably introduced when averaging energy densities in practical operational conditions. Thus, although the following illustrating measurements were taken with the chamber exhibiting limited statistical field homogeneity, the procedure shows qualitative results whose quantitative accuracy increases as the extent of averaging decreases or the intrinsic ergodicity is better approached. A more accurate investigation is possible when using a vector network analyzer and antennas of different lengths.

A theoretical investigation of local averaging and its effects is given in App G.

4.2.2 Method

Data for 27 discrete locations, equally spaced a distance 10mm between locations along one radius in the azimuthal plane at 2.5GHz (see Sec 3.1.9.2), were amalgamated to generate a synthetic aperture of variable length 3...273mm and constant width 3mm. For $|E_z|$, this procedure simulates[29] a linear dipole antenna of variable length. The synthetic aperture is realized via spatial rms averaging of the individual data sets for arbitrary τ, i.e. assuming a spatially perfectly incoherent (random) field. For $|E_x|$ and $|E_y|$, the procedure yields an aperture of variable width but constant length equal to the length of the dipoles.

4.2.3 Results

Figs 122–129 show the effect of varying aperture size on various chamber parameters.

Fig 122 shows the sweep data for various aperture widths. As this width increases, so does the local averaging i.e. the minima increase and maxima decrease in the sweep data.

Fig 123 compares the measured coefficients of variation ν_α for the full sample with the theoretical 'point' values for χ_2 and χ_6 distribution functions for the ideal chamber. It is clear that a danger exists in interpreting chamber characteristics on the basis of this statistic only: the

[29]Realistic dipole antennas will show some deviation from the results presented here due to continuity of induced current distributions, compared to spatially sampled fields and currents.

measured values eclipse the theoretical values at some nonzero aperture size. Note also that the ν_α are very sensitive to changes for small apertures.

Fig 124 illustrates that the match between theoretical and measured cdfs for the stirrer data rapidly improves as the antenna aperture increases to about 43mm. Further increasing the aperture causes the mismatch to increase again. This is further illustrated by the variation of the crosscorrelation coefficients as a function of aperture size, shown in Fig 125. The mismatch for the cdf of the total field field, however, is largely constant with respect to changing the aperture size.

Figs 126–127 show the measured and average planar and total statistical field anisotropy coefficients $A_{\alpha\beta}$, respectively. The values of the $A_{\alpha\beta}$ tend to be become more tightly clustered around zero, and the value of A_{tot} is overall lower in comparison with the 'point' measured value in Fig 37. The magnitude of $\langle A_{\alpha\beta} \rangle$ is seen to decrease as the aperture size increases. This results underpins the theoretical result of the effect of local averaging on wave chaos.

Fig 128 shows the variation of the insertion loss with aperture size, typically by about 4dB across the measured range. This has important implications for the uncertainty for the mean steady-state chamber quality factor.

Fig 129 shows the normalized spectral bandwidths δ_α and ϵ_α A small but consistent mean increase with aperture size is noted for small averaging lengths, as expected (App G). For larger $k\mathcal{T}$, the increase becomes saturated because the reverberant field is known to be less than perfect at 2.5GHz in this chamber, hence the intrinsic cavity ergodicity and averaging of energy densities are only approximately valid. The normalized spectral bandwidths are preferred measures for 'true' stirring performance, also because of their known theoretical values for ideal chambers [34, Sec 12.4].

Although it is difficult to extrapolate the present results to other frequencies and chamber particulars, it appears from these results that the maximum aperture should be kept as small as possible, and certainly well below 40mm ($\sim \lambda/3$) to yield results that are representative for true 'point' measurements. This is still one order of magnitude larger than the recommendation on the basis of the normalized spectral bandwidth (App G). If such limitation on the maximum aperture size is not being observed (e.g. to limit the cost of power amplification, requiring larger antennas), then the uncertainty on the chamber characterization necessarily increases.

4.3 Peak restoration and estimation of true maximum field strength

4.3.1 Cubic spline interpolation

The sample maximum of M equidistant sample data points can inevitably only be an estimate for the 'true' maximum for mode-stirred operation of the chamber, a value which does exist in any realistic chamber[30] and which could be determined if continuous (as opposed to discrete) data were available. Finding the true maximum of the continuous trace is important because even the transitions (rotations) between discrete stirrer positions (steps) are continuous, hence the EUT will effectively be subjected to the maximum of the continuous process, rather than to the maximum of the discrete process. This true maximum is usually estimated statistically from extreme value theory for order statistics, which are based on underlying continuous distributions. However, these distributions presume ideal $\chi^{(2)}_{2p}$ chamber field distributions. For imperfect chamber operation, particularly at lower frequencies, an alternative method must therefore be sought. The estimate depends on the sample autocorrelation, i.e. the stirrer step size, and (for nonstationary processes) the stirrer starting position. Experimentally, the 'true' ensemble maximum could be found from sampled data by making an infinite number of experiments for different stirrer positions (starting positions and stirrer steps), which is clearly an unrealistic task. As an alternative, for a sufficiently small but finite stirrer step size, one may post-process the sampled data by performing a high-performance data interpolation in order to find a better estimate for the true sample maximum. This procedure will succeed provided the data points are spaced not farther apart than half the reciprocal of the Nyquist frequency for the (unknown) mode-*stirring* tuner sweep which is finite for any real chamber. In this case, the Whitakker–Kotelnikov–Shannon sampling theorem for exact retrieval of the tuner sweep data for the mode-stirring is satisfied.

Various mathematical software packages offer a range of interpolation techniques of which cubic spline interpolation usually yields the best ('smoothest') interpolated data. Fig 130 compares the measured (discrete) and interpolated (smoothed) data, using the MATLAB^{TM} cubic spline interpolator, for the first 40 data points of the trace of $|E_x|$ at 2.5GHz. The interpolation is seen to be especially effective in estimating the local extrema in cases where a peak has been sampled asymmetrically on both sides of it.

If mode-stirring sweep data are known in analogue, i.e. continuous functional form then superior sampling schemes (e.g. Fourier sampling) other than the above standard 'point' sampling can

[30]In an ideal reverberation chamber such is not the case, because the stirrer data would then be pure white, i.e. having zero autocorrelation between different wall positions which allows for discontinuities in the stirrer data. In any real chamber, no matter how small the imperfections, the data will always form a continuous trace on the microscale, thus exhibitibng a finite maximum.

be performed on these functions, in order to obtain more accurate sampled data. The optimal[31] sampling technique consists of projection of the tuner sweep on a set of orthonormal functions (orthogonal or principal component or Karhunen–Loève expansion). The latter depend on the autocorrelation function of the tuner sweep. In the stir domain, the optimum sampling function $h(\tau)$ for the stirrer data function $|E_\alpha(\tau)|$ then follows as:

$$h(\tau) = \int_{-\infty}^{\infty} \left[\frac{s_{|E_\alpha||E_\alpha|}(\varpi)}{\sum_m s_{|E_\alpha||E_\alpha|}(\varpi - m\Delta\varpi)} \right] \exp(j\varpi\tau)\mathrm{d}\varpi$$

where $s_{|E_\alpha||E_\alpha|} = \mathcal{F}\left[\rho_{|E_\alpha||E_\alpha|}(\tau)\right](\varpi)$ is the two-sided autospectral power density function of $|E_\alpha(\tau)|$. Here ϖ is defined by the so-called reciprocal lattice of τ [9]. However, sweep data are only rarely available in analogue format as some form of digitization is almost always needed to measure or store the sweep data. In this case, the best one can do is to construct near-optimum transform data using one of several transformation techniques (Fourier-, cosine-, sine-, ...transformation) on the standard sampled data. Fortunately, for typical lengths of stirrer data (several tens of sample points or more), the differences with the optimum sampling results are very small.

4.3.2 Digital Laplace filtering

When sophisticated data interpolation routines are not available, simpler data processing techniques can be devised that still give improved results for the estimation of the maximum of the continuous trace. However, it is easily seen that simple linear interpolation will not give improvement regarding estimation of the max-to-mean field strength: for two measurement points on both sides of the 'true' peak, the linearly interpolated values will only take values between those of the two measurement points. This yields an estimate that is worse than, say, the maximum of both sample values.

One simple and powerful technique, also used in digital signal restoration and sharpening, is the use of digital filtering based on the use of 2nd-order discrete Laplace operators. For use in restoration of reverberation data, they have the key advantage over 1st-order differences of being isotropic, i.e. independent of the rotation direction of the electric field in the course of the stirring process. This makes them especially useful for application to vector random fields. The 1D 2nd-order Laplacian for a discrete stirrer data sequence $E_\alpha(\tau/\Delta\tau)$ is:

$$\nabla^2 E_\alpha(\tau/\Delta\tau, \Delta\tau) = E_\alpha[(\tau + \Delta\tau)/\Delta\tau] + E_\alpha[(\tau - \Delta\tau)/\Delta\tau] - 2E_\alpha[\tau/\Delta\tau],$$

following from two subsequent 1st-order differences. Since the sampling of the continuous tuner sweep causes the high spatial frequency contents of the sweep to be eliminated (as a direct result

[31] as defined in the sense of minimizing the mean square error between the true and the sampled tuner sweep

of the sampling theorem), the sampling causes, in particular, the loss of sharp features in the sweep data, yielding a blurred version of the original tuner sweep. Assume then that the sampled data $E'_\alpha(\tau)$ could equivalently be constructed, hypothetically, by adding to the (unknown) original data E_α a small fraction δ of the sum of field values at immediate[32] neighboring points[33], i.e.

$$E_\alpha(\tau/\Delta\tau, \Delta\tau) = E_\alpha(\tau/\Delta\tau) + \delta\{E_\alpha[(\tau + \Delta\tau)/\Delta\tau] + E_\alpha[(\tau - \Delta\tau)/\Delta\tau]\}$$

then we can estimate the original tuner sweep by subtracting a small fraction ζ of the Laplacian of the blurred sequence from the blurred sequence itself:

$$E'_\alpha(\tau/\Delta\tau, \Delta\tau) \approx (1 - \zeta\nabla^2)\, E_\alpha(\tau/\Delta\tau, \Delta\tau)$$

One usually takes $\zeta = \delta$. The factor $\zeta \ll 1$ is to be determined empirically for best results: too large a value emphasizes the peaks, giving unrealistic values. It is therefore recommended to determine the value of ζ from a comparison with spline interpolated data first.
Fig 130 shows the results, again for the first 40 data points of the sweep data for $|E_x|$ at 2.5GHz. The Figure compares the raw sampled data and interpolated data with the filtered data obtained by subtracting 8% of the Laplacian of the sampled data from the sampled data itself ($\zeta = 0.08$). With reference to the raw measured data, it can be seen that sharper peaks occur, of about the same magnitude as the spline-interpolated data, thus improving the estimation of the max-to-mean ratio. Investigating many different stirrer sequences, we found $\zeta = 0.08$ to be a typical value for reverberation processes. Note that the technique at the same time sharpens the local minima, which can even become negative. For estimation of field strengths and power densities, the technique should therefore be restricted to the definition and sharpening of maxima only.

5 Summary

The measurements with the Schmid & Partner electric field probe in the *NPL* untuned stadium reverberation chamber confirm many of the results obtained previously based on energy density measurement [34, Sec 13]. The measurements and data analysis also lead to the following additional observations:

1. At 2.5GHz, the field probe data are found to exhibit a spread s that is nearly inversely proportional to the measured average field strength:

   - for $|E_x|$ and $|E_y|$:

$$s_{x,y} \approx 4.03|E_{x,y}|^{-0.86} \quad \text{(high amplification setting)} \tag{23}$$

$$s_{x,y} \approx 1.74|E_{x,y}|^{-0.94} \quad \text{(low amplification setting)} \tag{24}$$

[32] More sophisticated higher-order differencing schemes over extended data intervals could also be considered.

[33] For measurement by finite-sized field probes or antennas this is precisely the mechanism by which the electromagnetic imaging becomes blurred, as a result of local spatial averaging.

- for $|E_z|$:

$$s_z \approx 2.24|E_z|^{-0.87} \quad \text{(high amplification setting)}$$
$$s_z \approx |E_z|^{-1} \quad \text{(low amplification setting)}$$

It is particularly noted that the proportionality constants differ by about a factor two between dipole elements. Hence the noise performance is significantly less isotropic than the quoted isotropy for the average field strengths.

2. At 2.5GHz, the inhomogeneity of the insertion loss in radial direction was determined based on measurements at 25 positions equally spaced by 10mm along a radial direction down to a distance of $\lambda/3$ from the cavity wall, each for $M = 275$ ($\sim N = 183$) stirrer positions. This inhomogeneity was found to be within ± 3.3dB for $|E_x|$, within ± 4.0dB for $|E_y|$, within ± 2.0dB for $|E_z|$ and within ± 2.5dB for $|E_t|$.

3. The field inhomogeneity coefficients show different radial dependencies for the three measurement directions: the transverse (x, y) directions show a modulated quasi-periodic behaviour, whereas the variation of the z-component is smaller and not periodic.

4. Close to the wall, the stirring capability in a plane parallel to the plane which is locally tangent plane to the wall is hardly affected by the presence of the wall. Therefore, the widely used '$\lambda/4$'-criterion for minimum distance to the walls to achieve proper reverberation is a criterion for full 3D field isotropy and homogeneity, not for field stochasticity. This implies that EMC testing for directions parallel to the wall can still be done close to the cavity wall, provided the input power is increased accordingly.

5. At 2.5GHz, the measured bootstrap-averaged field anisotropies for $M = 275$ samples ($N = 183$ equivalent independent samples) at radial distance $r = 91$mm are:

   - $|\langle A_{xy}\rangle| = -10.73$dB (standard error $= -15.2$dB);
   - $|\langle A_{yz}\rangle| = -12.16$dB (standard error $= -15.3$dB);
   - $|\langle A_{zx}\rangle| = -19.77$dB (standard error $= -15.1$dB);
   - $|\langle A_{tot}\rangle| = -12.58$dB (standard error $= -14.8$dB).

   At $r = 345$mm, i.e. 5mm off the cavity wall:

   - $|\langle A_{xy}\rangle| = -6.92$dB (standard error $= -14.9$dB);
   - $|\langle A_{yz}\rangle| = -0.87$dB (standard error $= -17.6$dB);
   - $|\langle A_{zx}\rangle| = -1.43$dB (standard error $= -16.2$dB);
   - $|\langle A_{tot}\rangle| = -4.48$dB (standard error $= -15.5$dB).

6. At 8.2GHz the measured bootstrap-averaged values for the field anisotropy for $M = 1200$ samples ($N = 400$ equivalent independent samples) at the same location $r = 91$mm are:

   - $|\langle A_{xy}\rangle| = -18.58$dB;
   - $|\langle A_{yz}\rangle| = -17.10$dB;
   - $|\langle A_{zx}\rangle| = -15.82$dB;

   $|\langle A_{tot}\rangle| = -16.27$dB.

   with comparable standard errors as for 2.5GHz. These average statistical field anisotropies are somewhat larger than the values obtained using energy density measurements with a larger Rx aperture [34, Sec 5.2]. This discrepancy demonstrates that the effect of a decrease in the degree of spatial local averaging is a *decrease* in the perceived stirring quality of the chamber.

7. The measured effect of local averaging has been further confirmed by theoretical calculations of the variance function and scale of fluctuation, in the present case, and for the general case through simulation of a synthetic Rx antenna with aperture of variable width, based on probe 'point' measured data. This simulation confirms a decrease of field anisotropy coefficients with increasing aperture size.

8. Improper decimation of data gives rise to a better match between the theoretical and measured cumulative distribution functions of the mean-normalized field. This might, wrongly, give the impression of better stirring being achieved in such cases. By contrast, the distribution of the deviations between the theoretical and measured cumulative distribution functions is sensitive to the correct data decimation, because such a distribution deviates farther from Gauss normality for decimations which are either too large or too small. The use of distributions of deviations (pointwise cdf mismatch) is thus recommended over the use of single test statistics (Kholmogorov–Smirnov, Cramér–von Mises, etc.). Proper decimation should always be observed when comparing with ideal-chamber characteristics, and more powerful decorrelation techniques need to be implemented.

9. The average field anisotropy coefficients are not markedly affected by the rate of subsampling of the tuner sweep, although denser subsampling does help in reducing their uncertainties. This suggests that such coefficients are more robust to residual correlation compared to comparison of distribution functions.

10. The max-to-mean ratio for the total electric field can be characterized with an uncertainty that is about a factor two smaller than for any of the field components.

11. Differences, though relatively small, are found between the mean of the ratio of received power to input power, compared to the ratio of the mean received power to the mean input power. The differences are larger at 2.5GHz than at 8.2GHz.

12. The use of cubic spline interpolation or digital Laplace filtering for post-processing of the measured data enables one to estimate the max-to-mean ratio for mode-stirred operation more accurately, in particular for less than perfect chamber operation conditions.

13. Numerical simulation of a noncorrugated 3D stadium using a finite-integration technique shows that the field uniformity (both field isotropy and homogeneity) is weakest near the cylindrical axis of the chamber and, particularly, near its center point. This underlines the fact that a chamber devoid of symmetries offers the best prospect for good reverberation.

14. Predicted and measured level crossing statistics for the total field or total power density show good agreement at 8.2GHz. The extensions of the theory given here to incorporate finite local averaging levels allow these statistics to be used in a realistic measurement set-up, showing second-order dependence on the averaging length.

6 Conclusions

The statistical analysis of stirrer data for individual field components and total field at 2.5GHz and 8.2GHz confirms the findings in [34]. Field anisotropy coefficients are found to enable reverberation quality to be assessed with great sensitivity, even when alternative methods (matching of cdfs, max-to-mean ratios within 95%, 99% confidence intervals, ...) show the reverberant field as 'very good' and make further distinction of performance and uncertainty levels very difficult.

7 Acknowledgements

This work was sponsored by the UK Department of Trade and Industry National Measurement System Electrical Programme (NMS 1997–2000) under project EL97F320: 'Isotropic methods for EMC susceptibility and emission testing 1GHz–18GHz'.

Stimulating discussions with J Ladbury and D Hill (National Institute of Standards and Technology, Boulder, CO), G Freyer (NCEE, Monument, CO), M Hatfield (Naval Surface Warfare Center, Dahlgren, VA), T Lehman (Consultant, Belen, NM), J Page (Nokia, New Systems Technology, Farnborough, GB), P Corona (Istituto Universitario Navale, Napoli, I), O Egger and K Poković (Schmid &Partner Engineering AG, Zürich, CH), and R N Clarke and W Liang (National Physical Laboratory, Teddington, GB) are gratefully acknowledged.

References

[1] Watson, G N: *A treatise on the theory of Bessel functions;* 2nd ed, Cambridge University Press (1944).

[2] Doob, J L: Heuristic approach to the Kolmogorov–Smirnov theorems; *Ann Math Stat,* vol 20 (1949), pp 393–402.

[3] Feller, W: Fluctuation theory of recurrent events; *Trans Am Math Soc;* vol 67 no 111 (1949), pp 98–119.

[4] Marsh, H W (Jr): Correlation in wave fields; *US Naval Underwater Sound Laboratory Quart Rep,* (Mar 1950), pp 63–68.

[5] Donsker, M D: Justification and extension of Doob's heuristic approach to the Kolmogorov–Smirnov theorems; *Ann Math Stat,* vol 23 (1952), pp 271–281.

[6] Erdélyi, A: *Tables of integral transforms;* McGraw–Hill, NY (1954).

[7] Schröder, M: Eigenfrequenzstatistik und Anregungsstatistik in Räumen; *Acustica,* vol 4 (1954), pp 456–468.

[8] Schröder, M: Die statistischen Parameter der Frequenzkurven von grossen Räumen; *Acustica,* vol 4 (1954), pp 594–600.

[9] Peterson, D P and Middleton, D: Sampling and reconstruction of wave-number-limited functions in n-dimensional Euclidean spaces; *Informat Contr,* vol 5 (1962), pp 279–323.

[10] Parzen, E: *Stochastic processes;* Holden–Day, San Francisco (1962).

[11] Pearson, E S and Tukey, J W: Approximate means and standard deviations based on distances between percentage points of frequency curves; *Biometrika,* vol 52 (1965), p 533.

[12] Cramér, H: On the intersection between the trajectories of a normal stationary stochastic process and a high level; *Arkiv Mat,* vol 6 (1966), p 337.

[13] Habibi, A and Wintz, P A: Image coding by linear transformation and block quantization; *IEEE Trans Comm Techn,* vol 19 (1971), pp 50–62.

[14] Lebowitz, J L and Penrose, O: Modern ergodic theory; *Physics Today,* (Feb 1973), pp 23–29.

[15] Oppenheim, A V and Shafer, R W: *Digital Signal Processing;* Prentice-Hall, Englewood Cliffs, NJ (1975).

[16] Vanmarcke, E: On the distribution of the first-passage time for normal stationary random processes; *J Appl Mech,* vol 42 (1975), pp 215–220.

[17] Benettin, G and Strelcyn, J-M: Numerical experiments on the free motion of a point mass moving in a plane convex region: stochastic transition and entropy; *Phys Rev A,* vol 17 no 2 (1978), pp 773–785.

[18] Silverman, B: Choosing the window width when estimating a density; *Biometrika,* vol 65 (1978), p 1

[19] Scott, D W: On optimal and data-based histograms; *Biometrika,* vol 66 (1979), p 605.

[20] Bunimovich, L A: On ergodic properties of nowhere dispersing billiards; *Comm Math Phys,* vol 65 (1979), pp 295–312.

[21] Vanmarcke, E: *Random fields: analysis and synthesis;* MIT Press, Cambridge, MA (1983)

[22] Scott, D W: Frequency polygons: theory and application; *J Am Statist Ass,* vol 80 (1985), p 348

[23] Bendat, J S and Piersol, A G: *Random data: analysis and measurement procedures;* 2nd ed, Wiley Interscience, NY (1986).

[24] Stuart, A and Ord, J K: *Kendall's advanced theory of statistics - vol 2;* Edward Arnold - Hodder & Stoughton, London, 5th ed (1991).

[25] Lehman, T H: A statistical theory of electromagnetic fields in complex cavities; *USAF Phillips Laboratory Interaction Notes,* Note 494 (1993).

[26] Mortessagne, F, Legrand, O and Sornette, D: Role of absorption distribution and generalization of exponential reverberation law in chaotic rooms; *J Acoust Soc Am,* vol 92 no 1 (1993), pp 154–161.

[27] Gradshteyn, I S and Ryzhik, I M: *Tables of integrals, series and products;* 5th ed, Academic Press, NY (1994).

[28] Schmid, T, Egger, O and Kuster, N: Automated E-field scanning system for dosimetric assessments; *EMV & Compliance Handbook,* vol 1 (1995), pp 9–16.

[29] Crawford, M L, Loughry, T A, Hatfield, M O and Freyer, G J: Band-limited, white Gaussian noise excitation for reverberation chambers and applications to radiated susceptibility testing; *NIST Technical Note 1375* (Jan 1996).

[30] Hatfield, M O, Freyer, G J and Slocum, M B: Reverberation characteristics of a large welded steel shielded enclosure; *US Naval Surface Warfare Center, Techn Rep NSWCDD/TR-96/149,* (Oct 1996).

[31] Aurich, R, Bäcker, A and Steiner, F: Mode fluctuations as fingerprints of chaotic and non-chaotic systems; *Int J Mod Phys B,* vol 11 no 7 (1997), pp 805–849.

[32] Spiegel, M R: *Mathematical Handbook;* 36th printing, McGraw-Hill, NY (1997)

[33] Arnaut, L R: Field anisotropy, field inhomogeneity and polarization bias in imperfect reverberation conditions; *NPL-CEM-DGSS Technical Report R980614* (Jun 1998).

[34] Arnaut, L R and West, P D: Evaluation of the *NPL* untuned stadium reverberation chamber using mechanical and electronic stirring techniques; *NPL Report CEM 11* (Aug 1998).

[35] Arnaut, L R: Relation between field isotropy and degree of polarization in reverberation chambers; *NPL-CEM-DGSS Technical Report R980806* (Aug 1998).

[36] Ladbury, J, Koepke, G and Camell, D: Evaluation of the NASA Langley Research Center mode-stirred chamber facility; *NIST Technical Note 1508* (Jan 1999).

[37] DASY3 - Dosimetric Assessment System; Software manual; *Schmid & Partner Engineering AG,* Zürich, CH (Apr 1999) (*http://www.speag.com*).

[38] Lundén, O, Jansson, L and Bäckström, M: Measurements of stirrer efficiency in mode-stirred reverberation chambers; *FOA Technical Report FOA-R-99-01129-612-SE,* (May 1999), p 13.

[39] Jansson, L and Bäckström, M: Directivity of equipment and its effect on testing in mode-stirred and anechoic chamber; *IEEE EMC Symposium* (02–06 Aug 1999, Seattle, WA), pp 17–22.

[40] Arnaut, L R: Ensemble decimation factors for reverberation chamber stirrer data; *NPL-CETM-DGSS Technical Report CETM12* (Aug 1999).

[41] Poković, K: Probe calibration for free space measurements; *PhD thesis (submitted),* ETH Zürich, CH (1999); *Schmid & Partner AG Technical Note,* (1999).

[42] Poković, K: Special considerations for probes optimized for close near-field evaluations in air; *submitted for publication* (1999).

[43] Joint Task Force IEC 61000-4-21 / CISPR 77B: Testing and measurement techniques. Annex J: Alternative procedure – Reverberation chamber method, Annex K: Overview to reverberation chambers.

[44] RTCA/DO-160D: Environmental conditions and test procedures for airborne equipment: 20. Radio frequency susceptibility (radiated and conducted), *RTCA Inc.;* Washington, DC (04 Mar 1997).

[45] Ladbury, J; private communication.

[46] Hill, D; private communication

[47] Page, J; private communication.

[48] Liang, W; private communication.

[49] Freyer, G: private communication

[50] Lehman, T: private communication.

[51] Egger, O: private communication

[52] Poković, K: private communication.

A Distributions, statistics and extreme values of field and energy density distribution functions

For easy reference, we list results for four particular cases of particular practical importance. Expressions are given for distributions and statistics of mean-normalized stirrer data X, the mean-normalized maximum W_N and mean-normalized minimum U_N for a sample of N independent data points.

A.1 Energy density for single field component

Pdf, cdf, mean, variance, coefficient of variation of mean-normalized field X (χ^2_2 distribution):

$$\begin{aligned} f_X(x) &= (1/2)\exp(-x/2) \\ F_X(x) &= 1-\exp(-x/2) \\ \mu_X &= 2 \\ \sigma_X^2 &= 4 \\ \nu_X &= 1 \end{aligned}$$

Pdf, cdf, mean, variance of mean-normalized maximum energy density[34] W_N:

$$f_{W_N}(w_N) = N[F_X(w_N)]^{N-1} f_X(w_N) = N[1-\exp(-w_N)]^{N-1}\exp(-w_N)$$

$$F_{W_N}(w_N) = [F_X(w_N)]^N = [1-\exp(-w_N/2)]^N$$

$$\mu_{W_N} = \sum_{k=1}^{N} k^{-1}$$

$$\gamma + \ln N + (2N)^{-1} - \sum_{m=2}^{\infty} \frac{m^{-1}\int_0^1 x(1-x)(2-x)\ldots[(m-1)-x]\mathrm{d}x}{N(N+1)\ldots(N+m-1)}$$

$$\gamma + \ln N + \frac{1/2}{N} - \frac{1/12}{N(N+1)} - \frac{1/12}{N(N+1)(N+2)}$$

$$\frac{19/80}{N(N+1)(N+2)(N+3)} - \frac{9/20}{N(N+1)(N+2)(N+3)(N+4)}$$

$$\gamma + \ln(N+1) - \frac{1/2}{N+1} - \frac{1/12}{(N+1)^2}$$

$$\sigma^2_{W_N} = \sum_{k=1}^{N} k^{-2}$$

$$\frac{\pi^2}{6} - \frac{1}{N+1} \quad \frac{1/2}{} - \frac{1/6}{}$$

[34] Expressions (34) and (35) are due to [45].

where $\gamma \triangleq 0.57722\ldots$ is the Euler constant.

Pdf, cdf, mean, variance of mean-normalized minimum energy density U_N:

$$f_{U_N}(u_N) = N[1-F_X(u_N)]^{N-1} f_X(u_N) = (N/2)\exp(-Nu_N/2) \quad (36)$$

$$F_{U_N}(u_N) = 1-[1-F_X(u_N)]^N = 1-\exp(-Nu_N/2) \quad (37)$$

$$\mu_{U_N} = 2/N \quad (38)$$

$$\sigma^2_{U_N} = 4/N^2 \quad (39)$$

A.2 Energy density for total field

Pdf, cdf, mean, variance, coefficient of variation of mean-normalized field X (χ^2_6 distribution):

$$f_X(x) = (x^2/16)\exp(-x/2)$$

$$F_X(x) = 1-(1+x/2+x^2/8)\exp(-x/2) \quad (41)$$

$$\mu_X = 6 \quad (42)$$

$$\sigma^2_X = 12 \quad (43)$$

$$\nu_X = 1/\sqrt{3} = 0.577350$$

Pdf, cdf, mean, variance of mean-normalized maximum field W_N:

$$f_{W_N}(w_N) = (Nw_N^2/16)\,[1-(1+w_N/2+w_N^2/8)\exp(-w_N/2)]^{N-1}\exp(-w_N/2) \quad (45)$$

$$F_{W_N}(w_N) = [1-(1+w_N/2+w_N^2/8)\exp(-w_N/2)]^N \quad (46)$$

$$\mu_{W_N} \approx F^{-1}_{W_N}(1/2) \approx \left[6(1/2)^{1/N}\right]^{1/3} \quad (N, w_N \gg 1) \quad (47)$$

Pdf, cdf, mean, variance of mean-normalized minimum field U_N:

$$f_{U_N}(u_N) = (Nu_N^2/2)\exp(-Nu_N/2)\left[\frac{1+u_N/2+u_N^2/8}{8}\right]^{N-1}$$

$$F_{U_N}(u_N) = 1-[(1+u_N/2+u_N^2/8)\exp(-u_N/2)]^N$$

$$\mu_{U_N} = \int_0^{+\infty} \frac{Nu_N^3}{2\cdot 8^{N-1}}\exp(-Nu_N/2)\left(1+u_N/2+u_N^2/8\right)^{N-1} \mathrm{d}u_N$$

$$\sum_{k=0}^{N-1}\sum_{l=0}^{N-k-1} \mathrm{C}^k_{N-1}\,\mathrm{C}^l_{N-k-1}\,2^{-(3N+3k+l-2)}N\int_0^{+\infty} u_N^{2k+l+3}\exp(-Nu_N/2)\mathrm{d}u_N$$

$$\sum_{k=0}^{N-1}\sum_{l=0}^{N-k-1} \mathrm{C}^k_{N-1}\,\mathrm{C}^l_{N-k-1}\,\frac{(2k+l+3)!}{2^{3N+k-5}\,N^{2k+l+2}}$$

$$\sigma^2_{U_N} = \left[\sum_{k=0}^{N-1}\sum_{l=0}^{N-k-1} \mathrm{C}^k_{N-1}\,\mathrm{C}^l_{N-k-1}\,\frac{(2k+l+3)!}{2^{3N+k-5}\,N^{2k+l+2}}\right]^2$$
$$\sum_{k=0}^{N-1}\sum_{l=0}^{N-k-1} \mathrm{C}^k_{N-1}\,\mathrm{C}^l_{N-k-1}\,\frac{(2k+l+4)!}{2^{3N+k-6}\,N^{2k+l+3}}$$

A.3 Field strength for single field component

Pdf, mean, variance, coefficient of variation of mean-normalized field X (χ_2 distribution):

$$f_X(x) = x\exp(-x^2/2) \quad (52)$$
$$F_X(x) = 1-\exp(-x^2/2) \quad (53)$$
$$\mu_X = \sqrt{\pi/2} \approx 1.253314\ldots \quad (54)$$
$$\sigma^2_X = 2-(\pi/2) \approx 0.429203\ldots \quad (55)$$
$$\nu_X = \sqrt{(4/\pi)-1} \approx 0.522723\ldots \quad (56)$$

Pdf, mean, variance, coefficient of variation of mean-normalized maximum field W_N:

$$f_{W_N}(w_N) = N\frac{\pi}{2}w_N[1-\exp(-w_N^2/2)]^{N-1}\exp(-w_N^2/2)$$
$$\mu_{W_N} = N\sum_{k=0}^{N-1}\frac{(-1)^k\,\mathrm{C}^k_{N-1}}{(k+1)^{3/2}}$$
$$\approx F^{-1}_{W_N}(1/2) = \sqrt{(4/\pi)\ln\left[1-(1/2)^{1/N}\right]^{-1}}$$
$$\sigma^2_{W_N} \quad (4/\pi)\sum_{k=1}^{N}k^{-2} - \mu^2_{W_N}(w_N)$$
$$\approx \frac{2\pi}{3} - \frac{4}{\pi}\ln[1-(1/2)^{1/N}]^{-1} - \frac{4/\pi}{N+1} - \frac{2/\pi}{(N+1)^2}$$

Pdf, cdf, mean, variance of mean-normalized minimum field strength U_N:

$$f_{U_N}(u_N) = N u_N \exp[-N u_N^2/2] \quad (60)$$
$$F_{U_N}(u_N) = 1-\exp[-N u_N^2/2] \quad (61)$$
$$\mu_{U_N} = \sqrt{\pi/(2N)} \quad (62)$$
$$\sigma^2_{U_N} = (2-\pi/2)/N$$

A.4 Field strength for total field

Pdf, mean, variance, coefficient of variation of mean-normalized field X (χ_6 distribution):

$$f_X(x) = (x^5/8)\exp(-x^2/2)$$
$$\mu_X = 15\sqrt{2\pi}/16 \approx 2.349964\ldots$$

$$\sigma_X^2 = (1536 - 450\pi)/256 \approx 0.477669\ldots \quad (66)$$

$$\nu_X = \sqrt{1536/(450\pi) - 1} \approx 0.294100\ldots \quad (67)$$

Pdf, mean, variance, coefficient of variation of mean-normalized maximum field W_N:

$$f_{W_N}(w_N) = C\,(N/8)\mu_X^6 w_N^5 \exp[-(\mu_X w_N)^2/2] \cdot \left\{1 - \left[1 + (\mu_X w_N)^2/2 + (\mu_X w_N)^4/16\right] \exp[-(\mu_X w_N)^2/2]\right\}^{N-1} \quad (68)$$

μ_{W_N} and σ_{W_N} are best calculated through numerical integration. A reasonable approximation for μ_{W_N} is given by the point of inflexion of the factor between curly brackets in Eqn (68) as a function of w_N, raised to its $(N-1)$th power and divided by μ_X. Alternatively, the mode of the distribution may be used as an approximation for μ_{W_N}.

It may be expected that the square root of the max-to-mean power density can serve as a good approximation for the estimated field strength. In doing so, however, the true value appears to be systematically underestimated.

B Low-cost conversion of anechoic chambers into reverberation chambers

One of the prime advantages of a mode-stirred or mode-tuned reverberation chamber as an EMC test facility, in comparison with open-area sites, full-size or compact (semi-)anechoic chambers, etc. is its low cost in manufacturing, installation and operation. It may therefore seem irrational to search for ways in which to generate reverberant fields by starting from an expensive anechoic or semi-anechoic enclosure. However, anechoic chambers are well-established and therefore often already in place in a test laboratory. One may wish to convert them, in an easily reversible manner if possible, into a reverberation facility. Such conversion not only saves on the cost of building an extra facility, but may also be inevitable, e.g. because of laboratory space or site limitations. Secondly, reverberation chambers do offer a more stringent test capability with respect to random incidence [30], so the conversion gives the user the benefit of an additional test capability.

The possibilities for conversion are restricted by the absorber lining of the room, which one generally prefers not to remove, thus (a) making high-field strength generation and testing hazardous or impossible and (b) preventing wall reflections which assist in setting up a random field in a dedicated reverberation chamber.

One way of generating a random field that mimics a reveberant field is by using a set of *incoherent* sources (e.g. noise sources) inside the anechoic chamber, distributed at differentlocations across the chamber. The superposition of their fields at the test location will therefore also be incoherent. For example, three dipole or horn antennas (or pairs thereof), placed equidistantly and in mutually orthogonal positions to the EUT (possibly on opposite sides of it for each pair, if bidirectionality of propagation is required for the testing) and with mutually orthogonal directions of polarization will generate a quasi-random field in any three mutually perpendicular directions. Each antenna is driven by a separate[35] noise source, contributing to a total field that is *locally* reverberant. One could also consider a set of mutually perpendicular incoherent antennas combined and located into a single location ('concentrated isotropic source'). The use of a single noise source, well-known in acoustic reverberation practice, has recently been suggested and used in EM reverberation chambers to create or enhance a stochastic cavity field [29].

Although the generation of random polarization and field isotropy (polarization uniformity) can be done using a small number of sources, the level of field homogeneity (spatial uniformity) and illumination isotropy (k-uniformity) is strongly dependent on the number of sources used, because these fields exhibit a r^{-1}-dependence. For small EUTs it may be sufficient to use a limited

[35]Driving all antennas by a single noise source would make the field coherent.

number of sources. It is well worth noting that the thus obtained EM field can only be partially reverberant (incoherent), because mutually orthogonal components of the electric field and magnetic field will remain correlated, unlike in true reverberation fields [46]. However, for EUTs which predominantly respond to either E or H, this should not pose a real problem as far as the generation of test conditions is concerned.

In estimating the effect of room absorption on the reverberation performance, one notes the analogy with a damped harmonic oscillator excited by white noise. Calculation shows that the normalized spectral bandwidth of this system will *increase* with increasing absorption.

C On increasing mode density at low frequencies

In [34, Sec 4], we presented some results on mode count and mode density in arbitrarily shaped cavities. A key result is the expression for the mode density:

$$\frac{\mathrm{d}N}{\mathrm{d}f} = \frac{8\pi V}{c}\left(\frac{f}{c}\right)^2 + \left[-\frac{4}{3\pi c}\int\int_{S=\partial V}\frac{\mathrm{d}s}{\overline{\varrho}(s)} + (6\pi c)^{-1}\int_{L=\partial S}\frac{[\pi-\varphi(l)][\pi-5\varphi(l)]\mathrm{d}l}{\varphi(l)}\right] \qquad (69)$$

where $\mathrm{d}N$ is the number of modes within a frequency interval $\mathrm{d}f$, $\overline{\varrho}$ is the average radius of curvature of the incremental surface element $\mathrm{d}s$ and φ is the dihedral internal angle along the incremental edge $\mathrm{d}l$ of a cavity of volume V with total surface area S and total edge length L.

At low frequencies, the term between brackets in (69) is dominant and should be maximized. Because the surface integral appears with the negative sign, one requires a maximization of $\varrho(s)$. If all walls are flat ($\varrho = \infty$), the term vanishes. Unfortunately, this clashes with requirements for large intrinsic cavity ergodicity, which requires the use of curved panels. A good intrinsic reverberation chamber i.e. one that requires relatively little stirring to achieve an adequate randomized field, should be based on a judicious combination of straight and curved wall panels [34, Sec 3]. Such a combination forms the key to good chamber design[36].

We are therefore left with maximizing the line integral. By keeping its integrand constant but increasing the total edge length L, e.g. by adding of (flat) metal panels inside the room, the chamber quality factor and usable volume decrease. This should therefore be done with care. Alternatively, one can seek to maximize the integrand, per edge, so that the total edge length can be kept minimal. The integrand is shown as a function of φ in Fig 131. The worst effect on low-frequency mode density occurs for $\varphi = \pi/\sqrt{5}$ ($\sim$80.5deg), where the integrand reaches its minimum, $-(\sqrt{5}-1)^2\pi \approx -4.800$. The integrand increases without bound the smaller φ is taken, below the first zero at $\pi/5$ or, to a lesser extent, the larger φ is taken above the second zero at π. Hence one could design a room with a ground plan whose corners satisfy both conditions. Consider, for example the 'bow-tie' room, whose ground plane is made up of bow-tie segments as shown in Fig 132, where each internal angle is either smaller than $\pi/5$ or larger than π. In practice, the acute angles cannot be decreased without bound however, because their walls rapidly form a waveguide below cut-off, making the corner regions of the room not contributing and, hence, ineffective. Alternatively, in the conversion of existing rooms it may prove useful to line the walls of the room with many short 'sharp' cones or pyramids with small opening angles so that their surface forms external angles $2\pi - \varphi \approx 2\pi$, i.e internal with respect to the room. Care must

[36] This is a result of the fact that the reflection of waves off the curved sections causes longer ringing in comparison with cavities with flat walls only, hence the decay is longer. In cases where rounding of corners or edges of cavity walls is not desirable, one could consider making the paddle blades curved.

be taken not to decrease V significantly in this process, as this would affect the performance at higher frequencies adversely. Dihedral angles between 36deg and 180deg, particularly the 90deg angles of prismatic cavities, yield a negative integrand and reduce the mode density. They should therefore be avoided when possible. Angles in excess of 180deg, i.e. convex conducting scatterers inside the room, always assist in increasing the LF mode density.

D Use of nonreciprocal loading for enhanced reverberation performance

The number of independent boundary conditions that can be generated in the mode mixing process can be increased by making use of nonreciprocal devices. This can be understood as follows.

In a travelling-wave model of a reverberation chamber, the field at a given location is built up by a large number of component fields (wavelets) that are associated with waves propagating 'up' and 'down' along a multitude of directions. By influencing how these waves *propagate* through the chamber (rather than, or in combination with, influencing their *reflection* by changing the boundary conditions through stirring), one obtains a different total field each time the *propagation* conditions are changed. In the limit for an unlimited number of such changes being possible, one arrives again at a statistically reverberant field.
Propagation conditions can be changed, for example, by passing waves through a nonreciprocal medium, e.g. by placing an electromagnet[37] placed inside or around a chamber. By producing a constant magnetic flux $\underline{B}$ inside a subregion inside the cavity and reversing its polarity and/or changing its magnitude, this will affect those wavelets that travel across the $\underline{B}$-region. In fact, such $\underline{B}$ could be given arbitrary directions making the number of possibilities for generating new boundary conditions virtually unlimited (e.g using three mutually orthogonal electromagnets driven by a pseudo-random noise generator to yield a statistically and spatially random biasing $\underline{B}$-field). Reversing the polarity of the feeding current, translating/rotating the coil etc. produces the necessary changes. This method can be called *electronic nonreciprocal stirring.* Even for a constant $\underline{B}$ the reverberant field is expected to be superior to a chamber without a constant $\underline{B}$: two paths crossing the place of the electromagnet will be affected differently depending on the angle between the wave vector $\underline{k}_i$ and $\underline{B}$ upon incidence with the electromagnet. Even single modes will be affected differently, e.g. depending on whether a single 'bouncing ball' eigenstate travels parallel and anti-parallel to the direction of $\underline{B}$ the mode will be affected differently.
Regarding size and placement, the same criteria apply as for mechanical stirrers because the aim is to maximize its impact on the local field. Thus, the coil should be electrically large and placed where the unstirred field exhibits a high energy density.

In this respect, its is worth mentioning that it can be shown that in the high-frequency limit, the variance of the mode fluctuations with respect to the Weyl law for nonreciprocal systems is only half that for corresponding reciprocal systems [31, Eqns (57)–(58)]. In other words, nonreciprocal systems are expected to follow the Weyl law for mode density more closely than reciprocal sys-

[37] Whereas a ferrite-loaded coil will produce higher flux densities but with additional total chamber losses, a (large) air coil minimizes the introduction of chamber losses. For the same reason, the use of unbiased ferrites should be avoided.

tems. Of course, this reduction in fluctuations does not affect the wave-chaotic properties, which are entirely governed by the distribution of these fluctuations rather than by their magnitudes.

E Autofiltering

We note the following feature of CW overmoded cavities, which appears not to have been noted before and which may have a profound effect on the mode density, chamber characterization and practical reverberation performance.

It is commonly assumed that *all* modes within the BW_Q of the measurement system will take part[38] in the cavity excitation. For steady-state CW excitation, the cavity field must be periodic, by definition, being a eigensolution of the wave equation. However, in general the superposition of two or more eigenmodes with arbitrarily related eigenfrequencies will not yield a periodic signal. Only those modes whose frequencies are pairwise interrelated as a *rational*[39] fraction can coexist and hence contribute to a periodic total field (e.g. [23, Sec 1.2]). As a result, modes whose frequencies are interrelated as irrational numbers will be suppressed for steady-state excitation and will appear as 'missing' in the cavity spectrum. This phenomenon we call *autofiltering*. Apart from additional obscuring of resonances due to line broadening, such autofiltering may, at least in part, be responsible for apparently 'disappearing' resonances, which were already observed during early reverberation experiments with cubic overmoded microwave cavities [7] where measured resonance frequencies were compared with theoretically predicted values.

Furthermore, resonances that 'go missing' for steady-state CW excitation can re-emerge in the spectrum when the source is switched off. Due to mode coupling, the permissible (sustained) resonances couple energy to the resonances that are forbidden in CW regime which can now coexist with the 'allowed' resonances because of the absence of the periodic boundary-value conditions. This makes CW pulse decay yet more complex: not only does every 'allowed' resonance decay with its own decay time, it may also trigger modes that did not exist at the time when the excitation was switched on and couple energy to them.

In determining the autofiltered spectrum of n cavity modes, a total of $n(n-1)/2$ pairwise intercomparisons must be made. The retained permissible pairs must subsequently be weighted by the composite resonance characteristic. For example, the intercomparison with the center frequency will yield the largest weight in the overall spectrum. The difficulty is in deciding on whether two resonance frequencies are related as rational or irrational numbers, especially when the eigenvalue problem to the cavity in question has to be solved numerically, i.e. with finite numerical accuracy (see App F). Secondly, it has been known for some time that very small perturbations to an idealized geometry already produce substantial shifts in the observed resonance frequencies [7].

[38] after weighting in accordance with the system resonance characteristic, which acts as a transfer function for the individual modes [34, Secs A.1, A.3].

[39] Modes with irrationally related frequencies give rise to so-called almost-periodic signals [23, Sec 1.2].

Thus, the realistic cavity may already possess a eigenspectrum – 'before' autofiltering – that is different from the theoretical one, even when applying tight mechanical tolerances to the construction. Therefore, any CW excited cavity will autofilter the spectrum in its own very complex but deterministic manner.

The main practical conclusion of this phenomenon is that, in the highly overmoded case, a fixed fraction of modes is excluded from the stirring process for steady-state excitation, thus reducing the actual mode density compared to the theoretical density that would apply if all cavity modes within the Q-bandwidth were able to coexist.

Autofiltering is a feature of CW excitation, and does not necessarily exist for pulse (i.e. wideband) excitation. This may partially be responsible for the discrepancy observed in the measured Q-factor for CW evaluation as opposed to the value derived from pulse excitation [34, Tbl 5]. The latter potentially allows for more modes within the BW_Q to participate, hence for longer ringing and thus higher Q_c.

F Numerical eigenmode analysis of the stadium reverberation chamber

F.1 Cavity spectrum using MAFIA^{TM} electromagnetic simulator

In [34, App A] we used the spherical resonator, because of its integrability, as a first approximation in the estimation of the mode count, mode density, modal and composite quality factors, bandwidth per mode etc. of the stadium chamber. Since the stadium is nonintegrable, one has to take recourse to the wideband measurement of the cavity spectrum or to numerical computation for its eigenmode analysis. We performed a numerical simulation using the E-module of the finite-integration time-domain code MAFIA^{TM}. A noncorrugated aluminium 3D stadium with hemispheres of radius $R = 350$mm and a central circular cylindrical section of height $a = 175$mm was modelled. This closely resembles the chamber in our experimental set-up, with exception of the the wall mounted wave diffractors which are difficult to model accurately, and the octagonal cylindrical section which was modelled as a circular cylinder to avoid difficulties in joining the cylinder to the circular bases of the hemispheres. Fig 133 shows 112 resonances at the low end of the spectrum of the stadium obtained with MAFIA^{TM}. The resonances exhibit twofold degeneracy, within the user-defined numerical accuracy for the resonance frequencies (0.1%), as a result of the cylindrical symmetry. The first resonance is found to be at $f = 331.2$MHz. Tbl 20 lists the first six resonance frequencies. In Fig 134, the cumulative mode count obtained from the MAFIA^{TM} simulation is compared with the classical Weyl formula:

$$N = \frac{8\pi V}{3}\left(\frac{f}{c}\right)^3 + \text{constant}$$

where $V = (4\pi R^3/3) + (\pi R^2 a)$, and with the extended Weyl formula for the 3D stadium [34, Sec A.1]:

$$N = \frac{8\pi V}{3}\left(\frac{f}{c}\right)^3 - \frac{16R}{3}\left(\frac{f}{c}\right) + \text{constant} \qquad (71)$$

which shows improved accuracy at lower frequencies in comparison with (70). The arbitrary integration constant in these expressions was set to zero in both cases. Good agreement is found between the counted (simulated) resonances and the prediction by the extended Weyl formula.

Figs 135–146 show the spatial distributions of the total electric field and total magnetic flux density in three central plane cuts. The legend to the left of the plots indicates the mode number and field type (e.g. B_1 signifies the magnetic flux of the first (i.e. fundamental) mode). Figs 147–149 and 150–152 show the magnitude and direction of polarization of these electric and magnetic quantities at 2.5GHz and 8.2GHz in a cross-section of the cavity, respectively. From these

and more extensive simulations, an increase in frequency is found to cause the region of relative inhomogeneity to concentrate around the cylindrical axis. Perhaps surprisingly, the center region is at the greatest distance from the cavity wall, suggesting that maximum reverberation quality (field uniformity) should be expected in this region. That this is not the case is to be explained by the fact that the key to good mode-stirring is the principle of 'breaking symmetry', hence by measuring at locations away from the cavity symmetry axis.

Fundamental limitations exist in finding the complete spectrum of the stadium through numerical computation. The simulator uses a Cartesian mesh, and therefore approximates the curved walls of the hemispheres as staircased boundaries. Because of the EM boundary conditions, the numerically obtainable resonances are necessarily constrained by the step size of the staircase. As a result of the discretized geometry, the difference between two computed consecutive resonances cannot be smaller than one half wavelength that corresponds to the unit step of the staircase, on average. Hence the number of numerical resonances obtained after one simulation depends on the mesh size. Results obtained using 10,000 meshing elements take approximately 15h run time on a UNIX UltraSPARC–II (2×360MHz, 128MB) workstation for computing the first 112 eigenmodes. Decreasing the resolution of the mesh was found to reduce the number of modes significantly. The frequency of missing modes increases more rapidly as their frequency increases. Although in the high-frequency limit the mode count solely depends on the cavity volume (thus, in particular, being independent of the staircasing), according to the Weyl formula, the lower part of the spectrum does depend on the details of the geometry and its numerical implementation.

The module also allows for small losses of the cavity walls to be incorporated, yielding numerical estimation of dissipated power and quality factors for each individual mode based on a perturbation analysis. The thus obtained Q-factors for the first six modes are shown in Tbl 20.

F.2 Optimization of stadium parameter for maximum Kholmogorov entropy

Numerical analysis of a 2D stadium has been performed earlier [17] in which the maximum Lyapounov number λ was computed as a function of the stadium parameter $\gamma = a/R$, as a measure for EM chaos. It was found that λ_{max} rapidly increases as γ increases from 0 to 1, reaching a maximum $\lambda_{max} \approx 0.43$ at $\gamma = 1$, and then slowly decreases as γ is further increased beyond 1. For our set-up, in which $\gamma = 0.25$, we have $\lambda_{max} \approx 0.32$. No numerical optimization of γ for our 3D chamber was performed at this stage.

G Local averaging

G.1 Introduction

Fundamental uncertainties exists in the measurement of statistical properties of reverberant fields. In the spatial domain, the uncertainties are caused by the nonzero size of the aperture of a field or power sensor. In the temporal (i.e. stir) domain, the uncertainties are a result of the nonzero width of the sampling interval (for mode stirring) or nonzero stirrer step size (for mode tuning) [34, Sec 12.2]. These finite widths give rise to local spatial and temporal averaging, respectively. Quantifying the extent of local averaging is crucial to allow for a correct interpretation of EMC test results and to accurately predict chamber characteristics such as maximum-to-mean ratio for the field, normalized spectral bandwidth, threshold crossing frequency, excursion lengths, etc. in the chamber calibration.

Local averaging smoothens 'events' in stirrer data, i.e. it rarefies the occurrence of local maxima and minima for the field or energy density at specific spatial locations and/or stirrer positions. This results in those EUTs which cannot (or may not be required to) withstand 'widely' spread (i.e. spatially 'large' scale) and/or 'long' term 'high' exposure to be more likely to fail the test. On the other hand, EUTs which cannot (or may not need) withstand 'strongly' localized and/or 'short' term (i.e. pulsed) 'high' intensity exposure may inadvertently pass the test because of local averaging effects. Neither situation is desirable and thus averaging should be either minimized so as to conform to the test specification or, at least, properly quantified and accounted for.

Many EMC test articles can be considered as EUTs with internal spatial averaging, such as those in which conduction currents flow along at least one dimension (e.g. printed circuit boards). (The averaging is generally three-dimensional. We will limit our discussion here to 1D local averaging, although the concepts and methodology are readily extendible to vector processes.) By contrast, point-wise reacting test articles (e.g. conduction-free dielectric material specimens) do not exhibit spatial averaging effects.

Similar considerations regarding local averaging apply to the stir domain. If the chosen stirrer step is too large (in mode-tuned operation) of if the sampling rate is too large (in mode-tuned operation), such that the number of data points M is well below the number of 'equivalent', 'independent' stirrer positions, N, then the tuner sweep will appear smoothened in comparison with the tuner sweep obtained for $M = N$.

G.2 Measures of local averaging in spatial and stir domain

G.2.1 Variance function

G.2.1.1 General local averaging Local averaging of a given process $X(t)$ can be considered as a partitioning of data in intervals of width $\mathcal{T}$. Thus, a mapping of $X(t)$ onto the local averaged process $X_{\mathcal{T}}(t)$ can be defined. Consequently, local averaging reduces the sample variance $\sigma_{\mathcal{T}}^2$ in comparison with its value σ_0^2 for the original (nonpartitioned, point-wise) data[40]. The effect can be quantified by introducing the variance function $\gamma_{\mathcal{T}}$ for a spatial or temporal window of width $\mathcal{T}$ [21, Sec 5], [34, Sec 12.6]:

$$\gamma_{\mathcal{T}} = \frac{\mathrm{Var}[\mathcal{T}^{-1}\int_{t-\mathcal{T}/2}^{t+\mathcal{T}/2} X(u)\,\mathrm{d}u]}{\mathrm{Var}[X(t)]} = \frac{2}{\mathcal{T}}\int_0^{\mathcal{T}}\left[1-\frac{\tau}{\mathcal{T}}\right]\rho(\tau)\,\mathrm{d}\tau \tag{72}$$

and may hence serve as an alternative measure for the autocorrelation. One recognizes in the second equality in (72) a Cesàro integral, as encountered in the theory of ergodicity. This second equality only holds provided $x(t)$ is stationary at least in the wide sense. Note that $\gamma_{\mathcal{T}} = 1$ if $\rho(\tau) = 1$ for all τ, i.e. for a deterministic field $X(t)$ ($\sigma_X = \sigma_{X_{\mathcal{T}}} = 0$).

A proper, possibly composite correlation model for general reverberation chambers must take account of the characteristics of the short-to-medium-term reverberation process (exponential decay of energy density with time) as well as the long-term reverberation (exponential energy decay or decay inversely proportional with time when the absorption is nonuniform[41]). The use of the ensemble acf is recommended over the sample acf, because of the large variance that exists for the latter.

The coefficient of variation, $\zeta_{\mathcal{T}} = \sigma_{\mathcal{T}}/\mu$, scales in accordance with the standard deviation, because the mean is not influenced by local averaging. Hence $\sqrt{\gamma_{\mathcal{T}}}$ is at the same time a measure of the change in $\zeta_{\mathcal{T}}$ for the process when subjected to local averaging. Therefore, a measured value for $\zeta_{\mathcal{T}}$ which is significantly lower than its theoretical value may be due to a considerable level of local averaging in the measured process, among other possible origins e.g. understirring [33].

G.2.1.2 Variance function for stirrer step In good approximation, an on average exponential energy decay in the spectral stir (i.e. Fourier ω-) domain was found in [34, Sec 12.2] for the

[40] We will sometimes denote σ_0^2 simply by $sigma^2$ in the following.

[41] The latter only contributes in intrinsically chaotic (nonintegrable) chambers as observed in [26] and [34, Sec 10.2.2].

reverberation process[42]: $g(\omega) = \beta \exp(-\beta\omega)$ with $\omega > 0$. On application of the Wiener-Khinchine theorem, the associated stirrer autocorrelation function for the energy density is then obtained after inverse Fourier cosine [43] transformation as [40]:

$$\rho(\tau) = (\pi/2)\, \mathcal{F}_C^{-1}[g(\omega)](\tau) = \left[1 + (\tau/\beta)^2\right]^{-1}$$

Substitution of (73) into (72) yields:

$$\gamma_{\mathcal{T}} = \frac{2\tan^{-1}(\mathcal{T}/\beta)}{\mathcal{T}/\beta} - \frac{\ln\left[1 + (\mathcal{T}/\beta)^2\right]}{(\mathcal{T}/\beta)^2}, \qquad (74)$$

which is verified to approach zero in the limit $\mathcal{T} \to \infty$, as required for cavity ergodicity in the mean, and is asymptotically proportional to $\mathcal{T}^{-1}$. The variation of $\gamma_{\mathcal{T}}$ as a function of $\mathcal{T}/\beta$ as given by (74) is shown in Fig 153. For very small and very large $\mathcal{T}/\beta$, the effect of changes in $\mathcal{T}/\beta$ on the variance becomes negligible on a linear scale for $\gamma_{\mathcal{T}}$.

The variance function enables one to estimate the reduction in the variance for the stirrer data as a function of the width of the averaging interval. Especially valuable is the inverse procedure (*inverse local averaging*), in which estimates for idealized point measurements are obtained from measurements over small but finite widths of the sensor aperture and stirrer step size. This enables stirrer data obtained using different stirring methods and/or stirrer step sizes and/or sensors to be compared on an equal footing. In addition, it yields more accurate estimates for the statistics of the random field to which the EUT is being exposed.

For our earlier horn antenna measurements at 8.2GHz with $\mathcal{T} = 2.60$mrad and $\beta = 0.0178$ [34, Tbl 7], (74) yields $\gamma_{\mathcal{T}} = 0.996$, i.e. $\sigma_{\mathcal{T}} = 0.998\sigma_0$. The present electric field probe measurements at this frequency with $\mathcal{T} = 4.33$mrad and $\beta_x = 0.0127$, $\beta_y = 0.055$ and $\beta_z = 0.049$ yield $\gamma_{\mathcal{T}_x} = 0.981$, $\gamma_{\mathcal{T}_y} = 0.999$ and $\gamma_{\mathcal{T}_z} = 0.999$, i.e. $\sigma_{\mathcal{T}_x} = 0.990\sigma_{0x}$, $\sigma_{\mathcal{T}_y} = 0.999\sigma_{0y}$ and $\sigma_{\mathcal{T}_z} = 0.999\sigma_{0z}$, respectively. Clearly, in this example, the effect of finite stirrer step size is negligible in both cases as compared to the point process, i.e. one with vanishingly small step size.

To understand the effect of data decimation for 'small' stirrer steps, we can expand (74) for $\mathcal{T} = m\mathcal{T}'$, yielding:

$$\gamma_{\mathcal{T}'} = 1 - \frac{(m\mathcal{T}'/\beta)^2}{6} \qquad (m\mathcal{T}'/\beta \ll 1$$

[42] Compared to [34, Sec 12.2] we here use a different normalization, i.e. such that $\int_0^\infty g(\omega)\mathrm{d}\omega = 1$.

[43] When using the two-sided normalized spectral density $s(\omega)$, the inverse Fourier transformation should be taken: $\rho(\tau) = (2\pi)\mathcal{F}^{-1}[s(\omega)](\tau)$. Since the acf and psdf are even functions of their arguments, the inverse Fourier cosine transformation can in this case be rescaled to an inverse Fourier transform.

showing a quadratic dependence on the decimation factor m for small averaging intervals. Therefore, upon local averaging the standard deviation of the stirring process decreases from unity, to first approximation, as $\sqrt{1-(m\mathcal{T}'/\beta)^2/6} \approx 1-(m\mathcal{T}'/\beta)^2/12$.

For the magnitude of the total field, a rigorous expression for $\rho(\tau)$ is as yet lacking. However, we may again use (73) and, hence, (74) for all practical purposes (Fig 155), because the differences which exist between $\rho_{|E_t|}(\tau)$ and $\rho_{|E_t|^2}(\tau)$ appear to be of second order, across the entire range for τ, and are decreasing for increasing frequency (compare measured values of $\gamma_{\mathcal{T}}$ for $|E_t$ and $|E_t|^2$ in Figs 9 and 74).

G.2.1.3 Variance function for sensor aperture Consider the spatial acf for the energy density (squared magnitude) associated with the total electric or magnetic field [50]:

$$\rho(\tau) = \mathrm{sinc}^2(k\tau$$

with $k = 2\pi/\lambda$. Substitution of (76) into (72) yields:

$$\gamma_{\mathcal{T}} = \frac{2\,\mathrm{Si}(2k\mathcal{T})}{k\mathcal{T}} - 2\,\mathrm{sinc}^2(k\mathcal{T}) - \frac{\ln(2k\mathcal{T})}{(k\mathcal{T})^2} - \frac{\gamma}{(k\mathcal{T})^2} - \frac{\mathrm{Ci}(2k\mathcal{T})}{(k\mathcal{T})^2}$$

where $\mathrm{Si}(x) = \int_0^x \mathrm{sinc}(u)\mathrm{d}u$ and $\mathrm{Ci}(x) = \int_x^\infty \mathrm{cosc}(u)\mathrm{d}u$ with $\mathrm{sinc}(u) = \sin(u)/u$ and $\mathrm{cosc}(u) = \cos(u)/u$ are the standard sine and cosine integral functions, respectively [32, Sec 35], and where $\gamma = 0.57722\ldots$ is the Euler constant. In deriving (77), use was made of the results:

$$\int \mathrm{sinc}^2(u)\mathrm{d}u = \mathrm{Si}(2u) + \frac{\cos(2u)-1}{2u}$$

$$\int u\,\mathrm{sinc}^2(u)\mathrm{d}u = \frac{\mathrm{Ci}(2u)+\ln(u)}{2}$$

Fig 154 shows $\gamma_{\mathcal{T}}$ as a function of $k\mathcal{T}$. Compared to $\gamma_{\mathcal{T}}$ for local stir averaging in Fig 153, $\gamma_{\mathcal{T}}$ is now found to be marginally larger[44] for intermediate values of the normalized interval width $k\mathcal{T}$ replacing $\mathcal{T}/\beta$ (see in particular the insets to Figs 153 and 154), but the asymptotics are identical

[44]The question may arise as to whether this difference does not violate the ergodicity of the mean, which can be loosely stated as stir averages and spatial averages being equal for almost all (i.e. except for a set of zero weight) cavity field configurations. Note, however, that this condition should only be met as an asymptotic scalar solution (geometrical optics), for we do not claim microwave cavities at finite frequencies to be perfectly ergodic. We do note, however, that the curves in Figs 153 and 154 reach their asymptotics in the same manner, i.e. they coincide for $k\mathcal{T}, \mathcal{T}/\beta \to \infty$ and $k\mathcal{T}, \mathcal{T}/\beta \to 0$, which are the only two values for $k\mathcal{T}$ and $\mathcal{T}/\beta$ that can occur asymptotically. Therefore, ergodicity is not violated.

in both cases. Thus, for processes which are ergodic in their first- and second-order statistics, one can conceive local stirrer averaging over the stirrer 'arc' (in mode-tuning) or sampling width (in mode-stirring), $\mathcal{T}_{stir}$, with spectral parameter β as being nearly equivalent in the mean to local spatial averaging over a distance $\mathcal{T}_{spat} = \mathcal{T}_{stir}/(k\beta)$.

The variance function for spatial averaging can now be used to estimate the reduction in the variance for the stirrer data as a function of the width of the antenna aperture. For our earlier antenna measurements at 8.2GHz, we used a Narda–640 horn with aperture width $\mathcal{T} = 55$mm, i.e. $k\mathcal{T} = 9.446$. Then (77) yields[45] $\gamma_{\mathcal{T}} = 0.282$, i.e. $\sigma_{\mathcal{T}} = 0.531\sigma_0$. In contrast, the dipole elements of the electric field probe have aperture widths $\mathcal{T} = 3$mm ($k\mathcal{T} = 0.515$), yielding at the same frequency $\gamma_{\mathcal{T}} = 0.985$, i.e. $\sigma_{\mathcal{T}} = 0.993\sigma_0$. Clearly, for the energy density the local spatial averaging by the antenna has a markedly larger effect than the local stirrer step averaging.

For the magnitude of the total electric or magnetic field the spatial acf is, in analogy with the result for scalar (acoustic) random fields [4]:

$$\rho(\tau) = \mathrm{sinc}(k\tau)$$

resulting in the variance function

$$\gamma_{\mathcal{T}} = \frac{2\ \mathrm{Si}(k\mathcal{T})}{k\mathcal{T}} + \frac{2\left[\cos(k\mathcal{T}) - 1\right]}{(k\mathcal{T})^2}$$

which for small arguments $k\mathcal{T}$ shows again a quadratic variation:

$$\gamma_{\mathcal{T}} = 1 - \frac{(k\mathcal{T})^2}{36} + \qquad (k\mathcal{T} \ll 1)$$

whereas for large $k\mathcal{T}$:

$$\gamma_{\mathcal{T}} \approx 2\ \mathrm{Si}(k\mathcal{T})/(k\mathcal{T}) = \pi/(k\mathcal{T}) + \qquad (k\mathcal{T} \gg 1)$$

i.e. again approaching zero as $\mathcal{T}^{-1}$ The complete dependence of $\gamma_{\mathcal{T}}$ on $k\mathcal{T}$ for the total field is shown in .

In conclusion, the reduction in the measured standard deviation resulting from local spatial

[45]Here the acf for a Cartesian component should be used strictly. The present calculation only serves in getting an approximate value for $\gamma_{\mathcal{T}}$.

or stir averaging demonstrates the need to distinguish between chamber imperfections and measurement limitations when measuring statistical fields, as pointed out in Sec 1. The proposed procedure is thus to first eliminate the effect of local averaging, i.e. estimating σ_0 for the idealized point measurement from the measured σ_T and then compare σ_0 with the theoretical value for (physically) ideal reverberation.

A trivial but important remark is that for the correct application of the correction, $\rho(\tau)$ and γ_T must refer to the same field quantity, e.g. using the power acf for use with the variance on the received power etc.

G.2.2 Scale of fluctuation

G.2.2.1 General local averaging The scale of fluctuation is defined as $\theta_T \triangleq \lim_{T\to\infty}(T\gamma_T)$ which can be interpreted as a correlation distance.

G.2.2.2 Scale of fluctuation for stirrer step For the energy density and, approximately, for the magnitude of the total field in the stir domain, we obtain using (74):

$$\theta_T = \pi\beta$$

Since γ_T decays in inverse proportion to T for $T \to \infty$, the scale of fluctuation is to be understood as the rate of inverse linear decay of σ_T^2 under long-term averaging ($T \to \infty$, or more precisely $T \gg \theta_T$) with reference to the point value σ_0^2. The value of $\theta_T = \pi\beta/2$ represents the optimum stirrer sampling rate, in the sense of minimizing both the reconstruction error for the true (continuous) tuner sweep from measured sampled data and the sampling overhead. The ratio:

$$T/\theta_T = T/(\pi\beta)$$

which is approximately equal to γ_T^{-1} for sufficiently large T, can be interpreted as the 'equivalent' number of 'independent' observations in the sampling interval $[0, T]$ (see [21, Sec 5.1]). This can be compared with the estimate based on the '$|\rho^{-1}(e^{-1})|$'-criterion in the stir domain, which defines the equivalent number of independent samples N from the decimation factor m for which $\rho(\tau = m\Delta\tau) = e^{-1}$ as [40]:

$$N = \frac{M}{m} = \frac{T}{m\Delta\tau} = \frac{T}{\beta\sqrt{e-1}}$$

for $\rho(\tau)$ given by (73). Both estimates differ by no less than a factor $\sqrt{e-1}/\pi \approx 41.7\%$, for this correlation model!

G.2.2.3 Scale of fluctuation for sensor aperture Using (77), we obtain for the scale of spatial fluctuation of the energy density:

$$\theta_{\mathcal{T}} = \pi/k$$

The optimum spatial sampling width is $\theta_{\mathcal{T}}/2 = \lambda/4$, as can be expected by considering the spatial variation of the energy density of a narrowband process to exhibit a random periodicity with mean value $\lambda/2$. The equivalent number of independent samples for spatial sampling is then:

$$\mathcal{T}/\theta_{\mathcal{T}} = k\mathcal{T}/\pi$$

This estimate can again be compared to the value obtained for the $|\rho^{-1}(e^{-1})|$-criterion in the spatial domain, viz. the value $k\tau$ for which $\mathrm{sinc}^2(k\tau) = 1/e$, i.e. for $\tau \approx 1.645/k \approx \lambda/4$. The corresponding number of independent samples is then

$$N = \frac{M}{m} = \frac{\mathcal{T}}{m\Delta\tau} \approx \frac{k\mathcal{T}}{1.645}$$

which differs from the previous estimate by a factor $1.645/\pi \approx 52.4\%$.

For the total field, the scale of spatial fluctuation is the same as for the power density, (87), but it is to be noted that this asymptote is now reached more slowly ($\mathcal{T}\gamma_{\mathcal{T}} \sim \mathrm{Si}(k\mathcal{T})/k$) than for the power density ($\mathcal{T}\gamma_{\mathcal{T}} \sim \mathrm{Si}(2k\mathcal{T})/k$). The corresponding correlation length follows from $\rho(\tau) = \mathrm{sinc}(k\tau) \geq e^{-1}$ as $\tau \approx 2.20/k \approx \lambda/3$, which is slightly different from the above correlation length for power density. This is of course a result of choosing a nonzero value for the threshold level. As a consequence, the number of 'equivalent', 'independent' samples in the spatial domain will be slightly larger for power density measurements compared to the number for total field magnitude measurements. The corresponding number of independent samples is then:

$$N = \frac{M}{m} = \frac{\mathcal{T}}{m\Delta\tau} \approx \frac{k\mathcal{T}}{2.20}$$

which now differs from the previous estimate by a factor $2.20/\pi \approx 70.0\%$.

The dependency of $\sigma^2_{\mathcal{T}}$ on $\mathcal{T}$ poses the question of characterizing the uncertainty of the physical process in a manner which is independent of its measurement, i.e. of the value of $\mathcal{T}$. This can be done by defining the uncertainty density, $\sigma^2_0\theta_{\mathcal{T}}$, which is a quantity that does not depend on $\mathcal{T}$. It is thus recommended to express results for reverberation chambers in terms of this uncertainty density if abstraction is to made of the stirrer stepping or sampling and the antennas or field probes used.

G.2.3 Point–interval correlation functions for local averaging

G.2.3.1 General local averaging The variance function can be used to express the correlation coefficient $\varrho_{TT'}$ between local averages taken over two overlapping or disjoint intervals T and T' as [21, Sec 5.2]:

$$\varrho_{TT'} = \frac{\sum_{k=0}^{3}(-1)^k\, T_k^2\, \gamma_{T_k}}{2TT'\sqrt{\gamma_T\, \gamma_{T'}}}$$

where T_0, T_1, T_2 and T_3 are defined as the oriented distances between the end point of T and the starting point of T', between the starting point of T and the starting point of T', between the starting point of T and the end point of T', and between the end point of T and the end point of T', respectively. As an important limiting case, we can consider the correlation coefficient ϱ_{T0} between the point value at the center of the sampling interval ($|T_k| = T/2$) and the local average across the full width T. Such a point–interval correlation function quantifies the representativity of an interval measurement for the ideal point value at the center of this interval, as in a realistic situation of a measurement of a random field across a finite interval. This center point can be considered as an interval T' of vanishingly small width, inside T and at equal distances from the start point and end point of T. One thus obtains from (91) for $T' \to 0$, after calculation:

$$\varrho_{T0} = \gamma_{T/2} + \frac{T}{4}\left(\frac{\mathrm{d}\gamma_T}{\mathrm{d}T}\right)_{T/2}$$

G.2.3.2 Point–interval correlation function in stir domain For this case, (92) is the correlation between a stirrer point measurement, i.e. using a vanishingly small stirrer step (mode-tuning) or sampling time (mode-stirring), and a realistic stirrer interval measurement, for a finite stirrer step (mode-tuning) or sampling width and rate of the field or power sensor (mode-stirring), caused by the nonzero sampling time width for the field or power sensor. Equation (92) reduces with (74) to:

$$\varrho_{T0} = \frac{\tan^{-1}[T/(2\beta)]}{\quad}$$

which is shown as a function of T/β in Fig 157. For $T/\beta \ll 1$, $\tan^{-1}[T/(2\beta)]/[T/(2\beta)] = 1 - [T/(2\beta)]^2/3 + \ldots$. For $T/\beta \gg 1$, the expression reduces to $\varrho_{T0} \sim \pi\beta/T$. In the limit $T \to 0$, we retrieve perfect correlation between two coincident points ($\varrho_{00} \to 1$). This result again underlines that the correlation between the idealized point value and the actual distributed measurement value weakens as local averaging increases.

G.2.3.3 Point–interval correlation function in spatial domain This function expresses the representativity of measurements using field or power sensors made finite aperture size with respect to the ideal point values which hold at their aperture center. From (77) and (92), we obtain for the measured energy density:

$$\varrho_{\mathcal{T}0} = \frac{2\ \mathrm{Si}(k\mathcal{T})}{k\mathcal{T}} + \frac{2\left[\cos(k\mathcal{T}) - 1\right]}{(k\mathcal{T})^2}$$

which is shown in Fig 157. As this is equivalent to (81), the approximations (82) and (83) equally apply.

For the magnitude of the total field, the correlation function is, with (81):

$$\varrho_{\mathcal{T}0} = \frac{\mathrm{Si}(k\mathcal{T}/2)}{k\mathcal{T}/2}$$

which is shown in Fig 157 and approximated for small apertures ($k\mathcal{T} \ll 1$) as $1 - (k\mathcal{T})^2/72$.

G.3 Spectral measures for stirring performance under local averaging

G.3.1 First normalized spectral bandwidth

G.3.1.1 General first normalized spectral bandwidth We now show that the first as well as second normalized spectral bandwidths on average *increase* upon increasing local averaging. The first normalized spectral bandwidth $\delta_{\mathcal{T}}$ is defined as:

$$\delta_{\mathcal{T}} \triangleq \sqrt{1 - \frac{\lambda_{1\mathcal{T}}^2}{\lambda_{0\mathcal{T}}\lambda_{2\mathcal{T}}}} \tag{96}$$

$$\sqrt{1 - \frac{\left\{\sigma_0^2 \int_0^\infty \left[\omega\ g(\omega)\ \mathrm{sinc}^2(\omega\mathcal{T}/2)\ \right] \mathrm{d}\omega\right\}^2}{\left\{\sigma_0^2 \int_0^\infty \left[g(\omega)\ \mathrm{sinc}^2(\omega\mathcal{T}/2)\right]\mathrm{d}\omega\right\}\left\{\sigma_0^2 \int_0^\infty \left[\omega^2\ g(\omega)\ \mathrm{sinc}^2(\omega\mathcal{T}/2)\right]\mathrm{d}\omega\right\}}} \tag{97}$$

G.3.1.2 First normalized spectral bandwidth for stirrer step With $g(\omega) = \beta\exp(-\beta\omega)$ and using [27, Eqn (3.946.2)]:

$$\int_0^\infty \frac{\exp(-px)\sin^{2m}(ax)}{x}\mathrm{d}x =$$

$$-1)^{(m+1)}2^{-2m}\sum_{k=0}^{m}(-1)^k \mathrm{C}_{2m}^k \ln\left[p^2 + (2m-2k)^2a^2\right] - 2^{-2m}\mathrm{C}_{2m}^m \ln(p),$$

using [27, Eqn (3.895.1)]:

$$\int_0^\infty \exp(-px)\sin^2(x)\mathrm{d}x = \frac{2}{p(p^2+4)} \tag{99}$$

and also using [27, Eqn (3.947.2)]:

$$\int_0^\infty \frac{\exp(-px)\sin^2(ax)}{x^2}\mathrm{d}x = a\,\tan^{-1}(2a/p) + (p/4)\ln[p^2/(p^2+4a^2)], \tag{100}$$

we obtain after calculation

$$\lambda_{0\mathcal{T}} = \frac{\beta^2\sigma_0^2}{\mathcal{T}^2}\left\{2\left(\frac{\mathcal{T}}{\beta}\right)\tan^{-1}\left[\frac{\mathcal{T}}{\beta}\right] - \ln\left[1+\left(\frac{\mathcal{T}}{\beta}\right)^2\right]\right\} = \sigma_0^2\gamma_{\mathcal{T}} = \sigma_{\mathcal{T}}^2 \tag{101}$$

$$\lambda_{1\mathcal{T}} = \frac{\beta\sigma_0^2}{\mathcal{T}^2}\ln\left[1+\left(\frac{\mathcal{T}}{\beta}\right)^2\right] \tag{102}$$

$$\lambda_{2\mathcal{T}} = \frac{2\sigma_0^2}{\mathcal{T}^2}\left[1+\left(\frac{\beta}{\mathcal{T}}\right)^2\right]^{-1} \tag{103}$$

hence

$$\delta_{\mathcal{T}} = \sqrt{1 - \frac{\left[1\right]}{2\left\{2\left(\frac{\mathcal{T}}{\beta}\right)\tan^{-1}\left[\frac{\mathcal{T}}{\beta}\right] - \ln\left[1+\left(\frac{\mathcal{T}}{\beta}\right)^2\right]\right\}}} \tag{104}$$

An approximation, valid for $\mathcal{T} \gg \theta_{\mathcal{T}}$ i.e. $\mathcal{T}/\beta \gg 1$ and arbitrary $g(\omega)$, is:

$$\delta_{\mathcal{T}} \approx \sqrt{1 - \frac{2}{\pi^2}\frac{\theta_{\mathcal{T}}}{\mathcal{T}}\ln^2\left[\frac{5.26\mathcal{T}}{\theta_{\mathcal{T}}}\right]} = \sqrt{1 - \frac{2}{\pi}\left(\frac{\beta}{\mathcal{T}}\right)\ln^2\left[\frac{5.26}{\pi}\left(\frac{\mathcal{T}}{\beta}\right)\right]} \tag{105}$$

G.3.1.3 First normalized spectral bandwidth for sensor aperture First the spatial spectral density function is obtained by Fourier transformation of (76). Since:

$$\begin{aligned}\int \mathrm{sinc}^2(ku)\cos(\Omega u)\mathrm{d}u \;=\; & \frac{-\Omega\left[\mathrm{cosc}(\Omega u) + \mathrm{Si}(\Omega u)\right]}{2k^2} \\ & + \frac{(2k+\Omega)\left\{\mathrm{cosc}[(2k+\Omega)u] + \mathrm{Si}[(2k+\Omega)u]\right\}}{4k^2} \\ & + \frac{(2k-\Omega)\left\{\mathrm{cosc}[(2k-\Omega)u] + \mathrm{Si}[(2k-\Omega)u]\right\}}{}\end{aligned}$$

where Ω is the Fourier, i.e. spatial spectral variable, we obtain

$$g(\Omega) = \frac{\pi}{2}\int_0^\infty \mathrm{sinc}^2(ku)\cos(\Omega u)\mathrm{d}u = \begin{cases} [1-\Omega/(2k)]/k, & 0 \le \Omega \le 2k \\ 0, & \Omega > 2k \end{cases}$$

as the spatial spectral density function. Then, using (78) and (79) and the fact that [32, Eqn (35.15)]:

$$\lim_{u\to 0}[\mathrm{Ci}(2u)+\ln(u)] = -\gamma - \ln(2) \tag{108}$$

we obtain:

$$\lambda_{0T} = \frac{2\sigma_0^2}{kT}\left[\mathrm{Si}(2kT) - \frac{2\sin^2(kT)+\gamma+\ln(2kT)+\mathrm{Ci}(2kT)}{2kT}\right] = \sigma_0^2\gamma_T = \sigma_T^2$$

$$\lambda_{1T} = \frac{2\sigma_0^2}{kT^2}[\mathrm{sinc}(2kT) - 1 + \gamma + \ln(2kT) + \mathrm{Ci}(2kT)]$$

$$\lambda_{2T} = \frac{2\sigma_0^2}{T^2}\left[1 - \mathrm{sinc}^2(kT)\right] \tag{111}$$

These expressions are to be substituted into (96), but do not lead to any major simplification for the resulting expression for δ_T. For $kT \to 0$, δ_T now approaches γ. Increasing T is seen to have the same effect on δ_T as increasing k, viz. an apparent whitening of the process.

G.3.2 Second normalized spectral bandwidth

G.3.2.1 General second normalized spectral bandwidth The second normalized spectral bandwidth is defined as:

$$\epsilon_T \triangleq \sqrt{1-\frac{\lambda_{2T}^2}{\lambda_{0T}\lambda_{4T}}} \tag{112}$$

$$\sqrt{1-\frac{\left[\sigma_0^2\int_0^\infty \omega^2 g(\omega)\,\mathrm{sinc}^2(\omega T/2)\,\mathrm{d}\omega\right]^2}{\left[\sigma_0^2\int_0^\infty g(\omega)\,\mathrm{sinc}^2(\omega T/2)\,\mathrm{d}\omega\right]\left[\sigma_0^2\int_0^\infty \omega^4\, g(\omega)\,\mathrm{sinc}^2(\omega T/2)\,\mathrm{d}\omega\right]}}$$

G.3.2.2 Second normalized spectral domain for stirrer step With $g(\omega) = \beta \exp(-\beta\omega)$:

$$\epsilon_{\mathcal{T}} = \sqrt{1 - \frac{\left[\sigma_0^2 \int_0^\infty \omega^2\ \beta \exp(-\beta\omega)\ \mathrm{sinc}^2(\omega\mathcal{T}/2)\ \mathrm{d}\omega\right]^2}{\left[\sigma_0^2 \int_0^\infty \beta \exp(-\beta\omega)\ \mathrm{sinc}^2(\omega\mathcal{T}/2)\ \mathrm{d}\omega\right]\left[\sigma_0^2 \int_0^\infty \omega^4\ \beta \exp(-\beta\omega)\ \mathrm{sinc}^2(\omega\mathcal{T}/2)\ \mathrm{d}\omega\right]}} \quad (114)$$

can be calculated. Using [27, Eqn (3.381.4)]:

$$\int_0^\infty x^{a-1} \exp(-px)\mathrm{d}x = \Gamma(a)/p^a$$

and using [27, Eqn (3.944.12)]:

$$\int_0^\infty x^n \exp(-px)\cos(bx)\mathrm{d}x \ = \ n!\left(\frac{p}{p^2+b^2}\right)^{n+1} \sum_{0\le 2k\le n+1} (-1)^k\ \mathrm{C}_{n+1}^{2k}\ (b/p)^{2k}$$

results in

$$\lambda_{4\mathcal{T}} = \frac{4\sigma_0^2}{\mathcal{T}^5}\left\{\left(\frac{\mathcal{T}}{\beta}\right)^3 \quad \left[\frac{(\beta/\mathcal{T})}{1+(\beta/\mathcal{T})^2}\right]\left[1 - 3\left(\frac{\mathcal{T}}{\beta}\right)^2\right]\right\}$$

hence

$$\epsilon_{\mathcal{T}} = \sqrt{1 - \frac{\left(\frac{\mathcal{T}}{\beta}\right)^3 \Big/ \left[1+\left(\frac{\beta}{\mathcal{T}}\right)^2\right]^2}{\left\{2\left(\frac{\mathcal{T}}{\beta}\right)\tan^{-1}\left(\frac{\mathcal{T}}{\beta}\right) - \ln\left[1+\left(\frac{\mathcal{T}}{\beta}\right)^2\right]\right\}\left\{\left(\frac{\mathcal{T}}{\beta}\right)^3 - \left[\frac{(\beta/\mathcal{T})}{1+(\beta/\mathcal{T})^2}\right]\left[1-3\left(\frac{\mathcal{T}}{\beta}\right)^2\right]\right\}}} \quad (118)$$

Again, for $\mathcal{T} \gg \theta_{\mathcal{T}}$ an approximation valid for general $g(\omega)$ can be used:

$$\epsilon_{\mathcal{T}} \ \approx \ \sqrt{1 - \frac{2}{\mathcal{T}\theta_{\mathcal{T}}(\lambda_{2\mathcal{T}}/\lambda_{0\mathcal{T}})}} \quad (119)$$

$$\approx \ \sqrt{1 - (4/\pi)[1+(\beta/\mathcal{T})^2]\{(1/2)\tan^{-1}(\mathcal{T}/\beta) - [\beta/(4\mathcal{T})]\ln[1+(\mathcal{T}/\beta)^2]\}} \quad (120)$$

G.3.2.3 Second normalized spectral bandwidth for sensor aperture With the aid of [27, Eqn (2.636.1)]:

$$\int x^n \sin^2(x)\mathrm{d}x \ = \ \frac{x^{n+1}}{2(n+1)} + \frac{n!}{4}\left\{\sum_{k=0}^{\lfloor n/2\rfloor} \frac{(-1)^{k+1}x^{n-2k}}{2^{2k}(n-2k)!}\sin(2x\right.$$

$$\left. + \sum_{k=0}^{\lfloor (n-1)/2\rfloor} \frac{(-1)^{k+1}x^{n-2k-1}}{2^{2k+1}(n-2k-1)!}\cos(2x)\right\} \quad (121)$$

the fourth spectral moment is calculated as:

$$\lambda_{4\mathcal{T}} = \frac{8\pi\sigma_0^2}{k\mathcal{T}^5}\left[\frac{(k\mathcal{T})^3}{6} + \frac{3}{4k\mathcal{T}} - \sin(2k\mathcal{T}) + \left(\frac{k\mathcal{T}}{2} - \frac{3}{4k\mathcal{T}}\right)\cos(2k\mathcal{T})\right]$$

With (109)–(111) this then leads to $\epsilon_{\mathcal{T}}$ from (112) but this does not simplify significantly.

Figs 158 and 159 show $\delta_{\mathcal{T}}$ and $\epsilon_{\mathcal{T}}$ for local stir and local spatial averaging, respectively. For $\mathcal{T}/\beta \to 0$ or $k\mathcal{T} \to 0$, $\delta_{\mathcal{T}}$ approaches $1/\sqrt{2} \approx 0.707$ or $\gamma \approx 0.577$, respectively, whereas $\epsilon_{\mathcal{T}}$ then approaches $\sqrt{5/6} = 0.913$ or 0.931, respectively, in accordance with previous results for point processes [34, Sec 12.4]. A local dip in the bandwidths for intermediate values of both $\mathcal{T}/\beta$ and $k\mathcal{T}$ is noticed. On this basis, it is concluded that the local averaging should be limited to about $x \leq 0.1$, where $x = \mathcal{T}/\beta$ or $k\mathcal{T}$, for the measurements to be representative for idealized point measurements.

In summary, the spectral bandwidth of the stirring process can be made to resemble that of a perfectly reverberant field (i.e. $\delta_0 = \epsilon_0 = 1$) as closely as desired, by increasing the antenna aperture width or sampling width accordingly.

G.4 Upward threshold crossing frequency under local averaging

G.4.1 General local averaging

G.4.1.1 Introduction The level crossing rate is an important statistic in the testing of EUTs, as explained in [34, Sec 12.6]. As a consequence of local averaging, the theoretical statistics of threshold crossings for point processes will show discrepancies with measured results or test field conditions. In particular, the crossing rate will be a monotonously decreasing function of $\mathcal{T}$ as can be readily understood from the 'levelling' property of the local averaging operation. For chosen values of the mode-stirring parameters and for a given level of input power, the upward threshold frequency incorporating local averaging can be used to define the maximum permissible value of $\mathcal{T}$ that will still achieve a specified number of crossings for a specified test level during the EMC test. Therefore, we here investigate the upward level crossing rate anew, in the light of the local averaging.

Extending our analysis of [34, Sec C.2], we find the upward threshold crossing rate $\nu_{\mathcal{T}}^{+}(b)$ for a distribution $f_{X_{\mathcal{T}}}(x_{\mathcal{T}})$ and a chosen threshold level $x_{\mathcal{T}} = b$ to be:

$$\nu_{\mathcal{T}}^{+}(b) = \frac{\mathrm{E}[|\dot{X}_{\mathcal{T}}|]}{2} f_{X_{\mathcal{T}}}(b)$$

Provided $\dot{X}_T$ and X_T are statistically independent and that $f_{\dot{X}_T}$ is Gauss normal, (123) reduces to:

$$\nu_T^{\pm}(b) = \sqrt{\frac{1-\rho_T}{\pi}}\frac{\sigma_0}{T} f_{X_T}(b) \tag{124}$$

Note that stationarity of $X_T(t)$ only guarantees that $X_T(t)$ and $\dot{X}_T(t)$, when evaluated and compared at the *same* instances ('times') t, are uncorrelated i.e. linearly independent.

For the χ_2 and χ_6 distributions these two conditions are satisfied because they constitute envelopes to complex Gauss normal processes in one and three dimensions, respectively. The Gauss normality of $\dot{X}_T$ can be verified from Fig 160, which compares the cdfs of the first-order differences of measured normalized field magnitudes $\mathrm{d}[|E_\alpha|/\sqrt{P_i}]/\mathrm{d}\tau$ at 8.2GHz with the cdf of the standardized Gauss normal distribution. The linear independence, as an approximate measure[46] of the full statistical independence, can be judged from Figs 161 and 162, showing the crosscorrelation function and its associated cdf, respectively, between $|E_\alpha|/\sqrt{P_i}$ and $\mathrm{d}[|E_\alpha|/\sqrt{P_i}]/\mathrm{d}\tau$ again at 8.2GHz. The linear and, hence, statistical dependence may seem to be not so small, as also witnessed from the deviation of the cdf of the crosscorrelation function from Gauss normality, in Fig 162. This is at least partly a result of the fact that only (discrete) differences could be computed from the (discrete) mode-tuned tuner sweep data as estimates for the (continuous) derivative of the continuous trace of the stirring process. This causes this estimate to be approximate and the first-order difference to be offset by half a stirrer step relative to the sampling positions of the tuner sweep data, resulting in $\Delta X(\tau + \Delta\tau/2)/\Delta\tau$ as a discrete approximation for $\mathrm{d}X/\mathrm{d}\tau$. The finite cross-correlations are mainly due to this shift in the ordinate.

By contrast, Fig 163 compares the cdfs of the 1st-order differences of the normalized energy densities $\mathrm{d}[(|E_\alpha|/\sqrt{P_i})^2]/\mathrm{d}\tau$ with the cdf of the standardized Gauss normal distribution. The graph indicates significant deviations from Gauss normality for the measured $\dot{X}_T$. Therefore a study of statistical distribution of first-order derivative processes will follow, preceding the further analysis of threshold crossings. The levels of crosscorrelations (Figs 164 and 165) are comparable to those for the derivatives of the field magnitudes.

G.4.1.2 Distribution of first-order derivative process for field magnitude and energy density The magnitudes of the Cartesian components of the field or of the total field are the absolute values of the complex processes defined from the associated in-phase and quadrature field components, per Cartesian field component:

[46]The use of correlation functions as *measures* of statistical dependence is recommended only for Gauss normal or near-normal variations [24, Sec 26.8].

$$|E_\alpha| = \sqrt{[\Re(E_\alpha)]^2 + [\Im(E_\alpha)]^2}, \qquad (\alpha = x, y, z) \tag{125}$$

$$|E_t| = \sqrt{\sum_{\alpha=x,y,z} |E_\alpha|^2}$$

Therefore, they can be interpreted as Cramér–Leadbetter envelopes of such complex processes in one or three dimensions, respectively. The derivatives of the associated pdfs χ_2 resp. χ_6 are known to be Gauss normal (e.g. [21, Secs. 4.3, 4.4]).

The distribution of the derivative of the energy density can then be found from $\mathrm{d}|E_\alpha|^2/\mathrm{d}\tau = 2|E_\alpha| \cdot (\mathrm{d}|E_\alpha|/\mathrm{d}\tau)$, which will be denoted for short as $|\dot{E}_\alpha|^2 = 2|E_\alpha| \cdot |\dot{E}_\alpha|$, i.e. as the distribution of a product of processes with known pdfs. If $|E_\alpha|$ and $|\dot{E}_\alpha|$ are independent, then the distribution of this product follows as:

$$f_{|\dot{E}_\alpha|^2}(z) = \int_{-\infty}^{+\infty} |2u|^{-1} \, f_{|E_\alpha|}(u/2) \, f_{|\dot{E}_\alpha|}(z/u) \, \mathrm{d}u \tag{127}$$

for $-\infty < z < +\infty$ and $\alpha = x, y, z, t$.

G.4.1.2.1 Cartesian field components Substituting the standard Rayleigh and Gaussian pdfs for $f_{|E_\alpha|}(u/2 > 0)$ and $f_{\mathrm{d}|\dot{E}_\alpha|/\mathrm{d}\tau}(z/u)$ in (127), respectively, and substituting $[u/(2\sqrt{2}\sigma_{|E_\alpha|})]^2$ for v, we obtain:

$$f_{|\dot{E}_\alpha|^2}(z) = \int_0^{+\infty} \left(4\sigma_{|E_\alpha|}\sigma_{|\dot{E}_\alpha|}\sqrt{\pi v}\right)^{-1} \exp\left[-v - \frac{\left[z/(4\sigma_{|E_\alpha|}\sigma_{|\dot{E}_\alpha|})\right]^2}{v}\right] \mathrm{d}v$$

Using [1, Eqn (15)], [27, Eqn (3.471.12)] restricted to real values for the parameter μ, i.e.:

$$\int_0^{+\infty} x^{\nu-1} \exp\left[-x - \frac{(\mu/2)^2}{x}\right] \mathrm{d}x = 2\,(\mu), \qquad (\mu \geq 0)$$

with $x = v$, $\nu = 1/2$, $\mu = z/(2\sigma_{|\dot{E}_\alpha|}\sigma_{E_\alpha})$ for $z \geq 0$, and noting that the result can be extended to negative real values of z by replacing μ in (129) with $|\mu|$, then (128) reduces to

$$f_{|\dot{E}_\alpha|^2}(|z|) = \left(2\sqrt{2\pi}\,\sigma_{|E_\alpha|}\sigma_{|\dot{E}_\alpha|}\right)^{-1} \left[\frac{|z|}{2\sigma_{|E_\alpha|}\sigma_{|\dot{E}_\alpha|}}\right]^{1/2} K_{1/2}\left[\frac{|z|}{2\sigma_{|E_\alpha|}\sigma_{|\dot{E}_\alpha|}}\right]$$

$$\left(4\sigma_{|E_\alpha|}\sigma_{|\dot{E}_\alpha|}\right)^{-1}\left\{\cosh\left[\frac{|z|}{2\sigma_{|E_\alpha|}\sigma_{|\dot{E}_\alpha|}}\right]\quad\sinh\left[\frac{|z|}{2\sigma_{|E_\alpha|}\sigma_{|\dot{E}_\alpha|}}\right]\right\}$$

$$\left[2\left(2\sigma_{|E_\alpha|}\sigma_{|\dot{E}_\alpha|}\right)\right]^{-1}\exp\left[-\frac{|z|}{2\sigma_{|E_\alpha|}\sigma_{|\dot{E}_\alpha|}}\right]\qquad(-\infty<z<+\infty)$$

Using [6, Eqn (27)], [27, Eqn (6.561.16)], i.e

$$\int_0^{+\infty}x^\mu K_\nu(x)\mathrm{d}x\;=\;2^{\mu-1}\;\Gamma[(1+\mu+\nu)/2]\;\Gamma[(1+\mu-\nu)/2],\qquad(1+\mu\pm\nu>0)\qquad(131)$$

for $\mu=\nu=1/2$, $x=z/(2\sigma_{|E_\alpha|}\sigma_{\dot{E}_\alpha})$ it is verified that the distribution (130) is normalized Equation (131) can further be used to obtain the moments of the distribution, in particular:

$$\mathrm{E}[|\dot{E}_\alpha|^2]=\int_{-\infty}^{+\infty}zf_{|\dot{E}_\alpha|^2}(|z|)\mathrm{d}z=0,\quad\mathrm{E}\left[\left||\dot{E}_t|^2\right|\right]=\int_{-\infty}^{+\infty}|z|f_{|\dot{E}_t|^2}(z)\mathrm{d}z=2\sigma_{|E_\alpha|}\sigma_{|\dot{E}_\alpha|}$$

$$\mathrm{Var}[|\dot{E}_\alpha|^2]=\mathrm{Var}\left[\left||\dot{E}_\alpha|^2\right|\right]=\int_{-\infty}^{+\infty}z^2f_{|\dot{E}_\alpha|^2}(|z|)\mathrm{d}z-\left[\mathrm{E}[|\dot{E}_\alpha|^2]\right]^2=8\left(\sigma_{|E_\alpha|}\sigma_{|\dot{E}_\alpha|}\right)^2$$

which is then used to write (130) finally as:

$$f_{|\dot{E}_\alpha|^2}(|z|)=\left[2(\sigma_z/\sqrt{2})\right]^{-1}\exp\left[-\frac{|z|}{\sigma_z/\sqrt{2}}\right],\qquad(-\infty<z<+\infty)\qquad(134)$$

where $\sigma_z^2\equiv\mathrm{Var}[|\dot{E}_\alpha|^2]$. The factor '2' in (134) reflects the fact that this exponential distribution is Laplacian, i.e. two-sided, because the tuner sweep data for $|E_\alpha|$ show increases as well as decreases between data points. The cdf associated with (134) is shown in Fig 163.

G.4.1.2.2 Total field Substituting the χ_6 and Gauss normal pdfs for $f_{|E_t|}(u/2>0)$ and $f_{|\dot{E}_t|}(z/u)$ in (127), respectively; denoting $v=[u/(2\sqrt{2}\sigma_{|E_t|})]^2$, and again using (129) we now obtain:

$$\begin{aligned}f_{|\dot{E}_t|^2}(|z|)\;=\;&\left(16\sqrt{2\pi}\sigma_{|E_t|}\sigma_{|\dot{E}_t|}\right)^{-1}\left[\frac{|z|}{2\sigma_{|E_t|}\sigma_{|\dot{E}_t|}}\right]^{5/2}K_{5/2}\left[\frac{|z|}{2\sigma_{|E_t|}\sigma_{|\dot{E}_t|}}\right]\\&\left(32\sigma_{|E_t|}\sigma_{|\dot{E}_t|}\right)^{-1}\left[\left(\frac{|z|}{2\sigma_{|E_t|}\sigma_{|\dot{E}_t|}}\right)^2+3\left(\frac{|z|}{2\sigma_{|E_t|}\sigma_{|\dot{E}_t|}}\right)+3\right]\\&\left\{\cosh\left[\frac{|z|}{2\sigma_{|E_t|}\sigma_{|\dot{E}_t|}}\right]-\sinh\left[\frac{|z|}{2\sigma_{|E_t|}\sigma_{|\dot{E}_t|}}\right]\right\}\\&\left[16\left(2\sigma_{|E_t|}\sigma_{|\dot{E}_t|}\right)\right]^{-1}\left[\left(\frac{|z|}{2\sigma_{|E_t|}\sigma_{|\dot{E}_t|}}\right)^2+3\left(\frac{|z|}{2\sigma_{|E_t|}\sigma_{|\dot{E}_t|}}\right)+3\right]\exp\left[-\frac{|z|}{2\sigma_{|E_t|}\sigma_{|\dot{E}_t|}}\right]\\&(-\infty<z<+\infty)\qquad(135)\end{aligned}$$

with mean and variance:

$$\mathrm{E}[|\dot{E}_t|^2] = \int_{-\infty}^{+\infty} z f_{|\dot{E}_t|^2}(z)\mathrm{d}z = 0, \quad \mathrm{E}\left[\left||\dot{E}_t|^2\right|\right] = \int_{-\infty}^{+\infty} |z| f_{|\dot{E}_t|^2}(z)\mathrm{d}z = 15\sigma_{|E_t|}\sigma_{|\dot{E}_t|}/4 \quad (136)$$

$$\mathrm{Var}[|\dot{E}_t|^2] = \mathrm{Var}[\left||\dot{E}_t|^2\right|] = \int_{-\infty}^{+\infty} z^2 f_{|\dot{E}_t|^2}(|z|)\mathrm{d}z = 15\left(\sigma_{|E_t|}\sigma_{|\dot{E}_t|}\right)^2$$

which is then used to write (135) finally as:

$$f_{|\dot{E}_t|^2}(|z|) = \left[16\left(2\sigma_z/\sqrt{15}\right)\right]^{-1}\left[\left(\frac{|z|}{2\sigma_z/\sqrt{15}}\right)^2 \quad \left(\frac{|z|}{2\sigma_z/\sqrt{15}}\right) + 3\right]\exp\left[-\frac{|z|}{2\sigma_z/\sqrt{15}}\right], \quad (-\infty < z < +\infty)$$

where now $\sigma_z^2 \equiv \mathrm{Var}[|\dot{E}_t|^2]$. The cdf associated with (138) is also shown in Fig 163.

G.4.2 Upward threshold crossing frequency for specific underlying distributions under extreme local averaging

$$\nu_T^+(b) = \sqrt{\frac{1-\rho_T}{2\pi^2 T^2 \gamma_T}}\exp\left[\frac{(b/\sigma_0)^2}{2\gamma_T}\right]$$

With the approximations for ρ_T and γ_T for large T, this can be reduced to

$$\left(2\pi^2\theta_T T\right) \quad \exp\left[-(b/\sigma_0)^2 T/(2\theta_T)\right], \qquad (T \gg \theta_T)$$

On the other hand, if the averaging interval is sufficiently small ($T \ll \theta_T$), then we may consider approximating $f_{X_T}(x_T)$, to first order, by $f_X(x)$ itself but in which σ_0 is being replaced by $\sigma_T = \sqrt{\gamma_T}\sigma_0$. The following upward threshold crossing rates are then obtained for specific distributions of the field magnitude or energy density of interest:

- χ_2 pdf:

$$\nu_T^+(b) = \sqrt{\frac{1-\rho_T}{\pi}}\frac{(b/\sigma_0)}{T\gamma_T}\exp\left[\frac{(b/\sigma_0)^2}{2\gamma_T}\right] \quad (141)$$

- χ_6 pdf:

$$\sqrt{\frac{1-\rho_{\mathcal{T}}}{\pi}}\frac{(b/\sigma_0)^5}{8\mathcal{T}\gamma_{\mathcal{T}}^3}\exp\left[-\frac{(b/\sigma_0)^2}{2\gamma_{\mathcal{T}}}\right] \tag{142}$$

- χ_2^2 pdf:

$$\nu_{\mathcal{T}}^{+}(b) = \frac{\sqrt{1-\rho_{\mathcal{T}}}}{4\mathcal{T}\gamma_{\mathcal{T}}\sigma_0}\exp\left[-\frac{(b/\sigma_0^2)}{2\gamma_{\mathcal{T}}}\right] \tag{143}$$

- χ_6^2 pdf:

$$\frac{\sqrt{30}\sqrt{1-\rho_{\mathcal{T}}}}{128}\frac{b^2/\sigma_0^5}{\mathcal{T}\gamma_{\mathcal{T}}^3}\exp\left[-\frac{(b/\sigma_0^2)}{2\gamma_{\mathcal{T}}}\right] \tag{144}$$

In these expressions $\rho_{\mathcal{T}}$ and $\gamma_{\mathcal{T}}$ are functions that are specific to the distribution in question, i.e. depending on whether field magnitude or energy density is the quantity of interest. For vanishingly small $\mathcal{T}$, these expressions reduce to:

- χ_2 pdf:

$$\nu_0^{+}(b) = \left(\sqrt{2\pi}\sigma_0\right)^{-1}\sqrt{\frac{\lambda_{2,|E_\alpha|}}{\lambda_{0,|E_\alpha|}}}\exp\left[-\frac{(b/\sigma_0)^2}{2}\right] \tag{145}$$

- χ_6 pdf:

$$\nu_0^{+}(b) = \left(8\sqrt{2\pi}\sigma_0^5\right)^{-1}\sqrt{\frac{\lambda_{2,|E_t|}}{\lambda_{0,|E_t|}}}\exp\left[-\frac{(b/\sigma_0)^2}{2}\right] \tag{146}$$

χ_2^2 pdf:

$$\left(4\sqrt{2}\sigma_0\right)^{-1}\sqrt{\frac{\lambda_{2,|E_\alpha|^2}}{\lambda_{0,|E_\alpha|^2}}}\exp\left[-\frac{(b/\sigma_0^2)}{2}\right] \tag{147}$$

- χ_6^2 pdf:

$$\nu_0^{+}(b) = \frac{\sqrt{15}}{128}\frac{b^2}{\sigma_0^5}\sqrt{\frac{\lambda_{2,|E_t|^2}}{\lambda_{0,|E_t|^2}}}\exp\left[-\frac{(b/\sigma_0^2)}{2}\right] \tag{148}$$

G.4.3 Upward threshold crossing frequency for stirrer step averaging

For the magnitude of the total field, the upward threshold crossing frequency is, from (73), (74) and (142):

$$\nu_T^+(b) = \frac{(b/\sigma_0)^5}{8\sqrt{\pi}} \frac{(\mathcal{T}^6/\beta^7)\,[1+(\mathcal{T}/\beta)^2]^{-1/2}}{[2(\mathcal{T}/\beta)\tan^{-1}(\mathcal{T}/\beta) - \ln[1+(\mathcal{T}/\beta)^2]]^3} \cdot \exp\left[-\frac{(b/\sigma_0)^2(\mathcal{T}/\beta)^2}{2\,[2(\mathcal{T}/\beta)\tan^{-1}(\mathcal{T}/\beta) - \ln[1+(\mathcal{T}/\beta)^2]]}\right]$$

Fig 168 shows ν_T^+ as a function of b/σ_0 for parameterized $\mathcal{T}/\beta$. The maxima are reached for intermediate values of (b/σ_0). They decrease in value and shift towards lower values of (b/σ_0) for increasing $\mathcal{T}/\beta$.

For the upward crossing rate of the energy density associated with the total field, we obtain from (73), (74) and (144):

$$\nu_T^+(b) = \frac{\sqrt{30}(b^2/\sigma_0^5)}{128} \frac{(\mathcal{T}^6/\beta^7)\,[1+(\mathcal{T}/\beta)^2]^{-1/2}}{[2(\mathcal{T}/\beta)\tan^{-1}(\mathcal{T}/\beta) - \ln[1+(\mathcal{T}/\beta)^2]]^3} \cdot \exp\left[-\frac{(b/\sigma_0^2)(\mathcal{T}/\beta)^2}{2\,[2(\mathcal{T}/\beta)\tan^{-1}(\mathcal{T}/\beta) - \ln[1+(\mathcal{T}/\beta)^2]]}\right]$$

Fig 169 shows this statistic as a function of b/σ_0 for parameterized $\mathcal{T}/\beta$. In comparison with the previous Figure, the decrease in the value of the maximum crossing rate is now much less pronounced.

For relatively small stirrer averaging, expanding (149) for small $(\mathcal{T}/\beta)$ yields:

$$\nu_T^+(b) = \frac{(b/\sigma_0)^5}{\sqrt{\pi}\beta}\left[1+\frac{11}{120}\left(\frac{\mathcal{T}}{\beta}\right)^4+\ldots\right]\exp\left[-\frac{(b/\sigma_0)^2}{2}\left(1+\frac{(\mathcal{T}/\beta)^2}{6}+\quad\right)\right]$$

which reduces to (146) in the limit $\mathcal{T} \to 0$. For the total power, expanding (150) for small $\mathcal{T}/\beta$ yields:

$$\nu_T^+(b) = \frac{\sqrt{30}(b^2/\sigma_0^5)}{128\,\beta}\left[1+\frac{11}{120}\left(\frac{\mathcal{T}}{\beta}\right)^4+\quad\right]\exp\left[\frac{b/\sigma_0^2}{2}\left(1+\frac{(\mathcal{T}/\beta)^2}{6}+\ldots\right)\right] \qquad (152)$$

which reduces to (148) for $\mathcal{T} \to 0$. Thus, for small stir averaging, the upward threshold crossing frequency for the total field varies in inverse proportion to β, as expected for a good stirring

process. For large thresholds b/σ_0, the threshold crossing rate for the total power hence decreases approximately quadratically with $\mathcal{T}/\beta$, whereas for sufficiently small b/σ_0 (viz. of the order of $(\mathcal{T}/\beta)^2$ or smaller), the variation is according to the fourth power of $\mathcal{T}/\beta$.

For $\mathcal{T}/\beta \gg 1$, from (84) and (140)

$$\nu_{\mathcal{T}}^{\pm}(b) \approx \left(2\pi^3\beta\mathcal{T}\right)^{-1/2} \exp\left[-(b/\sigma_0^2)\mathcal{T}/(2\pi\beta)\right] \tag{153}$$

G.4.4 Upward threshold crossing frequency for sensor aperture averaging

For the level crossings of the magnitude of the total field, substitution of (80) and (81) into (142) yields:

$$\nu_{\mathcal{T}}^{\pm}(b) = \frac{(b/\sigma_0)^5}{64\sqrt{\pi}} \frac{(k^6\mathcal{T}^5)\sqrt{1-\mathrm{sinc}(k\mathcal{T})}}{[k\mathcal{T}\,\mathrm{Si}(k\mathcal{T}) + \cos(k\mathcal{T}) - 1]^3} \cdot \exp\left[-\frac{(b/\sigma_0)^2(k\mathcal{T})^2}{4\,[k\mathcal{T}\,\mathrm{Si}(k\mathcal{T}) + \cos(k\mathcal{T}) - 1]}\right]$$

Expanding (154) for small $k\mathcal{T}$ yields, to first order:

$$\nu_{\mathcal{T}}^{\pm}(b) = \frac{k(b/\sigma_0)^5}{8\sqrt{6\pi}}\left[1 + \frac{7(k\mathcal{T})^2}{120} + \ldots\right] \exp\left[\frac{(b/\sigma_0)^2}{2}\left(1 + \frac{(k\mathcal{T})^2}{36} + \ldots\right)\right]$$

where the exponential decrease with increasing $\mathcal{T}$ will again dominate to yield an overall decrease of the high-level threshold crossing rate.

For the energy density of the total field, substitution of (76) and (77) into (144) yields:

$$\nu_{\mathcal{T}}^{\pm}(b) = \frac{\sqrt{30}(b^2/\sigma_0^5)}{128} \frac{(k^6\mathcal{T}^5)\sqrt{1-\mathrm{sinc}^2(k\mathcal{T})}}{[2k\mathcal{T}\,\mathrm{Si}(2k\mathcal{T}) - 2\sin^2(k\mathcal{T}) - \ln(2k\mathcal{T}) - \gamma - \mathrm{Ci}(2k\mathcal{T})]^3} \cdot \exp\left[-\frac{(b/\sigma_0^2)(k\mathcal{T})^2}{2\,[2k\mathcal{T}\,\mathrm{Si}(2k\mathcal{T}) - 2\sin^2(k\mathcal{T}) - \ln(2k\mathcal{T}) - \gamma - \mathrm{Ci}(2k\mathcal{T})]}\right] \tag{156}$$

For $k\mathcal{T} \ll 1$, this is approximated to first order as

$$\nu_{\mathcal{T}}^{\pm}(b) = \frac{\sqrt{10}\,k(b^2/\sigma_0^5)}{128}\left[1 + \frac{(k\mathcal{T})^2}{10} + \ldots\right] \left[-\frac{(b/\sigma_0^2)}{2}\left(1 + \frac{(k\mathcal{T})^2}{18} + \ldots\right)\right]$$

The expected linear increase of $\nu_{\mathcal{T}}^{\pm}(b)$ with increasing k is confirmed. The exponential decrease for increasing $\mathcal{T}$ will dominate, for sufficiently large b/σ_0, resulting in an overall lowering of the high-level threshold crossing frequencies with increasing aperture width.

Fig 170 shows $\nu_{\mathcal{T}}^{\pm}$ as a function of b/σ_0, for parameterized $k\mathcal{T}$, for the total field magnitude (underlying χ_6 df) with $k = 100$rad/m. For vanishingly small $k\mathcal{T}$, $\nu_{\mathcal{T}}^{\pm}(b/\sigma_0)$ reaches a maximum near the mean of the distribution, i.e. $\mu_X = 15\sqrt{2\pi}/16 \approx 2.350$. This maximum steadily decreases in value and occurs at increasingly smaller values of b/σ_0 the further $k\mathcal{T}$ is being increased. Conversely, Fig 171 shows ν_{b/σ_0}^{+} as a function of $\mathcal{T}$ for parameterized (b/σ_0) and $k = 100$rad/m. For $b/\sigma_0 \leq \mu_X$, $\nu_{b/\sigma_0}^{+}(\mathcal{T})$ reaches a maximum at some intermediate value of $\mathcal{T}$. For $b/\sigma_0 > \mu_X$, $\nu_{b/\sigma_0}^{+}(\mathcal{T})$ decreases monotonically. A cut-off width (transition or knee point) $\mathcal{T}_c$ for the averaging length emerges, separating a region of almost no change in $\nu_{b/\sigma_0}^{+}(\mathcal{T})$ (for small $\mathcal{T}$) from a region with rapid decay (for large $\mathcal{T}$). Furthermore, this cut-off length steadily decreases for increasing values of b/σ_0.

Similar dependencies are found for the total energy density (Figs 172 and 173) except that the decrease of the maximum $\nu_{\mathcal{T}}^{\pm}$ with increasing $\mathcal{T}$ now becomes less pronounced, although the value b/σ_0 at which this maximum occurs now decreases fmore rapidly with increasing $\mathcal{T}$.

G.5 Time to first passage

The probability for no upward threshold crossing of a chosen level b above the mean to occur during the interval $[0, \tau_0]$ can be estimated from the asymptotic result for $b \to +\infty$ [12]:

$$\mathcal{P}_{\mathcal{T}}(b, \tau_0) \approx \exp[-\nu_{\mathcal{T}}^{\pm}(b)\, \tau_0] \tag{158}$$

in which (123), (124) or (141)–(144) can be substituted. A chosen value of the first-passage probability $\mathcal{P}$ (failure probability) yields the mean time τ_0 before which the EUT will be subjected to the critical test level b (mean time to failure). As a result, the reliability rate for failure of the EUT to occur is, asymptotically, exponentially decreasing in general. The effect of local averaging on $\mathcal{P}_{\mathcal{T}}$ is an increase in the perceived reliability. For the situation of most practical interest, i.e. reliability when subjected to critical standardized field strength levels $b/\sigma_0 \gg 1$ and $\mathcal{T}/\beta \ll 1$ or $k\mathcal{T} \ll 1$, some small local averaging will result in an increase of the perceived reliability of the order $\exp[\mathcal{T}^2/\beta^3]$ or $\exp[k^3\mathcal{T}^2]$, respectively. The accuracy of the estimate (158) improves as b/σ_0 increases. The exponential law (158) is sufficiently accurate provided $\tau_0 \gg [\nu^+(b = \mu_X)]^{-1}$. For finite, but not very large b/σ_0, the estimate (158) can be further improved upon [21, Sec 4.4].

Figs 174–177 show the dependence of $\mathcal{P}_{\mathcal{T}}(b/\sigma_0)$ and $\mathcal{P}_{b/\sigma_0}(\mathcal{T})$ for the total field magnitude and

energy density, upon local spatial averaging. Note in particular the abrupt shift of the $\mathcal{P}_{\mathcal{T}}(b/\sigma_0)$ near $\mathcal{T} = 0.01 \ldots 0.1$ in Figs 175 and 177. Figs 178–181 show the corresponding dependencies for stir averaging.

G.6 Mean excursion lengths

As for the case of point-wise distributions, the mean excursion length for a threshold level b subject to local averaging of the process is critically dependent upon the underlying distribution function $f_{X_{\mathcal{T}}}(x_{\mathcal{T}})$ of that process:

$$\mathrm{E}[\mathcal{L}_{\mathcal{T}}(b)] = \frac{2}{\mathrm{E}[|\dot{X}_{\mathcal{T}}|]} \frac{1 - F_{X_{\mathcal{T}}}(b)}{f_{X_{\mathcal{T}}}(b)} \tag{159}$$

For statistically independent $X_{\mathcal{T}}$ and $\dot{X}_{\mathcal{T}}$ and Gauss normal $f_{\dot{X}_{\mathcal{T}}}(\dot{x}_{\mathcal{T}})$, e.g. for underlying χ_2 and χ_6 dfs, this reduces to:

$$\mathrm{E}[\mathcal{L}_{\mathcal{T}}(b)] = \sqrt{\frac{\pi}{1 - \rho_{\mathcal{T}}}} \frac{\mathcal{T}}{\sigma_0} \frac{1 - F_{X_{\mathcal{T}}}(b)}{f_{X_{\mathcal{T}}}(b)}$$

For χ_2^2 and χ_6^2, (132) and (136) should again be used in (159), respectively. Assuming again a small extent of averaging, such that the point-wise distribution can be assumed i.e. $f_{X_{\mathcal{T}}}(b) = f_X(b)$, we obtain:

- χ_2 pdf:

$$\mathrm{E}[\mathcal{L}_{\mathcal{T}}(b)] = \sqrt{\frac{\pi}{1 - \rho_{\mathcal{T}}}} \frac{\mathcal{T}\gamma_{\mathcal{T}}}{(b/\sigma_0)} \tag{161}$$

- χ_6 pdf:

$$\mathrm{E}[\mathcal{L}_{\mathcal{T}}(b)] = \sqrt{\frac{\pi}{1 - \rho_{\mathcal{T}}}} \frac{\mathcal{T}\gamma_{\mathcal{T}}^3}{(b/\sigma_0)^5} \frac{1 - \int_0^b [x^5/(8\gamma_{\mathcal{T}}^3\sigma_0^6)] \exp[-x^2/(2\gamma_{\mathcal{T}}\sigma_0^2)]\,\mathrm{d}x}{\exp[-b^2/(2\gamma_{\mathcal{T}}\sigma_0^2)]}$$

- χ_2^2 pdf:

$$\mathrm{E}[\mathcal{L}_{\mathcal{T}}(b)] = \frac{4\sigma_0\mathcal{T}\gamma_{\mathcal{T}}}{\sqrt{1 - \rho_{\mathcal{T}}}} \tag{163}$$

  Note its lack of dependence on b, which is clearly suspect (it predicts finite excursion lengths for infinite threshold levels). It is concluded that for this (Poisson) distribution, unlike for 'bell-shaped' pdfs, the application of the theory of recurrent events [3] may become unsustainable. Possibly, the assumption that the mean fraction of time in excess of the threshold relative to the overall run length, $\mathrm{E}[\tau_+/(\tau_+ + \tau_-)]$, is equal the ratio of the respective means,

$\mathrm{E}[\tau_+]/\mathrm{E}[(\tau_+ + \tau_-)]$, requires a more careful consideration, so that the factor $1 - F_{X_\mathcal{T}}(b)$ in (159) is to be replaced by a different b-dependent function for an underlying χ^2_2 pdf. Alternatively, the threshold crossings may not be independently distributed according to a Poisson process for the χ^2_2 df.

χ^2_6 pdf

$$\mathrm{E}[\mathcal{L}_\mathcal{T}(b)] = \frac{128}{\sqrt{30}} \frac{\sigma_0^5}{b^2} \frac{\mathcal{T}\gamma_\mathcal{T}^3}{\sqrt{1-\rho_\mathcal{T}}} \left[1 + \frac{b}{2\gamma_\mathcal{T}\sigma_0^2} + \frac{1}{2}\left(\frac{b}{2\gamma_\mathcal{T}\sigma_0^2}\right)^2\right]$$

As for χ^2_2, the first-order derivative needed in (164) has again a non-Gaussian distribution, so that the result may serve as an approximation only.

The specific expressions for the total field and total power density upon local stirrer and spatial averaging and their approximations for small $\mathcal{T}$ follow immediately from the foregoing expressions for the upward threshold crossing frequency.

For sufficiently large averaging widths, we can again assume the distribution functions under local averaging to tend to Gauss normality. For general b, the mean excursion length for underlying Gauss normal distributions $f_{X_\mathcal{T}}(x_\mathcal{T}) = (2\pi\gamma_\mathcal{T}\sigma_0^2)^{-1/2}\exp\left[-(x_\mathcal{T}/\sigma_0)^2/(2\gamma_\mathcal{T})\right]$, is obtained as:

$$\mathrm{E}[\mathcal{L}_\mathcal{T}(b)] = \sqrt{\frac{\pi}{1-\rho_\mathcal{T}}} \frac{\mathcal{T}}{\sigma_0} \frac{1 - \Phi[b/(\sqrt{\gamma_\mathcal{T}}\sigma_0)]}{(2\pi\gamma_\mathcal{T}\sigma_0^2)^{-1/2}\exp\left[-(b/\sigma_0)^2/(2\gamma_\mathcal{T})\right]} \tag{165}$$

with $\Phi[b/(\sqrt{\gamma_\mathcal{T}}\sigma_0)] = \int_{-\infty}^{b}(2\pi\gamma_\mathcal{T}\sigma_0^2)^{-1/2}\exp\left[-(x/\sigma_0)^2/(2\gamma_\mathcal{T})\right]\mathrm{d}x$. If $b/\sigma_0 \gg 1$, in addition to $X_\mathcal{T}$ having a Gauss normal distribution function, then the mean excursion length becomes:

$$\mathrm{E}[\mathcal{L}_\mathcal{T}(b)] \approx \frac{\sqrt{\pi}\theta_\mathcal{T}\sigma_0}{b} \qquad (\mathcal{T} \gg \theta_\mathcal{T},\ b \gg \sigma_0) \tag{166}$$

hence for stirrer averaging:

$$\mathrm{E}[\mathcal{L}_\mathcal{T}(b)] \approx \frac{\beta\pi^{3/2}\sigma_0}{b} \tag{167}$$

whereas for spatial averaging:

$$\mathrm{E}[\mathcal{L}_\mathcal{T}(b)] \approx \frac{\pi^{3/2}\sigma_0}{kb}$$

Figs 182 and 183 show $\mathrm{E}[\mathcal{L}_{\mathcal{T}}(b)]$ as a function of (b/σ_0), for parameterized $k\mathcal{T}$, for the total field (χ_6 distribution) and associated total power density (χ_6^2 distribution), respectively[47]. The steady decrease of $\mathrm{E}[\mathcal{L}_{\mathcal{T}}]$ with increasing (b/σ_0) and its decrease with increasing values of $k\mathcal{T}$ are confirmed. It is to be remembered that these graphs presume $f_{X_{\mathcal{T}}}(x_{\mathcal{T}}) \approx f_X(x)$, i.e. requiring sufficiently small $\mathcal{T}$, especially if $k\mathcal{T} \gg 1$.

Figs 184 and 185 show similar dependencies for the excursion lengths subject to local stir averaging, now with parameter $\mathcal{T}/\beta$.

G.7 Conclusion

The measurement of a reverberation process that is subject to local averaging is not only characterized by the sample mean and standard deviation, but also by the scale of fluctuation as a third parameter. If local averaging is considered along more than one dimension in parameter space, the previous results can easily be extended provided the averagings in the respective dimensions can be performed independently. If the local averaging is not negligible, then ignoring the scale of fluctuation may possibly lead to meaningless results or conclusions regarding the chamber or EUT, when assuming an idealized point process. We note parenthetically that the scale of fluctuation is inversely proportional with excitation frequency f as a direct consequence of the frequency dependence of ρ, the latter being analyzed in greater detail in [38].

[47]The cut-offs at the lower end of the curves for the total field are due to numerical instability of $[1 - F_{X_{\mathcal{T}}}(b)]/[f_{X_{\mathcal{T}}}(b)]$ for large $(b/\sigma_0, k\mathcal{T})$-products when calculating (162) numerically.

H Distribution of some goodness-of-fit statistics for measured field magnitude and energy density

H.1 Introduction

The testing of the hypothesis as to whether some given theoretical distribution is underlying a measured sample distribution is often performed on the basis of defining one or other single metric of deviation between the observed discrete sample cdf $F_N(x)$ for a sample size N, and the theoretical cdf at the observed values x_i, i.e. $F(x_i)$. Rejection or acceptance of the null hypothesis for Type I or Type II tests then follows, for chosen significance levels. Two commonly used metrics are the Kholmogorov–Smirnov statistic:

$$D_N = \sqrt{N}\,\sup_{x_i}|F_N(x) - F(x)| \triangleq \max_{x_i}|Y_N(x)| \tag{169}$$

i.e. a maximum-mismatch metric for absolute deviations, and the Cramér–von Mises statistic, defined as a Stieltjes integral:

$$W_N^2 = N\int_{-\infty}^{+\infty}[F_N(x) - F(x)]^2\,\mathrm{d}F(x) \tag{170}$$

i.e. an integrated curve mismatch for squared deviations, where $\mathrm{d}F(x) = f(x)\mathrm{d}x$ provided $f(x)$ exists across the support of $F(x)$. Each tuner sweep consisting of N data points yields a single realization d_N or w_N^2 of the random variable D_N or W_N^2, respectively.

Here, our aim is to find an alternative for the use of the classical tests of hypothesis for D_N and W_N^2, because the significance level is usually difficult to interpret in practically useful terms, and because a goodness-of-fit test often does not yield the correct type of uncertainty (I or II) of actual interest. Instead, we derive the *asymptotic* distributions and statistics of these metrics for $N \to \infty$. By then considering specific functionals on the asymptotic probability density functions, the asymptotic distributions of the original goodness-of-fit statistics are obtained. Application to actual measured stirrer data should show how large a typical sample size (mode-tuned tuner sweep) is required for such assumption to be sufficiently accurate. Supporting measured data for the distributions derived here are given in the main text (Sec 3.2.6.3).

H.2 Kholmogorov–Smirnov (K–S) statistic

For $N \to \infty$, the distribution of D_N tends in the wide sense[48] to the distribution of the random variable D defined by [2, 5]:

[48] i.e. with respect to its mean and covariance

$$D = \max_{0\le t\le 1}\left|(1-t)\,\mathcal{W}\left[\frac{t}{1-t}\right]\right| \triangleq \max_{0\le t\le 1}|Y(t)| \tag{171}$$

where $\mathcal{W}(t)$ is a Wiener process and, therefore, $Y(t)$ is a Gauss normal process [2], provided $F(x)$ *is* the underlying distribution of $F_N(x)$ and is continuous. Since $|Y_N(t)| \equiv \sqrt{Y_N^2(t)}$ and $Y_N(t) \to Y(t)$ for $N \to \infty$, the distribution of D_N tends to the distribution of the sample maximum of a χ_1 df (chi distribution with one degree of freedom) if $N \to \infty$. The χ_1 df is a scaled one-sided Gauss normal distribution, with pdf, cdf, mean and variance easily computed using a variate transformation for the χ_1^2 df as:

$$f_{\chi_1}(x) = \sqrt{2/\pi}\,\exp(-x^2/2), \qquad (x \ge 0)$$

$$F_{\chi_1}(x) = \mathrm{erf}(x/\sqrt{2}), \qquad (x \ge 0) \tag{173}$$

$$\mu_{\chi_1} = 1/\sqrt{2}, \qquad \sigma_{\chi_1}^2 = 1/2 \tag{174}$$

respectively, where $\mathrm{erf}(x) = (2/\sqrt{\pi})\int_0^x \exp(-t^2)\mathrm{d}t$ is the standard error function. The distribution of the sample maximum W_D for χ_1 follows as:

$$\begin{aligned} f_{\chi_{1,N}}(w_D) &= N\left[\int_0^{w_D} f_{\chi_1}(x)\mathrm{d}x\right]^{N-1} f_{\chi_1}(x = w_D) \\ &\quad N\sqrt{2/\pi}\left[\mathrm{erf}(w_D/\sqrt{2})\right]^{N-1}\exp(-w_D^2/2) \end{aligned}$$

$$F_{\chi_{1,N}}(w_D) = \left[\mathrm{erf}(w_D/\sqrt{2})\right]^N$$

Mean and variance follow upon numerical integration. For large N, the former can be approximated by the median, i.e. $m_{D,N} \triangleq F_{\chi_{1,N}}^{-1}(0.5) = \sqrt{2}\,\mathrm{erf}^{-1}(0.5^{1/N})$. Confidence intervals for W_D are easily computed from (176). For example, the [2.5%, 97.5%]-interval follows as:

$$\left[F_{\chi_{1,N}}^{-1}(0.025),\ F_{\chi_{1,N}}^{-1}(0.975)\right] = \left[\sqrt{2}\,\mathrm{erf}^{-1}\left(0.025^{1/N}\right),\ \sqrt{2}\,\mathrm{erf}^{-1}\left(0.975^{1/N}\right)\right]$$

Figs 186–188 show the pdf $f_{\chi_{1,N}}(w_D)$, the cdf $F_{\chi_{1,N}}(w_D)$, the mean $\mu_{\chi_{1,N}}$ and the standard deviation $\sigma_{\chi_{1,N}}$ for various sample sizes N with $W_D \equiv D_N$. The graphs of $f_{\chi_1}(x)$ and $F_{\chi_1}(x)$ are given by those for $N = 1$ in Figs 186 and 187, viz. $f_{\chi_1,1}$ and $F_{\chi_1,1}(x)$, respectively. The asymptotic Gauss normality of the sample distributions when $N \to \infty$ is apparent. The agreement of these theoretical curves with measured distributions and statistics can be expected to steadily increase as $N \to \infty$.

Squared Kholmogorov–Smirnov statistic

Defining this metric as the square of the K–S statistic, i.e. D_N^2, the associated χ_1^2 pdf is:

$$f_{\chi_1^2}(x) = \frac{\exp(-x/2)}{\sqrt{2\pi x}} \qquad (x \geq 0) \tag{178}$$

The corresponding cdf, mean and standard deviation are found as:

$$F_{\chi_1^2}(x) = \frac{\gamma(1/2, x/2)}{\sqrt{\pi}} \qquad (x \geq 0) \tag{179}$$

$$\mu_{\chi_1^2} = 1, \qquad \sigma^2_{\chi_1^2} = 2 \tag{180}$$

where $\gamma(\alpha, x) = \int_0^x t^{\alpha-1}\exp(-t)\mathrm{d}t$ with $\Re[\alpha] > 0$ is the incomplete gamma function. Hence we have the relations:

$$\mu_{\chi_1} = (1/\sqrt{2})\, \mu_{\chi_1^2} = (1/\sqrt{2})\, \sqrt{\mu_{\chi_1^2}} \tag{181}$$

which is reminiscent of a corresponding relation between χ_2 and χ_2^2 dfs [36, Eqn (44)], and

$$\sigma^2_{\chi_1} = (1/4)\, \sigma^2_{\chi_1^2} = (\sqrt{2}/4)\, \sqrt{\sigma^2_{\chi_1^2}} \tag{182}$$

The sample maximum W_D^2 has a pdf:

$$\begin{aligned} f_{\chi_1^2,N}(w_D^2) &= N \left[\int_0^{w_D^2} f_{\chi_1^2}(x)\mathrm{d}x\right]^{N-1} f_{\chi_1^2}(w_D^2) \\ &\quad \frac{N}{\pi^{(N-1)/2}}\, \gamma^{N-1}(1/2, w_D^2/2)\, \frac{\exp(-w_D^2/2)}{\sqrt{2\pi w_D^2}} \end{aligned} \tag{183}$$

Figs 189–191 show $f_{\chi_1^2,N}(w_D^2)$, $F_{\chi_1^2,N}(w_D^2)$, $\mu_{\chi_1^2,N}$ and $\sigma_{\chi_1^2,N}$ for various sample sizes N, again with $f_{\chi_1^2}(x) \equiv f_{\chi_{1,1}^2}(w_D^2)$ and $F_{\chi_1^2}(x) \equiv F_{\chi_{1,1}^2}(w_D^2)$ with $W_D^2 \equiv D_N^2$. The agreement with measured distributions and statistics is expected to improve as $N \to \infty$.

Cramér–von Mises statistic

This test statistic W_N^2 tends, for $N \to \infty$, to the distribution of:

$$W^2 = \int_0^1 \{(1-t)\mathcal{W}[t/(1-t)]\}^2 \, \mathrm{d}t \triangleq \int_0^1 Y^2(t)\mathrm{d}t \tag{184}$$

where $Y(t)$ and $\mathcal{W}(t)$ are again Gauss normal and Wiener processes, respectively. Thus, $Y^2(t)$ has a χ_1^2 pdf. The first- and second-order statistics of W^2 can be found as follows. Since $Y(t)$ is Gauss normal, then [10, Sec 3–5]:

$$\mathrm{E}[Y(t)] = 0 \tag{185}$$

$$\mathrm{Cov}[Y(s), Y(t)] = \min(s,t)\,[1 - \max(s,t)] \tag{186}$$

The mean and covariance of a process that is defined via quadratic operations on a zero-mean Gauss normal process [10, Sec 3–4] follow as:

$$\mathrm{E}[Y^2] = 0$$

$$\mathrm{Cov}[Y^2(s), Y^2(t)] = 2\mathrm{Cov}^2[Y(s), Y(t)] = 2\,\{\min(s,t)\,[1 - \max(s,t)]\}^2$$

Hence, finally,

$$\mathrm{E}[W^2] = \int_0^1 \mathrm{E}[Y^2(t)]\mathrm{d}t = 0 \tag{189}$$

$$\mathrm{Var}[W^2] = \mathrm{Var}\left[\int_0^1 Y^2(t)\mathrm{d}t\right] = \int_0^1 \int_0^1 \mathrm{Cov}[Y^2(s), Y^2(t)]\mathrm{d}s\mathrm{d}t = 1/45$$

I Tables

I.1 Field statistics

Field statistics for stirrer data (f=2.5GHz, r=91mm, m=2):

Avg:
(Ex) = 30.2261V/m (29.6076dBV/m)
(Ey) = 28.0698V/m (28.9648dBV/m)
(Ez) = 29.9004V/m (29.5135dBV/m)
(Et) = 55.6200V/m (34.9046dBV/m)
(Pi) = 0.0569mW (-12.4524dBm)

Std:
(Ex) = 17.8297V/m (25.0229dBV/m)
(Ey) = 19.0969V/m (25.6193dBV/m)
(Ez) = 18.5392V/m (25.3618dBV/m)
(Et) = 22.9049V/m (27.1986dBV/m)
(Pi) = 0.0112mW (-19.5122dBm)

Max:
(Ex) = 97.9867V/m (39.8233dBV/m)
(Ey) = 87.0292V/m (38.7933dBV/m)
(Ez) = 99.6108V/m (39.9661dBV/m)
(Et) = 126.9026V/m (42.0694dBV/m)
(Pi) = 0.0895mW (-10.4802dBm)

Max/Avg:
(Ex) = 3.2418 (10.2157dB)
(Ey) = 3.1005 (9.8285dB)
(Ez) = 3.3314 (10.4526dB)
(Et) = 2.2816 (7.1648dB)
(Pi) = 1.5748 (1.9722dB)

Med:
(Ex) = 27.1853V/m (28.6867dBV/m)
(Ey) = 23.2484V/m (27.3279dBV/m)
(Ez) = 26.4082V/m (28.4348dBV/m)
(Et) = 51.8541V/m (34.2957dBV/m)
(Pi) = 0.0583mW (-12.3399dBm)

VarCoef:
(Ex) = 0.5899 (-4.5848dB)
(Ey) = 0.6803 (-3.3455dB)
(Ez) = 0.6200 (-4.1517dB)
(Et) = 0.4118 (-7.7060dB)
(Pi) = 0.1968 (-7.0598dB)

Min:
(Ex) = 2.0751V/m (6.3409dBV/m)
(Ey) = 2.0050V/m (6.0424dBV/m)
(Ez) = 2.7856V/m (8.8983dBV/m)
(Et) = 9.0634V/m (19.1458dBV/m)
(Pi) = 0.0342mW (-14.6589dBm)

Max/Min:
(Ex) = 47.2196 (33.4824dB)
(Ey) = 43.4054 (32.7509dB)
(Ez) = 35.7595 (31.0678dB)
(Et) = 14.0016 (22.9236dB)
(Pi) = 2.6174 (4.1787dB)

Table 1: Field statistics @ $f = 2.5$GHz, $r = 91$mm ($m_\alpha = 2$).

Field statistics for stirrer data (f=2.5GHz, r=91mm, m=1):

Avg:
(Ex) = 30.9372V/m (29.8096dBV/m)
(Ey) = 28.3530V/m (29.0520dBV/m)
(Ez) = 30.3554V/m (29.6447dBV/m)
(Et) = 56.3690V/m (35.0208dBV/m)
(Pi) = 0.0571mW (-12.4372dBm)

Med:
(Ex) = 28.7750V/m (29.1803dBV/m)
(Ey) = 23.8891V/m (27.5640dBV/m)
(Ez) = 26.4680V/m (28.4544dBV/m)
(Et) = 54.5530V/m (34.7364dBV/m)
(Pi) = 0.0583mW (-12.3450dBm)

Std:
(Ex) = 17.9524V/m (25.0825dBV/m)
(Ey) = 18.3486V/m (25.2720dBV/m)
(Ez) = 18.7087V/m (25.4409dBV/m)
(Et) = 22.6308V/m (27.0940dBV/m)
(Pi) = 0.0111mW (-19.5491dBm)

VarCoef:
(Ex) = 0.5803 (-4.7272dB)
(Ey) = 0.6471 (-3.7799dB)
(Ez) = 0.6163 (-4.2038dB)
(Et) = 0.4015 (-7.9268dB)
(Pi) = 0.1944 (-7.1119dB)

Max:
(Ex) = 98.1590V/m (39.8386dBV/m)
(Ey) = 89.2145V/m (39.0087dBV/m)
(Ez) = 99.7860V/m (39.9814dBV/m)
(Et) = 130.8491V/m (42.3354dBV/m)
(Pi) = 0.0895mW (-10.4802dBm)

Min:
(Ex) = 2.0788V/m (6.3562dBV/m)
(Ey) = 2.0086V/m (6.0577dBV/m)
(Ez) = 2.3001V/m (7.2350dBV/m)
(Et) = 9.0794V/m (19.1611dBV/m)
(Pi) = 0.0327mW (-14.8596dBm)

Max/Avg:
(Ex) = 3.1729 (10.0290dB)
(Ey) = 3.1466 (9.9567dB)
(Ez) = 3.2873 (10.3367dB)
(Et) = 2.3213 (7.3146dB)
(Pi) = 1.5692 (1.9569dB)

Max/Min:
(Ex) = 47.2196 (33.4824dB)
(Ey) = 44.4172 (32.9510dB)
(Ez) = 43.3828 (32.7463dB)
(Et) = 14.4117 (23.1743dB)
(Pi) = 2.7411 (4.3793dB)

Table 2: Field statistics @ $f = 2.5$GHz, $r = 91$mm ($m_\alpha = 1$).

Field statistics for stirrer data (f=2.5GHz, r=345mm, m=2):

Avg:
(Ex) = 10.1945V/m (20.1673dBV/m)
(Ey) = 7.6278V/m (17.6480dBV/m)
(Ez) = 33.2053V/m (30.4242dBV/m)
(Et) = 36.5175V/m (31.2500dBV/m)
(Pi) = 0.0564mW (-12.4874dBm)

Std:
(Ex) = 6.1929V/m (15.8378dBV/m)
(Ey) = 4.8528V/m (13.7199dBV/m)
(Ez) = 18.4528V/m (25.3213dBV/m)
(Et) = 18.2506V/m (25.2255dBV/m)
(Pi) = 0.0111mW (-19.5454dBm)

Max:
(Ex) = 34.1214V/m (30.6605dBV/m)
(Ey) = 23.6055V/m (27.4603dBV/m)
(Ez) = 95.4761V/m (39.5979dBV/m)
(Et) = 96.9263V/m (39.7288dBV/m)
(Pi) = 0.0862mW (-10.6448dBm)

Max/Avg:
(Ex) = 3.3470 (10.4932dB)
(Ey) = 3.0947 (9.8123dB)
(Ez) = 2.8753 (9.1737dB)
(Et) = 2.6542 (8.4788dB)
(Pi) = 1.5285 (1.8426dB)

Med:
(Ex) = 8.7203V/m (18.8106dBV/m)
(Ey) = 6.4283V/m (16.1619dBV/m)
(Ez) = 27.7054V/m (28.8513dBV/m)
(Et) = 30.5887V/m (29.7112dBV/m)
(Pi) = 0.0577mW (-12.3872dBm)

VarCoef:
(Ex) = 0.6075 (-4.3295dB)
(Ey) = 0.6362 (-3.9281dB)
(Ez) = 0.5557 (-5.1029dB)
(Et) = 0.4998 (-6.0245dB)
(Pi) = 0.1969 (-7.0580dB)

Min:
(Ex) = 1.7913V/m (5.0632dBV/m)
(Ey) = 0.9014V/m (-0.9021dBV/m)
(Ez) = 5.6850V/m (15.0946dBV/m)
(Et) = 10.3008V/m (20.2575dBV/m)
(Pi) = 0.0330mW (-14.8145dBm)

Max/Min:
(Ex) = 19.0487 (25.5973dB)
(Ey) = 26.1889 (28.3624dB)
(Ez) = 16.7945 (24.5033dB)
(Et) = 9.4095 (19.4714dB)
(Pi) = 2.6120 (4.1698dB)

Table 3: Field statistics @ $f = 2.5\text{GHz}$, $r = 345\text{mm}$ ($m_\alpha = 2$).

Field statistics for stirrer data (f=2.5GHz, r=345mm, m=1):

Avg:
(Ex) = 10.3505V/m (20.2993dBV/m)
(Ey) = 7.6960V/m (17.7253dBV/m)
(Ez) = 33.1389V/m (30.4068dBV/m)
(Et) = 36.6531V/m (31.2822dBV/m)
(Pi) = 0.0565mW (-12.4787dBm)

Med:
(Ex) = 8.8384V/m (18.9275dBV/m)
(Ey) = 6.3731V/m (16.0870dBV/m)
(Ez) = 28.2571V/m (29.0226dBV/m)
(Et) = 32.1079V/m (30.1322dBV/m)
(Pi) = 0.0580mW (-12.3693dBm)

Std:
(Ex) = 6.5269V/m (16.2941dBV/m)
(Ey) = 4.8689V/m (13.7486dBV/m)
(Ez) = 18.8654V/m (25.5133dBV/m)
(Et) = 18.5208V/m (25.3532dBV/m)
(Pi) = 0.0111mW (-19.5551dBm)

VarCoef:
(Ex) = 0.6306 (-4.0052dB)
(Ey) = 0.6327 (-3.9767dB)
(Ez) = 0.5693 (-4.8935dB)
(Et) = 0.5053 (-5.9290dB)
(Pi) = 0.1960 (-7.0764dB)

Max:
(Ex) = 37.4413V/m (31.4670dBV/m)
(Ey) = 23.6291V/m (27.4690dBV/m)
(Ez) = 116.5067V/m (41.3270dBV/m)
(Et) = 118.3266V/m (41.4616dBV/m)
(Pi) = 0.0862mW (-10.6448dBm)

Min:
(Ex) = 1.5934V/m (4.0465dBV/m)
(Ey) = 0.9023V/m (-0.8934dBV/m)
(Ez) = 4.7127V/m (13.4654dBV/m)
(Et) = 9.2136V/m (19.2886dBV/m)
(Pi) = 0.0330mW (-14.8145dBm)

Max/Avg:
(Ex) = 3.6173 (11.1678dB)
(Ey) = 3.0703 (9.7436dB)
(Ez) = 3.5157 (10.9203dB)
(Et) = 3.2283 (10.1794dB)
(Pi) = 1.5254 (1.8340dB)

Max/Min:
(Ex) = 23.4977 (27.4205dB)
(Ey) = 26.1889 (28.3624dB)
(Ez) = 24.7218 (27.8616dB)
(Et) = 12.8426 (22.1731dB)
(Pi) = 2.6120 (4.1698dB)

Table 4: Field statistics @ $f = 2.5$GHz, $r = 345$mm ($m_\alpha = 1$

Field statistics for stirrer data (f=8.2GHz, r=91mm, m=3):

Avg:
(Ex) = 27.4248V/m (28.7629dBV/m)
(Ey) = 27.3319V/m (28.7334dBV/m)
(Ez) = 28.4359V/m (29.0773dBV/m)
(Et) = 51.8704V/m (34.2984dBV/m)
(Pi) = 0.0269mW (-15.7093dBm)

Med:
(Ex) = 25.4658V/m (28.1192dBV/m)
(Ey) = 25.7214V/m (28.2059dBV/m)
(Ez) = 27.0110V/m (28.6308dBV/m)
(Et) = 51.7967V/m (34.2860dBV/m)
(Pi) = 0.0267mW (-15.7311dBm)

Std:
(Ex) = 14.6759V/m (23.3321dBV/m)
(Ey) = 14.0483V/m (22.9525dBV/m)
(Ez) = 14.5508V/m (23.2577dBV/m)
(Et) = 15.5150V/m (23.8150dBV/m)
(Pi) = 0.0022mW (-26.6585dBm)

VarCoef:
(Ex) = 0.5351 (-5.4308dB)
(Ey) = 0.5140 (-5.7809dB)
(Ez) = 0.5117 (-5.8196dB)
(Et) = 0.2991 (-10.4834dB)
(Pi) = 0.0804 (-10.9492dB)

Max:
(Ex) = 91.7801V/m (39.2550dBV/m)
(Ey) = 75.7166V/m (37.5838dBV/m)
(Ez) = 70.5125V/m (36.9653dBV/m)
(Et) = 97.6400V/m (39.7926dBV/m)
(Pi) = 0.0332mW (-14.7911dBm)

Min:
(Ex) = 0.6140V/m (-4.2371dBV/m)
(Ey) = 0.1810V/m (-14.8441dBV/m)
(Ez) = 0.2287V/m (-12.8160dBV/m)
(Et) = 11.3358V/m (21.0891dBV/m)
(Pi) = 0.0222mW (-16.5328dBm)

Max/Avg:
(Ex) = 3.3466 (10.4921dB)
(Ey) = 2.7703 (8.8504dB)
(Ez) = 2.4797 (7.8880dB)
(Et) = 1.8824 (5.4942dB)
(Pi) = 1.2354 (0.9182dB)

Max/Min:
(Ex) = 149.4878 (43.4921dB)
(Ey) = 418.2115 (52.4279dB)
(Ez) = 308.3646 (49.7813dB)
(Et) = 8.6134 (18.7035dB)
(Pi) = 1.4934 (1.7418dB)

Table 5: Field statistics @ $f = 8.2\text{GHz}$, $r = 91\text{mm}$ ($m_\alpha = 3$).

Field statistics for stirrer data (f=8.2GHz, r=91mm, m=1):

Avg:
(Ex) = 27.4430V/m (28.7686dBV/m)
(Ey) = 27.2111V/m (28.6949dBV/m)
(Ez) = 28.3650V/m (29.0557dBV/m)
(Et) = 51.8623V/m (34.2970dBV/m)
(Pi) = 0.0269mW (-15.7087dBm)

Med:
(Ex) = 24.9728V/m (27.9493dBV/m)
(Ey) = 26.3191V/m (28.4054dBV/m)
(Ez) = 26.6506V/m (28.5142dBV/m)
(Et) = 51.7665V/m (34.2810dBV/m)
(Pi) = 0.0267mW (-15.7374dBm)

Std:
(Ex) = 14.7228V/m (23.3598dBV/m)
(Ey) = 14.0612V/m (22.9604dBV/m)
(Ez) = 14.6216V/m (23.2999dBV/m)
(Et) = 15.3744V/m (23.7360dBV/m)
(Pi) = 0.0022mW (-26.6509dBm)

VarCoef:
(Ex) = 0.5365 (-5.4088dB)
(Ey) = 0.5167 (-5.7345dB)
(Ez) = 0.5155 (-5.7557dB)
(Et) = 0.2964 (-10.5611dB)
(Pi) = 0.0805 (-10.9422dB)

Max:
(Ex) = 91.7857V/m (39.2555dBV/m)
(Ey) = 80.0913V/m (38.0717dBV/m)
(Ez) = 70.5169V/m (36.9659dBV/m)
(Et) = 101.5197V/m (40.1310dBV/m)
(Pi) = 0.0339mW (-14.7011dBm)

Min:
(Ex) = 0.3400V/m (-9.3701dBV/m)
(Ey) = 0.1811V/m (-14.8436dBV/m)
(Ez) = 0.0677V/m (-23.3894dBV/m)
(Et) = 8.5524V/m (18.6417dBV/m)
(Pi) = 0.0218mW (-16.6109dBm)

Max/Avg:
(Ex) = 3.3446 (10.4869dB)
(Ey) = 2.9433 (9.3768dB)
(Ez) = 2.4861 (7.9102dB)
(Et) = 1.9575 (5.8340dB)
(Pi) = 1.2611 (1.0076dB)

Max/Min:
(Ex) = 269.9467 (48.6256dB)
(Ey) = 442.3472 (52.9153dB)
(Ez) = 1041.7482 (60.3553dB)
(Et) = 11.8704 (21.4893dB)
(Pi) = 1.5523 (1.9098dB)

Table 6: Field statistics @ $f = 8.2$GHz, $r = 91$mm ($m_\alpha = 1$)

I.2 Theoretical vs. measured mean-normalized field

X	ν_X	n_X
$\|E_x\|/\langle\|E_x\|\rangle$	$\sqrt{\frac{4}{\pi}-1} \approx 0.5227$	0.5899
$\|E_y\|/\langle\|E_y\|\rangle$	$\sqrt{\frac{4}{\pi}-1} \approx 0.5227$	0.6803
$\|E_z\|/\langle\|E_z\|\rangle$	$\sqrt{\frac{4}{\pi}-1} \approx 0.5227$	0.6200
$\|E_t\|/\langle\|E_t\|\rangle$	$\sqrt{\frac{1536}{450\pi}-1} \approx 0.2941$	0.4118

Table 7: Theoretical vs. measured coefficients of variation for mean-normalized field @ f 2.5GHz, $r = 91$mm: decimated data set ($m_\alpha = 2$).

X	ν_X	n_X
$\|E_x\|/\langle\|E_x\|\rangle$	$\sqrt{\frac{4}{\pi}-1} \approx 0.5227$	0.5803
$\|E_y\|/\langle\|E_y\|\rangle$	$\sqrt{\frac{4}{\pi}-1} \approx 0.5227$	0.6471
$\|E_z\|/\langle\|E_z\|\rangle$	$\sqrt{\frac{4}{\pi}-1} \approx 0.5227$	0.6163
$\|E_t\|/\langle\|E_t\|\rangle$	$\sqrt{\frac{1536}{450\pi}-1} \approx 0.2941$	0.4015

Table 8: Theoretical vs. measured coefficients of variation for mean-normalized field @ $f =$ 2.5GHz, $r = 91$mm: full data set ($m_\alpha = 1$).

X	ν_X	n_X
$\|E_x\|/\langle\|E_x\|\rangle$	$\sqrt{\frac{4}{\pi}-1} \approx 0.5227$	0.6075
$\|E_y\|/\langle\|E_y\|\rangle$	$\sqrt{\frac{4}{\pi}-1} \approx 0.5227$	0.6362
$\|E_z\|/\langle\|E_z\|\rangle$	$\sqrt{\frac{4}{\pi}-1} \approx 0.5227$	0.5557
$\|E_t\|/\langle\|E_t\|\rangle$	$\sqrt{\frac{1536}{450\pi}-1} \approx 0.2941$	0.4998

Table 9: Theoretical vs. measured coefficients of variation for mean-normalized field @ f 2.5GHz, $r = 345$mm: decimated data set ($m_\alpha = 2$).

X	ν_X	n_X
$\|E_x\|/\langle\|E_x\|\rangle$	$\sqrt{(\frac{4}{\pi}-1} \approx 0.5227$	0.6306
$\|E_y\|/\langle\|E_y\|\rangle$	$\sqrt{\frac{4}{\pi}-1} \approx 0.5227$	0.6327
$\|E_z\|/\langle\|E_z\|\rangle$	$\sqrt{\frac{4}{\pi}-1} \approx 0.5227$	0.5639
$\|E_t\|/\langle\|E_t\|\rangle$	$\sqrt{\frac{1536}{450\pi}-1} \approx 0.2941$	0.5053

Table 10: Theoretical vs. measured coefficients of variation for mean-normalized field @ f 2.5GHz, r = 345mm: full data set ($m_\alpha = 1$).

X	ν_X	n_X
$\|E_x\|/\langle\|E_x\|\rangle$	$\sqrt{\frac{4}{\pi}-1} \approx 0.5227$	0.5351
$\|E_y\|/\langle\|E_y\|\rangle$	$\sqrt{\frac{4}{\pi}-1} \approx 0.5227$	0.5140
$\|E_z\|/\langle\|E_z\|\rangle$	$\sqrt{\frac{4}{\pi}-1} \approx 0.5227$	0.5117
$\|E_t\|/\langle\|E_t\|\rangle$	$\sqrt{\frac{1536}{450\pi}-1} \approx 0.2941$	0.2991

Table 11: Theoretical vs. measured coefficients of variation for mean-normalized field @ f = 8.2GHz, r = 91mm: decimated data set ($m_\alpha = 3$).

X	ν_X	n_X
$\|E_x\|/\langle\|E_x\|\rangle$	$\sqrt{\frac{4}{\pi}-1} \approx 0.5227$	0.5365
$\|E_y\|/\langle\|E_y\|\rangle$	$\sqrt{\frac{4}{\pi}-1} \approx 0.5227$	0.5167
$\|E_z\|/\langle\|E_z\|\rangle$	$\sqrt{\frac{4}{\pi}-1} \approx 0.5227$	0.5155
$\|E_t\|/\langle\|E_t\|\rangle$	$\sqrt{\frac{1536}{450\pi}-1} \approx 0.2941$	0.2964

Table 12: Theoretical vs. measured coefficients of variation for mean-normalized field @ f = 8.2GHz, r = 91mm: full data set ($m_\alpha = 1$).

I.3 Theoretical vs. measured mean-normalized maximum field

W	theory $([F^{-1}_{W_N}(0.025)\ldots\mu_{W_N}\ldots F^{-1}_{W_N}(0.975)])$	measured (w_M)
$\max(\lvert E_x\rvert)/\langle\lvert E_x\rvert\rangle$	$[2.2329\ldots2.6987\ldots3.3639]$	3.2418
$\max(\lvert E_y\rvert)/\langle\lvert E_y\rvert\rangle$	$[2.2329\ldots2.6987\ldots3.3639]$	3.1005
$\max(\lvert E_z\rvert)/\langle\lvert E_z\rvert\rangle$	$[2.2329\ldots2.6987\ldots3.3639]$	3.3314
$\max(\lvert E_t\rvert)/\langle\lvert E_t\rvert\rangle$	$[1.5812\ldots1.8271\ldots2.2340]$	2.2816

Table 13: Theoretical vs. measured max-to-mean field W with 95% confidence interval @ f = 2.5GHz, r = 91mm: decimated data (M = 137, N = 275/1.5 = 183).

W	theory $([F^{-1}_{W_N}(0.025)\ldots\mu_{W_N}\ldots F^{-1}_{W_N}(0.975)])$	measured (w_M)
$\max(\lvert E_x\rvert)/\langle\lvert E_x\rvert\rangle$	$[2.2329\ldots2.6987\ldots3.3639]$	3.1729
$\max(\lvert E_y\rvert)/\langle\lvert E_y\rvert\rangle$	$[2.2329\ldots2.6987\ldots3.3639]$	3.1466
$\max(\lvert E_z\rvert)/\langle\lvert E_z\rvert\rangle$	$[2.2329\ldots2.6987\ldots3.3639]$	3.2873
$\max(\lvert E_t\rvert)/\langle\lvert E_t\rvert\rangle$	$[1.5812\ldots1.8271\ldots2.2340]$	2.3213

Table 14: Theoretical vs. measured max-to-mean field W with 95% confidence interval @ f = 2.5GHz, r = 91mm: full data (M = 275, N = 275/1.5 = 183).

W	theory $([F^{-1}_{W_N}(0.025)\ldots\mu_{W_N}\ldots F^{-1}_{W_N}(0.975)])$	measured (w_M)
$\max(\lvert E_x\rvert)/\langle\lvert E_x\rvert\rangle$	$[2.2329\ldots2.6987\ldots3.3639]$	3.3471
$\max(\lvert E_y\rvert)/\langle\lvert E_y\rvert\rangle$	$[2.2329\ldots2.6987\ldots3.3639]$	3.0947
$\max(\lvert E_z\rvert)/\langle\lvert E_z\rvert\rangle$	$[2.2329\ldots2.6987\ldots3.3639]$	2.8753
$\max(\lvert E_t\rvert)/\langle\lvert E_t\rvert\rangle$	$[1.5812\ldots1.8271\ldots2.2340]$	2.6542

Table 15: Theoretical vs. measured max-to-mean field W with 95% confidence interval @ f = 2.5GHz, r = 345mm: decimated data (M = 137, N = 275/1.5 = 183).

W	theory $([F^{-1}_{W_N}(0.025)\ldots\mu_{W_N}\ldots F^{-1}_{W_N}(0.975)])$	measured (w_M)
$\max(\lvert E_x\rvert)/\langle\lvert E_x\rvert\rangle$	$[2.2329\ldots2.6987\ldots3.3639]$	3.6173
$\max(\lvert E_y\rvert)/\langle\lvert E_y\rvert\rangle$	$[2.2329\ldots2.6987\ldots3.3639]$	3.0703
$\max(\lvert E_z\rvert)/\langle\lvert E_z\rvert\rangle$	$[2.2329\ldots2.6987\ldots3.3639]$	3.5157
$\max(\lvert E_t\rvert)/\langle\lvert E_t\rvert\rangle$	$[1.5812\ldots1.8271\ldots2.2340]$	3.2283

Table 16: Theoretical vs. measured max-to-mean field W with 95% confidence interval @ f = 2.5GHz, r = 345mm: full data (M = 275, N = 275/1.5 = 183).

W	theory $([F^{-1}_{W_N}(0.025)\ldots\mu_{W_N}\ldots F^{-1}_{W_N}(0.975)])$	measured (w_M)
$\max(\lvert E_x\rvert)/\langle\lvert E_x\rvert\rangle$	$[2.4439\ldots2.9174\ldots3.5085]$	3.3099
$\max(\lvert E_y\rvert)/\langle\lvert E_y\rvert\rangle$	$[2.4439\ldots2.9174\ldots3.5085]$	2.9422
$\max(\lvert E_z\rvert)/\langle\lvert E_z\rvert\rangle$	$[2.4439\ldots2.9174\ldots3.5085]$	2.4836
$\max(\lvert E_t\rvert)/\langle\lvert E_t\rvert\rangle$	$[1.7242\ldots1.9363\ldots2.2669]$	1.8648

Table 17: Theoretical vs. measured max-to-mean field W with 95% confidence interval @ f = 8.2GHz, r = 91mm: decimated data (M = 400, N = 1200/3 = 400).

W	theory $([F^{-1}_{W_N}(0.025)\ldots\mu_{W_N}\ldots F^{-1}_{W_N}(0.975)])$	measured (w_M)
$\max(\lvert E_x\rvert)/\langle\lvert E_x\rvert\rangle$	$[2.4439\ldots2.9174\ldots3.5085]$	3.3446
$\max(\lvert E_y\rvert)/\langle\lvert E_y\rvert\rangle$	$[2.4439\ldots2.9174\ldots3.5085]$	2.9434
$\max(\lvert E_z\rvert)/\langle\lvert E_z\rvert\rangle$	$[2.4439\ldots2.9174\ldots3.5085]$	2.4861
$\max(\lvert E_t\rvert)/\langle\lvert E_t\rvert\rangle$	$[1.7242\ldots1.9363\ldots2.2669]$	1.9575

Table 18: Theoretical vs. measured max-to-mean field W with 95% confidence interval @ f = 8.2GHz, r = 91mm: full data (M = 1200, N = 1200/3 = 400).

Parameter	2.5GHz ($r = 91$mm)	2.5GHz ($r = 345$mm)	8.2GHz ($r = 91$mm)
β_x	0.0261	0.0490	0.0137
β_y	0.0321	−0.0049	0.0155
β_z	0.0640	0.0223	0.0149
δ_x	0.620	0.665	0.687
δ_y	0.639	0.633	0.670
δ_z	0.623	0.644	0.635
ϵ_x	0.823	0.849	0.904
ϵ_y	0.828	0.823	0.887
ϵ_z	0.808	0.824	0.867

Table 19: Spectral parameters and spectral bandwidths @ 2.5GHz, $r = 91$mm, 345mm and 8.2GHz, $r = 91$mm.

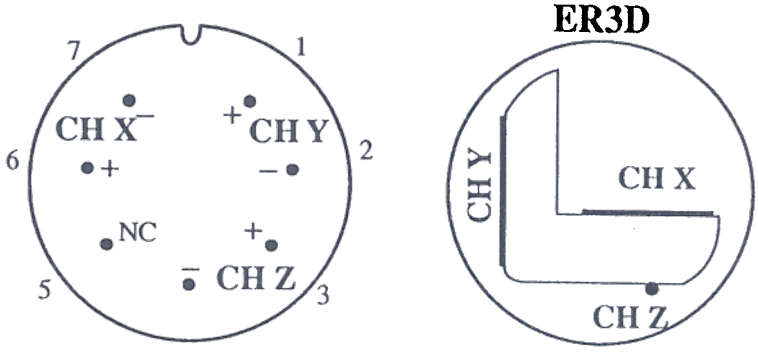
Mode	Resonance frequency (MHz)	Quality factor (−)
1	331.17	11,909
2	331.20	11,929
3	358.64	11,558
4	464.41	10,798
5	467.27	13,219
6	467.30	13,211

Table 20: Numerical simulation results (MAFIA^{TM}) for first few resonances of stadium cavity.

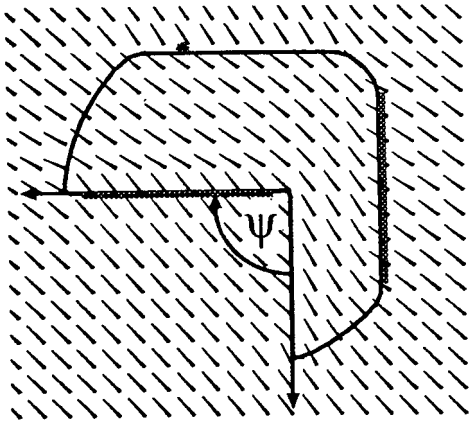
J Figures



(a)



(b)



(c)

Figure 1: (a) 3-axis electric field probe (Schmid & Partner ER3Dxxx family); (b) connector plan and front view; (c) local near-field distortions [Poković, 1999].

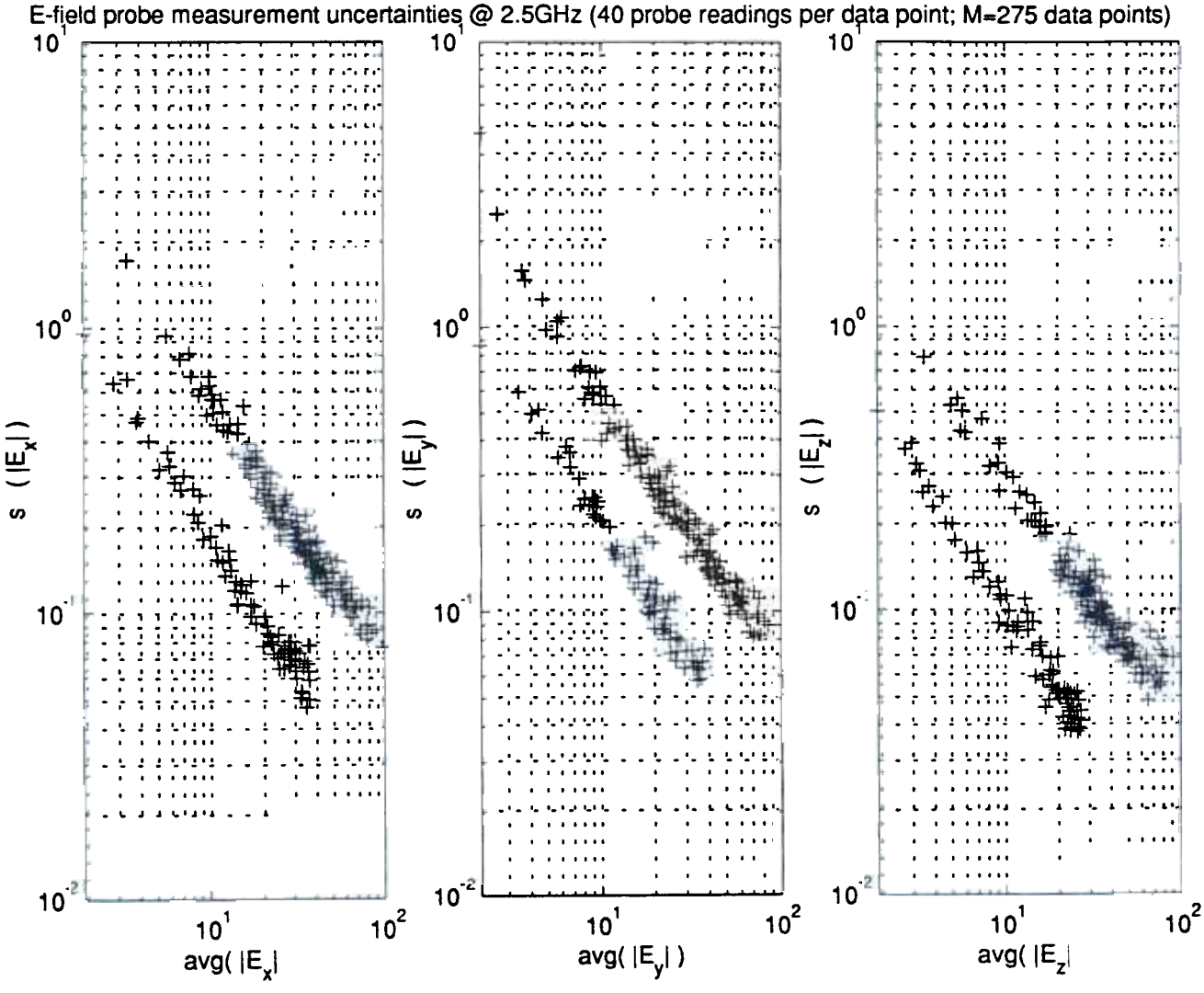
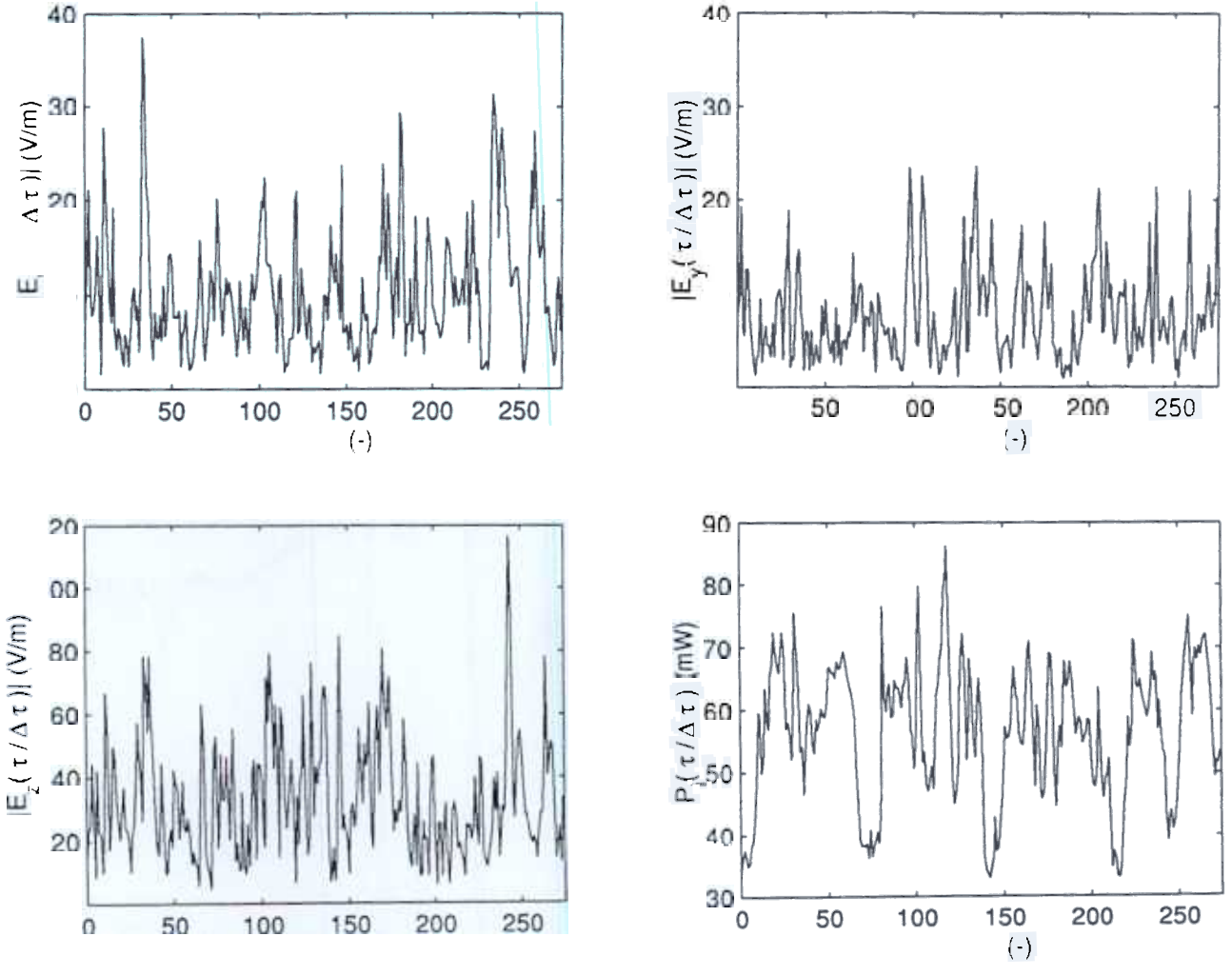
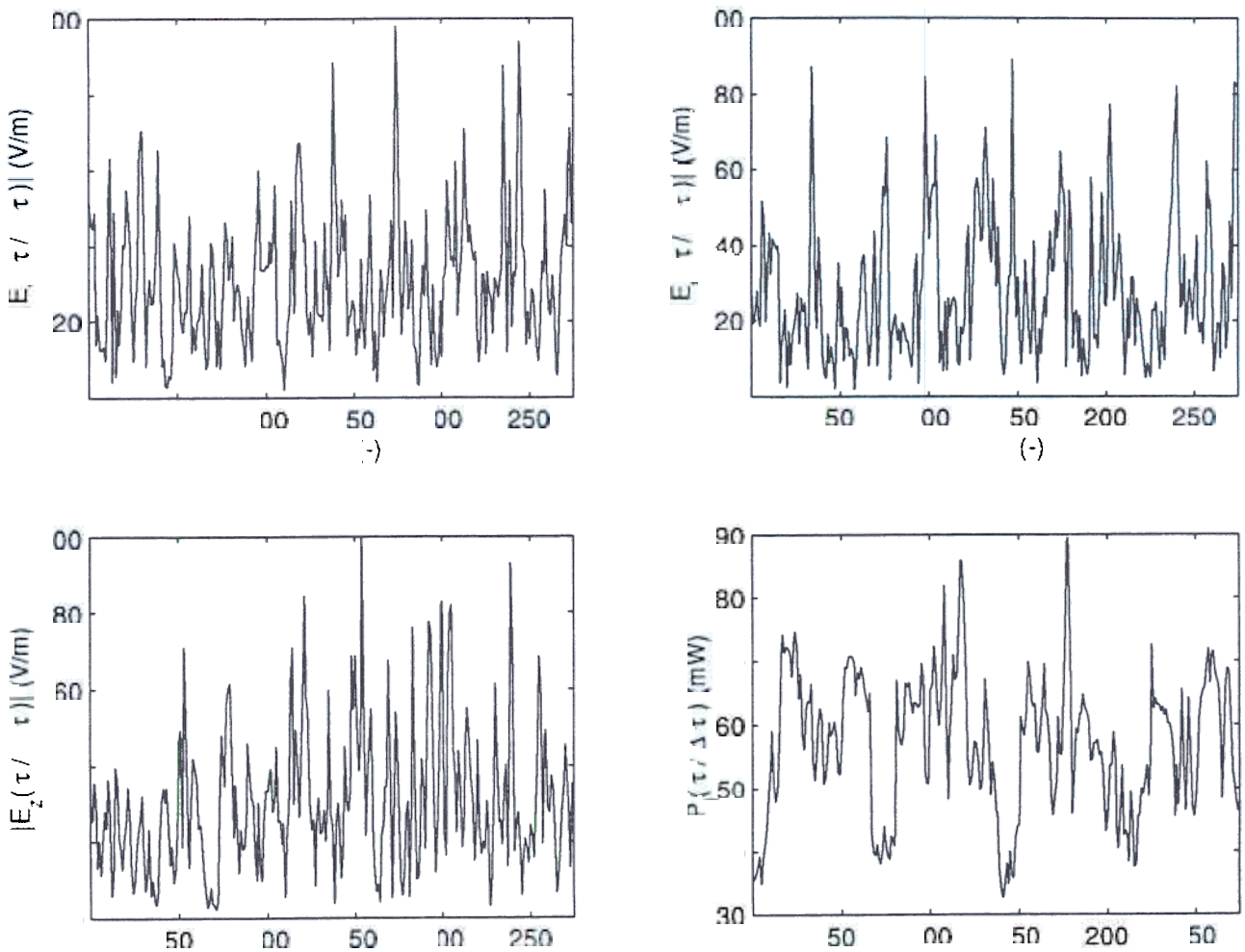


Figure 2: Spread as a function of average field strength for S&P probe measurements @ f = 2.5GHz, r = 91mm for 40 readings per sample and sample size M = 275.



ig ee @ *f* 5GH 345mm


00
20
00 50 00 250
-)
00
80
60
40
20
50 00 50 200 250
(-)
00
80
60
50 00 50 00 250
90
80
60
50
30
50 00 50 200 50

igu *f* GHz.

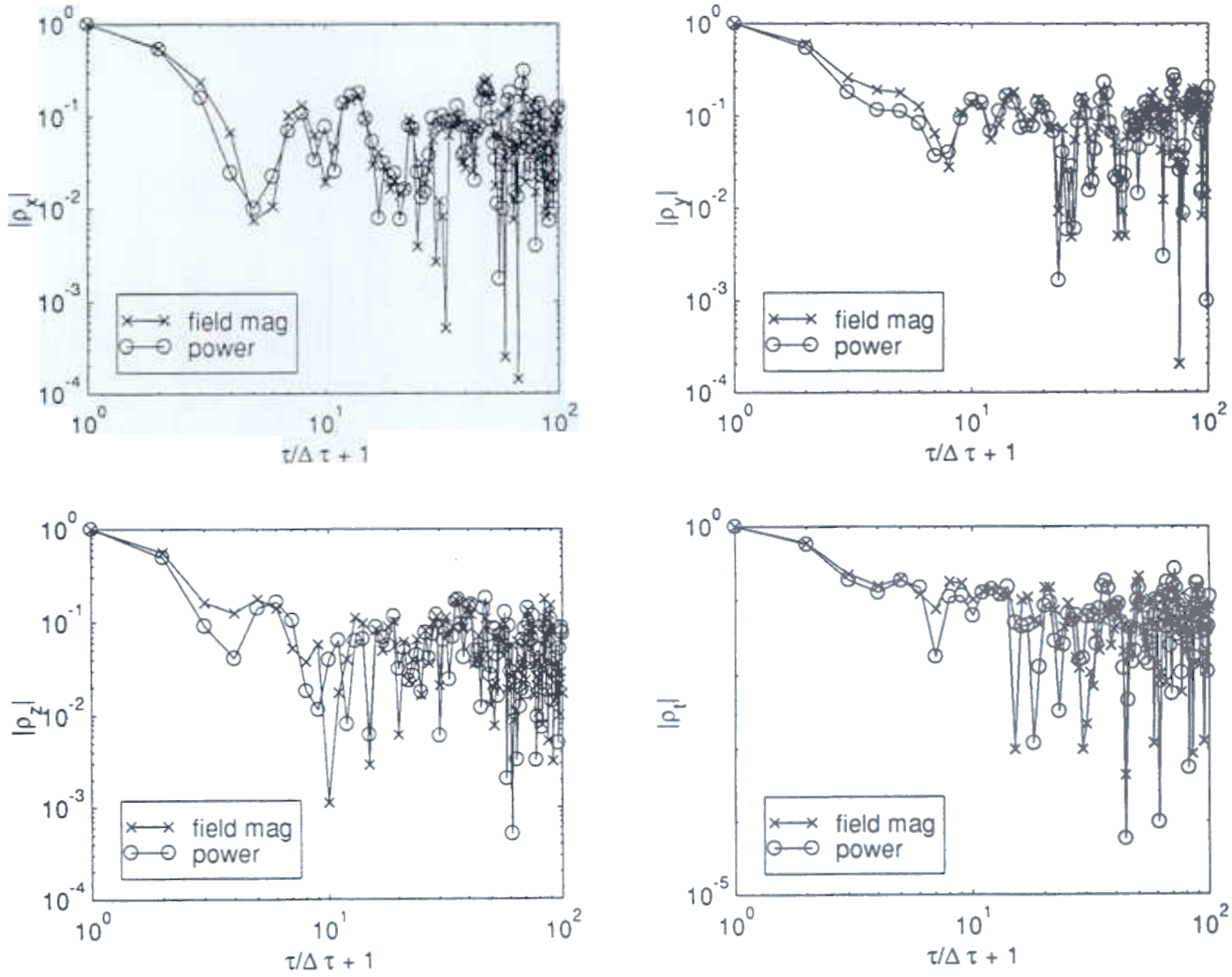


Figure 5: Autocorrelation functions $|\rho_\alpha|$ for power and field magnitude for $|E_\alpha|$ ($\alpha = x, y, z, t$) as a function of wall position $\tau/\Delta\tau$ @ $f = 2.5$GHz, $r = 91$mm.

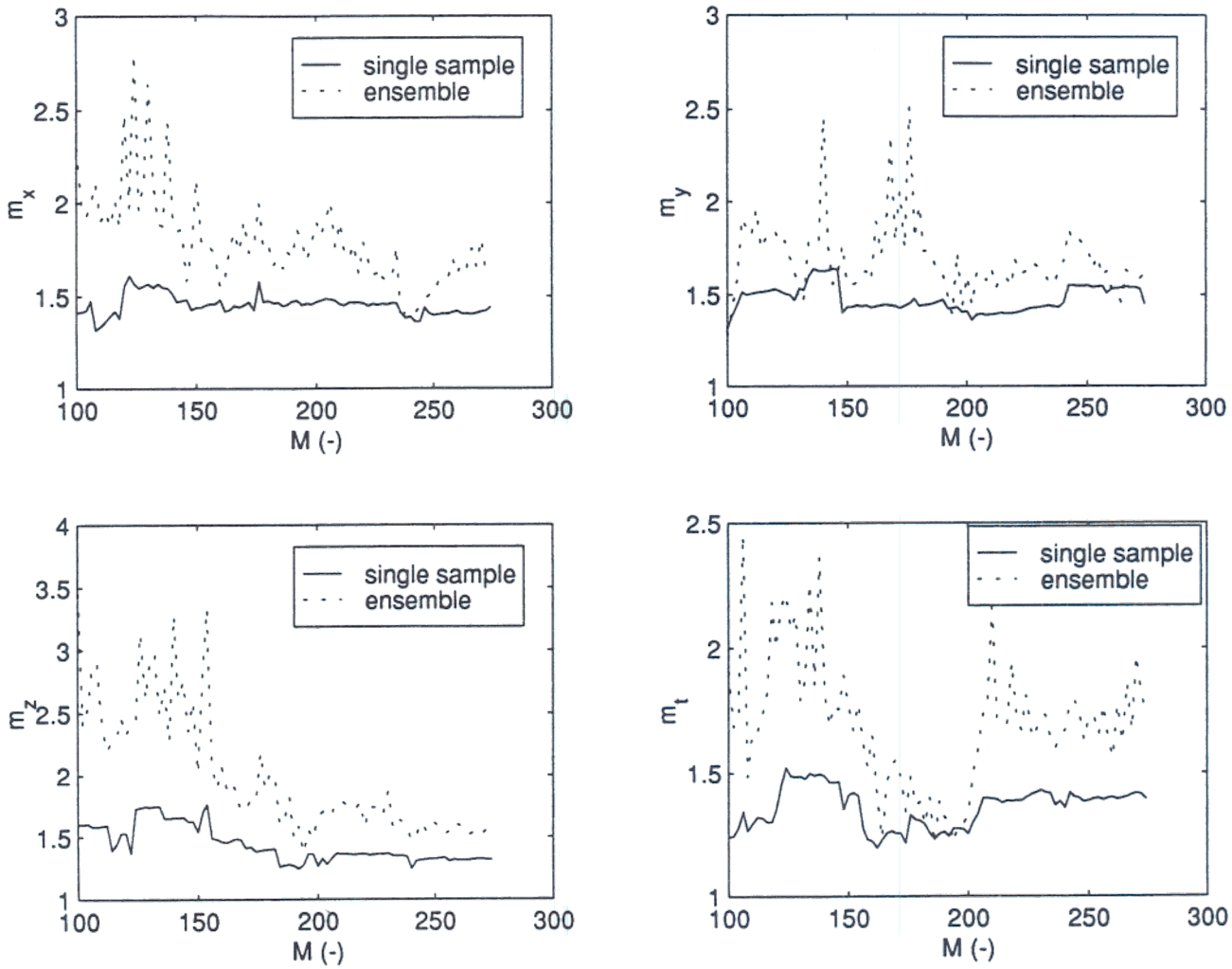


Figure 6: Single-sample and ensemble decimation factors m_α for $|E_\alpha|^2$ ($\alpha = x, y, z, t$) as a function of sample size M @ $f = 2.5$GHz, $r = 91$mm.

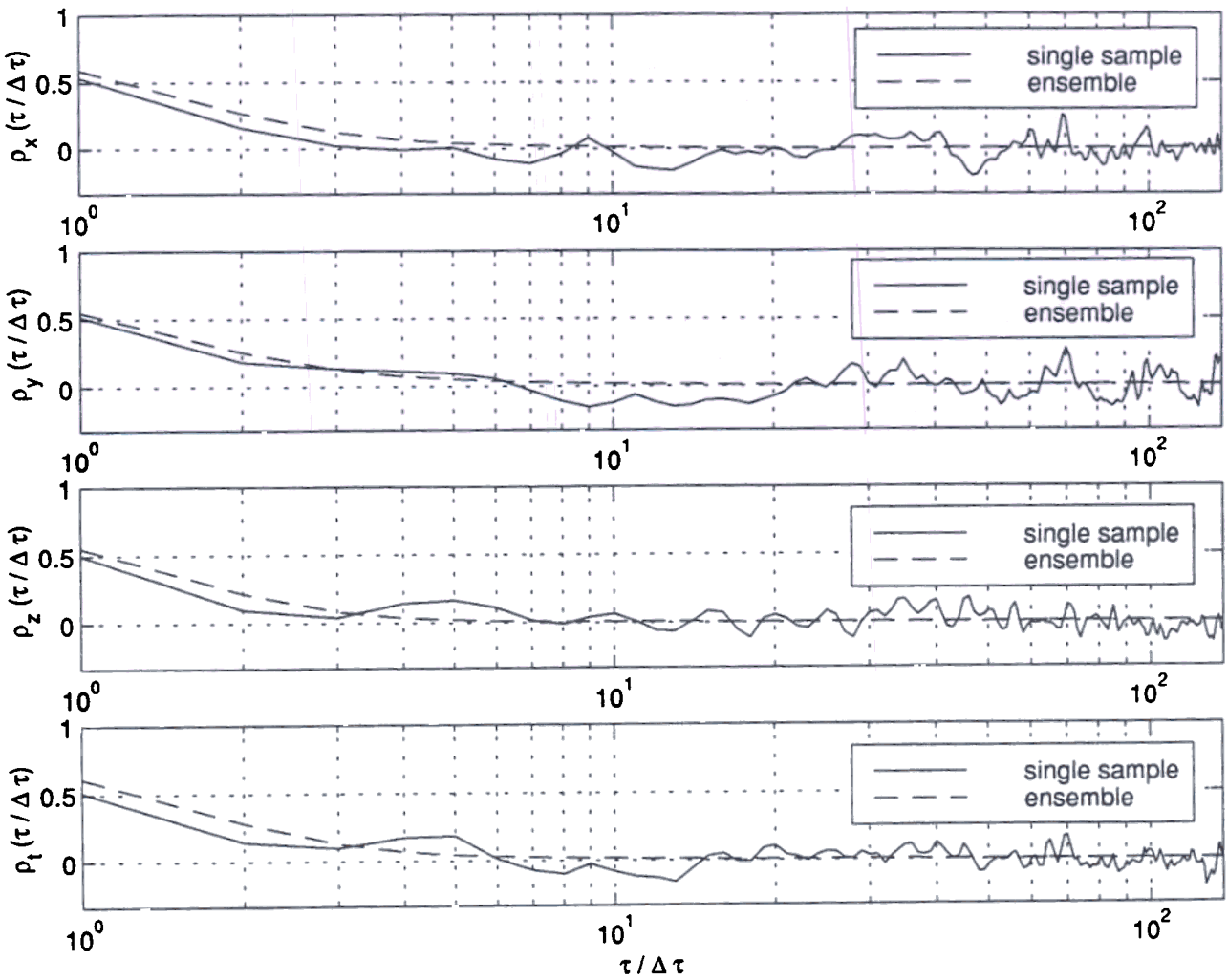


Figure 7: Single-sample and ensemble power autocorrelation functions ρ_α for $|E_\alpha|$ $(\alpha = x, y, z, t)$ as a function of wall position $\tau/\Delta\tau$ @ $f = 2.5\text{GHz}, r = 91\text{mm}$.

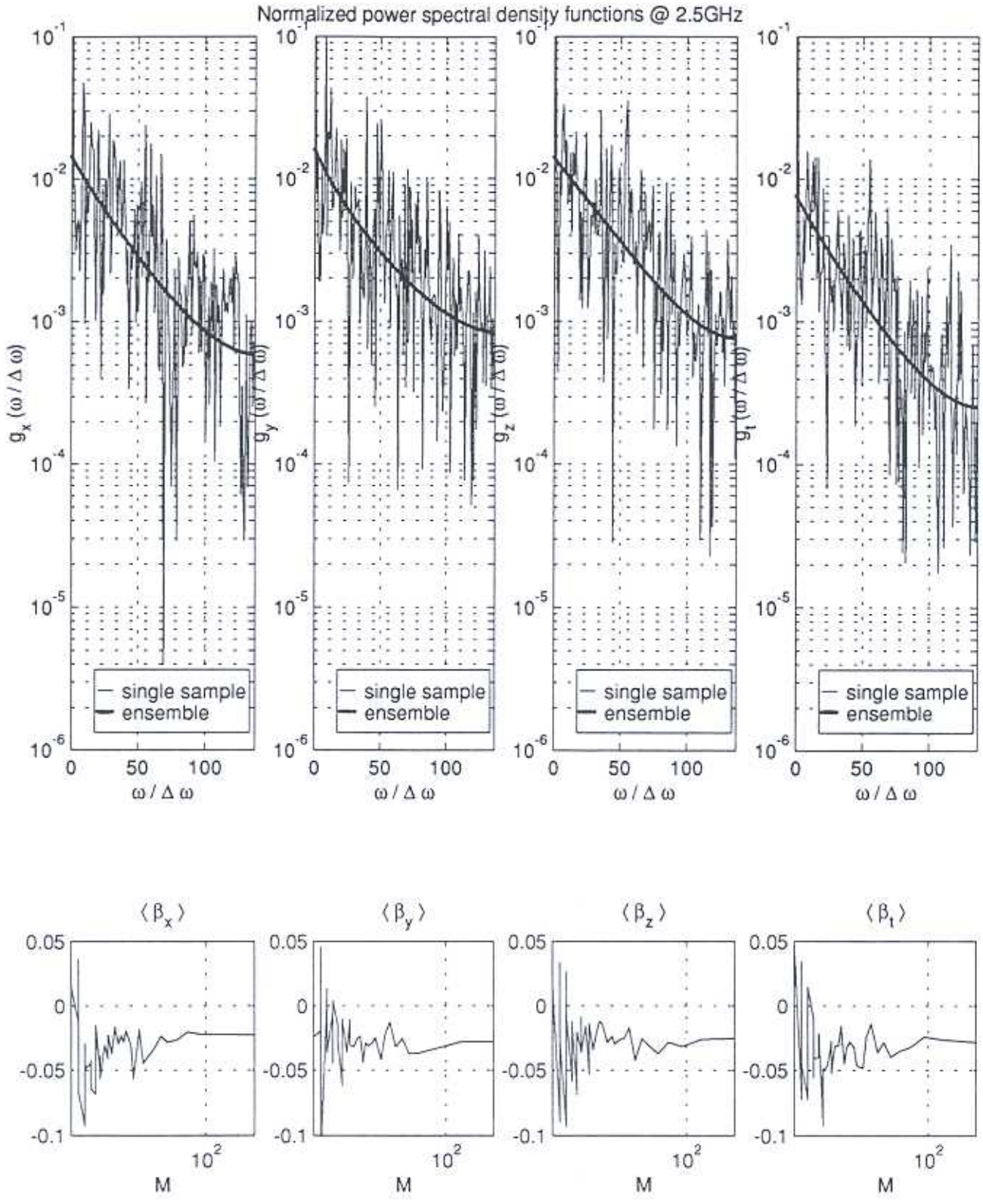


Figure 8: Single-sample and ensemble power autospectral density functions g_α for $|E_\alpha|$ ($\alpha = x, y, z, t$) as a function of spectral wall position $\omega/\Delta\omega$ @ $f = 2.5$GHz, $r = 91$mm, with Bartlett estimates of spectral parameters β_α for smoothed density function (1st-order exponential model).

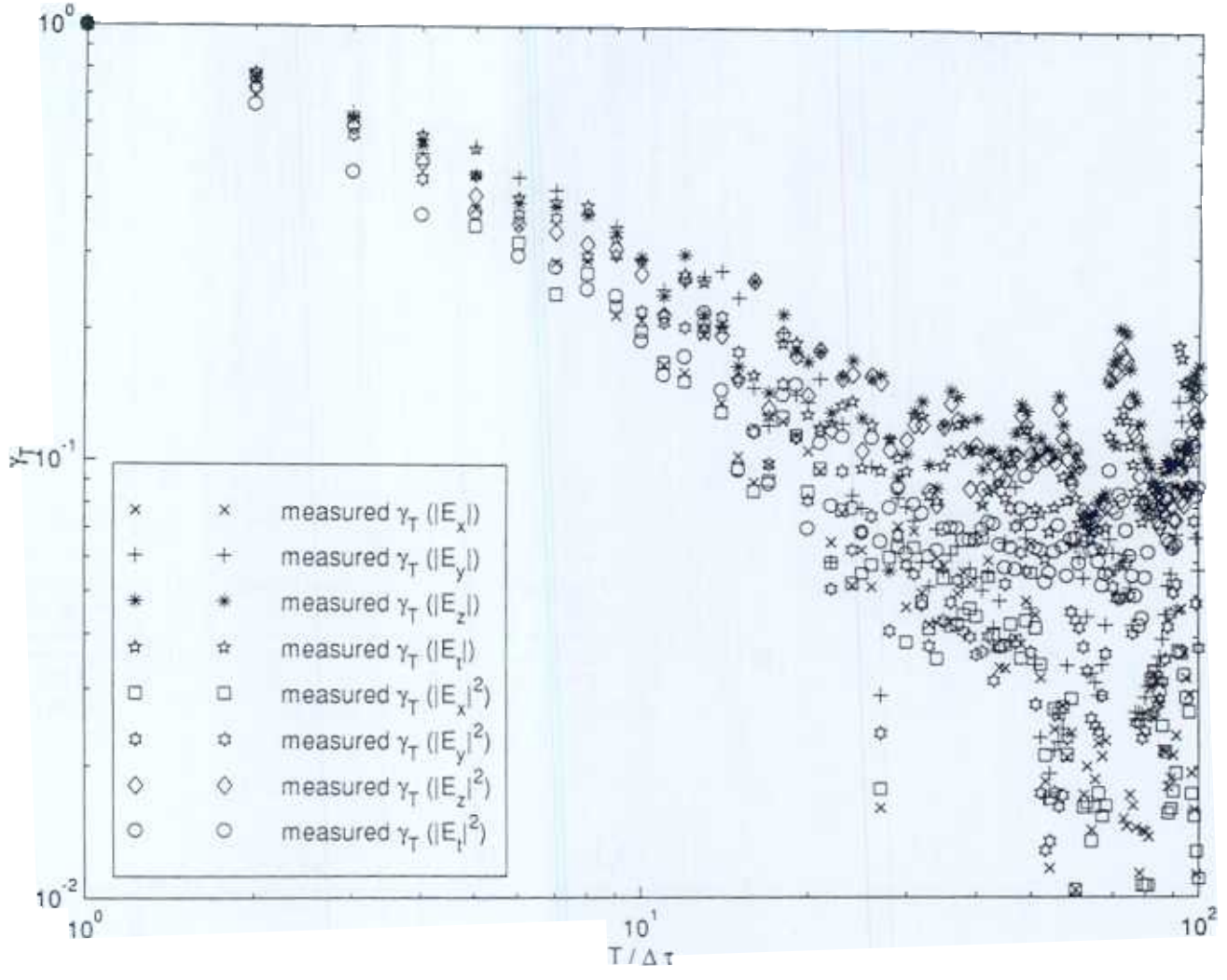


Figure 9: Field and power variance functions for $|E_\alpha|$ ($\alpha = x, y, z, t$) as a function of stirrer averaging length $\mathcal{T}/\Delta\tau$ @ $f = 2.5$GHz, $r = 91$mm.

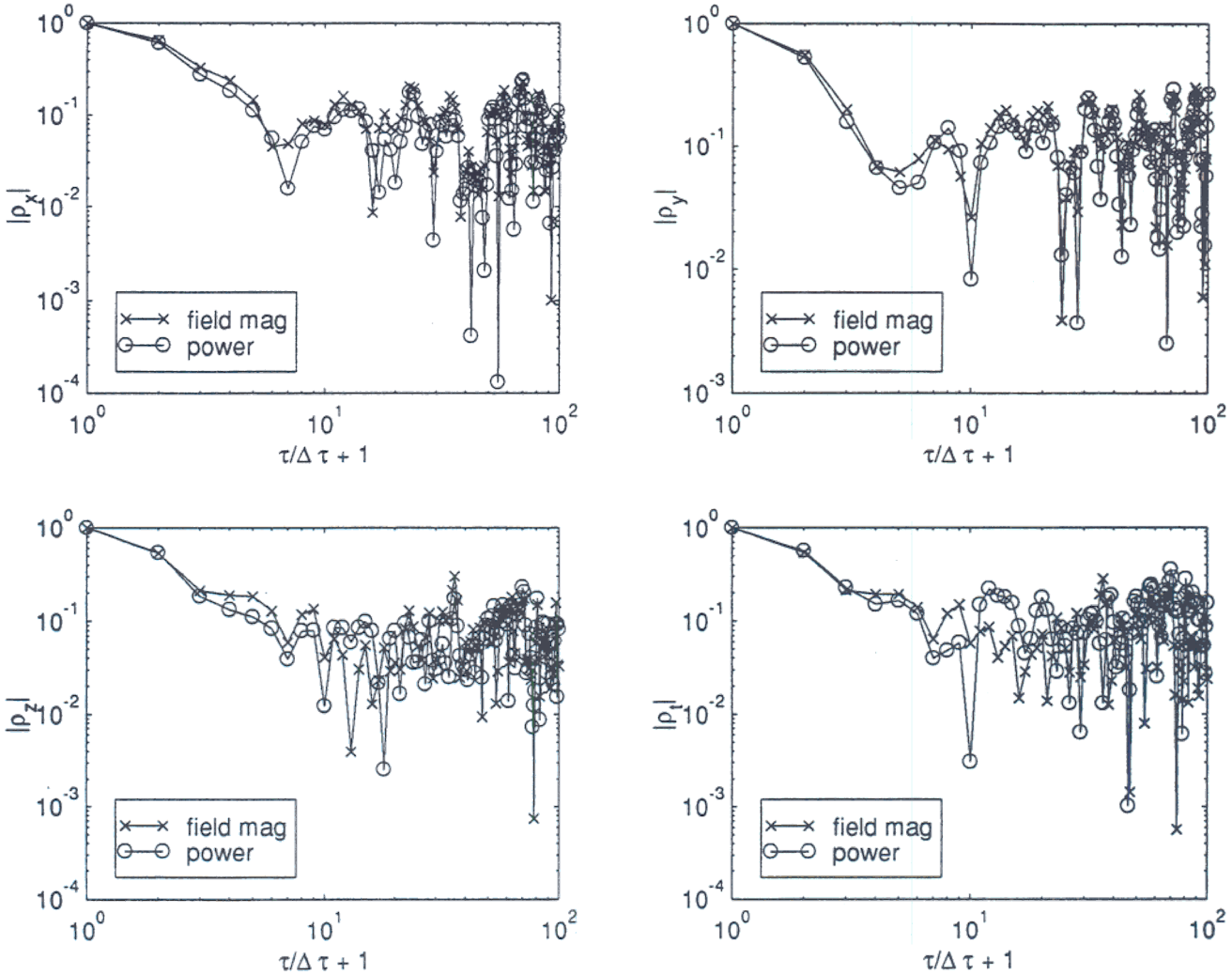


Figure 10: Autocorrelation functions $|\rho_\alpha|$ for power and field magnitude for $|E_\alpha|$ ($\alpha = x, y, z, t$) as a function of wall position $\tau/\Delta\tau$ @ $f = 2.5$GHz, $r = 345$mm.

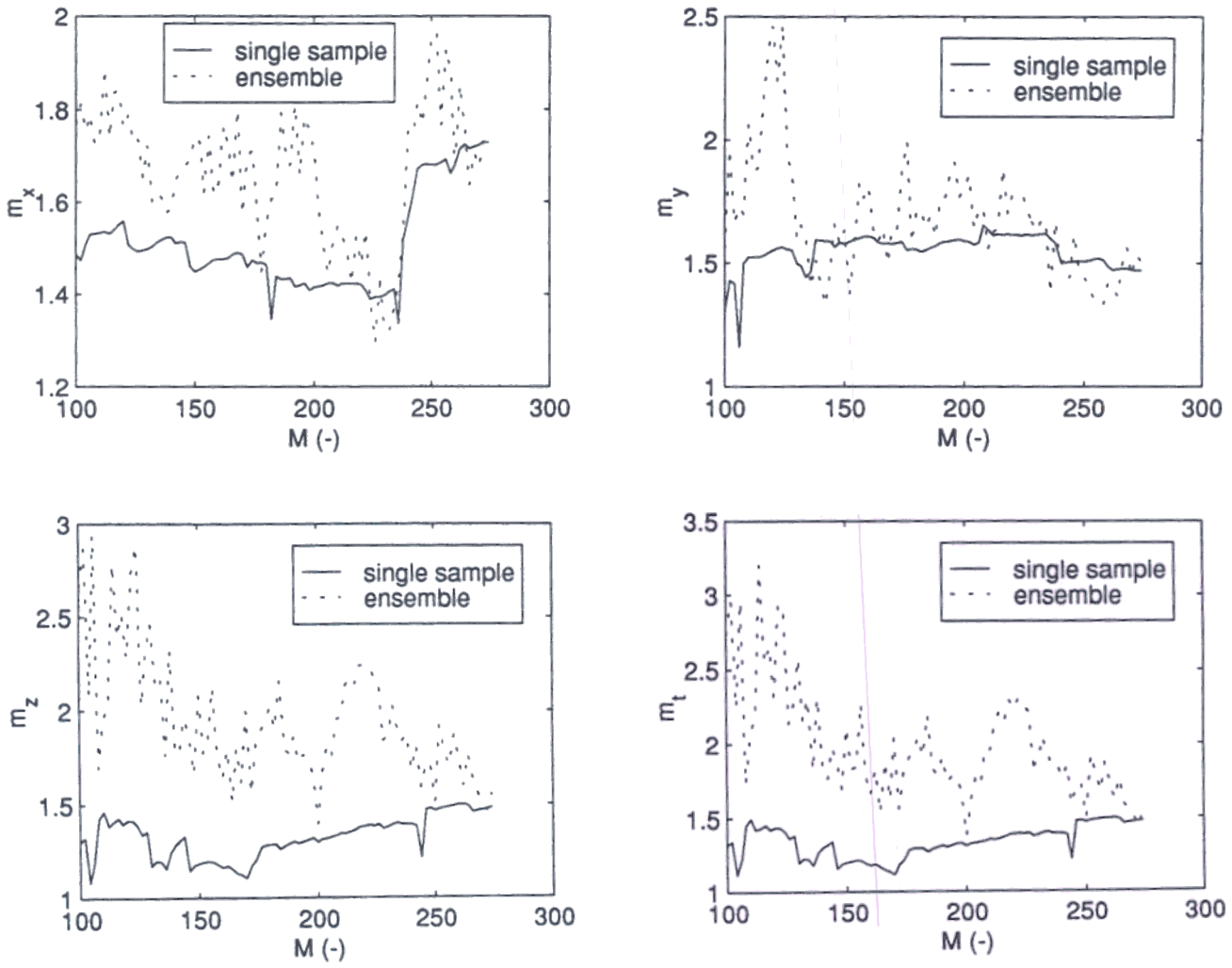


Figure 11: Single-sample and ensemble decimation factors m_α for $|E_\alpha|^2$ $(\alpha = x, y, z, t)$ as a function of sample size M @ $f = 2.5$GHz, $r = 345$mm.

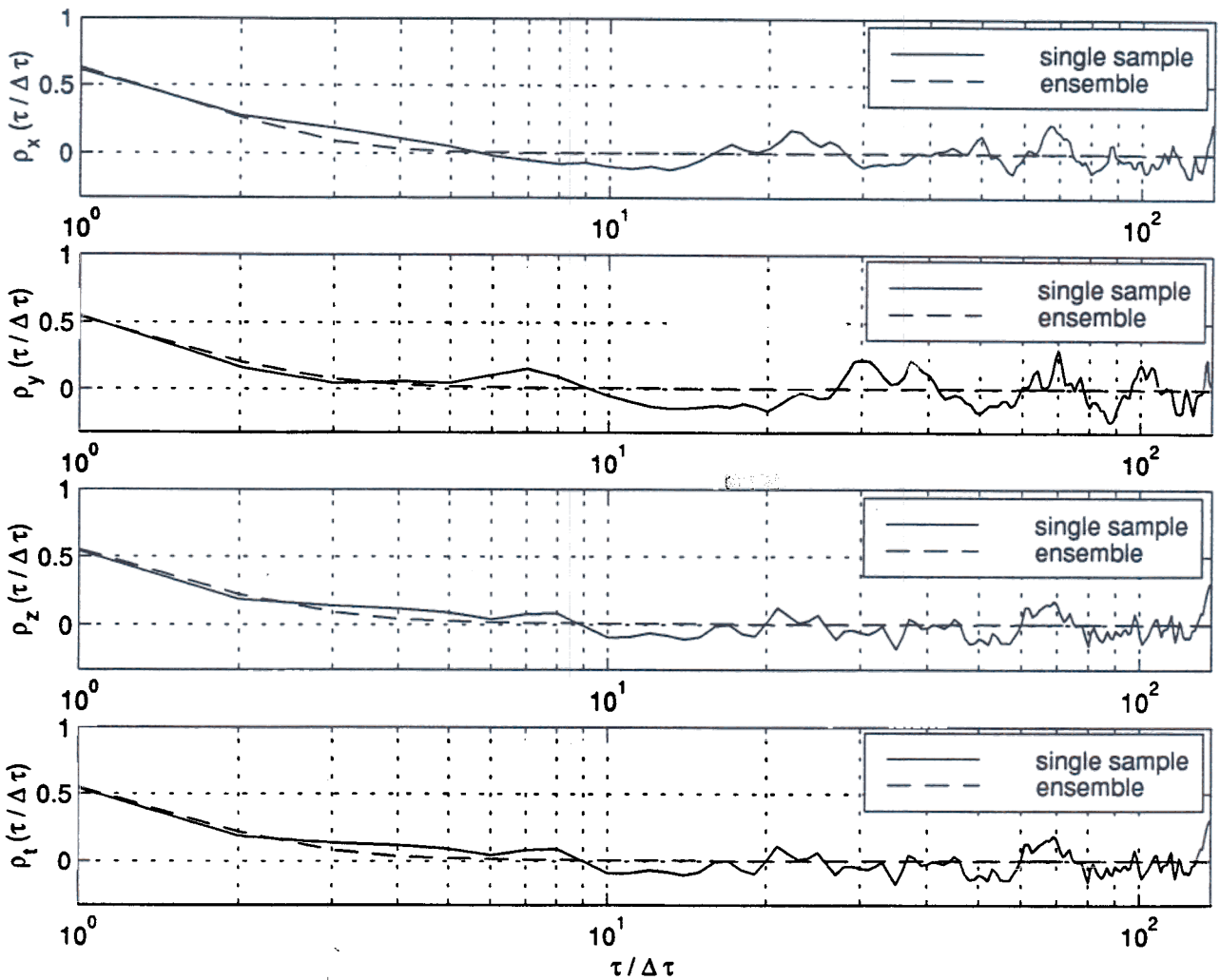


Figure 12: Single-sample and ensemble power autocorrelation functions ρ_α for $|E_\alpha|$ ($\alpha = x, y, z, t$) as a function of wall position $\tau/\Delta\tau$ @ $f = 2.5$GHz, $r = 345$mm.

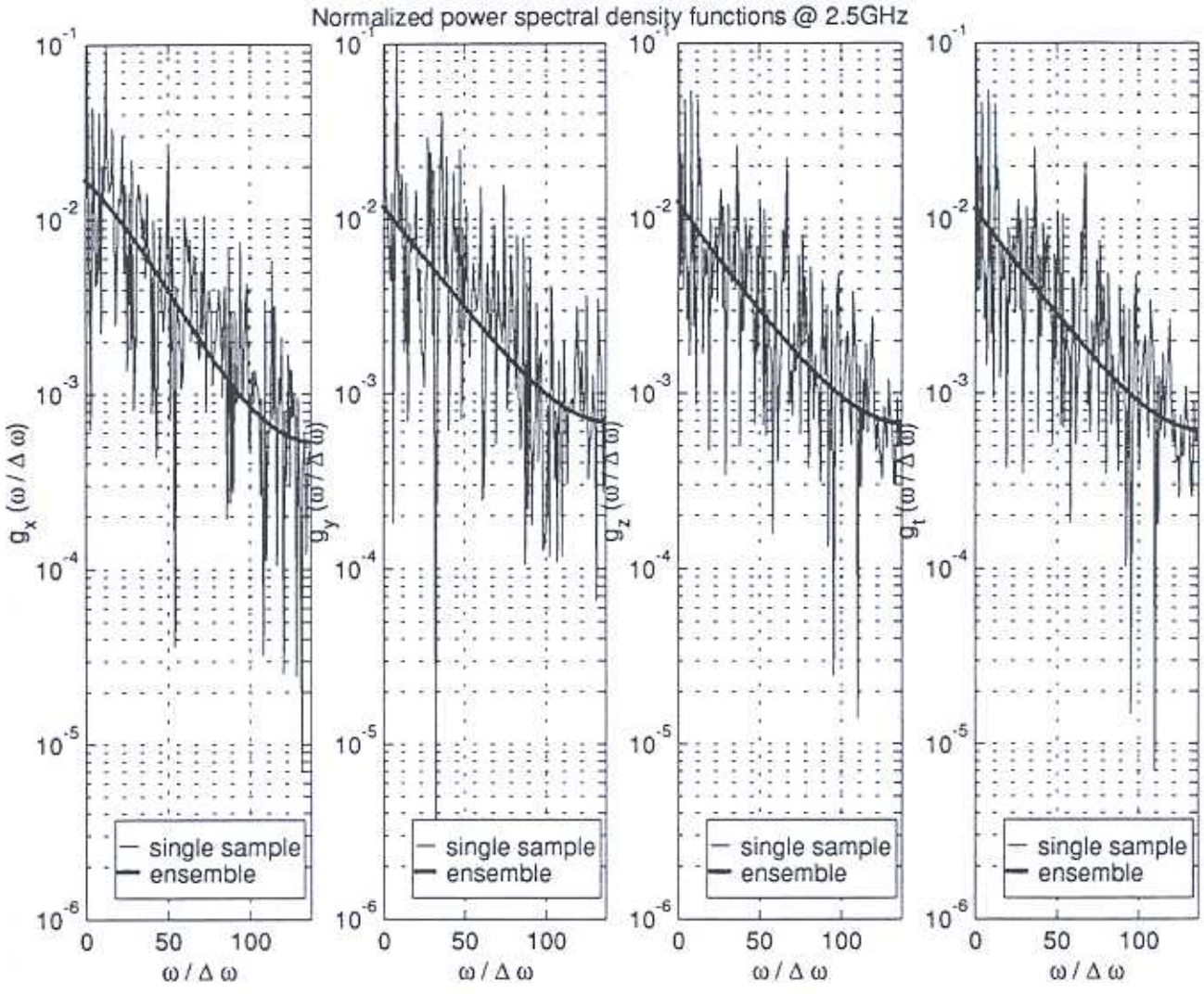


Figure 13: Single-sample and ensemble power autospectral density functions g_α for $|E_\alpha|$ ($\alpha = x, y, z, t$) as a function of spectral wall position $\omega/\Delta\omega$ @ $f = 2.5$GHz, $r = 345$mm.

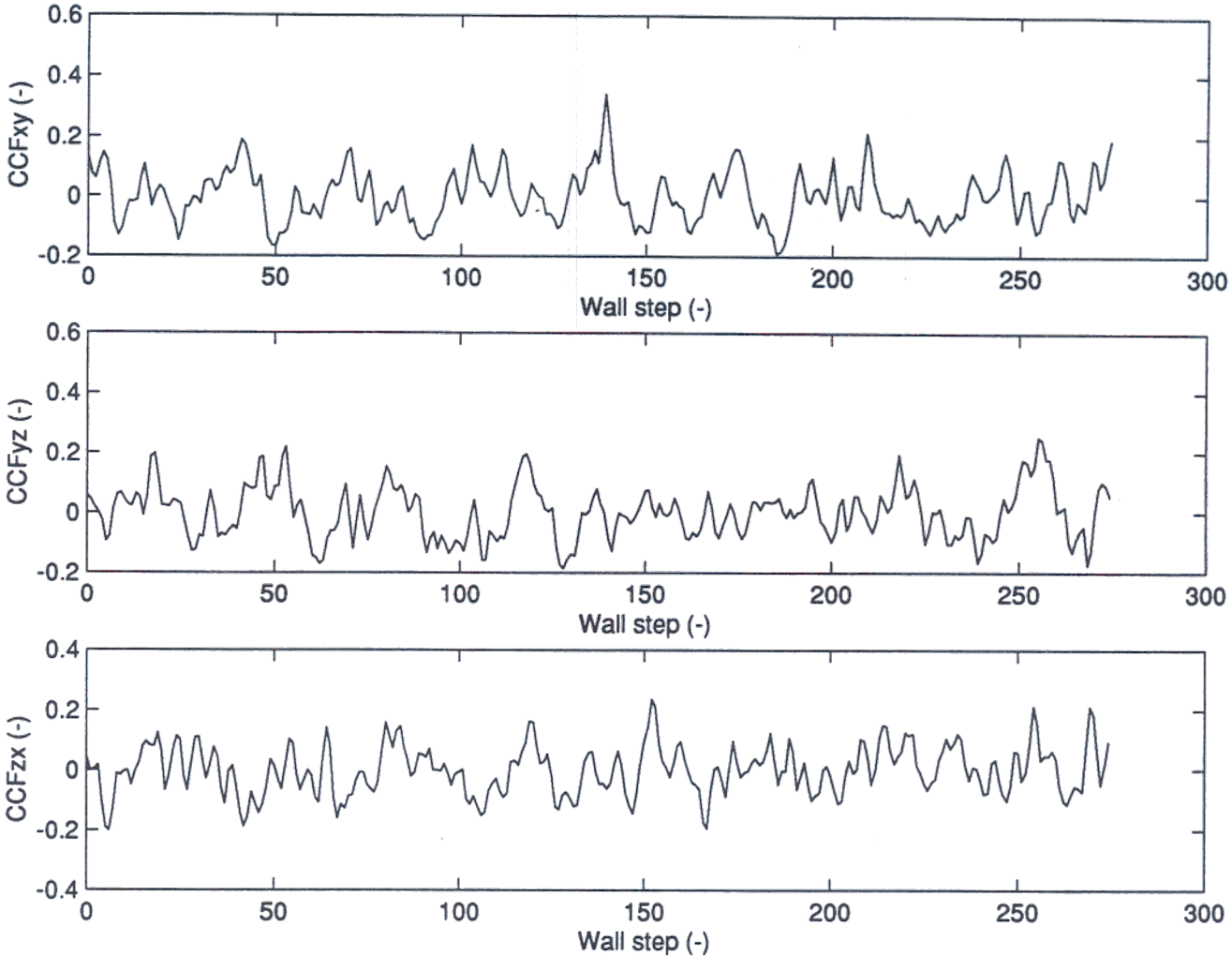


Figure 14: Power crosscorrelation functions $\rho_{\alpha\beta}$ for $|E_\alpha|$, $|E_\beta|$,$(\alpha, \beta = x, y, z)$ as a function of wall position $\tau/\Delta\tau$ @ $f = 2.5$GHz, $r = 91$mm.

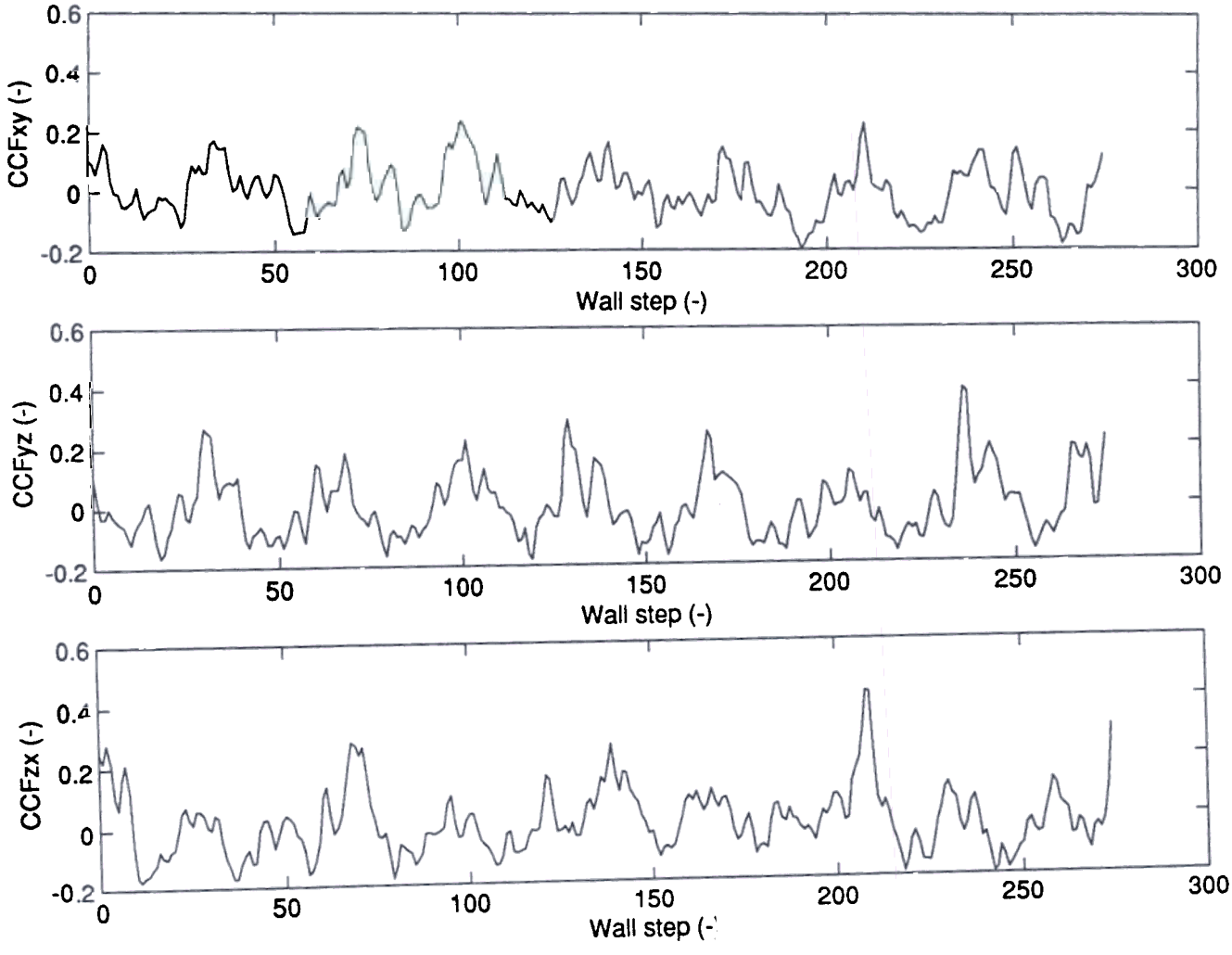


Figure 15: Power crosscorrelation functions $\rho_{\alpha\beta}$ for $|E_\alpha|$, $|E_\beta|$ $(\alpha, \beta = x, y, z)$ as a function of wall position $\tau/\Delta\tau$ @ $f = 2.5$GHz, $r = 345$mm.

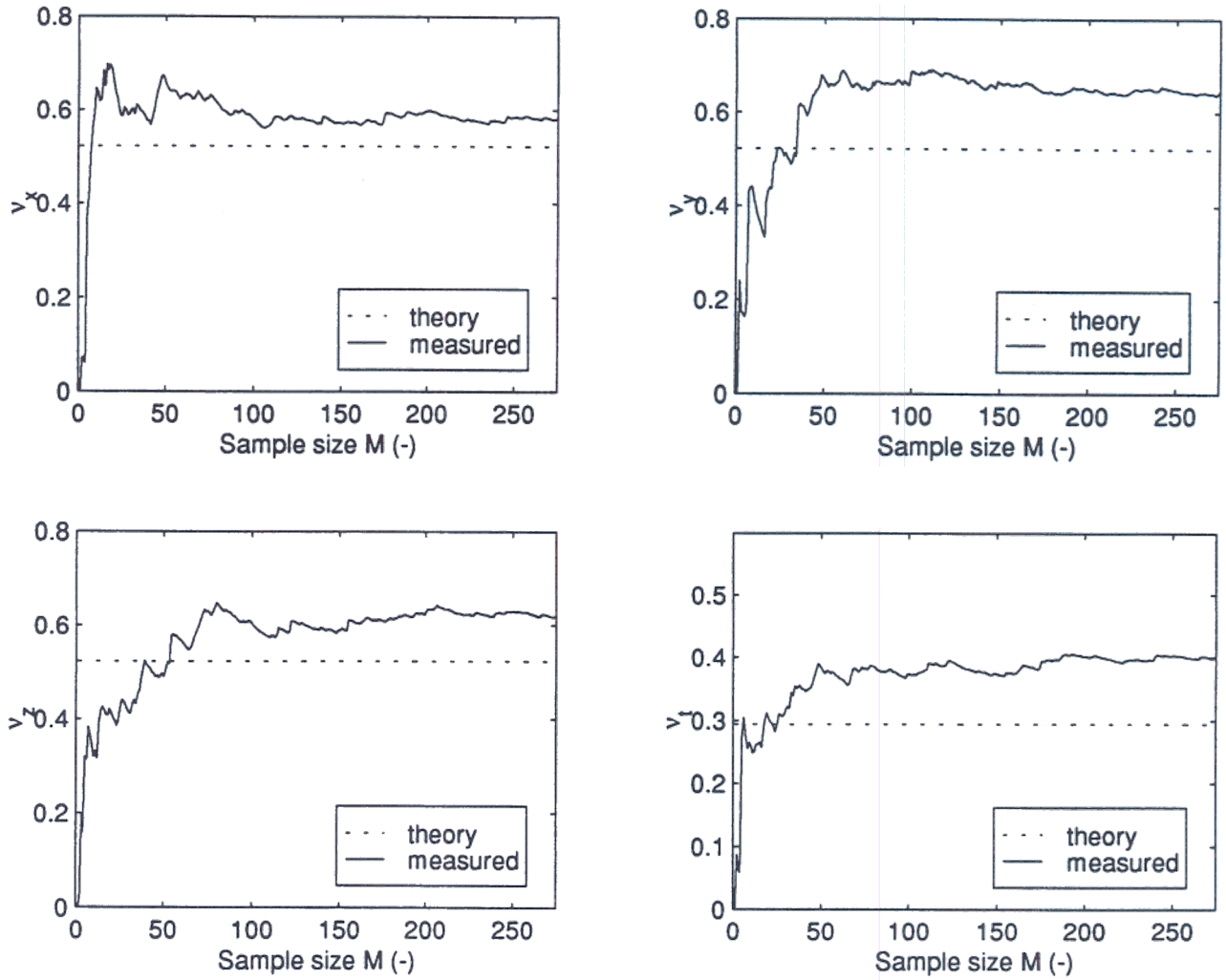


Figure 16: Coefficients of variation ν_α for $|E_\alpha|$ $(\alpha = x, y, z, t)$ as a function of sample size M @ $f = 2.5\text{GHz}$, $r = 91\text{mm}$.

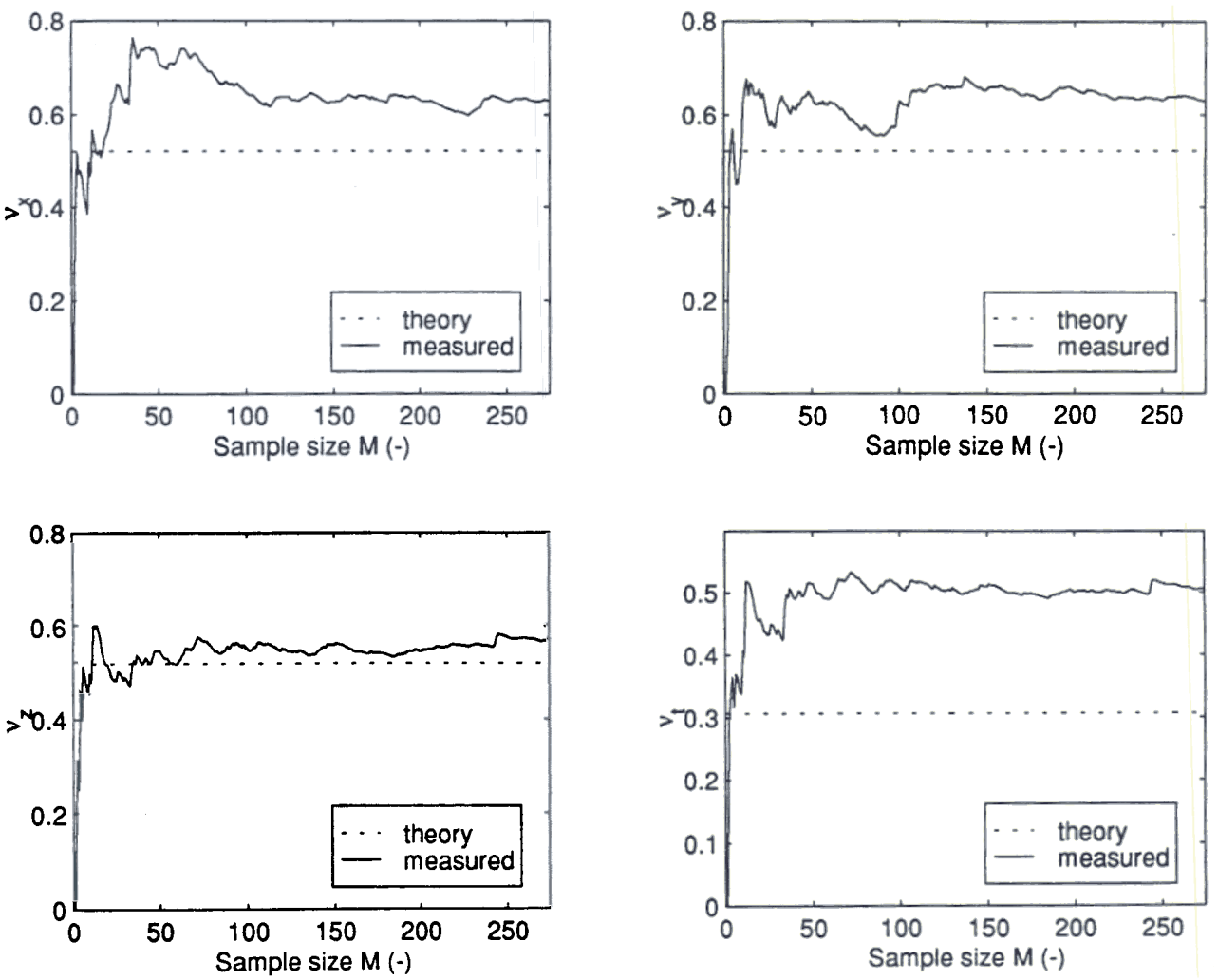


Figure 17: Coefficients of variation ν_α for $|E_\alpha|$ $(\alpha = x, y, z, t)$ as a function of sample size M @ $f = 2.5\text{GHz}, r = 345\text{mm}$.

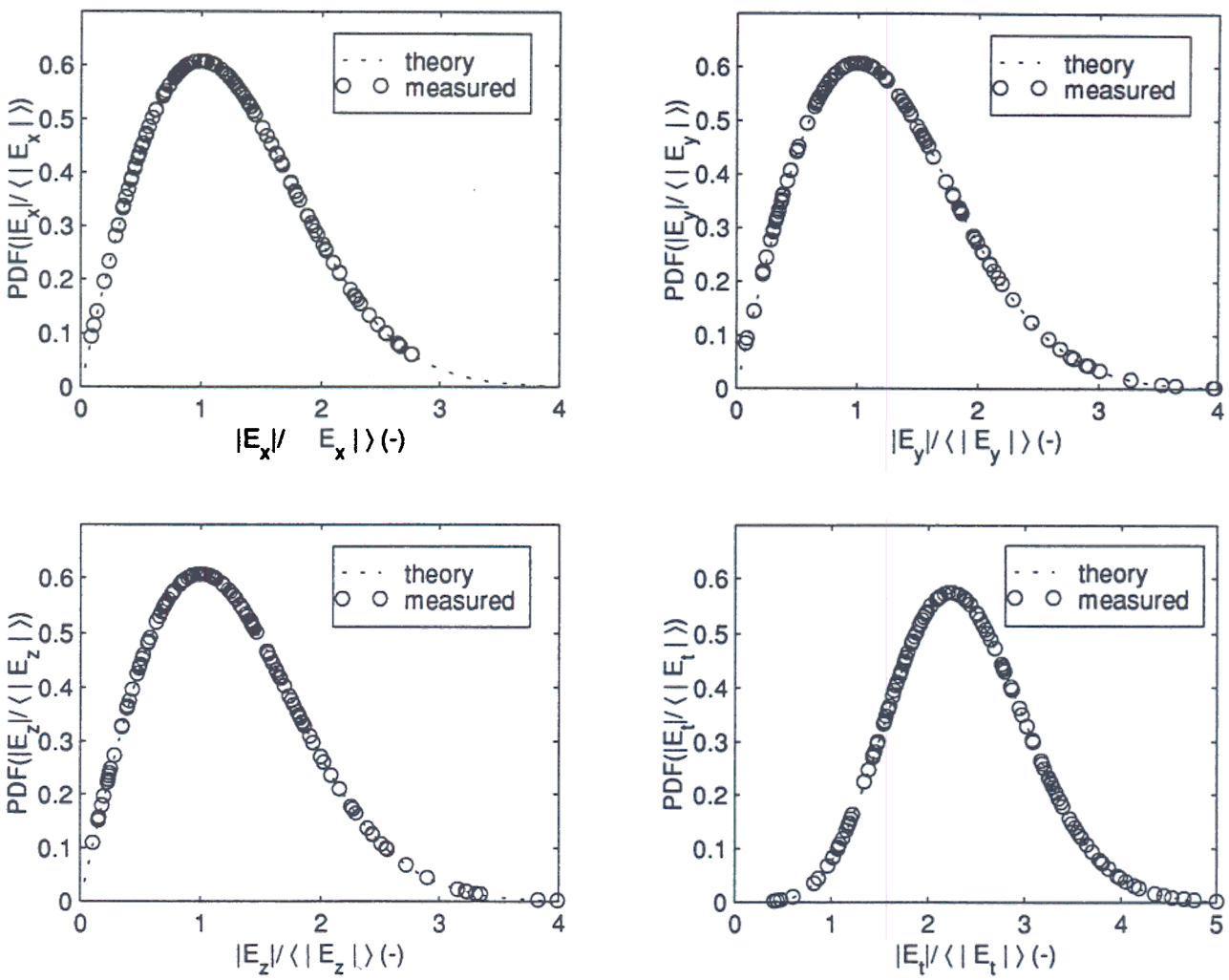


Figure 18: Probability density functions f_α of $|E_\alpha|/\langle|E_\alpha|\rangle$ ($\alpha = x, y, z, t$) @ $f = 2.5$GHz, $r = 91$mm for decimated data set ($m_\alpha = 2$). (See text for correct interpretation of Figure.)

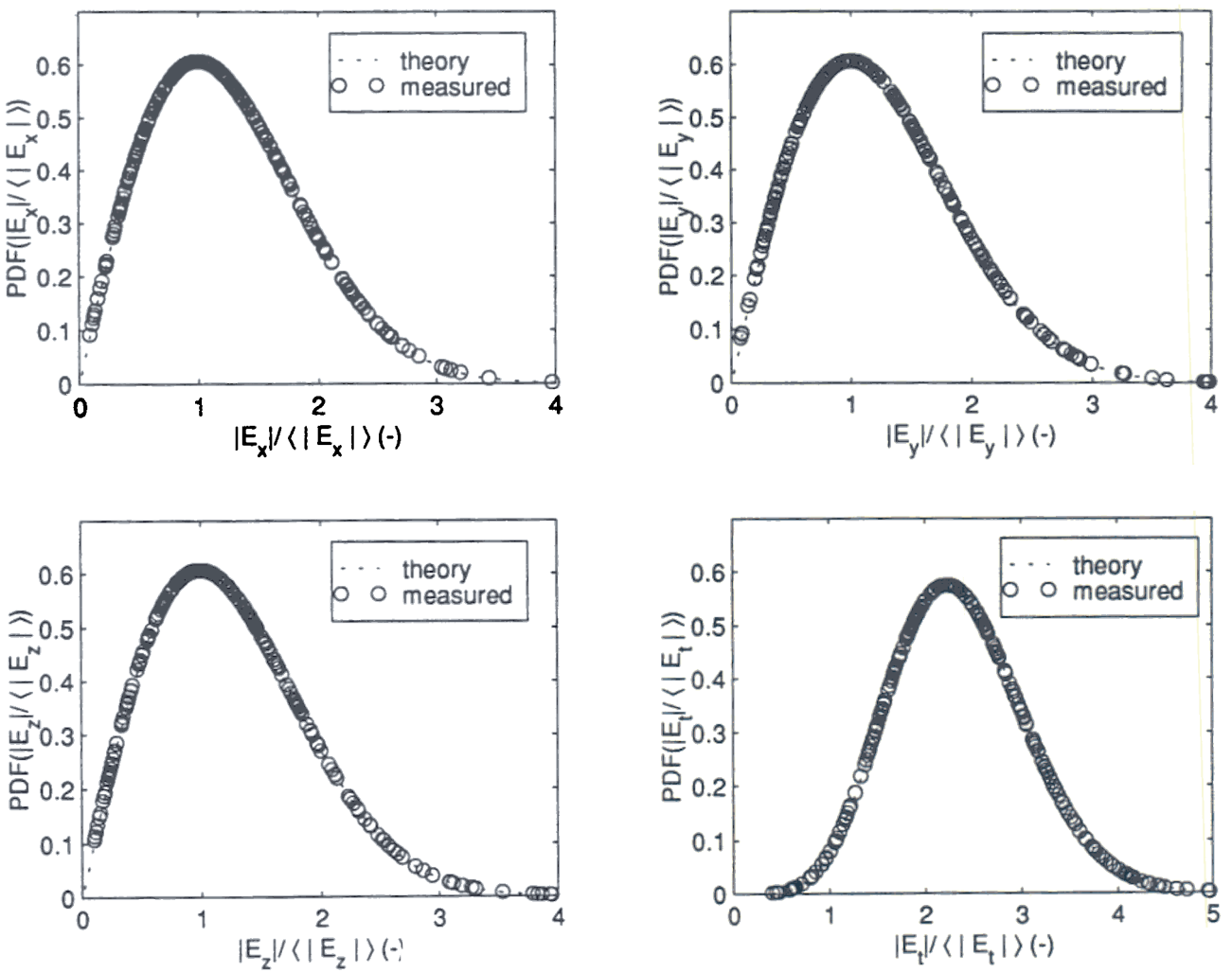


Figure 19: Probability density functions f_α of $|E_\alpha|/\langle|E_\alpha|\rangle$ ($\alpha = x, y, z, t$) @ $f = 2.5$GHz, $r = 91$mm for full data set. (See text for correct interpretation of Figure.)

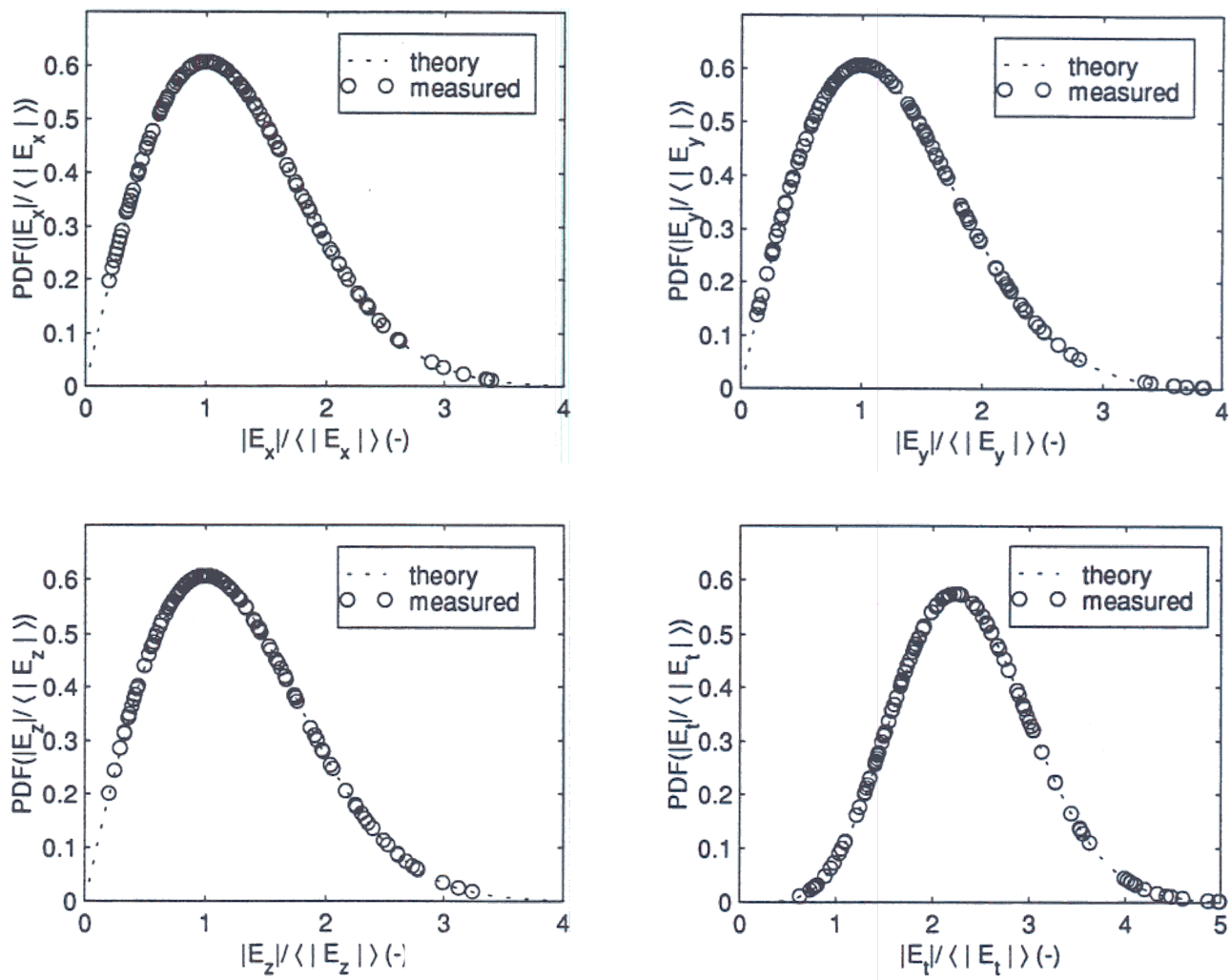


Figure 20: Probability density functions f_α of $|E_\alpha|/\langle|E_\alpha|\rangle$ ($\alpha = x, y, z, t$) @ $f = 2.5$GHz, $r = 345$mm for decimated data set ($m_\alpha = 2$). (See text for correct interpretation of Figure.)

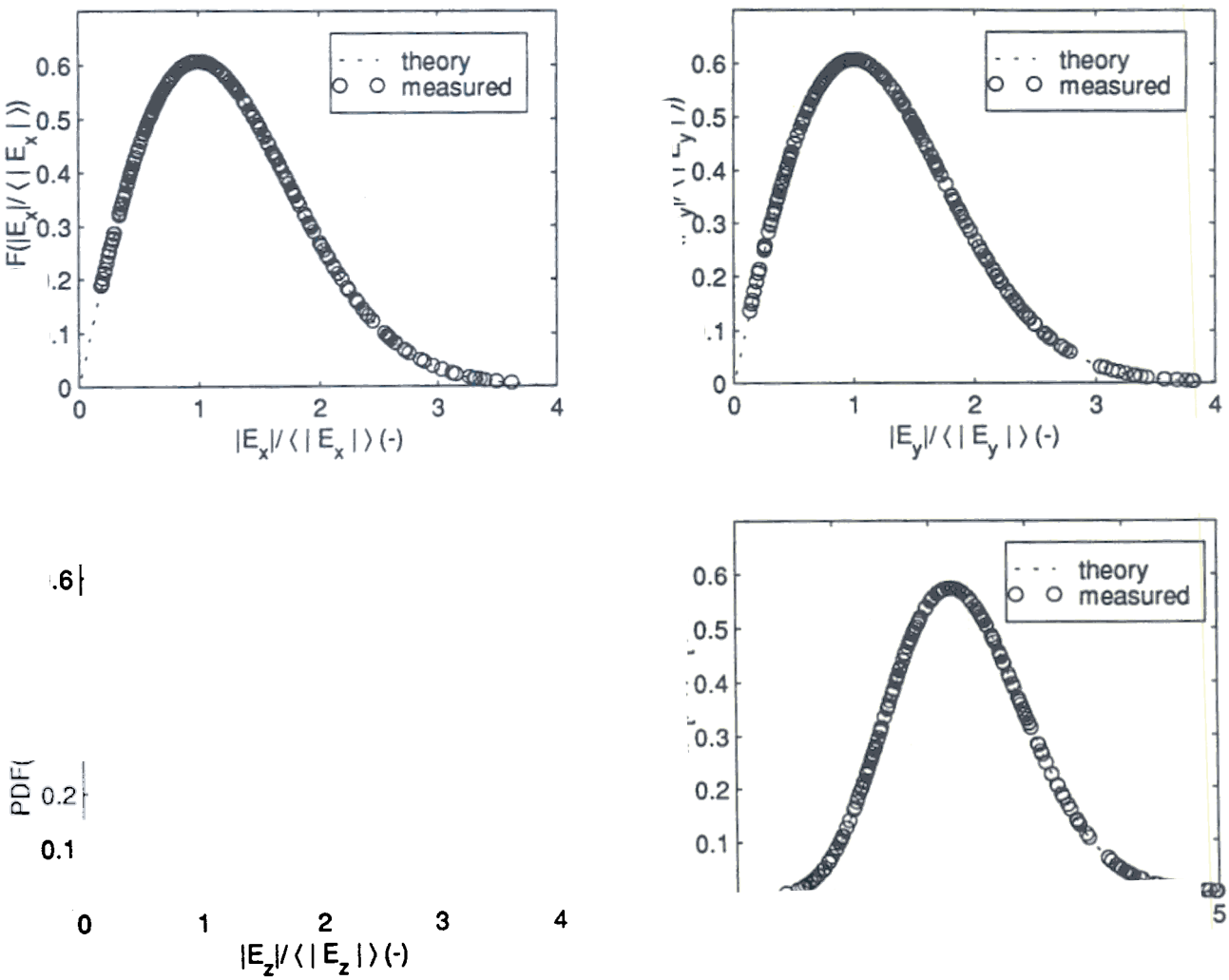


Figure 21: Probability density functions f_α of $|E_\alpha|/\langle|E_\alpha|\rangle$ ($\alpha = x, y, z, t$) @ $f = 2.5$GHz, $r = 345$mm for full data set. (See text for correct interpretation of Figure.)

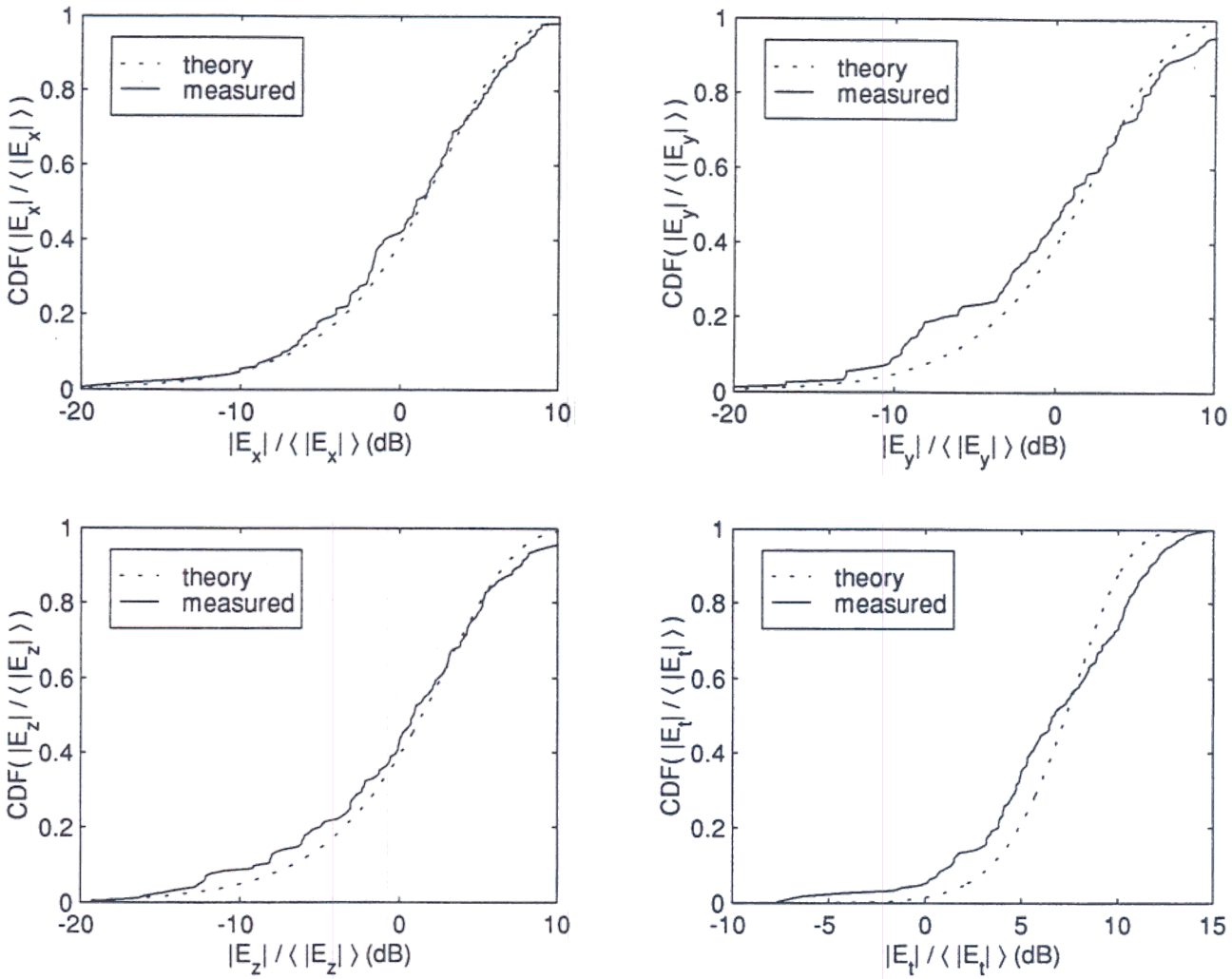


Figure 22: Cumulative distribution functions F_α of $|E_\alpha|/\langle|E_\alpha|\rangle$ ($\alpha = x, y, z, t$) @ $f = 2.5$GHz, $r = 91$mm for decimated data set ($m_\alpha = 2$).

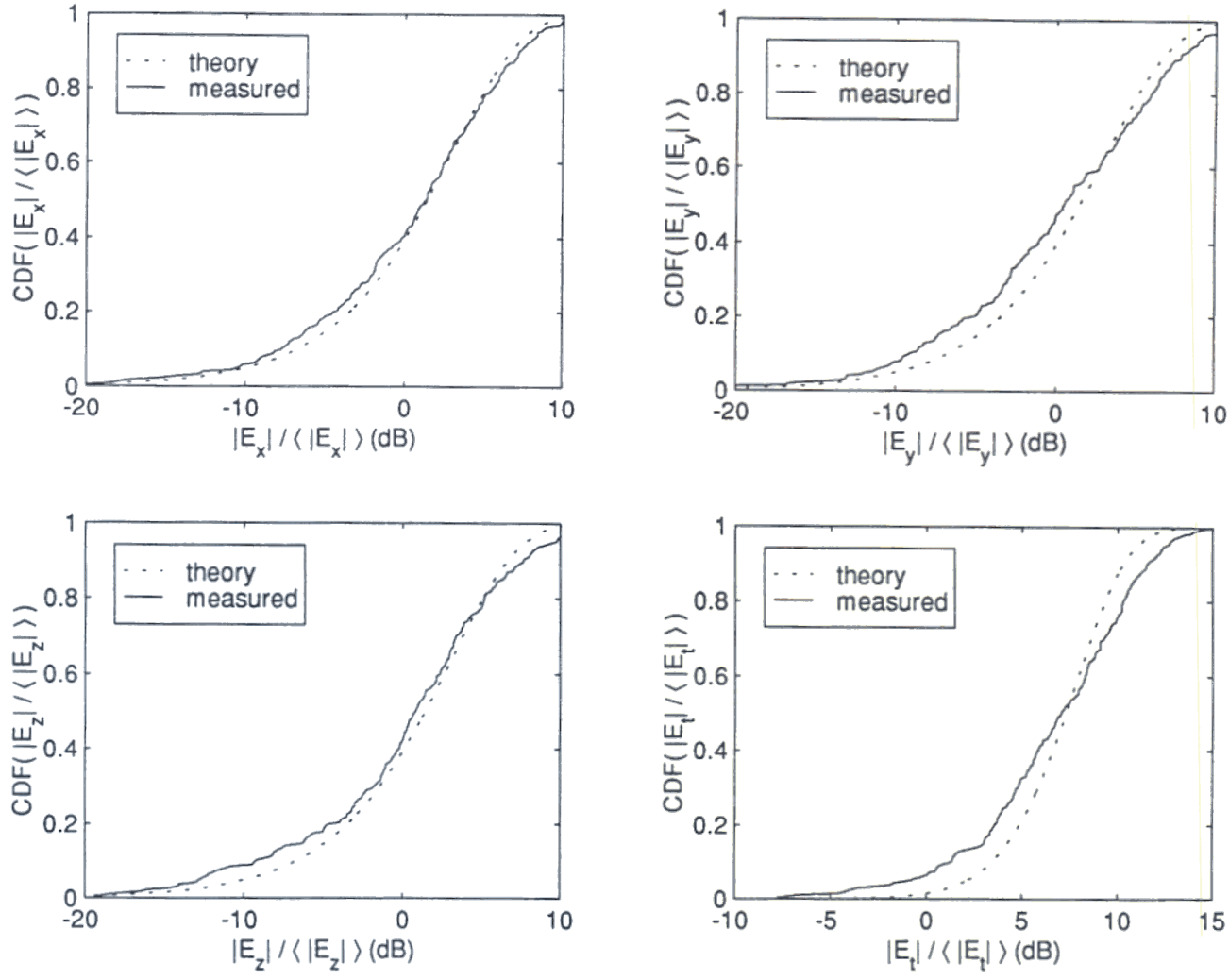


Figure 23: Cumulative distribution functions F_α of $|E_\alpha|/\langle|E_\alpha|\rangle$ ($\alpha = x, y, z, t$) @ $f = 2.5$GHz, $r = 91$mm for full data set.

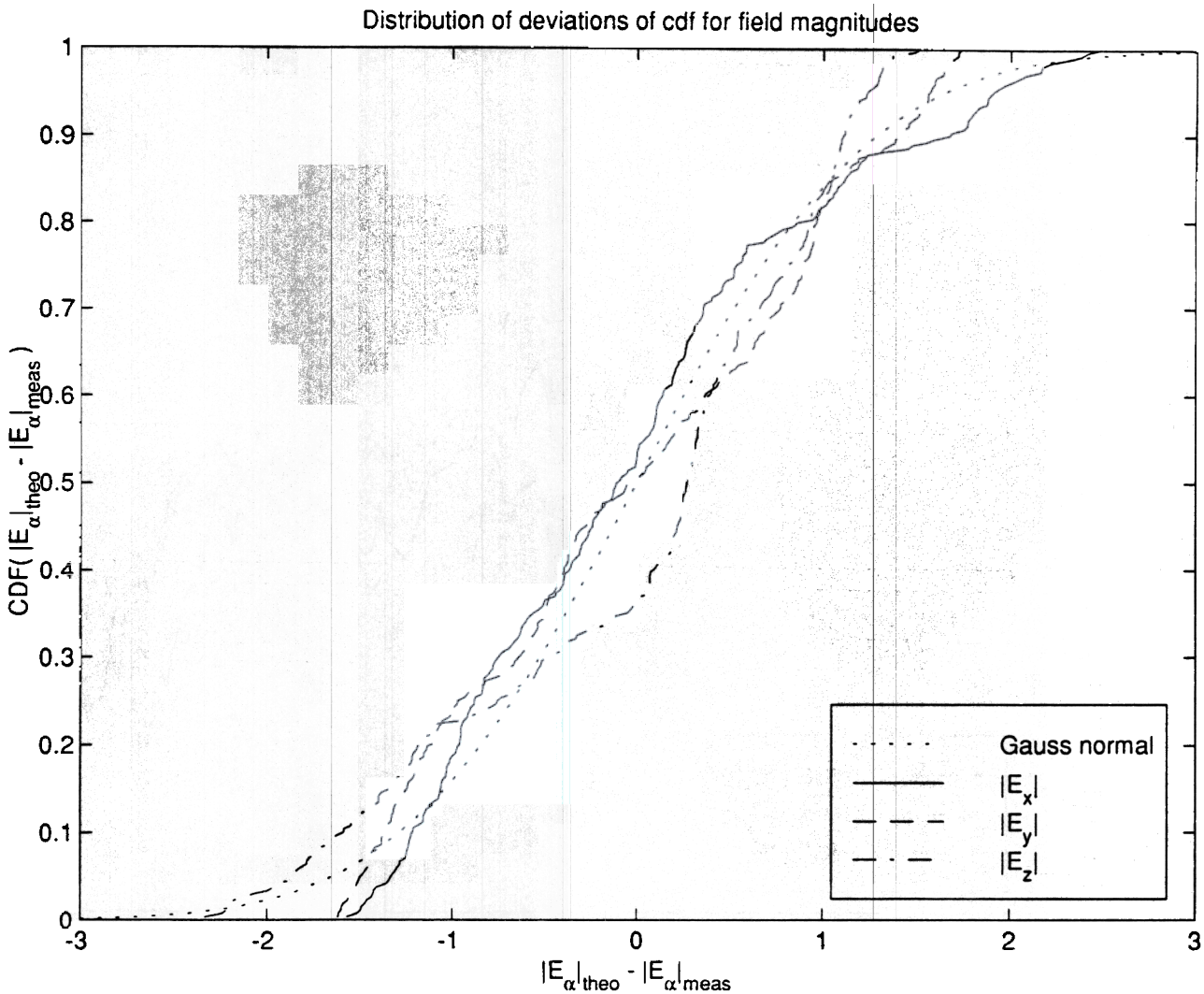


Figure 24: Cumulative distribution functions of standardized deviations $|E_\alpha|_{theo} - |E_\alpha|_{meas}$ $(\alpha = x, y, z)$ @ $f = 2.5$GHz, $r = 91$mm for full data set.

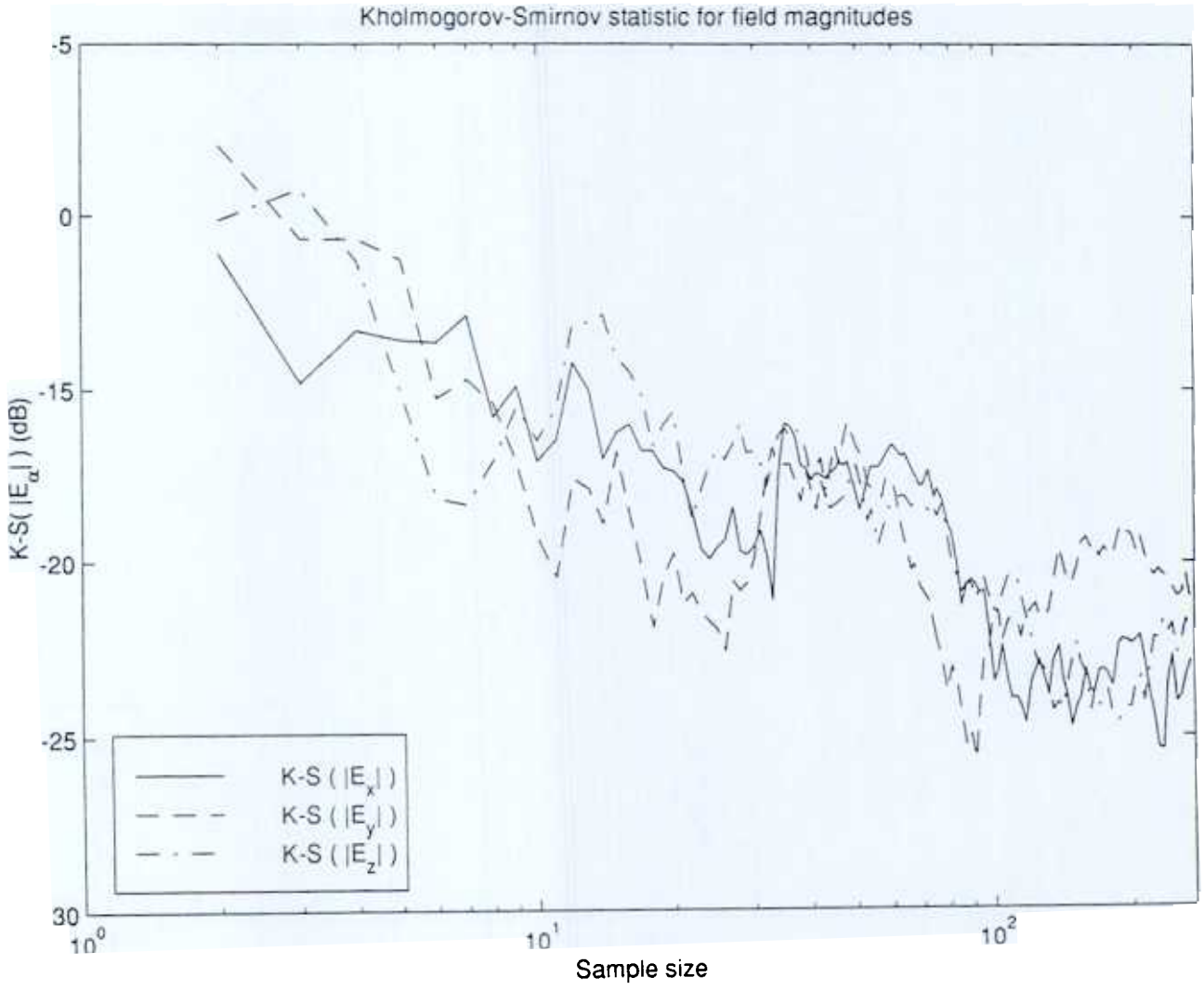


Figure 25: Kholmogorov–Smirnov test statistic between measured and theoretical cumulative distribution functions of $|E_\alpha|/\langle|E_\alpha|\rangle$ ($\alpha = x, y, z$) as a function of sample size M @ $f = 2.5$GHz, $r = 91$mm for full data set.

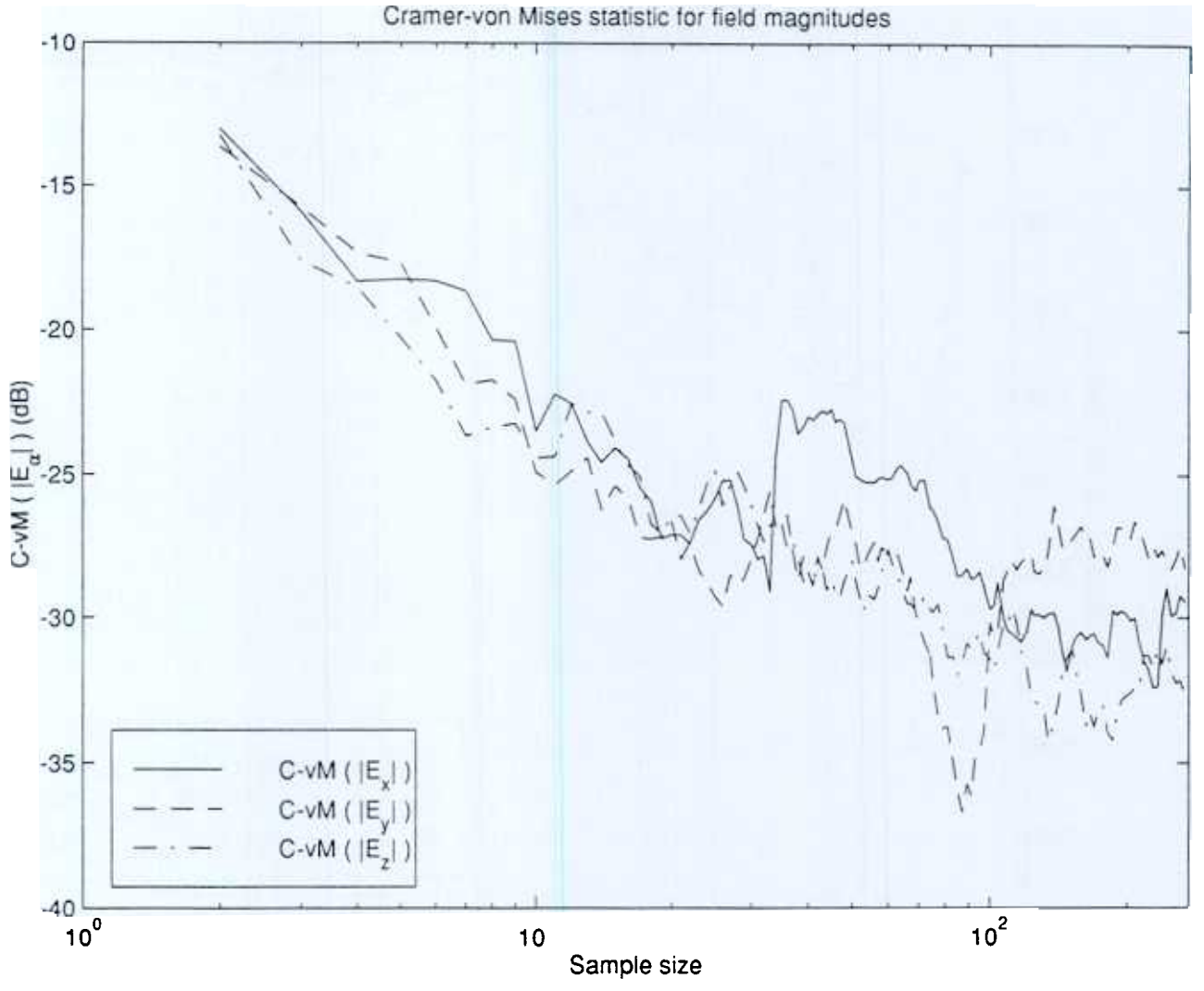


Figure 26: Cramér–von Mises test statistic between measured and theoretical cumulative distribution functions of $|E_\alpha|/\langle|E_\alpha|\rangle$ ($\alpha = x, y, z$) as a function of sample size M@ $f = 2.5$GHz, $r = 91$mm for full data set.

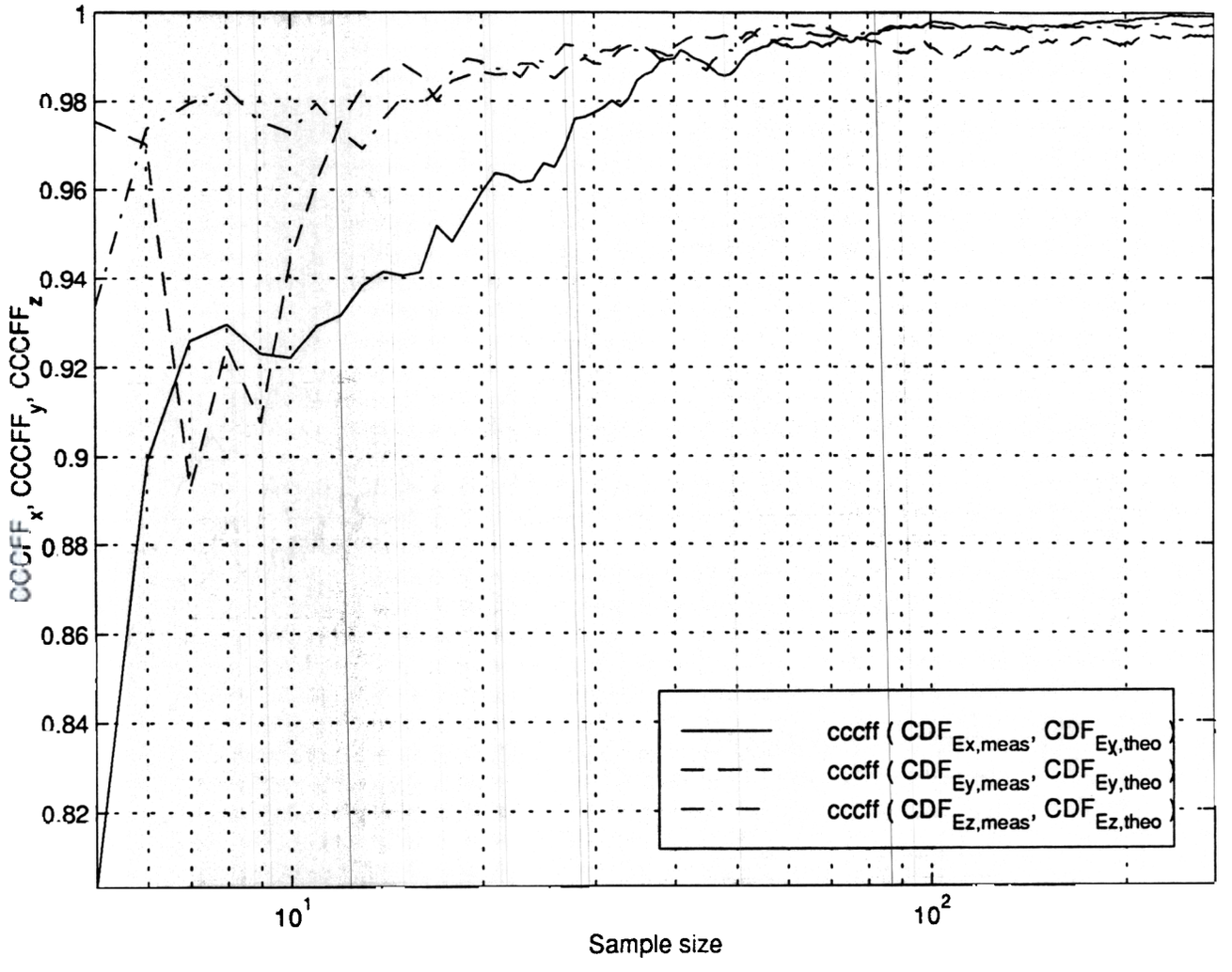


Figure 27: Crosscorrelation coefficients $\varrho_{\alpha\beta}$ between measured and theoretical cumulative distribution functions of $|E_\alpha|/\langle|E_\alpha|\rangle$, $|E_\beta|/\langle|E_\beta|\rangle$ $(\alpha, \beta = x, y, z)$ as a function of sample size M @ $f = 2.5\text{GHz}$, $r = 91\text{mm}$ for fulldata set.

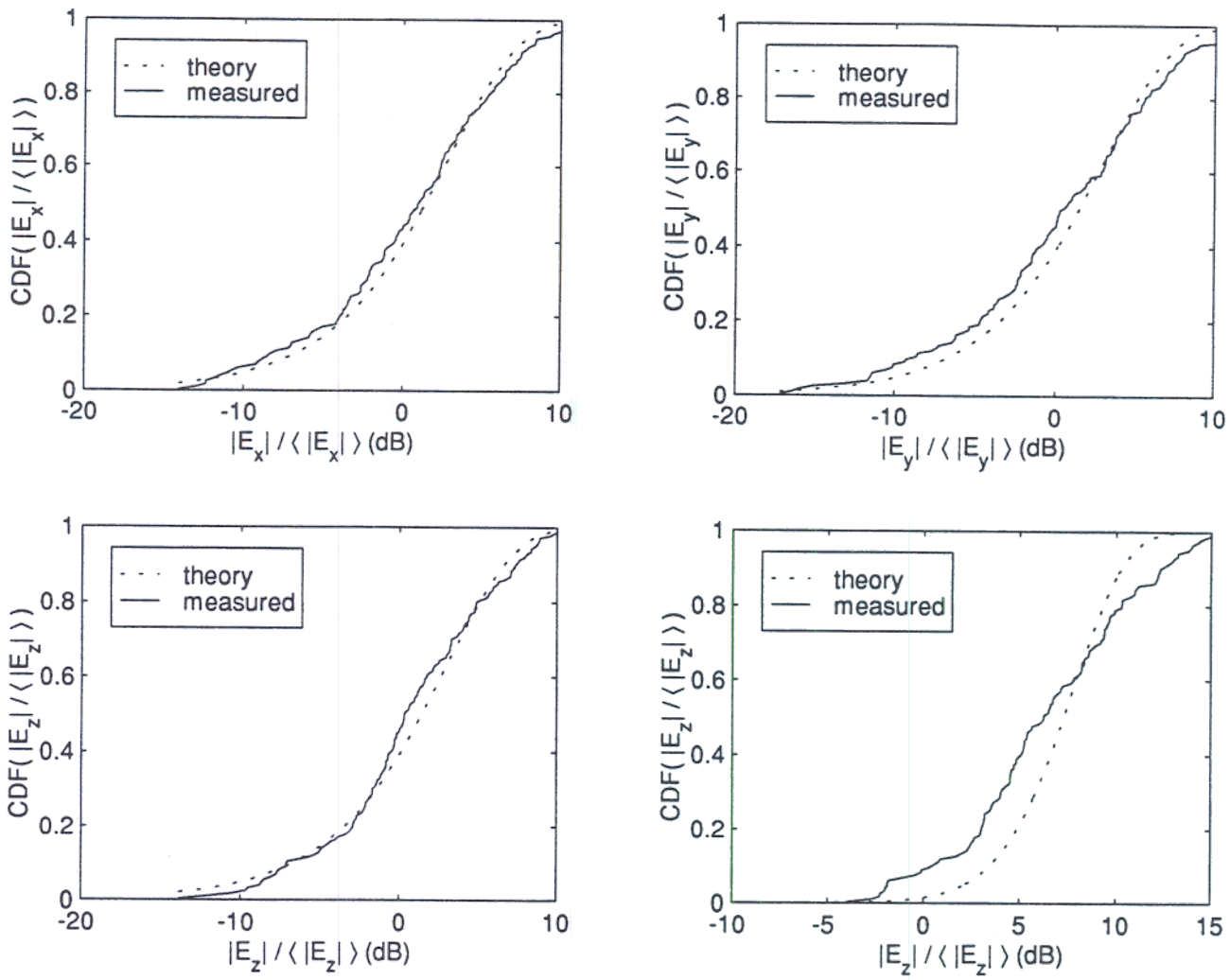


Figure 28: Cumulative distribution functions F_α of $|E_\alpha|/\langle|E_\alpha|\rangle$ ($\alpha = x, y, z, t$) @ $f = 2.5$GHz, $r = 345$mm for decimated data set ($m_\alpha = 2$).

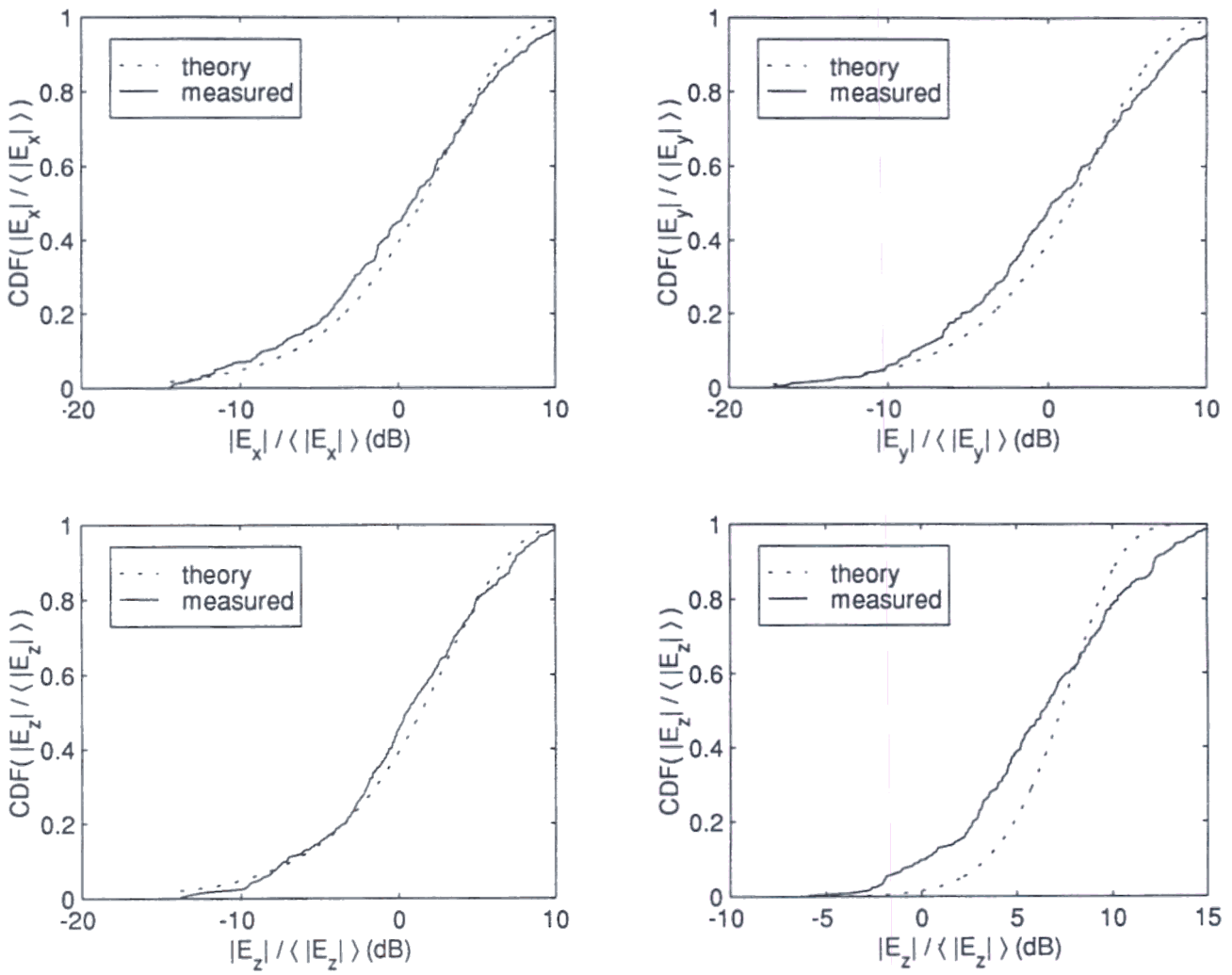


Figure 29: Cumulative distribution functions F_α of $|E_\alpha|/\langle|E_\alpha|\rangle$ ($\alpha = x, y, z, t$) @ $f = 2.5$GHz, $r = 345$mm for full data set.

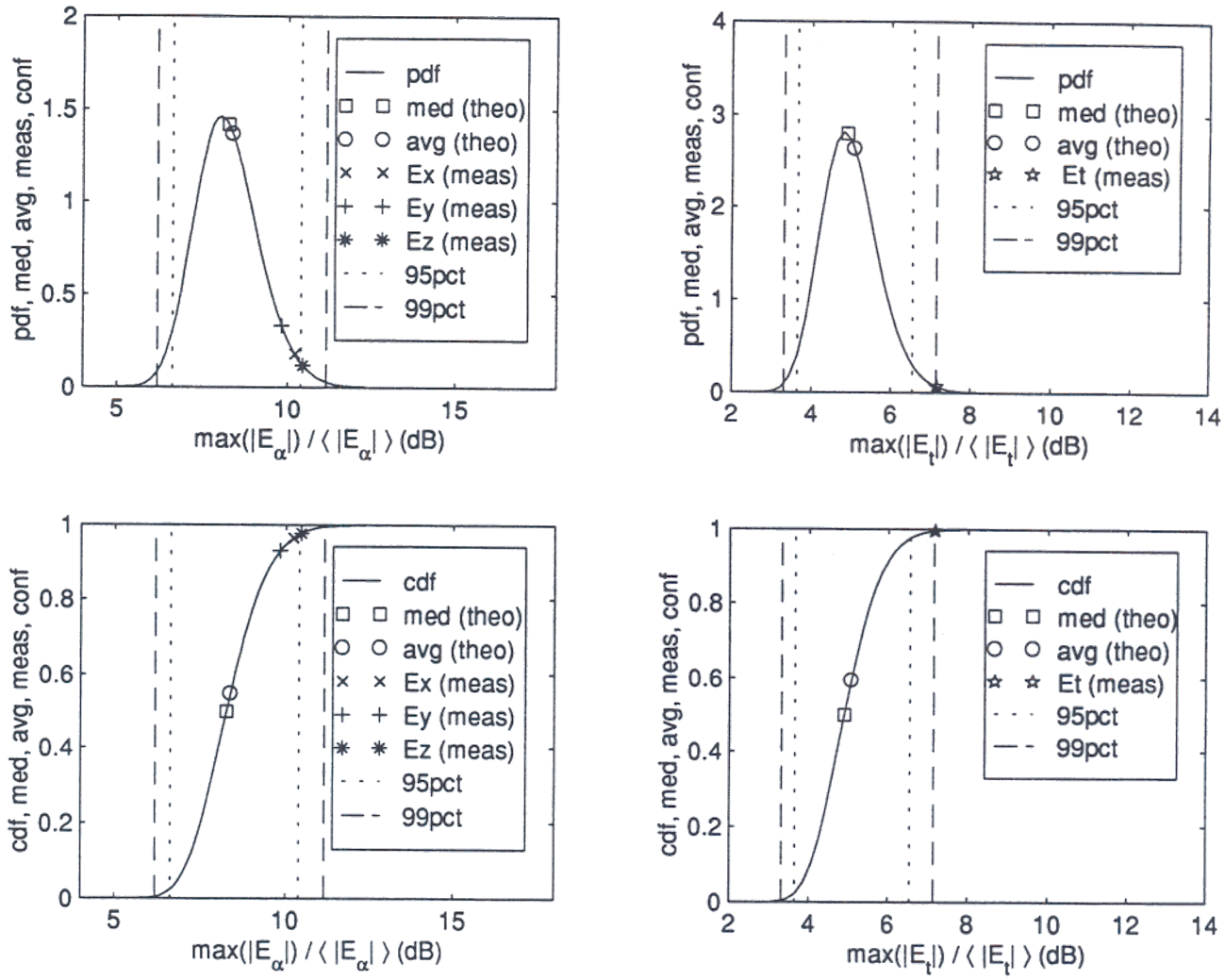


Figure 30: Distribution functions, theoretical median, theoretical mean, measured values, and 95% and 99% confidence intervals of max-to-mean field for $|E_\alpha|/\langle|E_\alpha|\rangle$ ($\alpha = x, y, z, t$) @ f = 2.5GHz, r = 91mm for decimated data set ($m_\alpha = 2$).

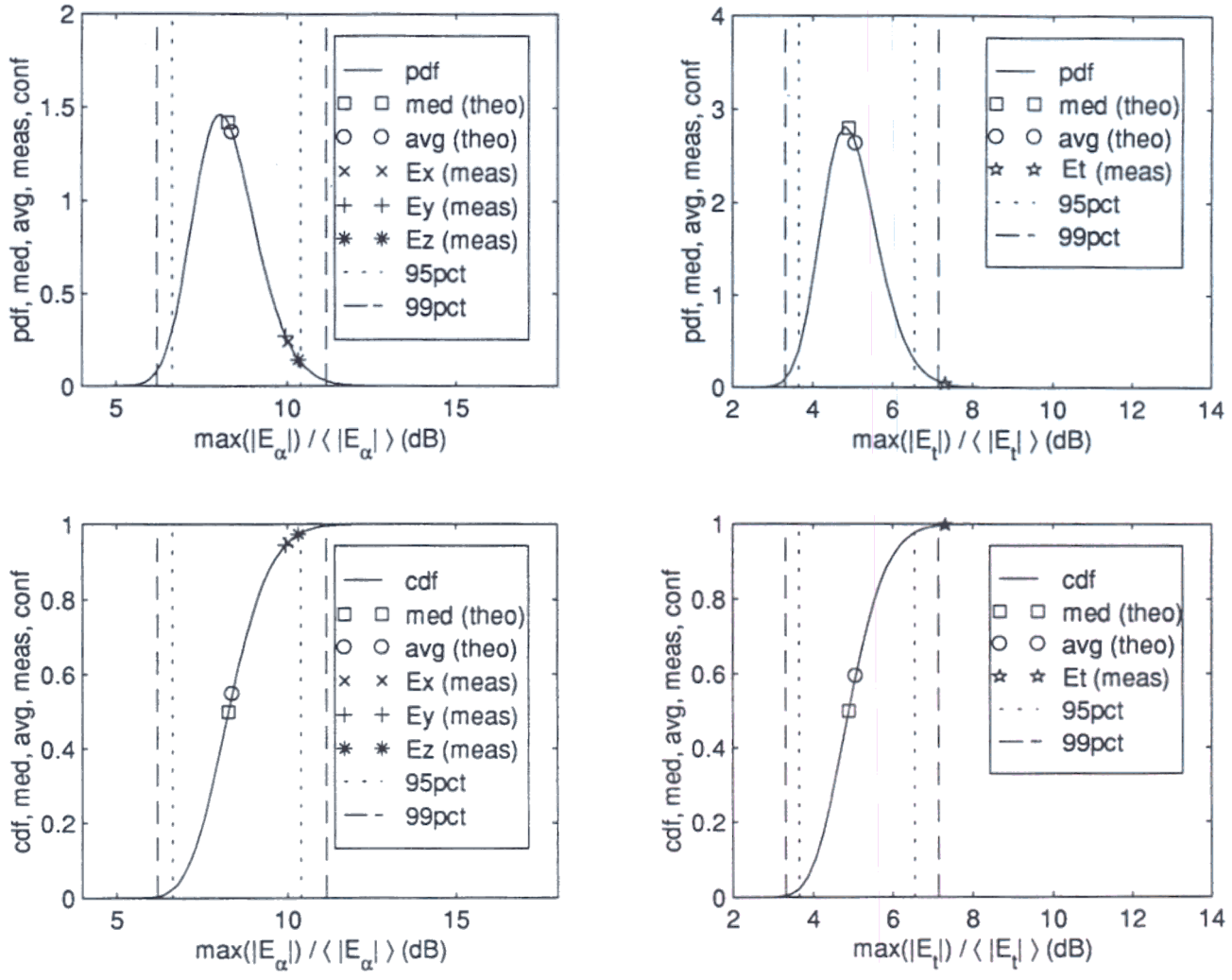


Figure 31: Distribution functions, theoretical median, theoretical mean, measured values, and 95% and 99% confidence intervals of max-to-mean field for $|E_\alpha|/\langle|E_\alpha|\rangle$ ($\alpha = x, y, z, t$) @ f = 2.5GHz, r = 91mm for full data set.

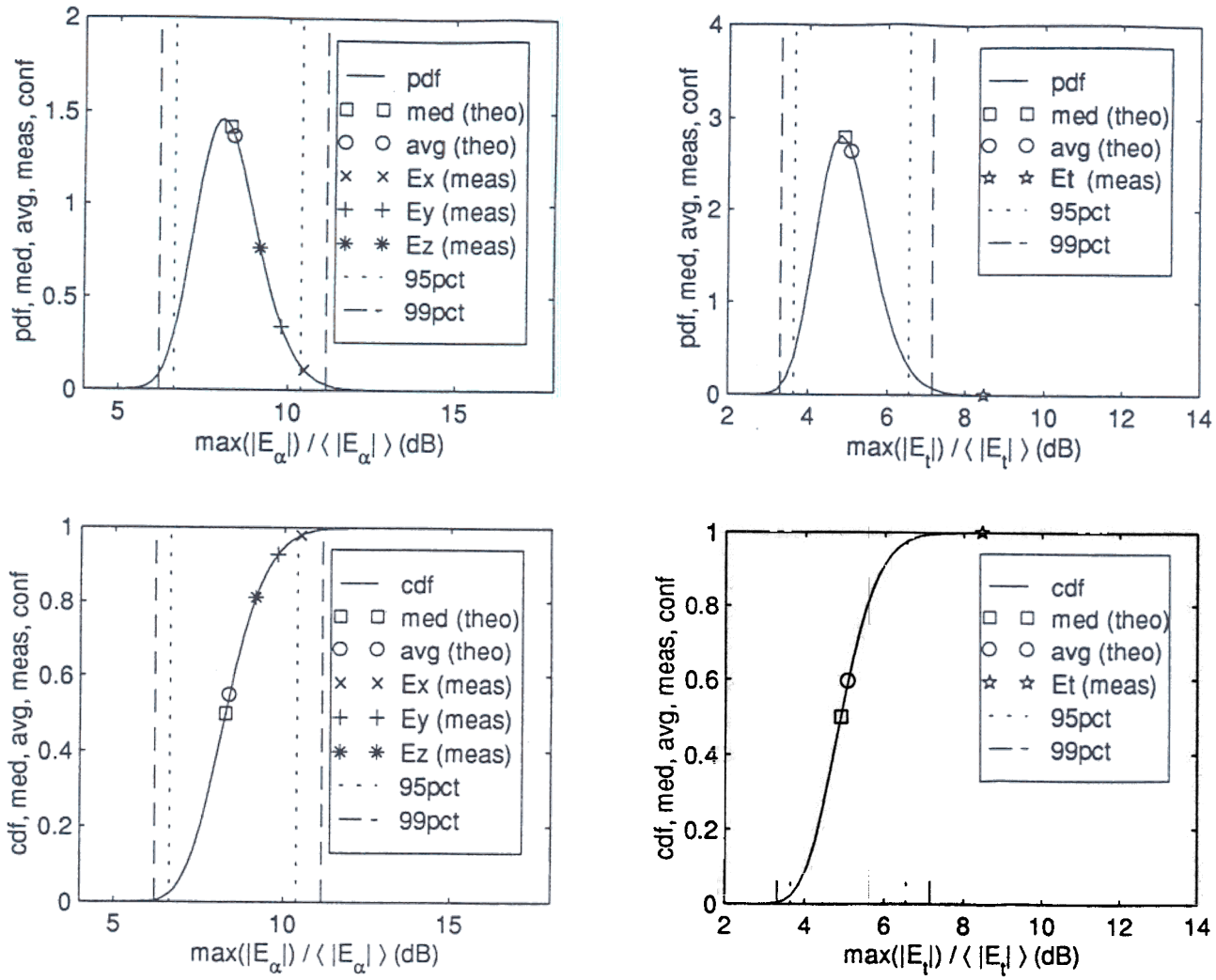


Figure 32: Distribution functions, theoretical median, theoretical mean, measured values, and 95% and 99% confidence intervals of max-to-mean field for $|E_\alpha|/\langle|E_\alpha|\rangle$ ($\alpha = x, y, z, t$) @ $f =$ 2.5GHz, $r = 345$mm for decimated data set ($m_\alpha = 2$).

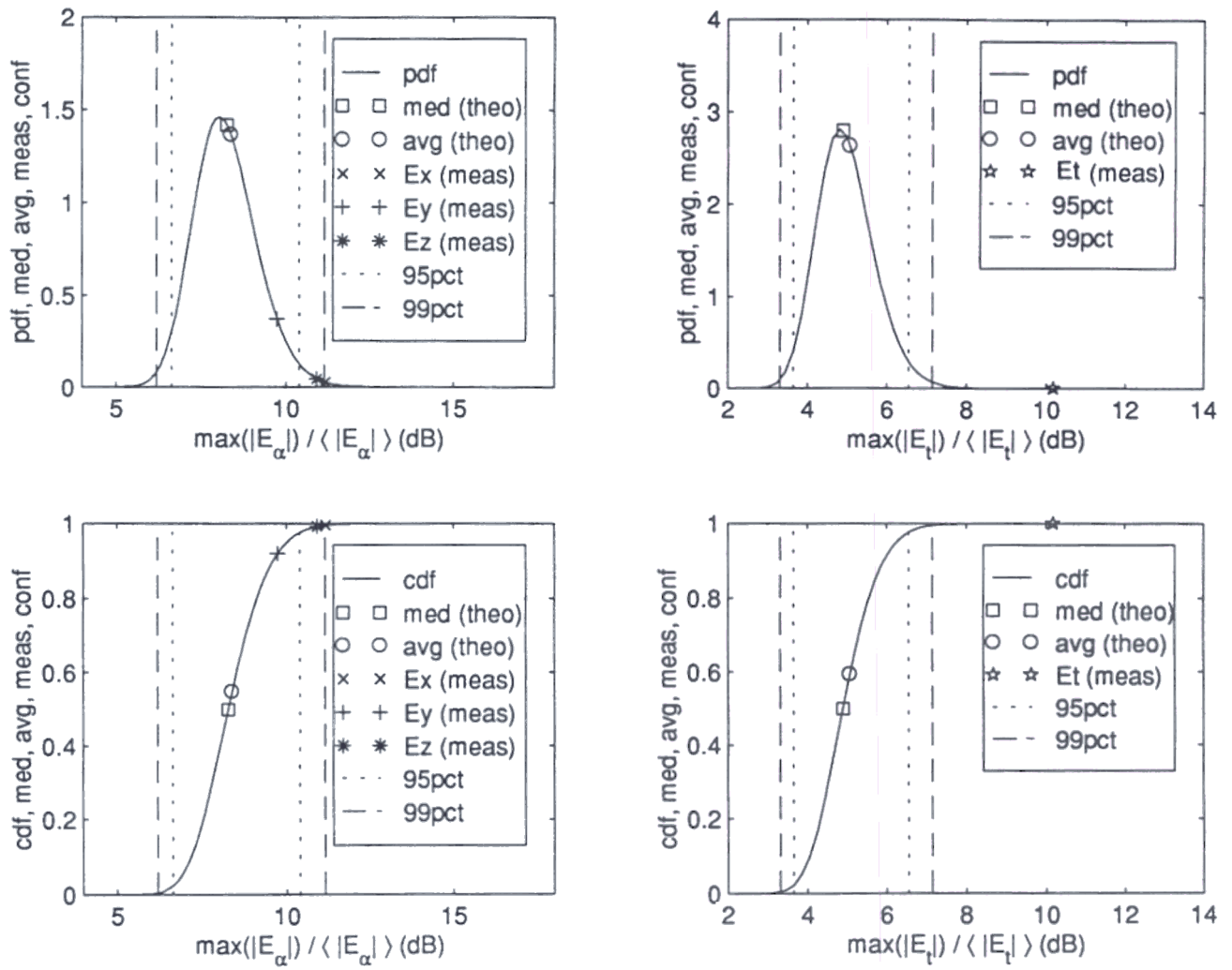


Figure 33: Distribution functions, theoretical median, theoretical mean, measured values, and 95% and 99% confidence intervals of max-to-mean field for $|E_\alpha|/\langle|E_\alpha|\rangle$ ($\alpha = x, y, z, t$) @ f = 2.5GHz, r = 345mm for full data set.

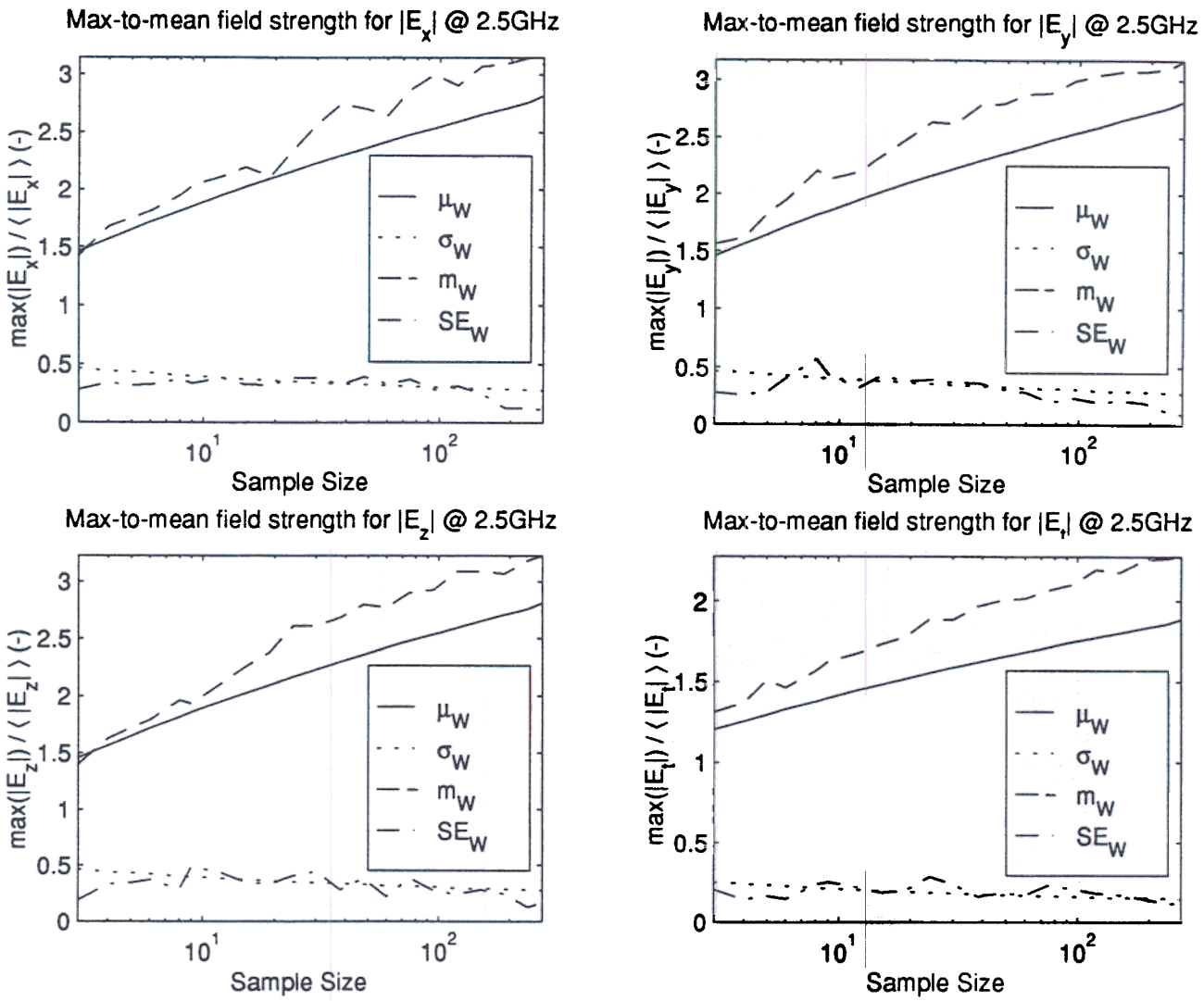


Figure 34: Theoretical and measured max-to-mean field for $|E_\alpha|/\langle|E_\alpha|\rangle$ ($\alpha = x, y, z, t$) as a function of sample size M @ $f = 2.5$GHz, $r = 91$mm.

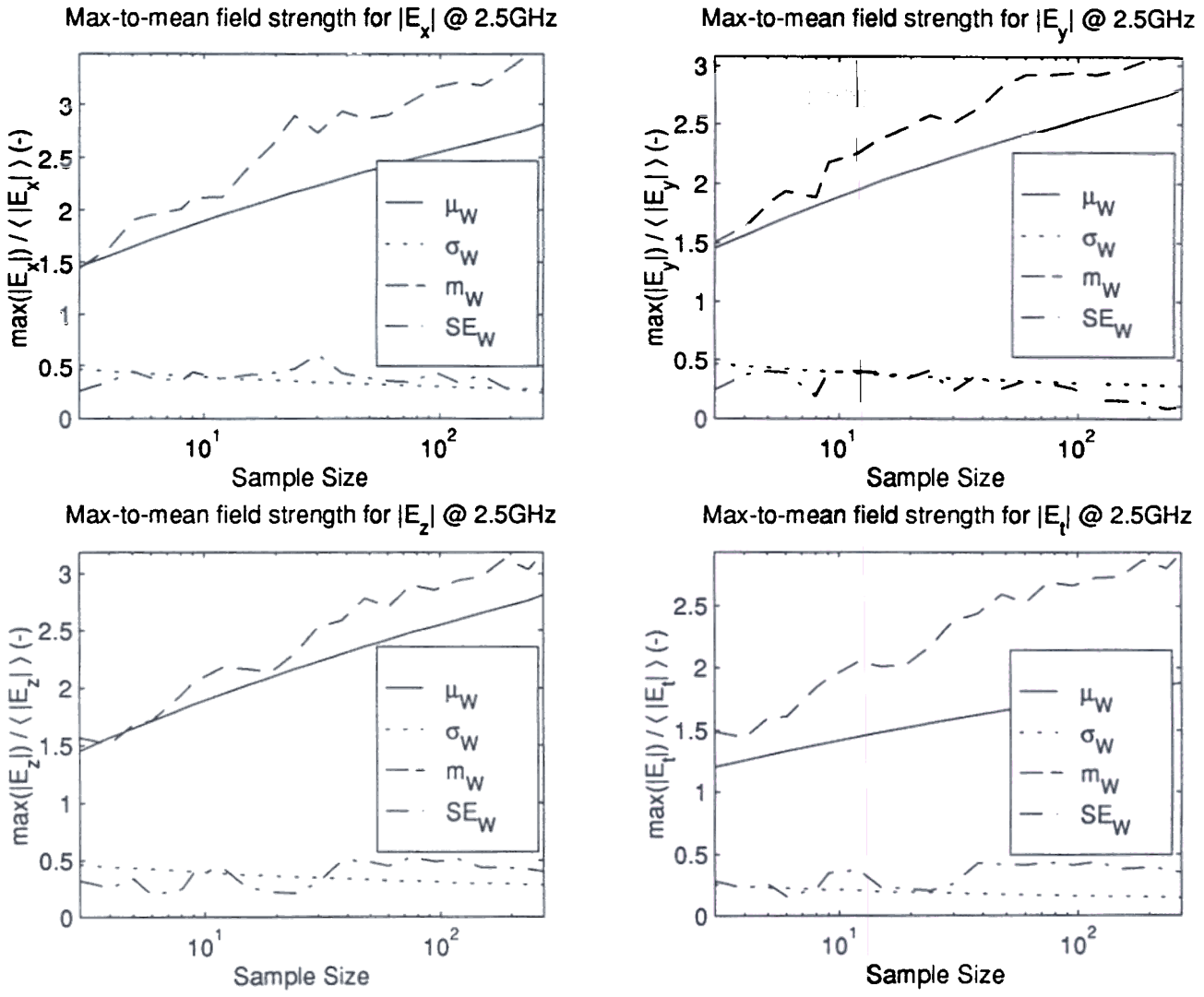


Figure 35: Theoretical and measured max-to-mean field for $|E_\alpha|/\langle|E_\alpha|\rangle$ $(\alpha = x, y, z, t)$ as a function of sample size M @ $f = 2.5$GHz, $r = 345$mm.

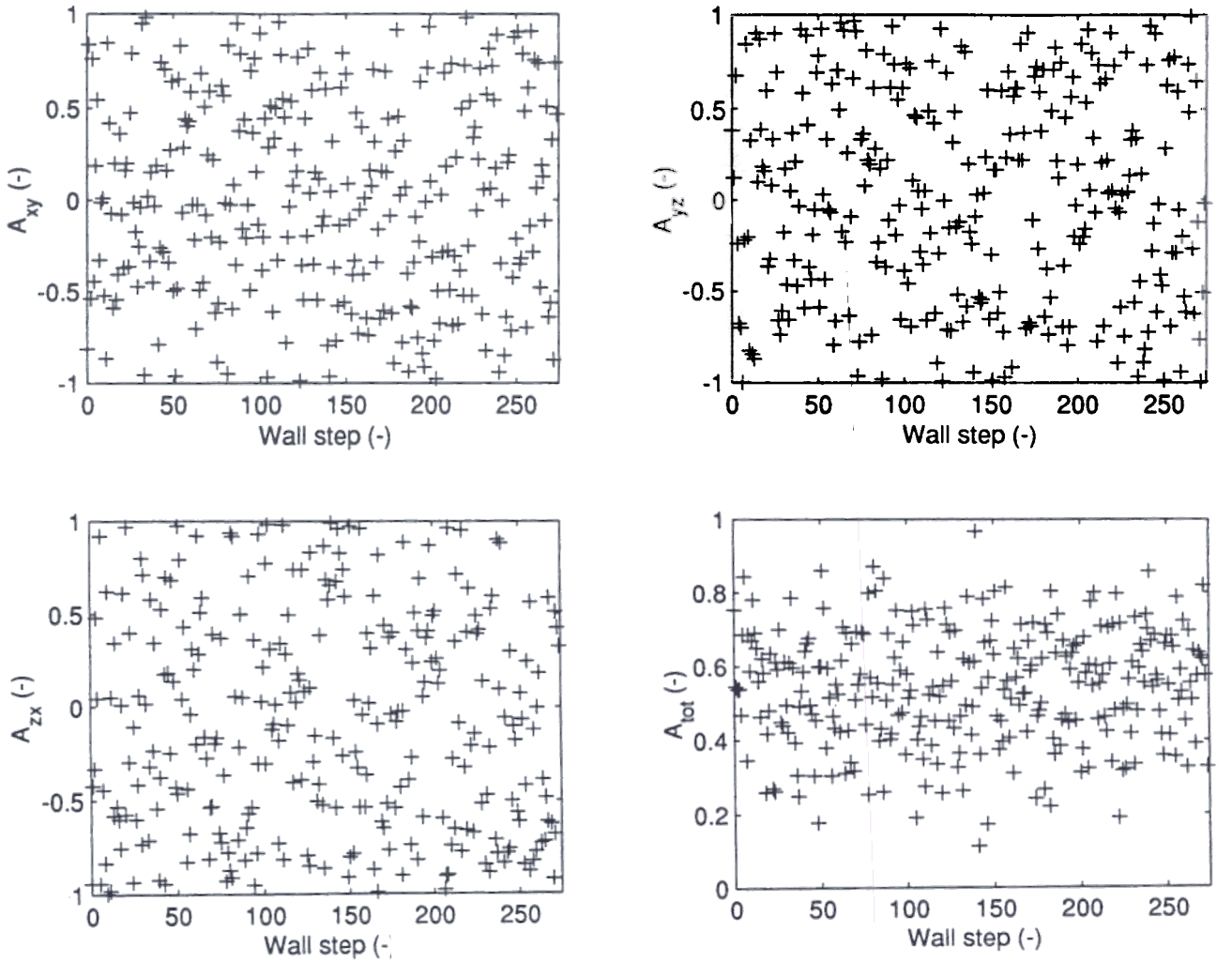


Figure 36: Theoretical (simulated) field anisotropy coefficients $A_{\alpha\beta}$ and A_{tot} for sample of size $M = 275$ taken from a perfectly reverberant field.

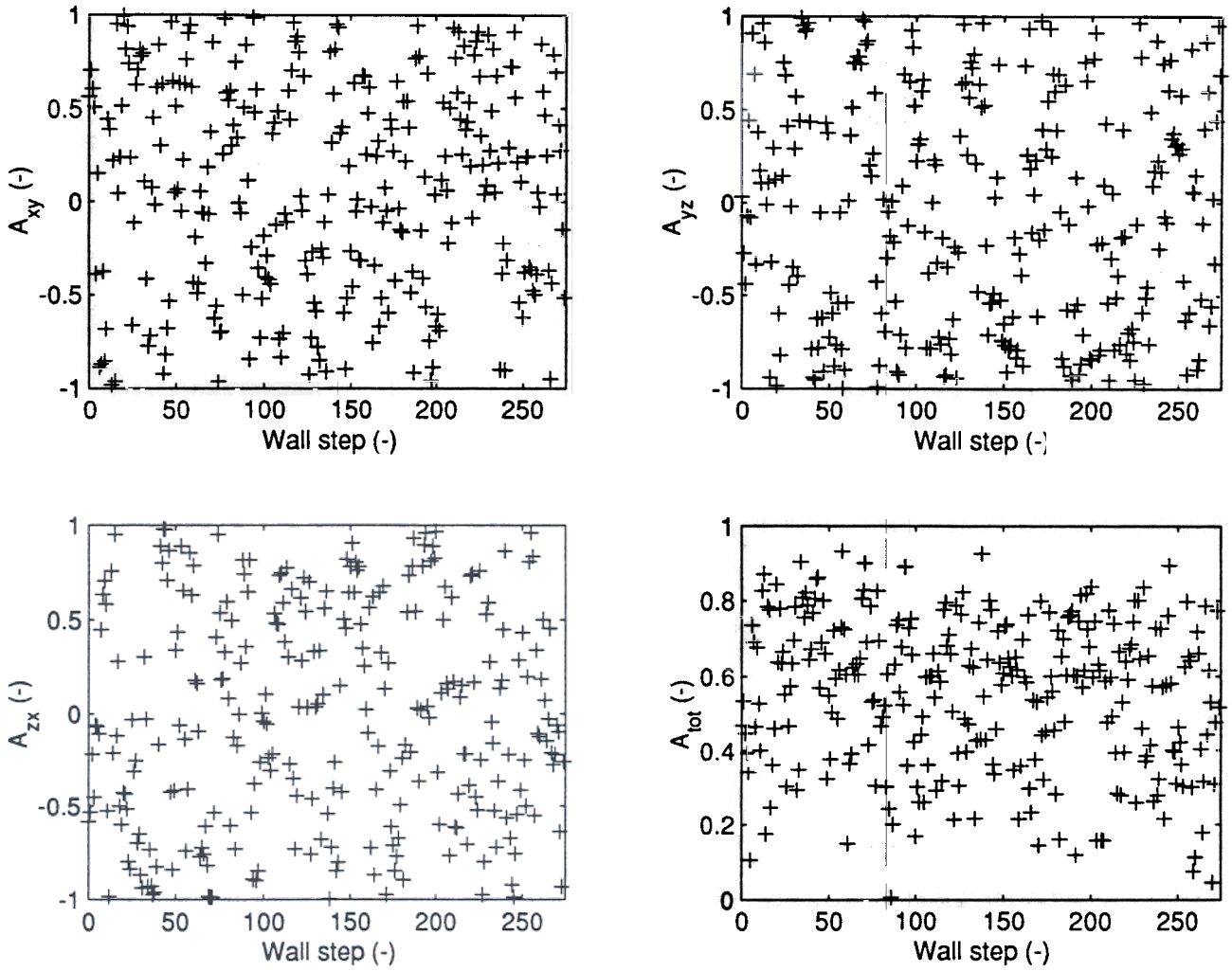


Figure 37: Measured field anisotropy coefficients $A_{\alpha\beta}$ and A_{tot} @ $f = 2.5$GHz, $r = 91$mm for full data set.

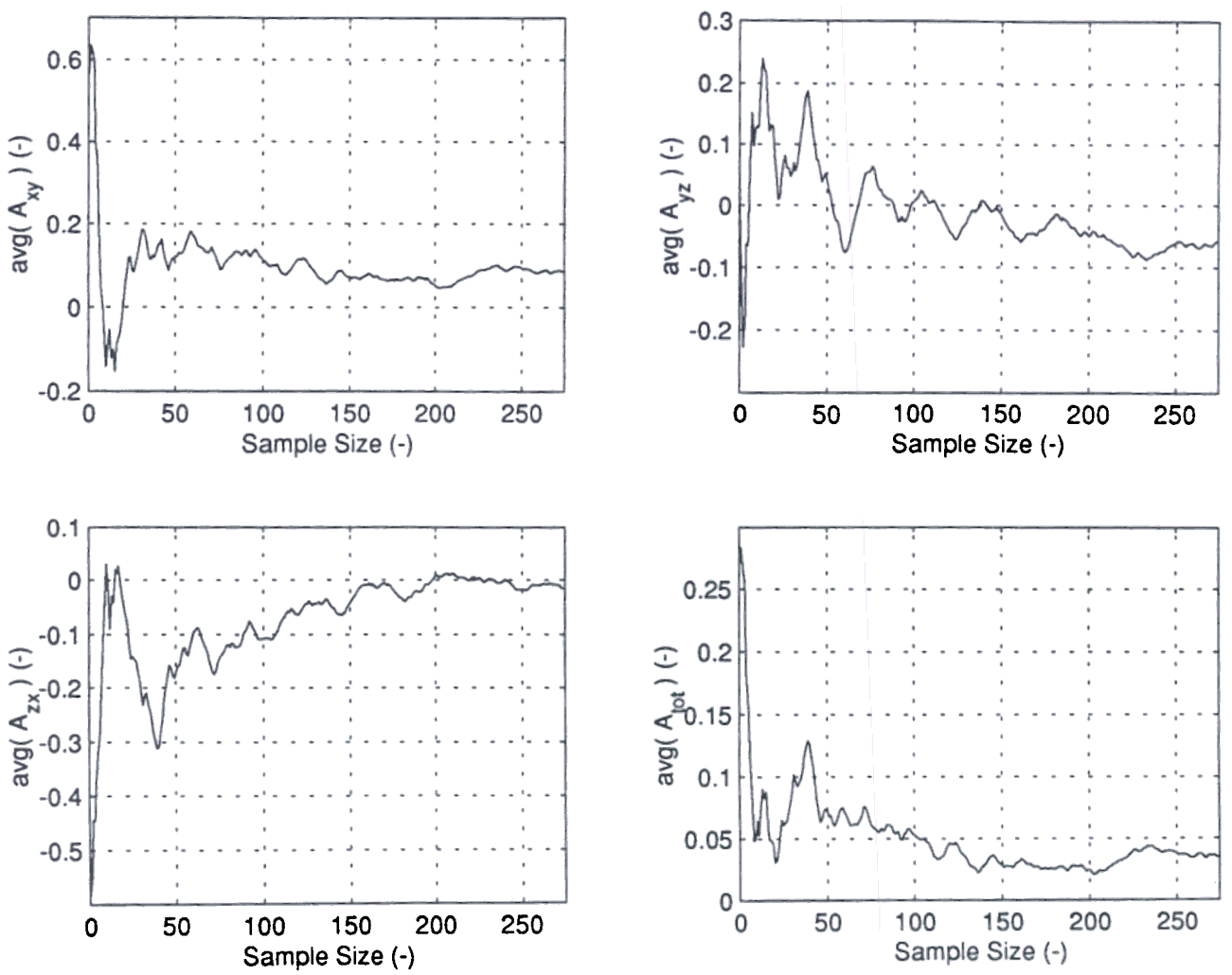


Figure 38: Single-sample average of measured field anisotropy coefficients $A_{\alpha\beta}$ and A_{tot} as a function of sample size M @ $f = 2.5$GHz, $r = 91$mm for full data set (linear scale).

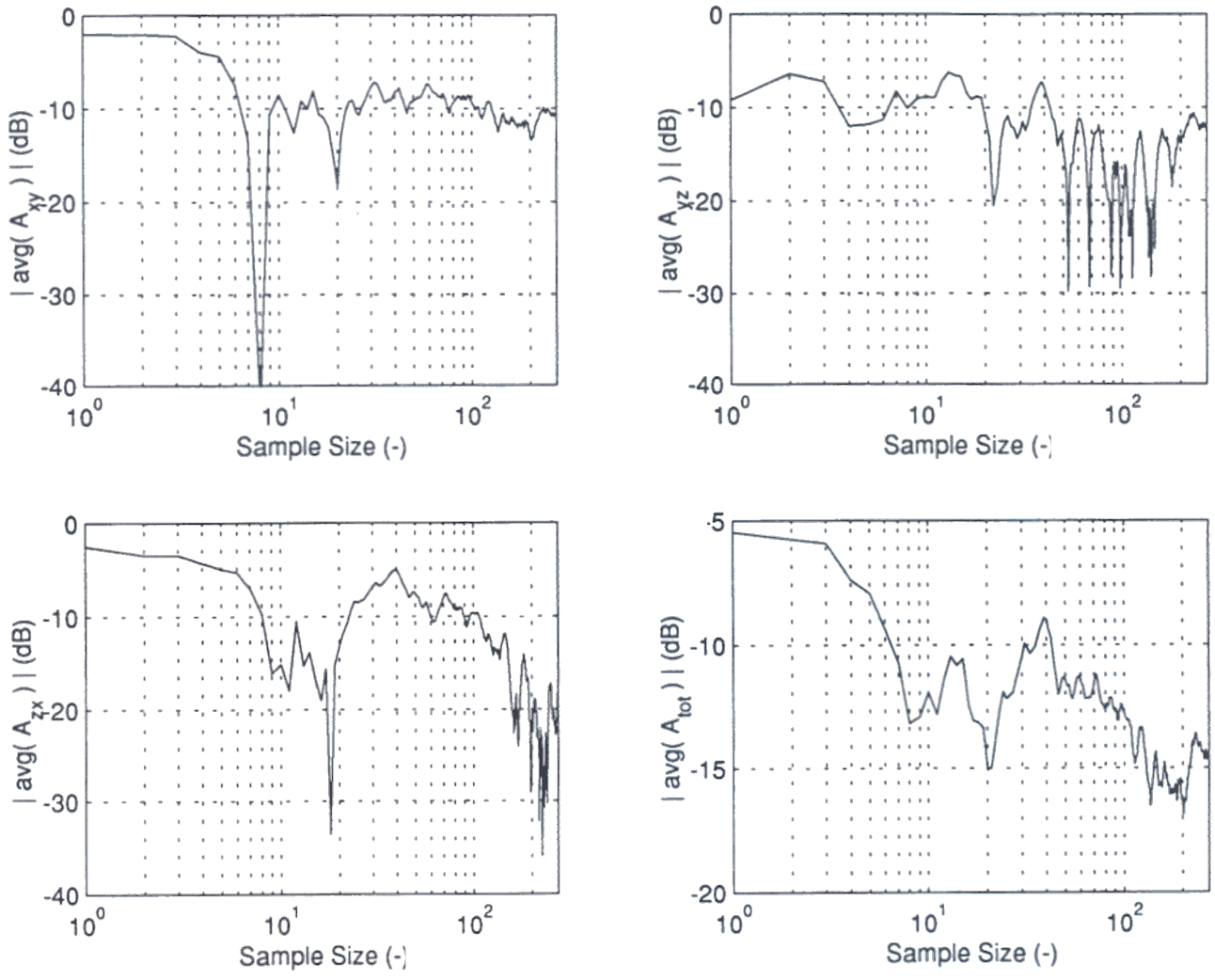


Figure 39: Magnitude of single-sample average of measured field anisotropy coefficients $A_{\alpha\beta}$ and A_{tot} as a function of sample size M @ $f = 2.5$GHz, $r = 91$mm for full data set (dB scale).

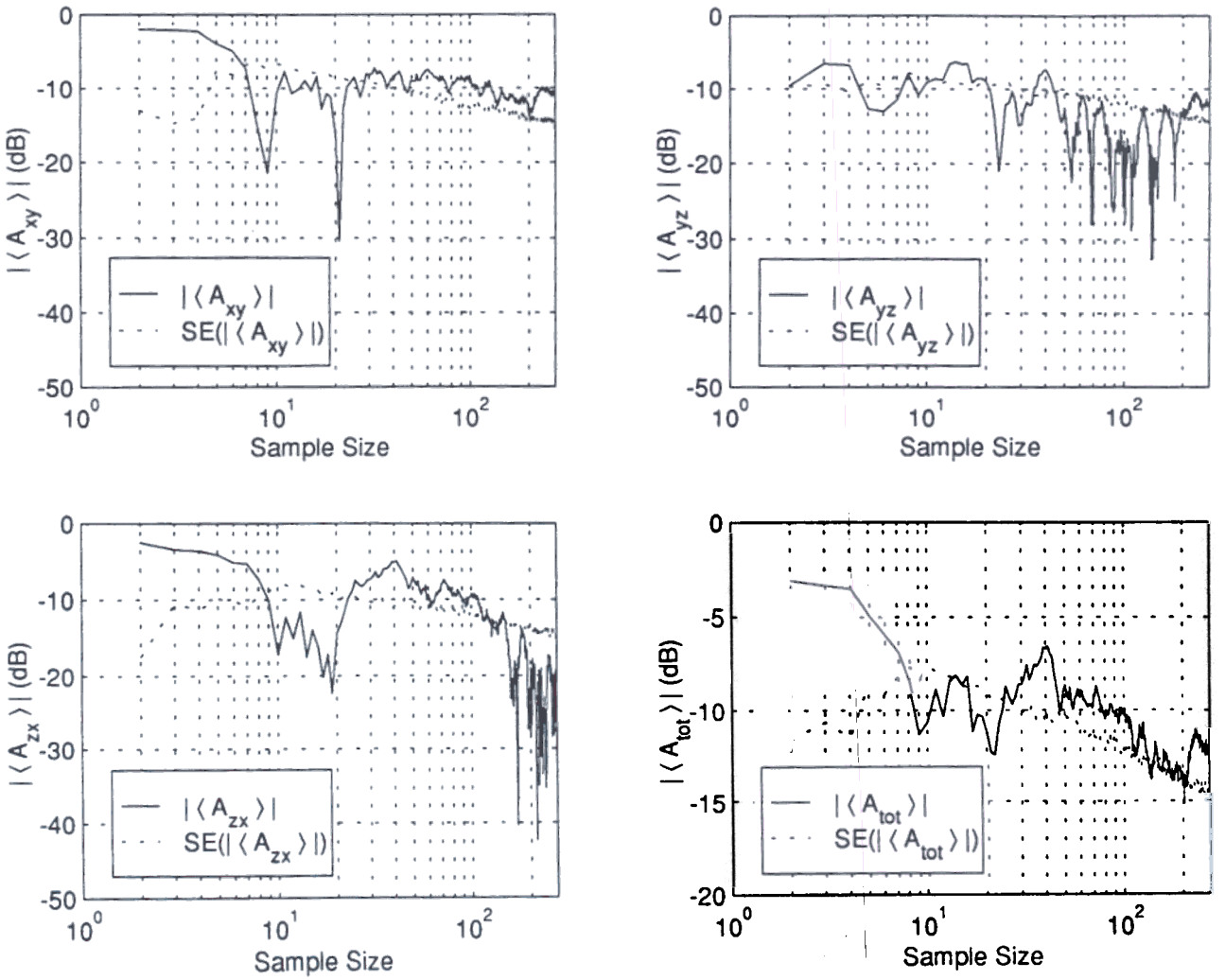


Figure 40: Magnitude of bootstrap average of measured field anisotropy coefficients $A_{\alpha\beta}$ and A_{tot} as a function of sample size M @ $f = 2.5$GHz, $r = 91$mm for full data set (dB scale).

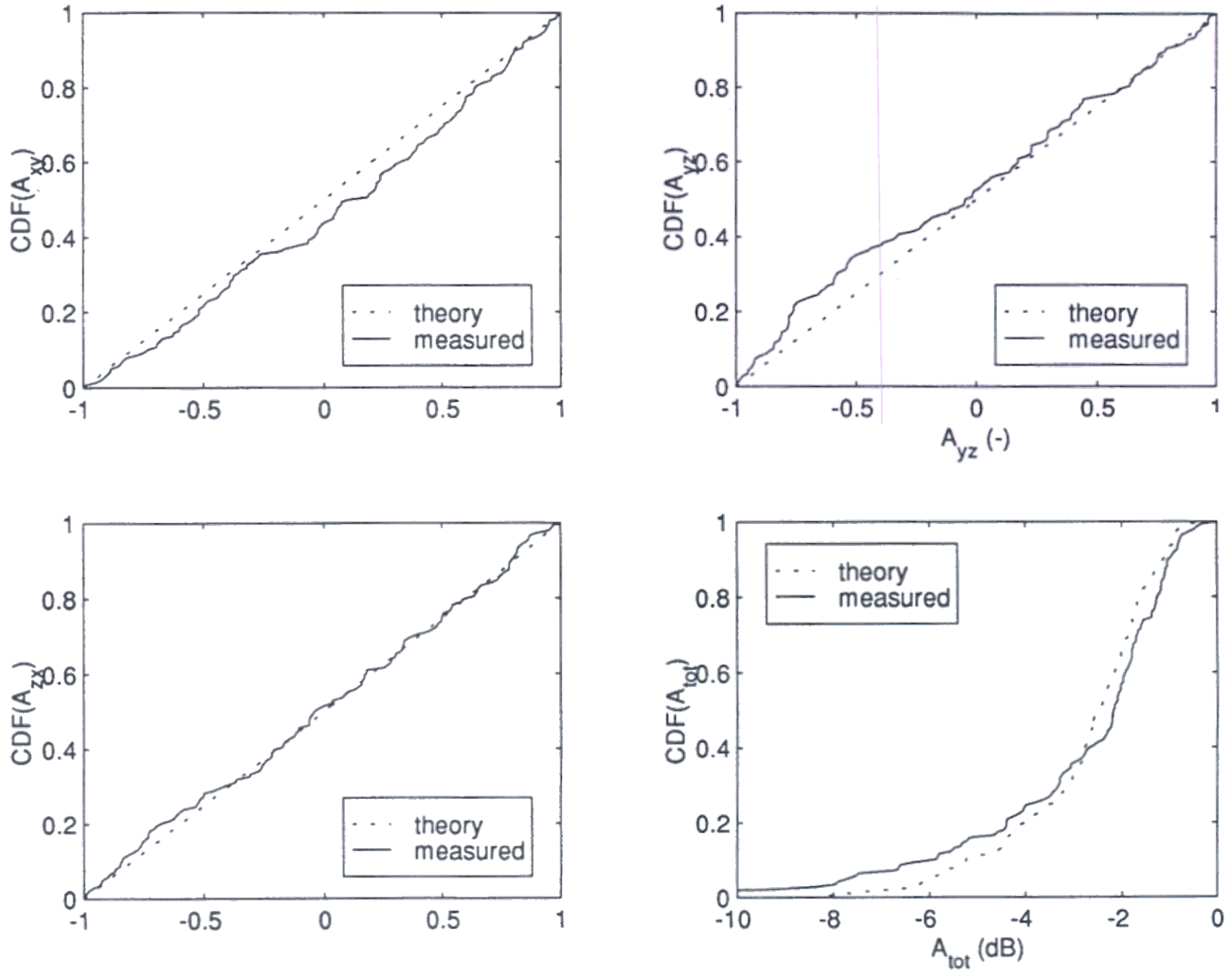


Figure 41: Theoretical and measured cumulative distribution functions of field anisotropy coefficients $A_{\alpha\beta}$ and A_{tot} @ $f = 2.5$GHz, $r = 91$mm for decimated data set ($m_\alpha = 2$).

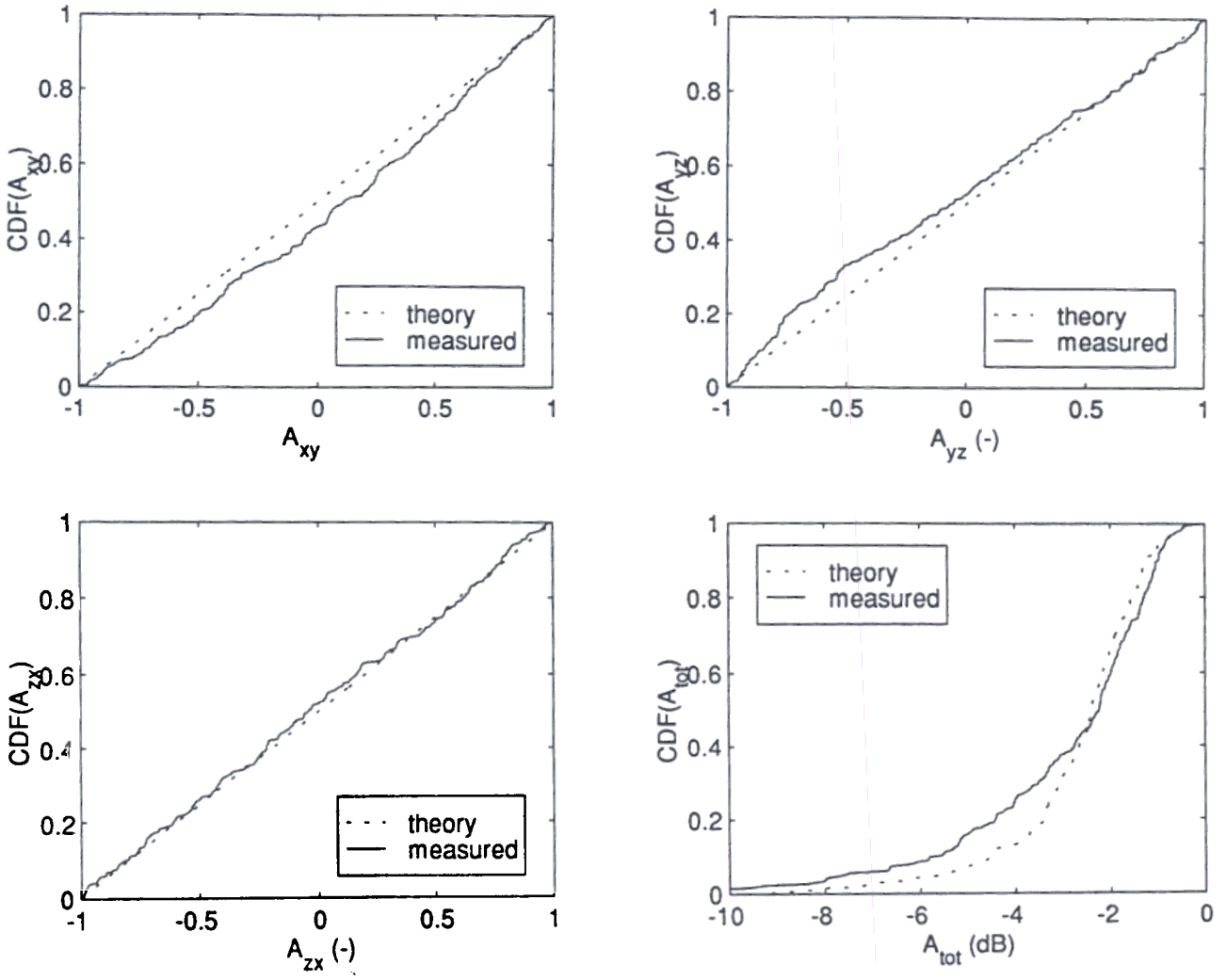


Figure 42: Theoretical and measured cumulative distributions of field anisotropy coefficients $A_{\alpha\beta}$ and A_{tot} @ $f = 2.5$GHz, $r = 91$mm for full data set.

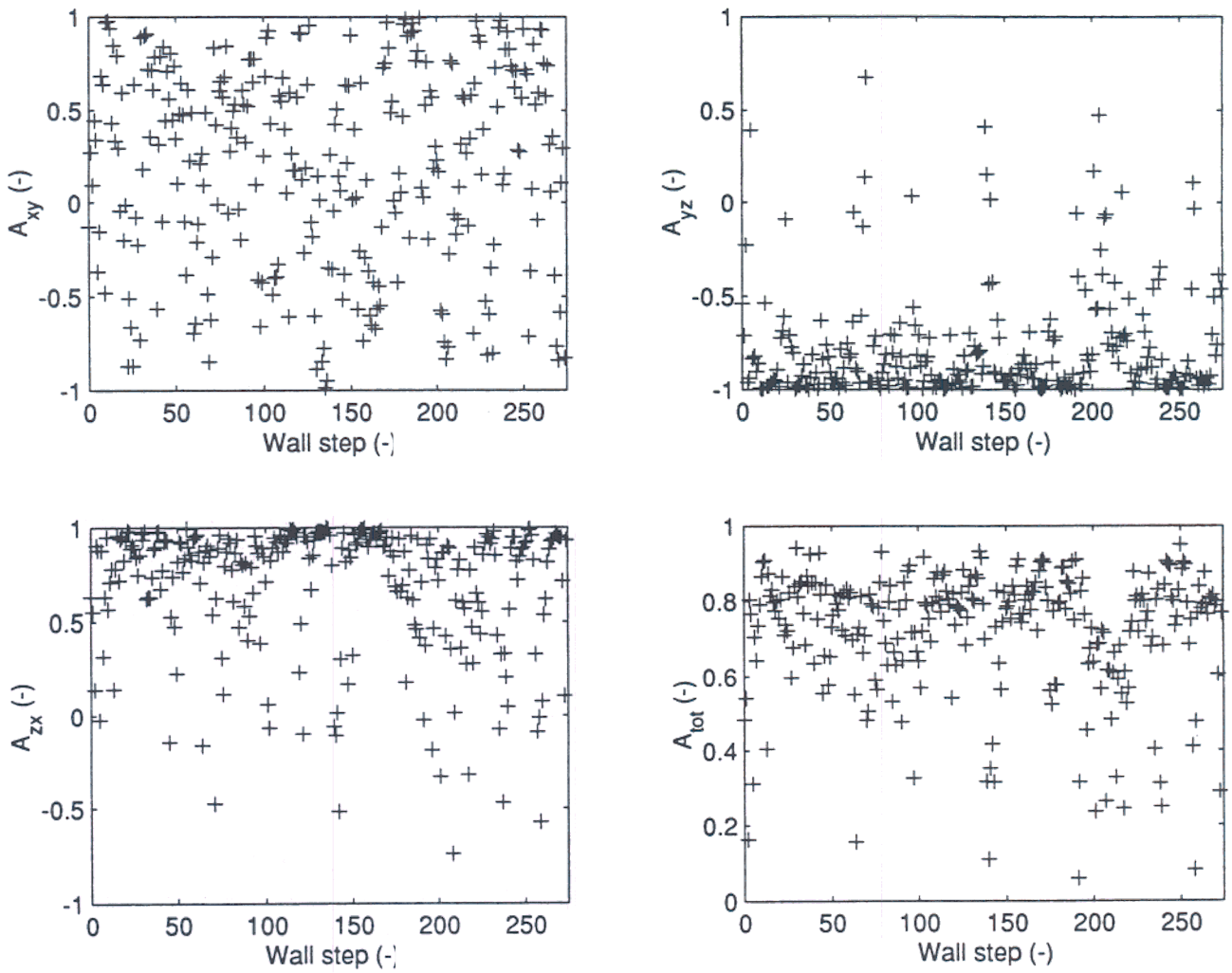


Figure 43: Measured field anisotropy coefficients $A_{\alpha\beta}$ and A_{tot} @ $f = 2.5$GHz, $r = 345$mm for full data set.

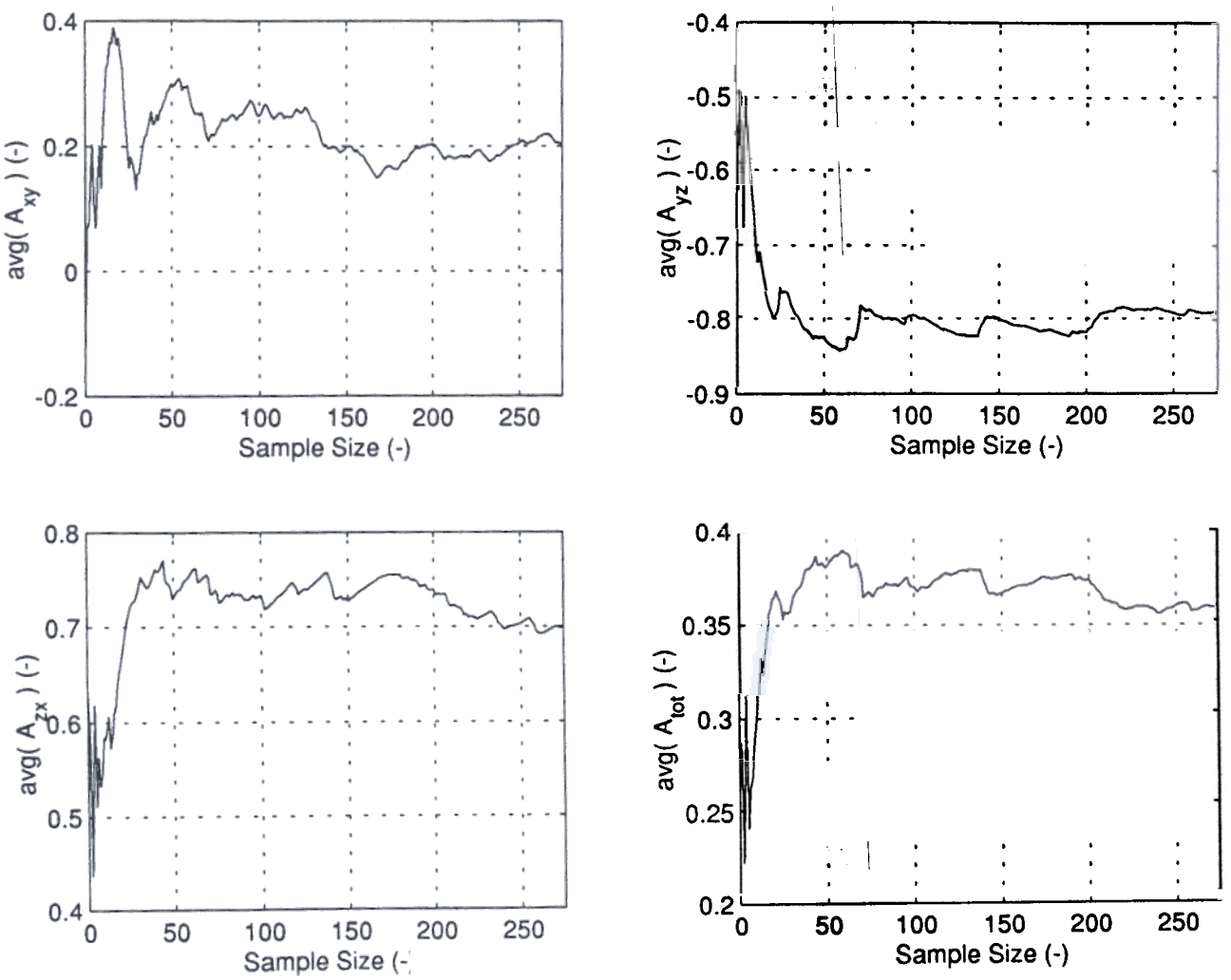


Figure 44: Single-sample average of measured field anisotropy coefficients $A_{\alpha\beta}$ and A_{tot} as a function of sample size M @ $f = 2.5$GHz, $r = 345$mm for full data set (linear scale).

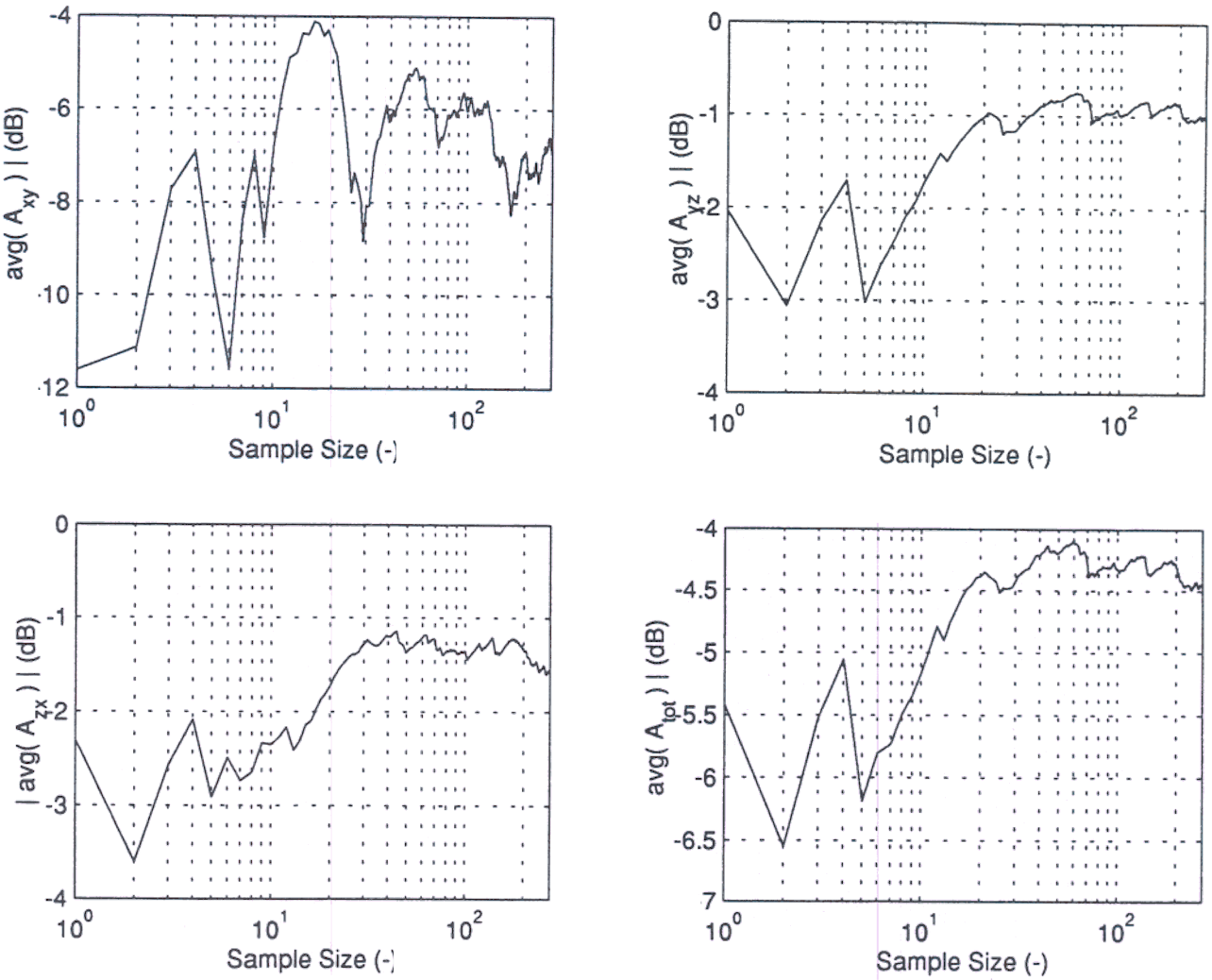


Figure 45: Magnitude of single-sample average of measured field anisotropy coefficients $A_{\alpha\beta}$ and A_{tot} as a function of sample size M @ $f = 2.5$GHz, $r = 345$mm for full data set (dB scale).

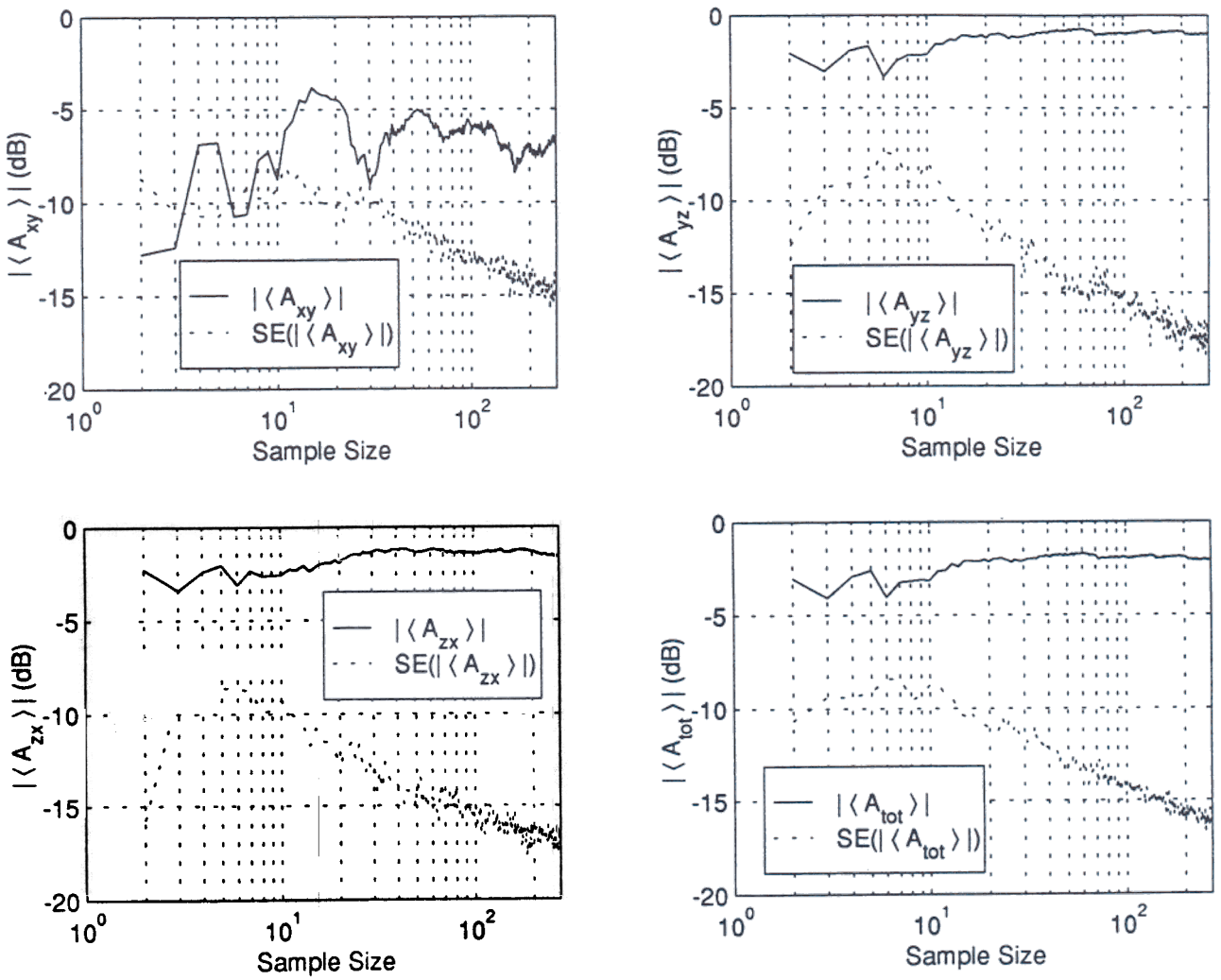


Figure 46: Magnitude of bootstrap average of measured field anisotropy coefficients $A_{\alpha\beta}$ and A_{tot} as a function of sample size M @ f = 2.5GHz, r = 345mm for full data set (dB scale).

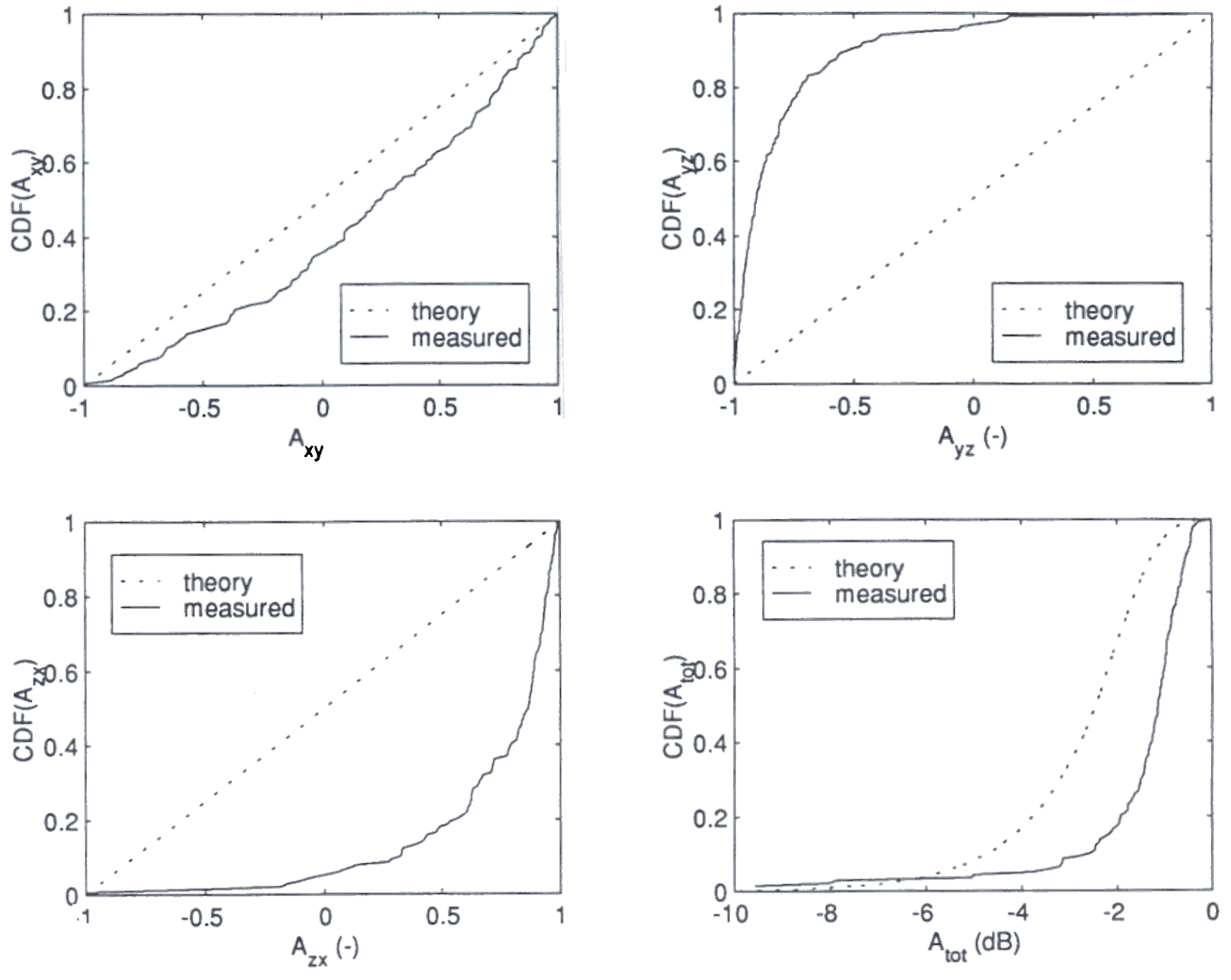


Figure 47: Theoretical and measured cumulative distribution functions of field anisotropy coefficients $A_{\alpha\beta}$ and A_{tot} @ $f = 2.5$GHz, $r = 345$mm for decimated data set ($m_\alpha = 2$).

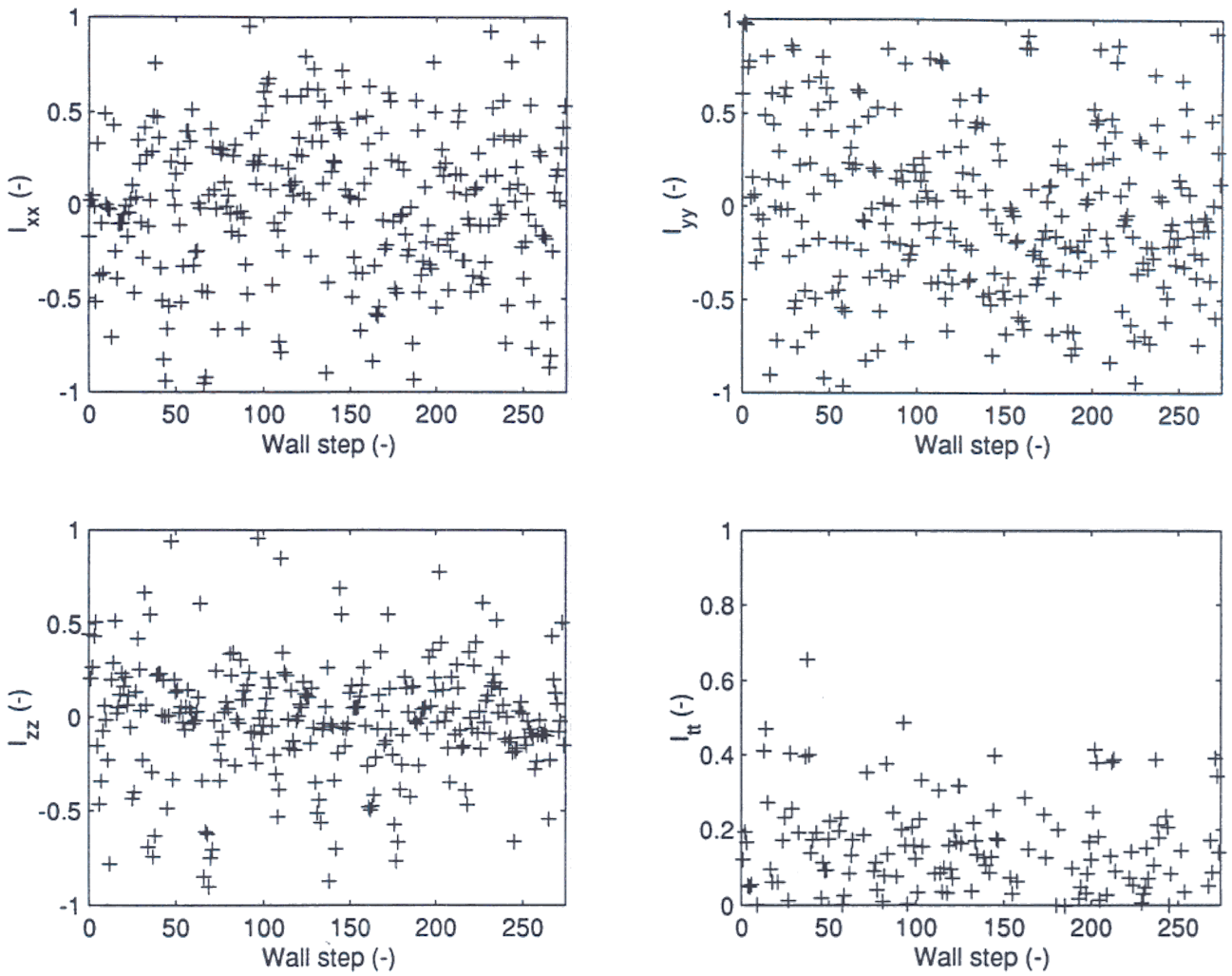


Figure 48: Measured field inhomogeneity coefficients $I_{\alpha\alpha}$ ($\alpha = x, y, z, t$) @ $f = 2.5$GHz, $r_0 = 91$mm, $r_1 = 101$mm for full data set.

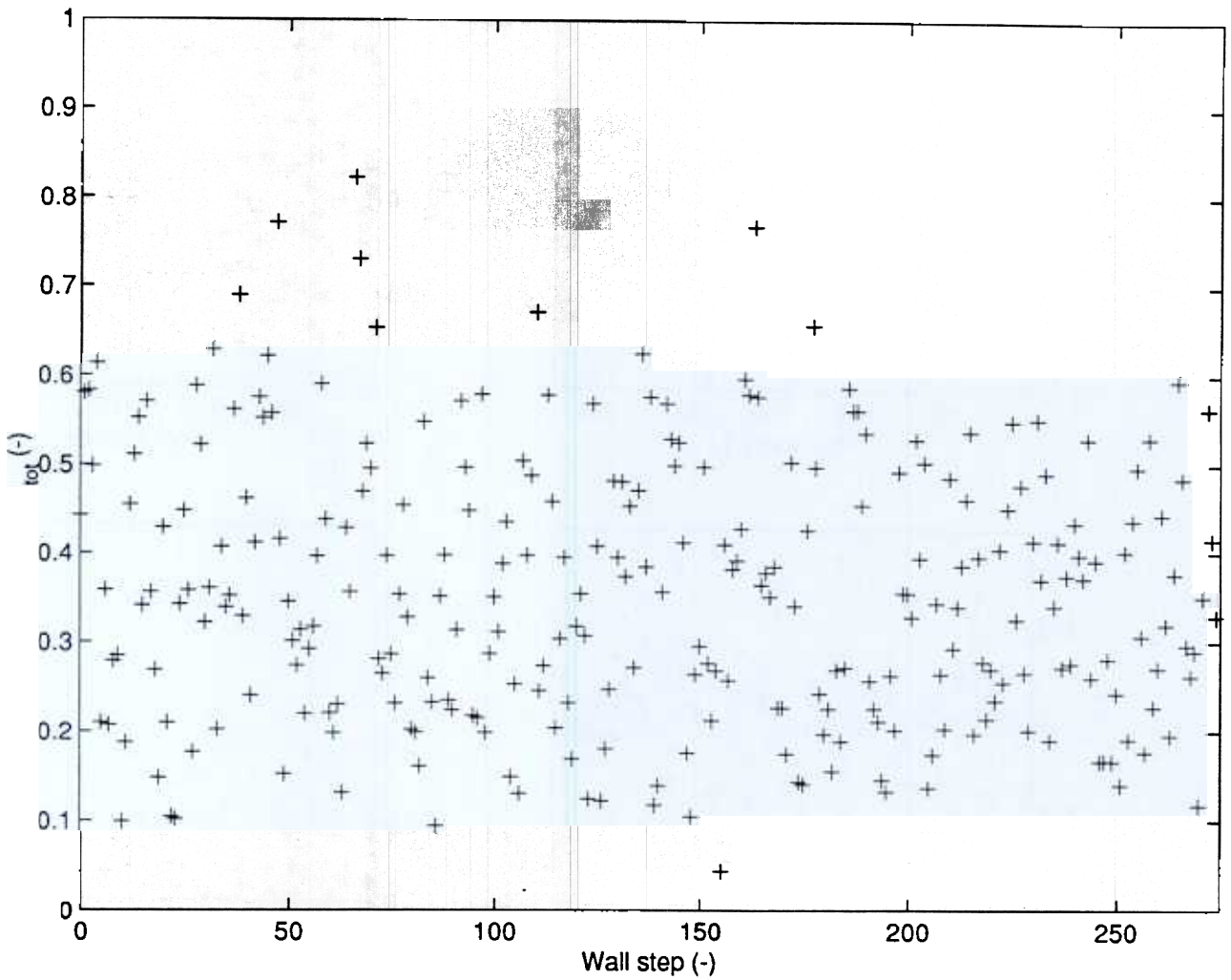


Figure 49: Total measured field inhomogeneity coefficient I_{tot} @ f = 2.5GHz, r_0 = 91mm, r_1 = 101mm for full data set.

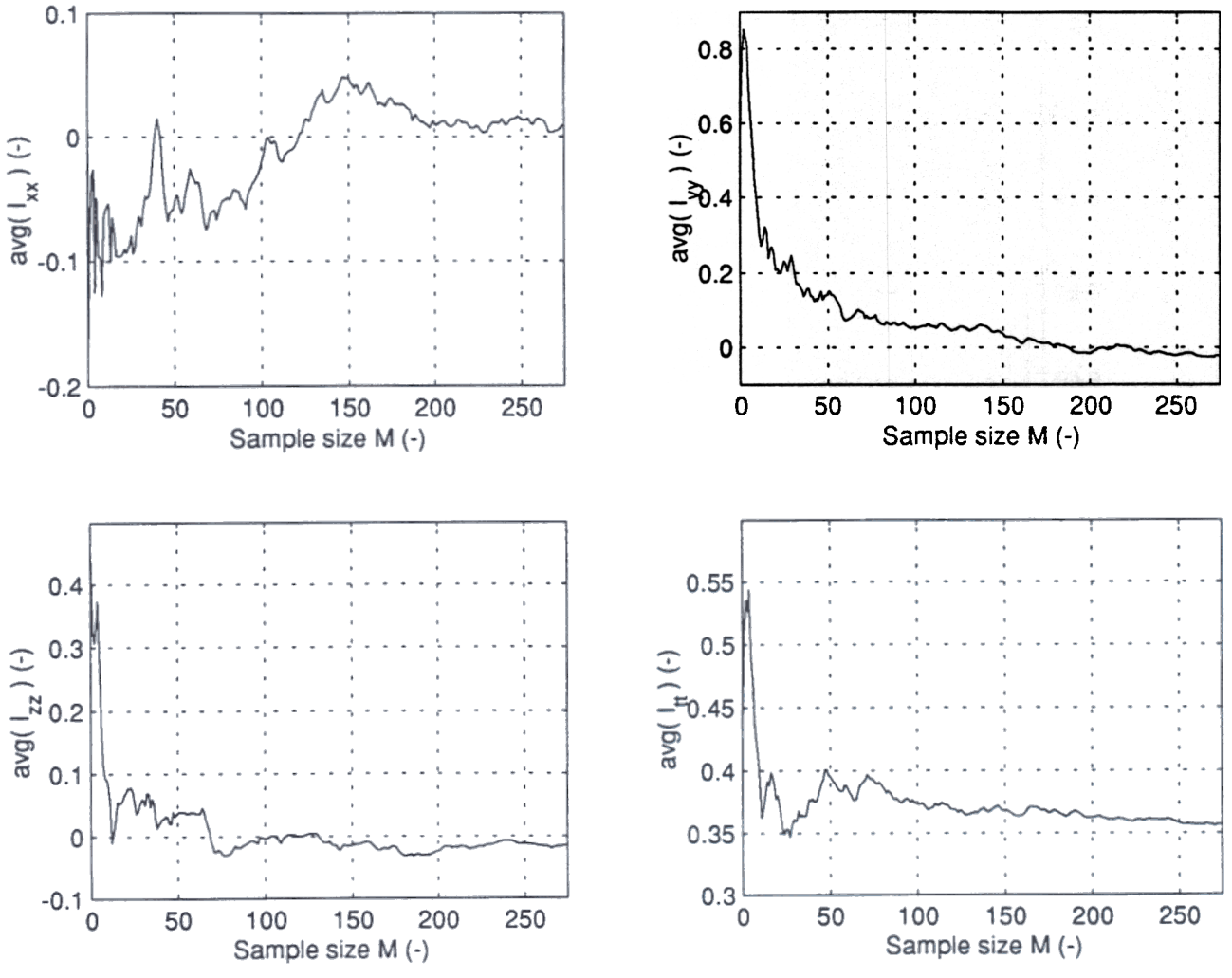


Figure 50: Single-sample average of measured field inhomogeneity coefficients $I_{\alpha\alpha}$ ($\alpha = x, y, z, t$) as a function of sample size M @ $f = 2.5$GHz, $r_0 = 91$mm, $r_1 = 101$mm for full data set (linear scale).

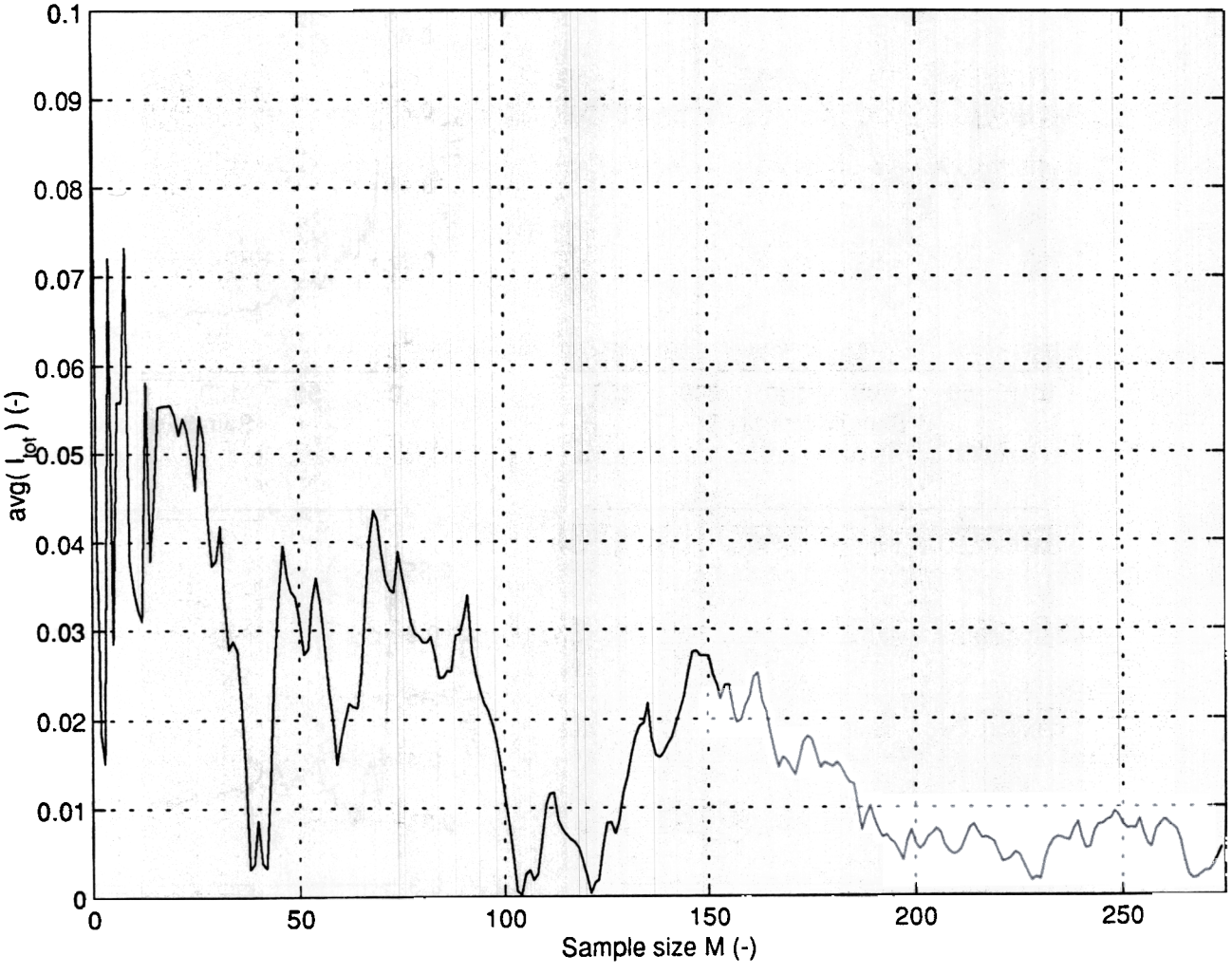


Figure 51: Single-sample average of total measured field inhomogeneity coefficient I_{tot} as a function of sample size M @ f = 2.5GHz, r_0 = 91mm, r_1 = 101mm for full data set (linear scale).

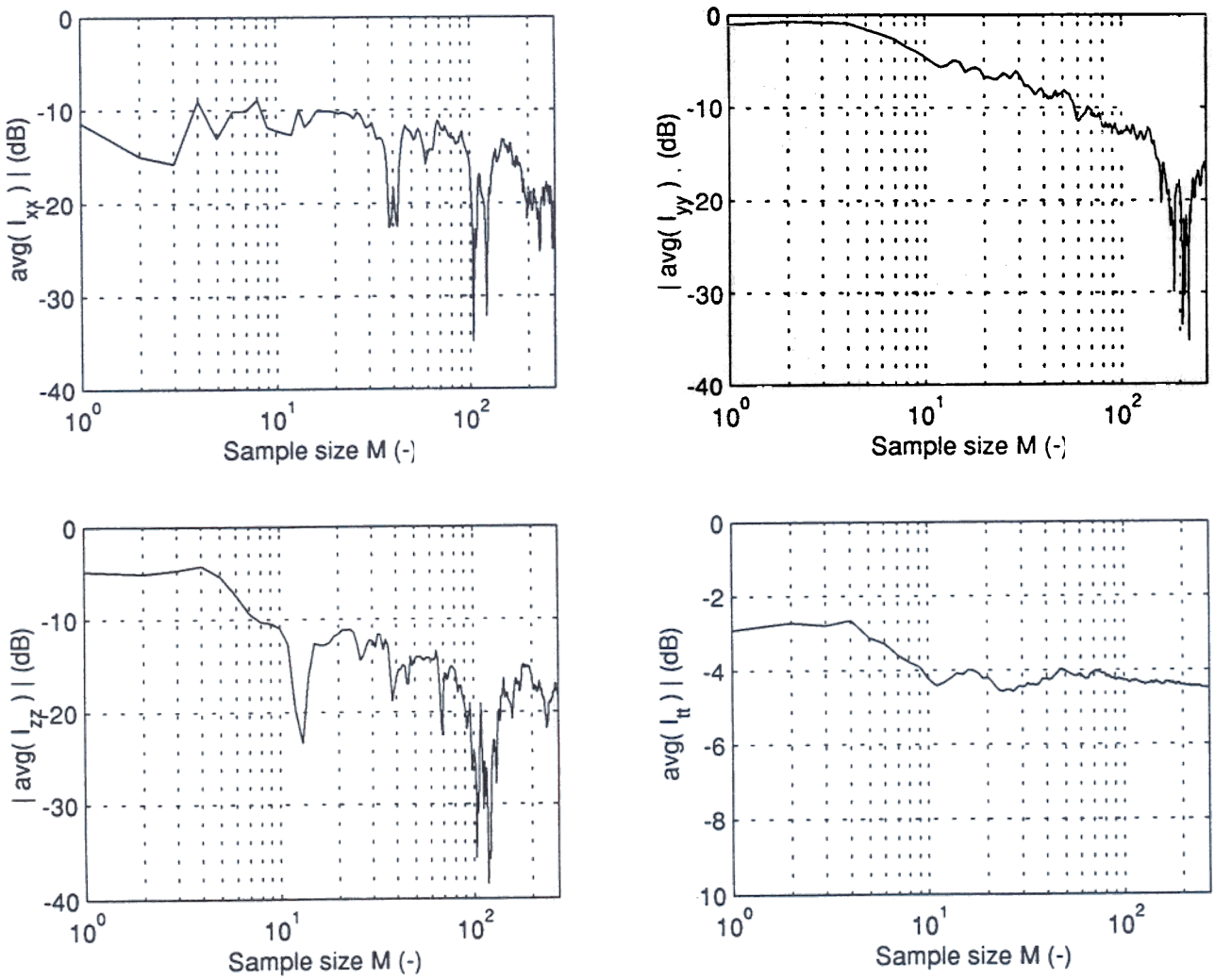


Figure 52: Magnitude of single-sample average of measured field inhomogeneity coefficients $I_{\alpha\alpha}$ ($\alpha = x, y, z, t$) as a function of sample size M @ $f = 2.5$GHz, $r_0 = 91$mm, $r_1 = 101$mm for full data set (dB scale).

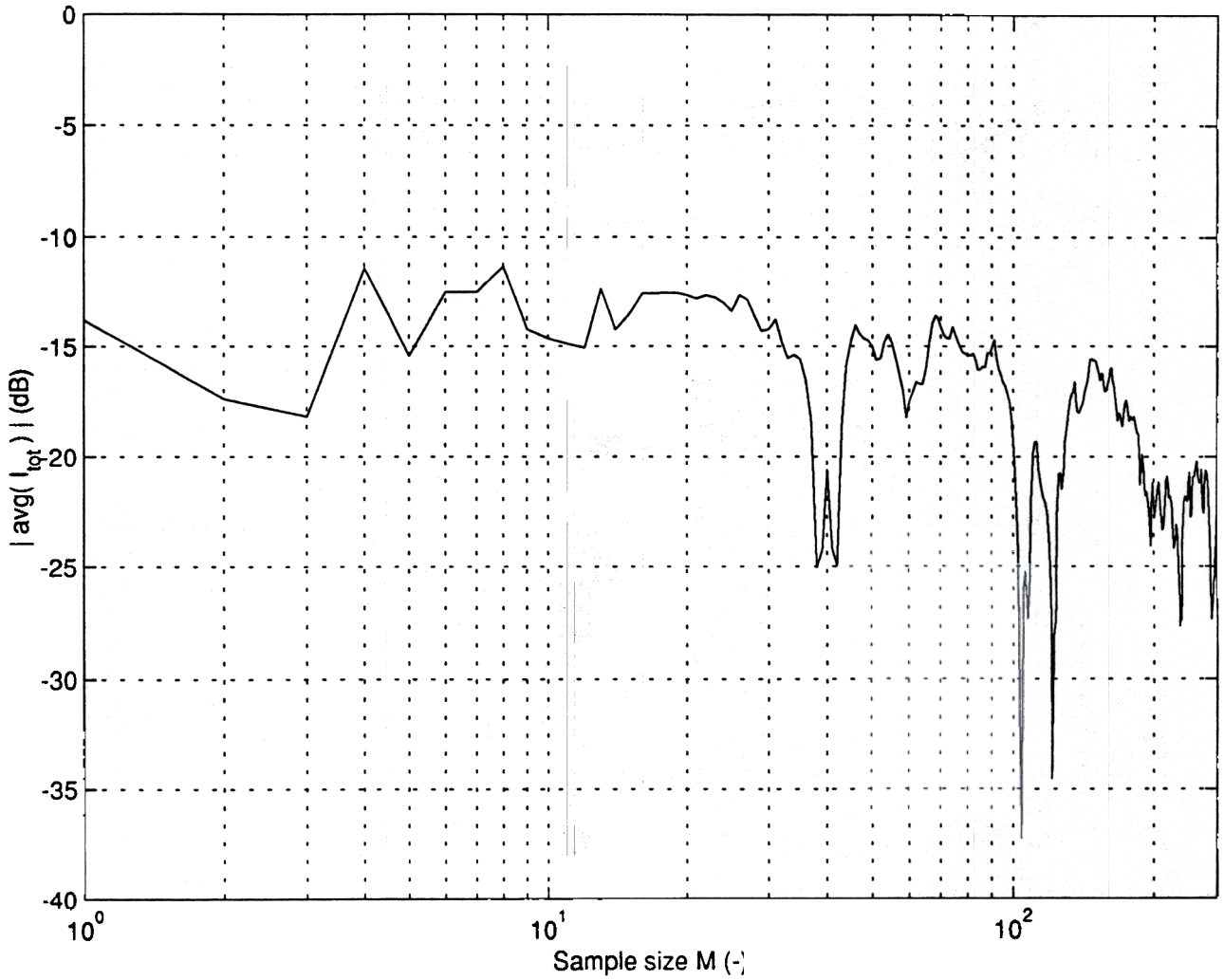


Figure 53: Magnitude of single-sample average of total measured field inhomogeneity coefficient I_{tot} as a function of sample size M @ f = 2.5GHz, r_0 = 91mm, r_1 = 101mm for full data set (dB scale).

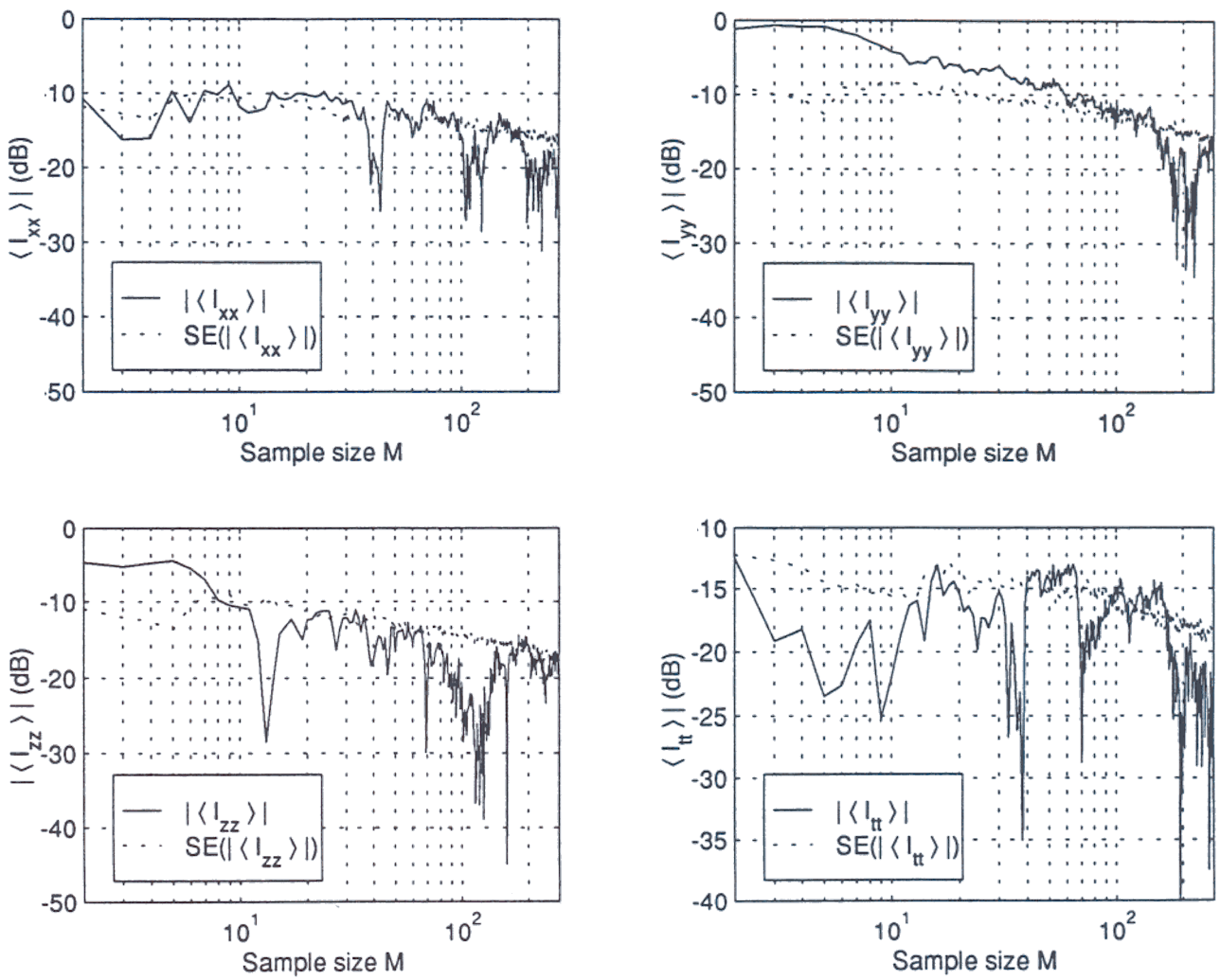


Figure 54: Magnitude of bootstrap average of measured field inhomogeneity coefficients $I_{\alpha\alpha}$ ($\alpha = x, y, z, t$) as a function of sample size M @ $f = 2.5$GHz, $r_0 = 91$mm, $r_1 = 101$mm for full data set (dB scale).

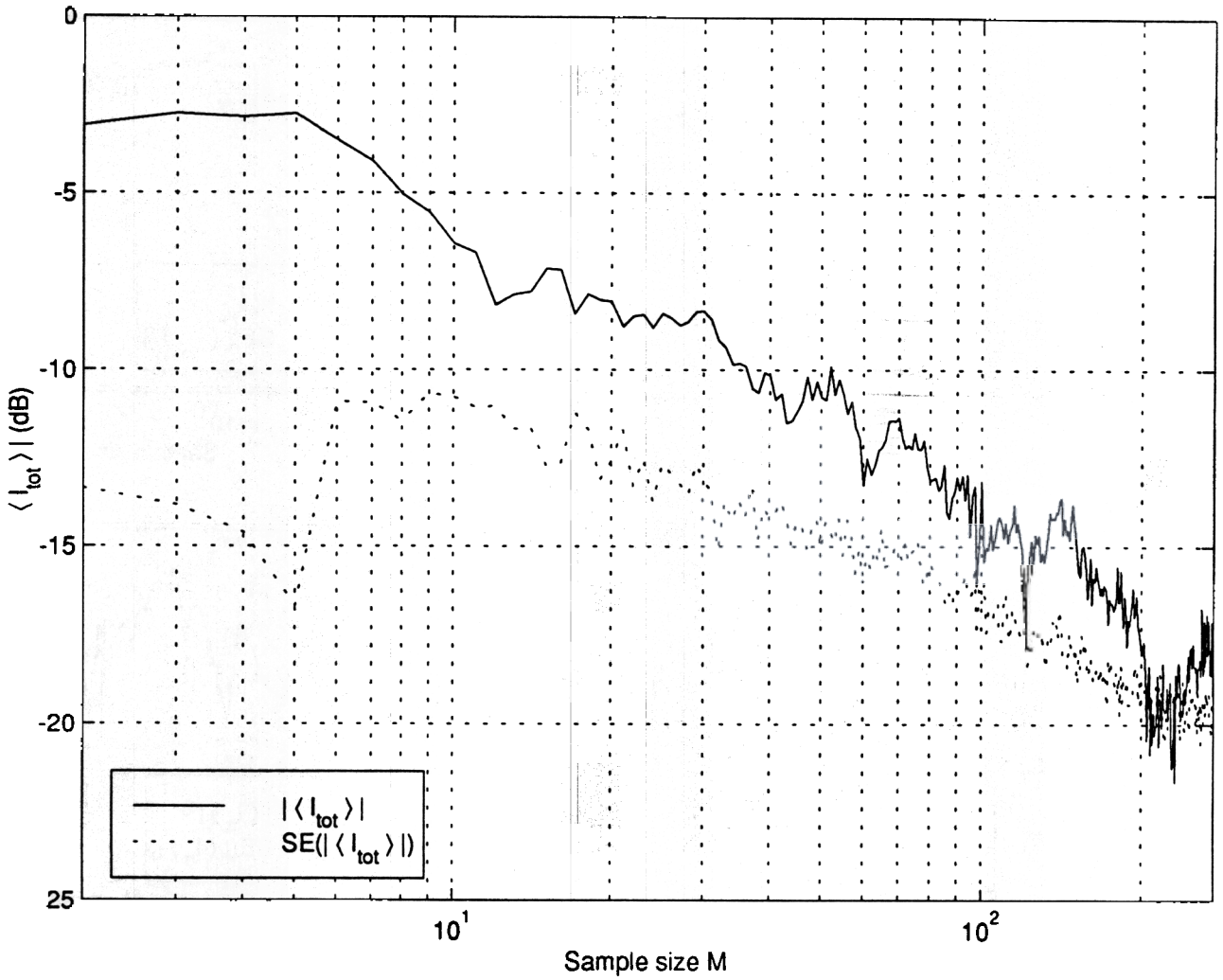


Figure 55: Magnitude of bootstrap average of total measured field inhomogeneity coefficient I_{tot} as a function of sample size M @ f = 2.5GHz, r_0 = 91mm, r_1 = 101mm for full data set (dB scale).

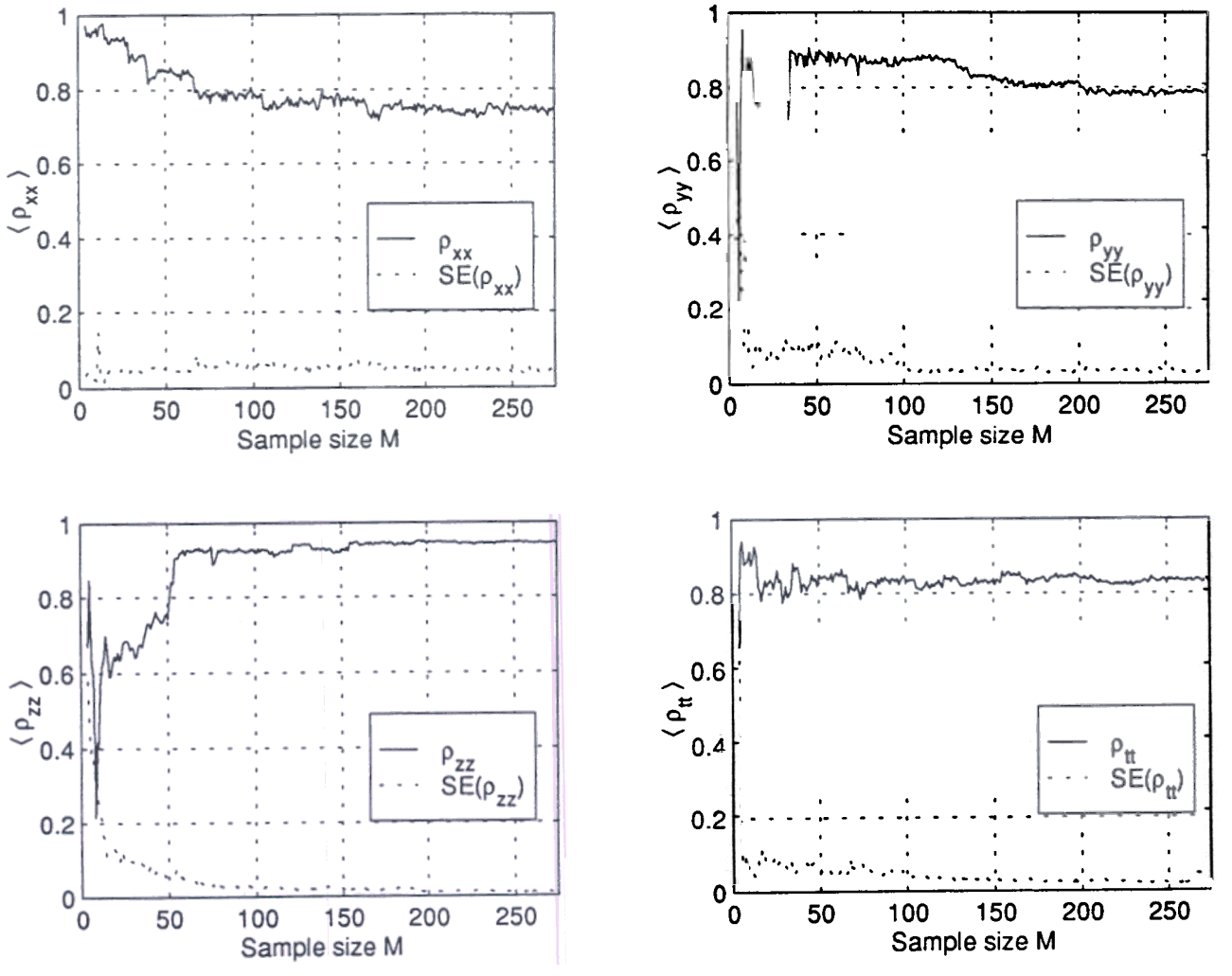


Figure 56: Spatial correlation coefficients between $|E_\alpha(r_0)|^2$ and $|E_\alpha(r_1)|^2$ as a function of sample size M @ $f = 2.5$GHz, $r_0 = 91$mm, $r_1 = 101$mm for full data set.

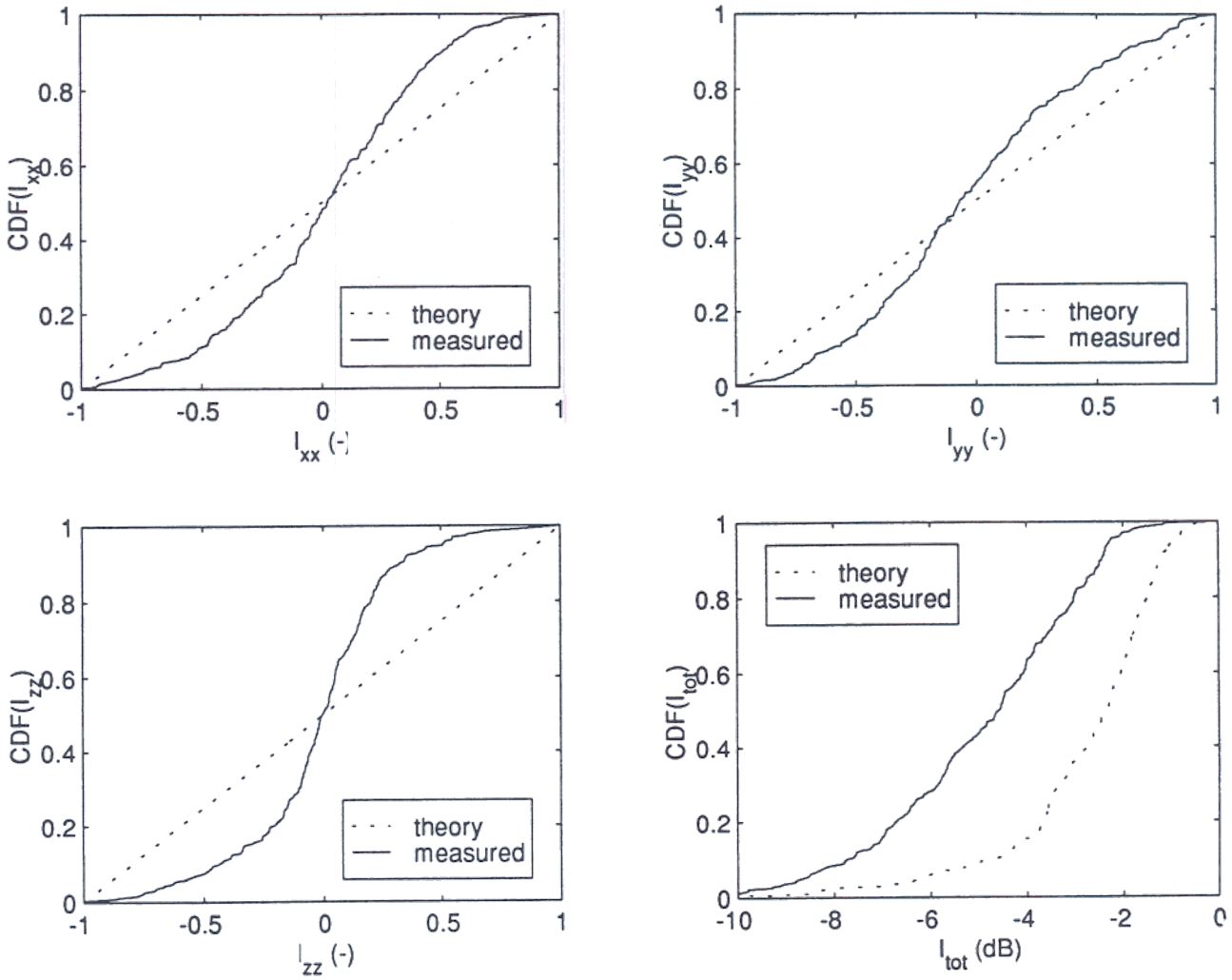


Figure 57: Theoretical and measured cumulative distribution functions of field inhomogeneity coefficients @ $f = 2.5$GHz, $r_0 = 91$mm, $r_1 = 101$mm for decimated data set ($m_\alpha = 2$).

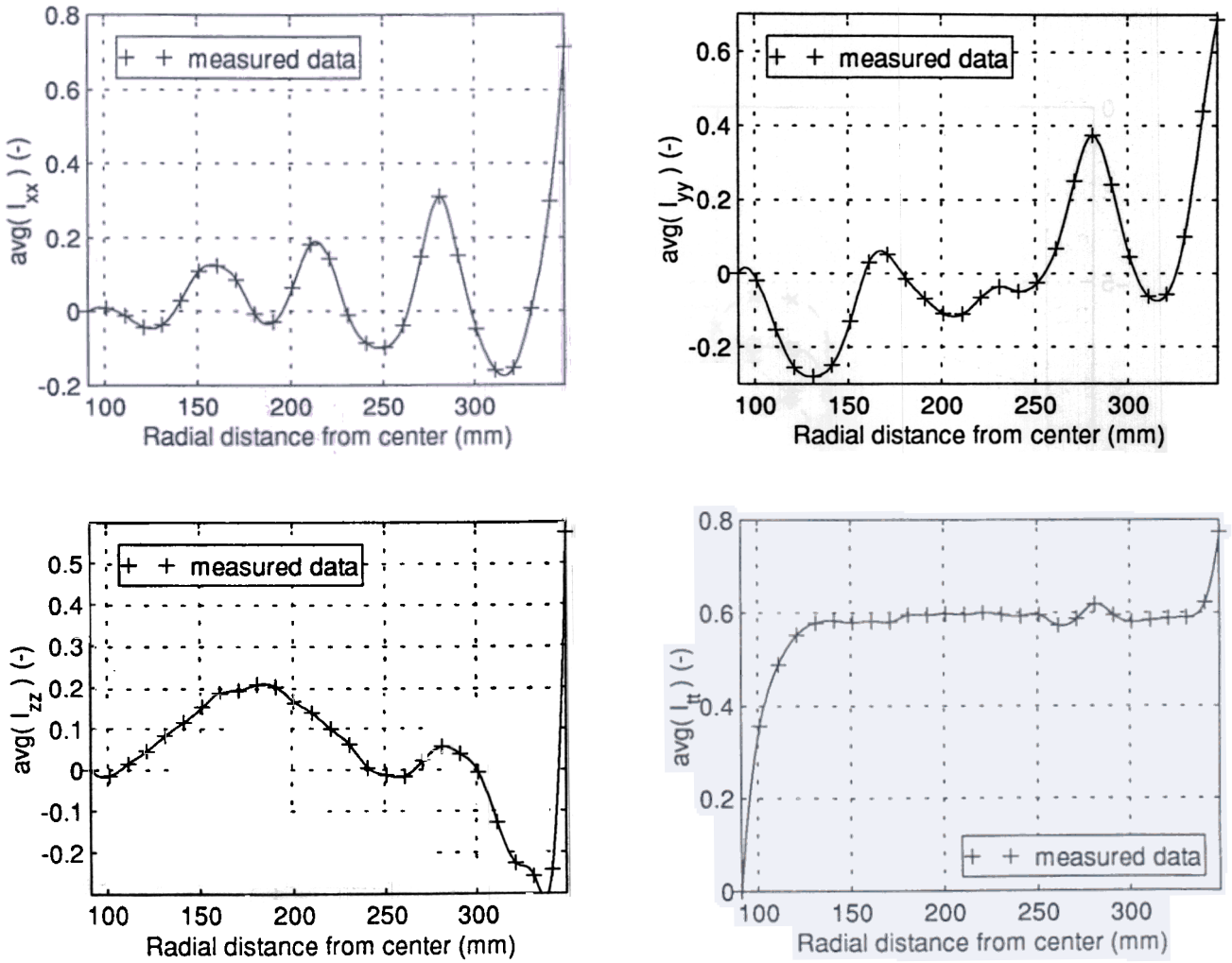


Figure 58: Radial dependence of field inhomogeneity coefficients $I_{\alpha\alpha}$ ($\alpha = x, y, z, t$) @ f = 2.5GHz, $r_0 = 91$mm, $r_1 = 101 \ldots 349$mm.

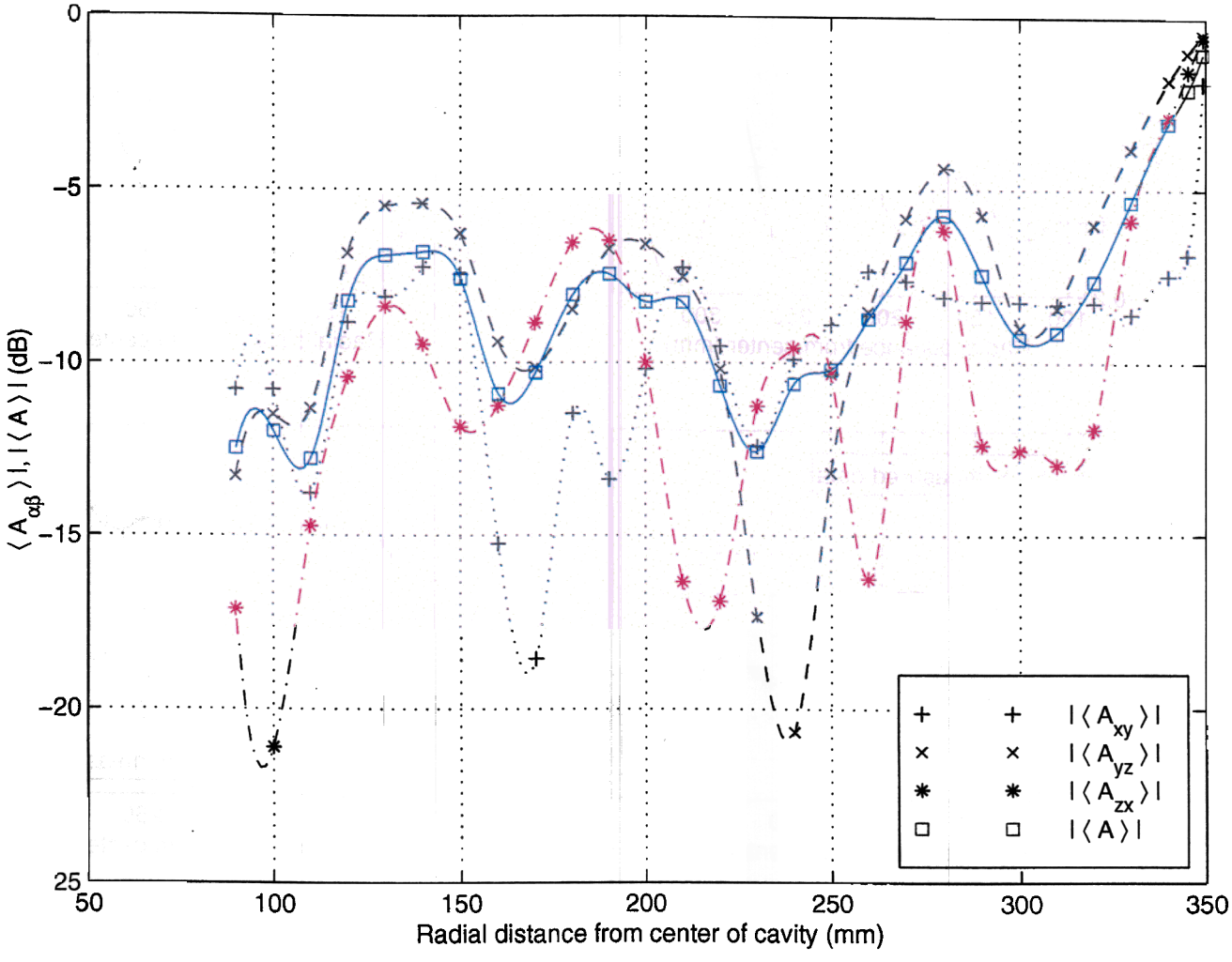


Figure 59: Radial dependence of magnitude of bootstrap averaged field anisotropy coefficients $A_{\alpha\beta}$ and A_{tot} @ $f = 2.5$GHz.

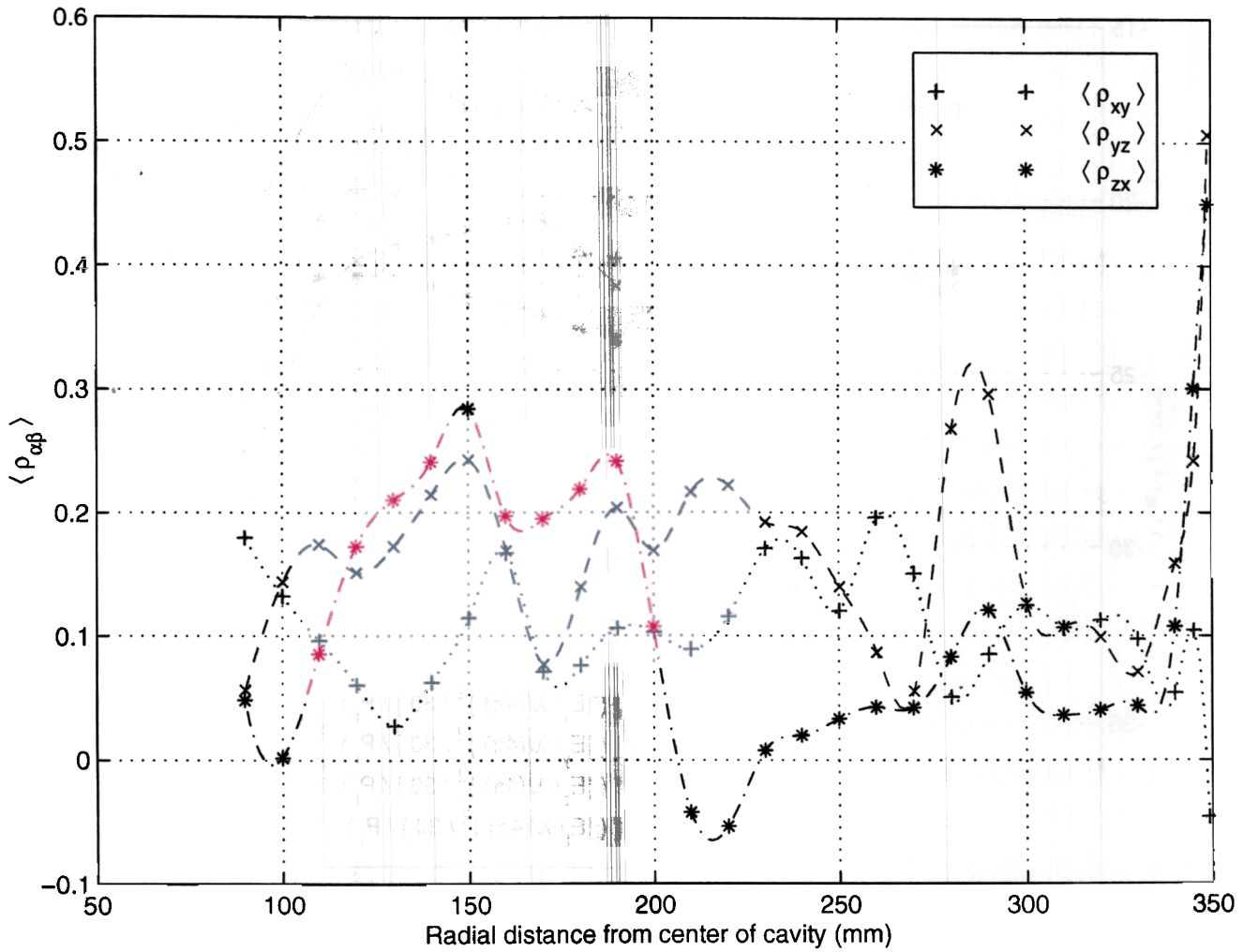


Figure 60: Radial dependence of bootstrap averaged crosscorrelation coefficients $\varrho_{\alpha\beta}$ @ f = 2.5GHz for full data set.

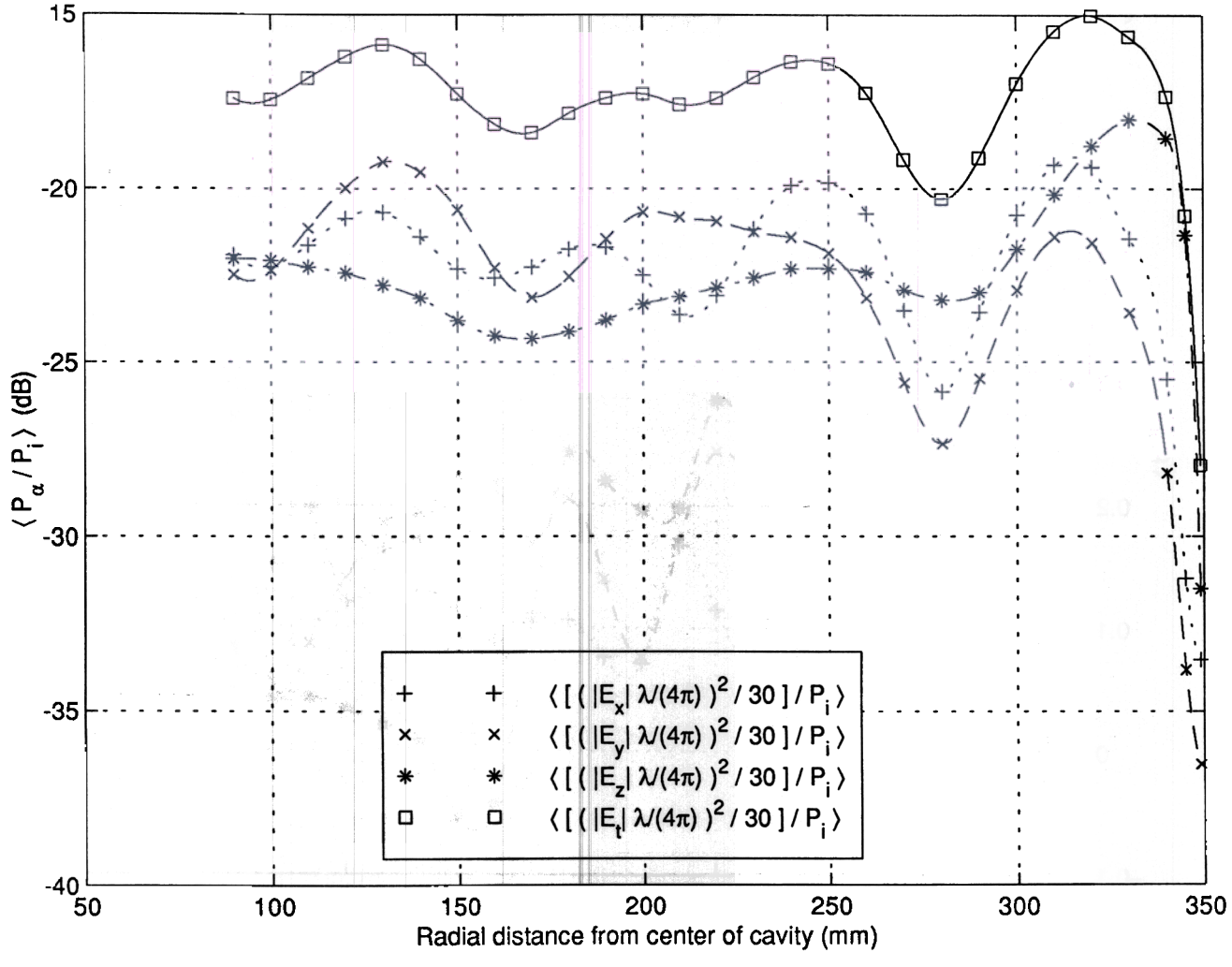


Figure 61: Radial dependence of bootstrap averaged transmission loss @ $f = 2.5$GHz.

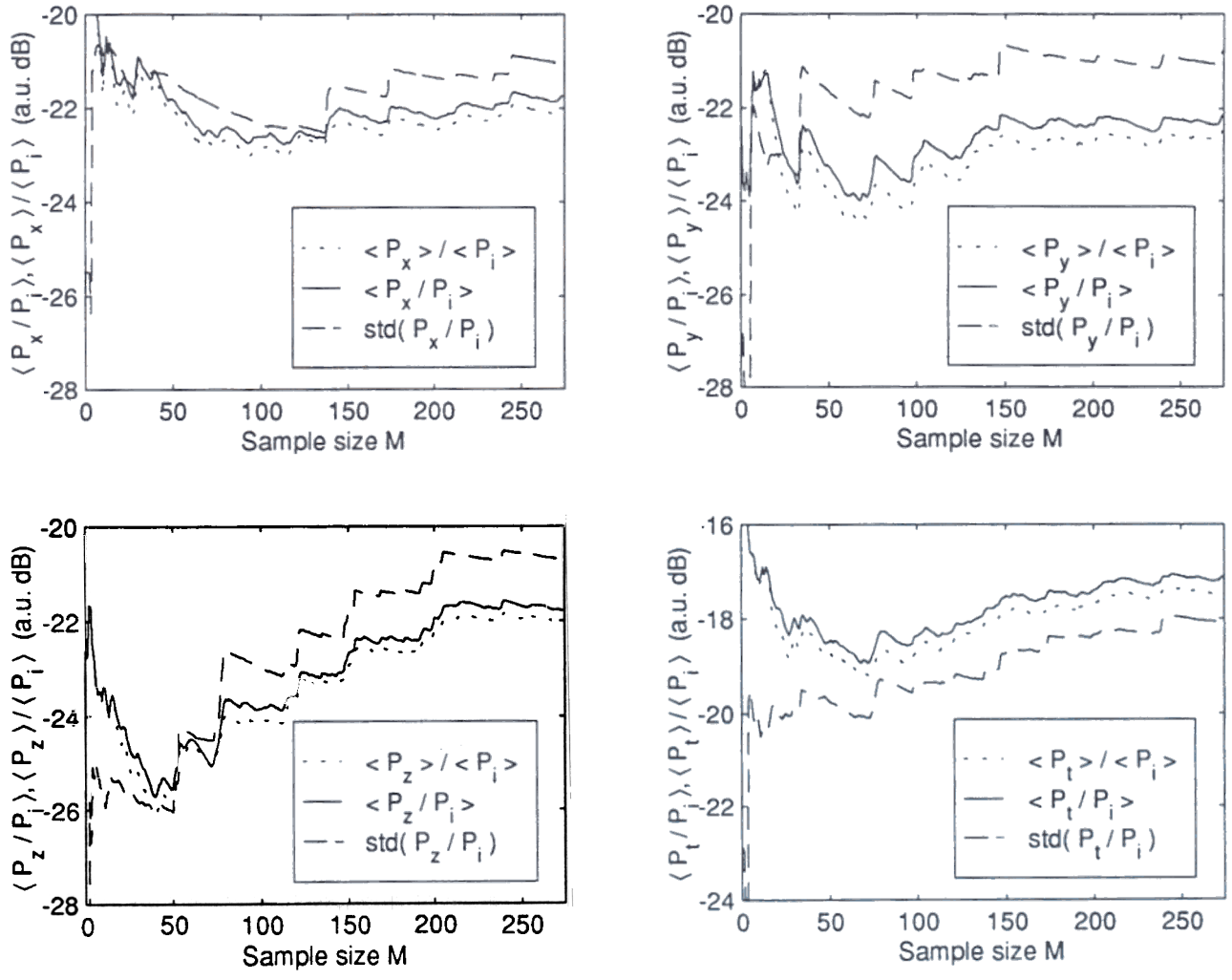


Figure 62: Mean of ratio of power densities vs. ratio of mean of power densities as a function of sample size M @ $f = 2.5$GHz, $r = 91$mm for full data set.

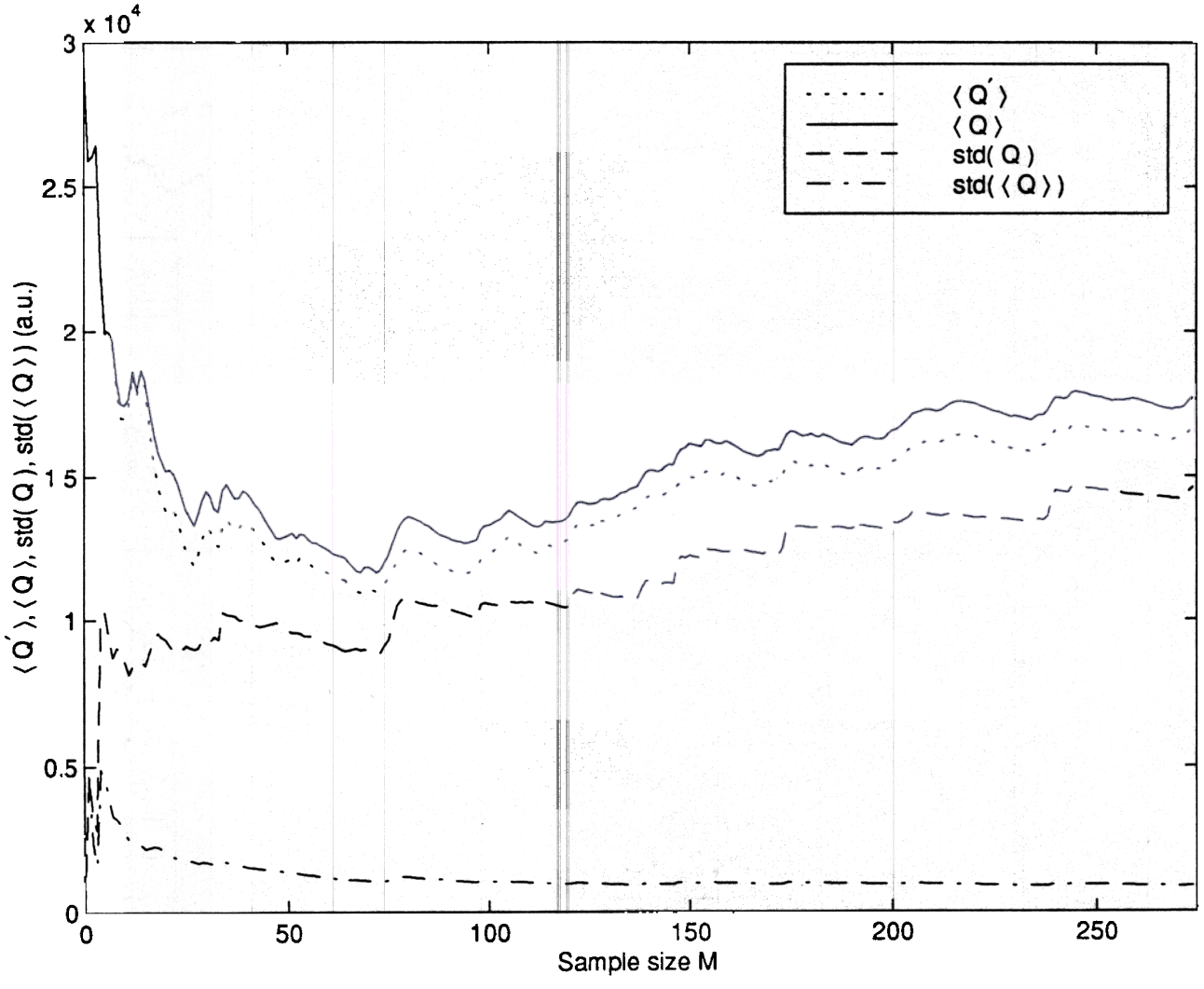
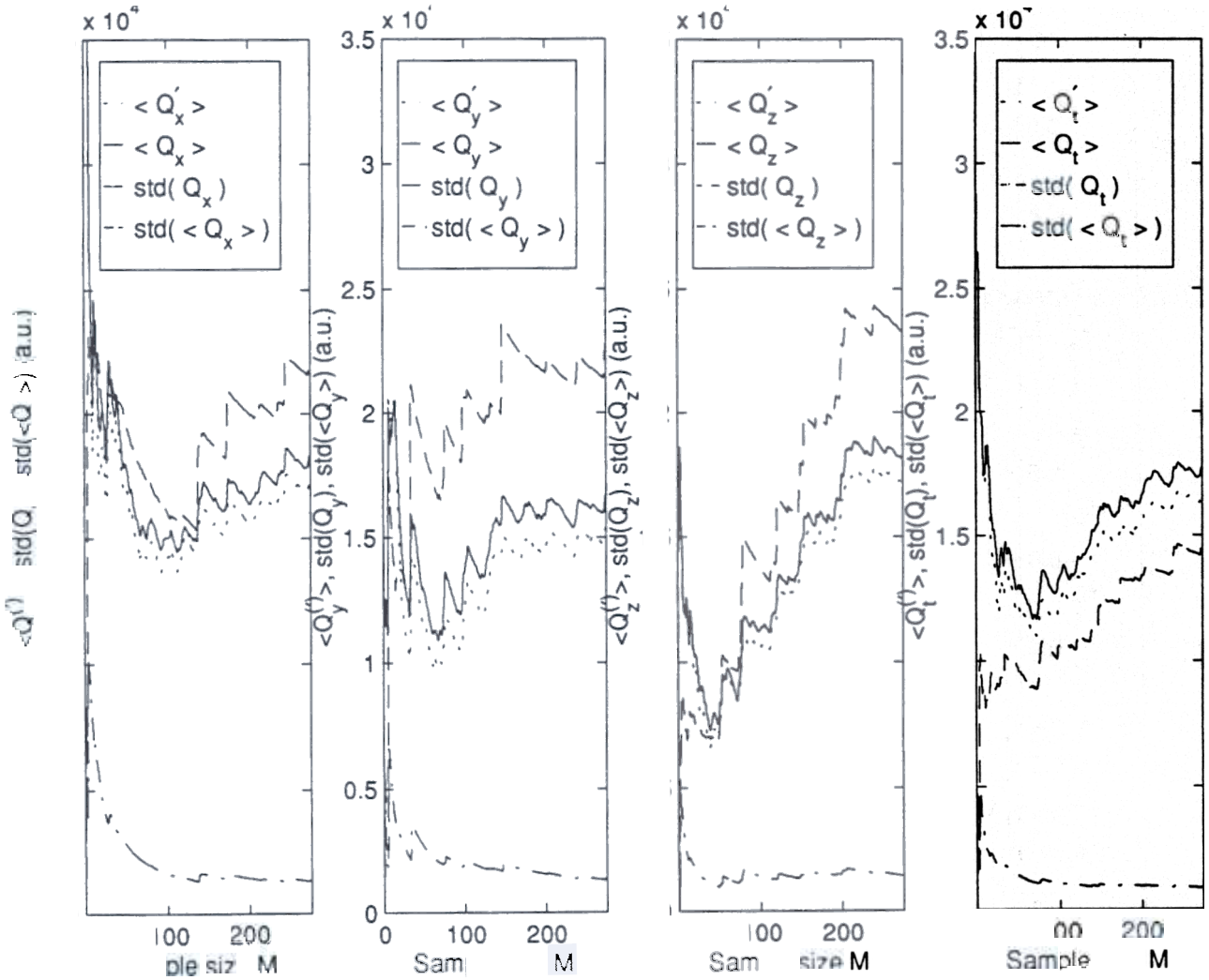


Figure 63: Theoretical composite quality factors computed for mean of ratio of total power densities vs. ratio of mean of total power densities as a function of sample size M @ $f = 2.5$GHz, $r = 91$mm for full data set (assuming free space wave impedance).



64 ore al **ali** al po

of of al po **as** **sa** le ***M*** @

GG **ill** pace ve ped

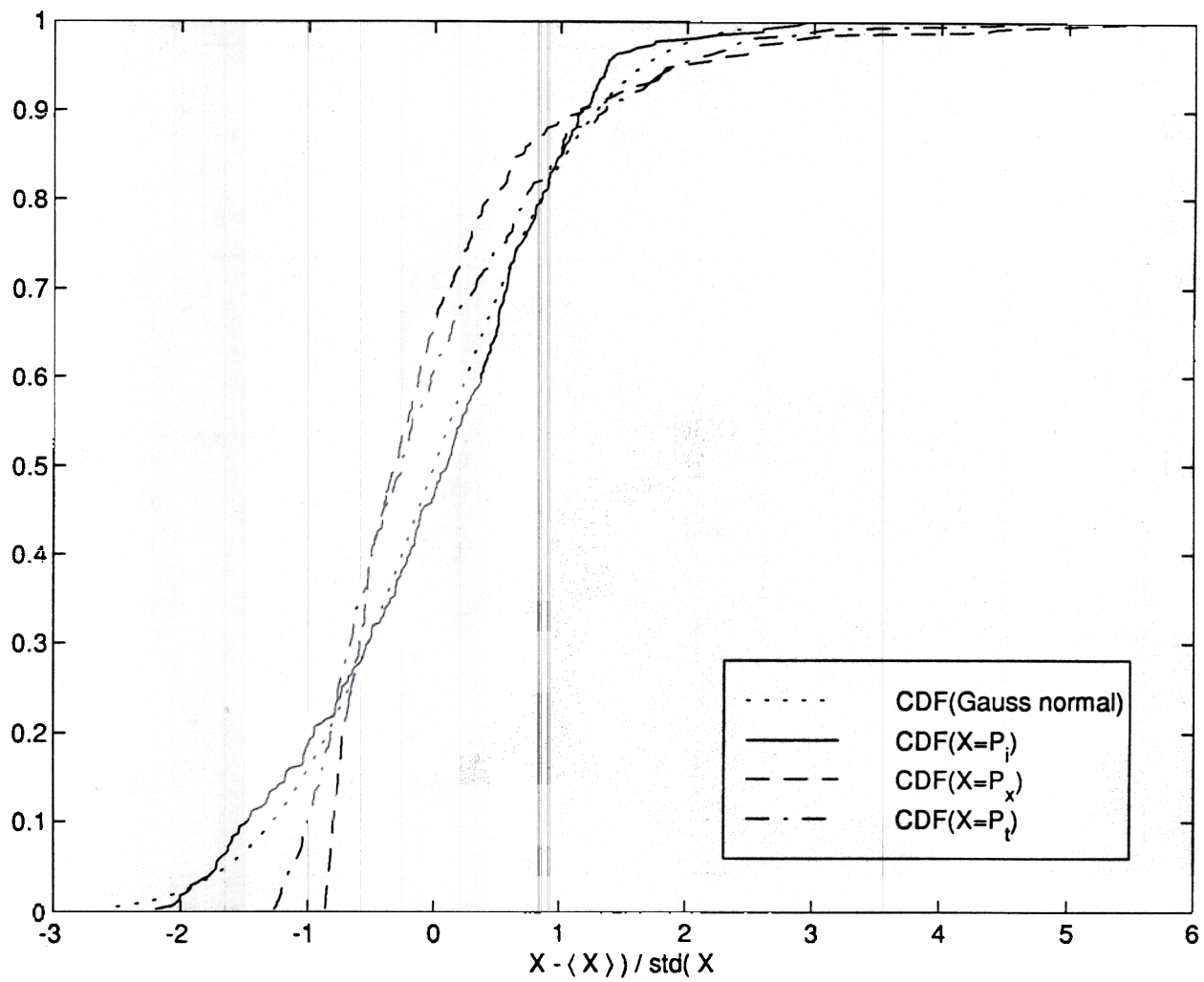


Figure 65: Cumulative distribution functions of measured input power P_i, received rectilinear power P_α and received total power P_t @ $f = 2.5$GHz, $r = 91$mm for full data set.

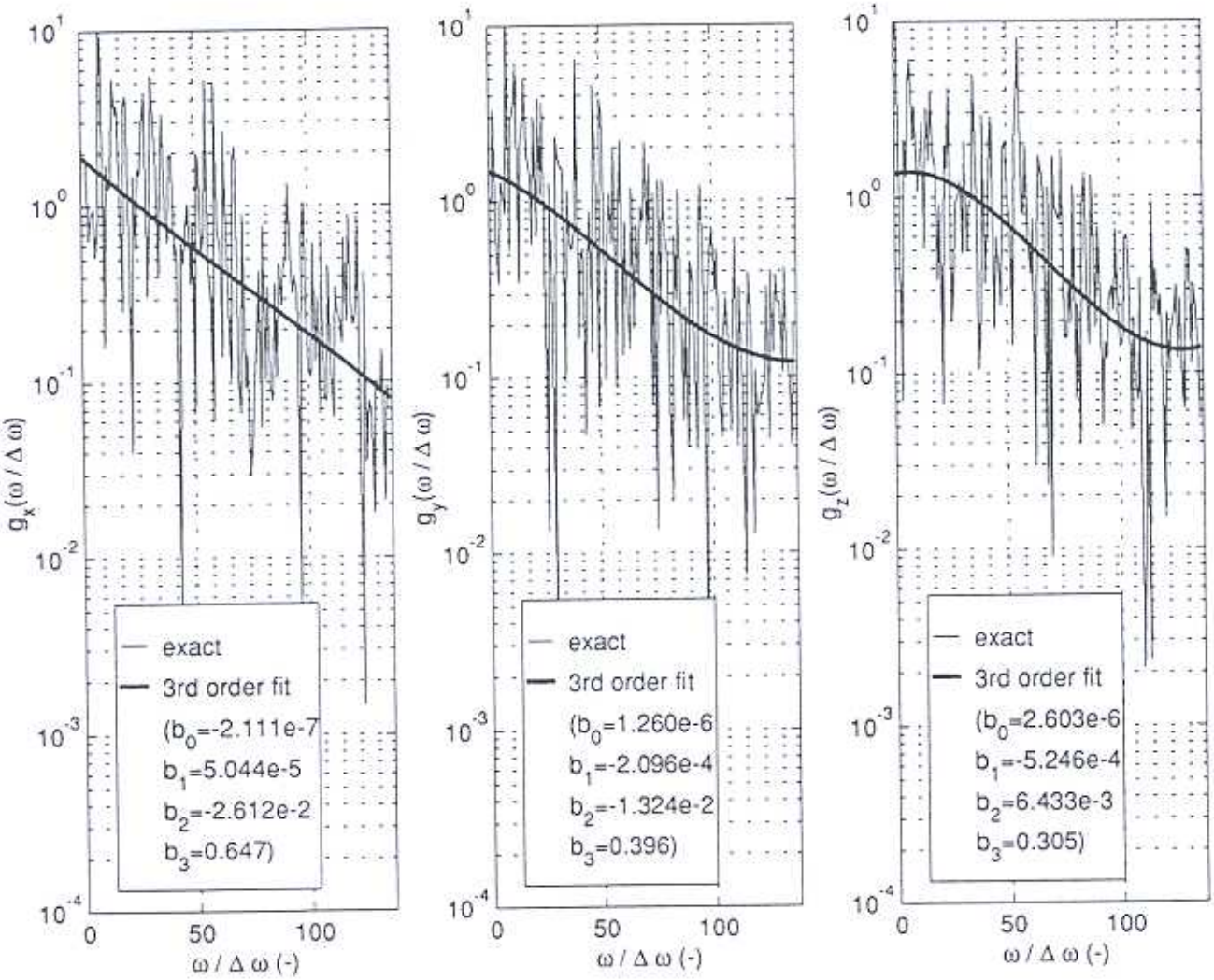


Figure 66: Normalized power autospectral density functions g_o and 3rd order exponential fits as a function of normalized spectral wall position $\omega/\Delta\omega$ @ $f = 2.5$GHz, $r = 91$mm for full data set.

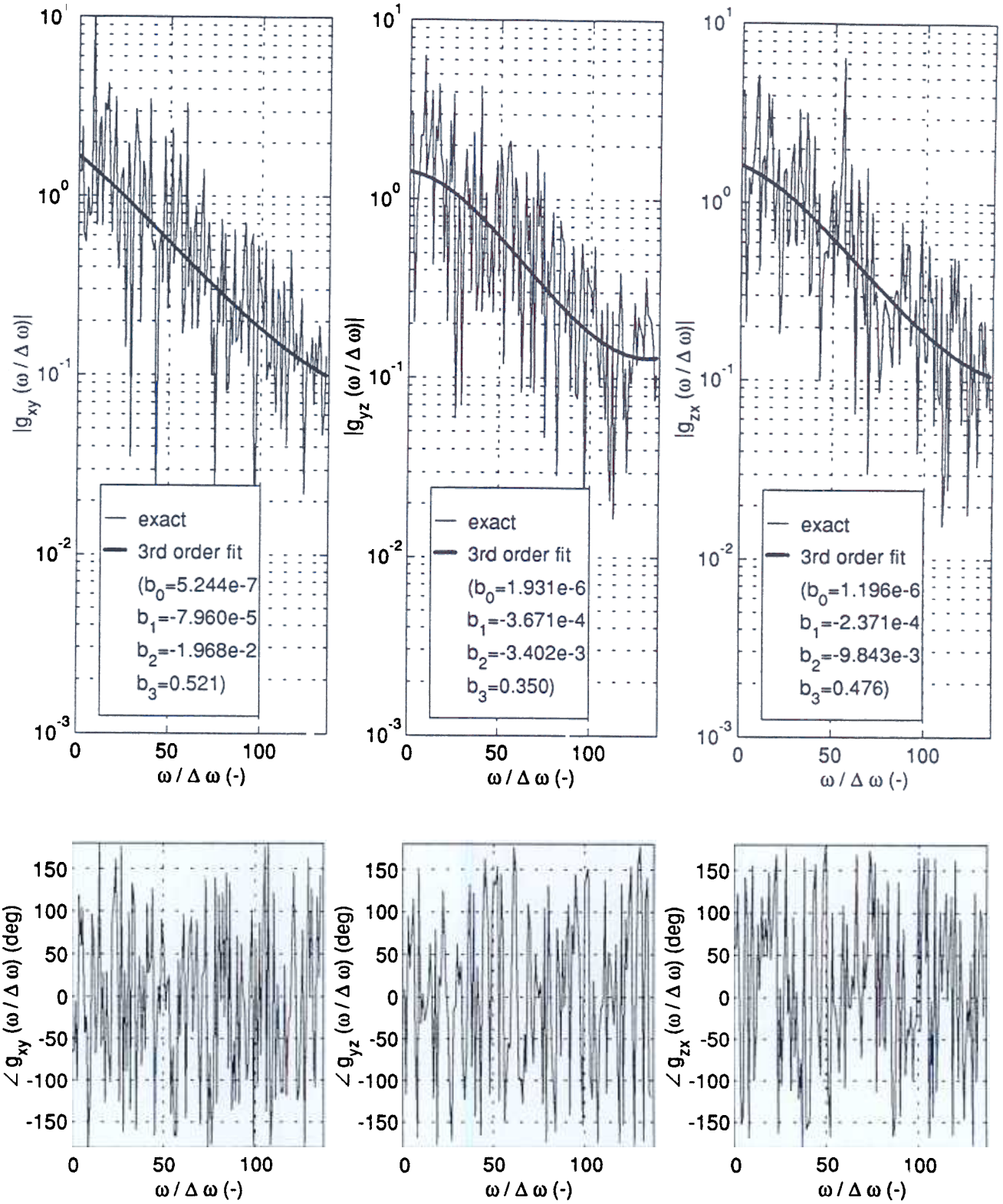


Figure 67: Normalized power crossspectral density functions $g_{\alpha\beta}$ and 3rd order exponential fits as a function of normalized spectral wall position $\omega/\Delta\omega$ @ $f = 2.5$GHz, $r = 91$mm for full data set.

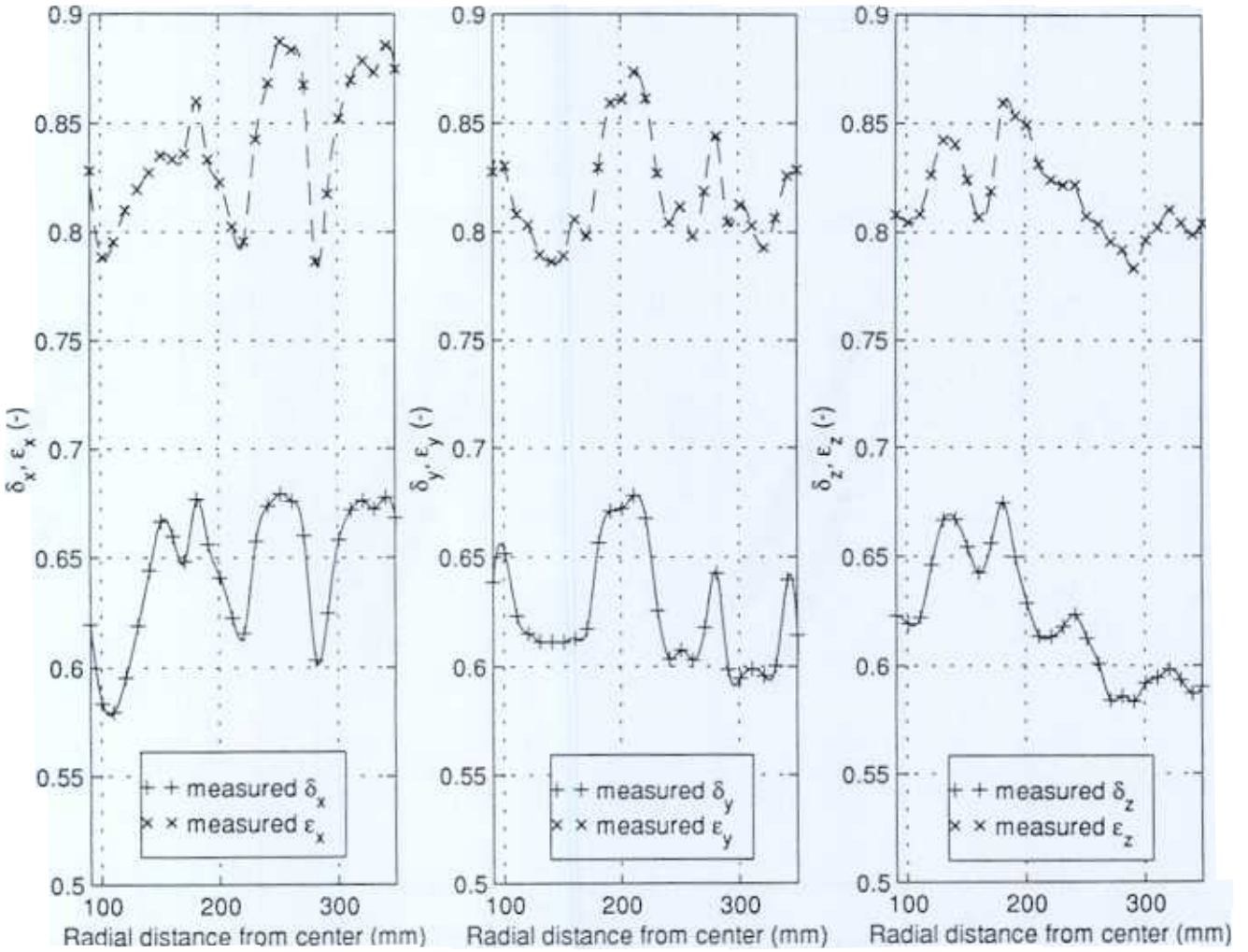


Figure 68: Normalized spectral bandwidths δ_α and ϵ_α as a function of radial distance @ f = 2.5GHz.

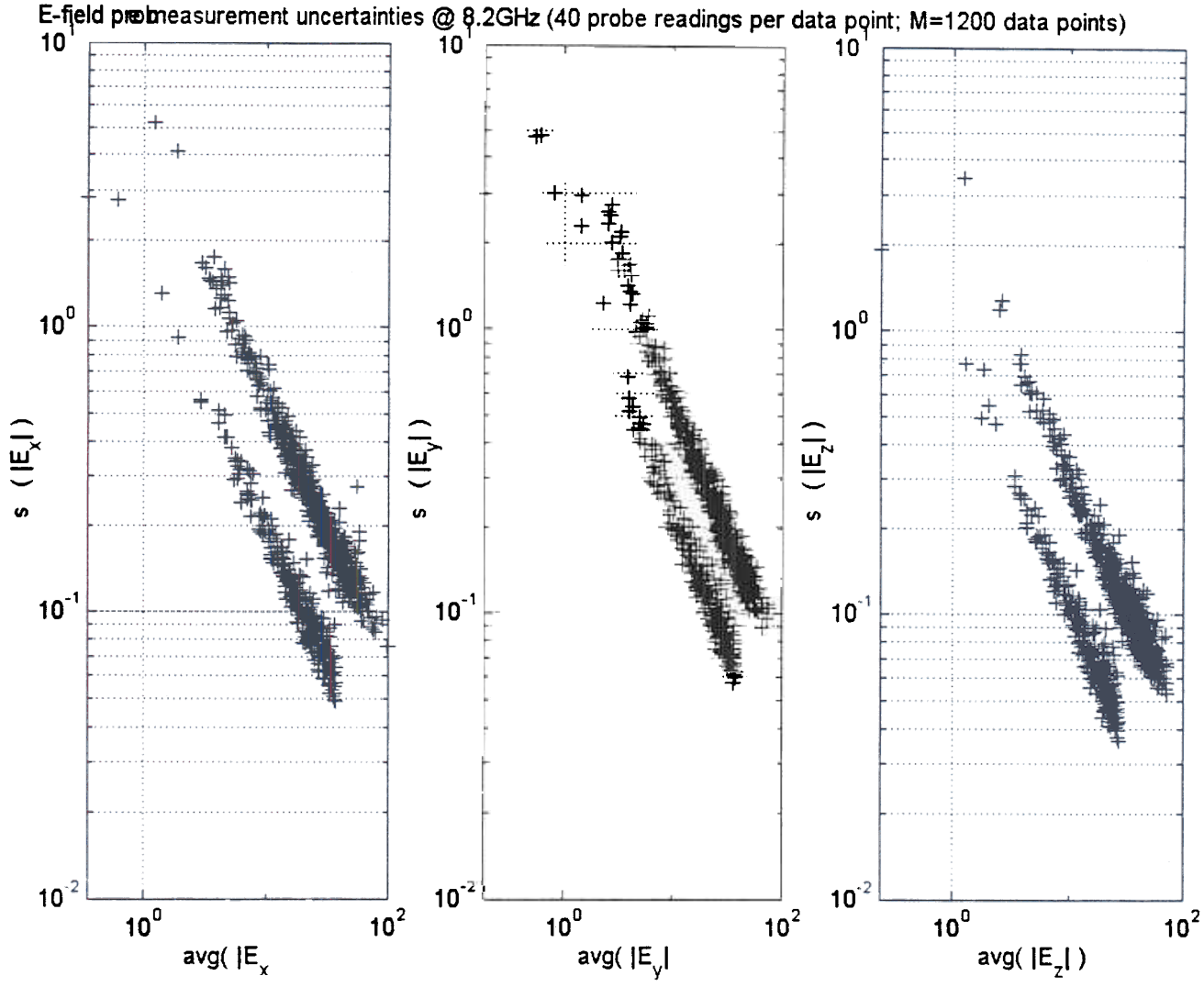


Figure 69: Spread as a function of average field strength for S&P probe measurements @ f 8.2GHz, r = 91mm for 40 readings per sample and sample size M = 1200.

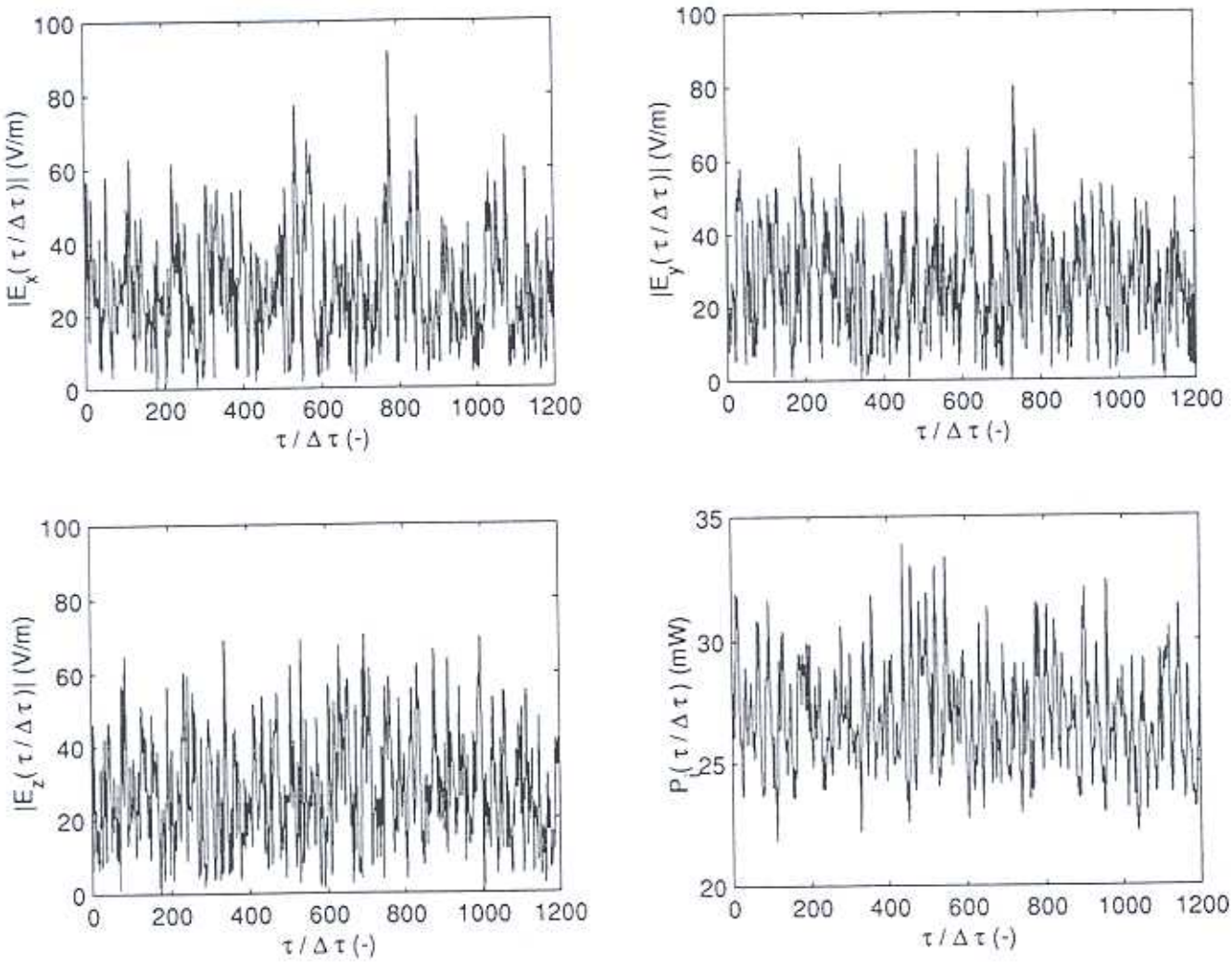


Figure 70: Sweep data @ $f = 8.2$GHz, $r = 91$mm.

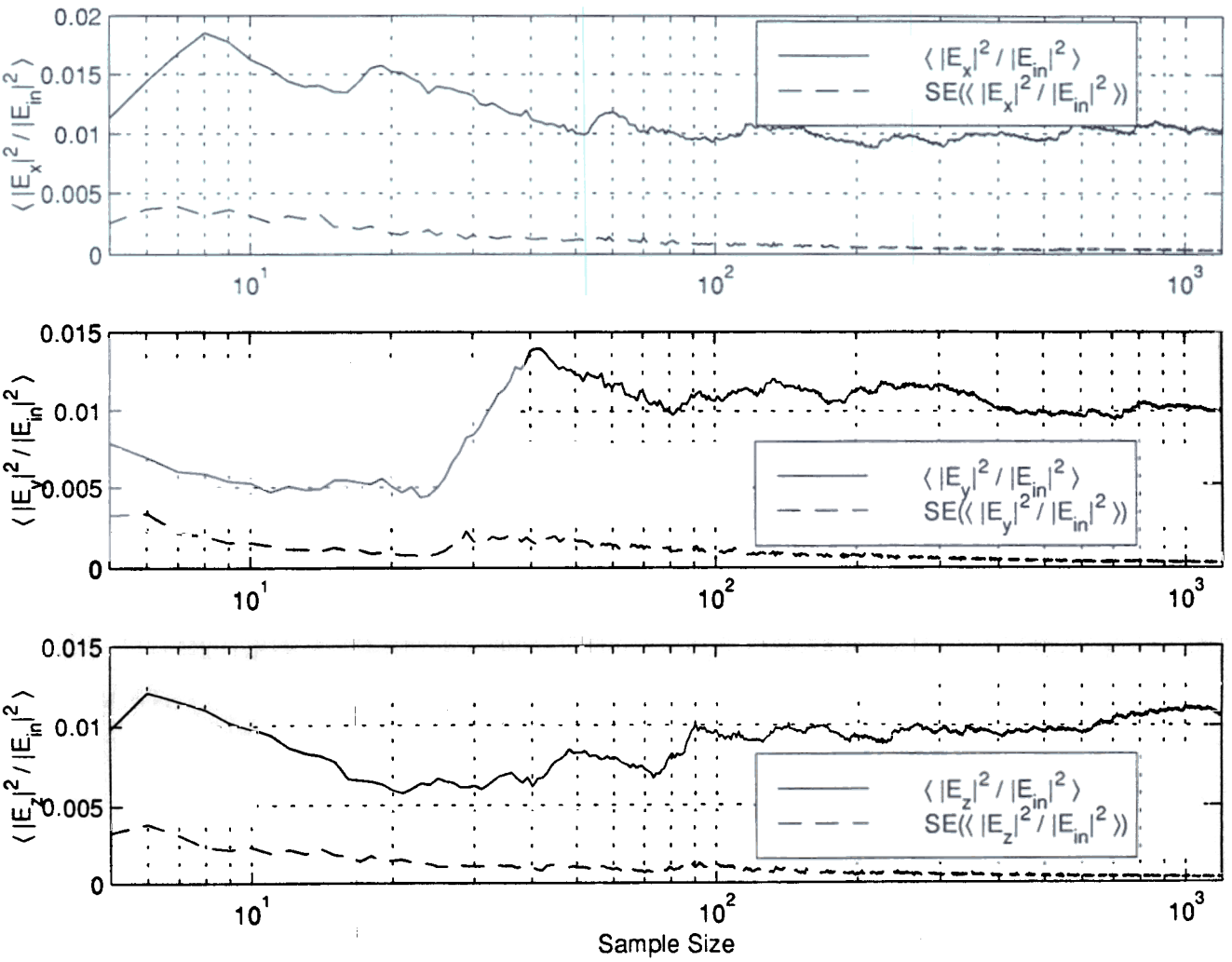


Figure 71: Average normalized squared field strength as a function of sample size M @ f = 8.2GHz, r = 91mm for full data set.

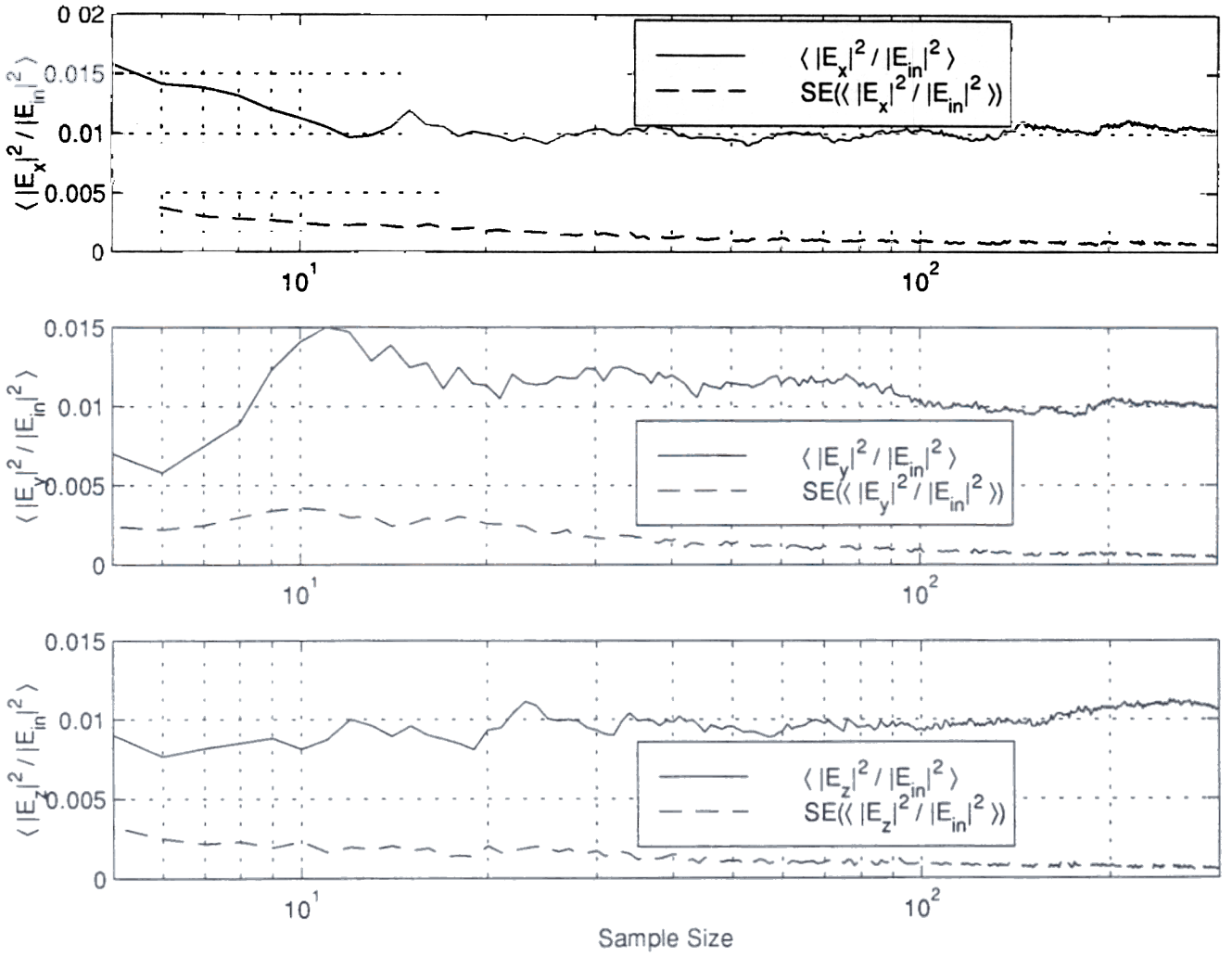


Figure 72: Average normalized squared field strength as a function of sample size N @ f = 8.2GHz, r = 91mm for decimated data set ($m_\alpha = 4$).

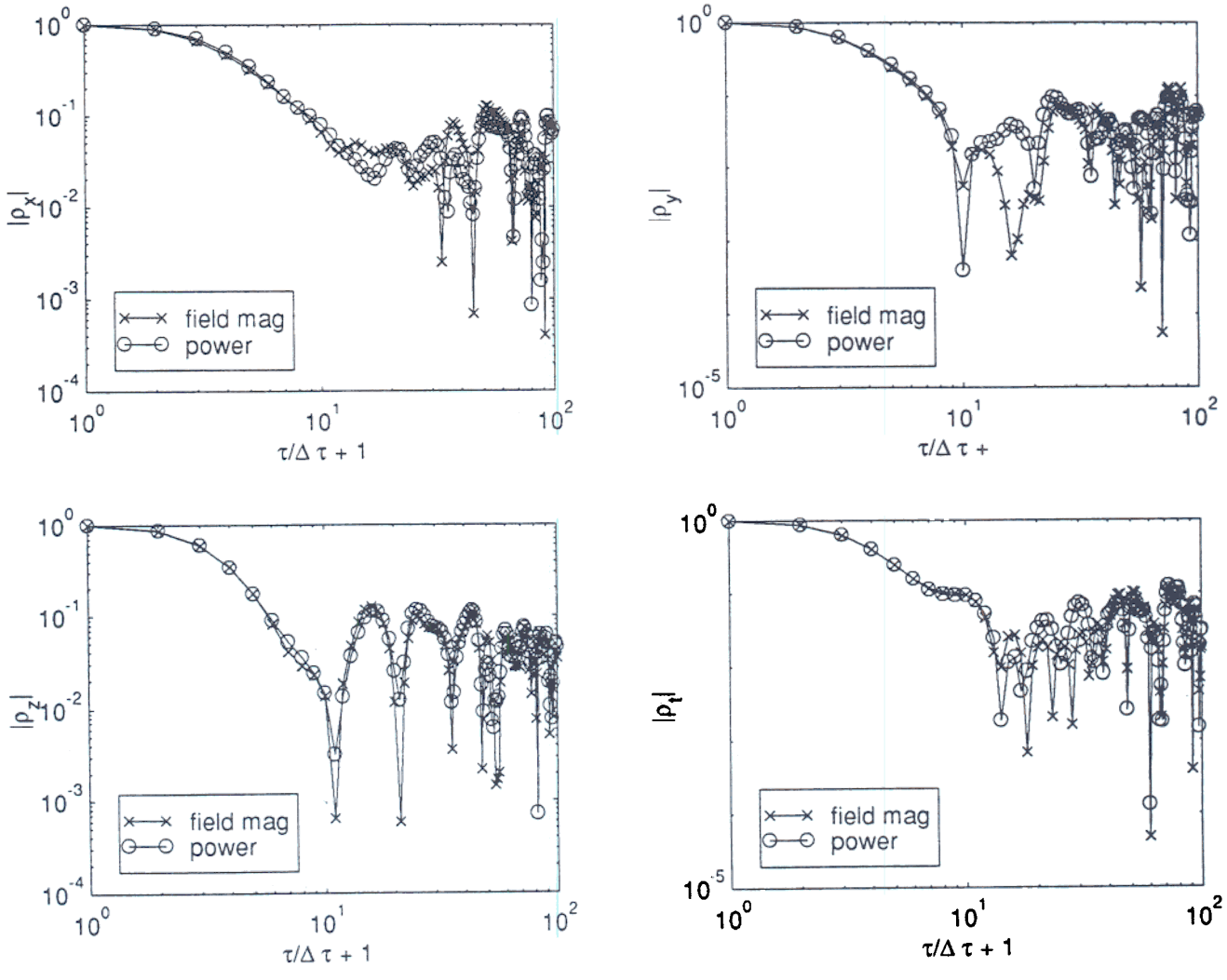


Figure 73: Autocorrelation functions $|\rho_\alpha|$ for power and field magnitude for $|E_\alpha|$ ($\alpha = x, y, z, t$) as a function of wall position $\tau/\Delta\tau$ @ $f = 8.2$GHz, $r = 91$mm.

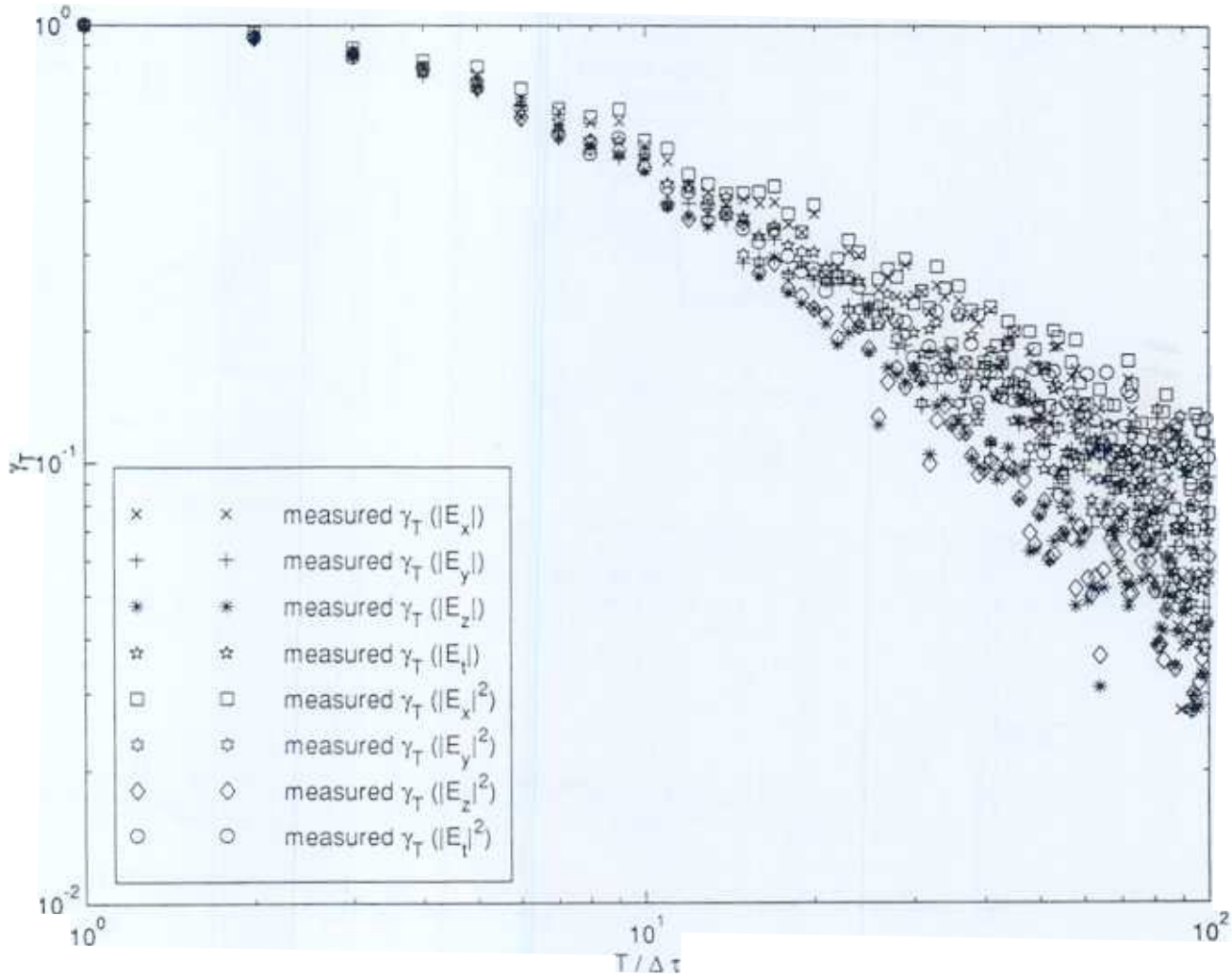


Figure 74: Field and power variance functions for $|E_\alpha|$ ($\alpha = x, y, z, t$) as a function of stirrer averaging length $\mathcal{T}/\Delta\tau$ @ $f = 8.2$GHz, $r = 91$mm.

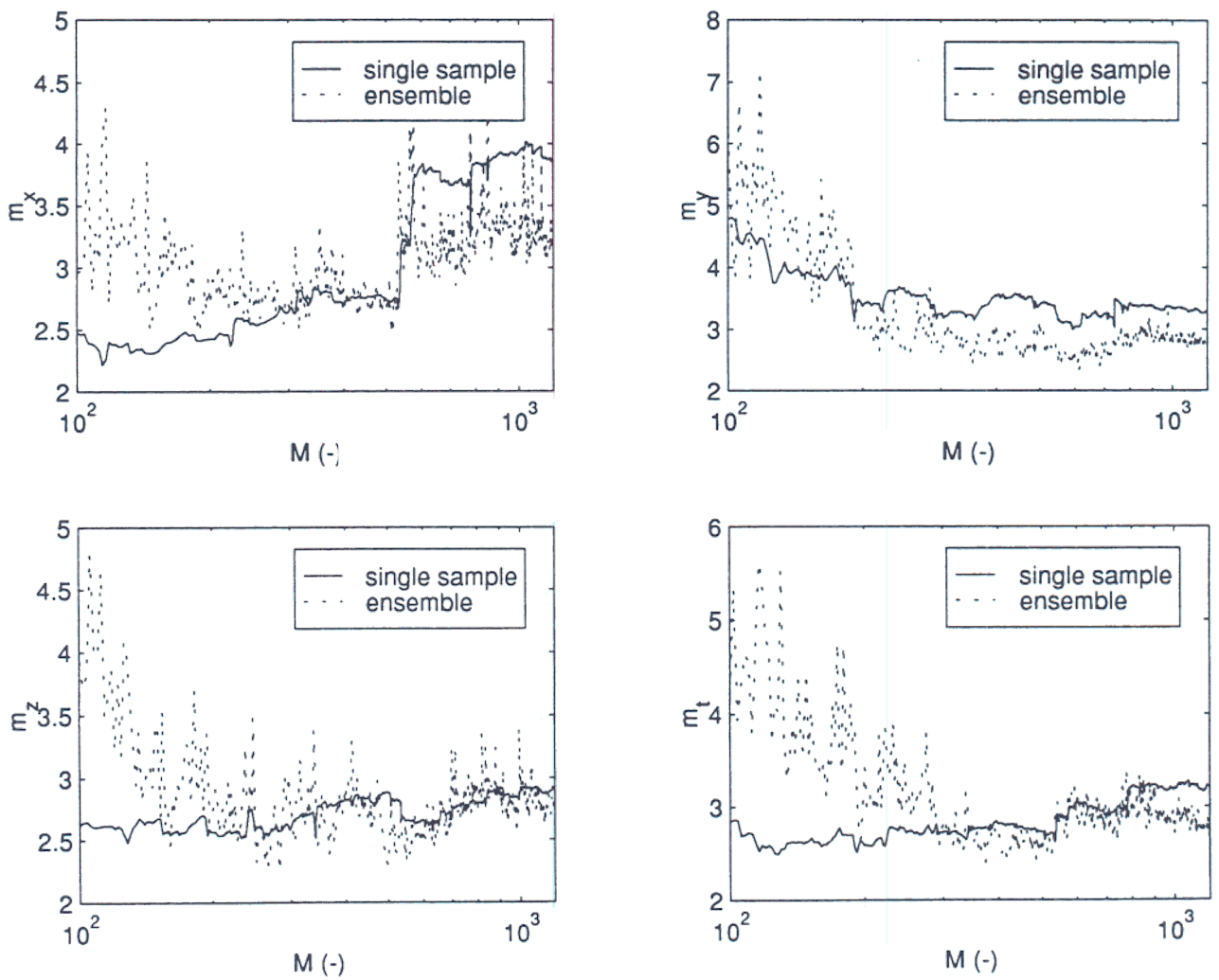


Figure 75: Single-sample and ensemble decimation factors m_α for $|E_\alpha|^2$ ($\alpha = x, y, z, t$) as a function of sample size M @ $f = 8.2$GHz, $r = 91$mm.

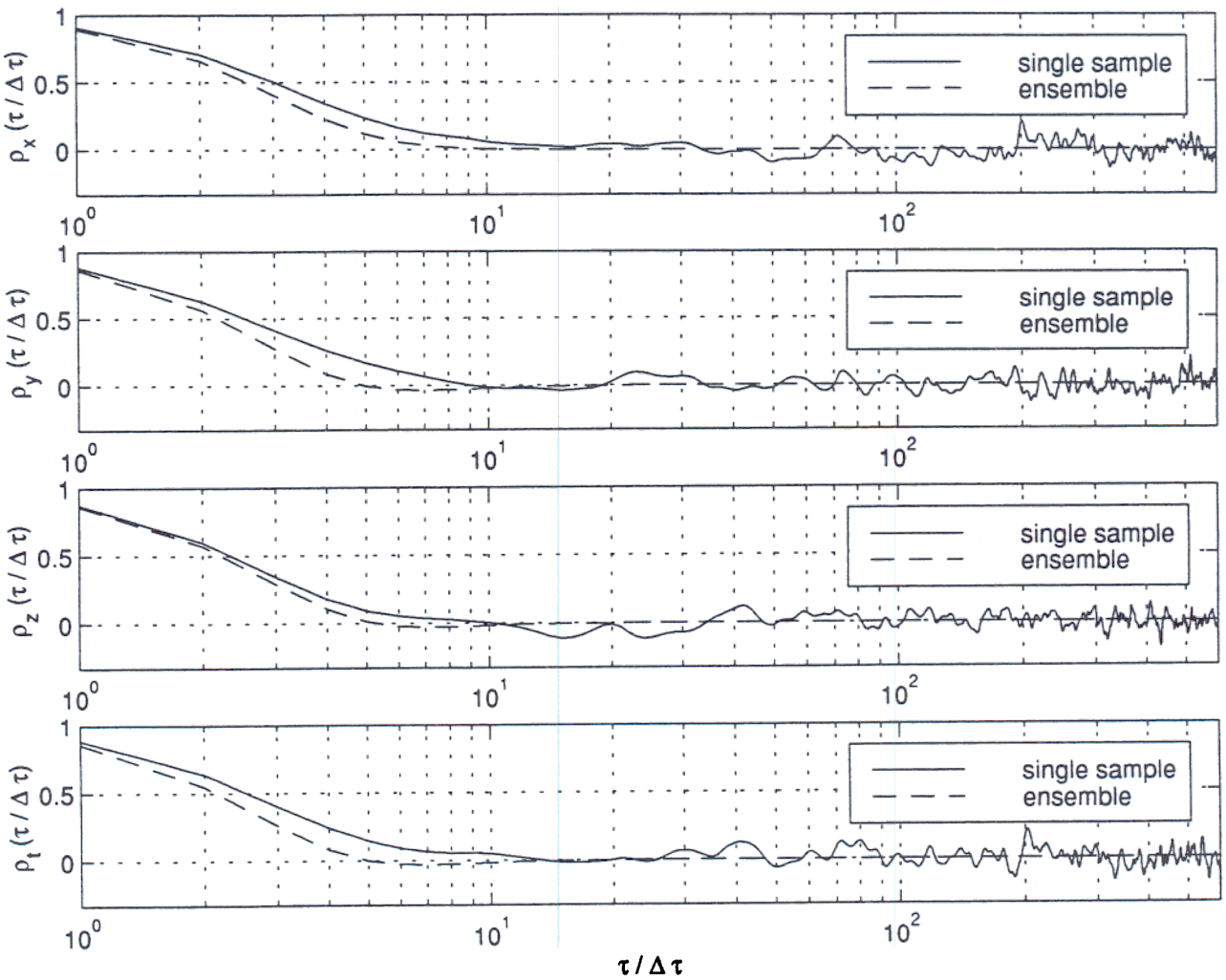


Figure 76: Single-sample and ensemble power autocorrelation functions ρ_α for $|E_\alpha|^2(\alpha = x, y, z, t)$ as a function of wall position $\tau/\Delta\tau$ @ $f = 8.2$GHz, $r = 91$mm.

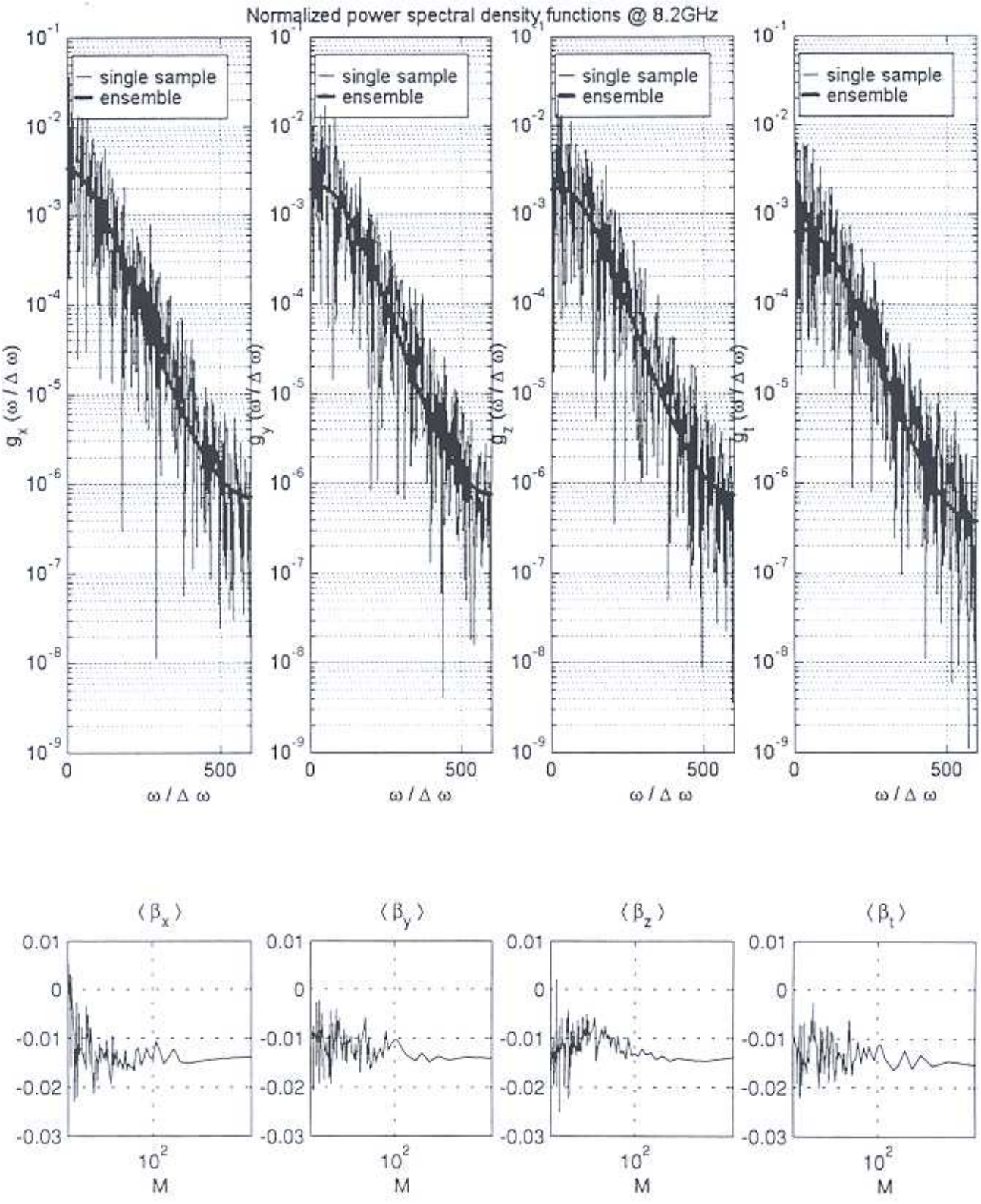


Figure 77: Single-sample and ensemble power autospectral density functions g_α for $|E_\alpha|$ ($\alpha = x, y, z, t$) as a function of spectral wall position $\omega/\Delta\omega$ @ $f = 8.2$GHz, $r = 91$mm, with Bartlett estimates of spectral parameters β_α for smoothed density function (1st-order exponential model).

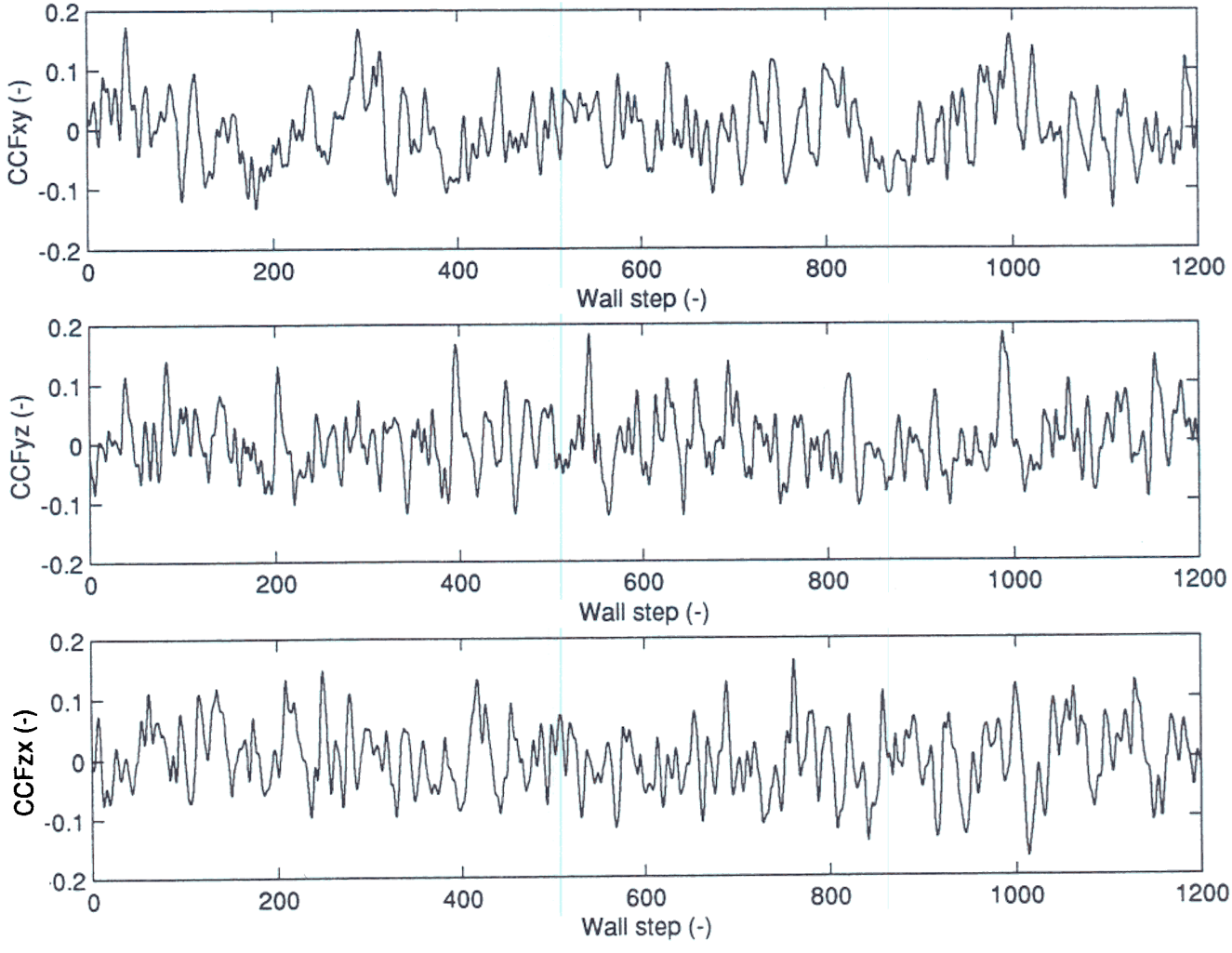


Figure 78: Power crosscorrelation functions $\rho_{\alpha\beta}$ for $|E_\alpha|,\ E_\beta|$ $(\alpha, \beta = x, y, z)$ as a function of wall position $\tau/\Delta\tau$ @ $f = 8.2$GHz, $r = 91$mm for full data set.

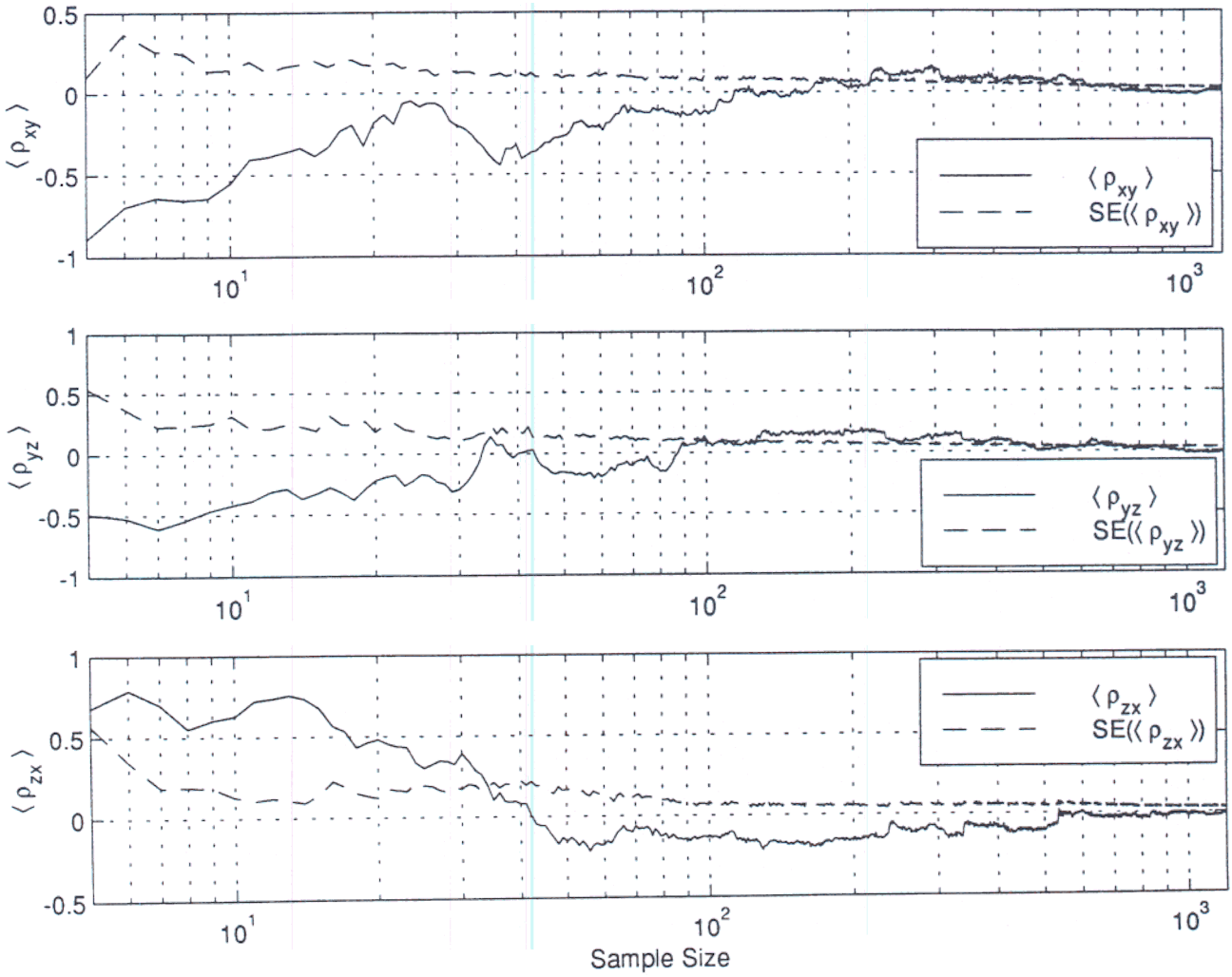


Figure 79: Power crosscorrelation coefficients $\varrho_{\alpha\beta}$ for $|E_\alpha|$, $|E_\beta|$ $(\alpha, \beta = x, y, z)$ as a function of sample size M @ $f = 8.2$GHz, $r = 91$mm for full data set.

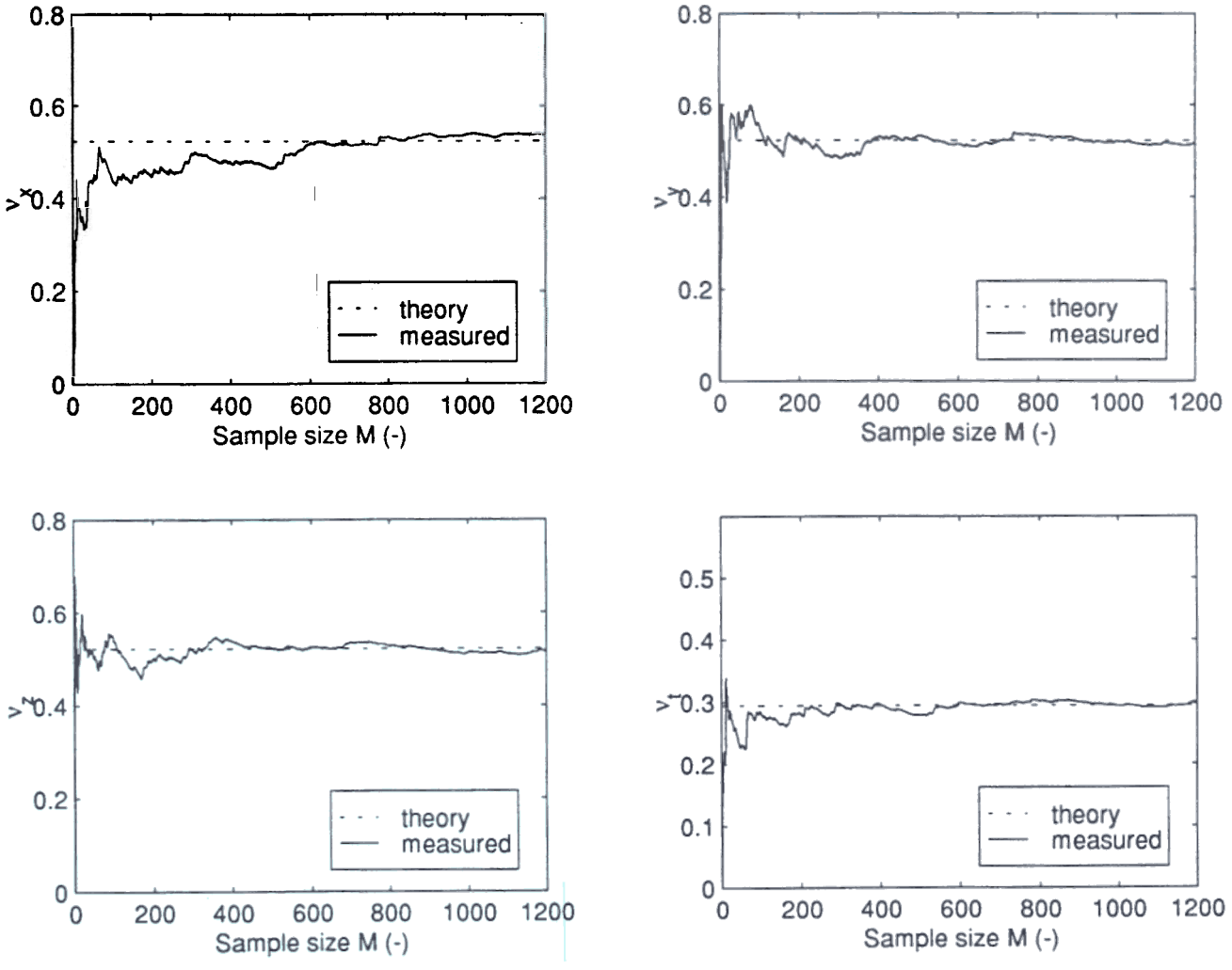


Figure 80: Coefficients of variation ν_α for $|E_\alpha|$ $(\alpha = x, y, z, t)$ as a function of sample size M @ $f = 8.2\text{GHz}$, $r = 91\text{mm}$.

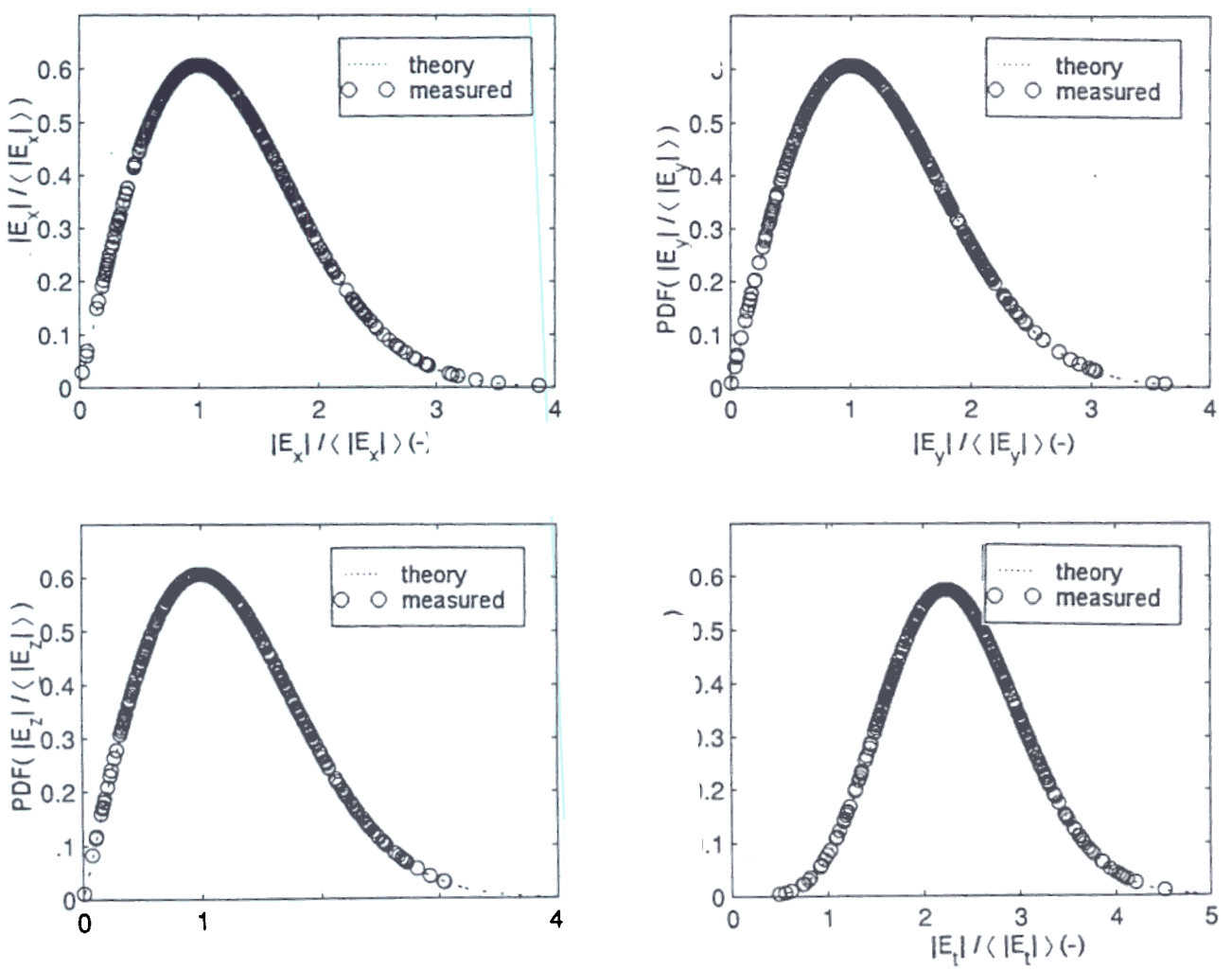


Figure 81: Probability density functions f_α of $|E_\alpha|/\langle|E_\alpha|\rangle$ ($\alpha = x, y, z, t$) @ $f = 8.2$GHz, $r = 91$mm for decimated data set ($m_\alpha = 3$). (See text for correct interpretation of Figure.)

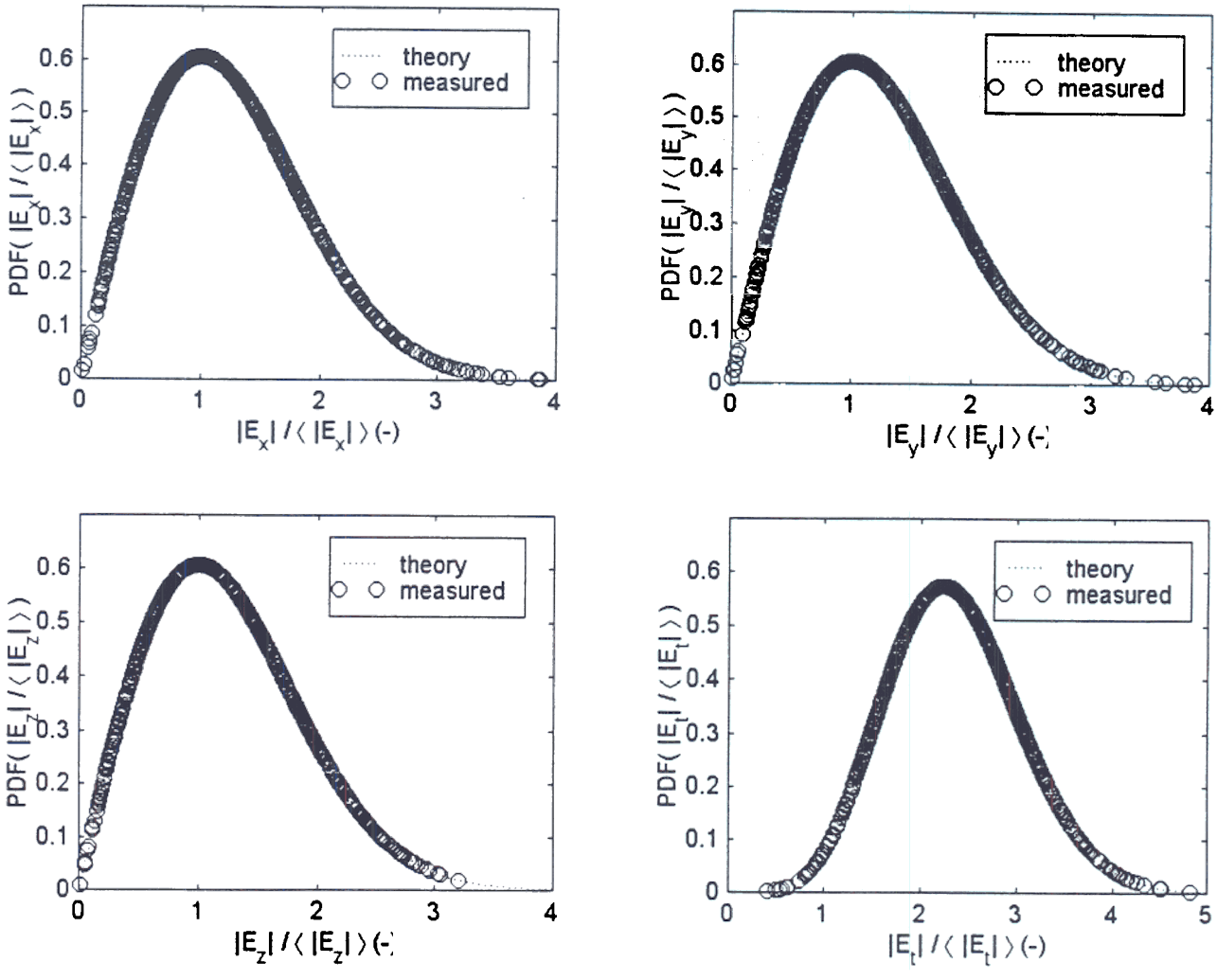


Figure 82: Probability density functions f_α of $|E_\alpha|/\langle|E_\alpha|\rangle$ ($\alpha = x, y, z, t$) @ $f = 8.2$GHz, $r =$ 91mm for full data set ($m_\alpha = 1$) (for demonstration only). (See text for correct interpretation of Figure.)

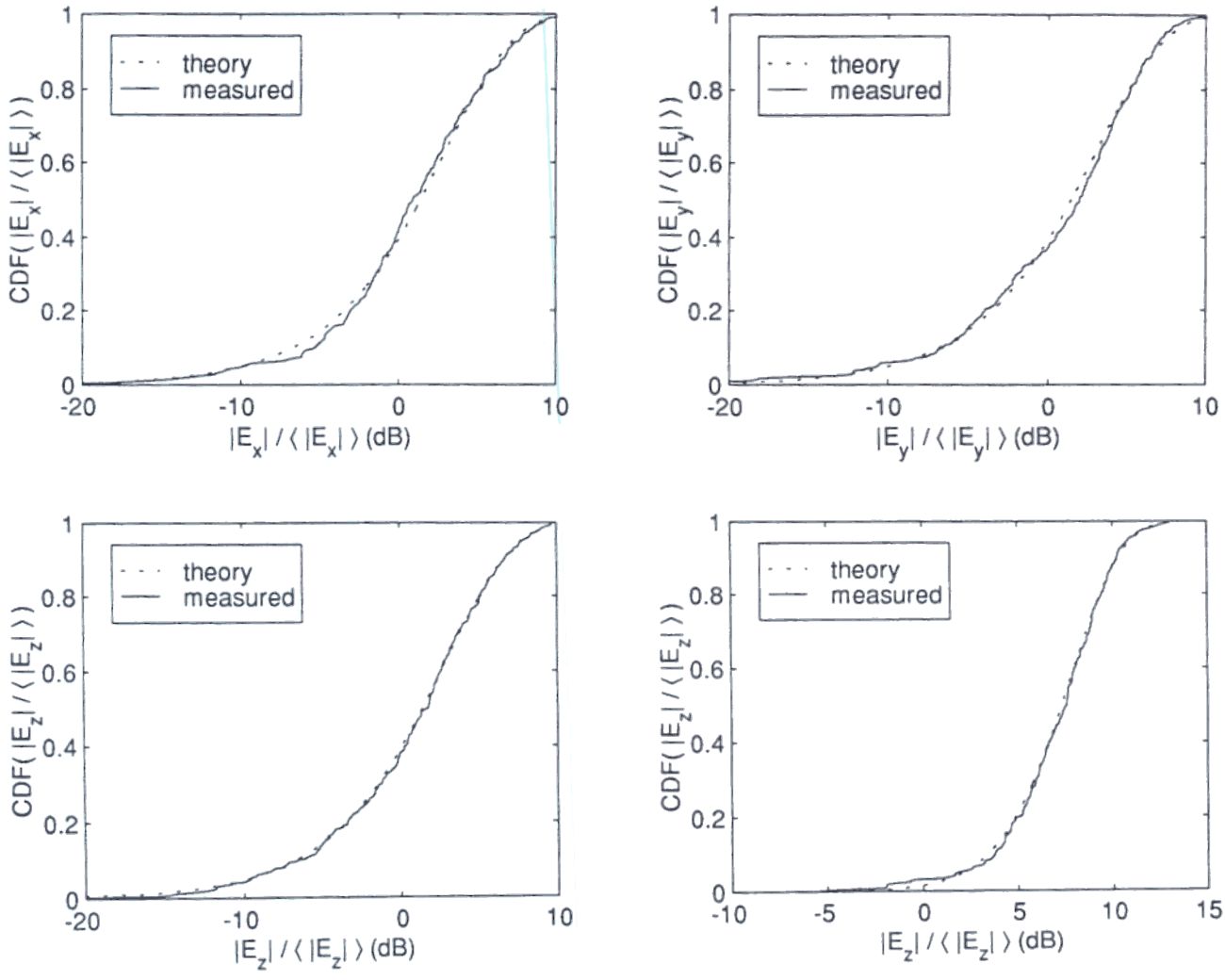


Figure 83: Cumulative distribution functions F_α of $|E_\alpha|/\langle|E_\alpha|\rangle$ ($\alpha = x, y, z, t$) @ $f = 8.2$GHz $r = 91$mm for decimated data set ($m_\sim = 3$).

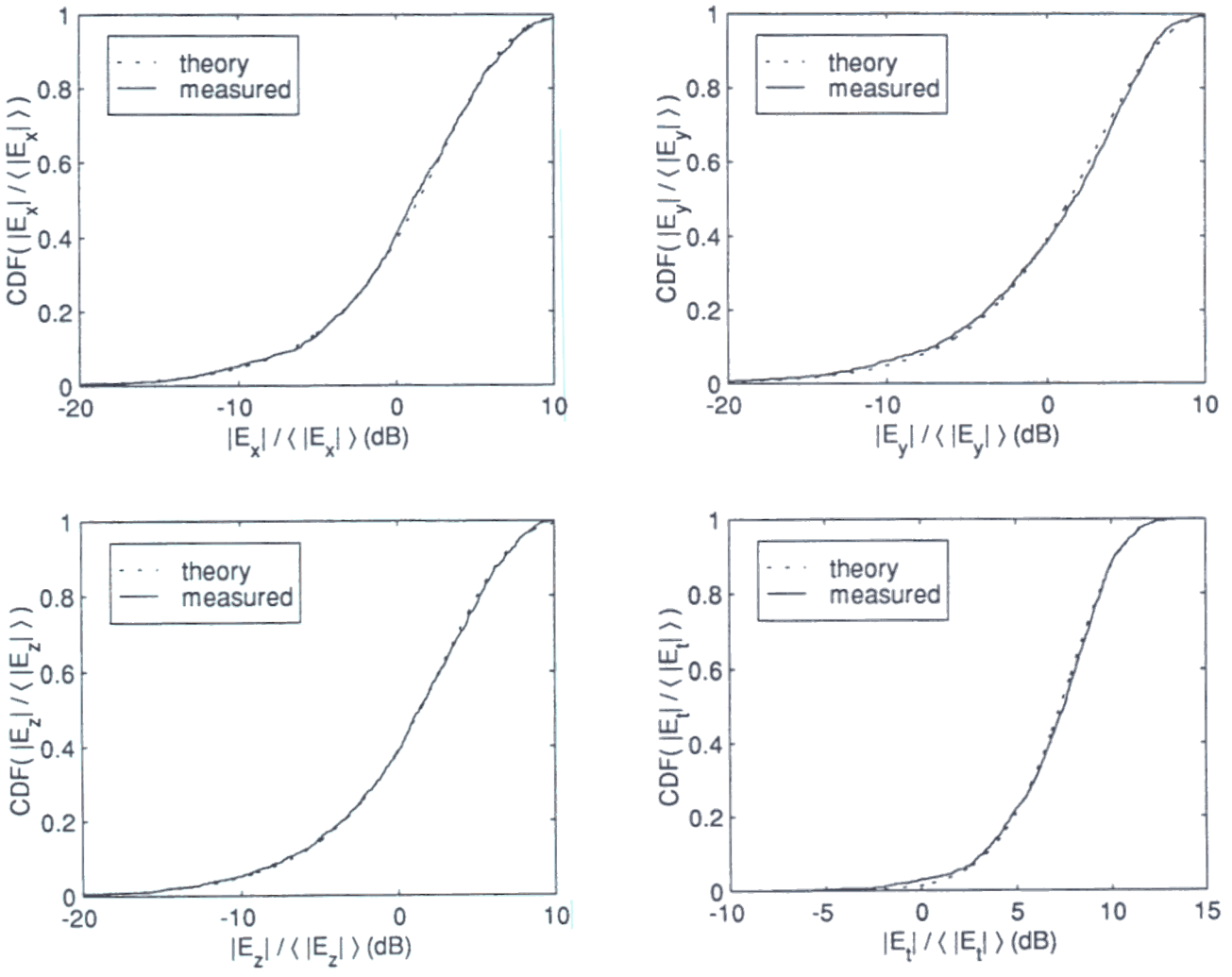


Figure 84: Cumulative distribution functions F_α of $|E_\alpha|/\langle|E_\alpha|\rangle$ ($\alpha = x, y, z, t$) @ $f = 8.2$GHz $r = 91$mm for full data set ($m_\alpha = 1$) (for demonstration only).

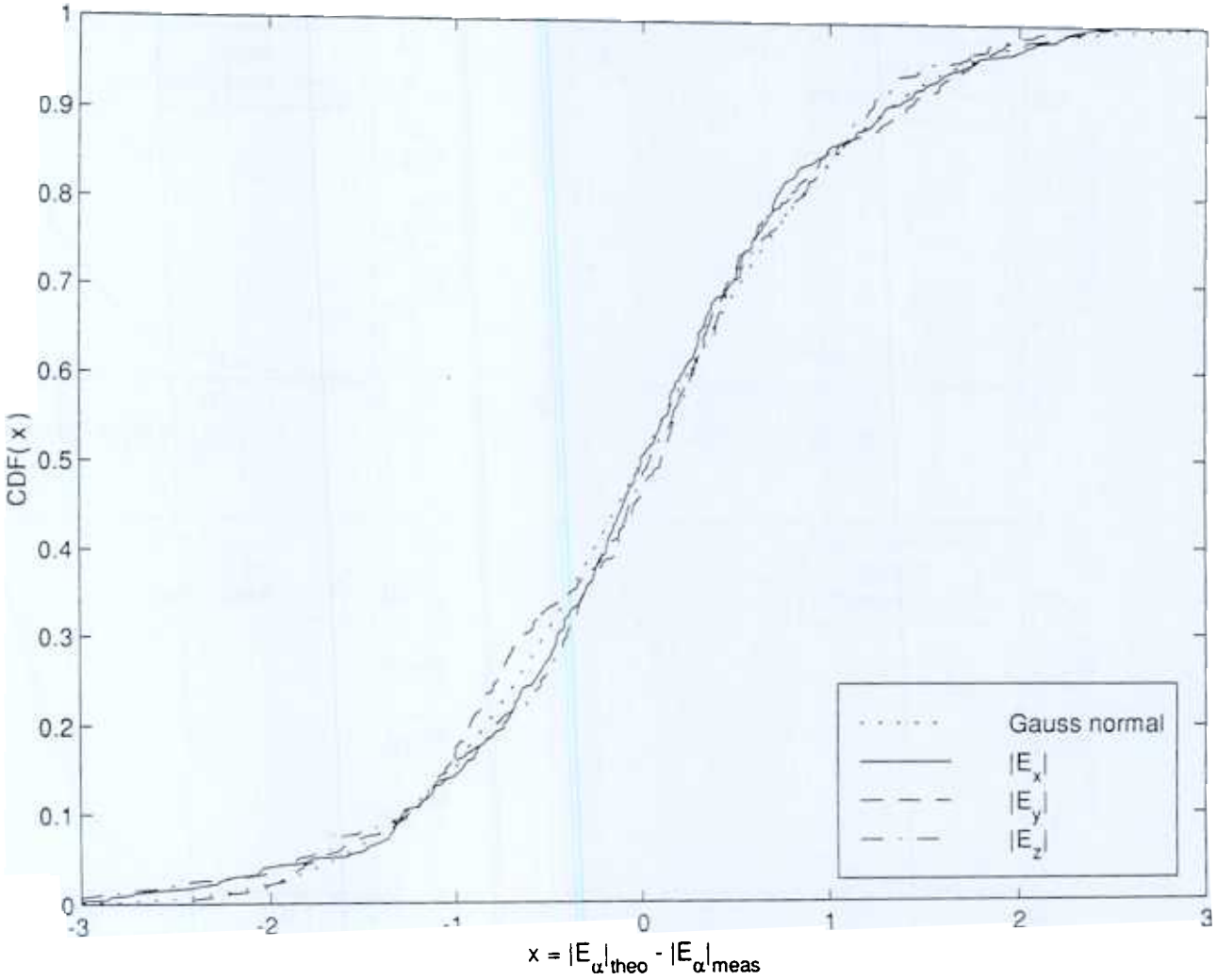


Figure 85: Cumulative distribution functions of standardized deviations $|E_\alpha|_{theo} - |E_\alpha|_{meas}$ ($\alpha = x, y, z$) @ $f = 8.2$GHz, $r = 91$mm for decimated data set ($m_\alpha = 3$).

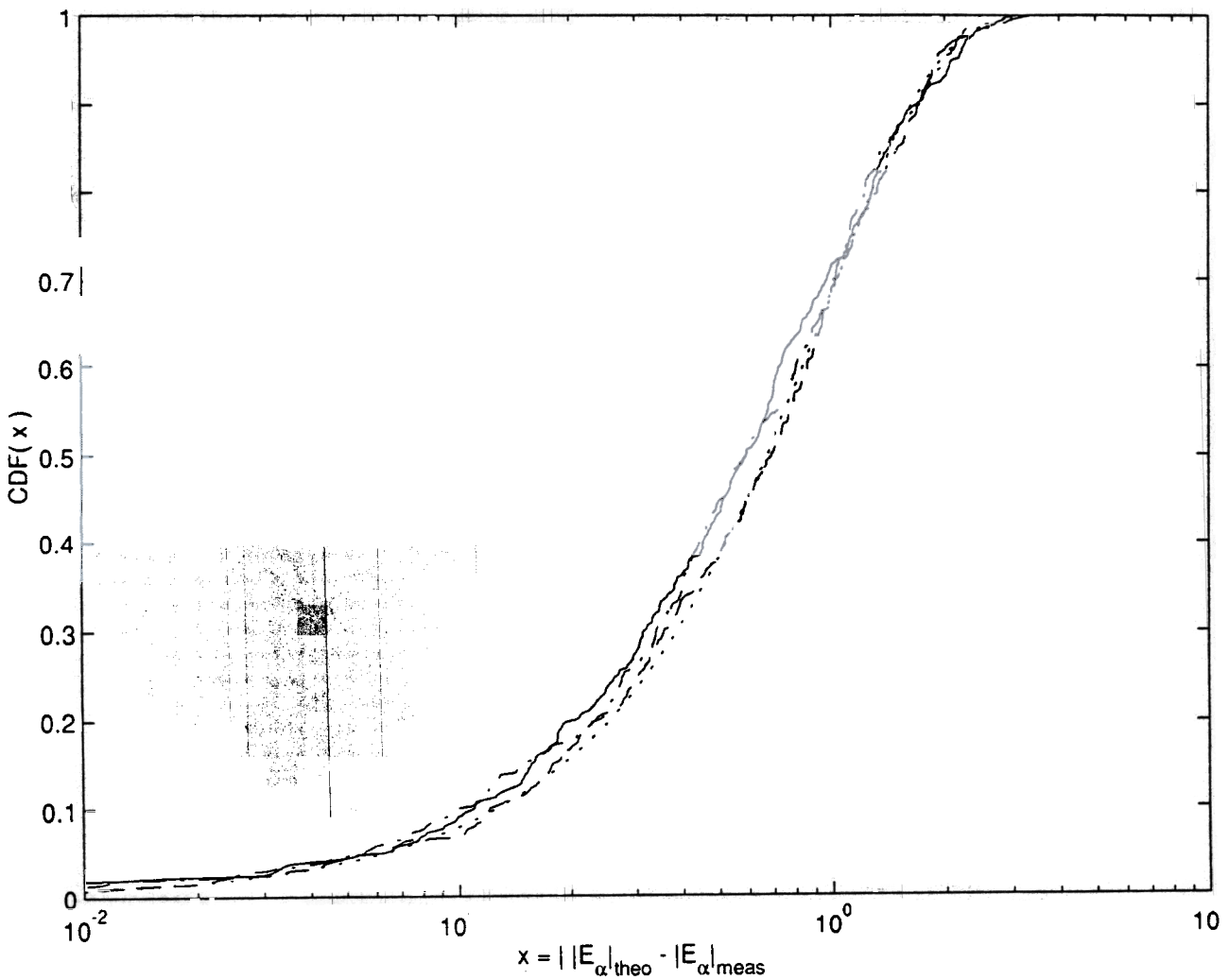


Figure 86: Cumulative distribution functions of standardized absolute deviations $||E_\alpha|_{theo} - |E_\alpha|_{meas}|$ ($\alpha = x, y, z$) @ $f = 8.2$GHz, $r = 91$mm for decimated data set ($m_\alpha = 3$).

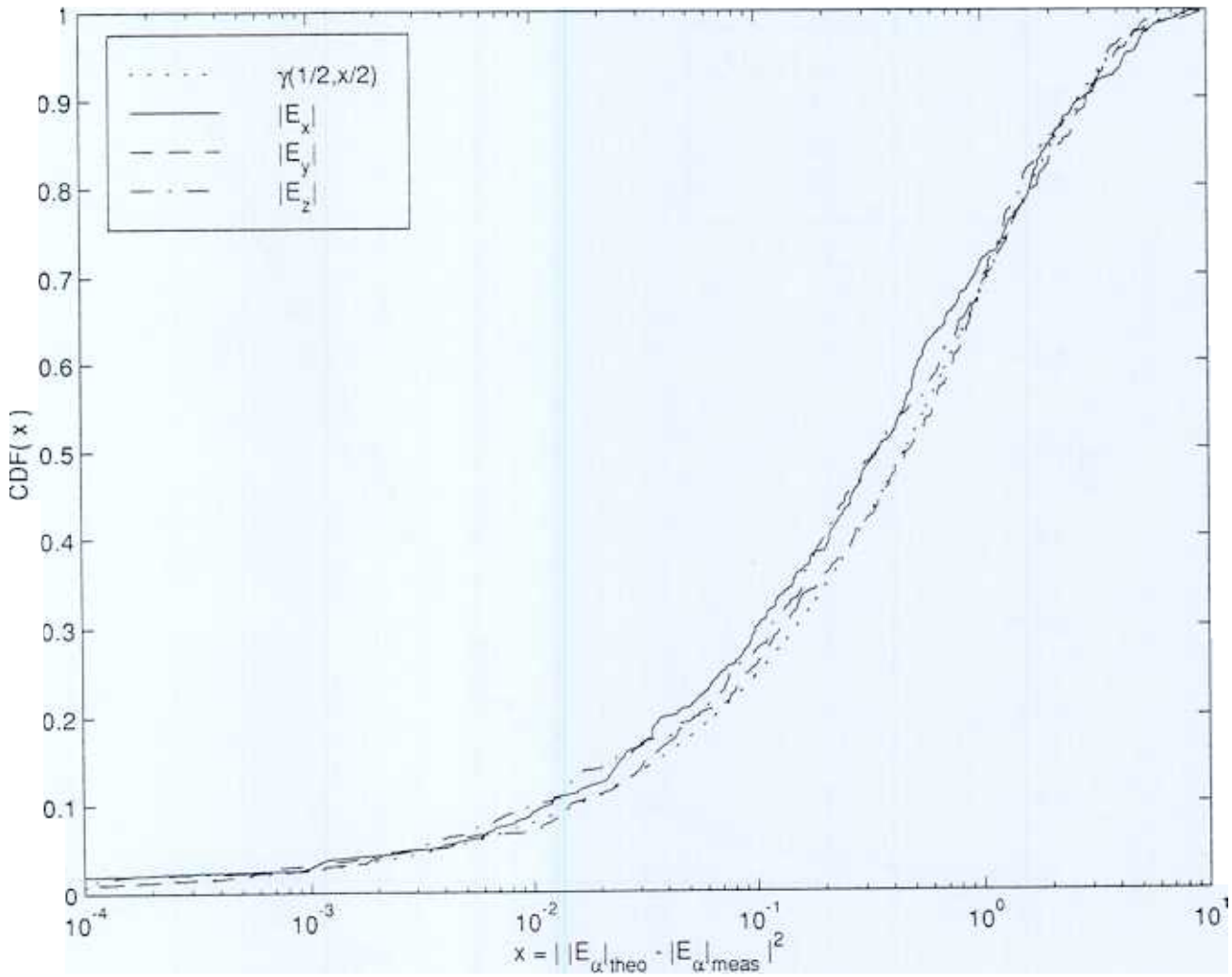


Figure 87: Cumulative distribution functions of standardized squared deviations $||E_\alpha|_{theo} - |E_\alpha|_{meas}|^2$ ($\alpha = x, y, z$) @ $f = 8.2$GHz, $r = 91$ mm for decimated data set ($m_\alpha = 3$).

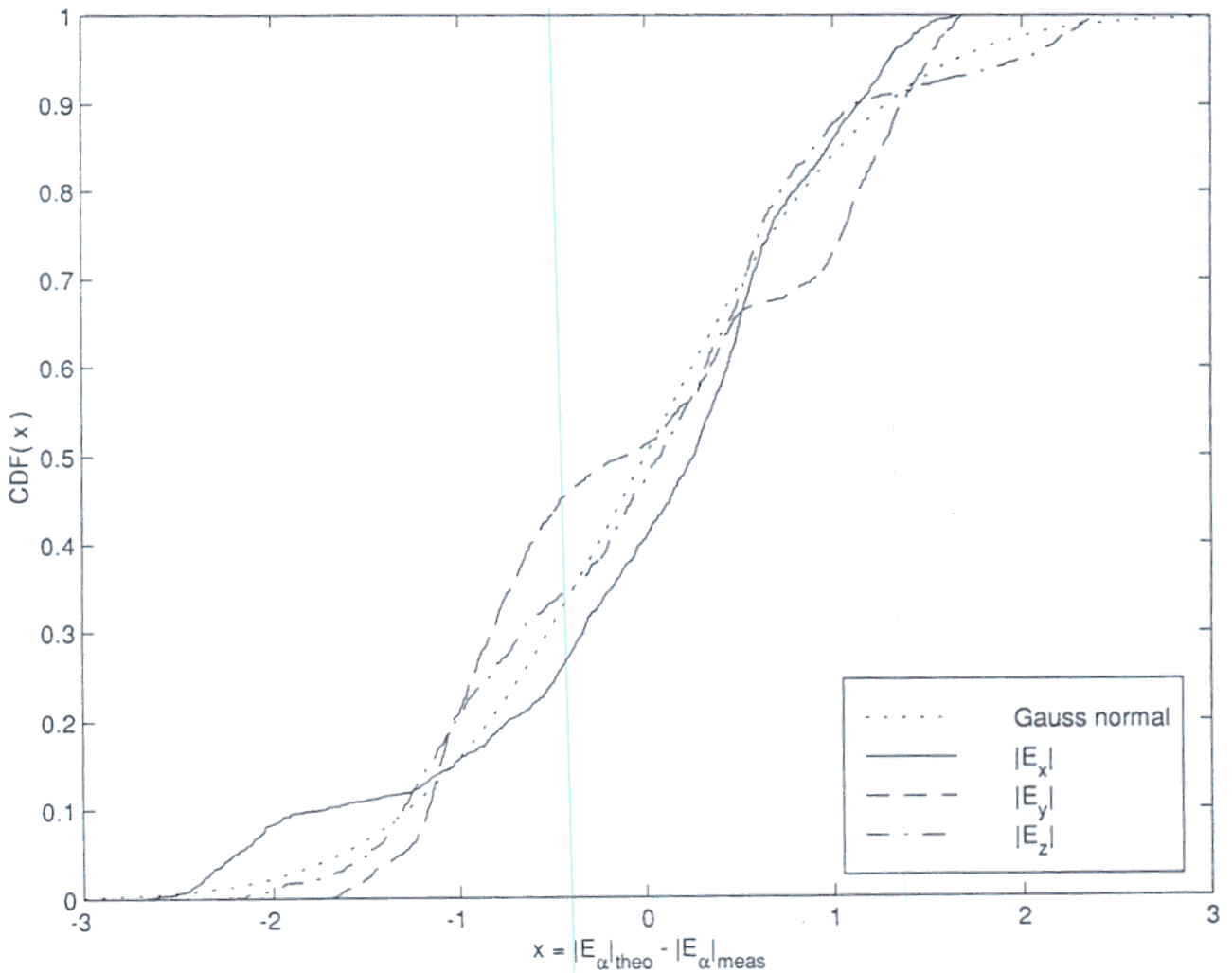


Figure 88: Cumulative distribution functions of standardized deviations $|E_\alpha|_{theo} - |E_\alpha|_{meas}$ ($\alpha = x, y, z$) @ $f = 8.2$GHz, $r = 91$mm for full data set.

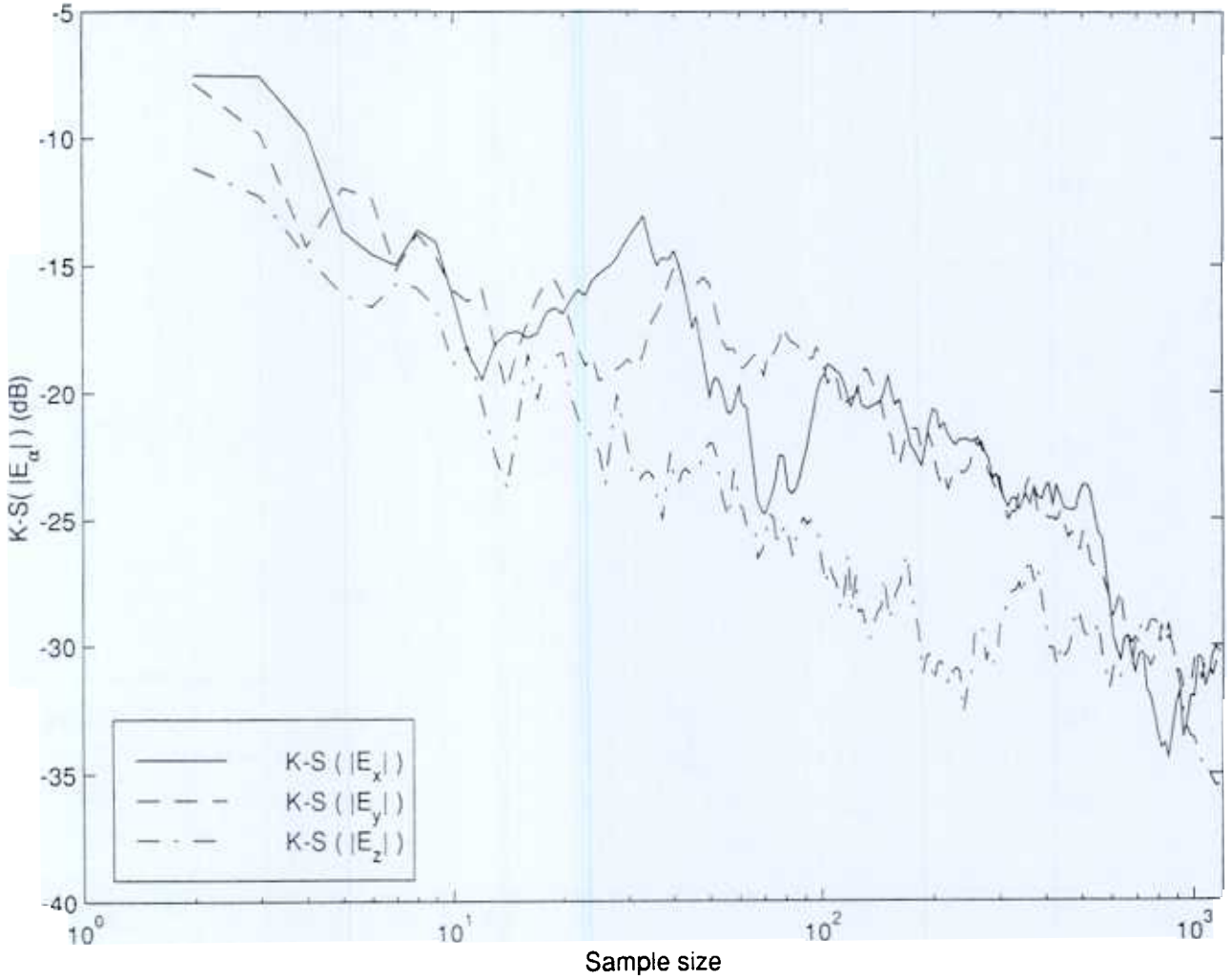


Figure 89: Kholmogorov–Smirnov test statistic between measured and theoretical cumulative distribution functions of $|E_\alpha|/\langle|E_\alpha|\rangle$ ($\alpha = x, y, z$) as a function of sample size M @ $f = 8.2$GHz, $r = 91$mm for full data set.

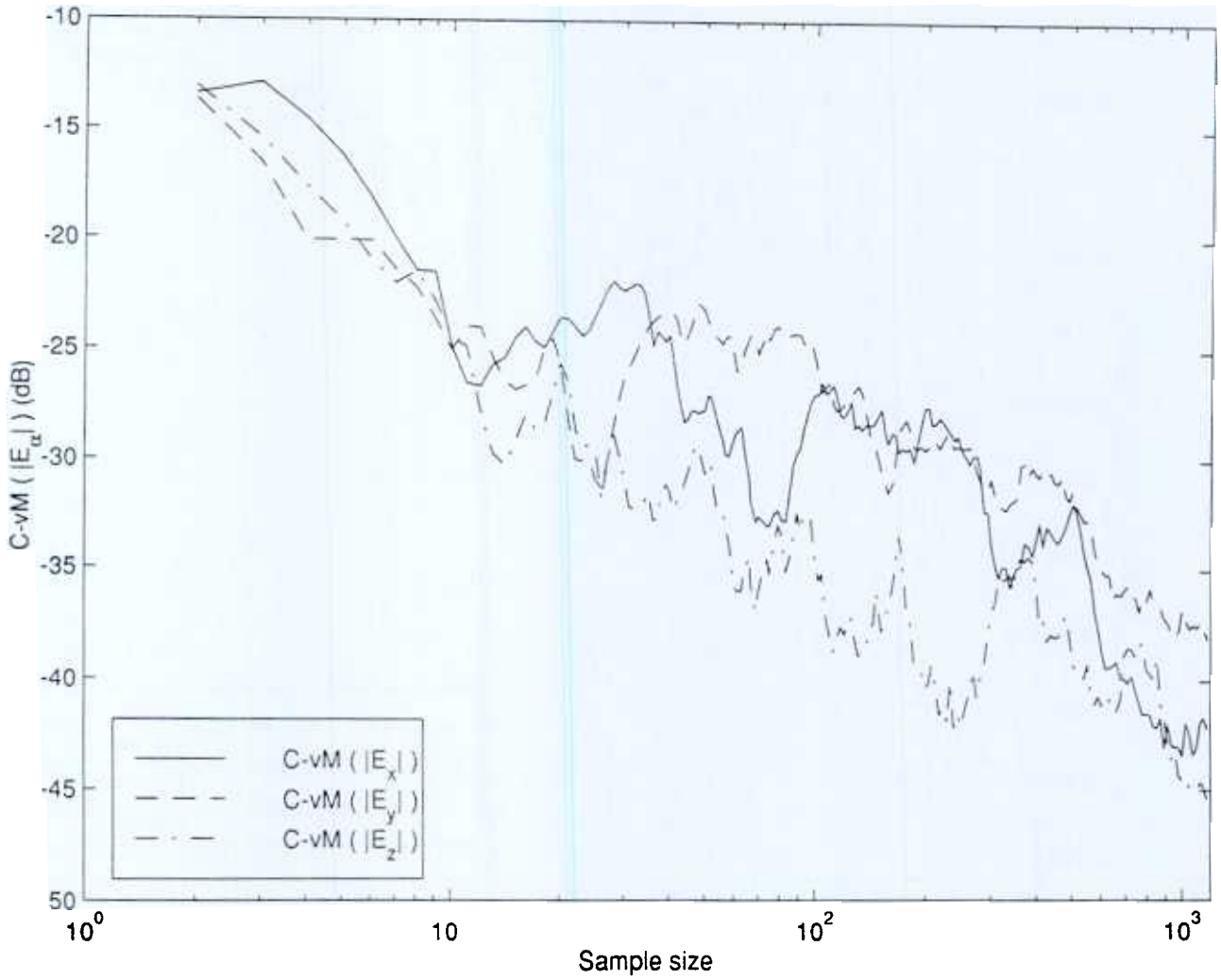


Figure 90: Cramér–von Mises test statistic between measured and theoretical cumulative distribution functions of $|E_\alpha|/\langle|E_\alpha|\rangle$ ($\alpha = x, y, z$) as a function of sample size M@ $f = 8.2$GHz, $r = 91$mm for full dataset.

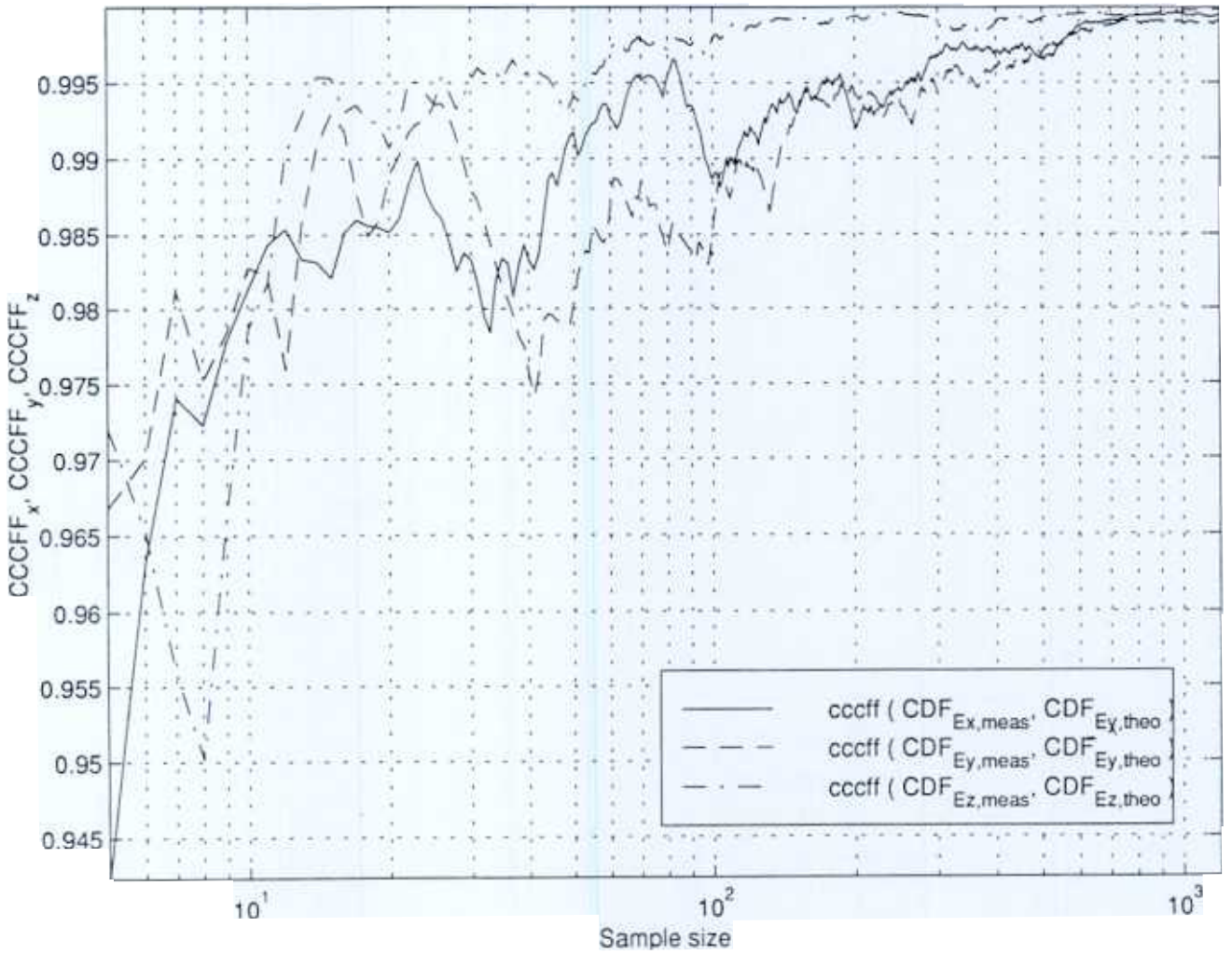


Figure 91: Crosscorrelation coefficients $\varrho_{\alpha\beta}$ between measured and theoretical cumulative distribution functions of $|E_\alpha|/\langle|E_\alpha|\rangle$, $|E_\beta|/\langle|E_\beta|\rangle$ $(\alpha, \beta = x, y, z)$ as a function of sample size M @ $f = 8.2$GHz, $r = 91$mm for full data set.

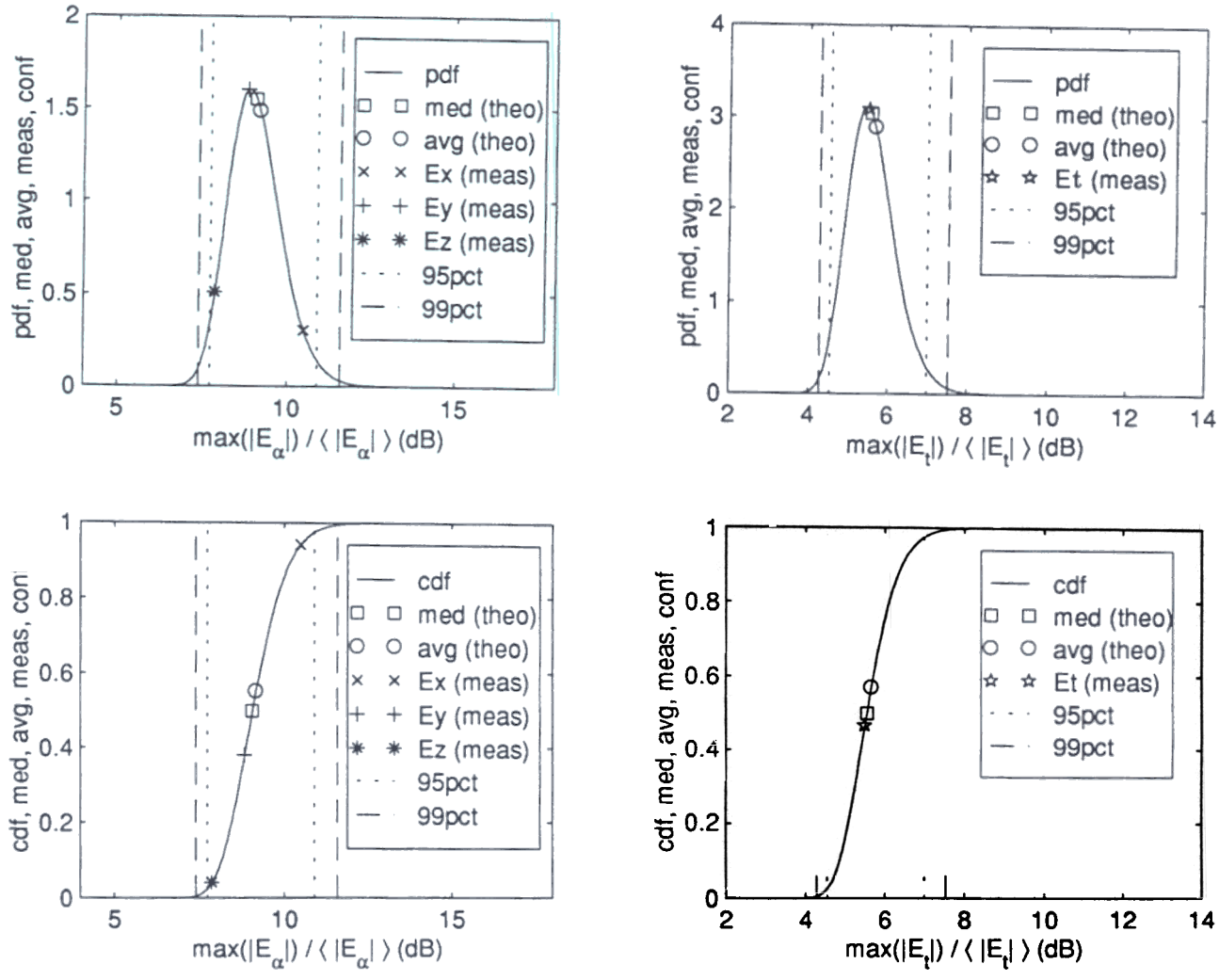


Figure 92: Distribution functions, theoretical median, theoretical mean, measured values, and 95% and 99% confidence intervals of max-to-mean field for $|E_\alpha|/\langle|E_\alpha|\rangle$ ($\alpha = x, y, z, t$) @ $f =$ 8.2GHz, $r = 91$mm for decimated data set ($m_\alpha = 3$).

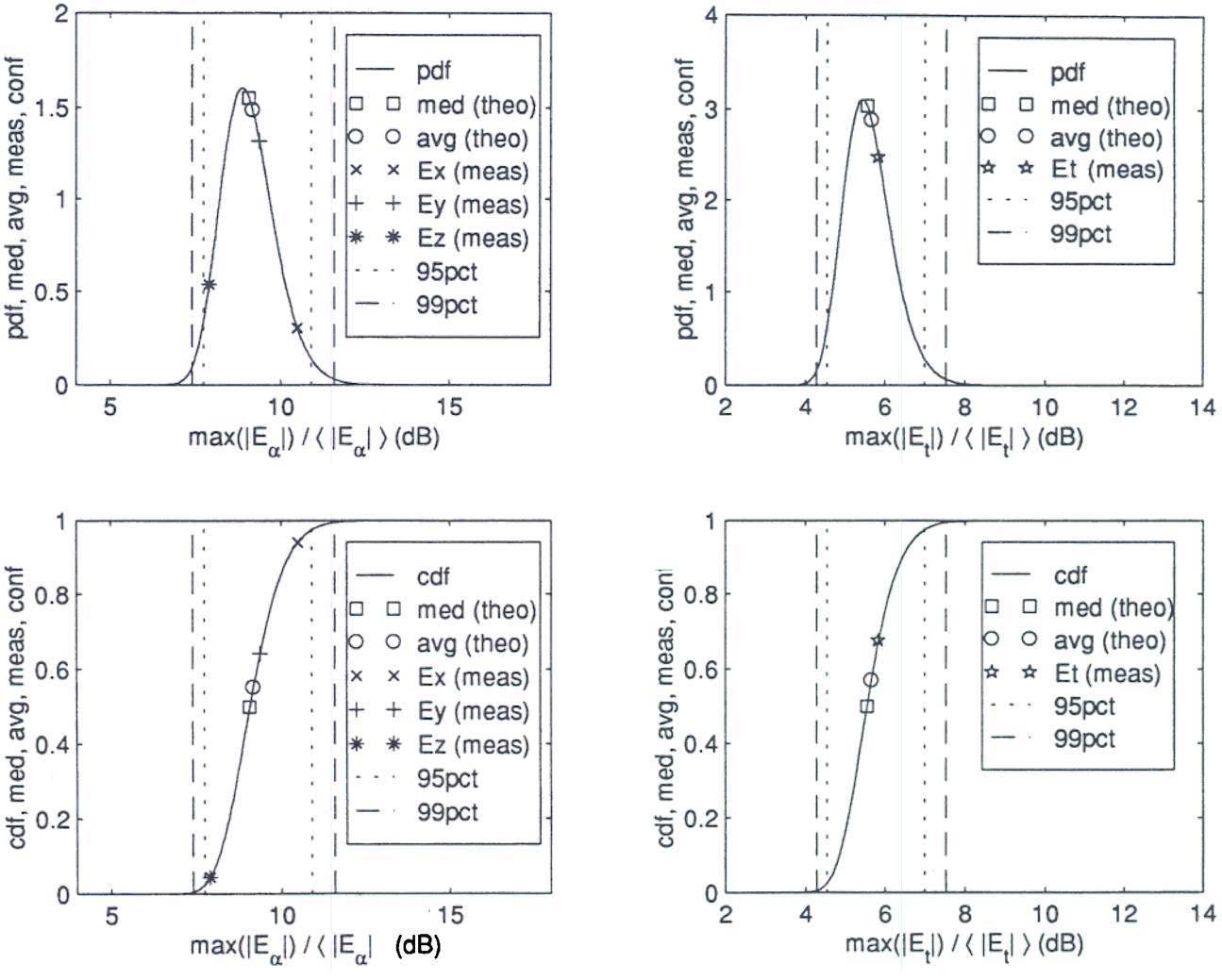


Figure 93: Distribution functions, theoretical median, theoretical mean, measured values, and 95% and 99% confidence intervals of max-to-mean field for $|E_\alpha|/\langle|E_\alpha|\rangle$ ($\alpha = x, y, z, t$) @ f = 8.2GHz, r = 91mm for full data set (for demonstration only).

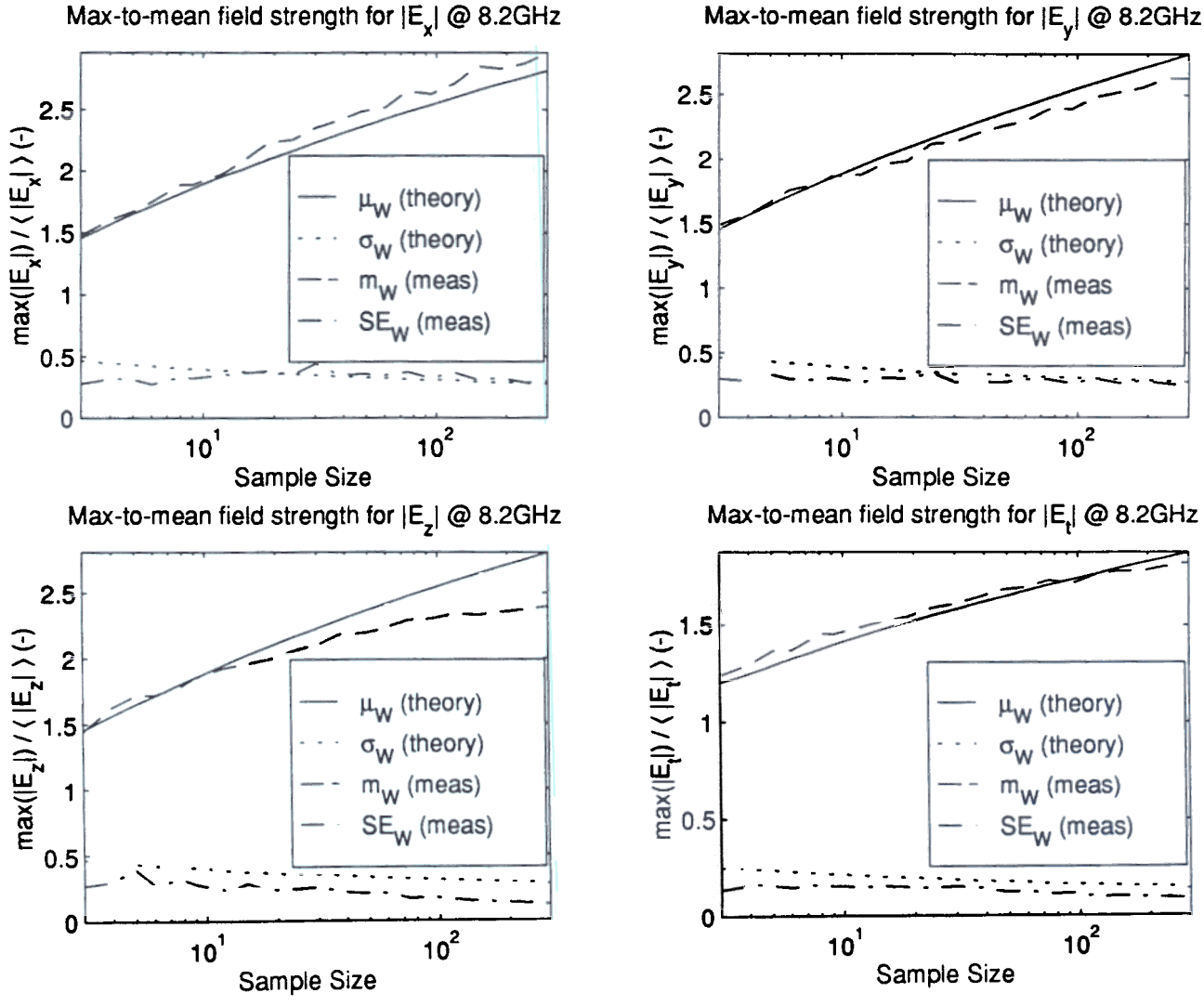


Figure 94: Theoretical and measured max-to-mean field for $|E_\alpha|/\langle|E_\alpha|\rangle$ ($\alpha = x, y, z, t$) as a function of sample size N @ $f = 8.2$GHz, $r = 91$mm.

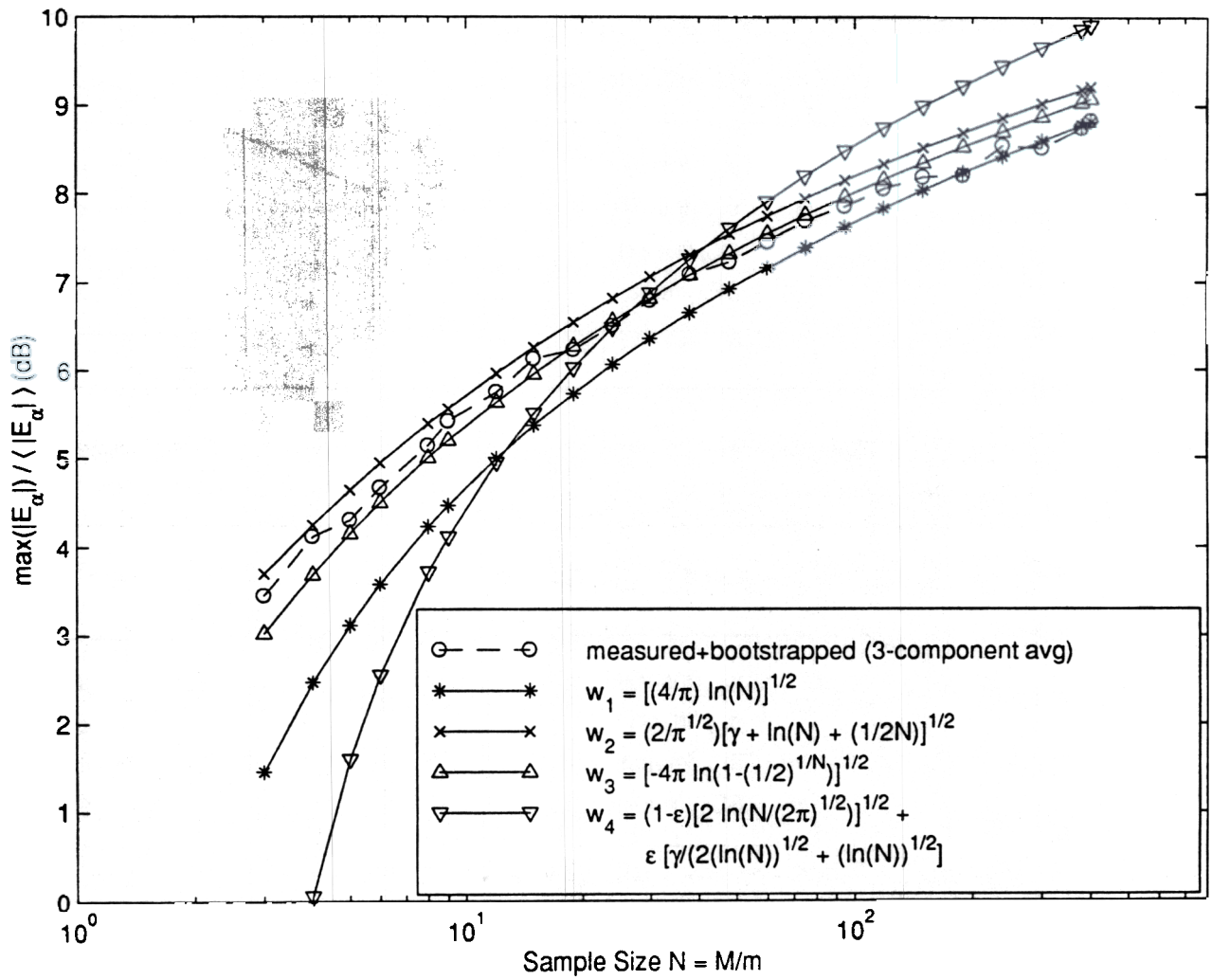


Figure 95: Comparison between measured max-to-mean field for $|E_\alpha|/\langle|E_\alpha|\rangle$ ($\alpha = x, y, z$) and various estimates a function of sample size N @ $f = 8.2$GHz, $r = 91$mm.

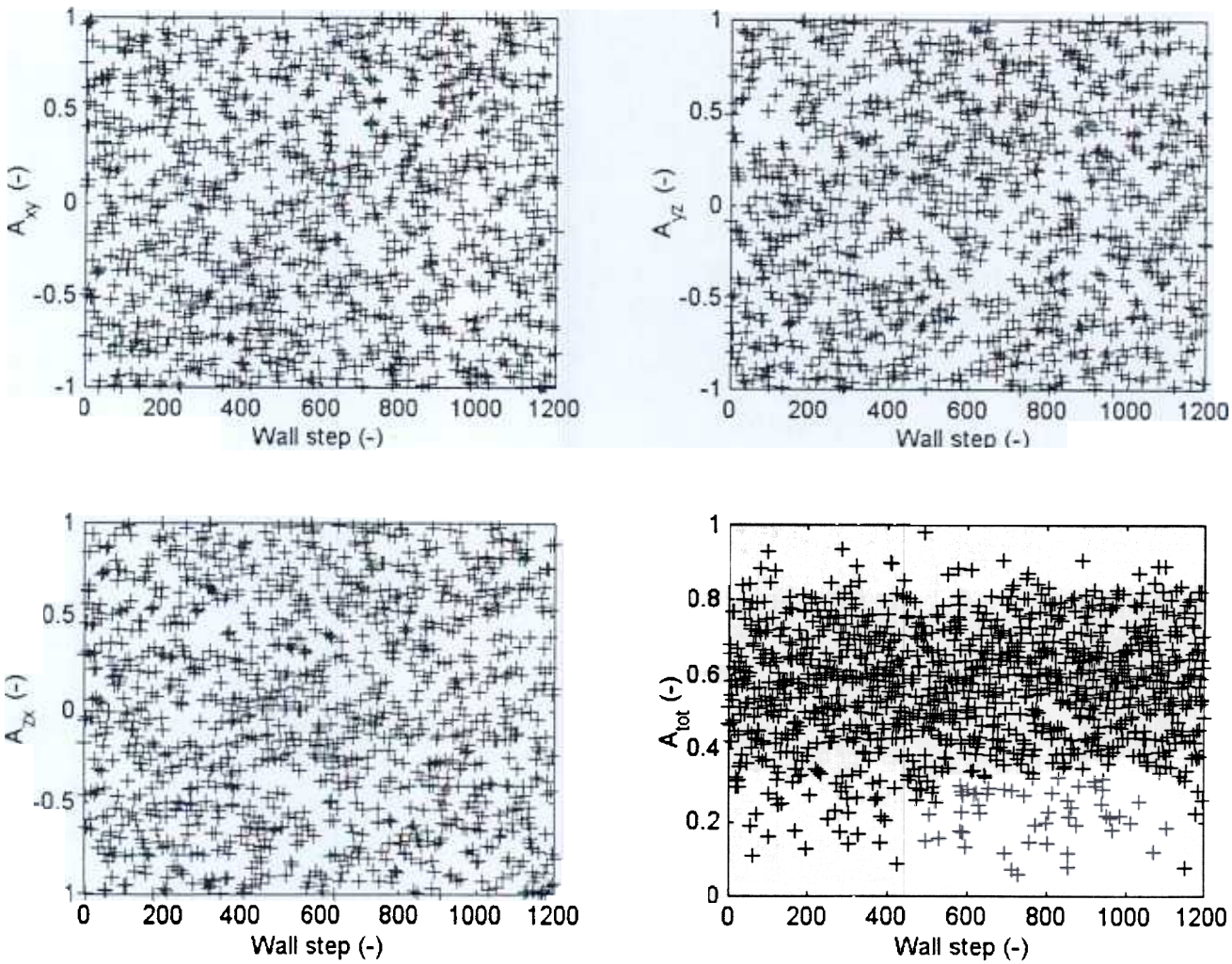


Figure 96: Theoretical (simulated) field anisotropy coefficients $A_{\alpha\beta}$ and A_{tot} for sample of size $M = 1200$ taken from a perfectly reverberant field.

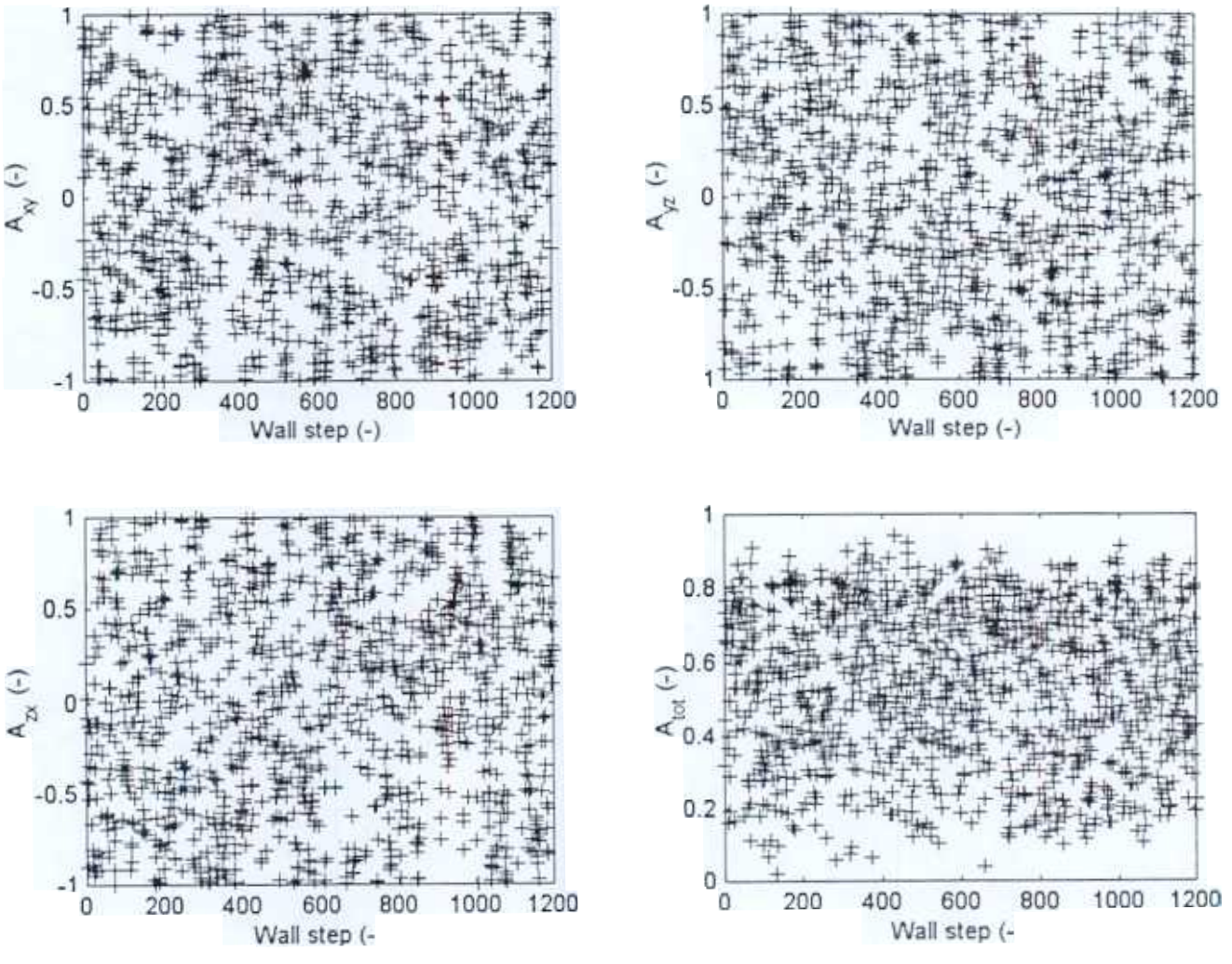


Figure 97: Measured field anisotropy coefficients $A_{\alpha\beta}$ and A_{tot} @ f = 8.2GHz, r = 91mm for full data set.

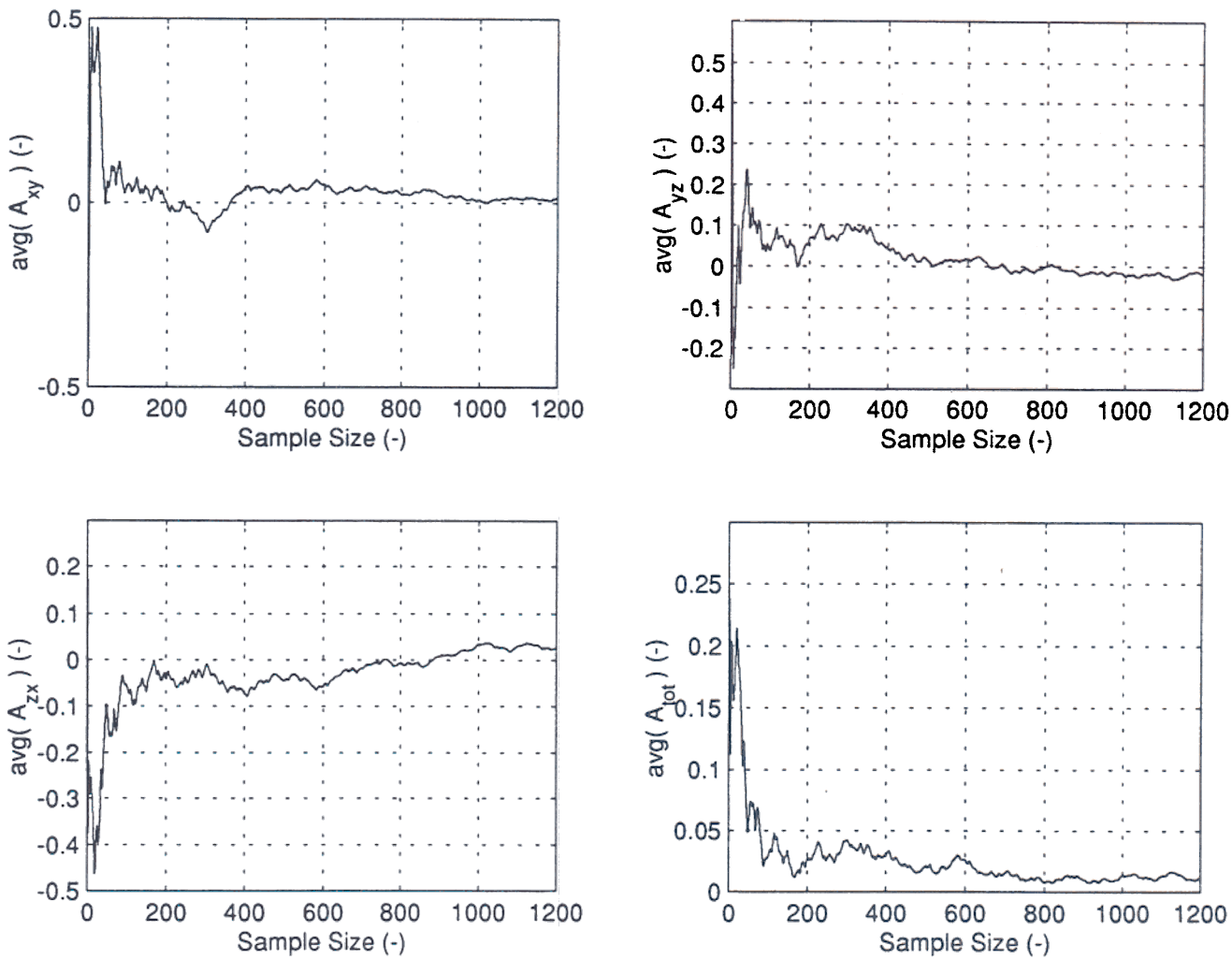


Figure 98: Single-sample average of measured field anisotropy coefficients $A_{\alpha\beta}$ and A_{tot} as a function of sample size M @ $f = 8.2$GHz, $r = 91$mm for full data set (linear scale).

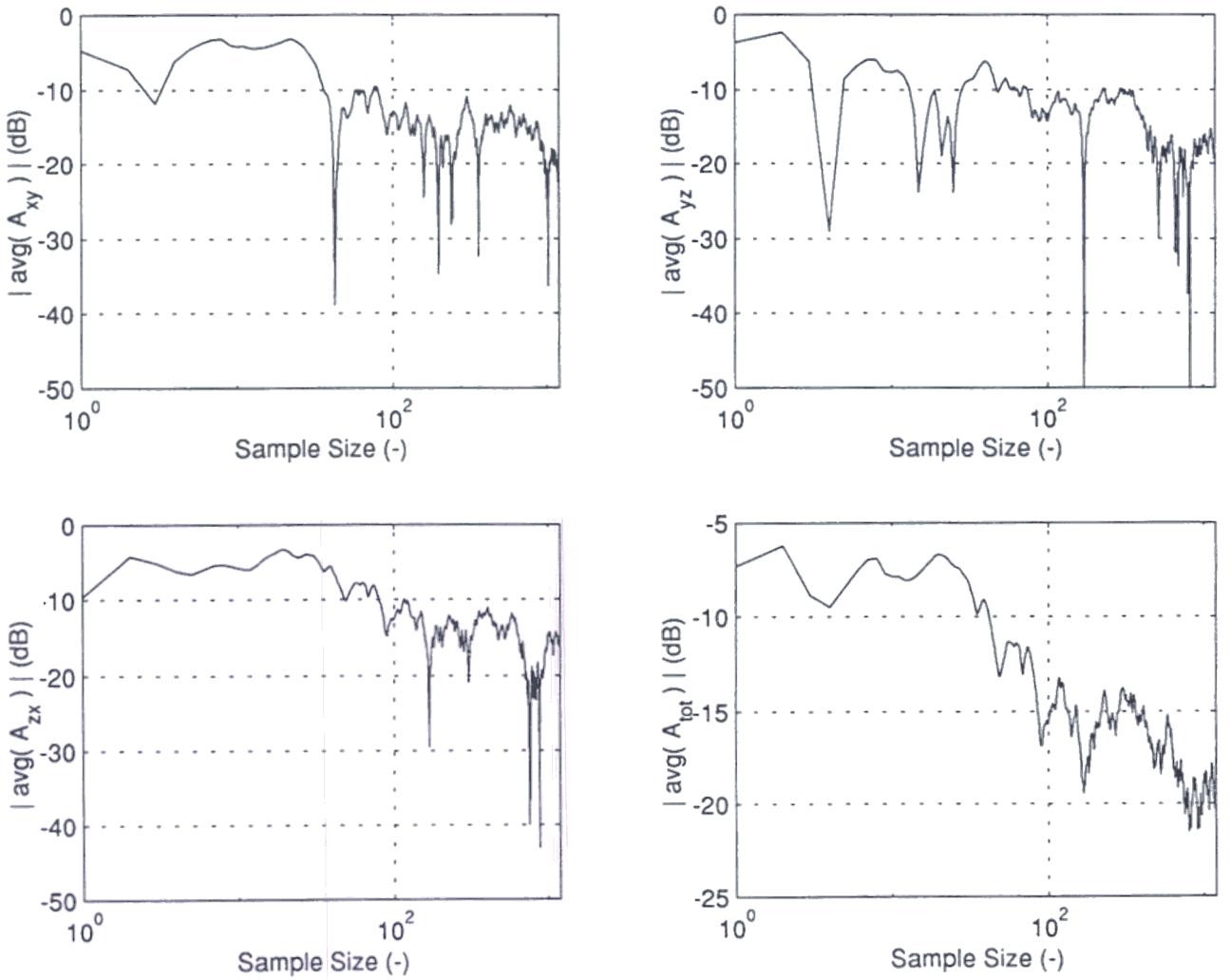


Figure 99: Magnitude of single-sample average of measured field anisotropy coefficients $A_{\alpha\beta}$ and A_{tot} as a function of sample size M @ $f = 8.2$GHz, $r = 91$mm for full data set (dB scale).

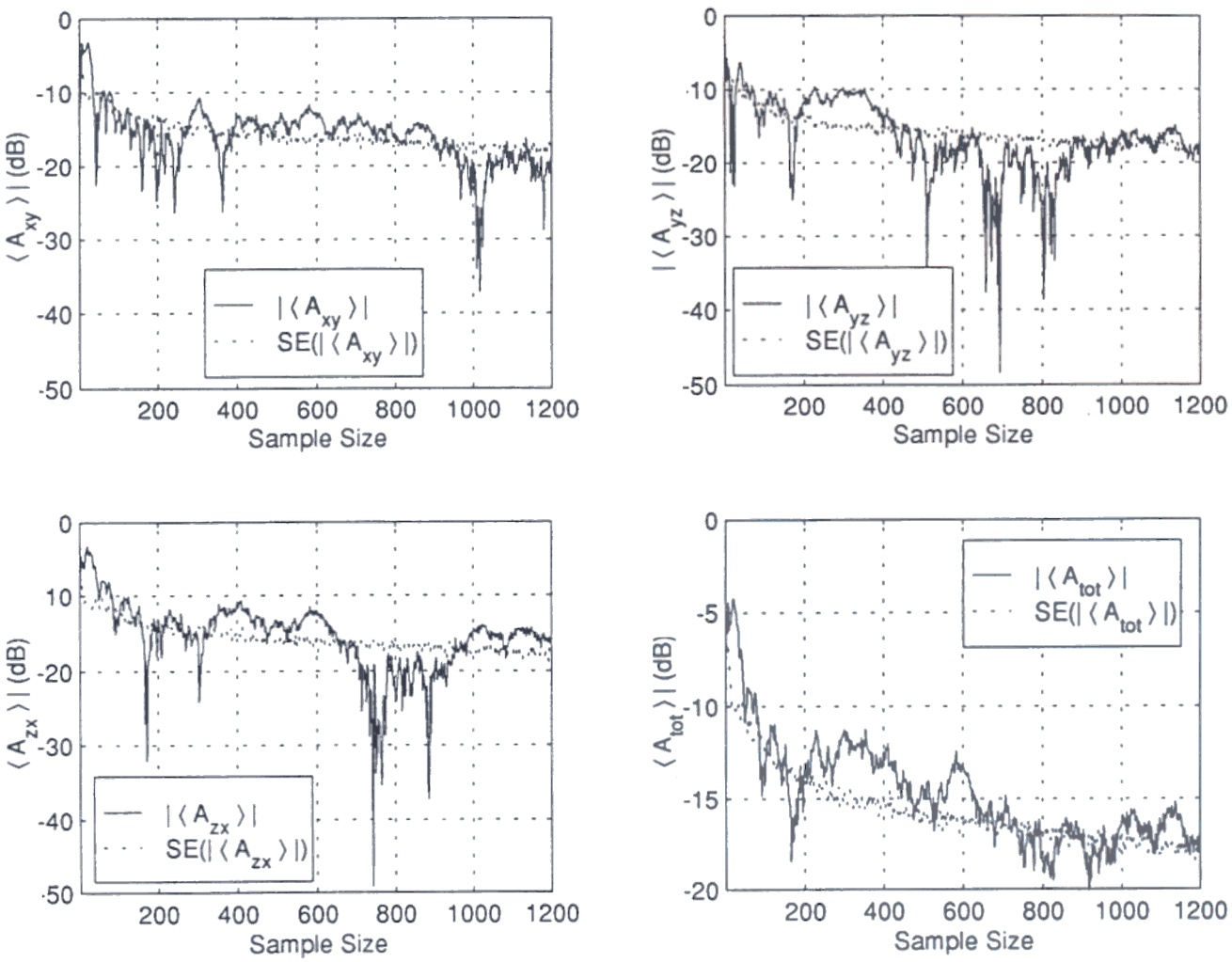


Figure 100: Magnitude of bootstrap average of measured field anisotropy coefficients $A_{\alpha\beta}$ and A_{tot} as a function of sample size M @ $f = 8.2$GHz, $r = 91$mm for full data set (dB scale).

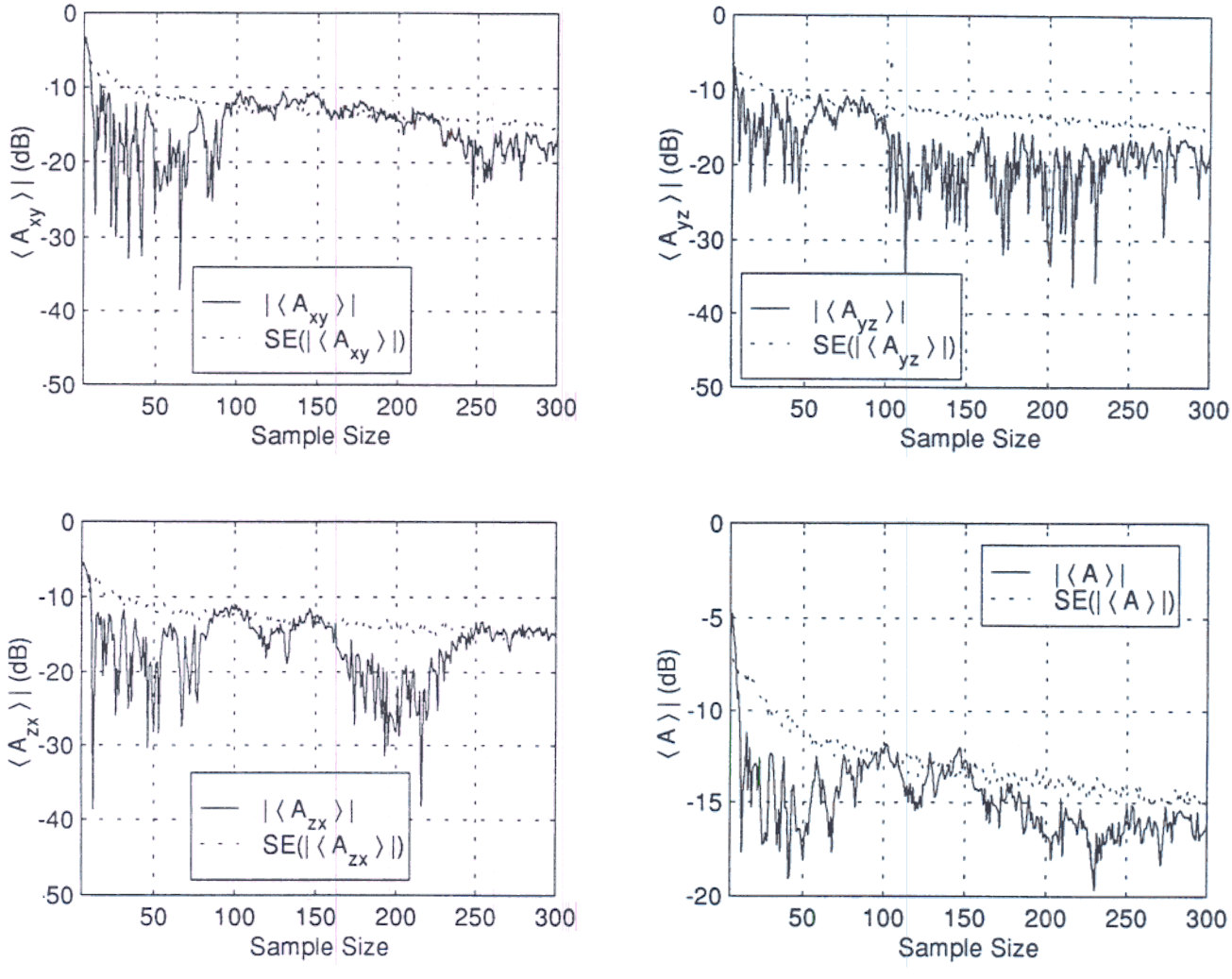


Figure 101: Magnitude of bootstrap average of measured field anisotropy coefficients $A_{\alpha\beta}$ and A_{tot} @ $f = 8.2$GHz, $r = 91$mm for decimated data set ($m_\alpha = 4$) (dB scale).

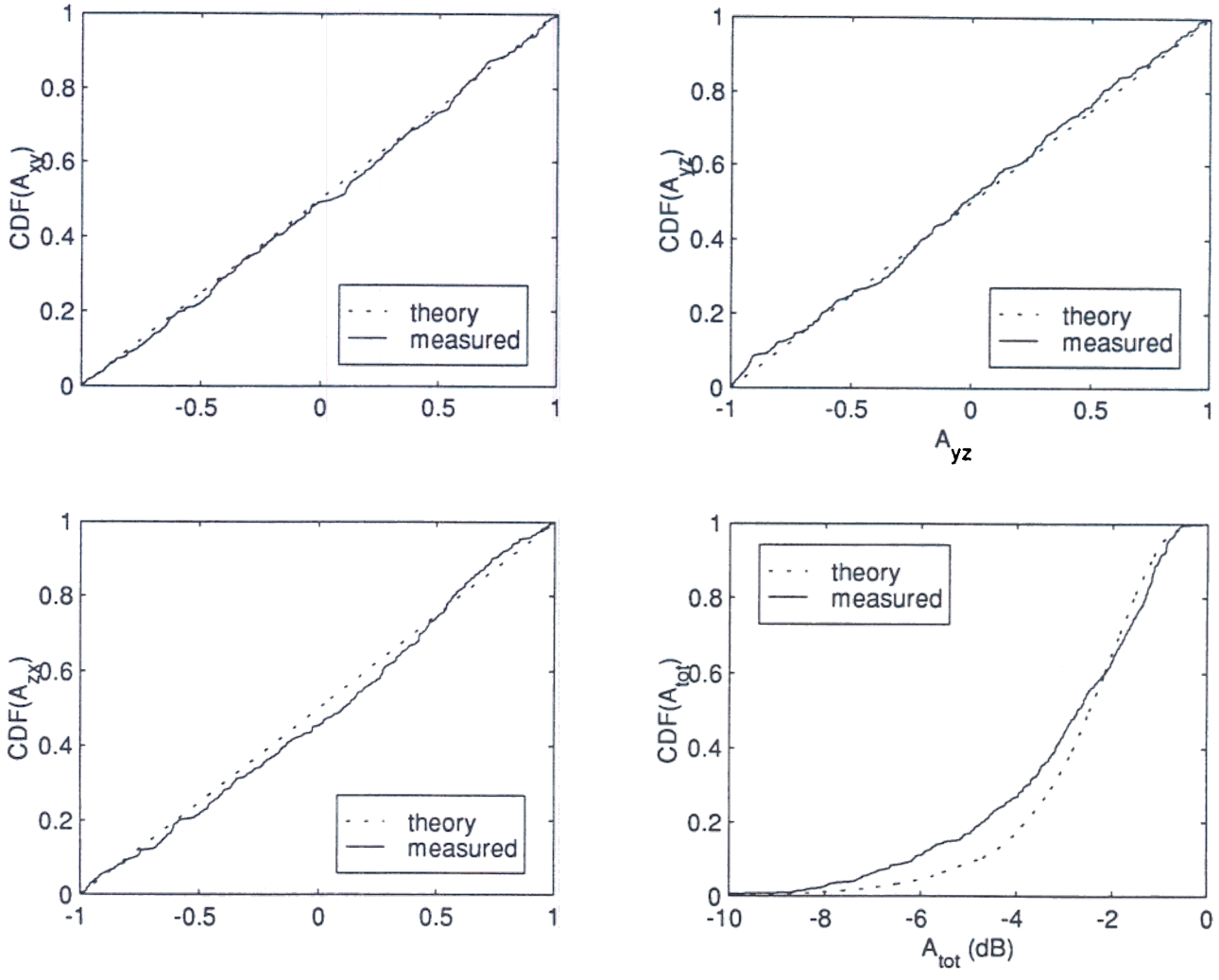


Figure 102: Theoretical and measured cumulative distribution functions of field anisotropy coefficients $A_{\alpha\beta}$ and A_{tot} @ $f = 8.2$GHz, $r = 91$mm for decimated data set ($m_\alpha = 3$).

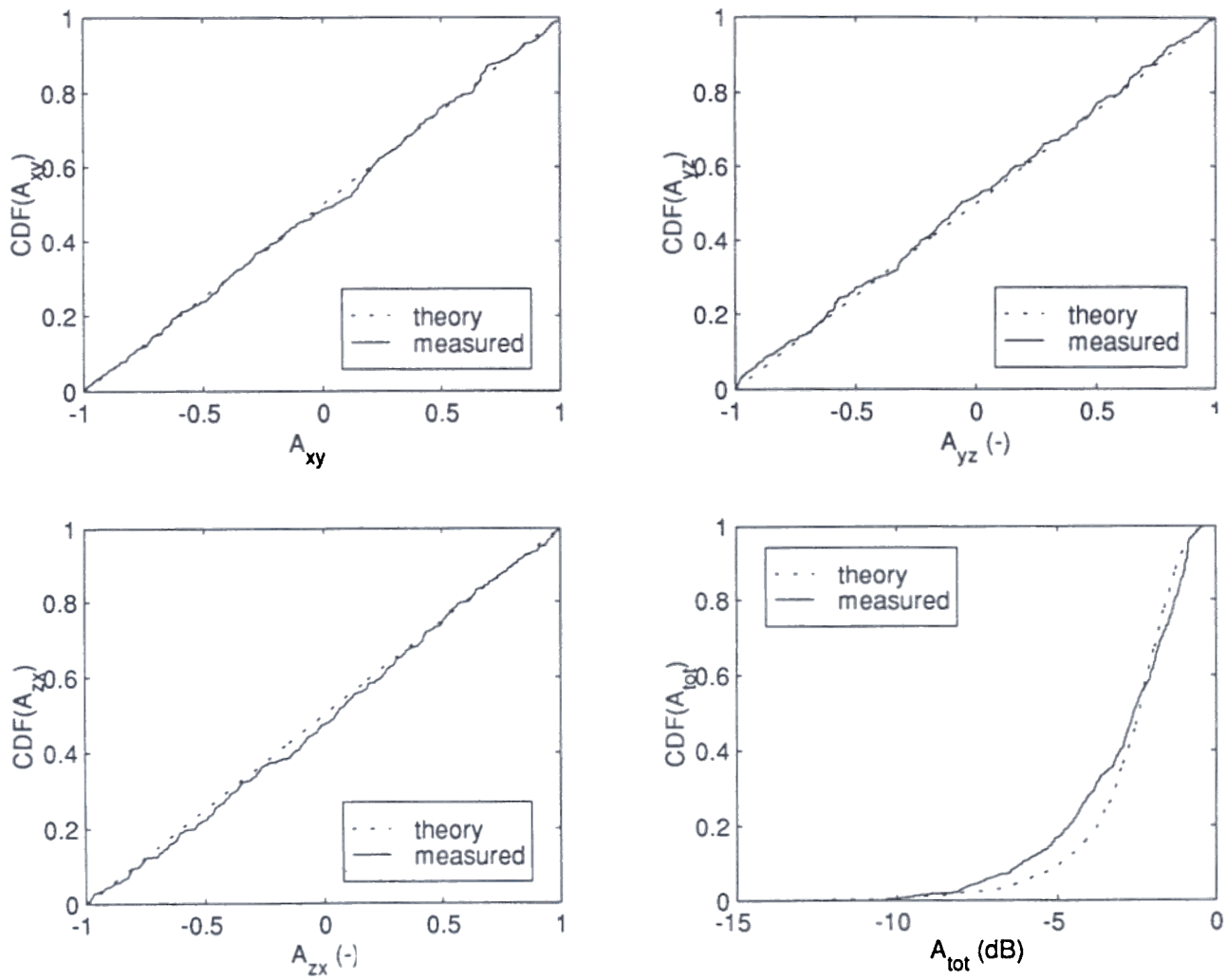


Figure 103: Theoretical and measured cumulative distribution functions of field anisotropy coefficients $A_{\alpha\beta}$ and A_{tot} @ $f = 8.2$GHz, $r = 91$mm for full data set (for demonstration only).

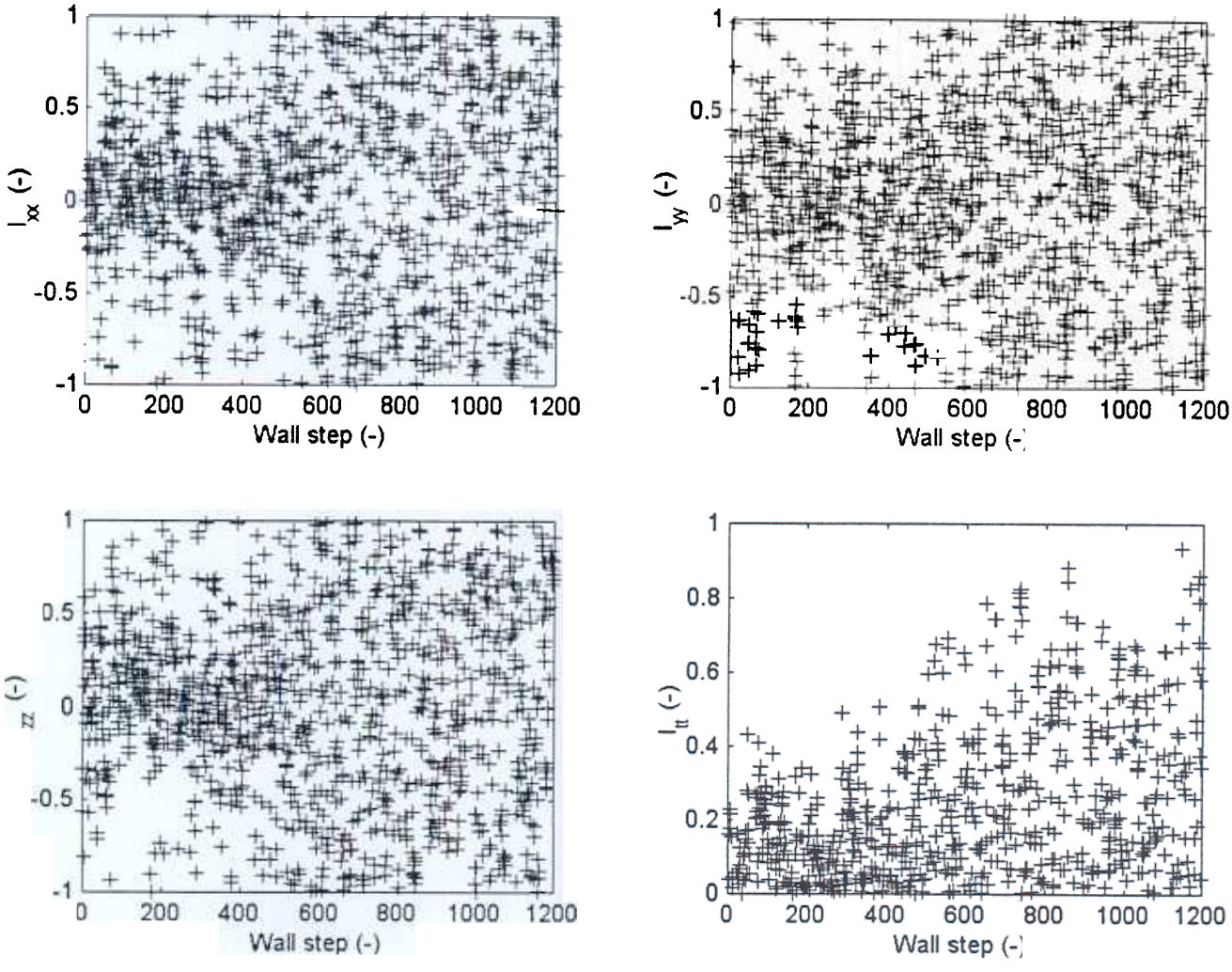


Figure 104: Measured field inhomogeneity coefficients $I_{\alpha\alpha}$ ($\alpha = x, y, z, t$) @ $f = 8.2$GHz, $r_0 = 91$mm, $r_1 = 94$mm for full data set.

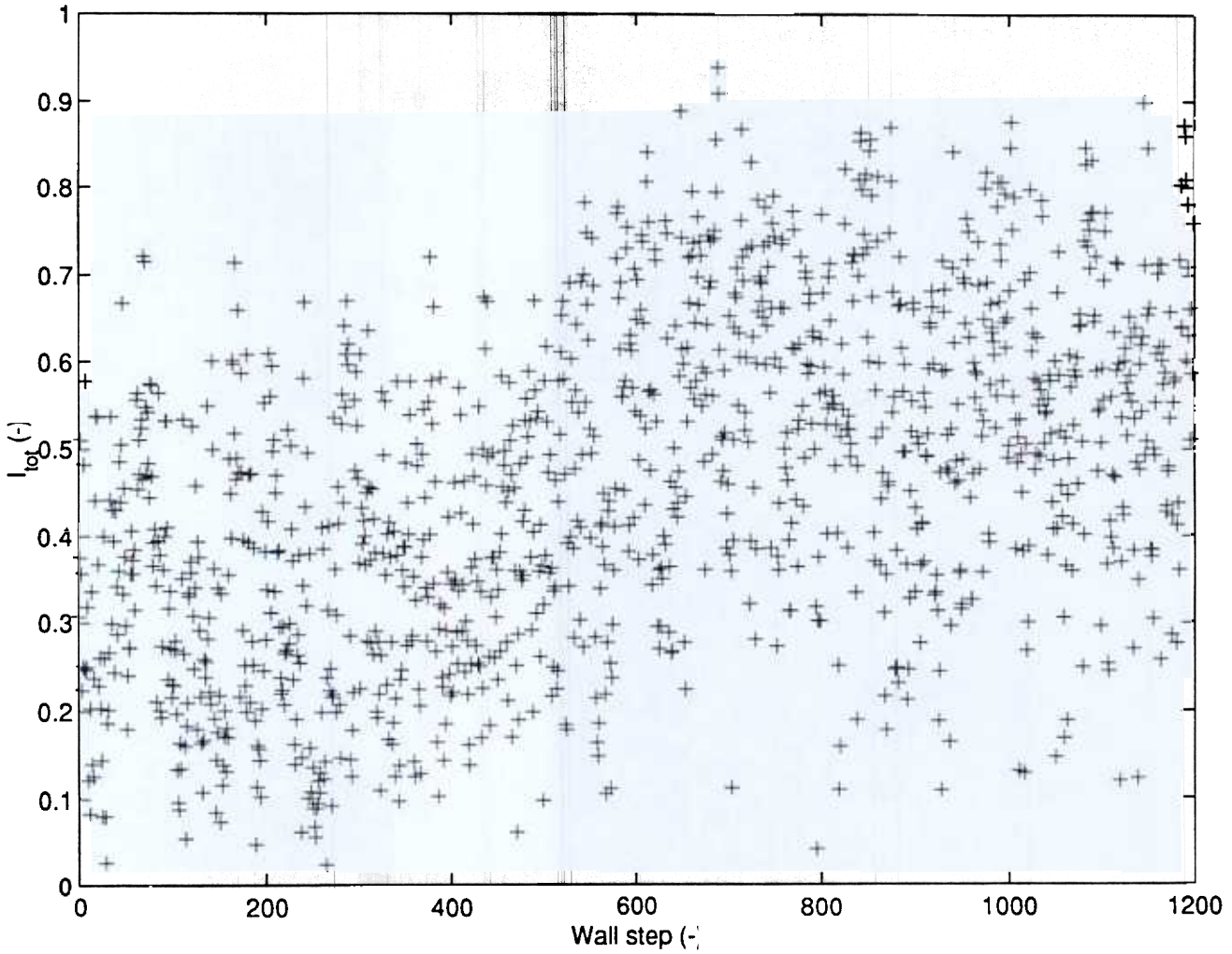


Figure 105: Total measured field inhomogeneity coefficients I_{tot} @ f = 8.2GHz, r_0 = 91mm, r_1 = 94mm for full data set.

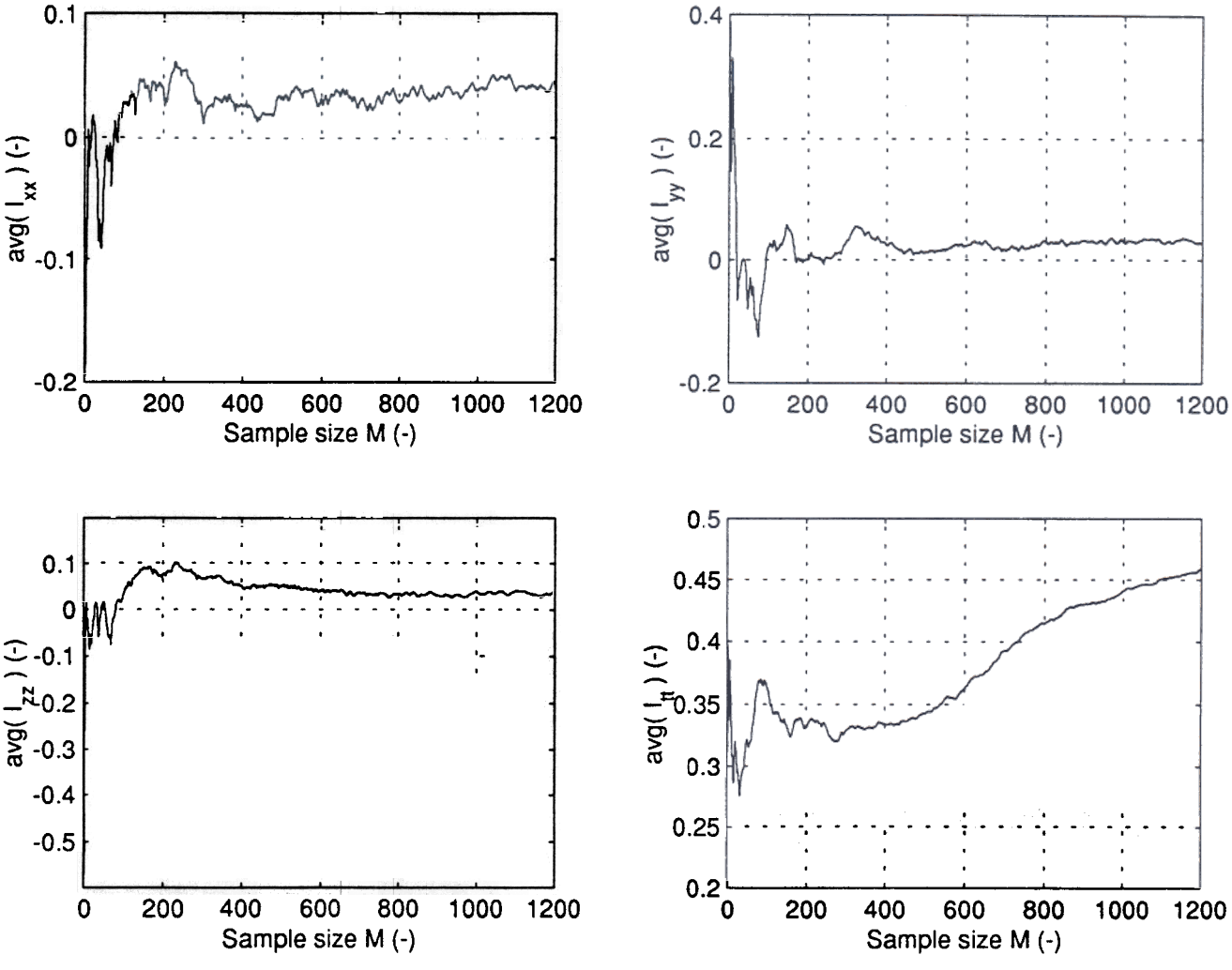


Figure 106: Single-sample average of measured field inhomogeneity coefficients $I_{\alpha\alpha}$ ($\alpha = x, y, z, t$) as a function of sample size M @ $f = 8.2$GHz, $r_0 = 91$mm, $r_1 = 94$mm for full data set (linear scale).

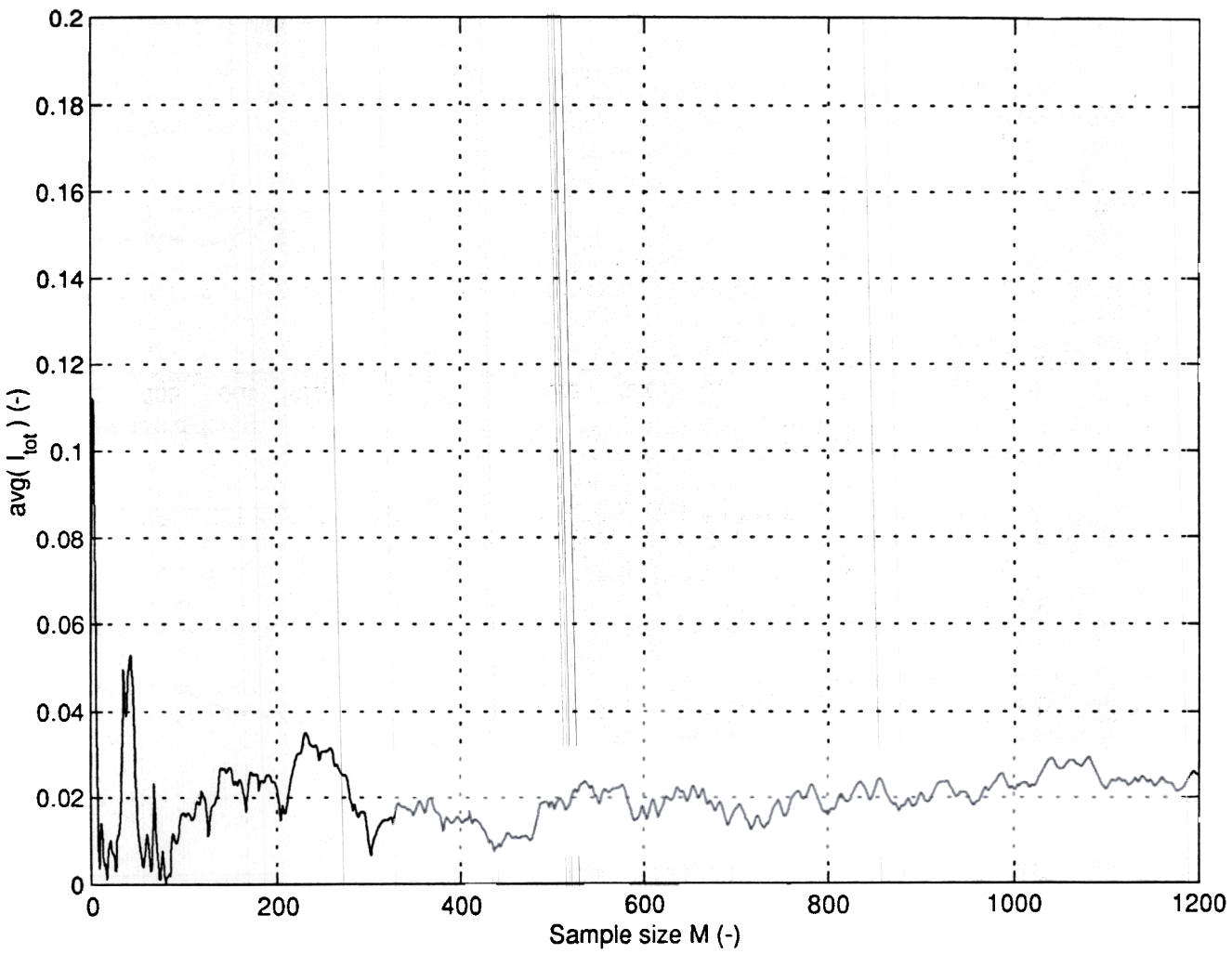


Figure 107: Single-sample average of total measured field inhomogeneity coefficients I_{tot} as a function of sample size M @ $f = 8.2\text{GHz}, r_0 = 91\text{mm}, r_1 = 94\text{mm}$ for full data set (linear scale).

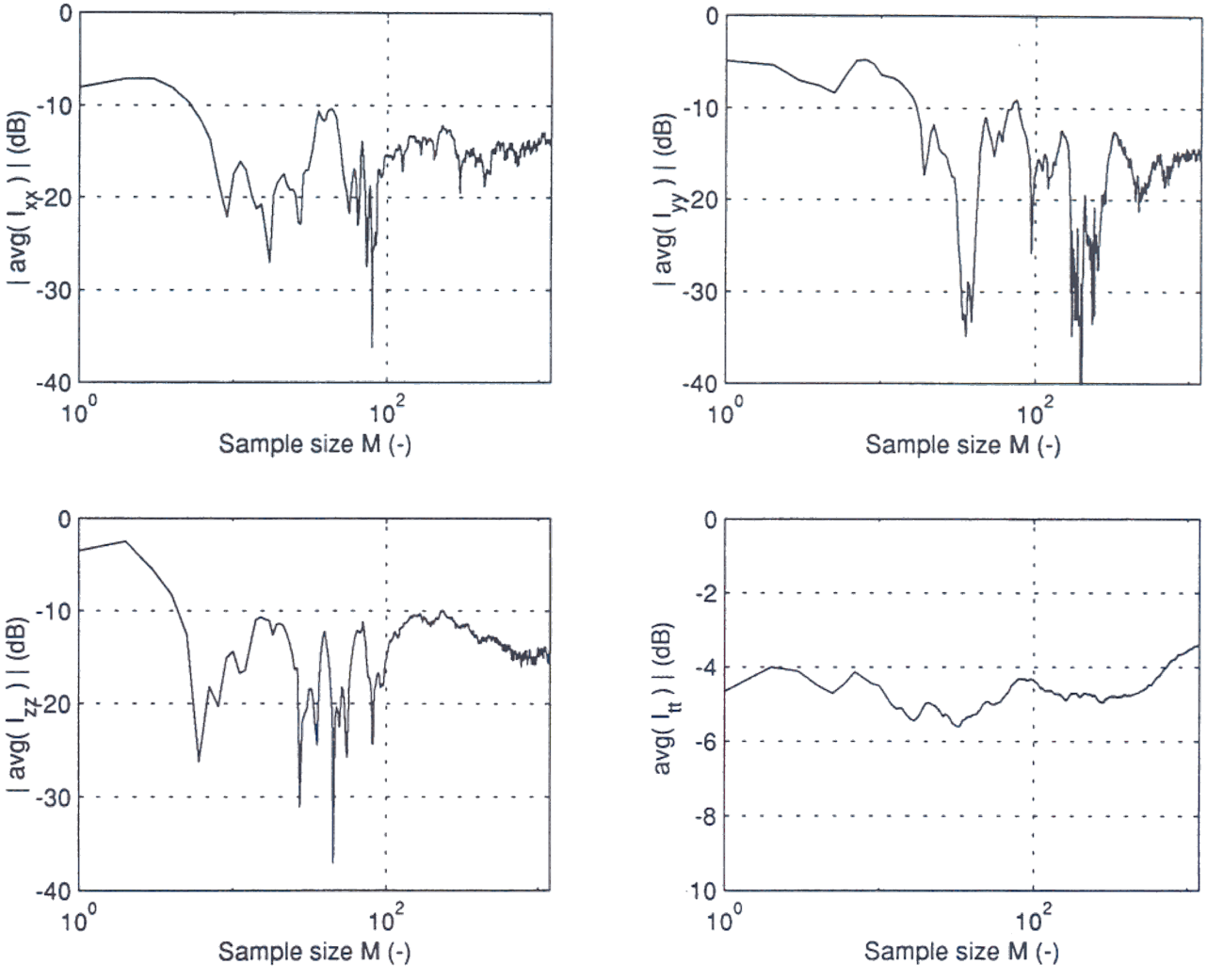


Figure 108: Magnitude of single-sample average of measured field inhomogeneity coefficients $I_{\alpha\alpha}$ ($\alpha = x, y, z, t$) as a function of sample size M @ $f = 8.2$GHz, $r_0 = 91$mm, $r_1 = 94$mm for full data set (dB scale).

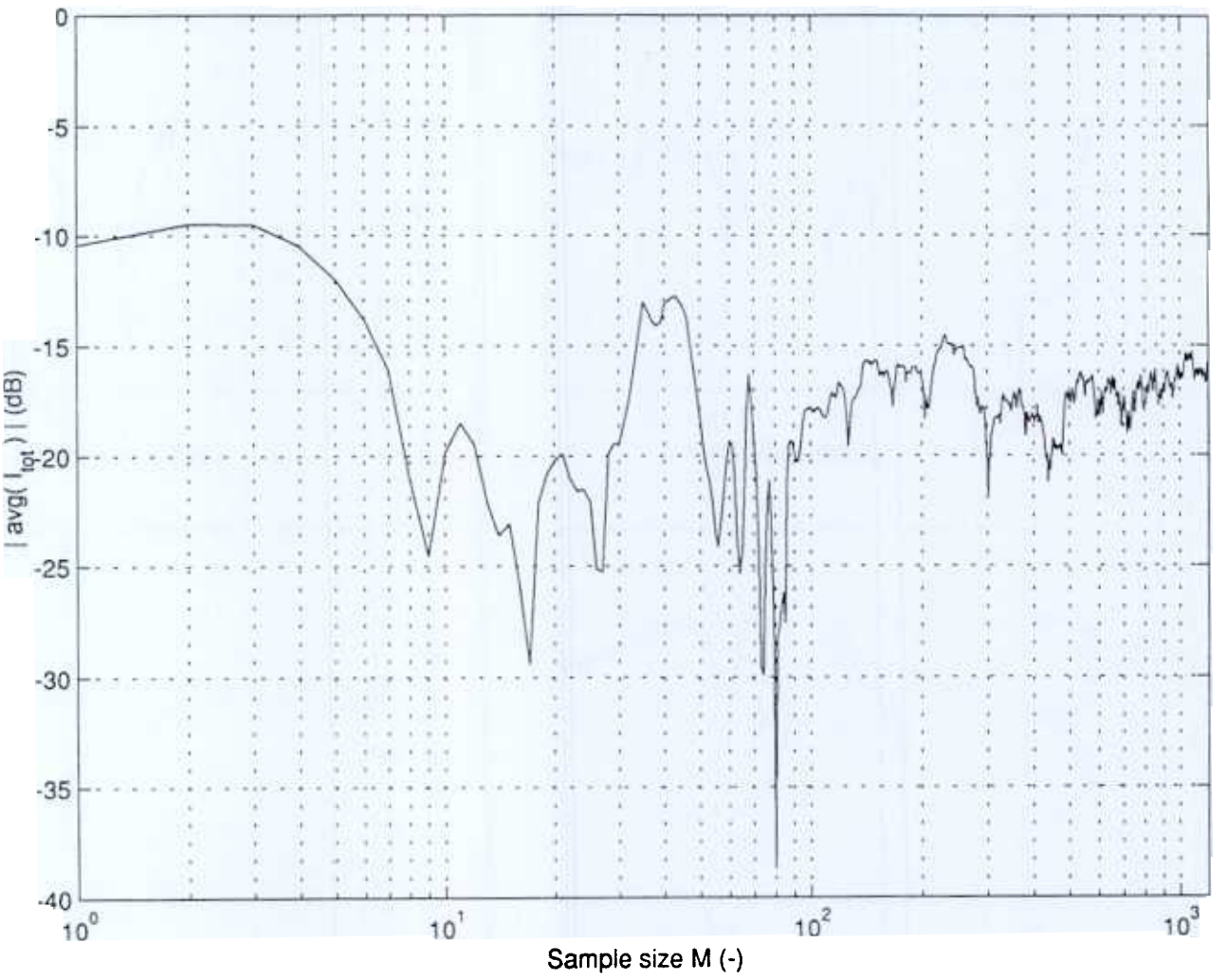


Figure 109: Magnitude of single-sample average of total measured field inhomogeneity coefficient I_{tot} as a function of sample size M @ f = 8.2GHz, r_0 = 91mm, r_1 = 94mm for full data set (dB scale).

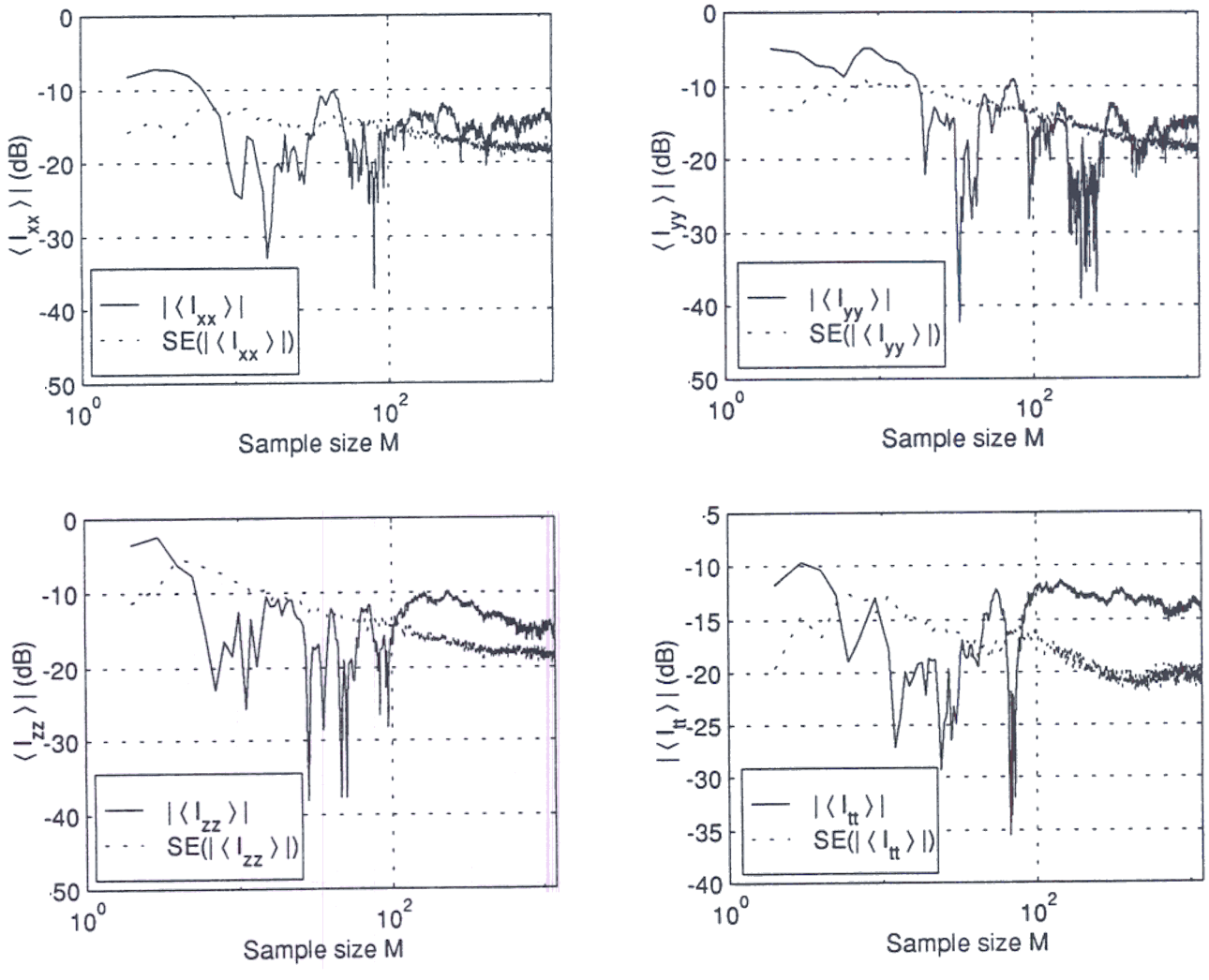


Figure 110: Magnitude of bootstrap average of measured field inhomogeneity coefficients $I_{\alpha\alpha}$ ($\alpha = x, y, z, t$) as a function of sample size M @ f = 8.2GHz, r_0 = 91mm, r_1 = 94mm for full data set (dB scale).

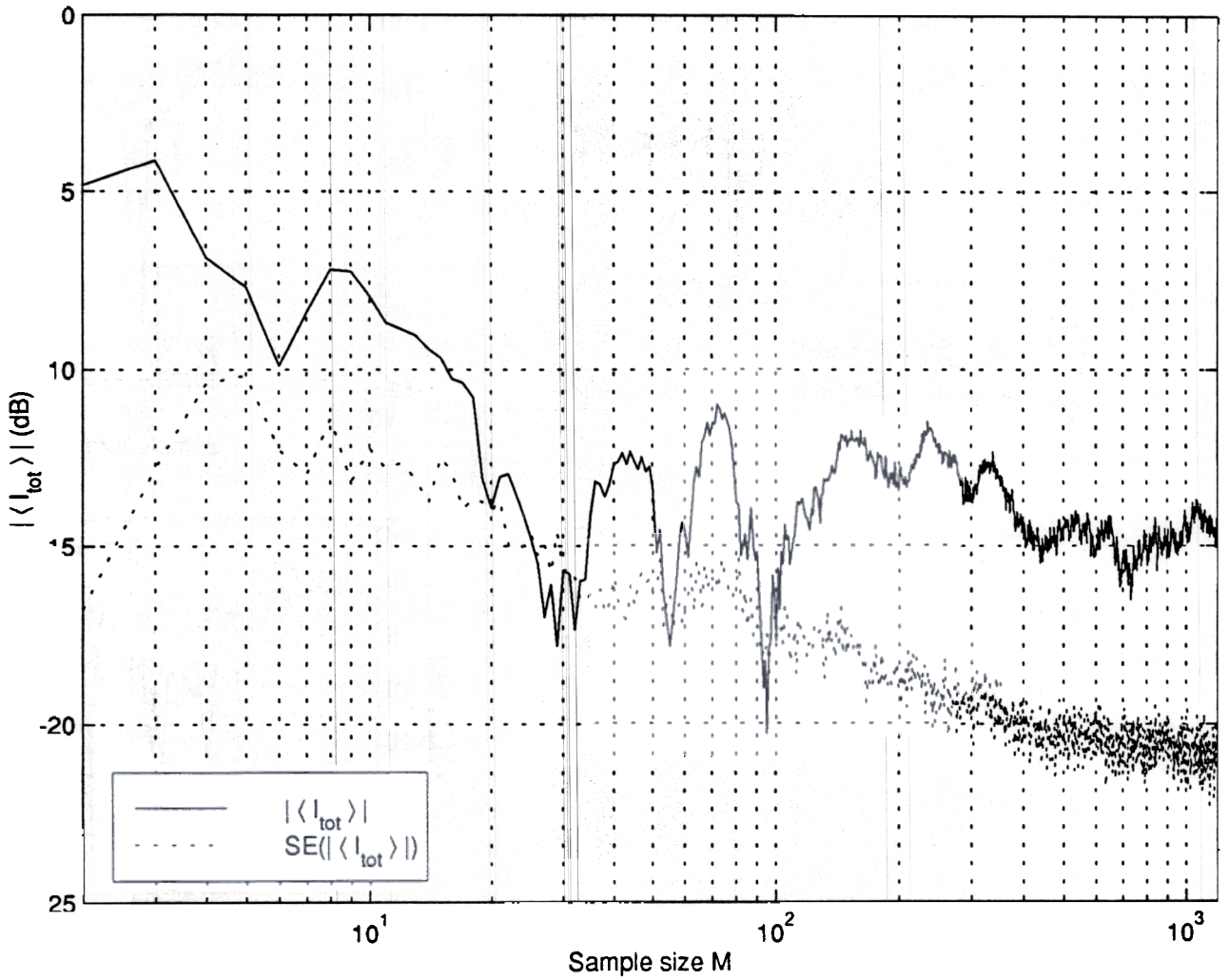


Figure 111: Magnitude of bootstrap average of total measured field inhomogeneity coefficient I_{tot} as a function of sample size M @ $f = 8.2$GHz, $r_0 = 91$mm, $r_1 = 94$mm for full data set (dB scale).

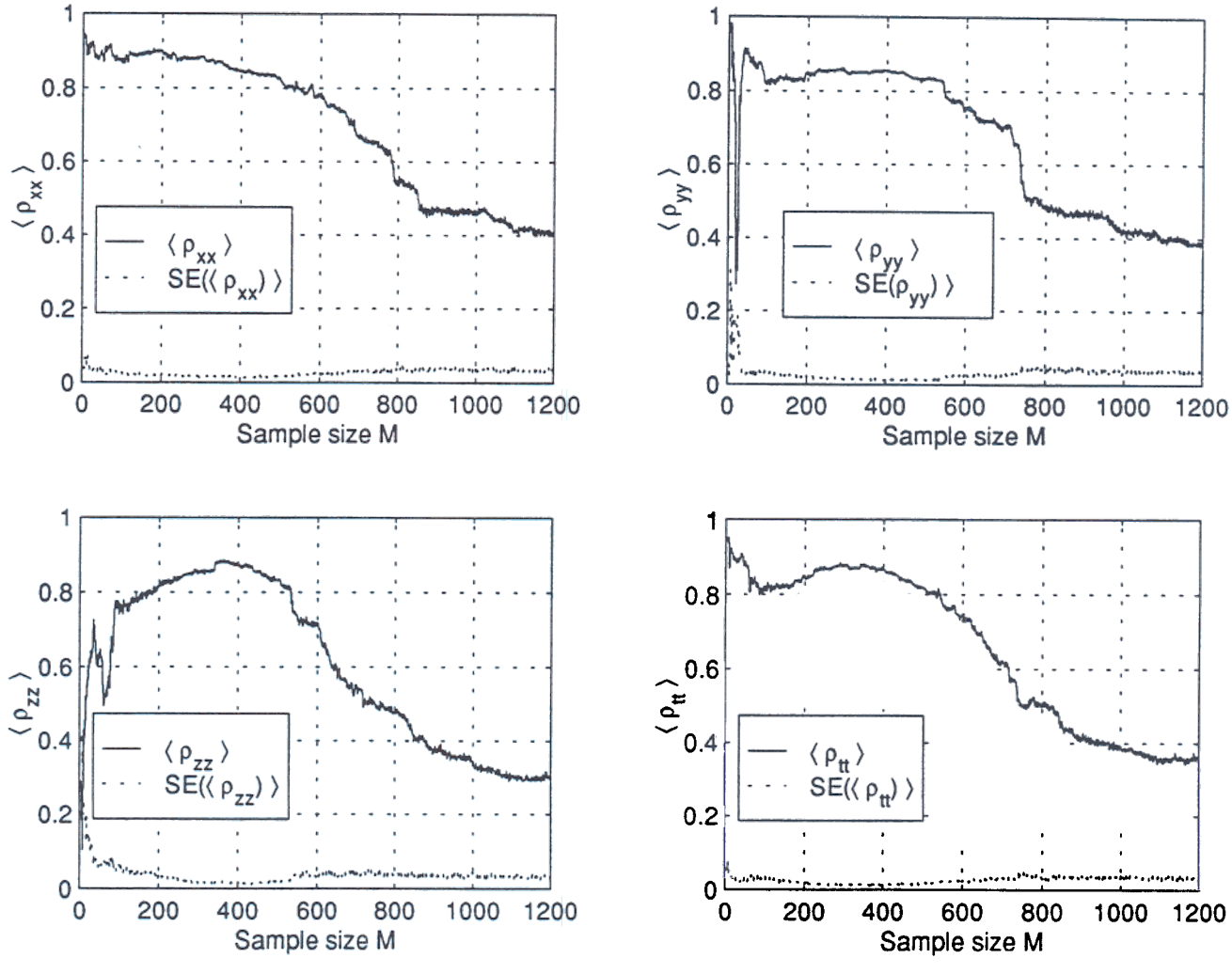


Figure 112: Spatial correlation coefficients between $E_\alpha(r_0)|^2$ and $|E_\alpha(r_1)|^2$ as a function of sample size M @ $f = 8.2$GHz, $r_0 = 91$mm, $r_1 = 94$mm for full data set.

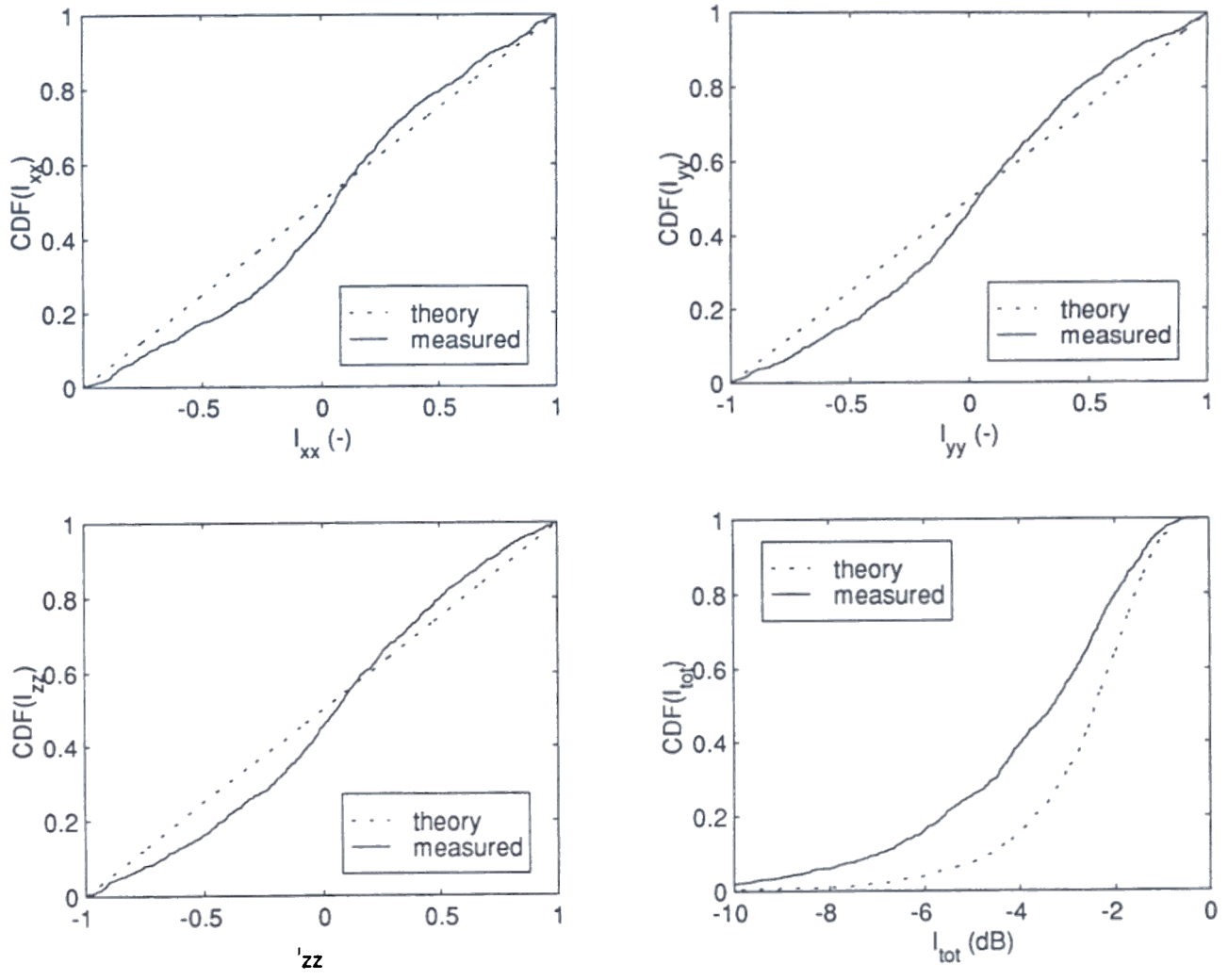


Figure 113: Theoretical and measured cumulative distribution functions of field inhomogeneity coefficients @ $f = 8.2$GHz, $r_0 = 91$mm, $r_1 = 94$mm for decimated data set ($m_\alpha = 3$).

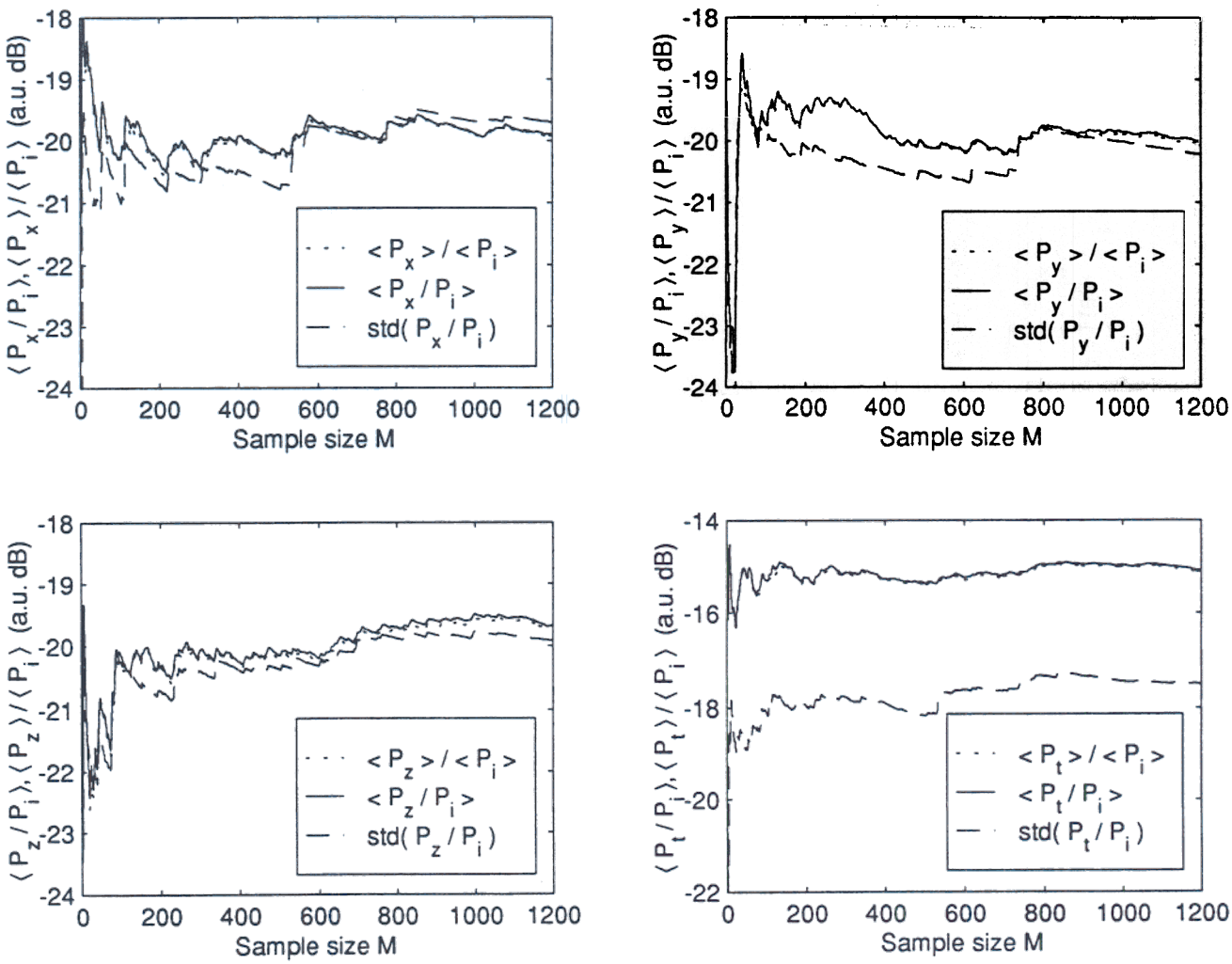


Figure 114: Mean of ratio of power densities vs. ratio of mean of power densities as a function of sample size M @ $f = 8.2$GHz, $r = 91$mm for full data set.

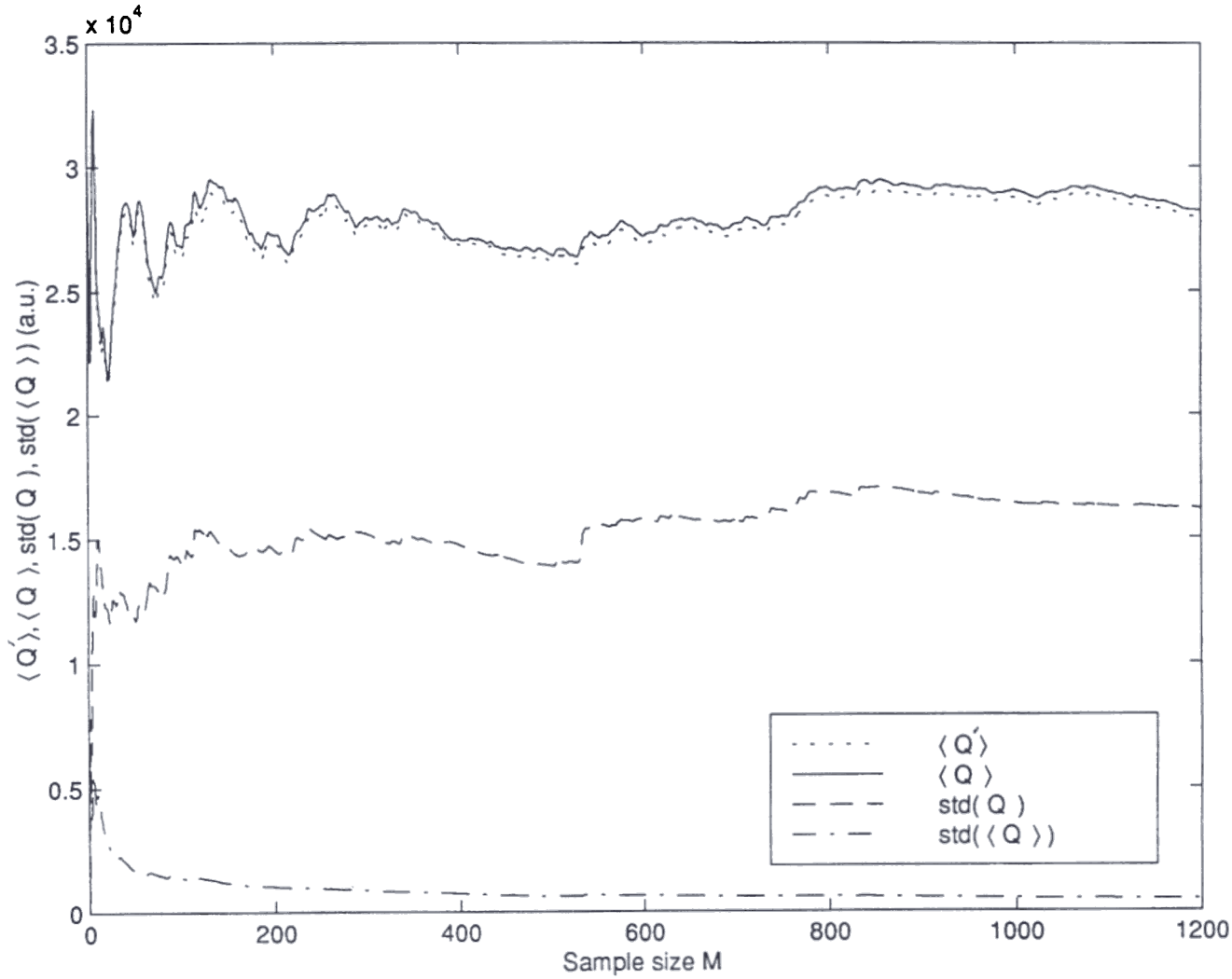


Figure 115: Theoretical composite quality factors computed for mean of ratio of total power densities vs. ratio of mean of total power densities as a function of sample size M @ $f = 8.2$GHz, $r = 91$mm for full data set (assuming free space wave impedance).

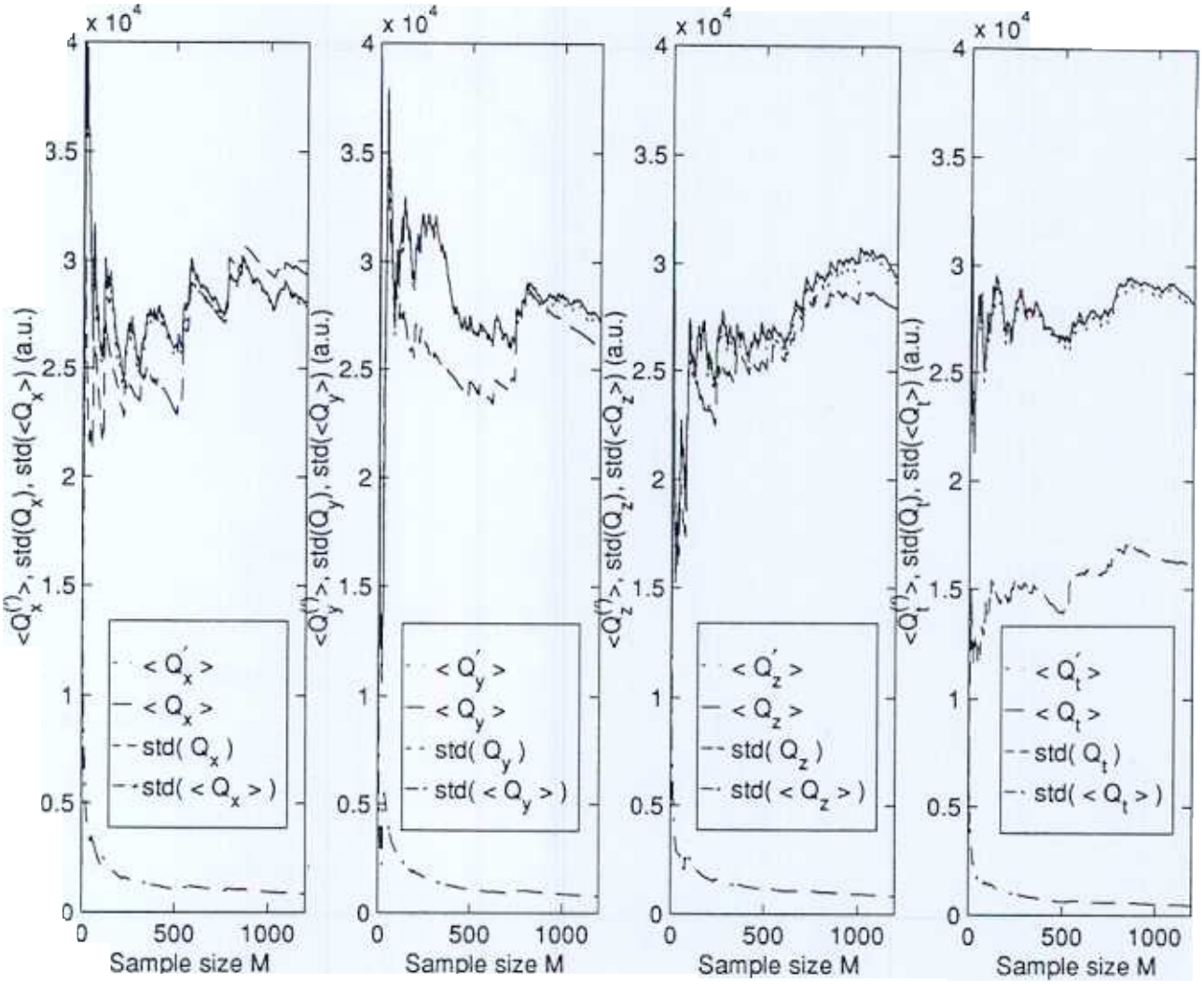


Figure 116: Theoretical composite quality factors computed for mean of ratio of individual power densities vs. ratio of mean of individual power densities as a function of sample size M @ $f = 8.2$GHz, $r = 91$mm for full data set (assuming free space wave impedance).

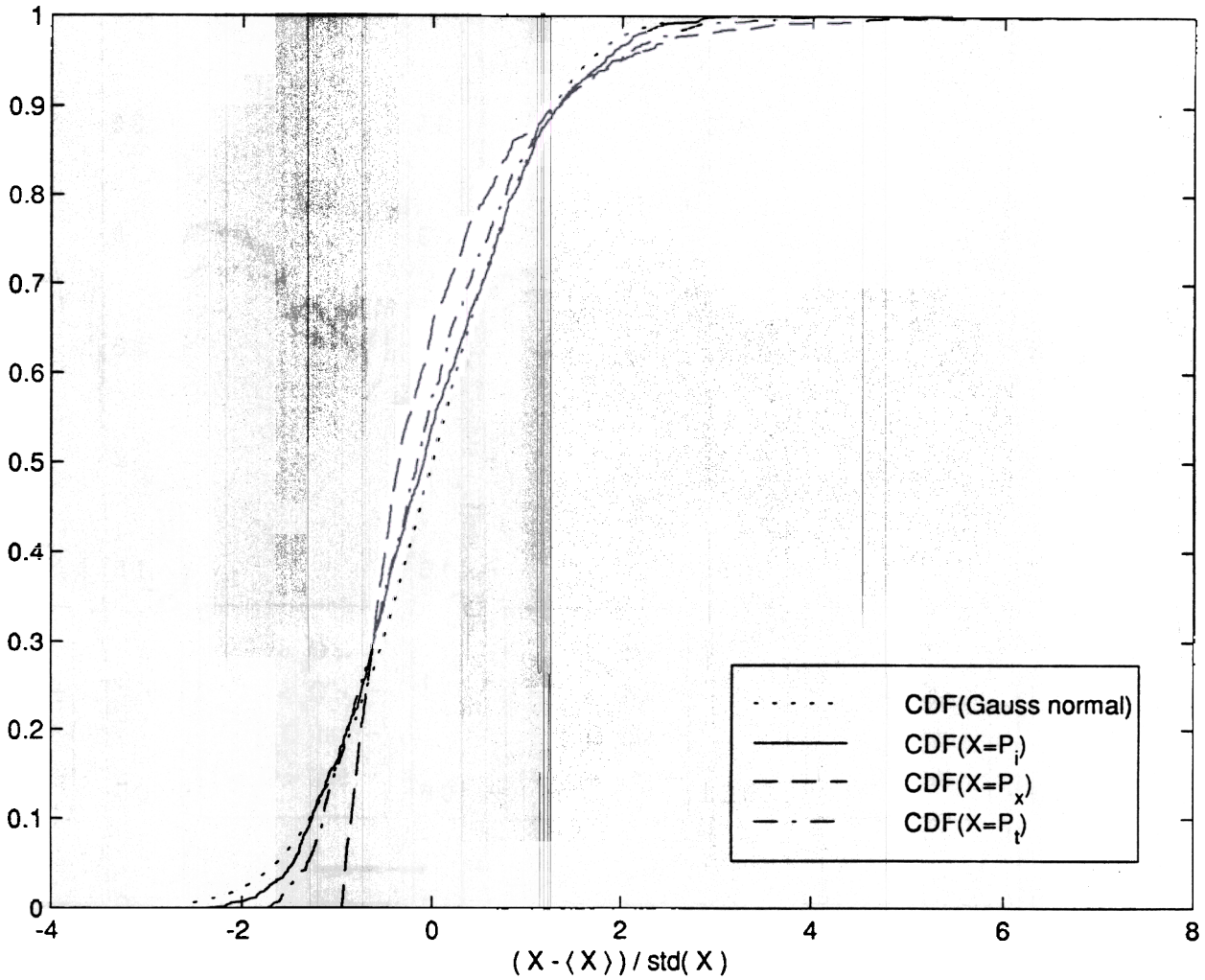


Figure 117: Cumulative distribution functions of measured input power P_i, received rectilinear power P_α and received total power P_t @ $f = 8.2$GHz, $r = 91$mm for full data set.

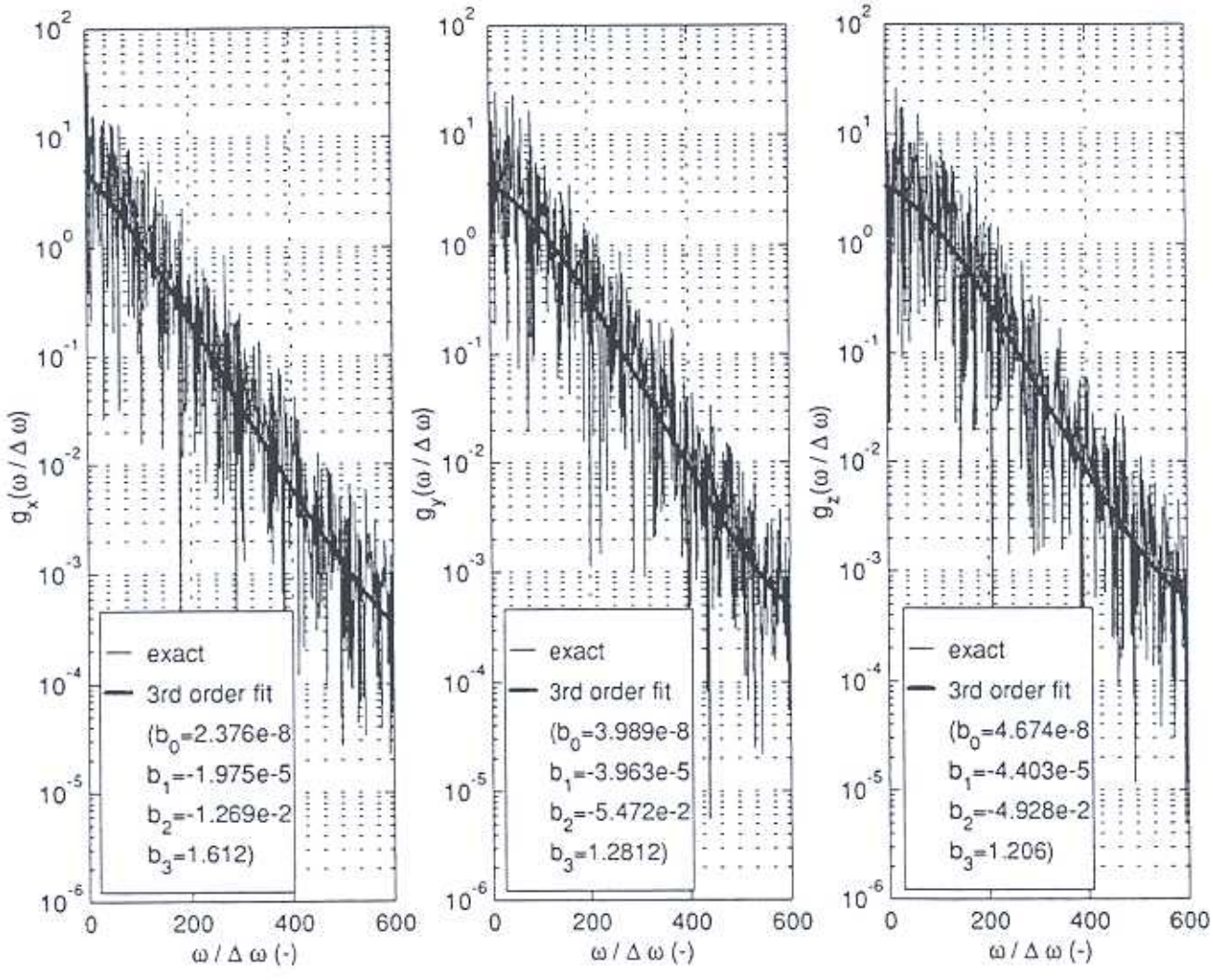


Figure 118: Normalized power autospectral density functions g_α and 3rd order exponential fits as a function of normalized spectral wall position $\omega/\Delta\omega$ @ $f = 8.2$GHz, $r = 91$mm for full data set.

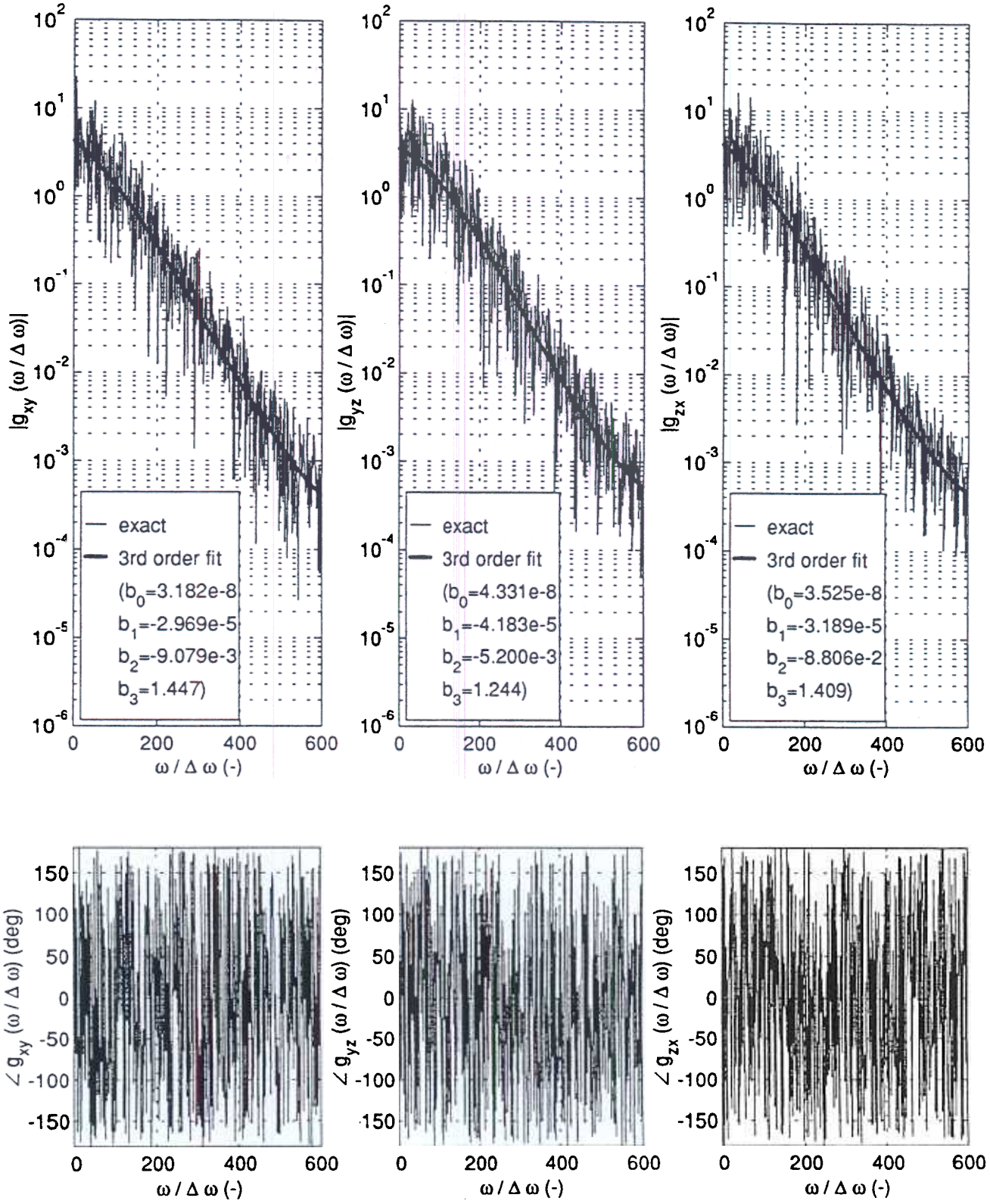


Figure 119: Normalized power cross-spectral density functions $g_{\alpha\beta}$ and 3rd order exponential fits as a function of normalized spectral wall position $\omega/\Delta\omega$ @ $f = 8.2$GHz, $r = 91$mm for full data set.

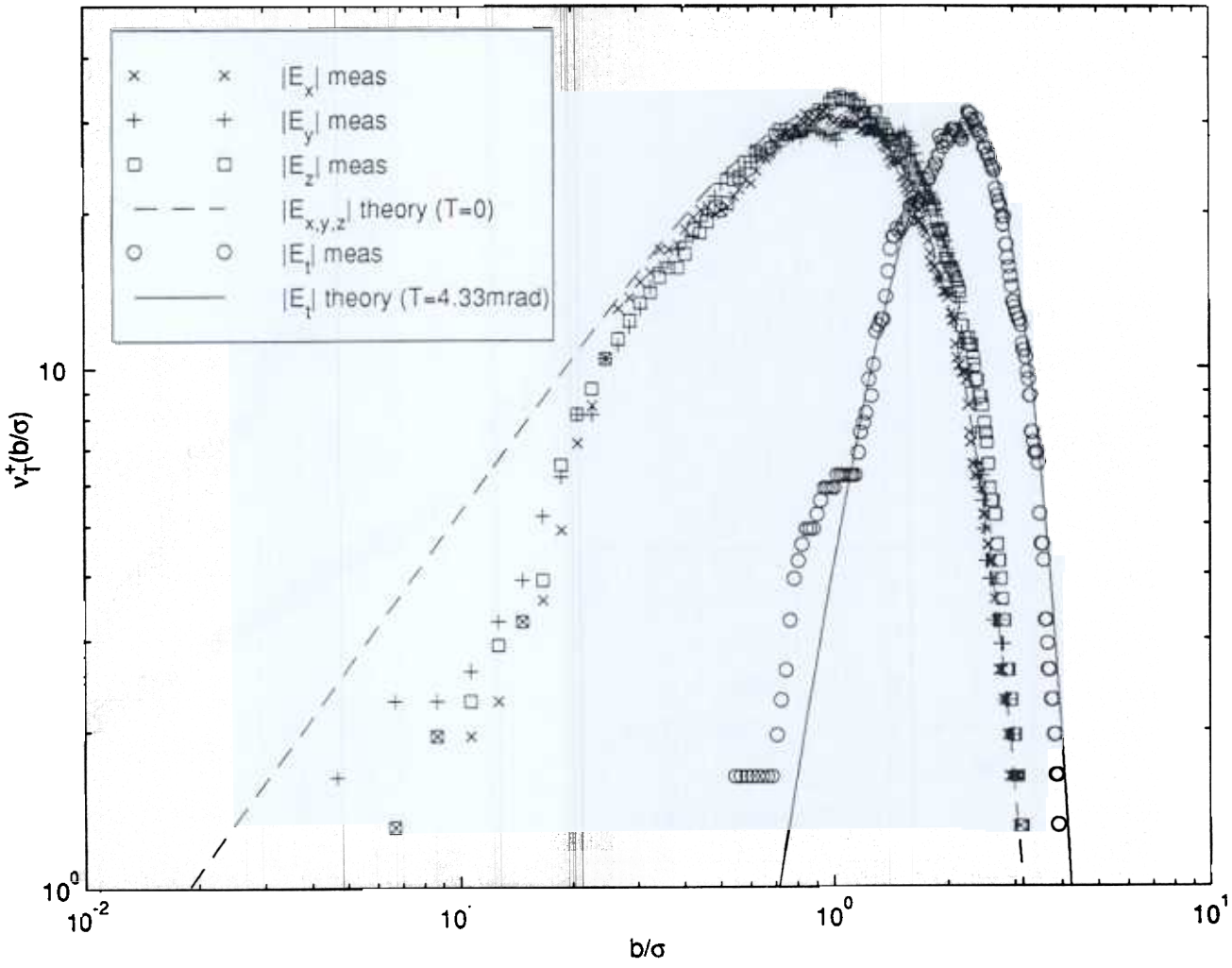


Figure 120: Theoretical and measured upward threshold crossing rate ν_T^+ for field magnitudes as a function of threshold level b/σ_0 @ f = 8.2GHz, r = 91mm for full data set.

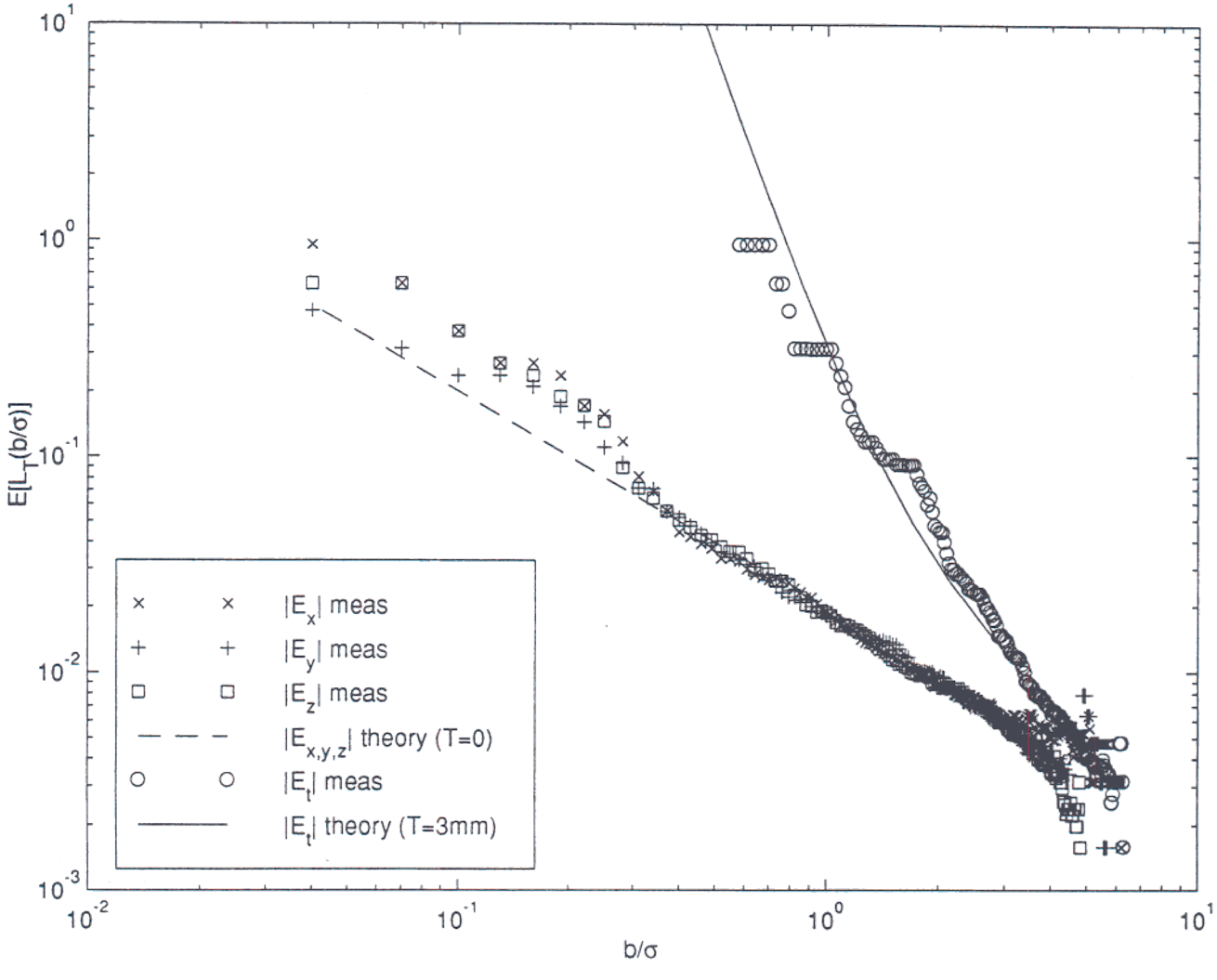


Figure 121: Theoretical and measured mean excursion length $\mathrm{E}[\mathcal{L}_T]$ for field magnitudes as a function of threshold level b/σ_0 @ $f = 8.2$GHz, $r = 91$mm for full data set.

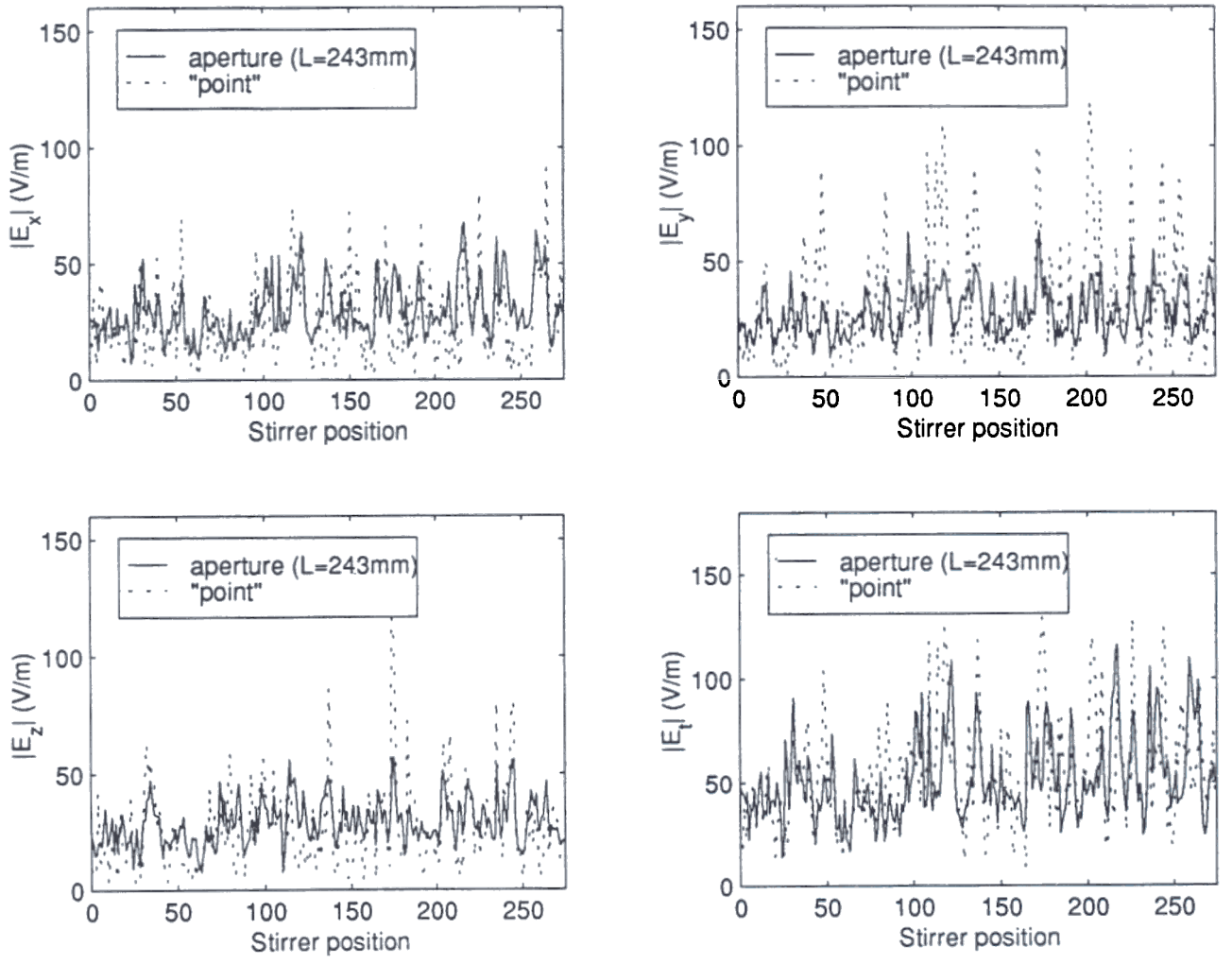


Figure 122: Sweep data for synthetic Rx apertures of minimum and maximum width L @ $f = 2.5$GHz

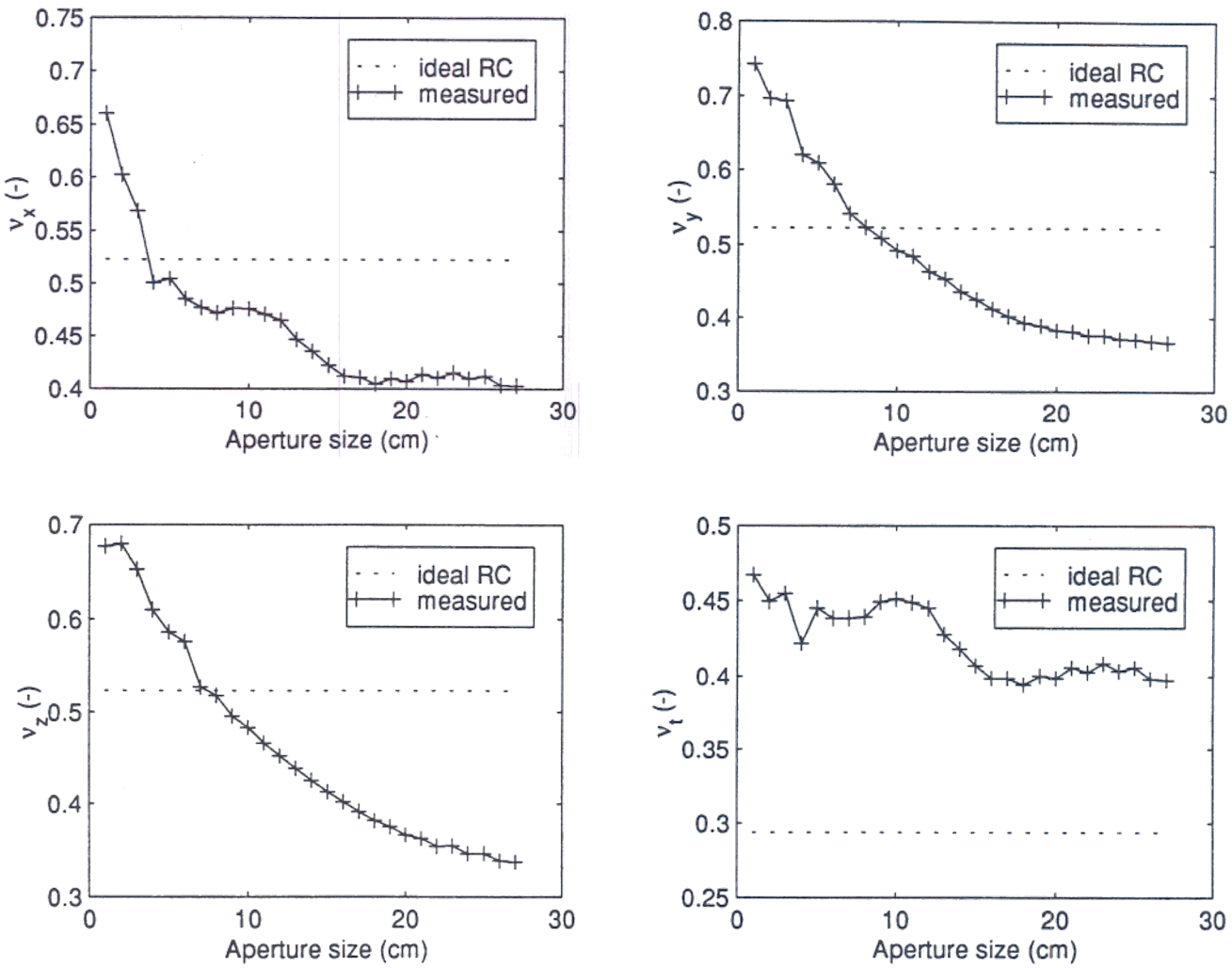


Figure 123: Coefficients of variation ν_α for $|E_\alpha|$ ($\alpha = x, y, z$) as a function of width L of synthetic Rx aperture @ $f = 2.5$GHz.

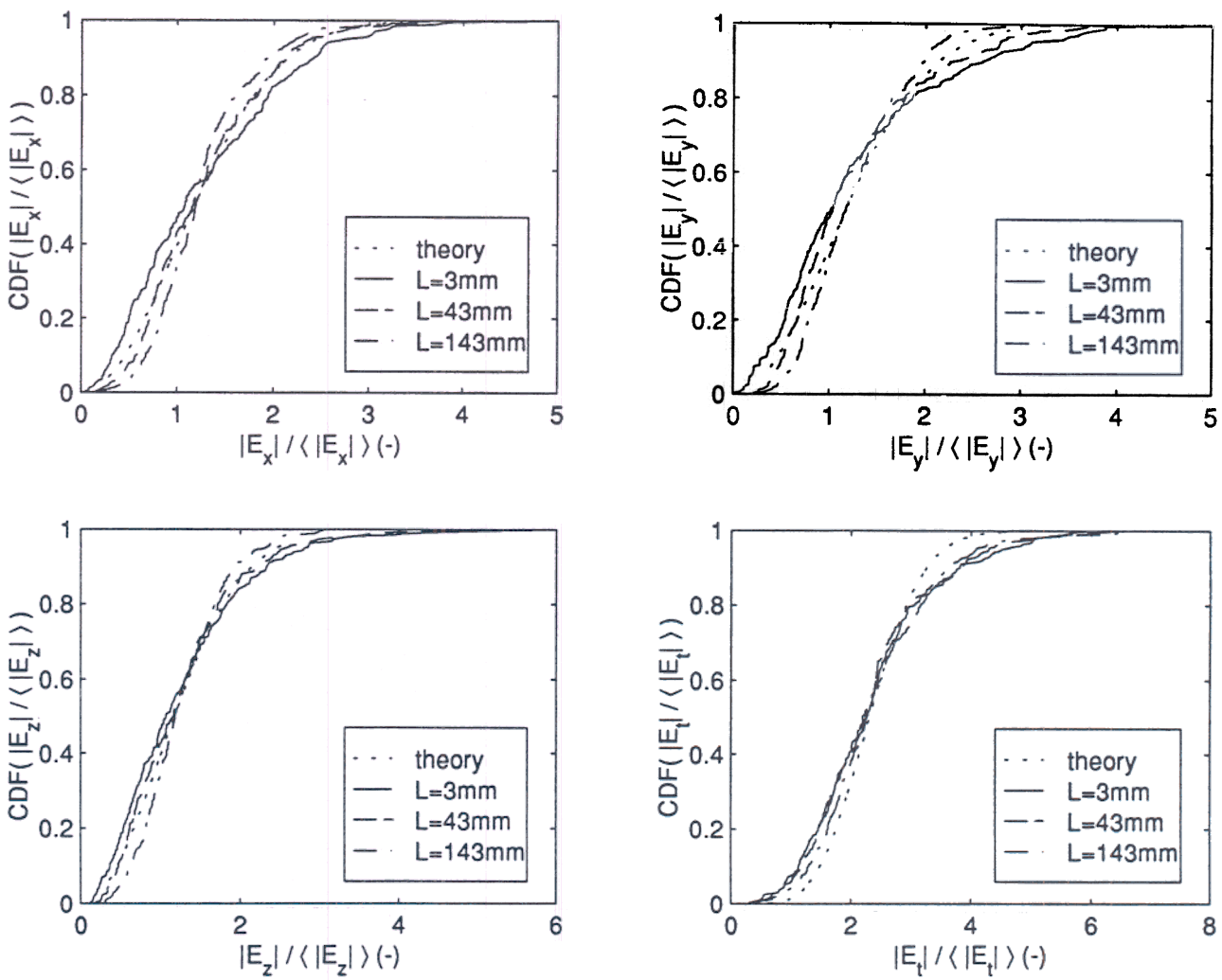


Figure 124: Theoretical and measured cumulative distribution functions of $|E_\alpha|/\langle|E_\alpha|\rangle$ (α x, y, z, t) for synthetic Rx apertures of various widths L @ $f = 2.5$GHz.

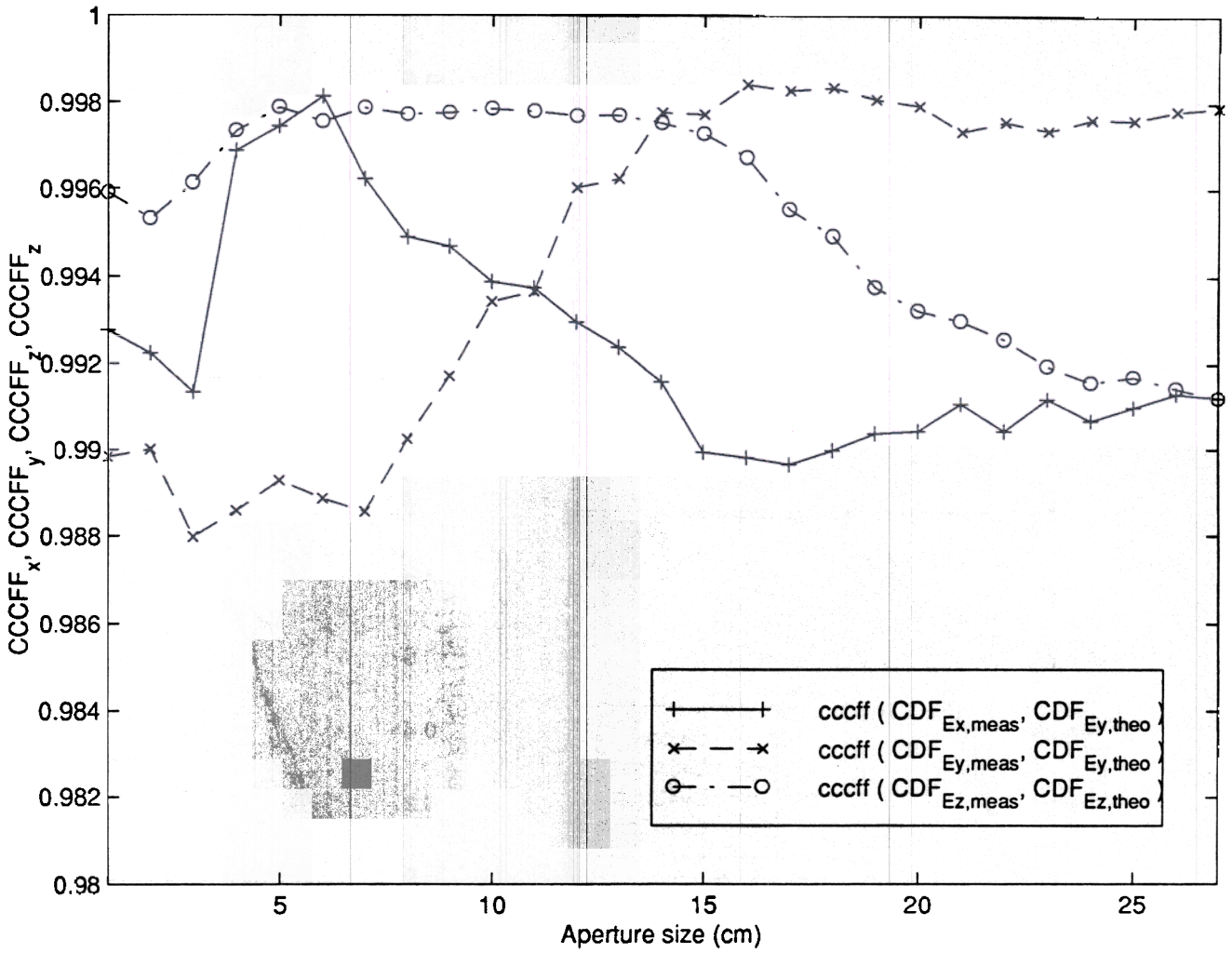


Figure 125: Crosscorrelation coefficients $\varrho_{\alpha\beta}$ between theoretical and measured cumulative distribution functions of $|E_\alpha|/\langle|E_\alpha|\rangle$, $|E_\beta|/\langle|E_\beta|\rangle$ $(\alpha, \beta = x, y, z, t)$ as a function of aperture width L @ $f = 2.5$GHz.

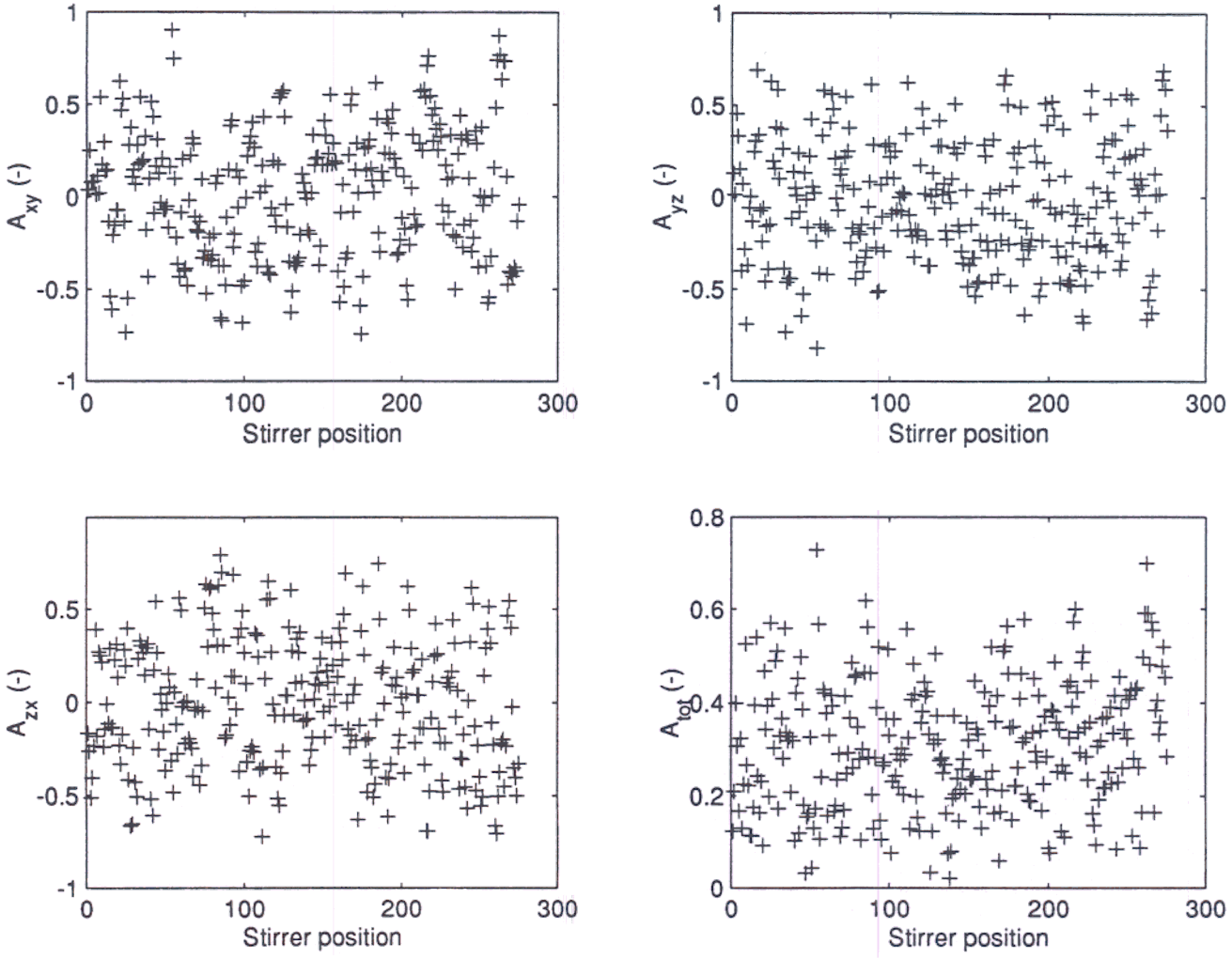


Figure 126: Measured field anisotropy coefficients $A_{\alpha\beta}$ and A_{tot} for synthetic Rx aperture of maximum width ($L = 243$mm) @ $f = 2.5$GHz.

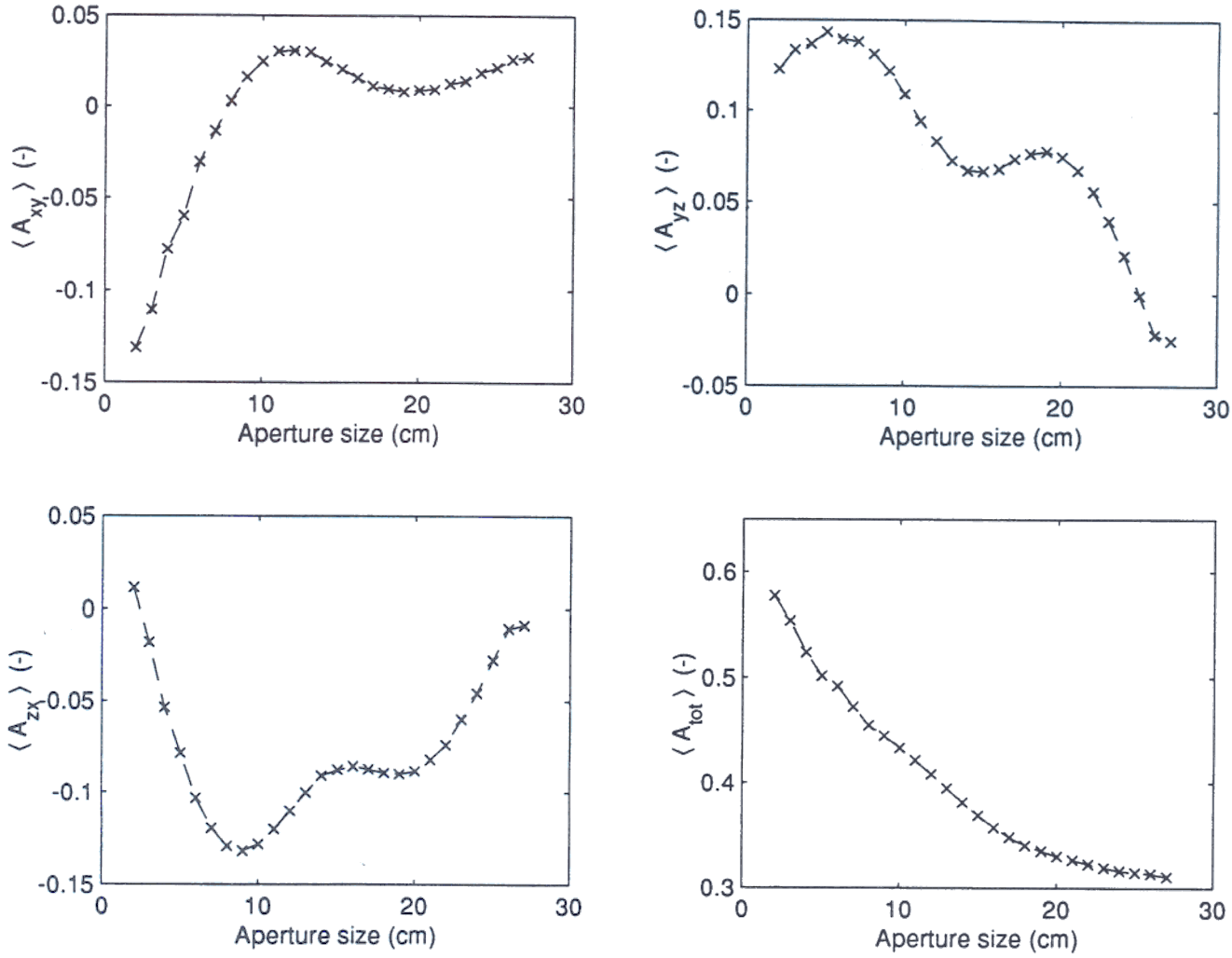


Figure 127: Single-sample average of measured field anisotropy coefficients $A_{\alpha\beta}$ and A_{tot} as a function of width L of synthetic Rx aperture @ $f = 2.5$GHz for full data set.

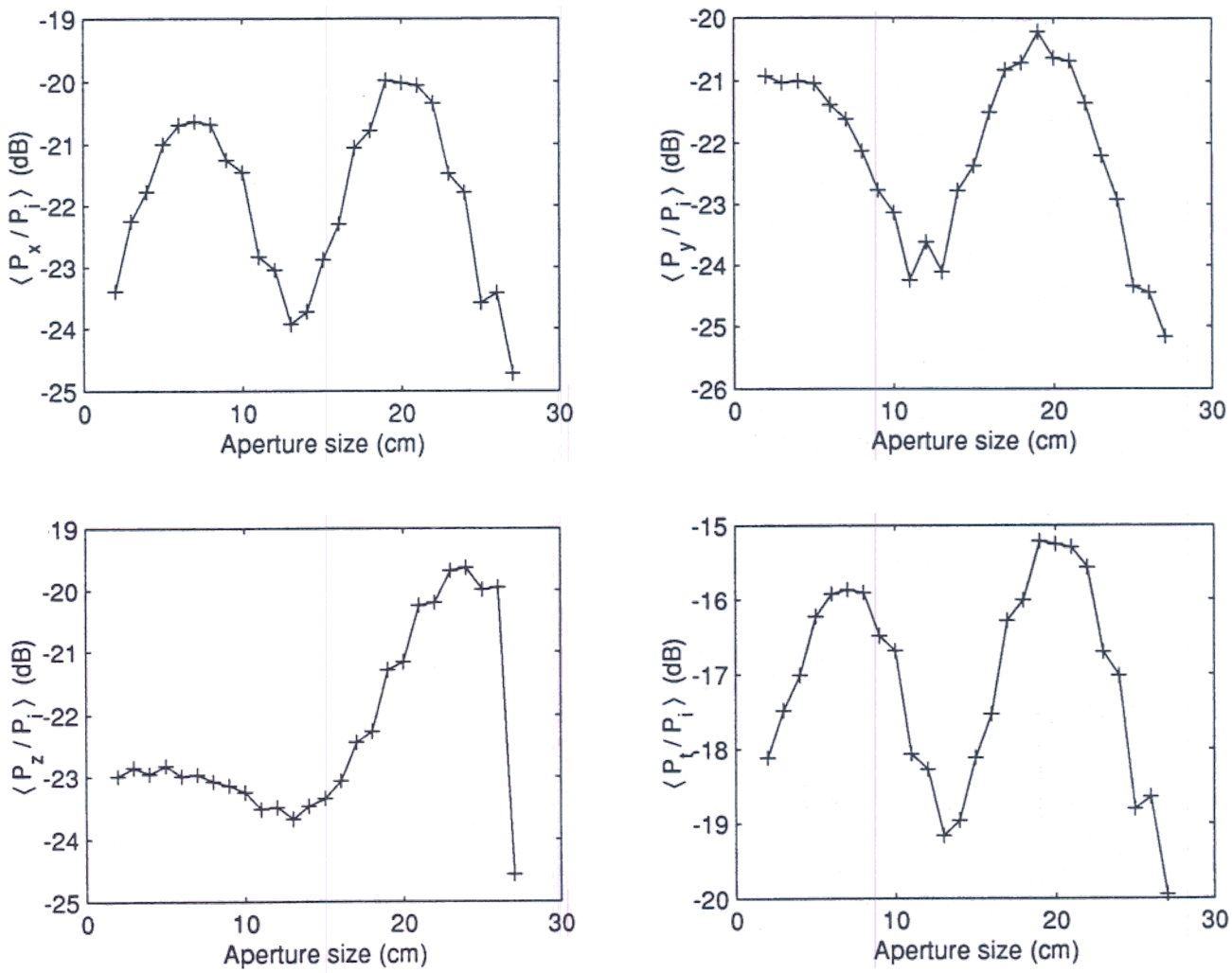


Figure 128: Bootstrap averaged insertion loss $\langle P_\alpha / P_i \rangle$ ($\alpha = x, y, z, t$) as a function of width L of synthetic Rx aperture @ $f = 2.5$GHz.

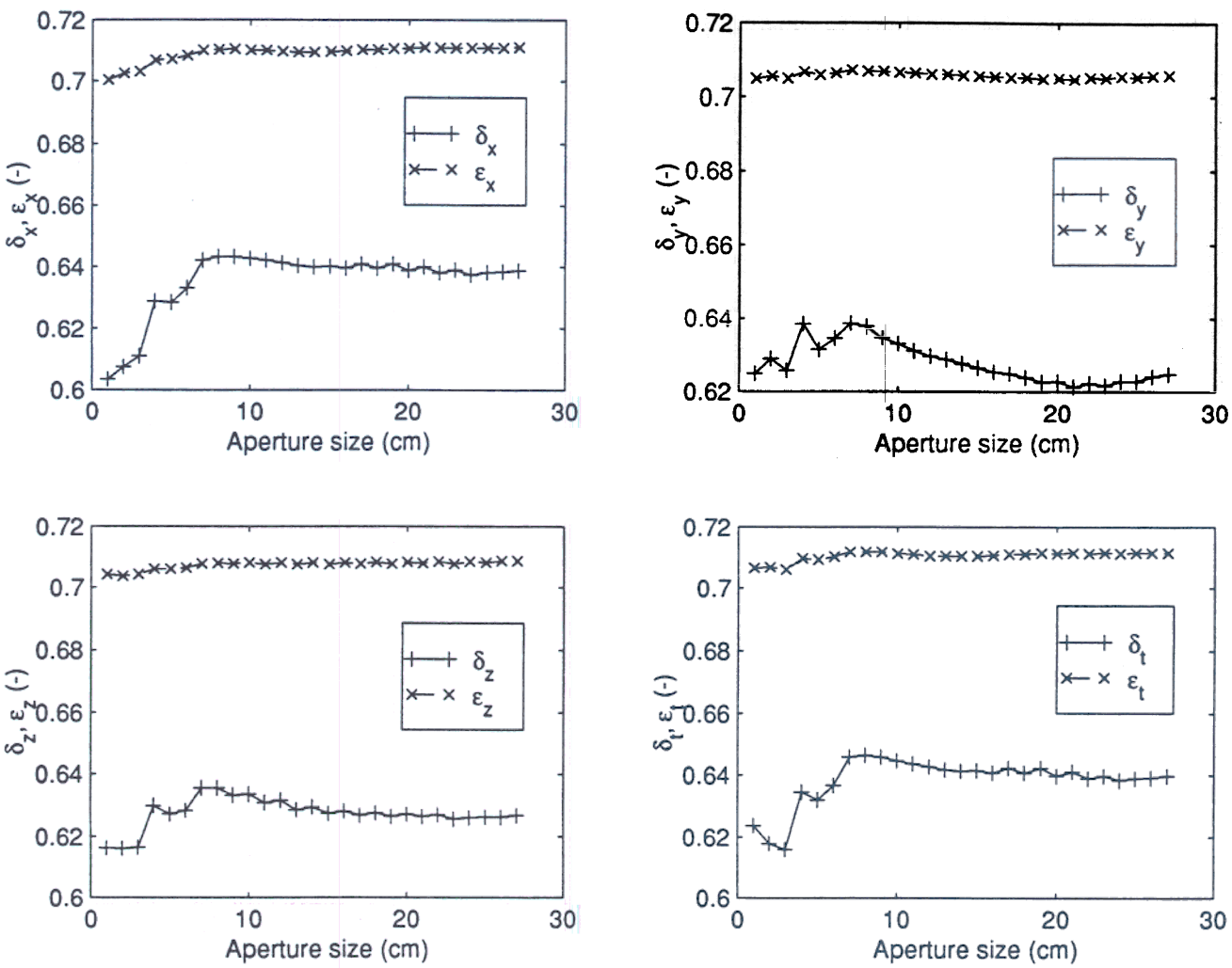


Figure 129: Normalized spectral bandwidths δ_α, ϵ_α ($\alpha = x, y, z, t$) as a function of width L of for synthetic Rx aperture @ $f = 2.5$GHz.

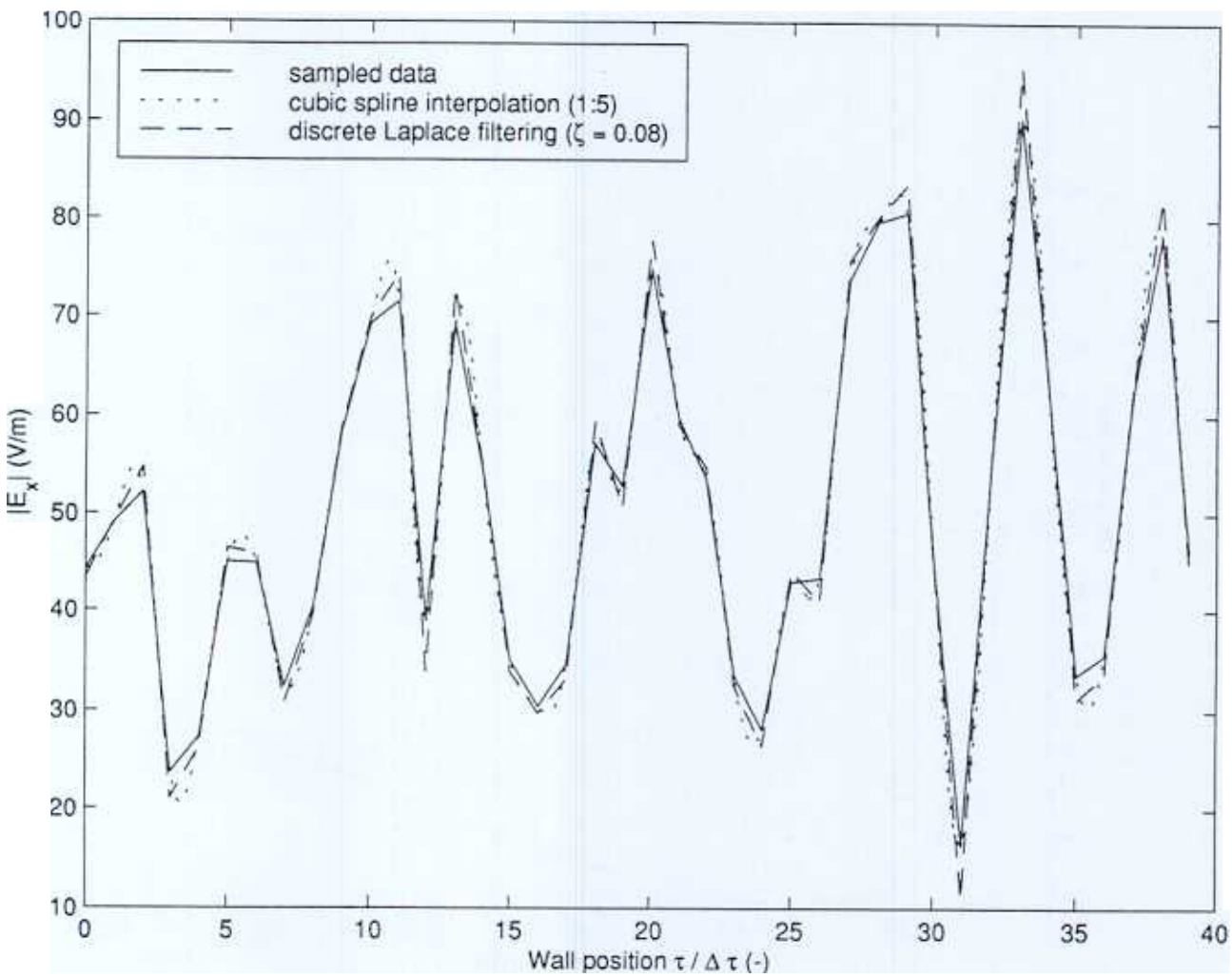


Figure 130: Peak restoration for stirrer data using cubic spline interpolation and digital Laplace filtering with $\zeta = 0.08$ @ $f = 2.5$GHz, $r = 91$mm (first 40 data points only).

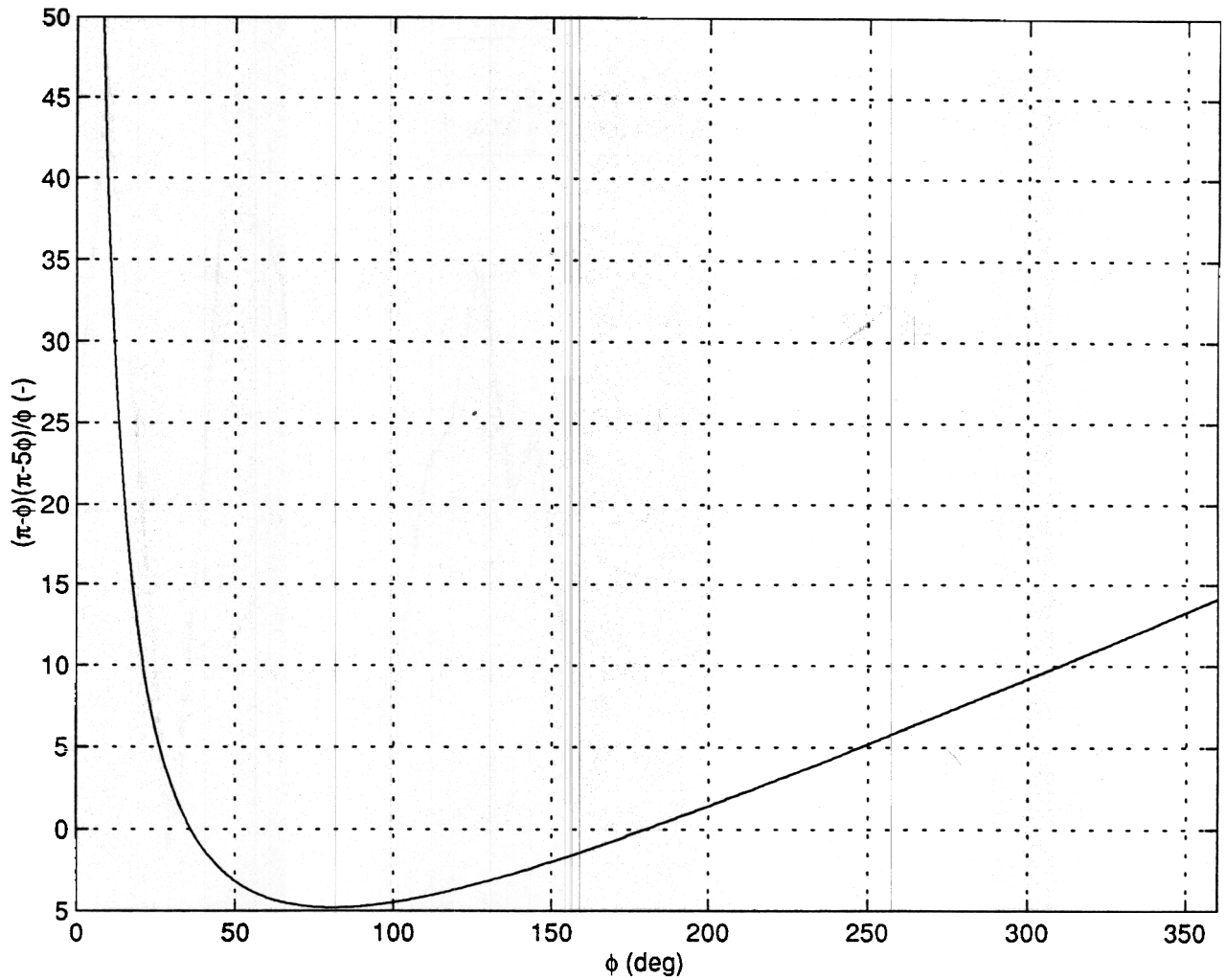


Figure 131: Integrand of edge line integral (edge length contribution to mode density) as a function of dihedral opening angle ϕ.

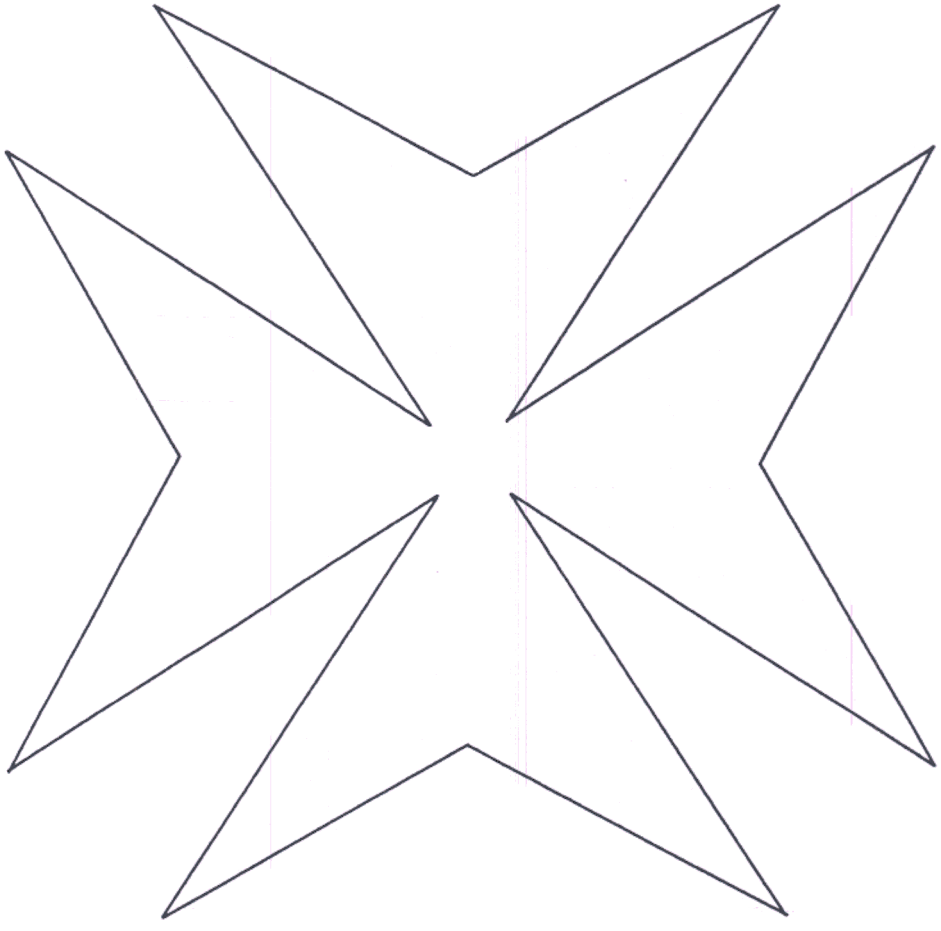
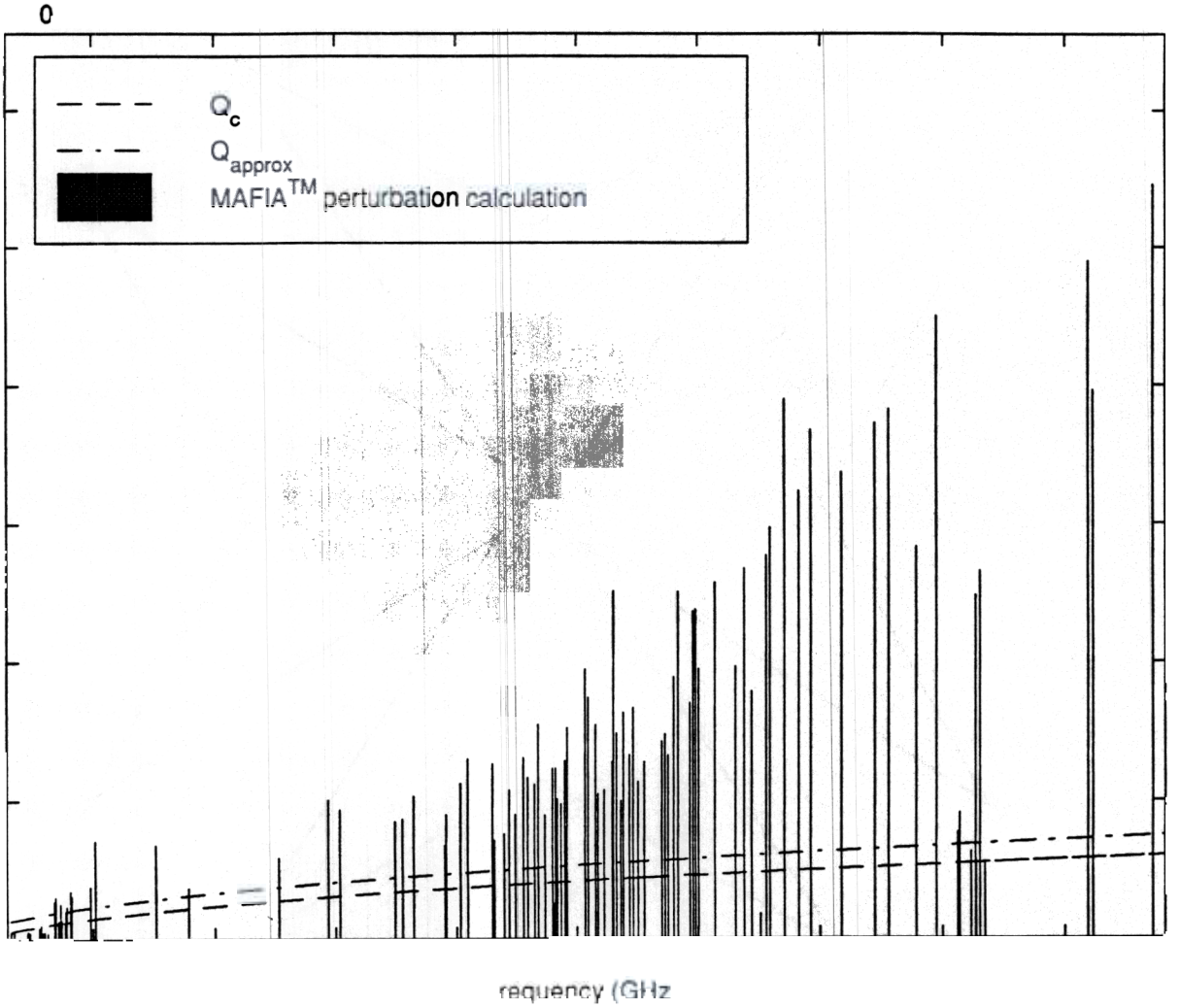


Figure 132: Ground plan of a 4-segment 'bow-tie' room.



adius R 35m

pole solution of MAFIA

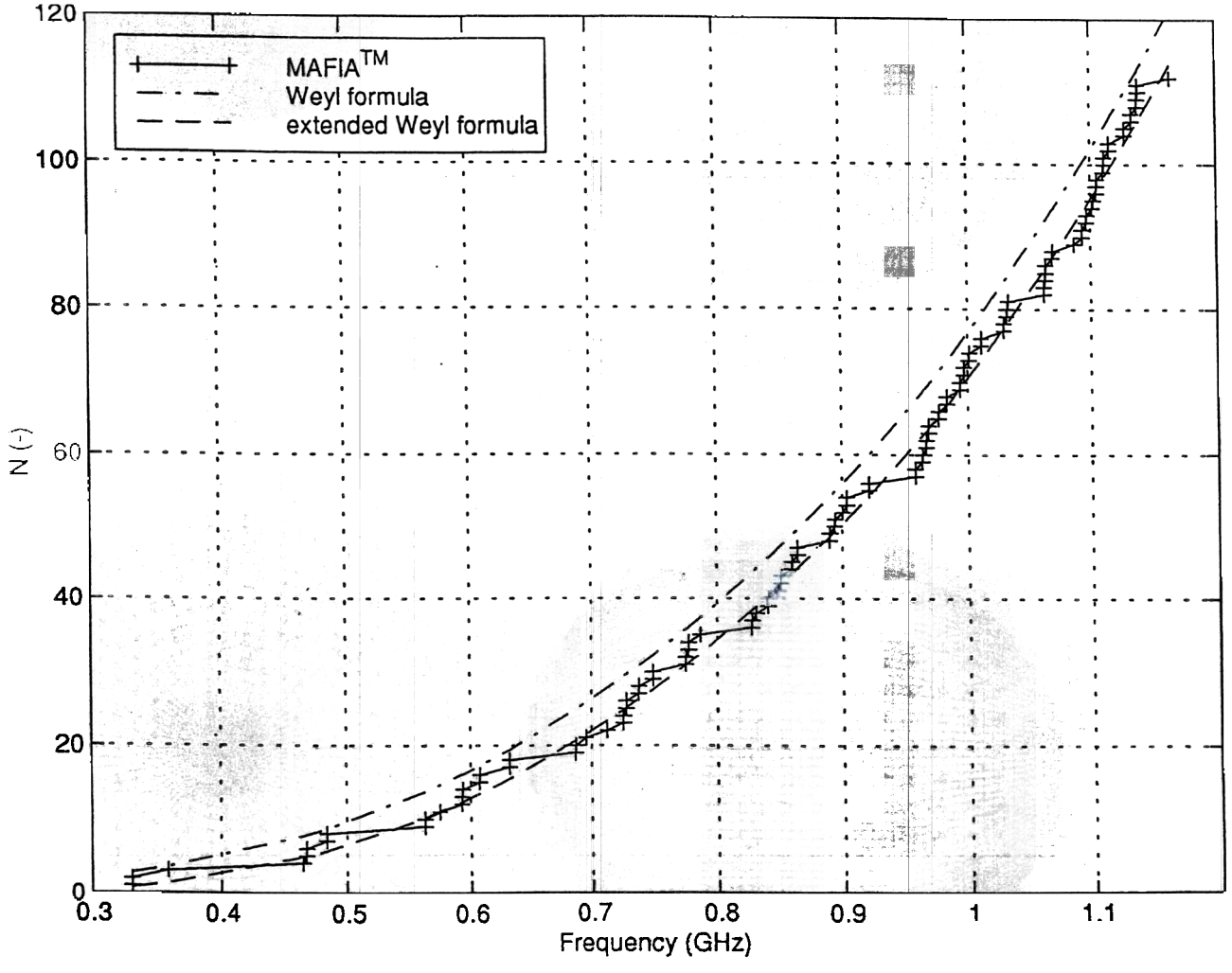


Figure 134: Comparison between cumulative mode count for 3D stadium cavity obtained with MAFIA™, classical Weyl formula and extended Weyl formula.

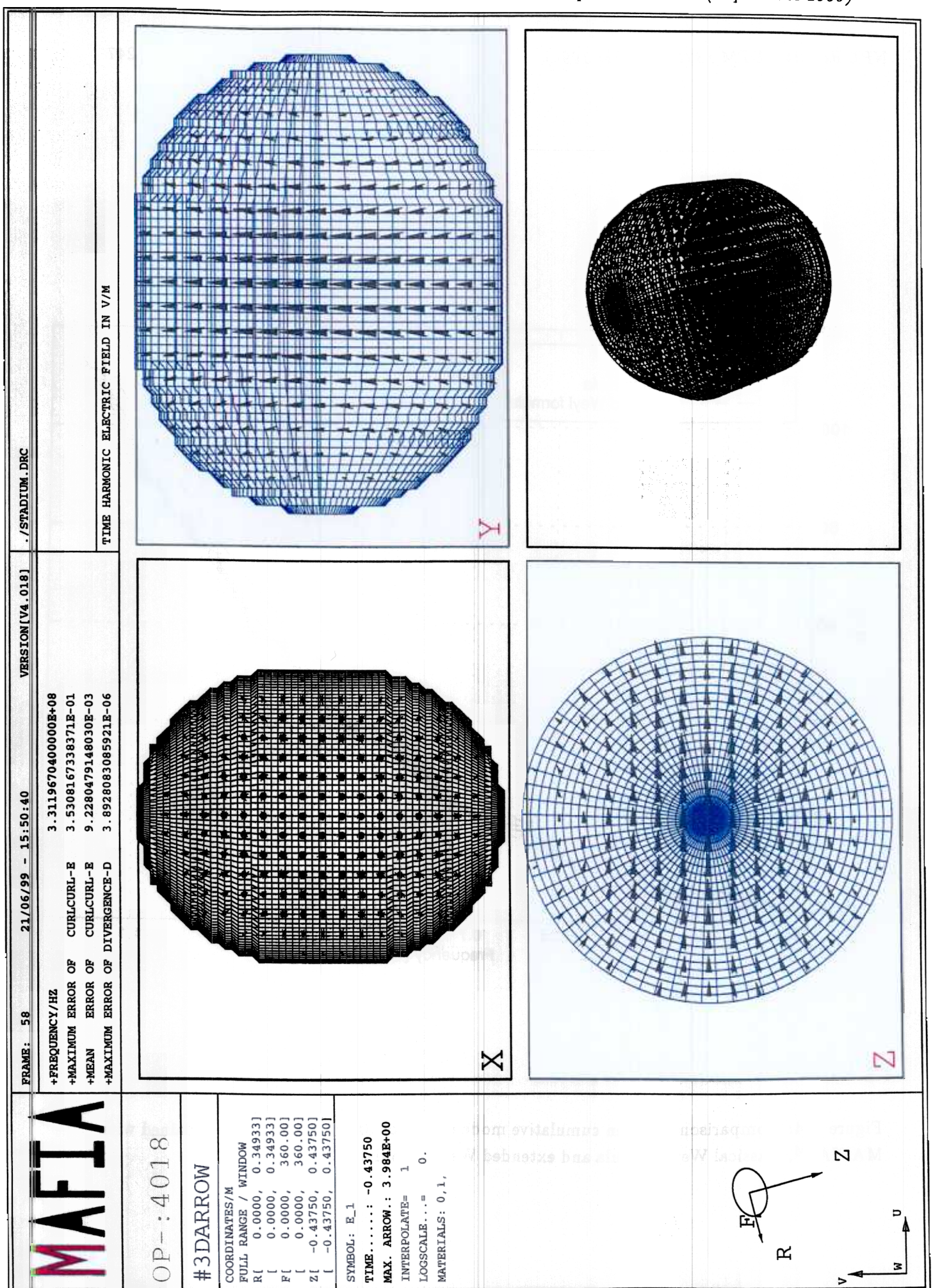


Figure 135: Distribution of $\underline{E}_t$ for 1st eigenmode of 3D stadium ($R = 0.35$m, $a = 0.175$m).

MAFIA

FRAME: 9 21/06/99 - 15:50:40 VERSION[V4.018]

./STADIUM.DRC

+FREQUENCY/HZ 3.3119670400000E+08
+MAXIMUM ERROR OF CURLCURL-E 3.5308167338371E-01
+MEAN ERROR OF CURLCURL-E 9.2280479148030E-03
+MAXIMUM ERROR OF DIVERGENCE-D 3.8928083085921E-06

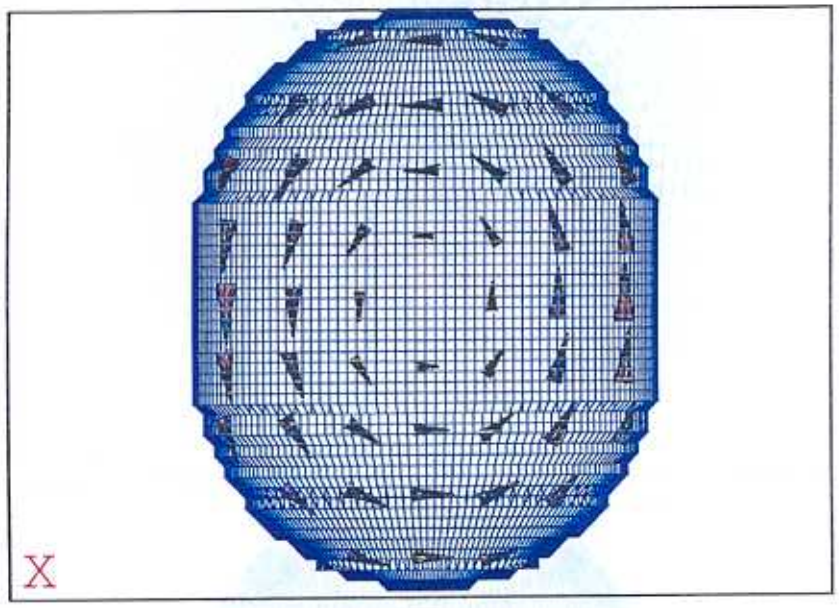
TIME HARMONIC MAGNETIC FLUX DENSITY IN VS/M**2

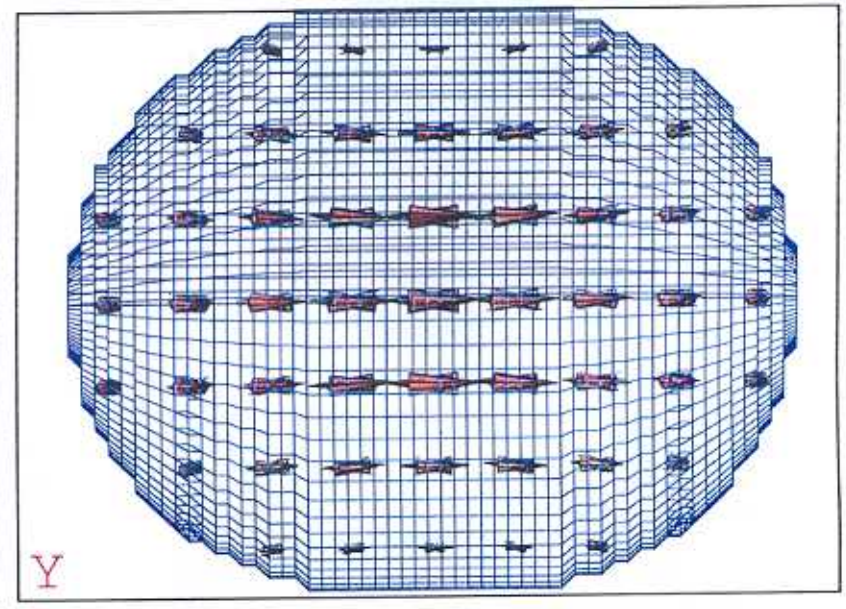
OP-:4018

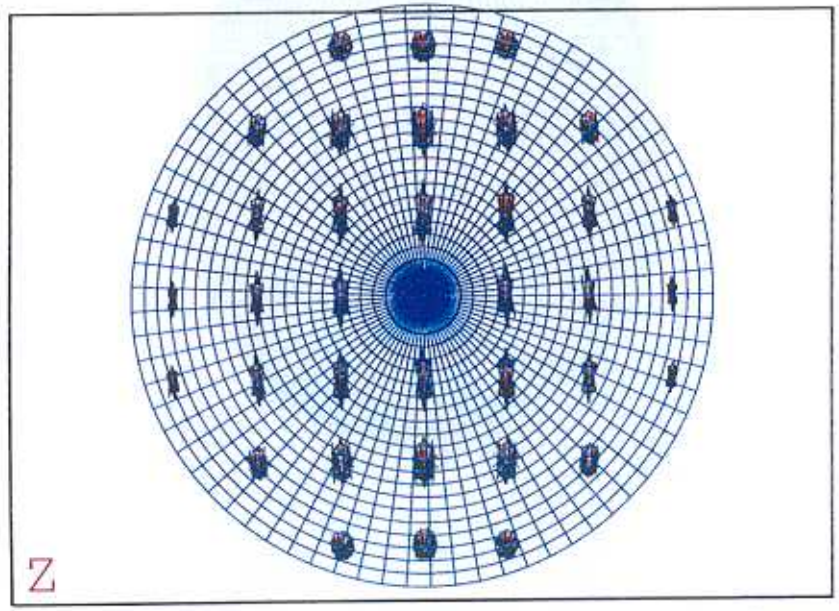
#3DARROW

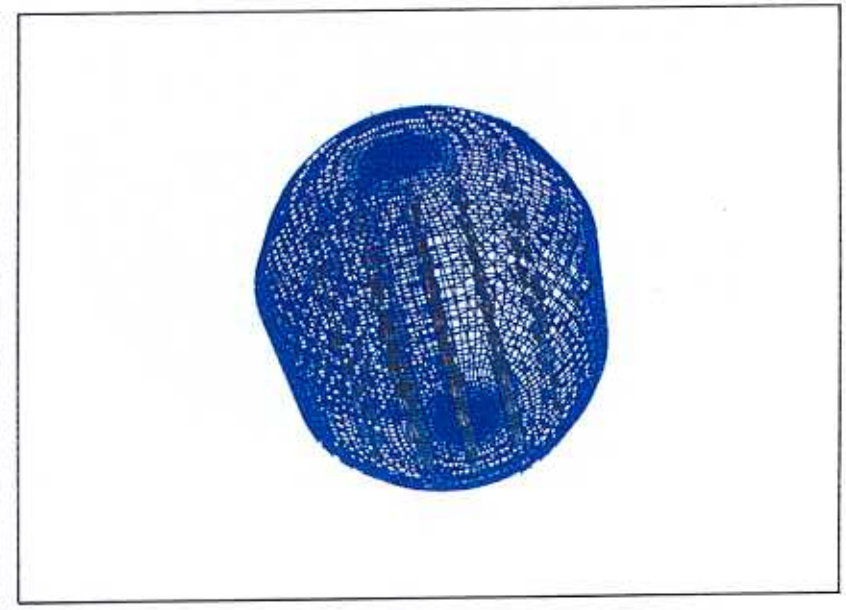
ORDINATES/M
ULL RANGE / WINDOW
[0.0000, 0.34933]
[0.0000, 0.34933]
[0.0000, 360.00]
[0.0000, 360.00]
[-0.43750, 0.43750]
[-0.43750, 0.43750]

YMBOL: B_1
IME.....: 0.
AX. ARROW.: 1.081E-08
NTERPOLATE= 1
OGSCALE...= 0.
ATERIALS: 0,1,









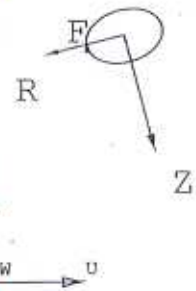


Figure 36: Distribution of B_1 for 1st eigenmode of 3D

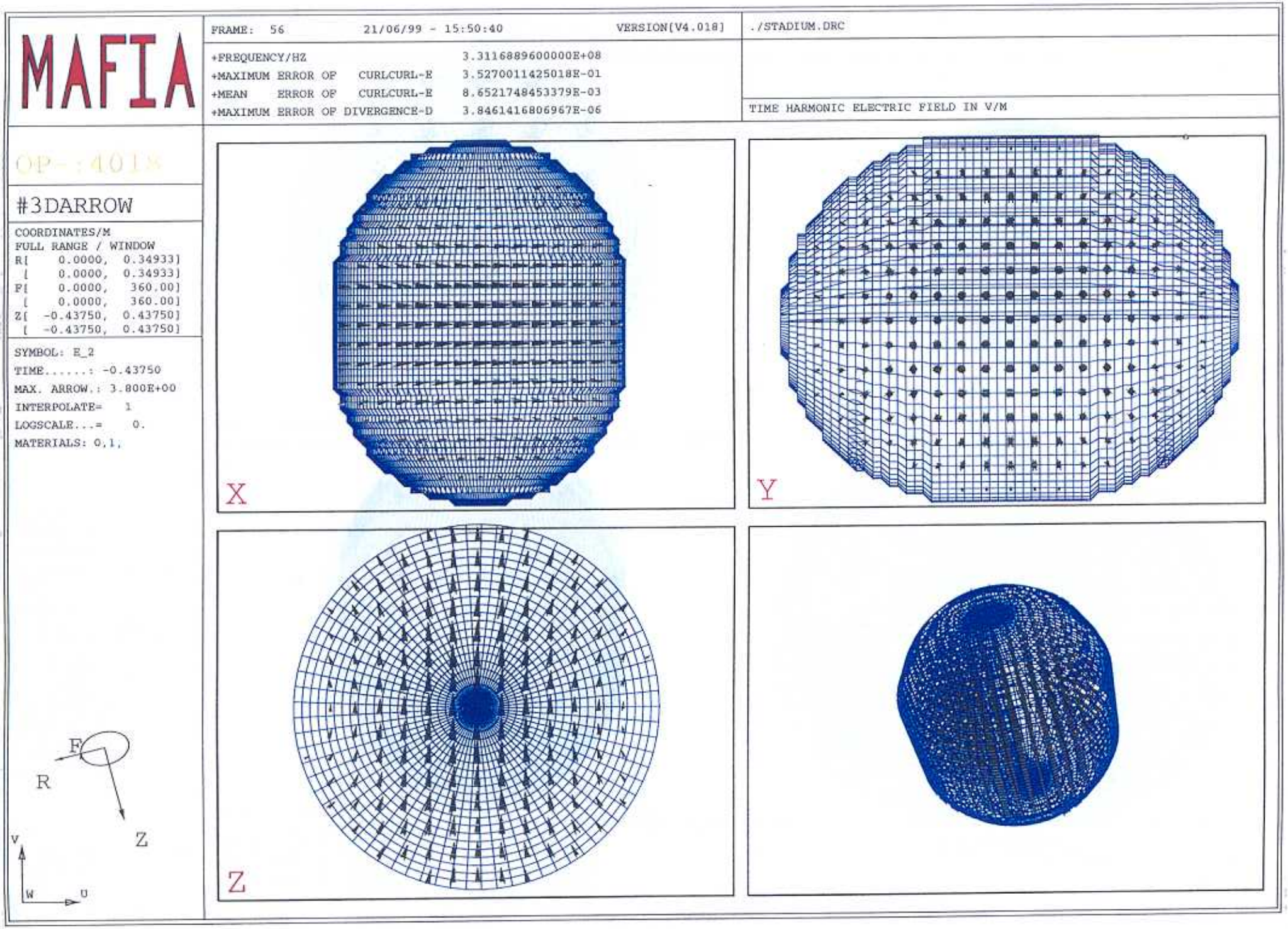


Figure 137: Distribution of $\underline{E}_z$ for 2nd eigenmode of 3D stadium ($R = 0.35$m, $a = 0.175$m).

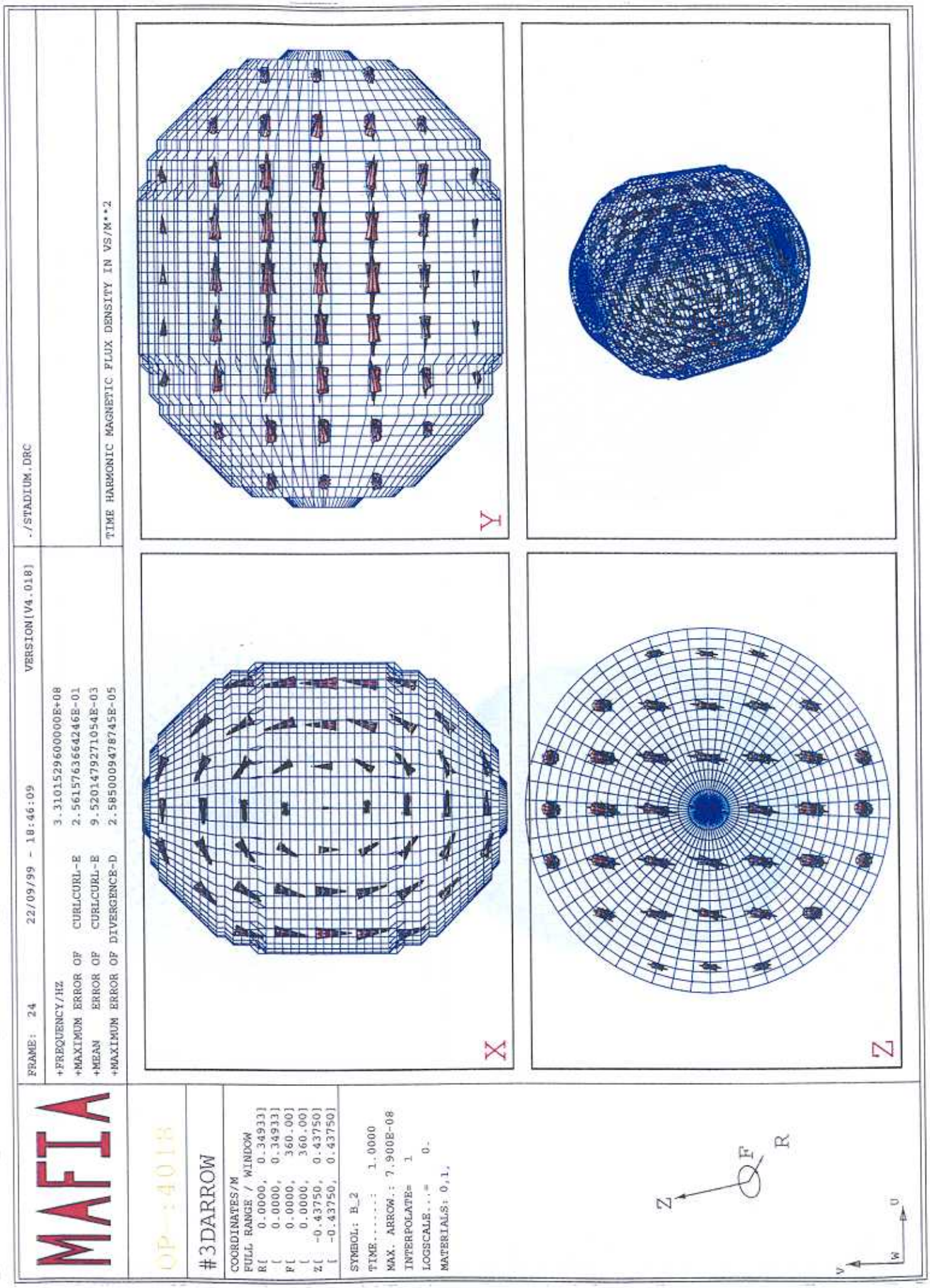


Figure 138: Distribution of $\underline{B}_t$ for 2nd eigenmode of 3D stadium ($R = 0.35$m, $a = 0.175$m).

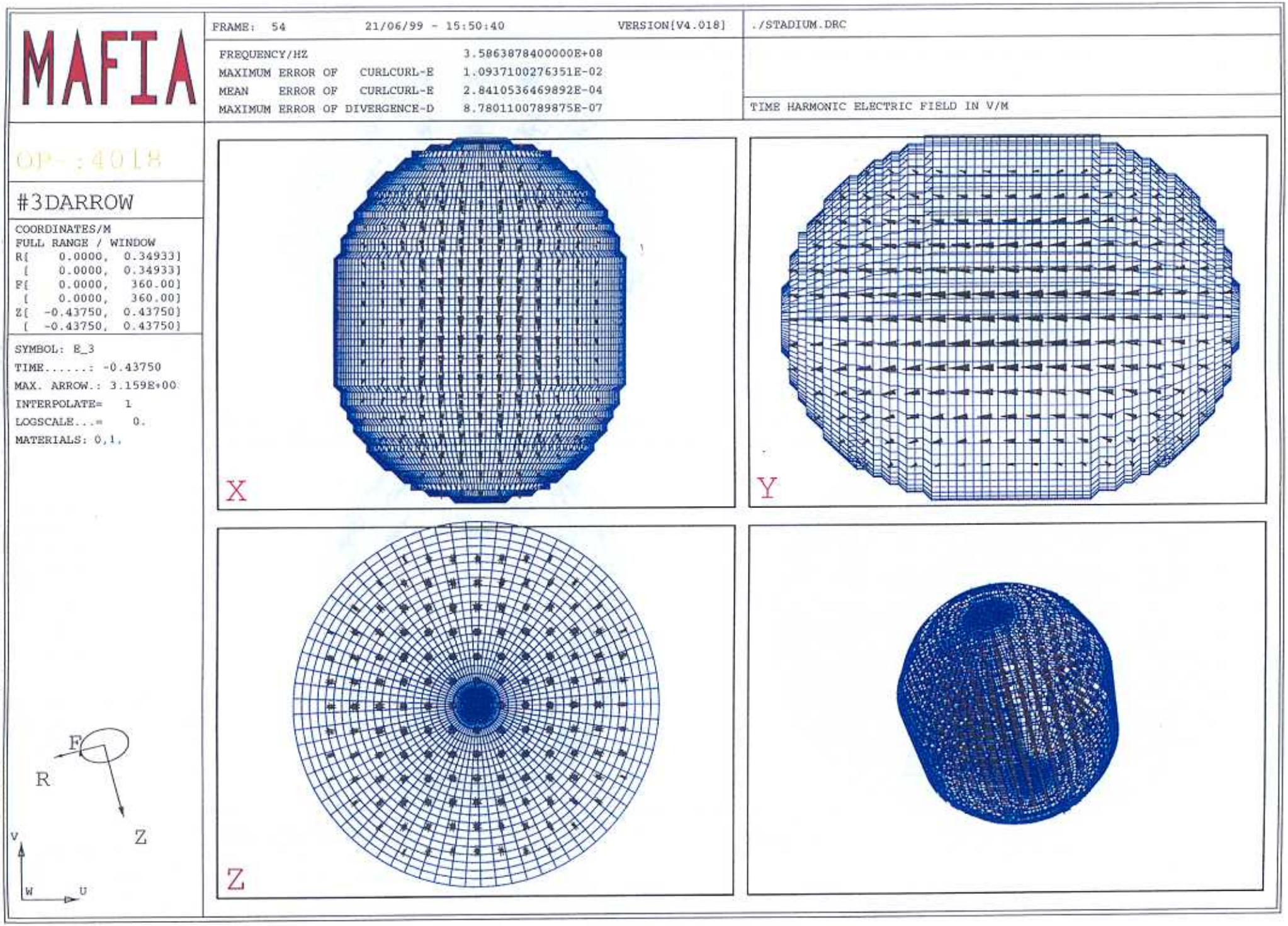


Figure 139: Distribution of $\underline{E}_t$ for 3rd eigenmode of 3D stadium ($R = 0.35$m, $a = 0.175$m).

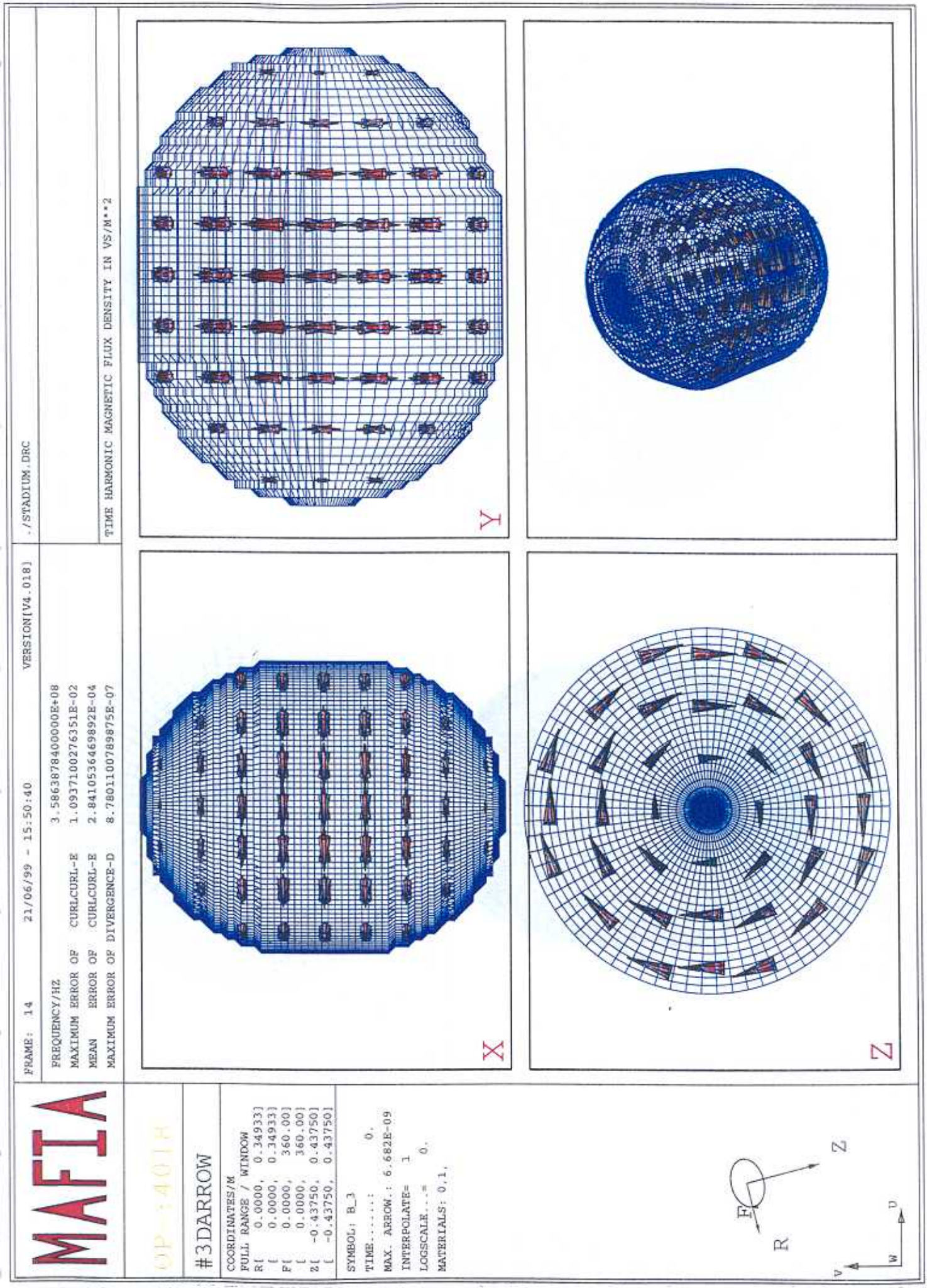


Figure 140: Distribution of $\underline{B}_t$ for 3rd eigenmode of 3D stadium ($R = 0.35$m, $a = 0.175$m).

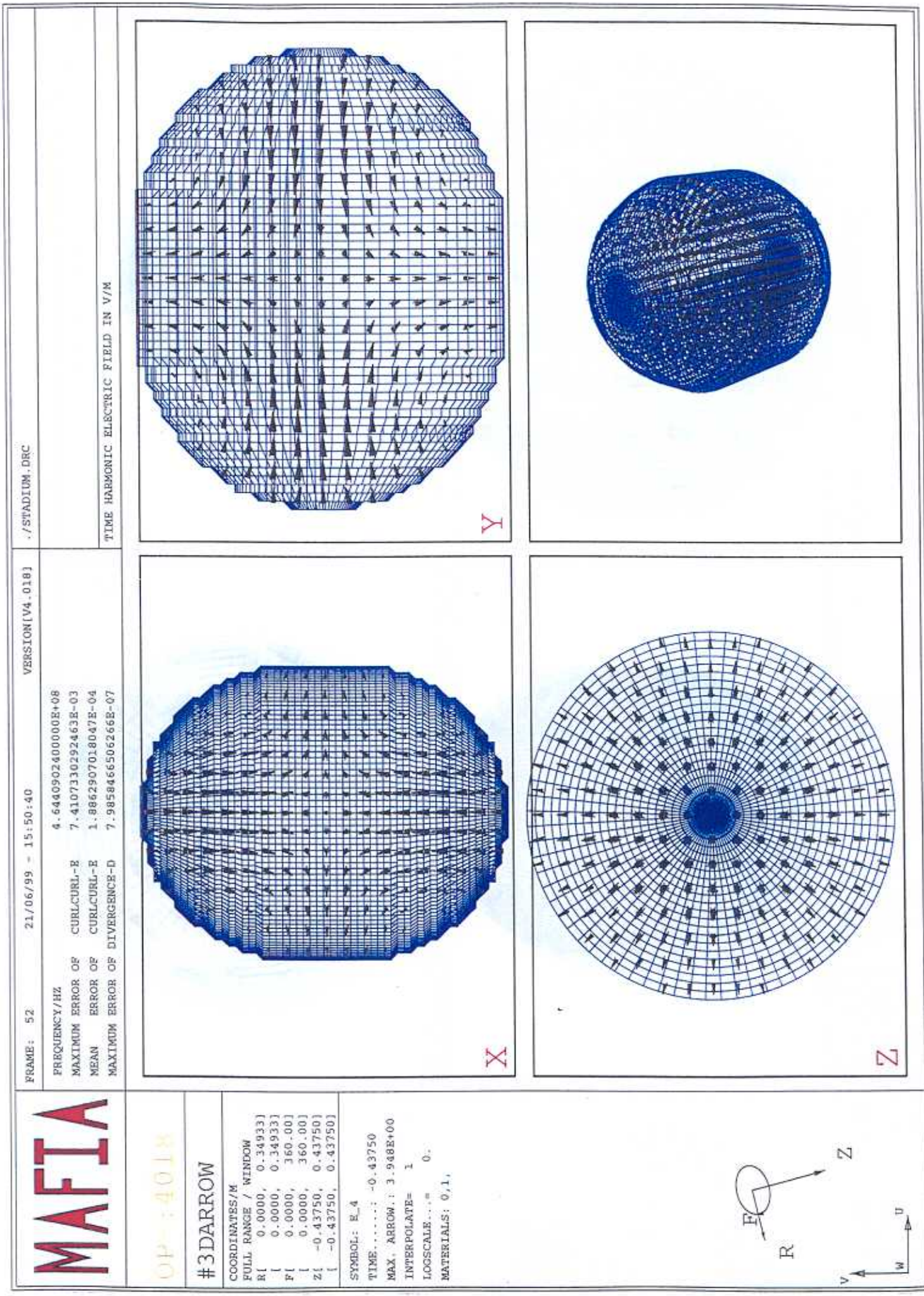


Figure 141: Distribution of $\underline{E}_t$ for 4th eigenmode of 3D stadium ($R = 0.35$m, $a = 0.175$m).

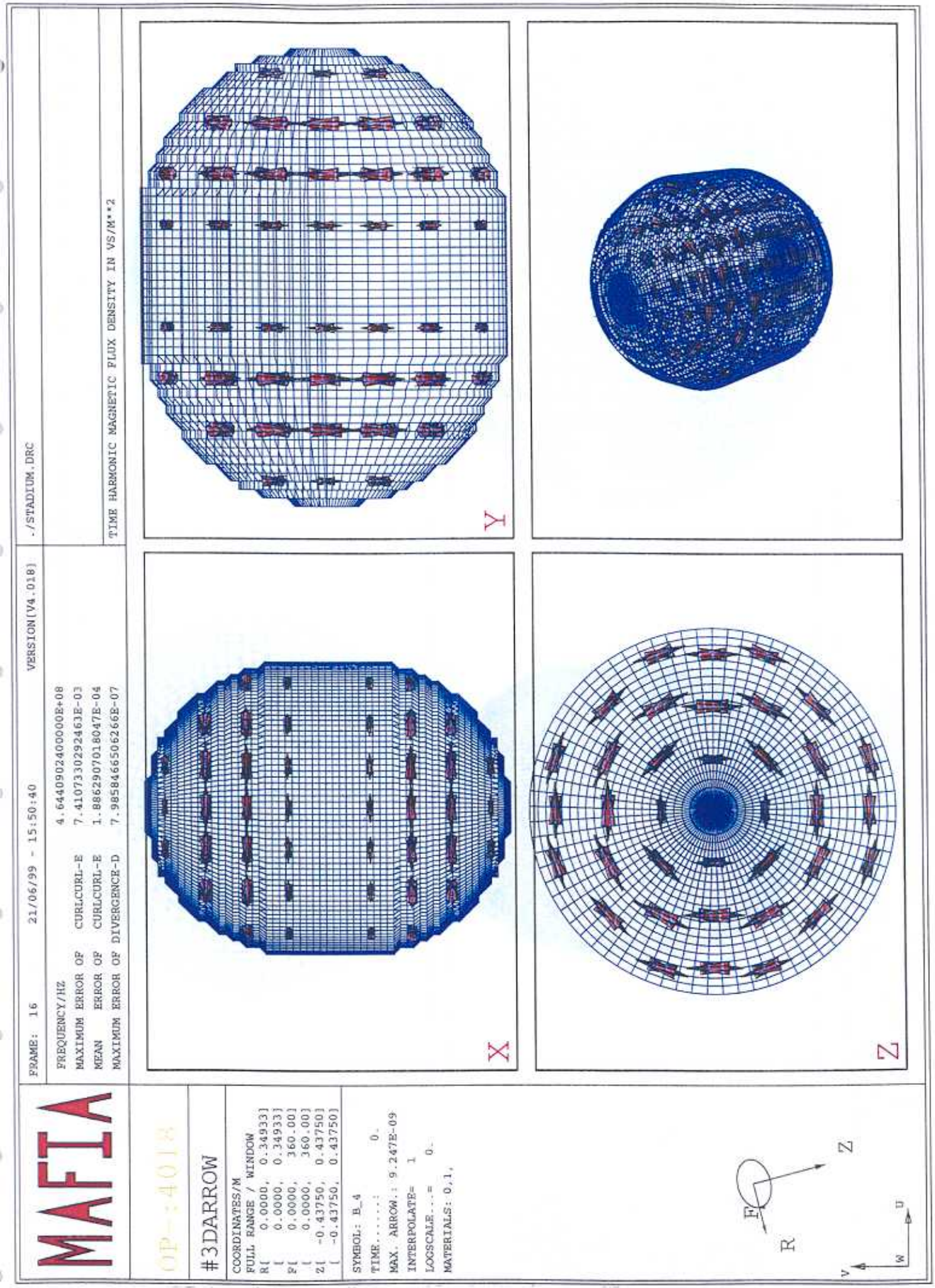


Figure 142: Distribution of B_t for 4th eigenmode of 3D stadium ($R = 0.35$m, $a = 0.175$m).

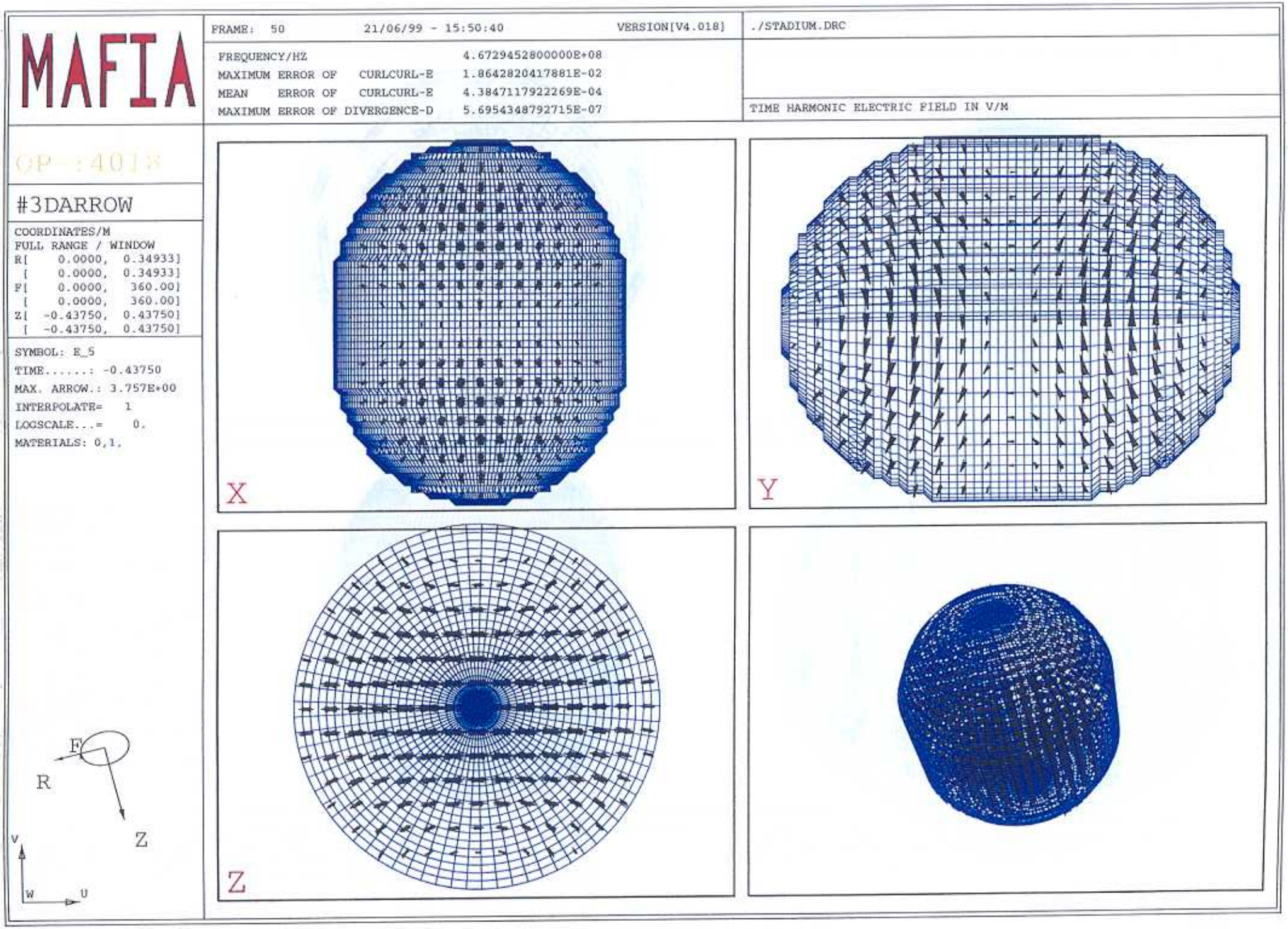


Figure 143: Distribution of $\underline{E}_t$ for 5th eigenmode of 3D stadium ($R = 0.35$m, $a = 0.175$m).

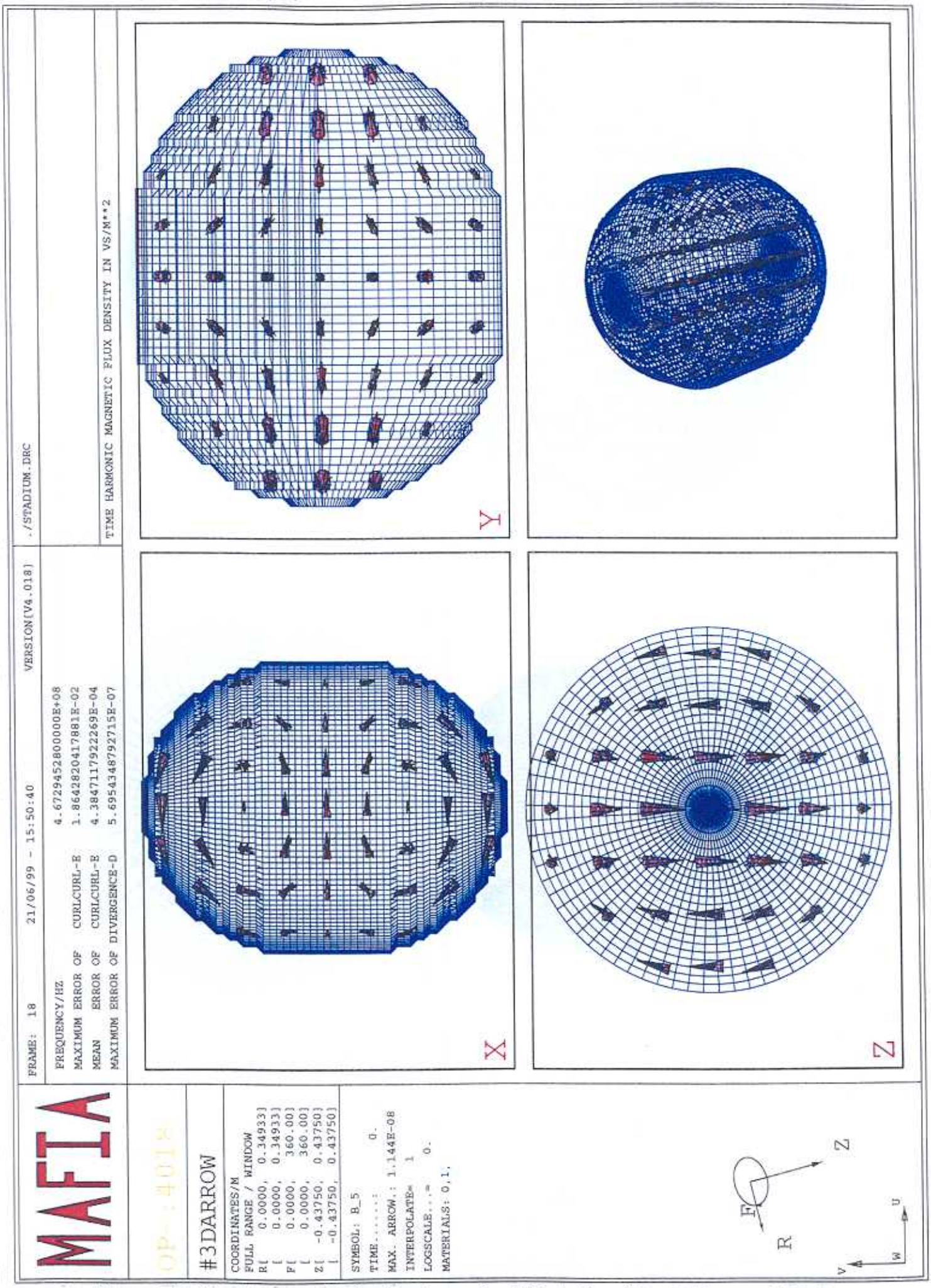


Figure 144: Distribution of $\underline{B}_t$ for 5th eigenmode of 3D stadium ($R = 0.35$m, $a = 0.175$m).

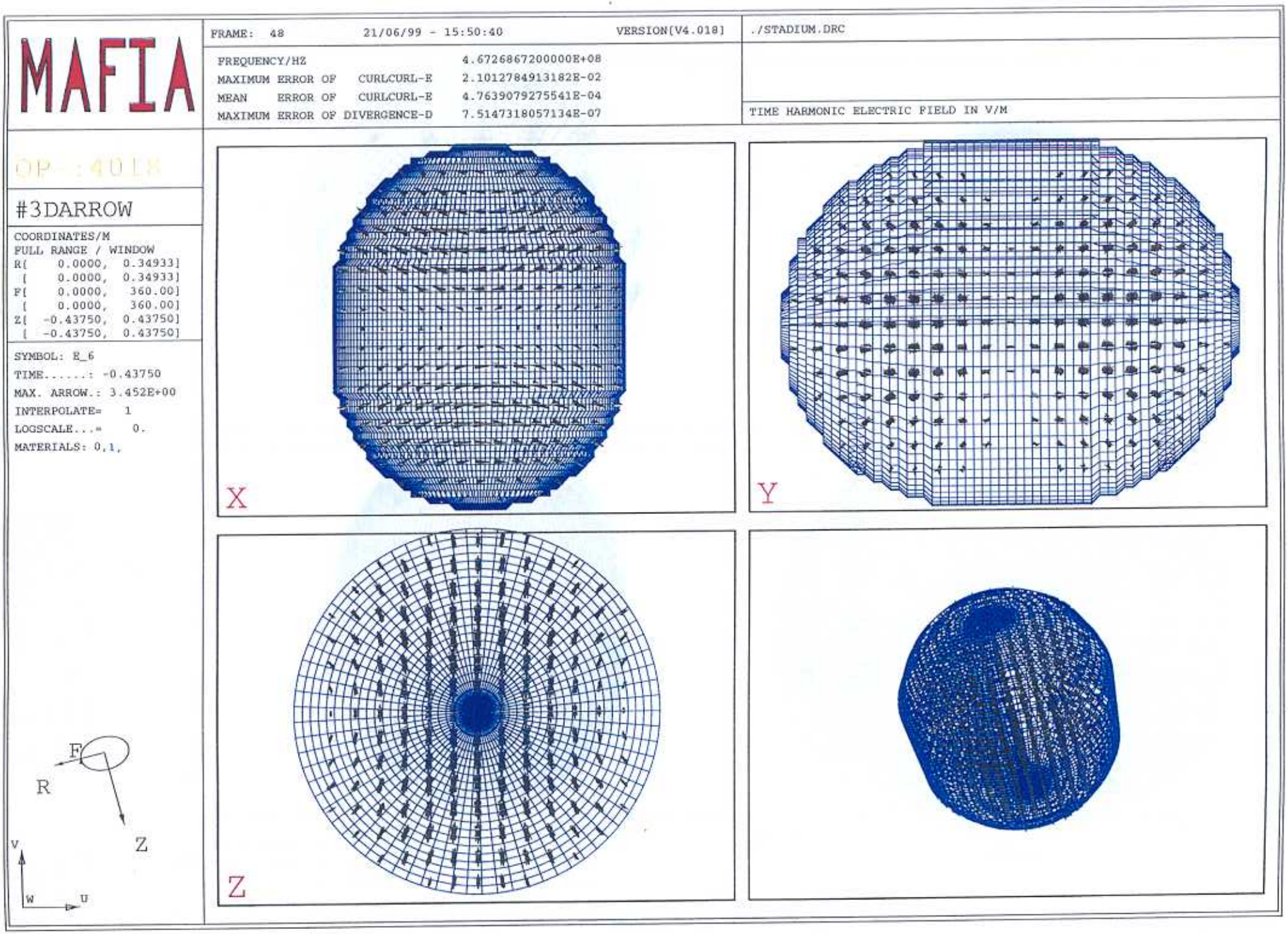


Figure 145: Distribution of $\underline{E}_t$ for 6th eigenmode of 3D stadium ($R = 0.35$m, $a = 0.175$m).

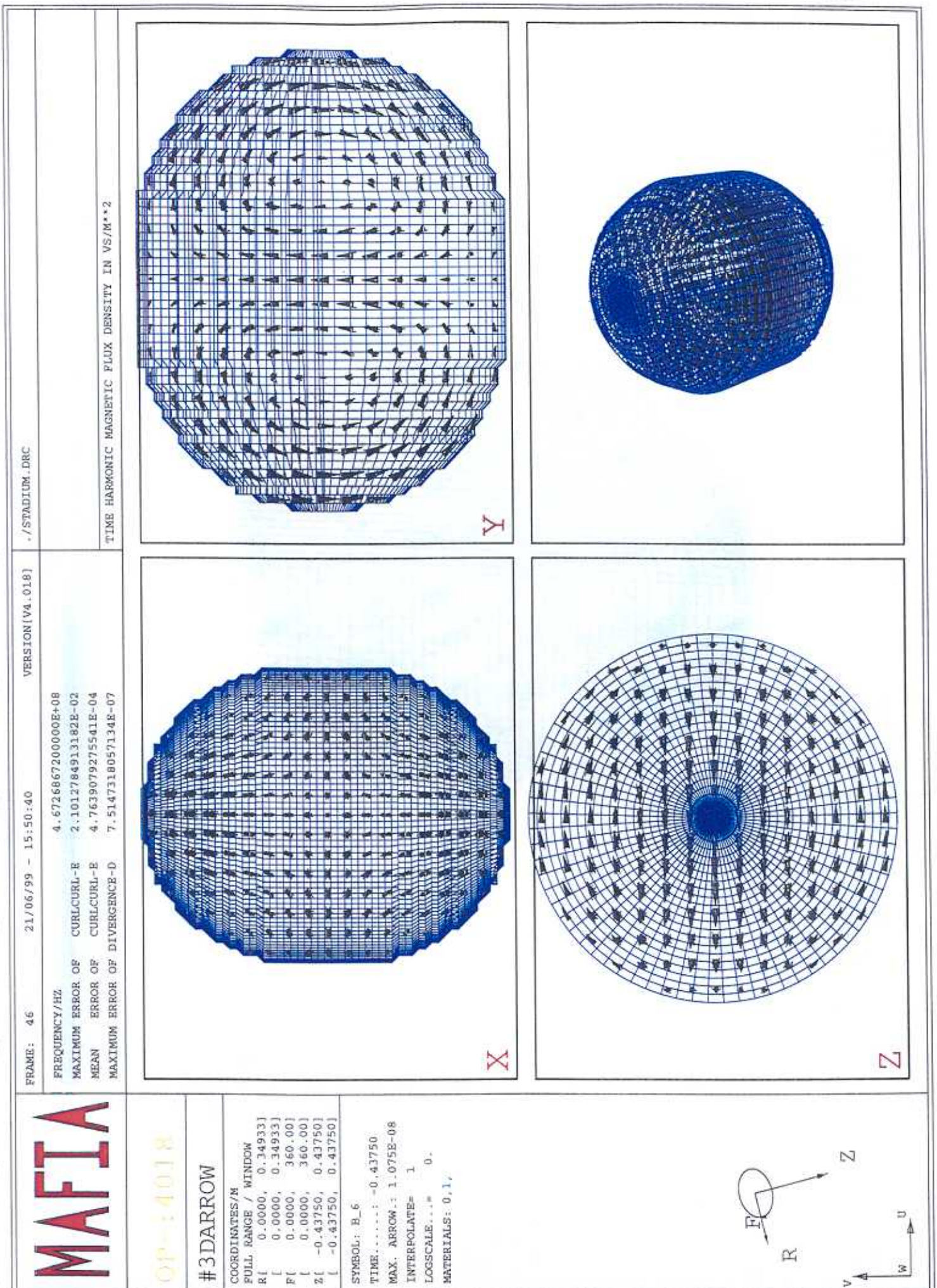


Figure 146: Distribution of $\underline{B}_t$ for 6th eigenmode of 3D stadium ($R = 0.35$m, $a = 0.175$m).

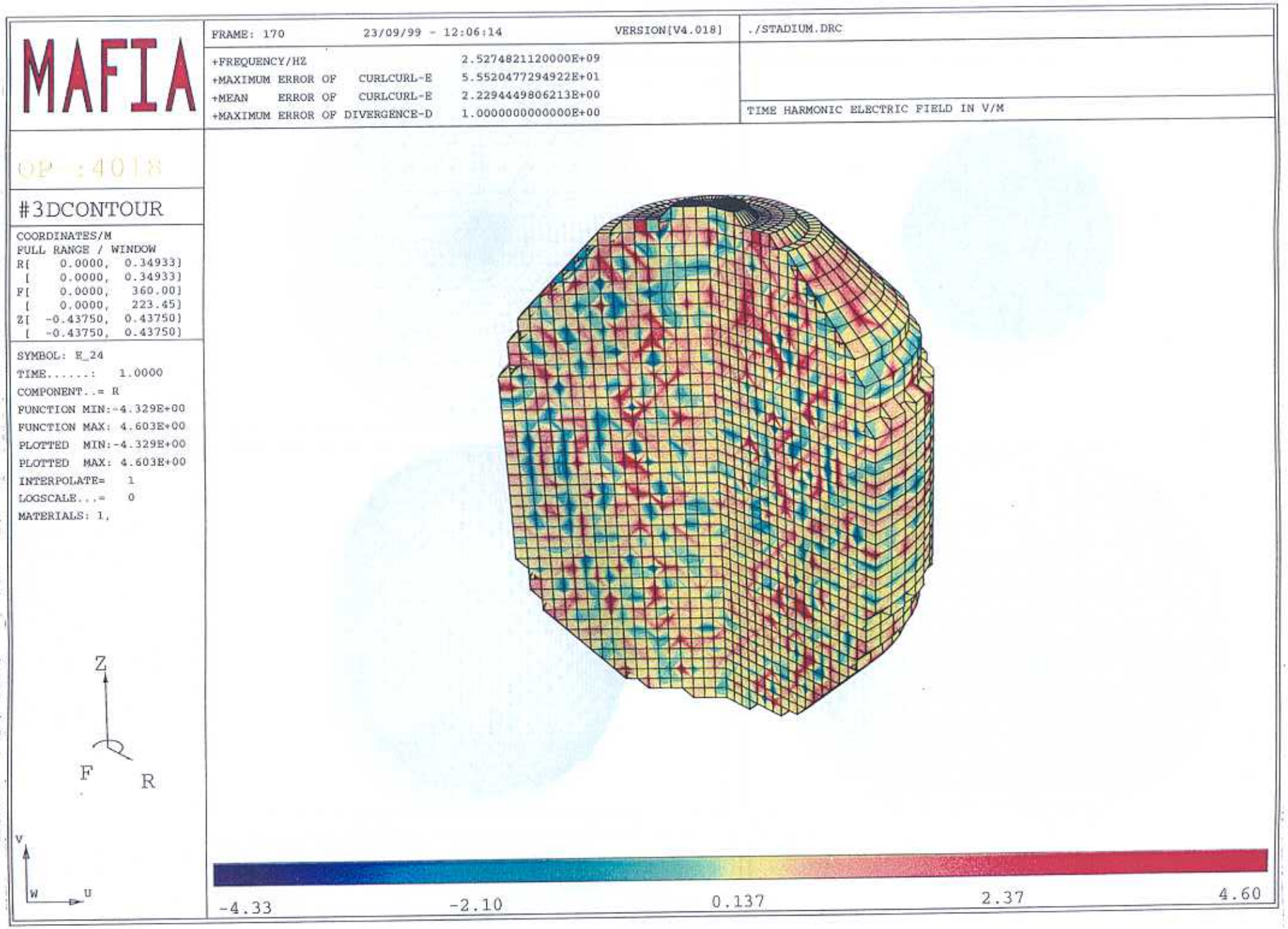


Figure 147: Distribution of $|\underline{E}_t|$ (V/m) in 3D stadium ($R = 0.35$m, $a = 0.175$m) @ $f = 2.53$GHz.

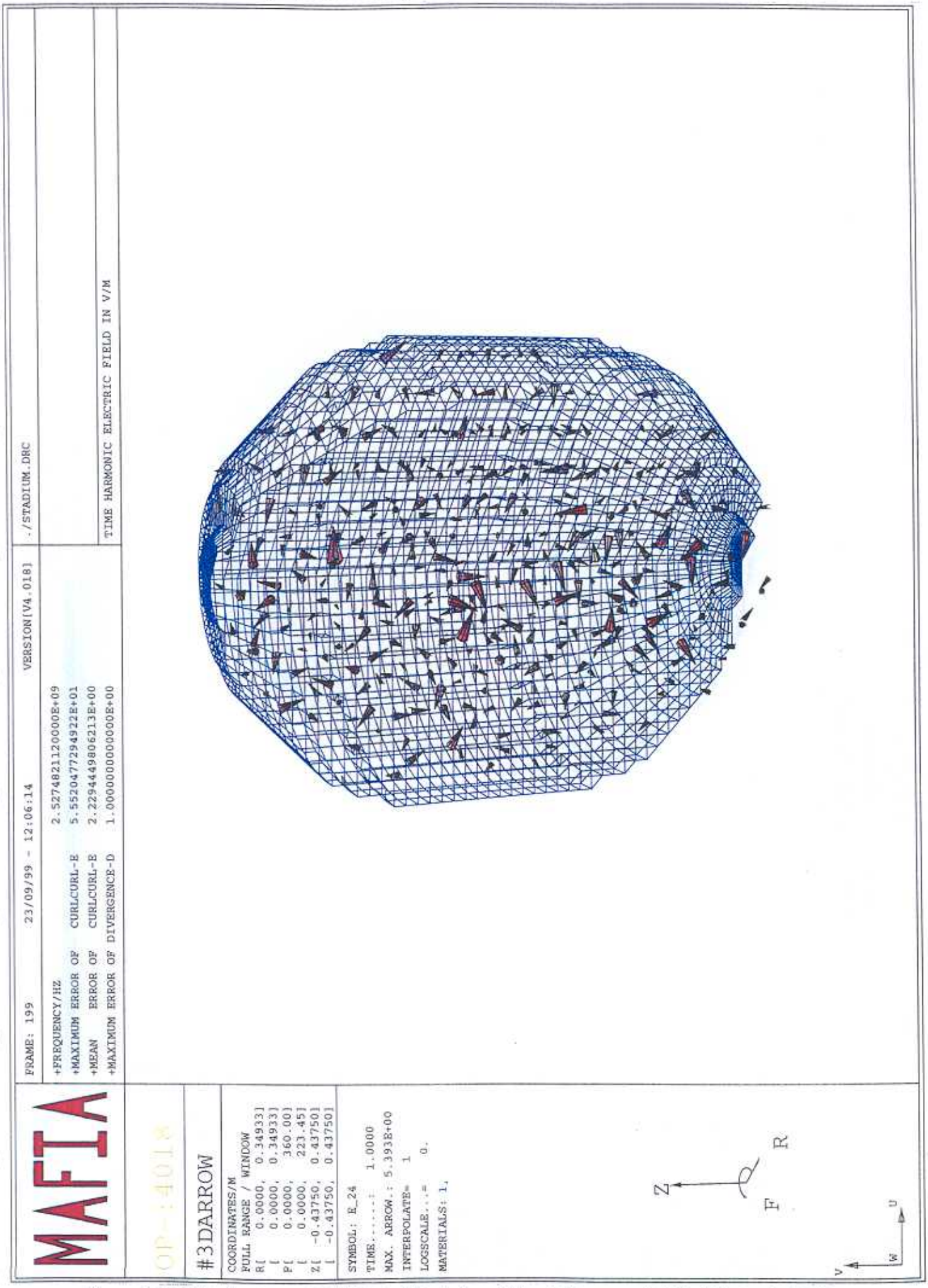


Figure 148: Distribution of $\underline{E}_z/|\underline{E}_z|$ in 3D stadium ($R = 0.35$m, $a = 0.175$m) @ $f = 2.53$GHz.

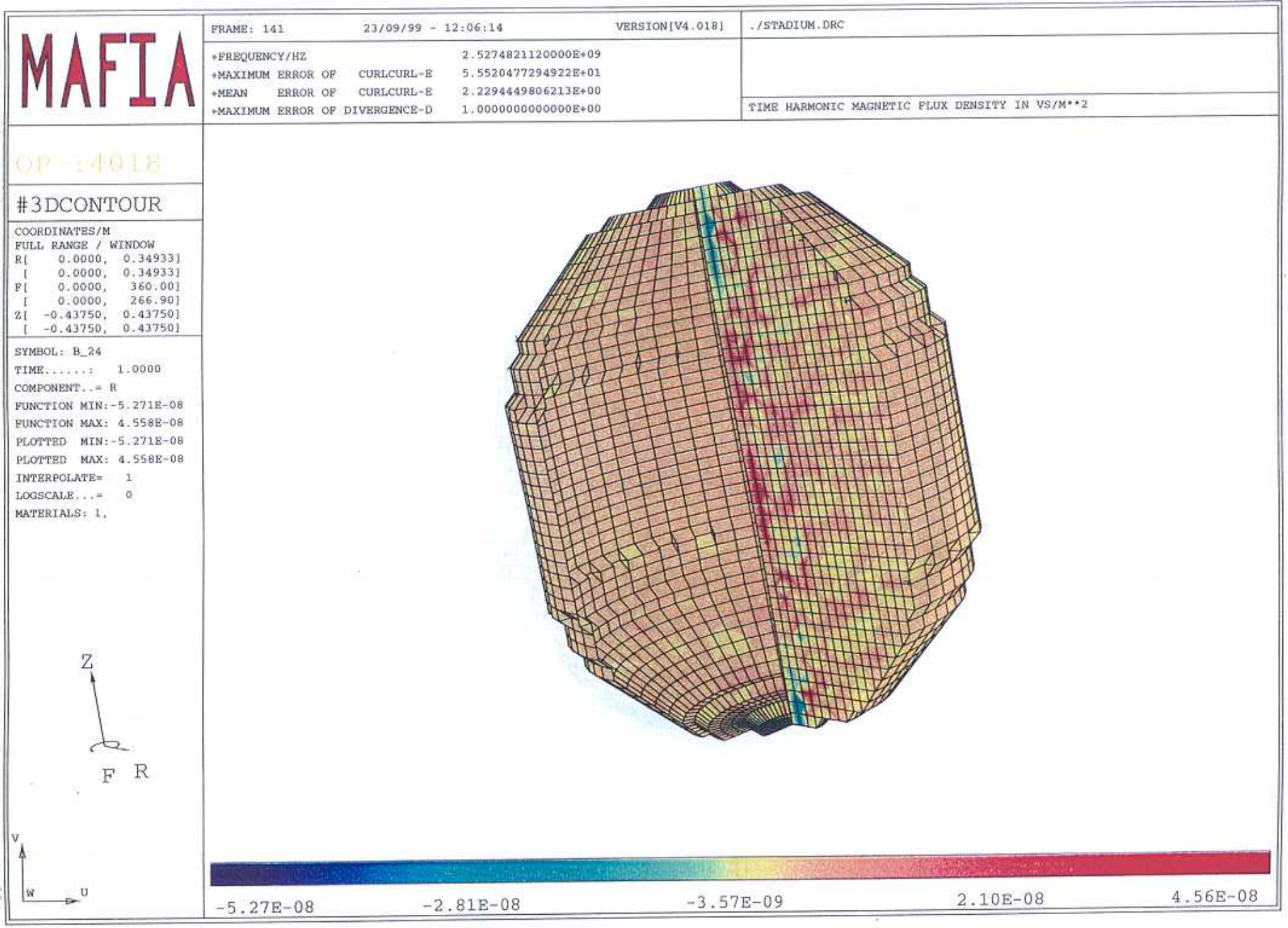


Figure 149: Distribution of $|\underline{B}_z|$ (Vs/m^2) in 3D stadium (R = 0.35m, a = 0.175m) @ f = 2.53GHz.

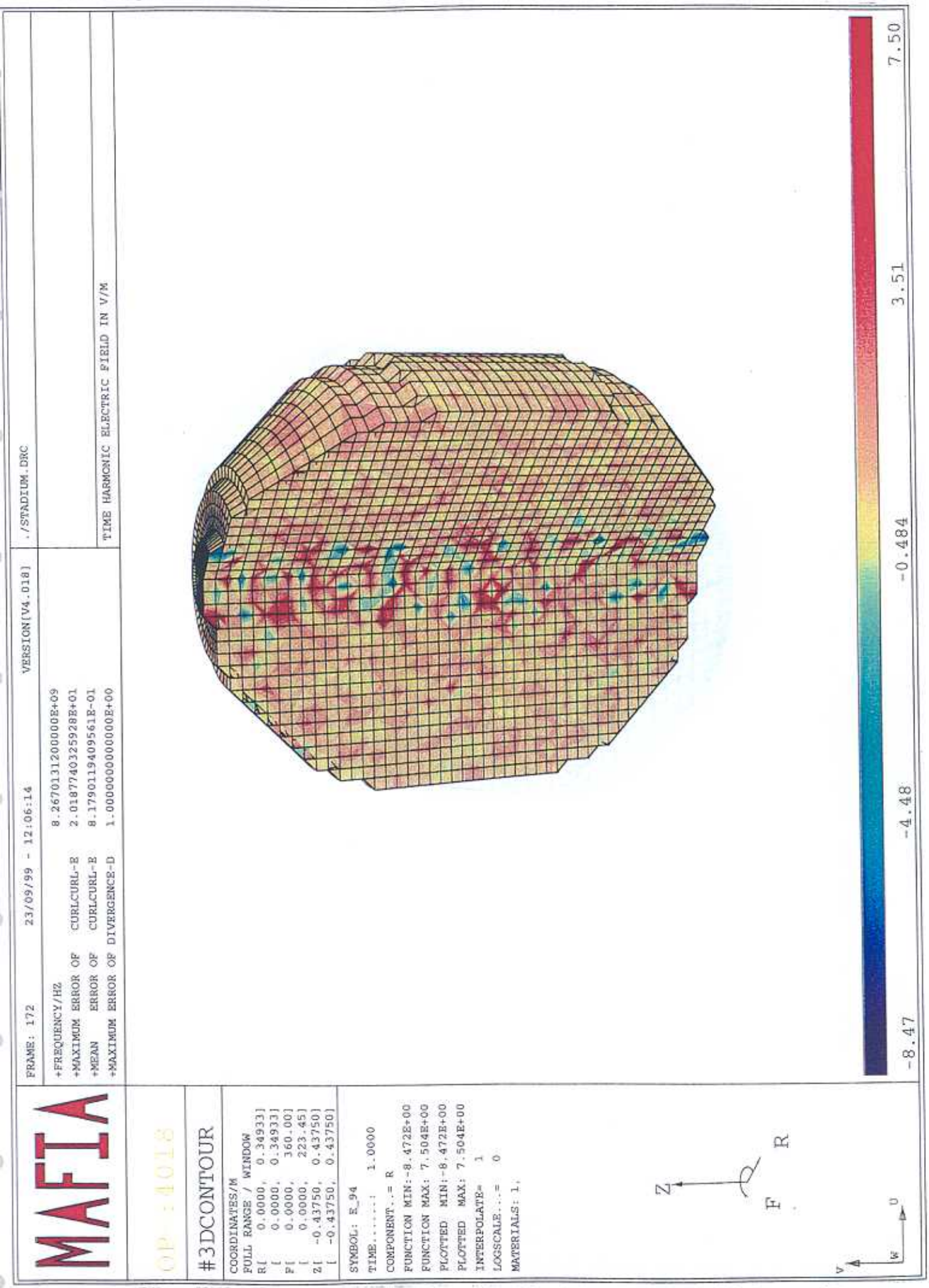


Figure 150: Distribution of $|\underline{E}_t|$ (V/m) in 3D stadium ($R = 0.35$m, $a = 0.175$m) @ $f = 8.26$GHz.

MAFIA

FRAME: 194 23/09/99 - 12:06:14 VERSION[V4.018] ./STADIUM.DRC

+FREQUENCY/HZ	8.2670131200000E+09
+MAXIMUM ERROR OF CURLCURL-E	2.0187740325928E+01
+MEAN ERROR OF CURLCURL-E	8.1790119409561E-01
+MAXIMUM ERROR OF DIVERGENCE-D	1.0000000000000E+00

TIME HARMONIC ELECTRIC FIELD IN V/M

OP-:4018

#3DARROW

COORDINATES/M
FULL RANGE / WINDOW
R[0.0000, 0.34933]
[0.0000, 0.34933]
F[0.0000, 360.00]
[0.0000, 223.45]
Z[-0.43750, 0.43750]
[-0.43750, 0.43750]

SYMBOL: E_94
TIME.....: 1.0000
MAX. ARROW.: 7.366E+00
INTERPOLATE= 1
LOGSCALE...= 0.
MATERIALS: 1,

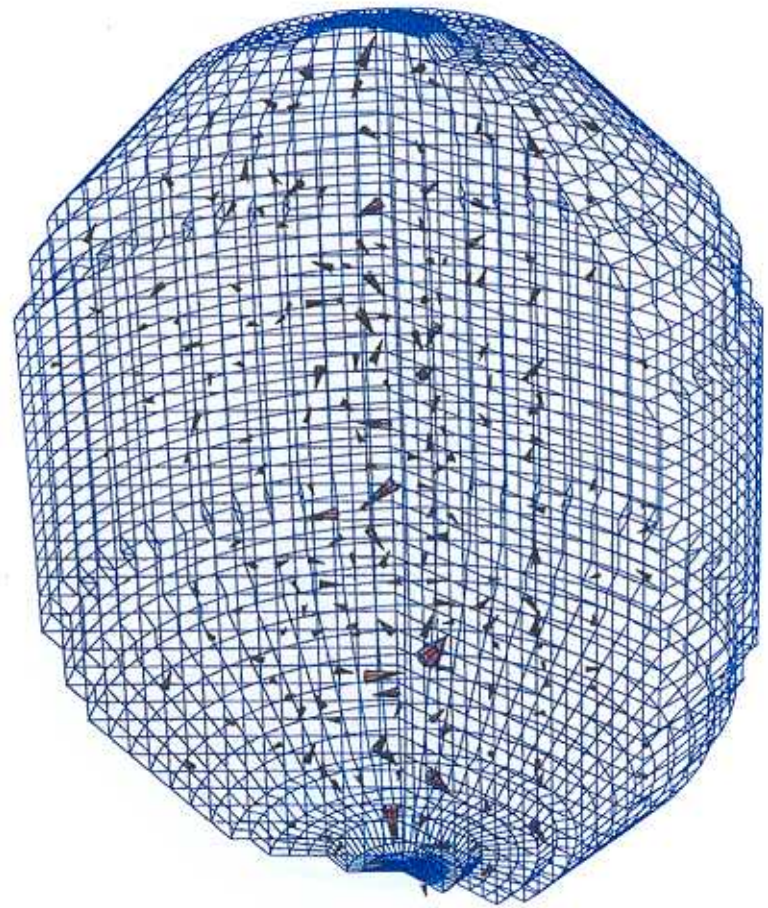


Figure 151: Distribution of $\underline{E}_t/|\underline{E}_t|$ in 3D stadium ($R = 0.35$m, $a = 0.175$m) @ $f = 8.26$GHz.

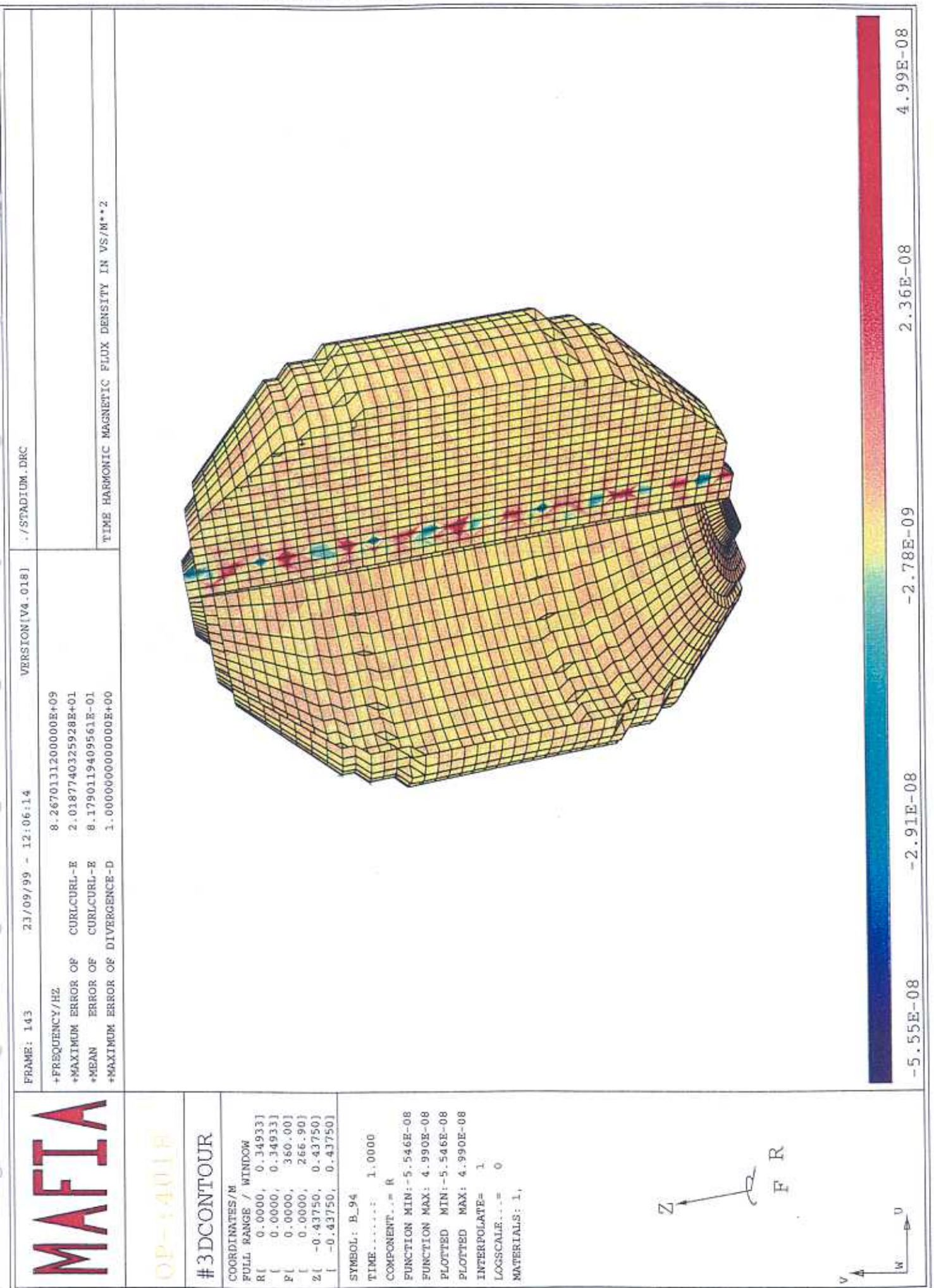


Figure 152: Distribution of $|\underline{B}_t|$ (Vs/m^2) in 3D stadium (R = 0.35m, a = 0.175m) @ f = 8.26GHz.

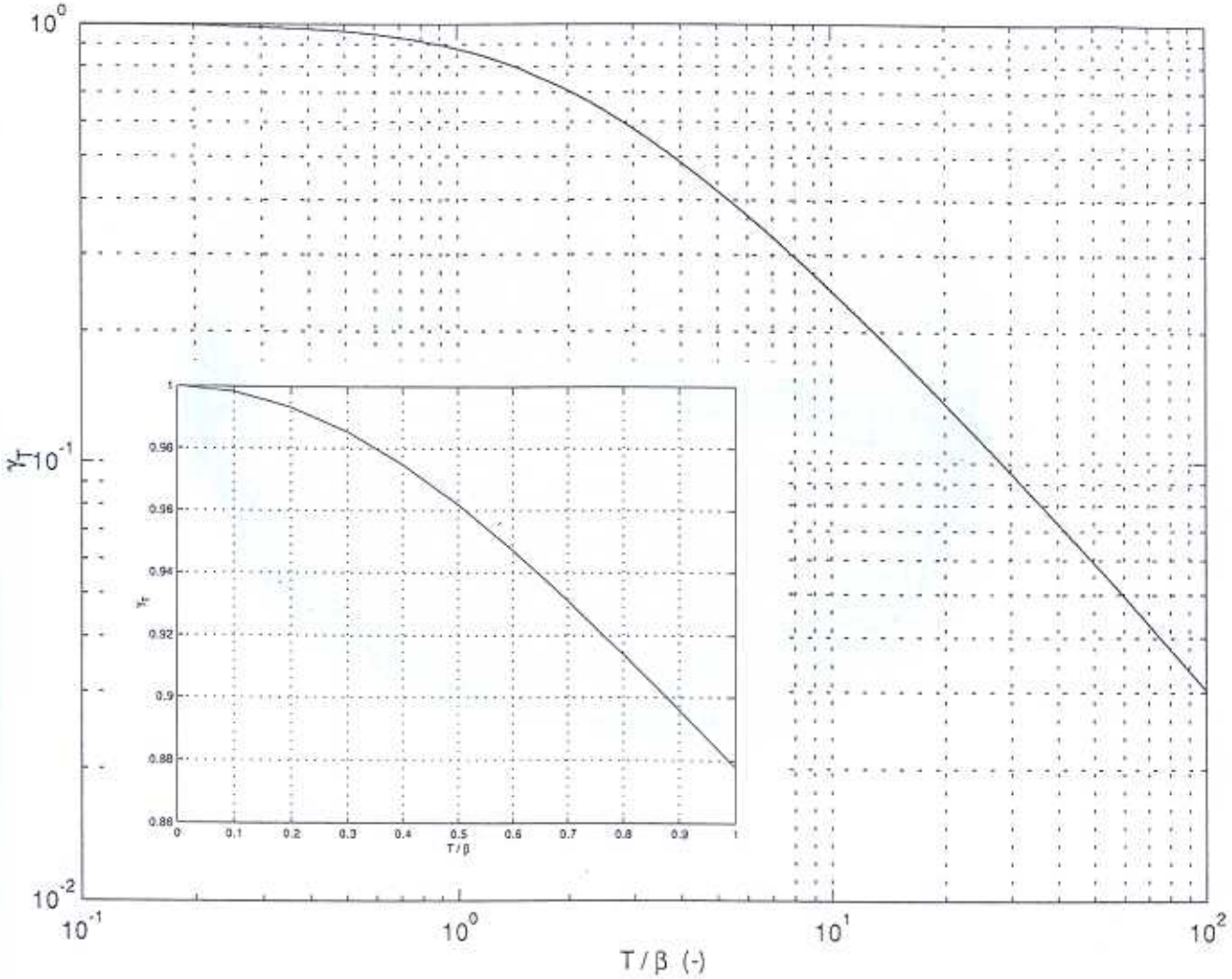


Figure 153: Variance function γ_T for power density as a function of normalized interval width T/β for local stir averaging.

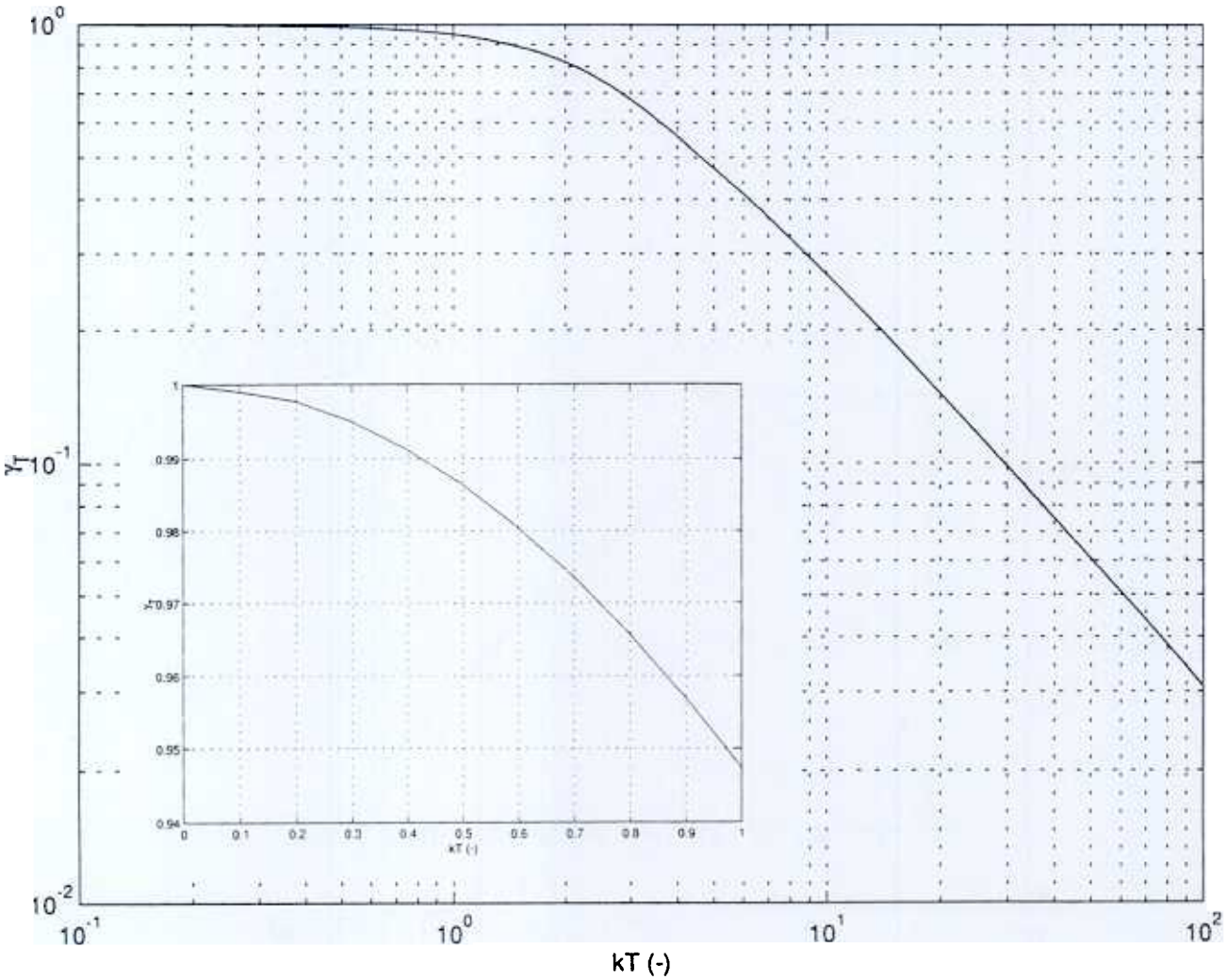


Figure 154: Variance function γ_T for power density as a function of normalized interval width kT for local spatial averaging.

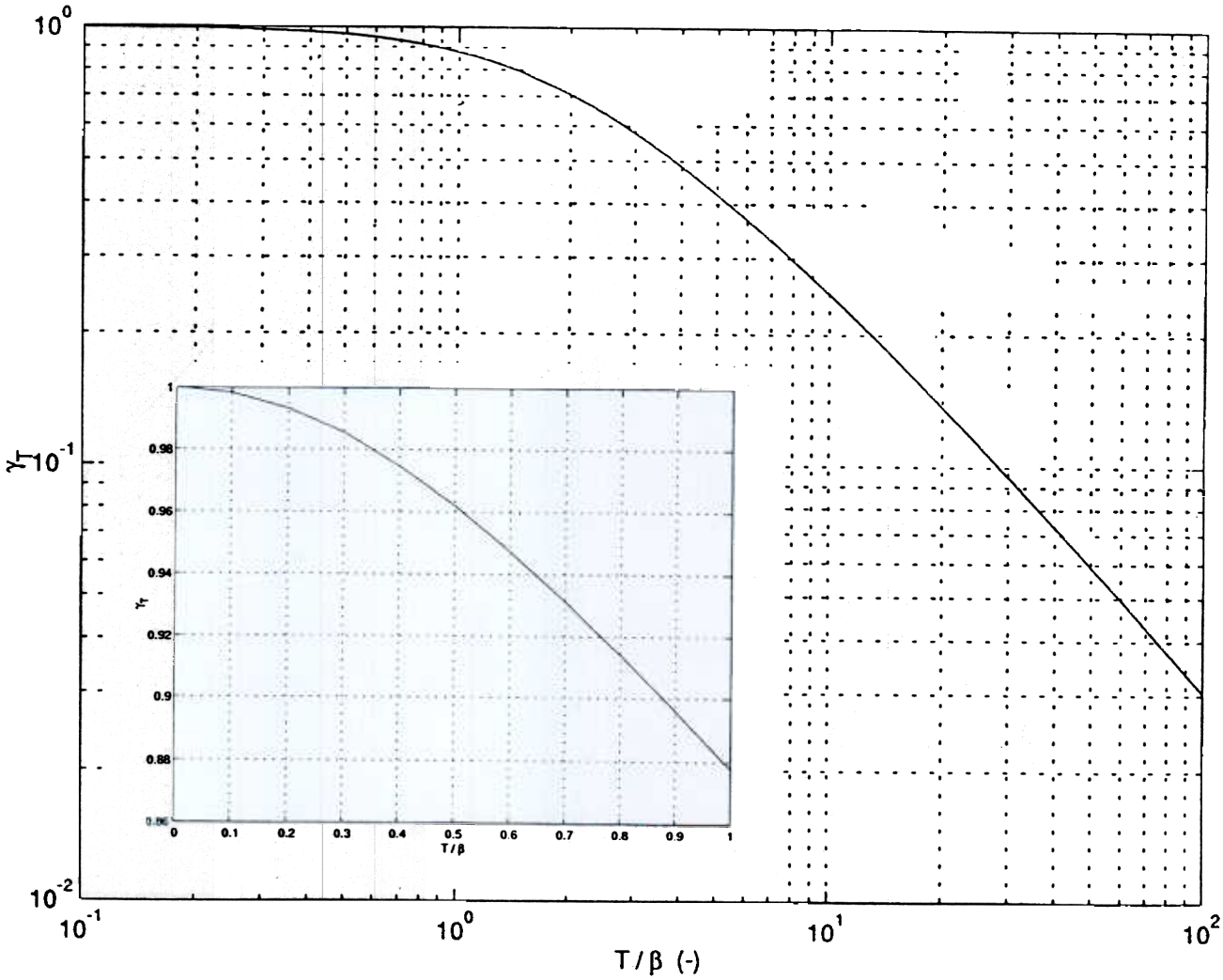


Figure 155: Variance function $\gamma_{\mathcal{T}}$ for magnitude of total field as a function of normalized interval width $k\mathcal{T}$ for local stir averaging.

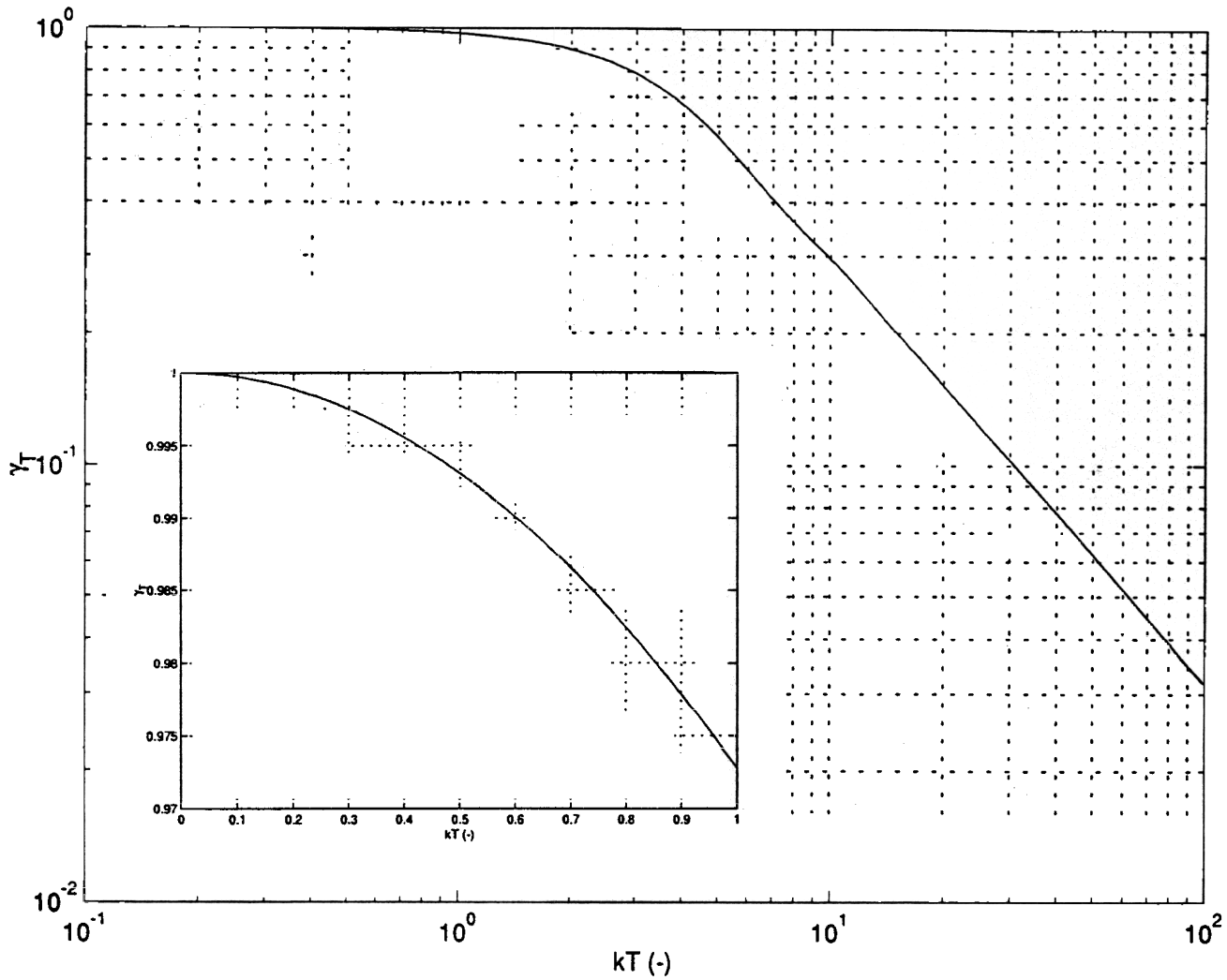


Figure 156: Variance function γ_T for magnitude of total field as a function of normalized interval width kT for local spatial averaging.

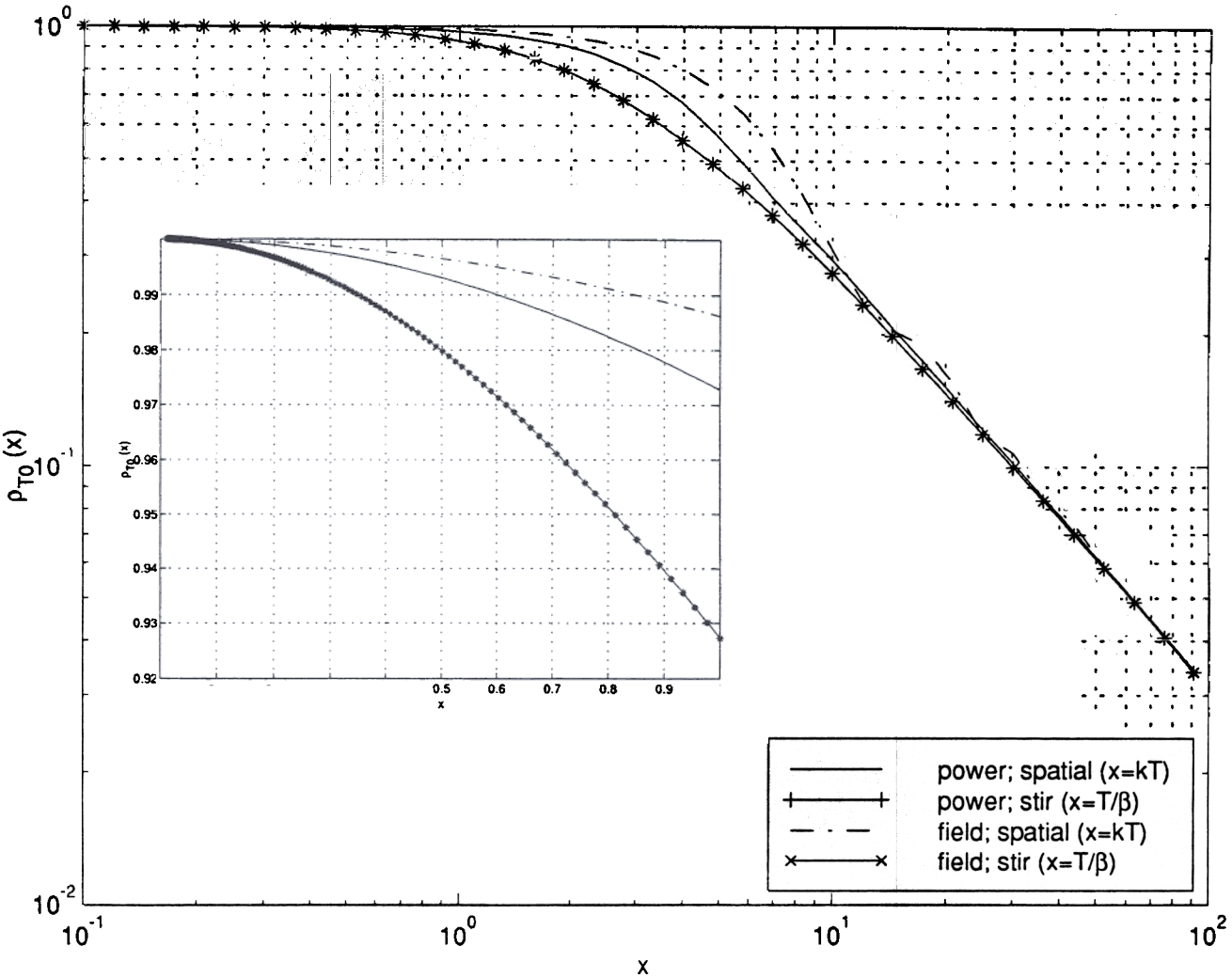


Figure 157: Point-interval correlation function $\varrho_{\mathcal{T}0}$ for power density and field magnitude as a function of normalized interval width $\mathcal{T}/\beta$ or $k\mathcal{T}$ for local spatial or stir averaging.

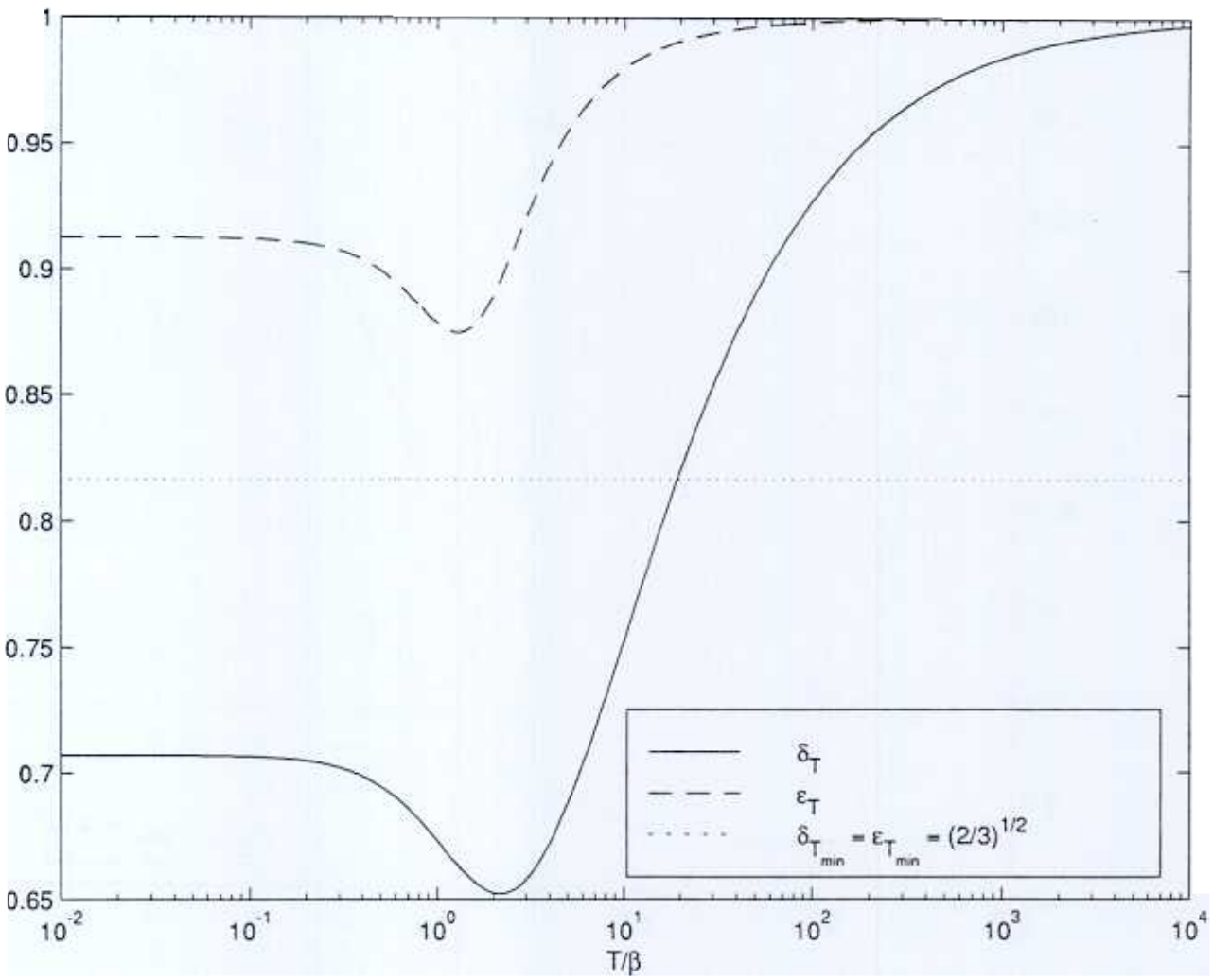


Figure 158: Normalized spectral bandwidths $\delta_{\mathcal{T}}$ and $\epsilon_{\mathcal{T}}$ as a function of normalized interval width $\mathcal{T}/\beta$ for local stir averaging.

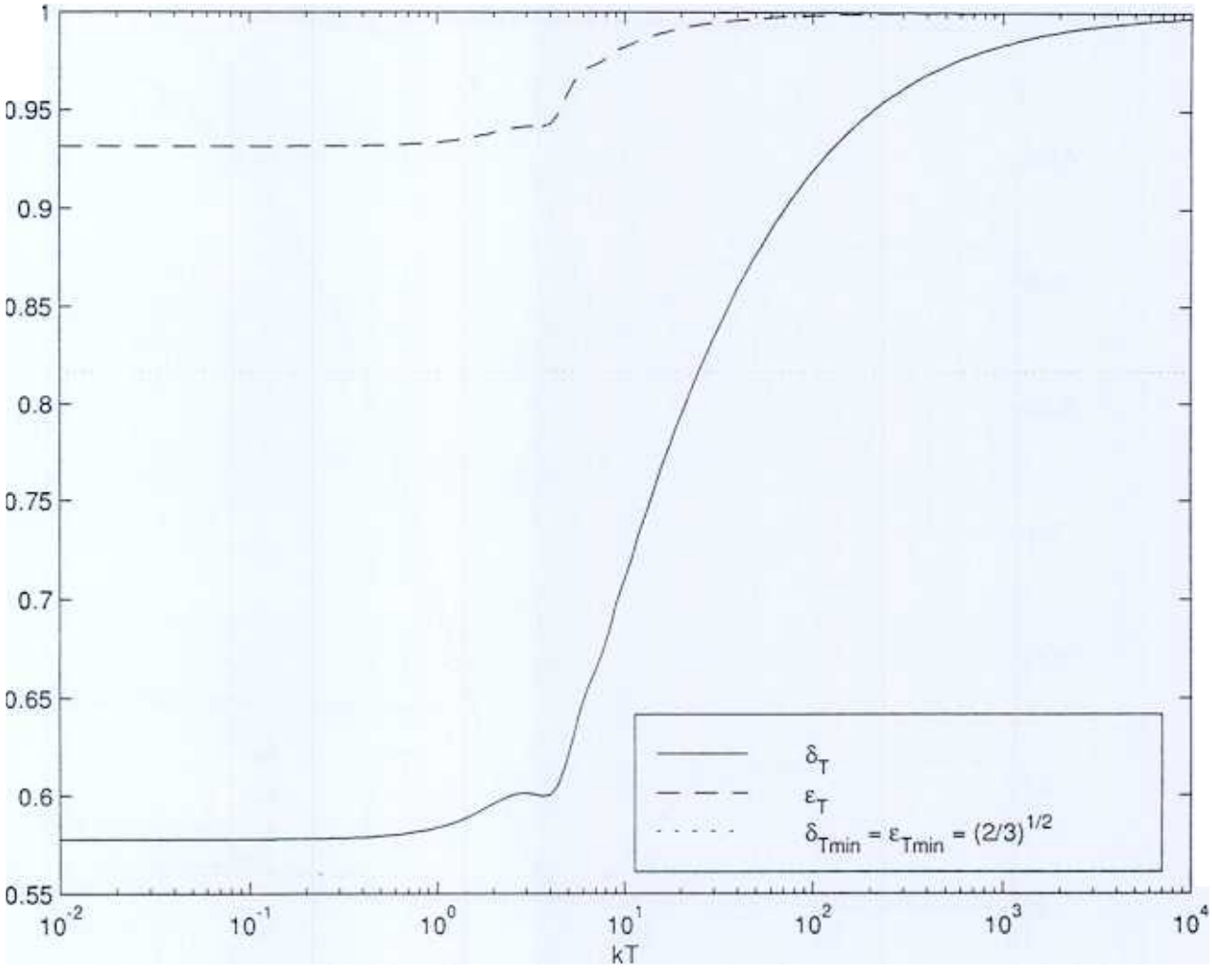


Figure 159: Normalized spectral bandwidths δ_T and ϵ_T as a function of normalized interval width kT for local spatial averaging.

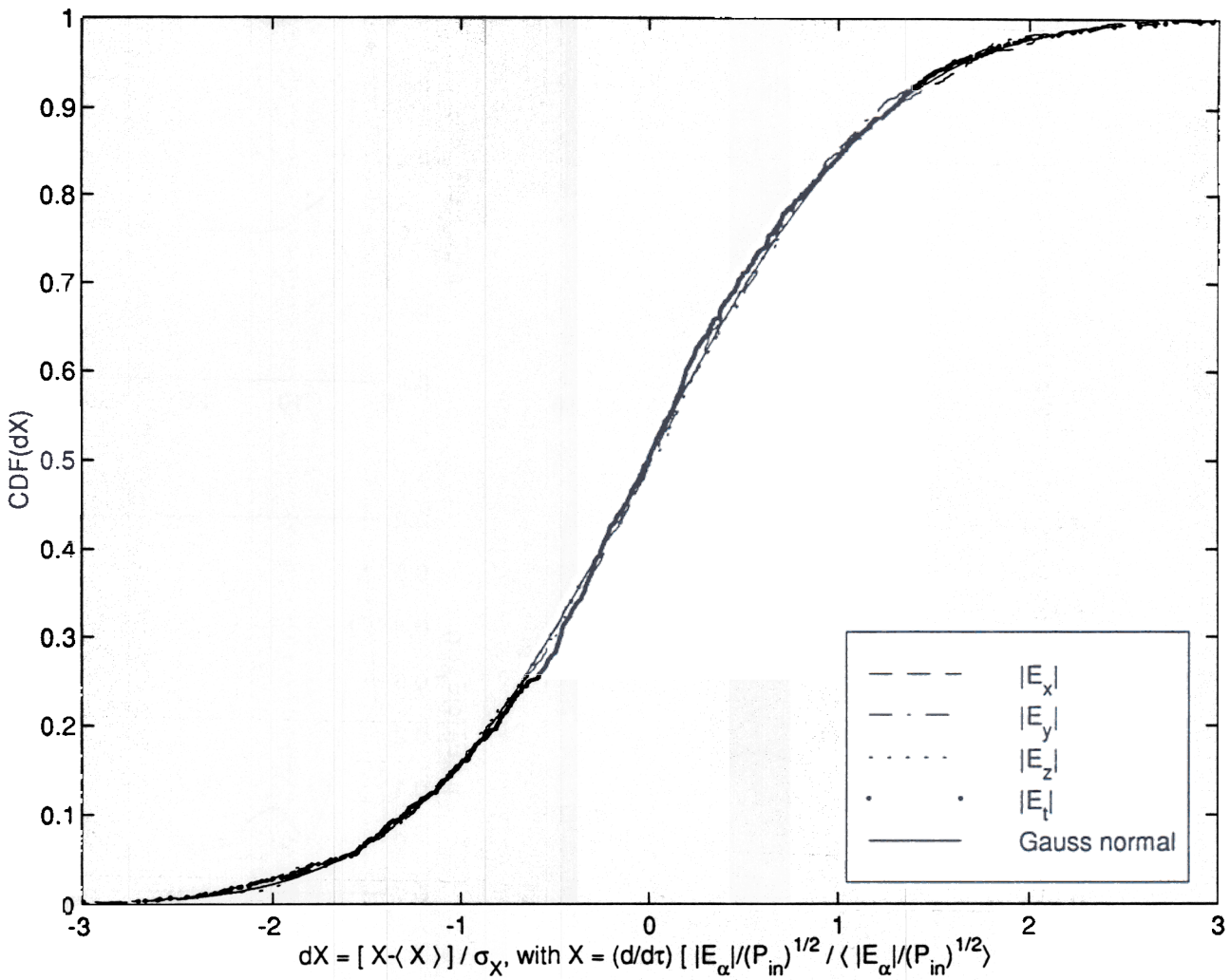


Figure 160: Cumulative distribution function of first-order difference of normalized measured $|E_\alpha(\tau)|$ and $|E_t(\tau)|$.

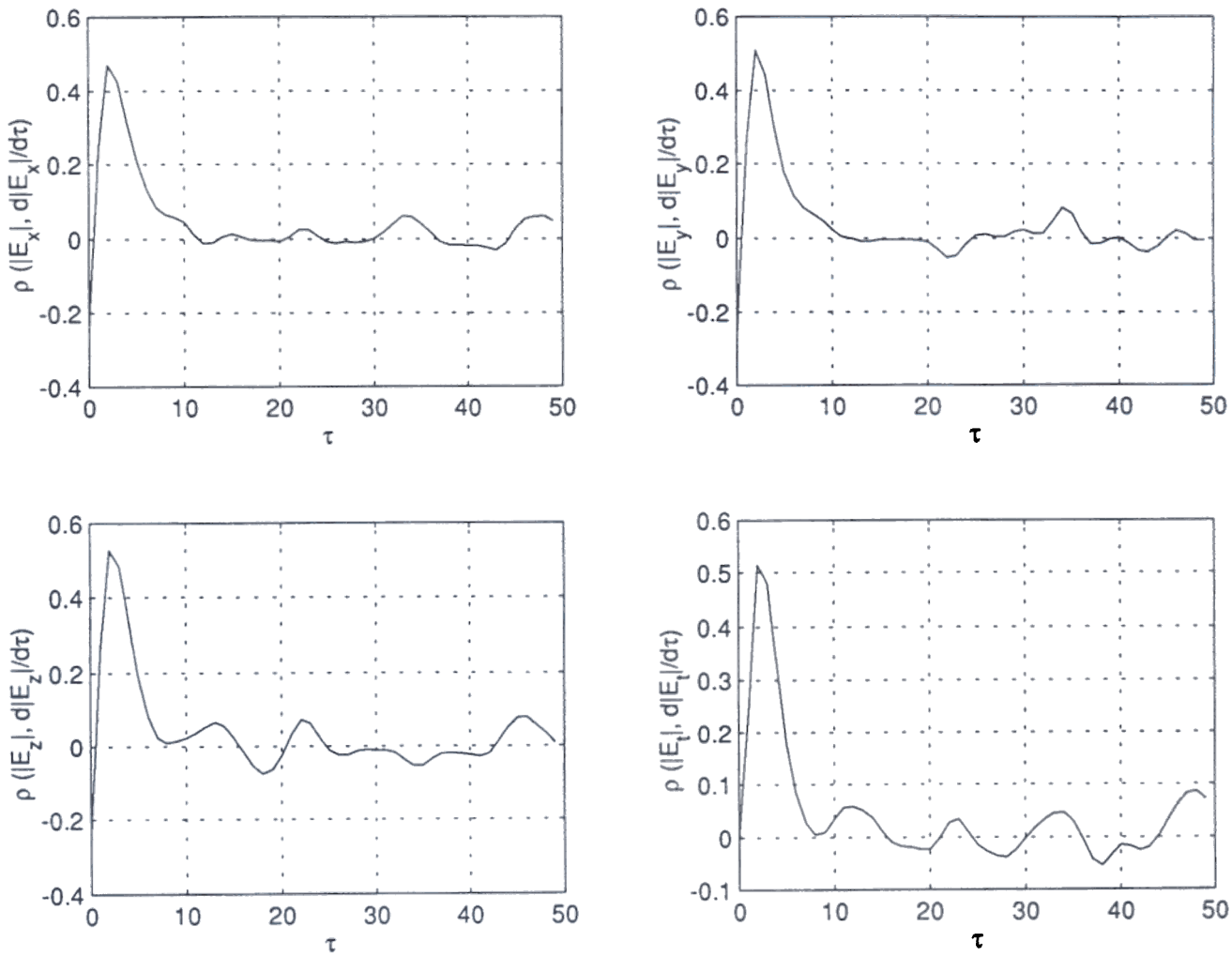


Figure 161: Crosscorrelation function between normalized measured $|E_\alpha(\tau)|$ or $|E_t(\tau)|$ and their first-order difference.

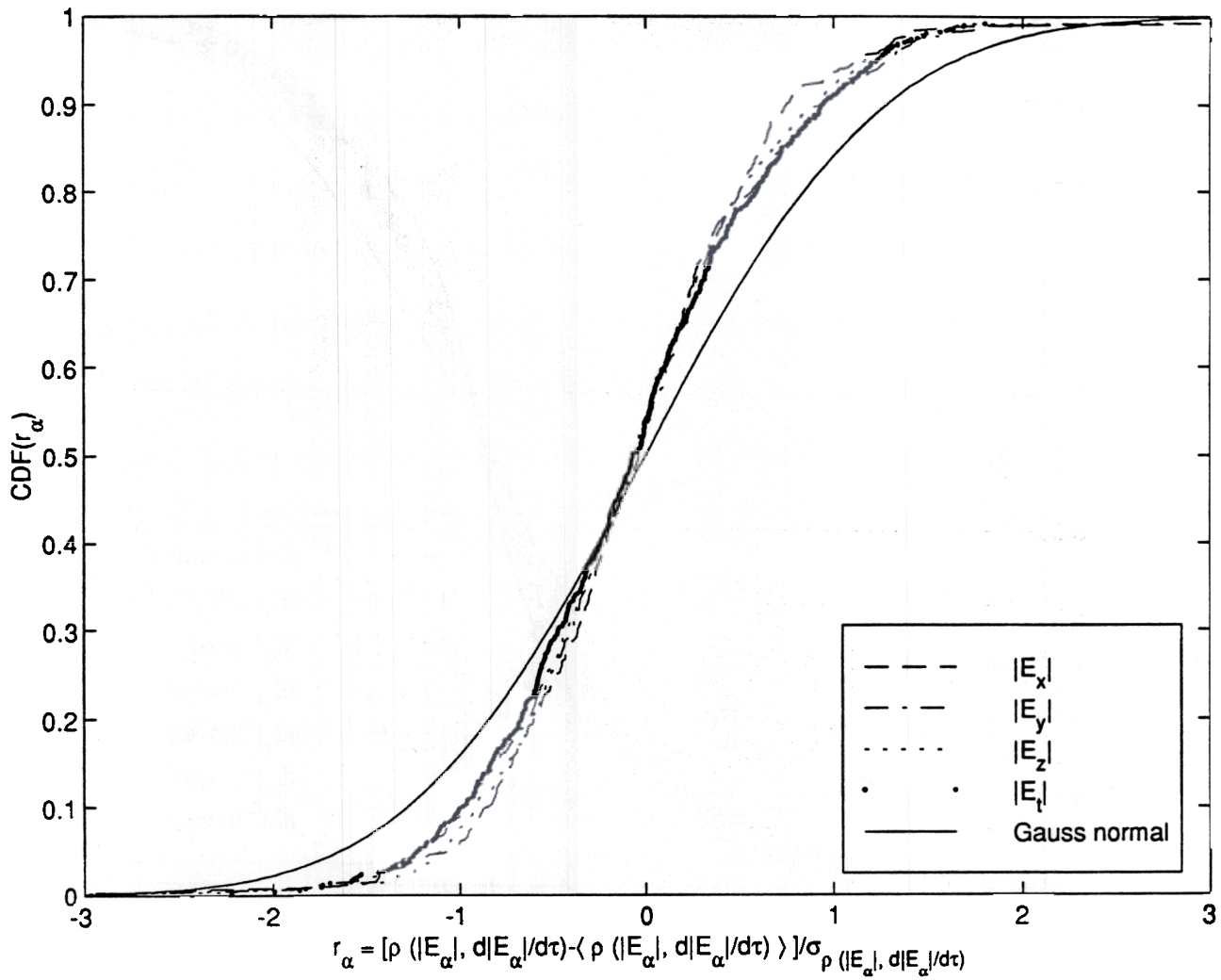


Figure 162: Cumulative distribution function of crosscorrelation function between normalized measured $|E_\alpha(\tau)|$ or $|E_t(\tau)|$ and their first-order difference.

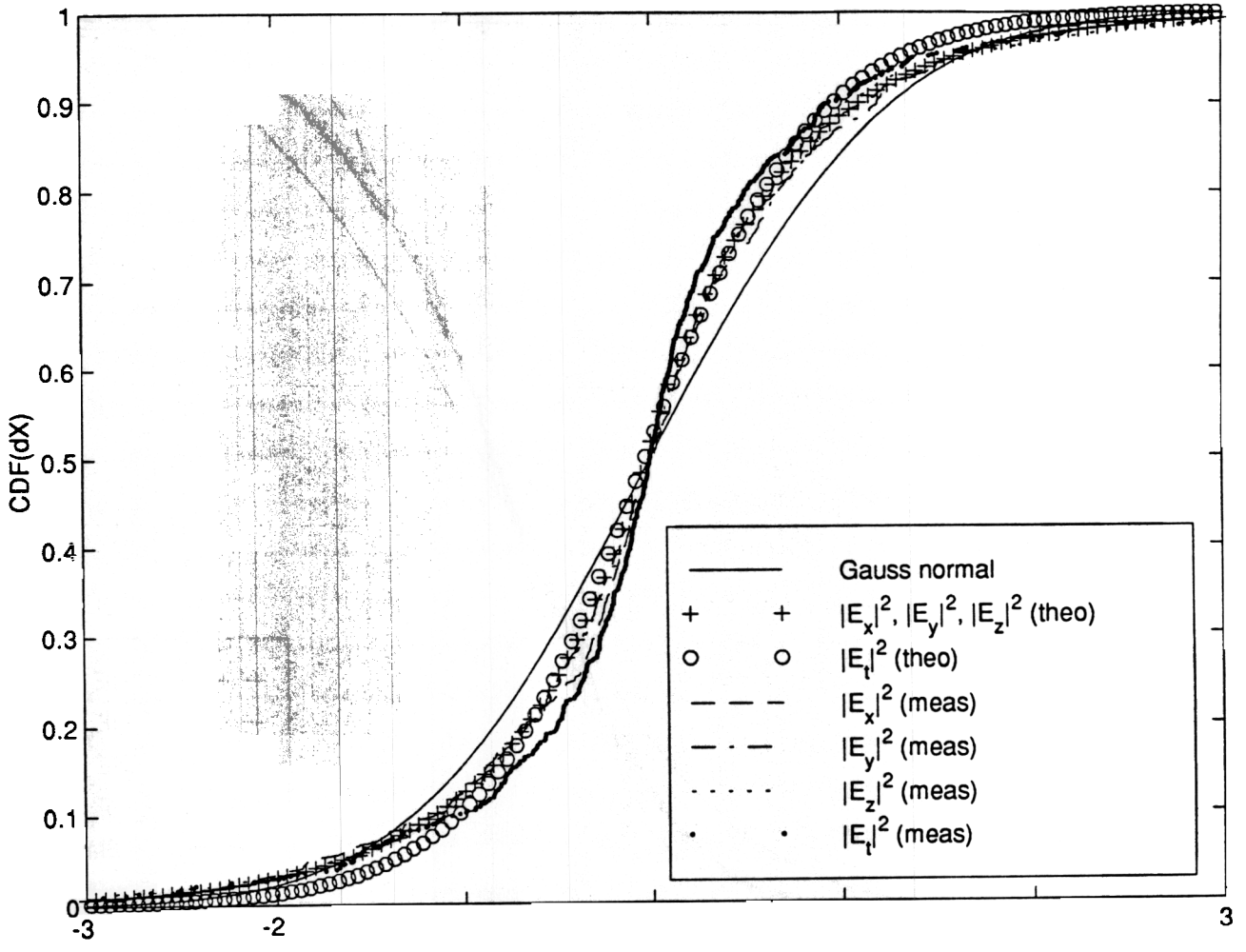


Figure 163: Cumulative distribution function of first-order difference of normalized measured $|E_\alpha(\tau)|^2$ and $|E_t(\tau)|^2$.

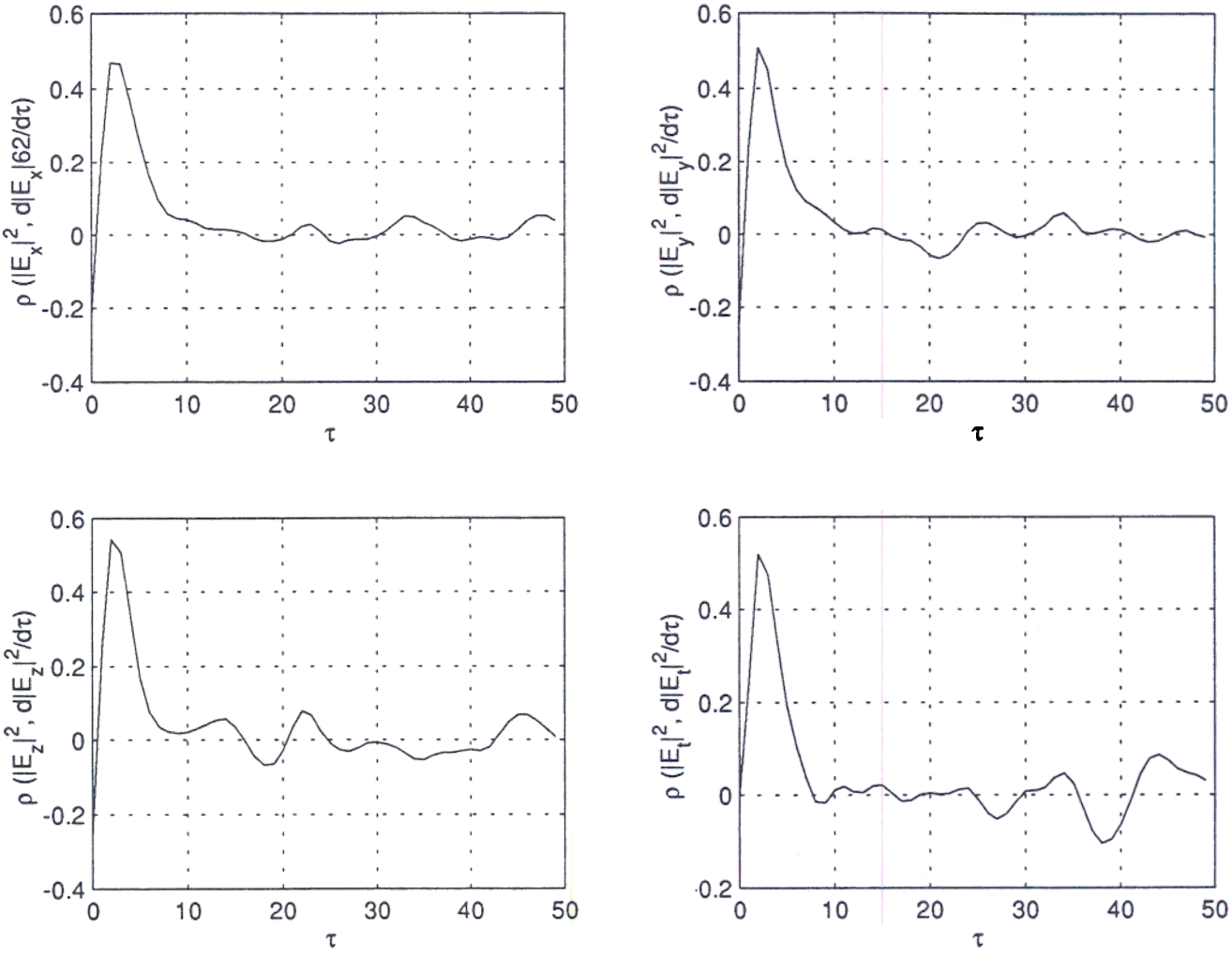


Figure 164: Crosscorrelation function between normalized measured $|E_\alpha(\tau)|^2$ or $|E_t(\tau)|^2$ and their first-order difference.

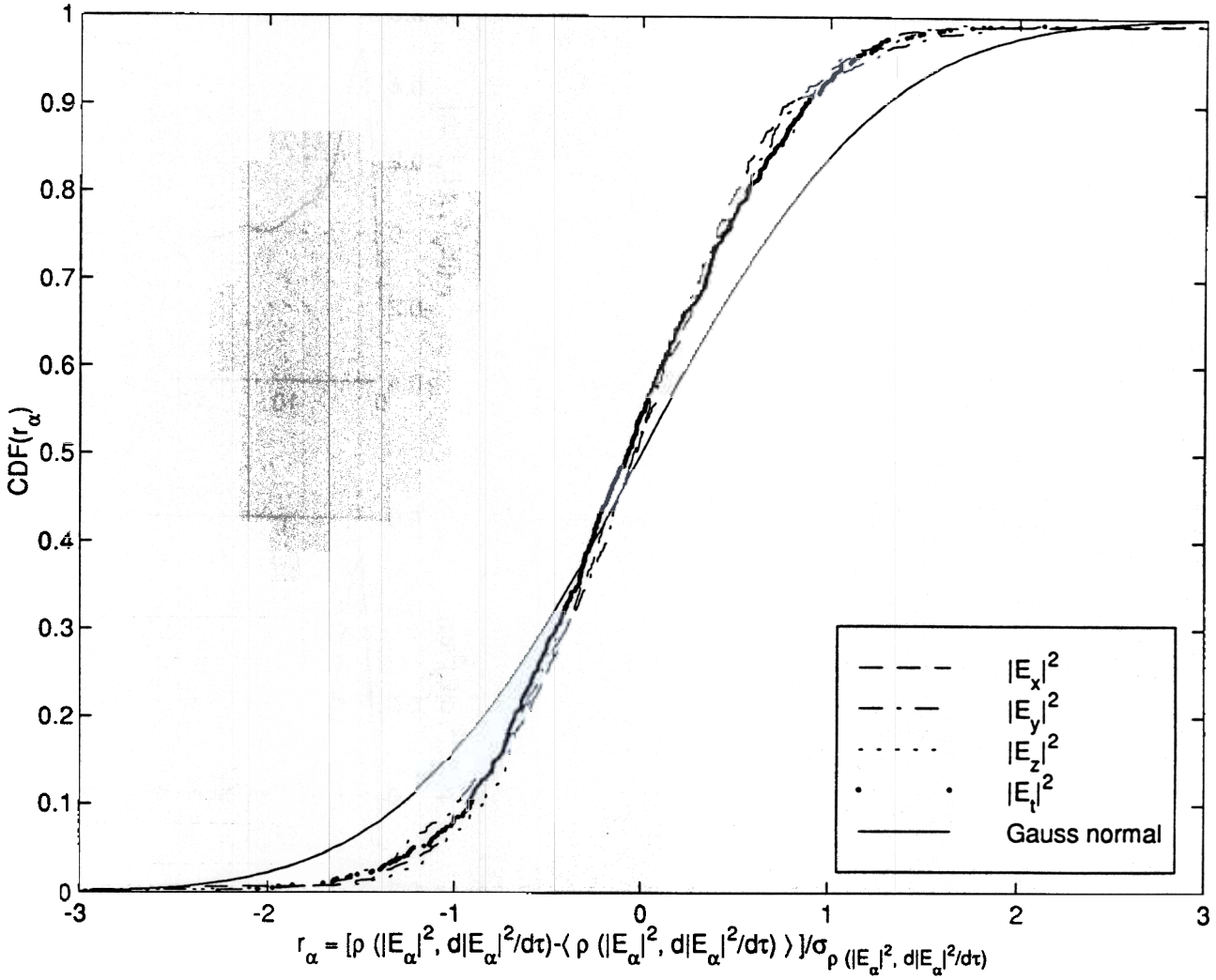


Figure 165: Cumulative distribution function of crosscorrelation function between normalized measured $|E_\alpha(\tau)|^2$ or $|E_t(\tau)|^2$ and their first-order difference.

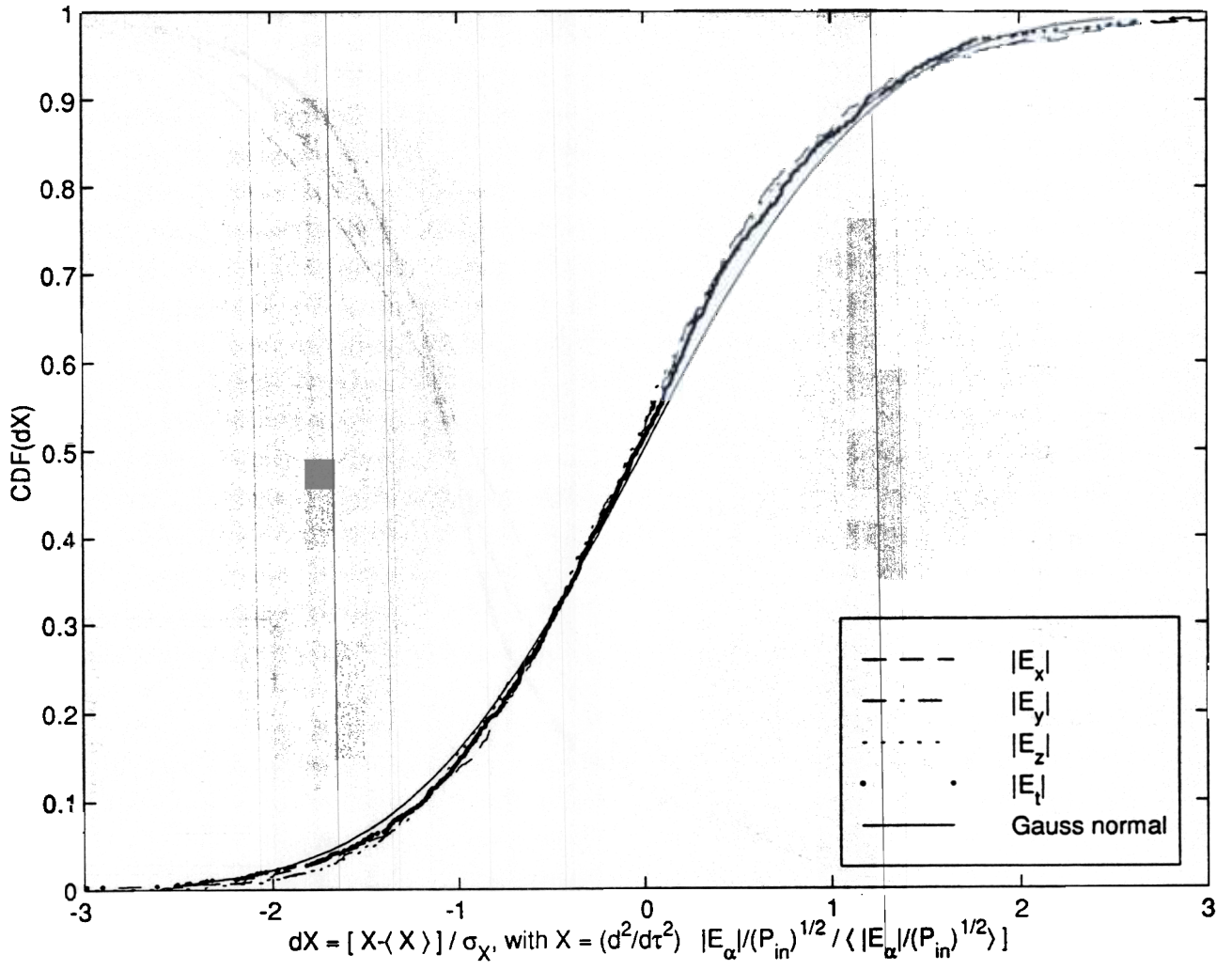


Figure 166: Cumulative distribution function of second-order difference of normalized measured $|E_\alpha(\tau)|$ and $|E_t(\tau)|$.

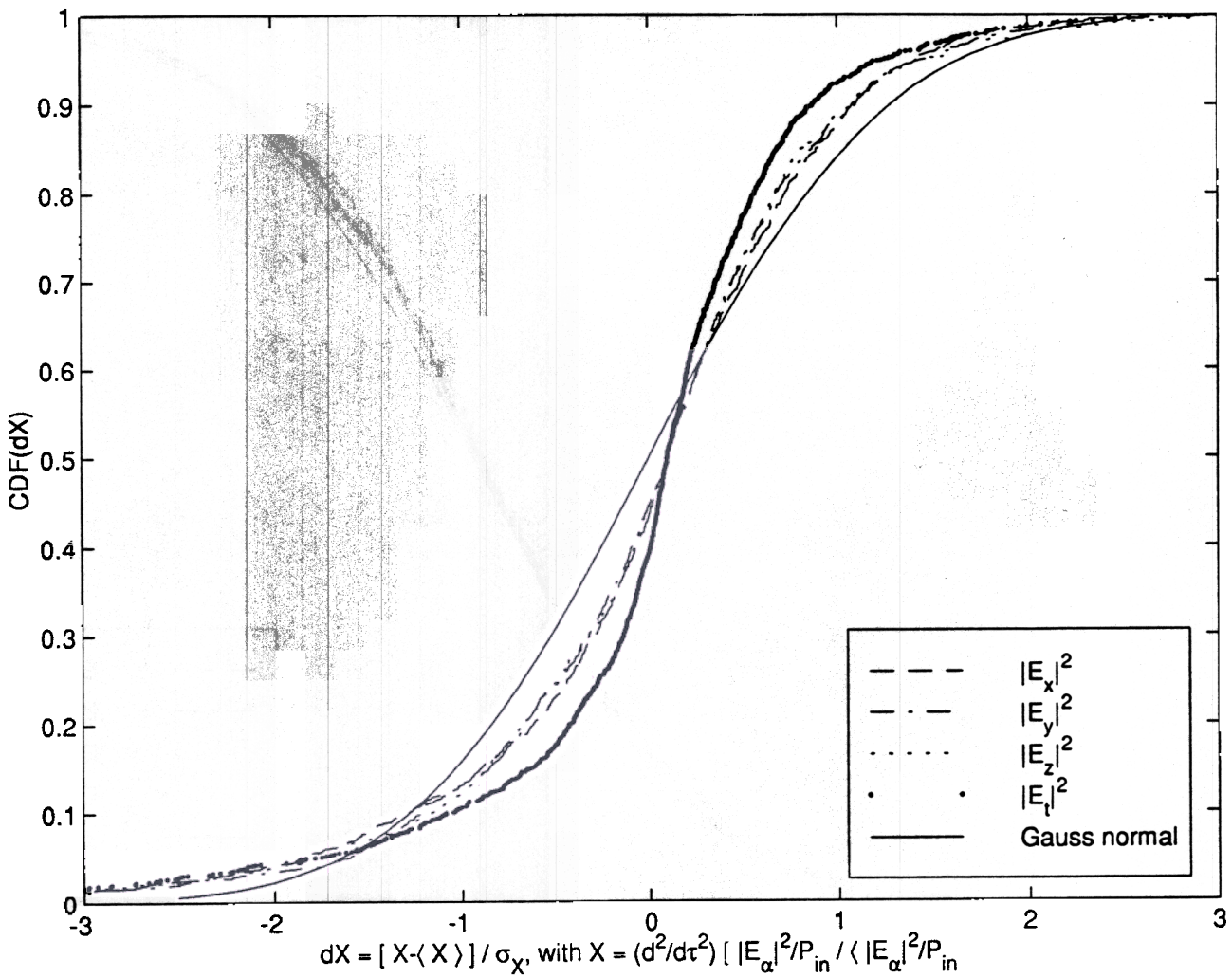


Figure 167: Cumulative distribution function of second-order difference of normalized measured $|E_\alpha(\tau)|^2$ and $|E_t(\tau)|^2$.

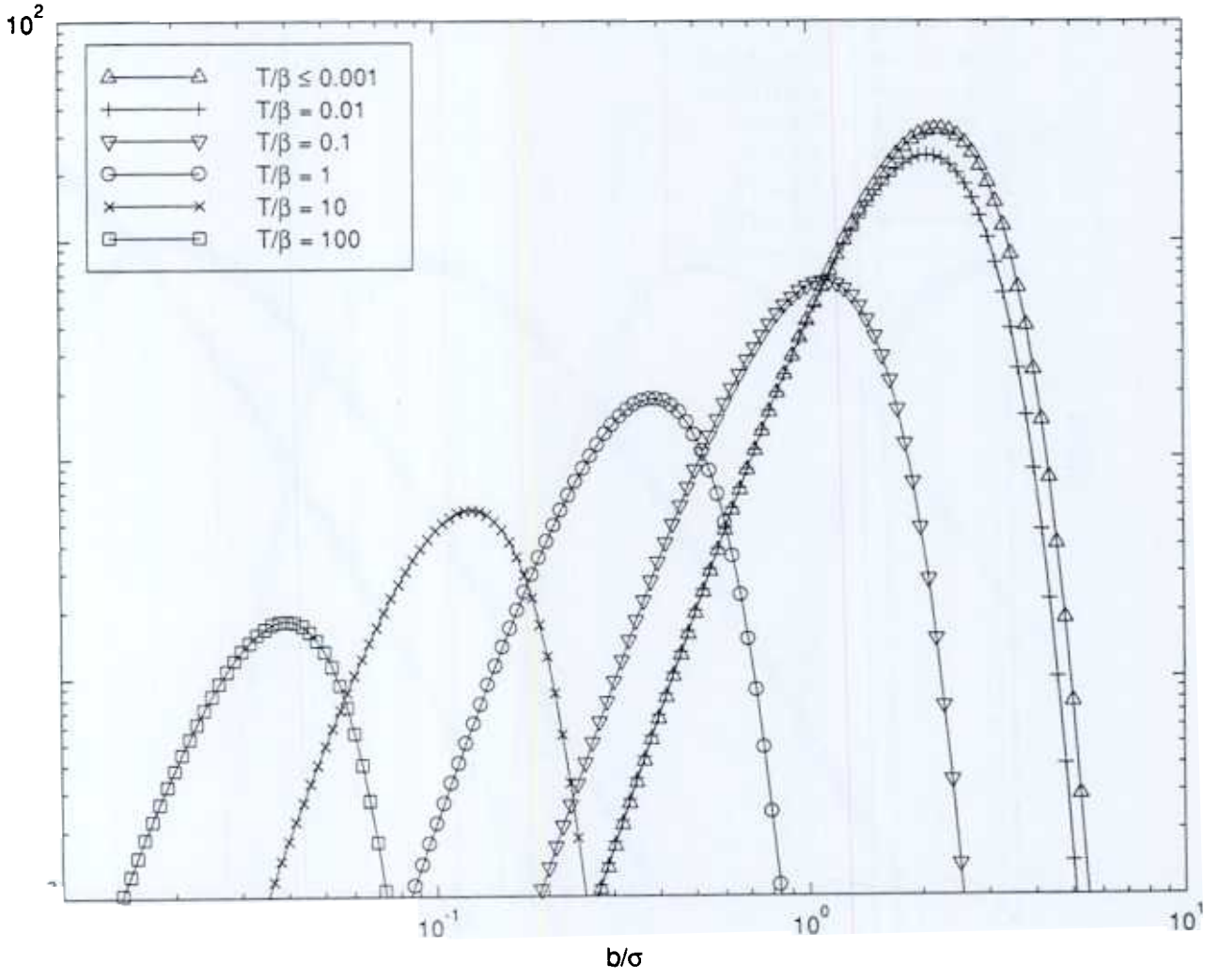
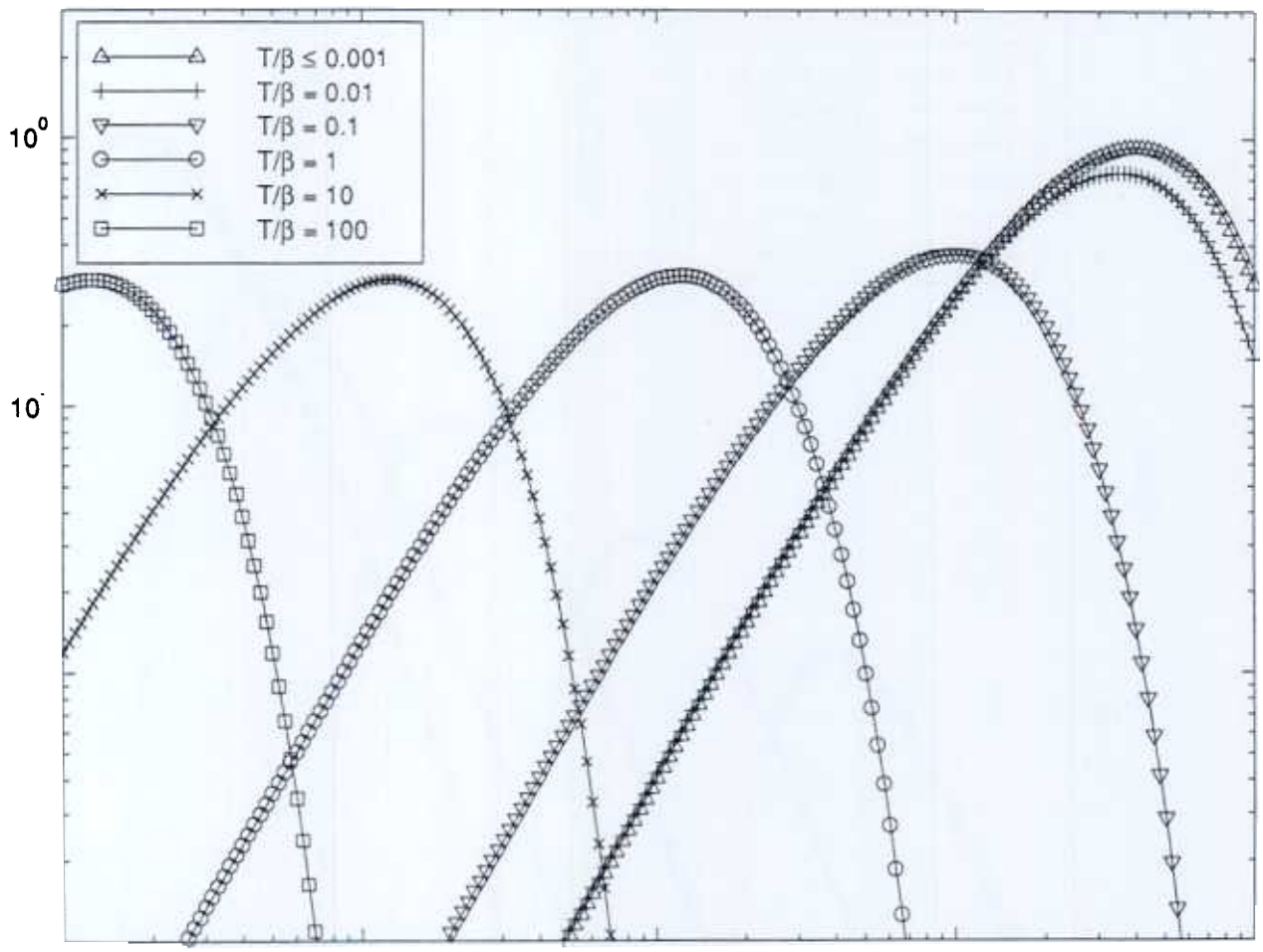


Figure 168: Upward threshold crossing frequency $\nu_T^+(b/\sigma_0)$ for magnitude of total field upon local stir averaging.


T/β ≤ 0.001
T/β = 0.01
T/β = 0.1
T/β = 1
T/β = 10
T/β = 100
10^0
10^-

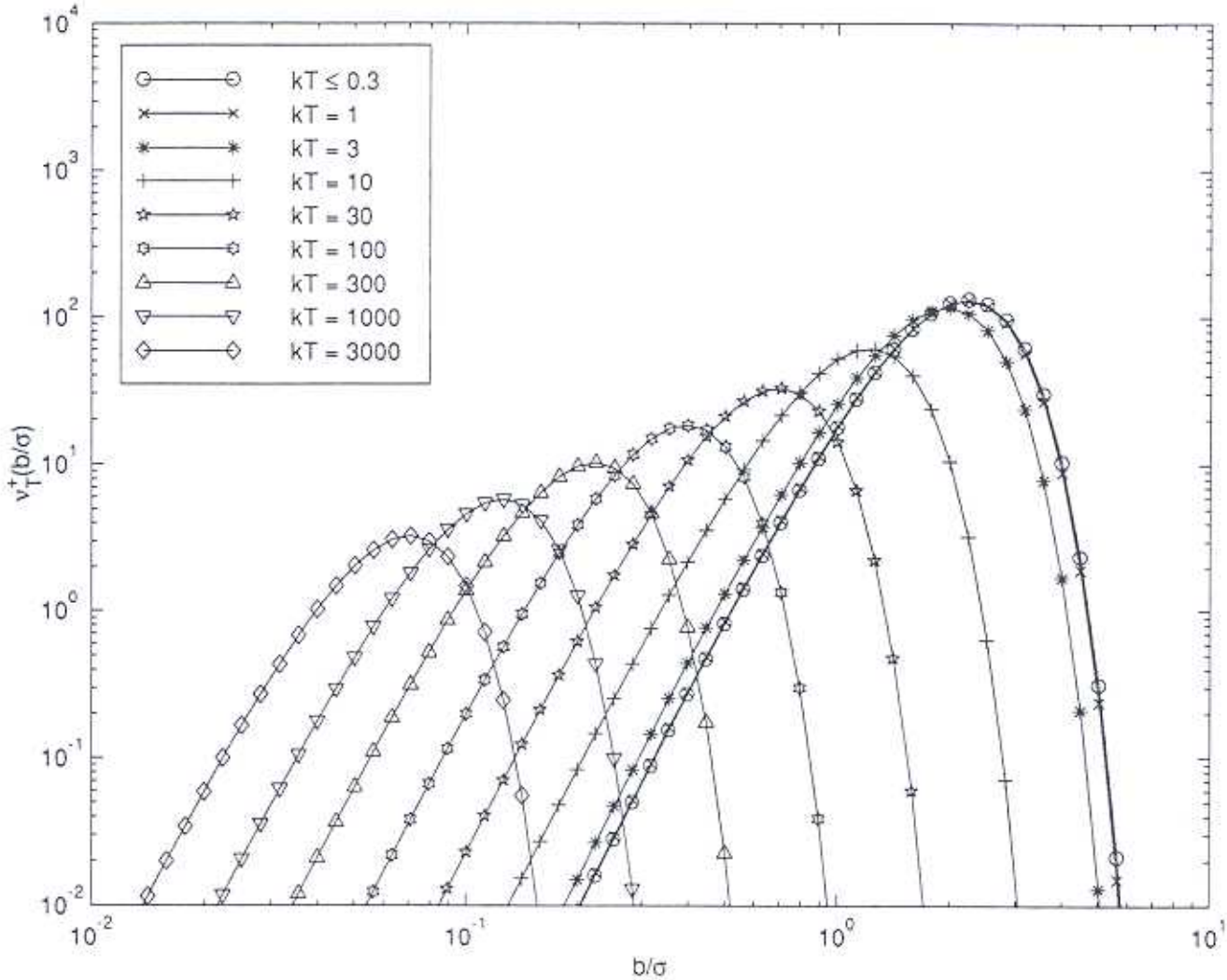


Figure 170: Upward threshold crossing frequency $\nu_T^+(b/\sigma_0)$ for magnitude of total field upon local spatial averaging.

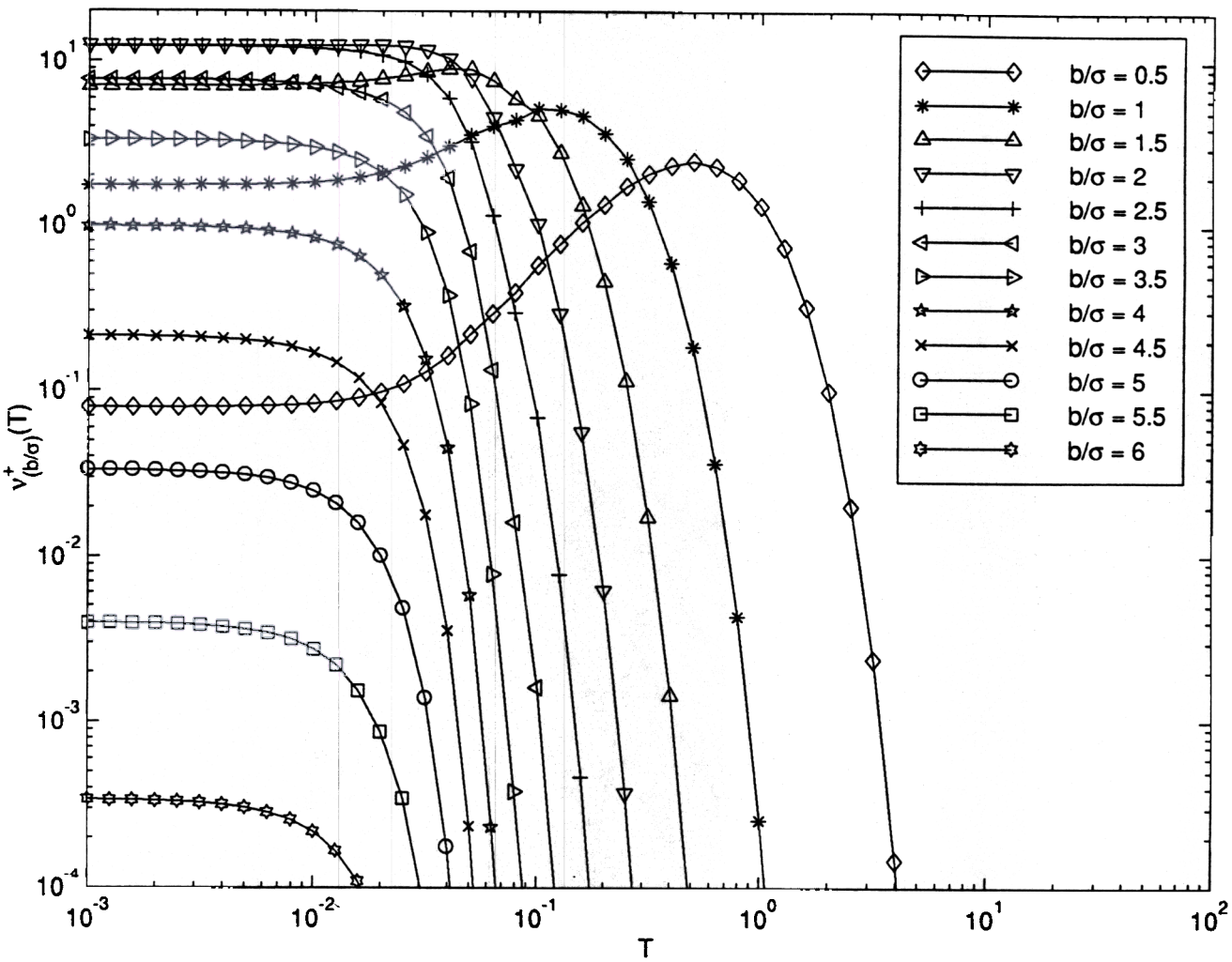


Figure 171: Upward threshold crossing frequency $\nu^+_{b/\sigma_0}(T)$ for magnitude of total field upon local spatial averaging.

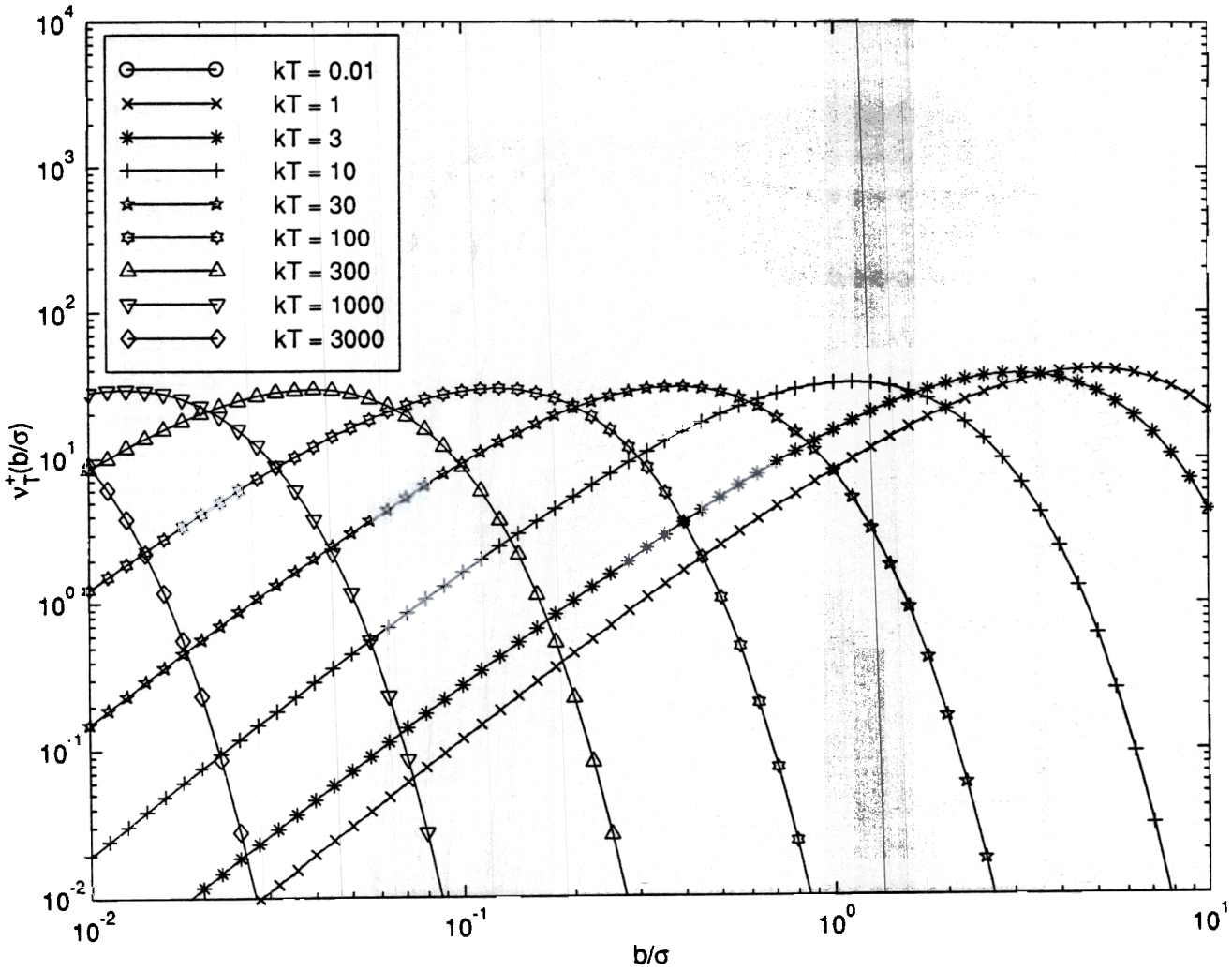


Figure 172: Upward threshold crossing frequency $\nu_T^+(b/\sigma_0)$ for total power density upon local spatial averaging.

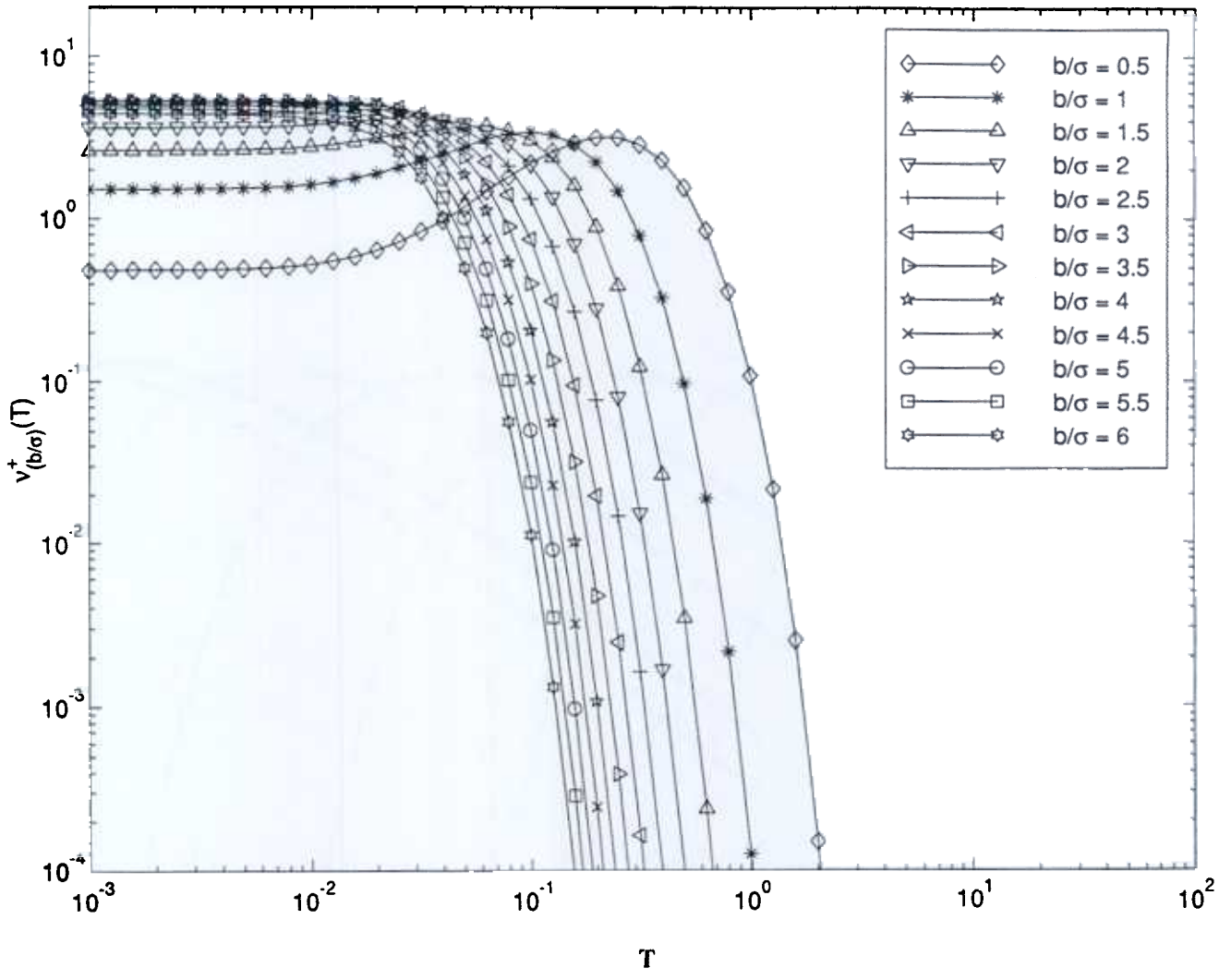


Figure 173: Upward threshold crossing frequency $\nu^+_{b/\sigma_0}(\mathcal{T})$ for total power density upon local spatial averaging.

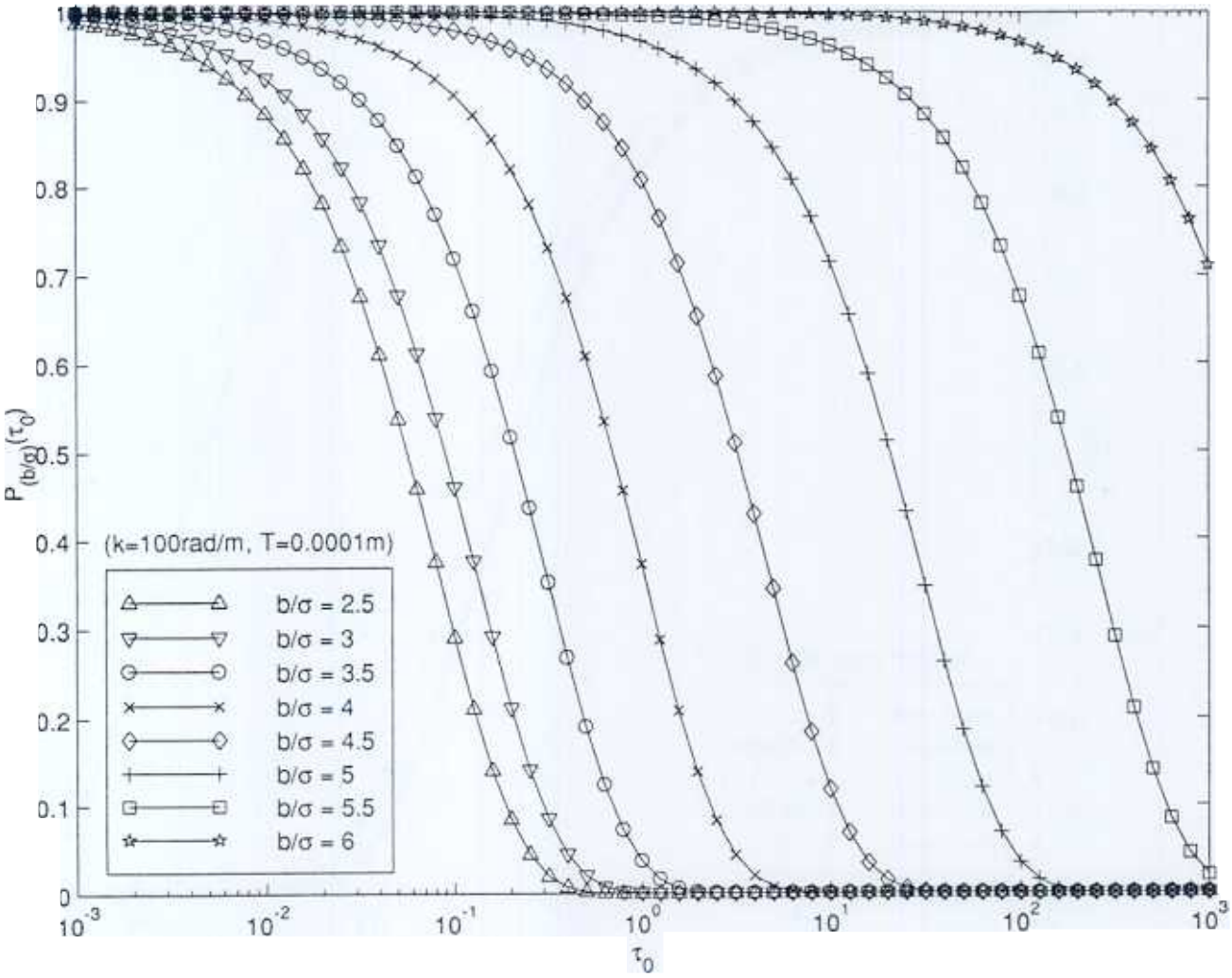


Figure 174: First-passage probability $\mathcal{P}_{b/\sigma_0}(\tau_0)$ for magnitude of total field upon local spatial averaging.

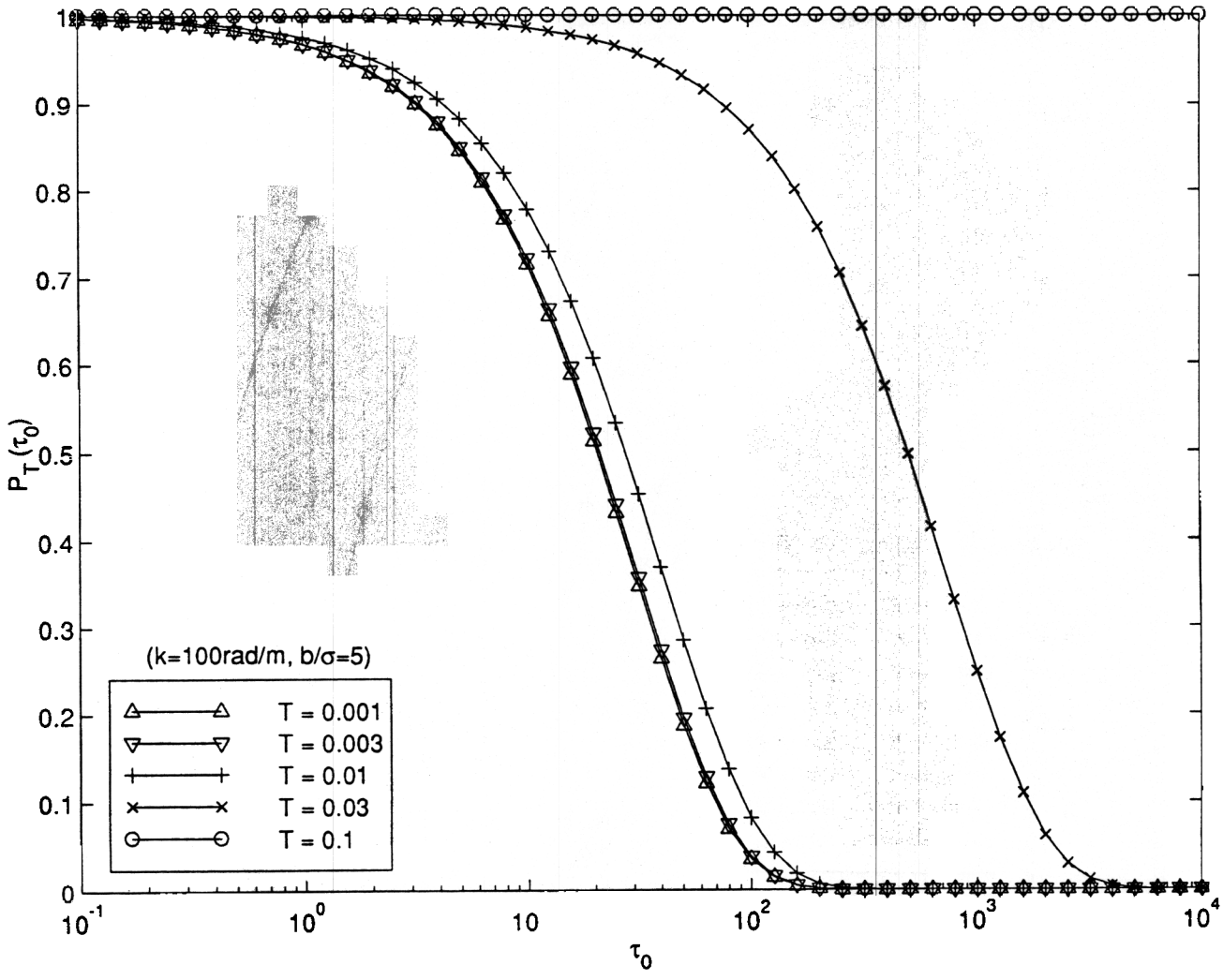


Figure 175: First-passage probability $\mathcal{P}_{\mathcal{T}}(\tau_0)$ for magnitude of total field upon local spatial averaging.

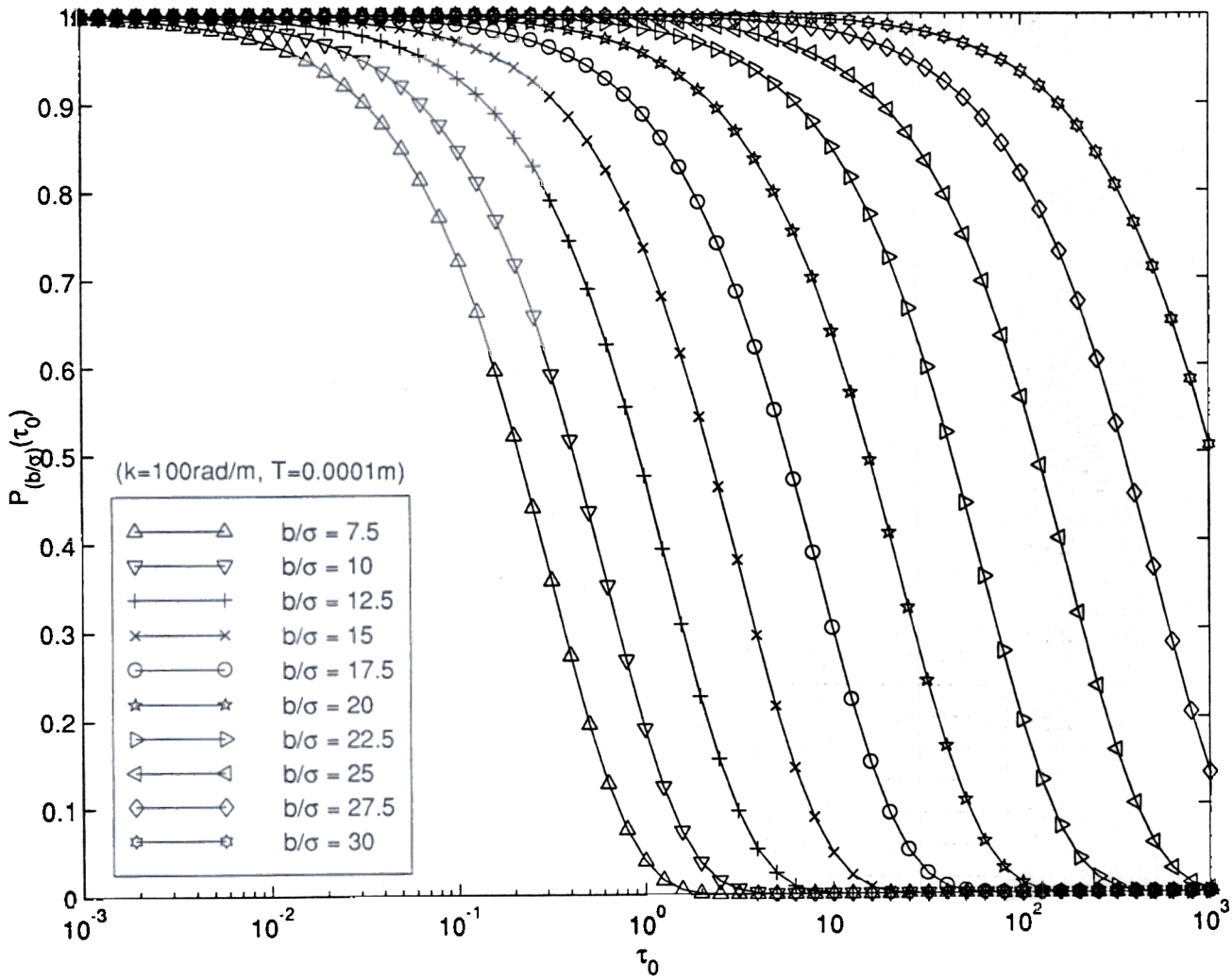


Figure 176: First-passage probability $\mathcal{P}_{b/\sigma_0}(\tau_0)$ for total power density upon local spatial averaging.

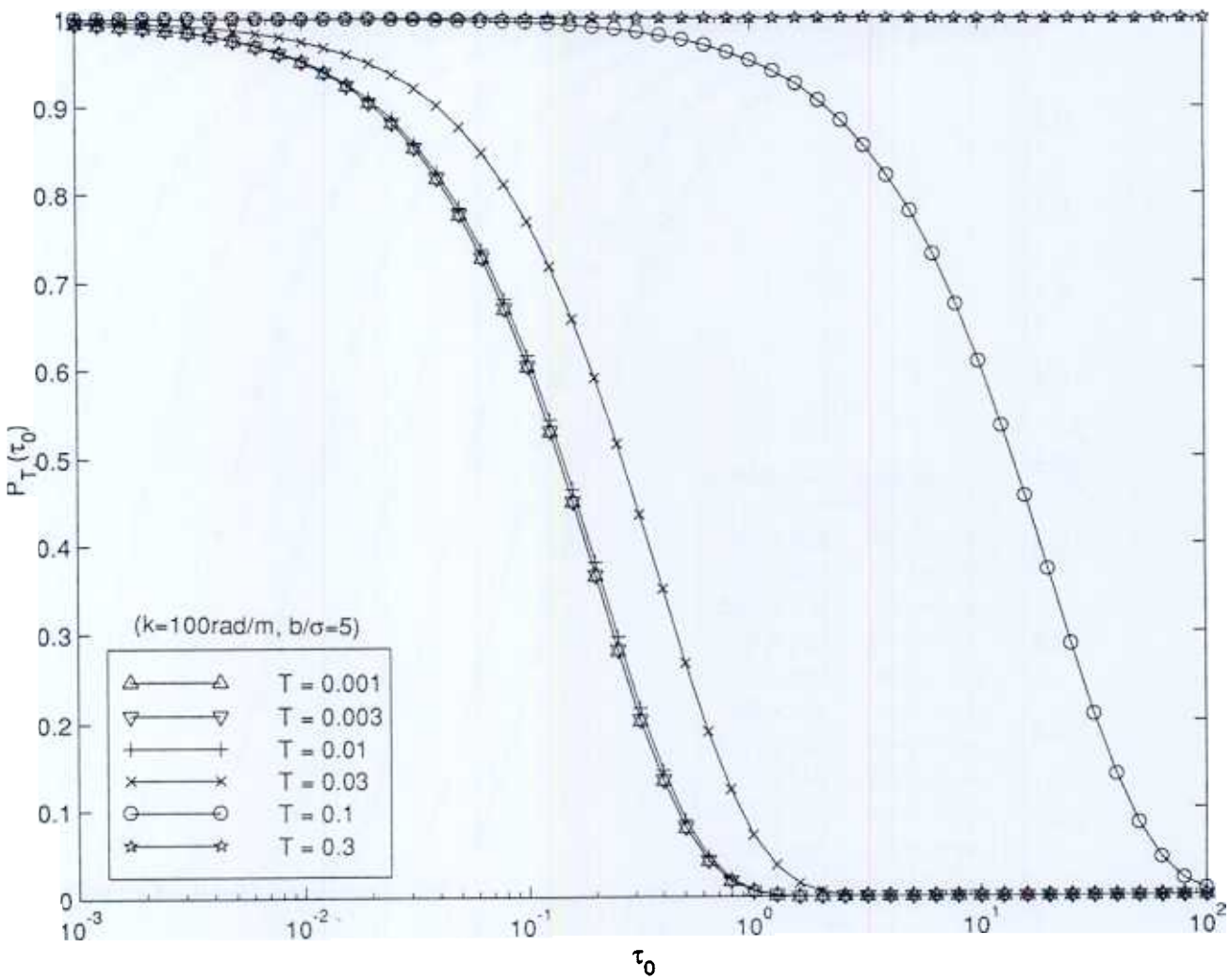


Figure 177: First-passage probability $\mathcal{P}_{\mathcal{I}}(\tau_0)$ for total power density upon local spatial averaging.

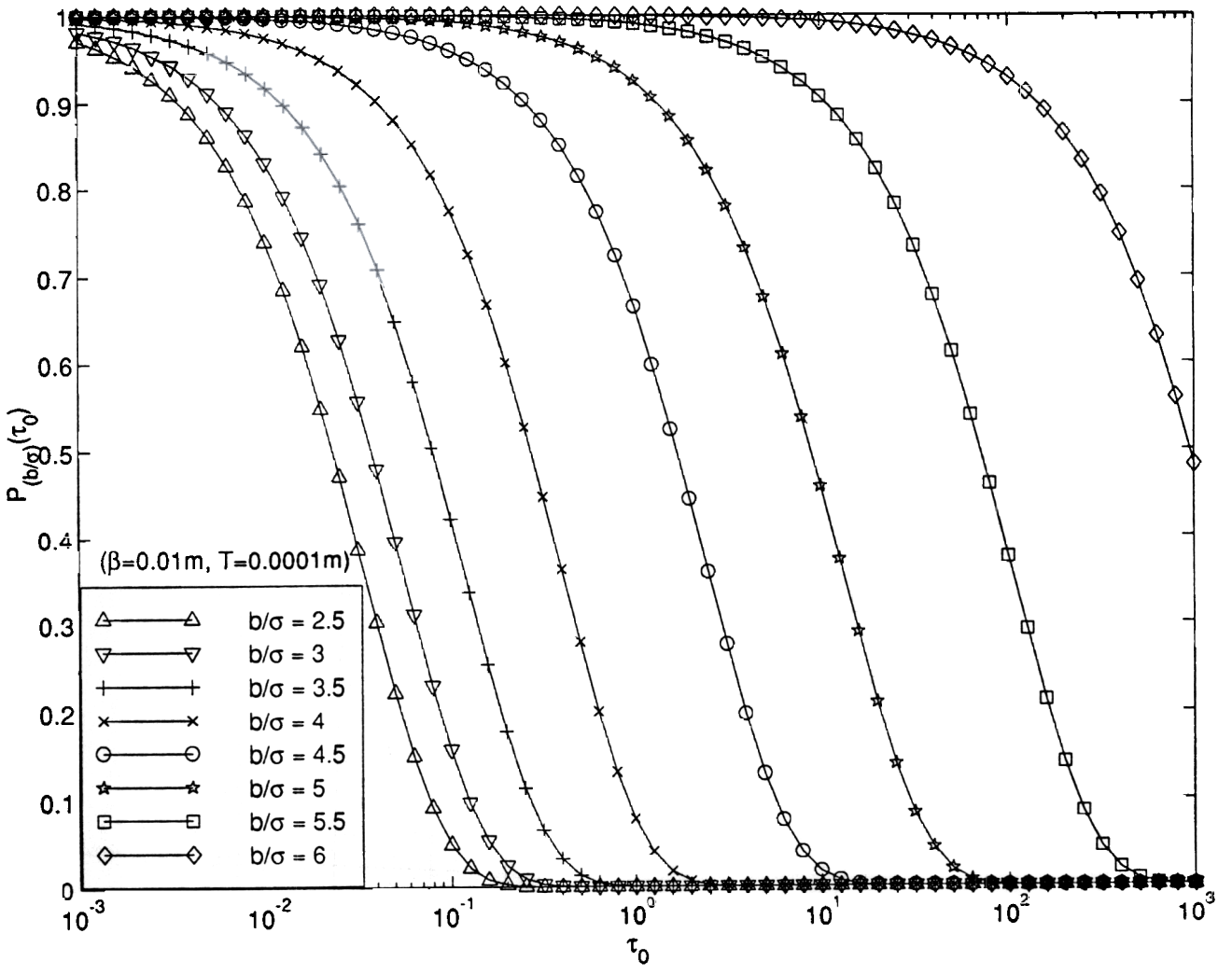


Figure 178: First-passage probability $\mathcal{P}_{b/\sigma_0}(\tau_0)$ for magnitude of total field upon local stir averaging.

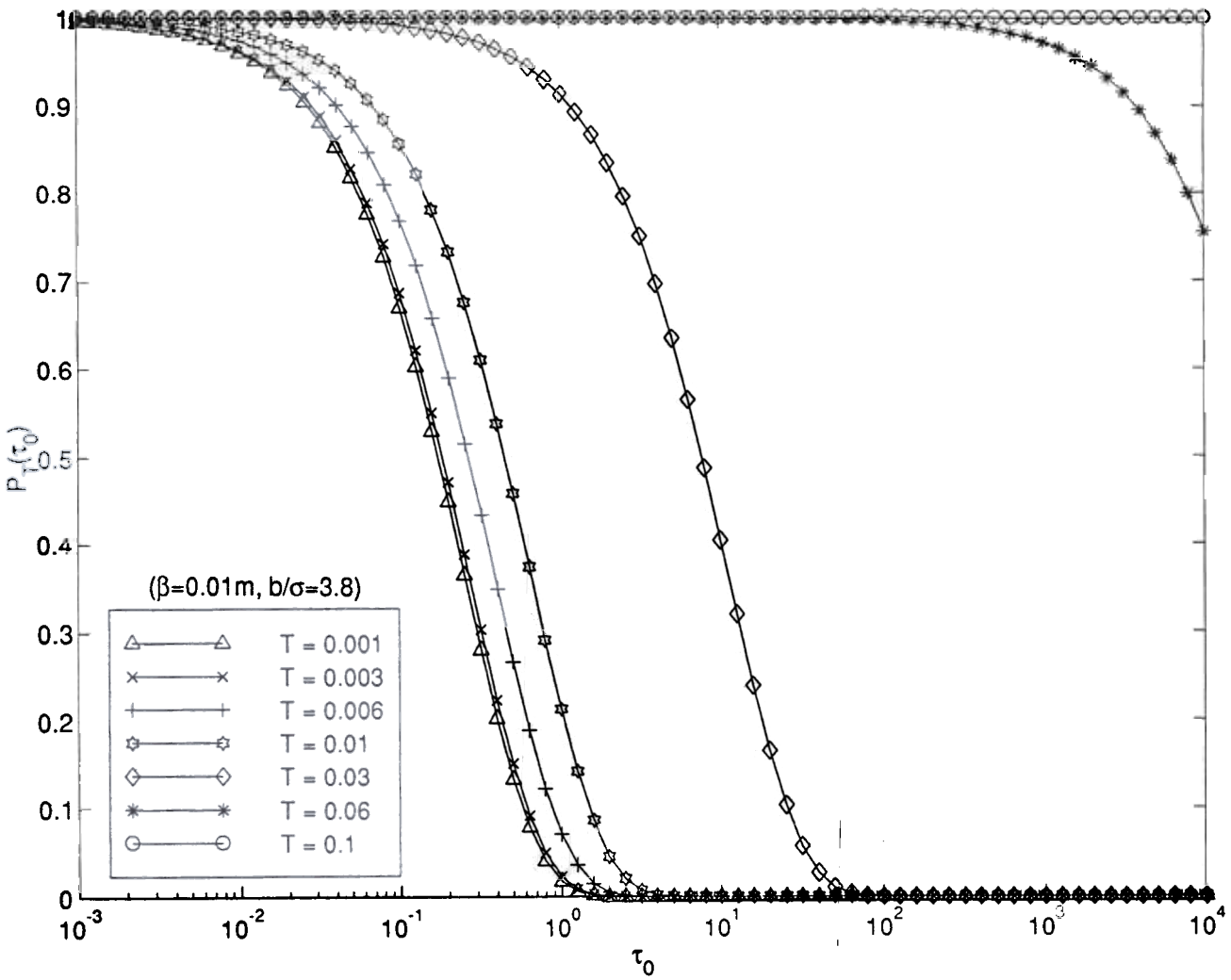


Figure 179: First-passage probability $\mathcal{P}_T(\tau_0)$ for magnitude of total field upon local stir averaging.

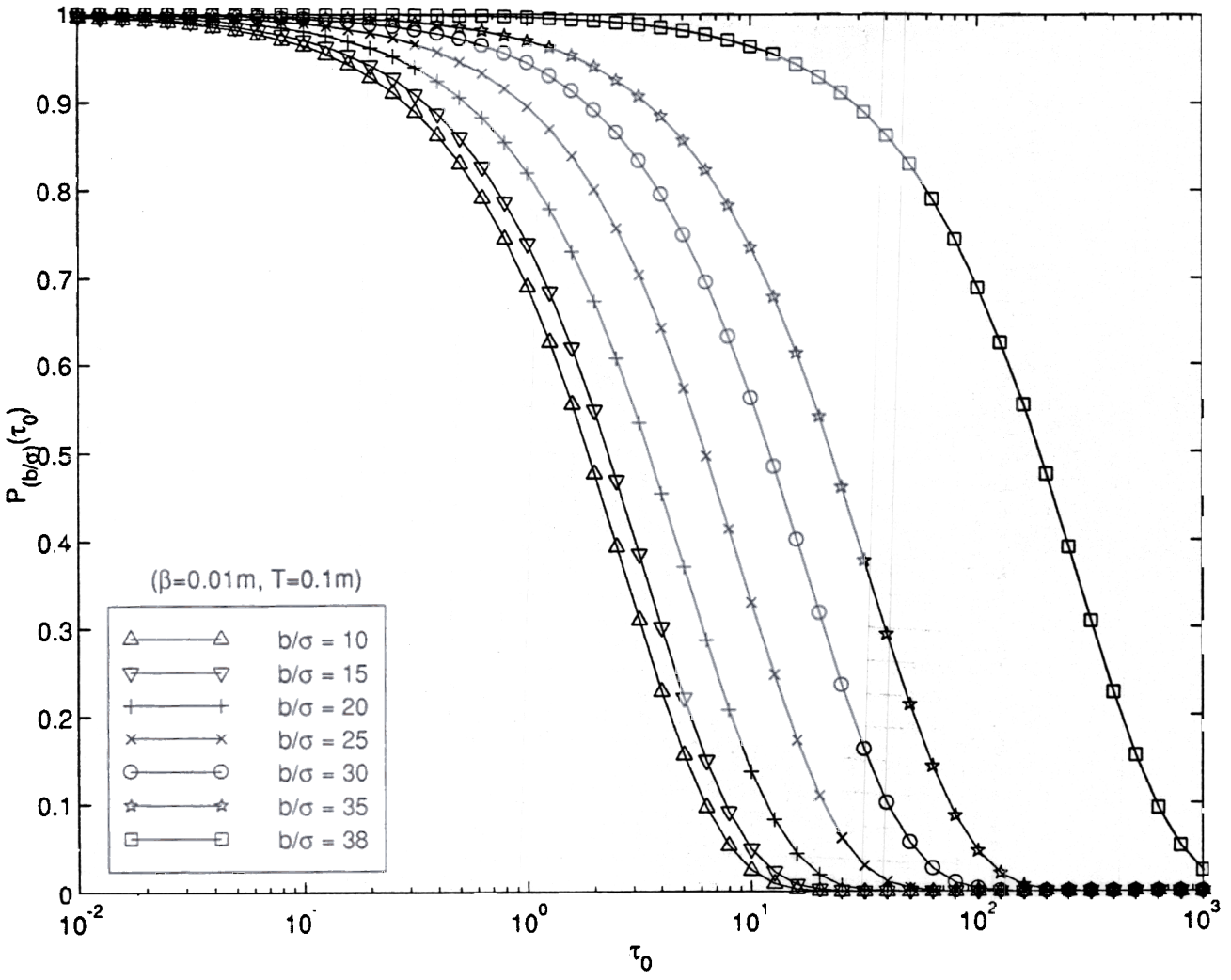


Figure 180: First-passage probability $\mathcal{P}_{b/\sigma_0}(\tau_0)$ for total power density upon local stir averaging.

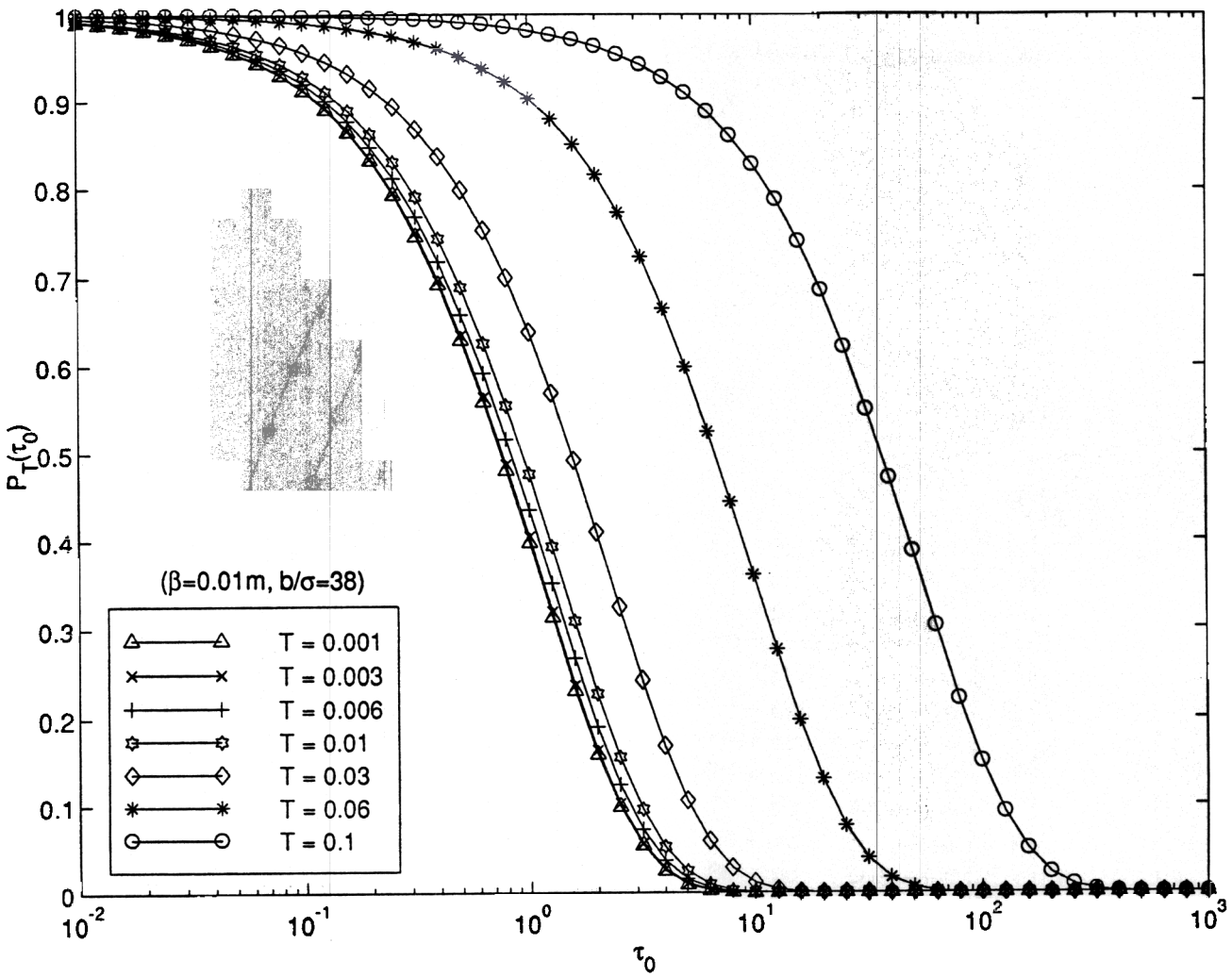


Figure 181: First-passage probability $\mathcal{P}_T(\tau_0)$ for total power density upon local stir averaging.

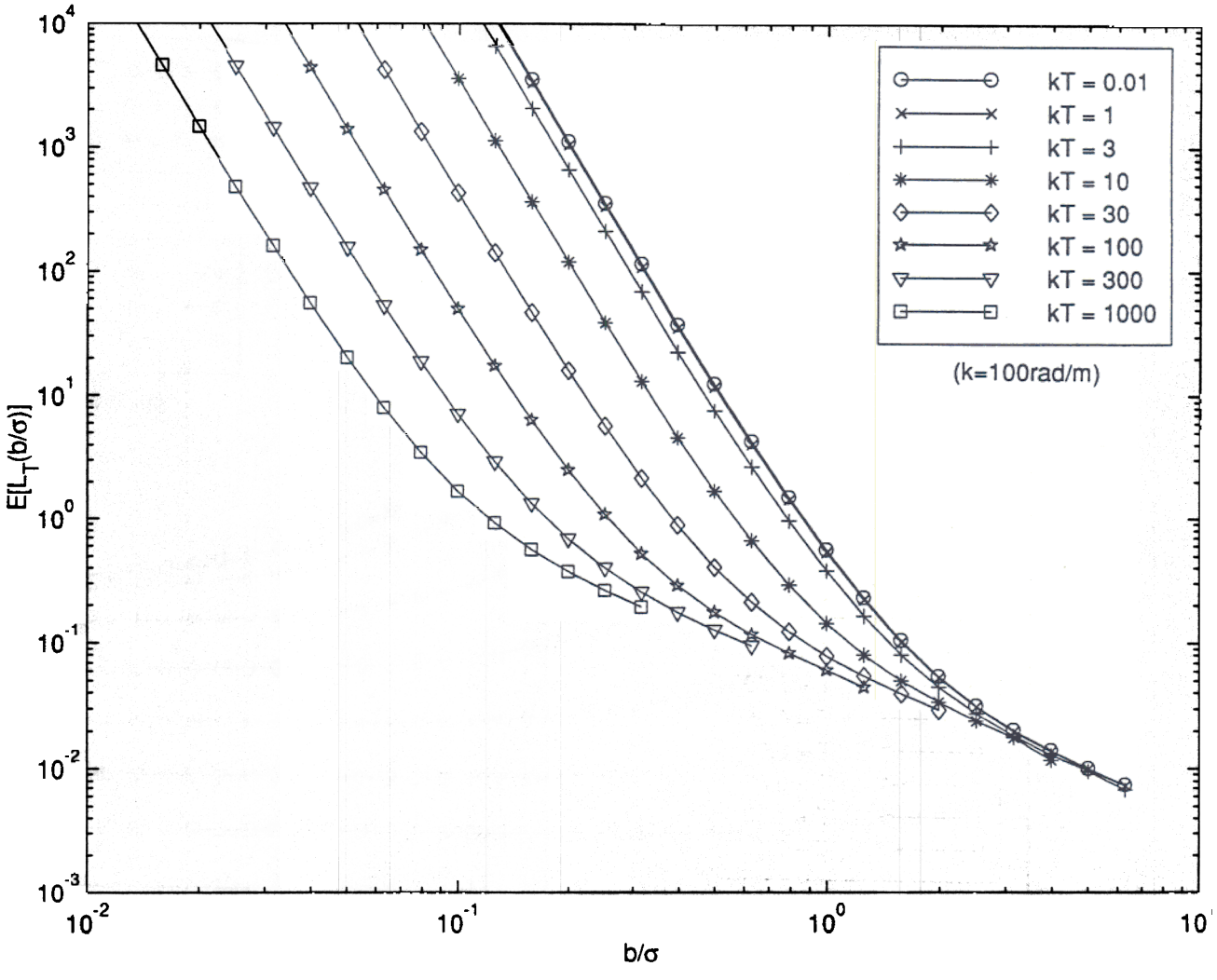


Figure 182: Mean excursion length $\mathrm{E}[\mathcal{L}_T(b)]$ for magnitude of total field upon local spatial averaging.

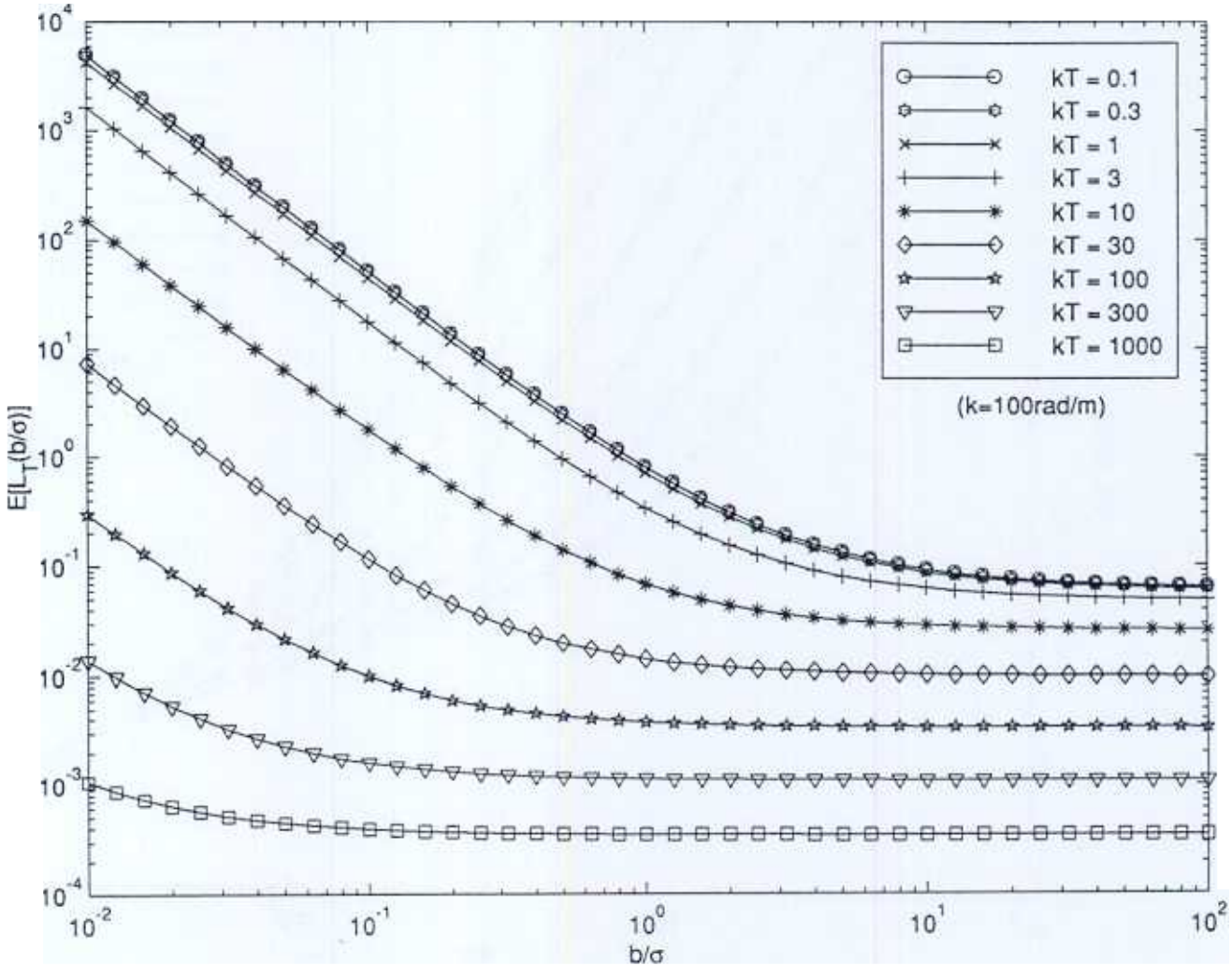


Figure 183: Mean excursion length $\mathrm{E}[\mathcal{L}_T(b)]$ for total power density upon local spatial averaging.

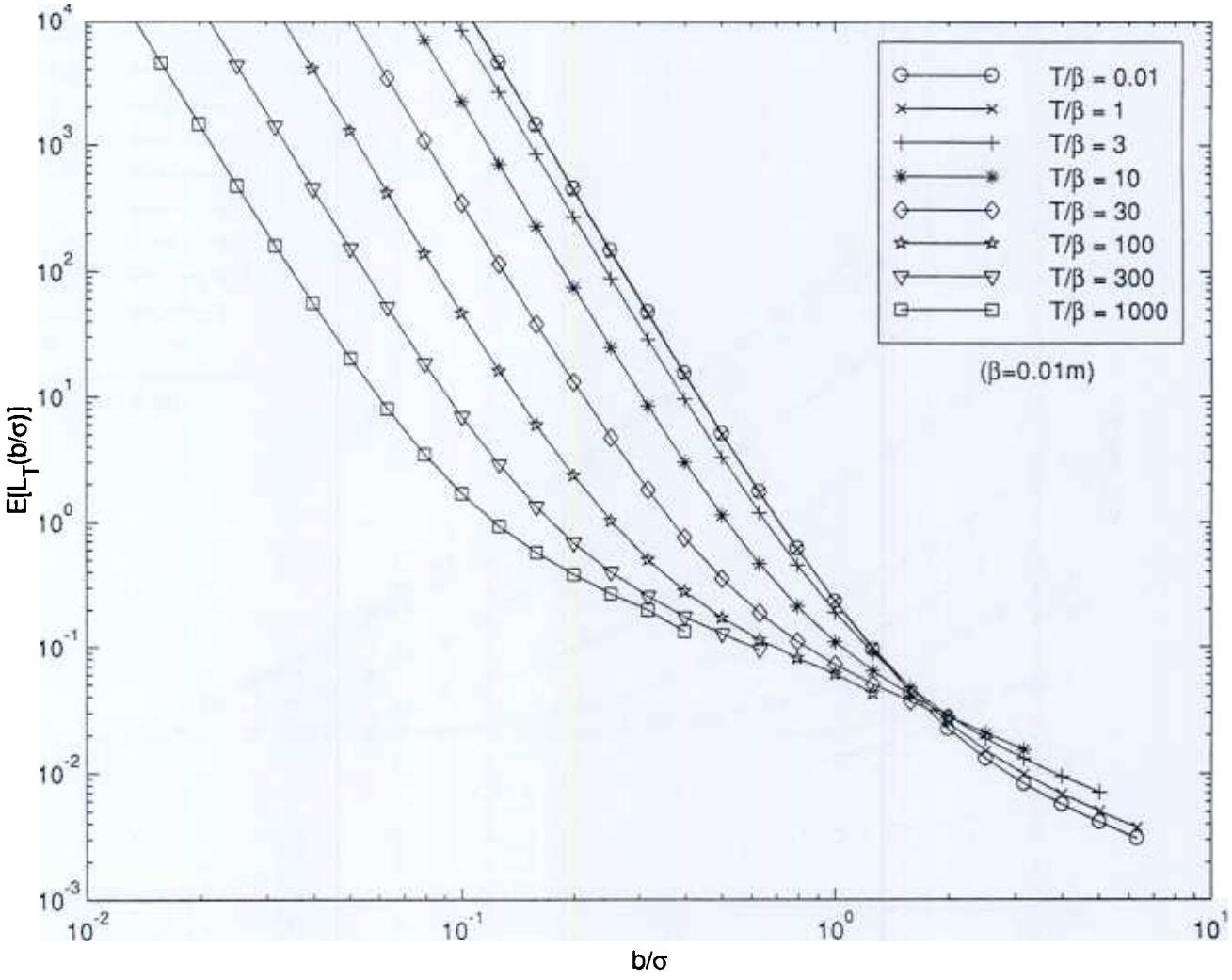


Figure 184: Mean excursion length $\mathrm{E}[\mathcal{L}_T(b)]$ for magnitude of total field upon local stir averaging.

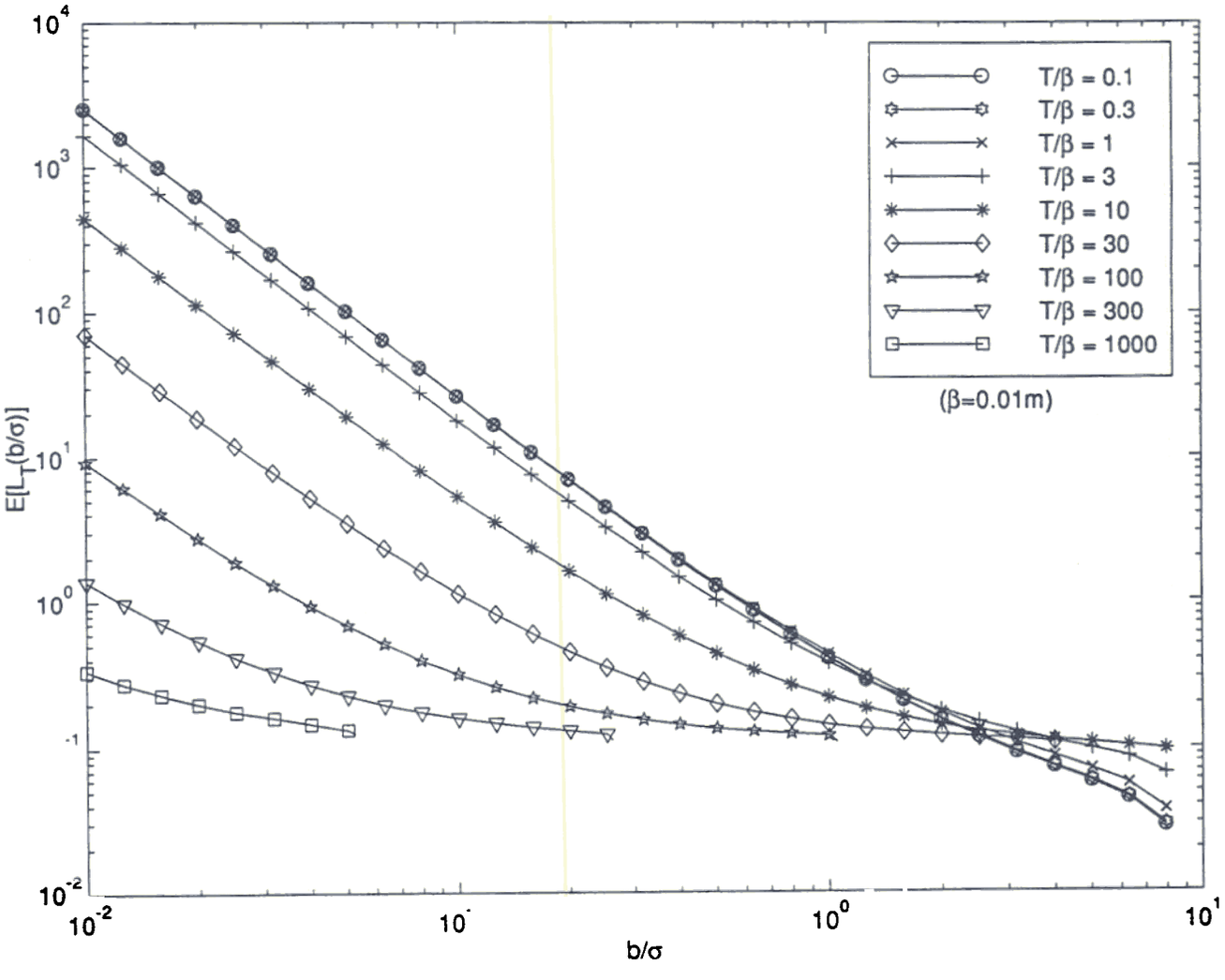


Figure 185: Mean excursion length $\mathrm{E}[\mathcal{L}_{\mathcal{T}}(b)]$ for total power density upon local stir averaging.

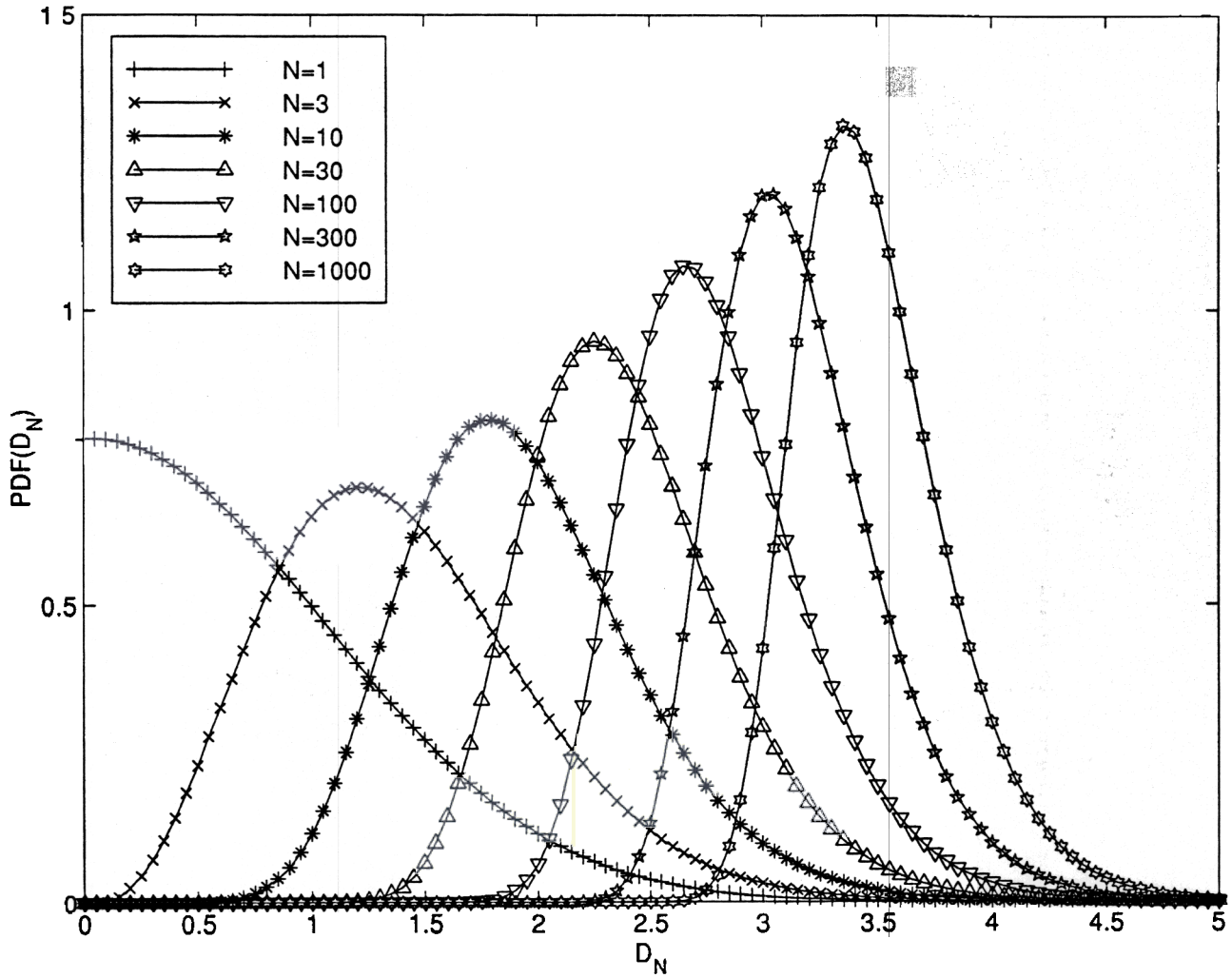


Figure 186: Asymptotic probability density function $f_{\chi_1(N)}(w_D)$ of max-to-mean ratio of sampled values of $f_{\chi_1}(x)$ for Kholmogorov–Smirnov statistic.

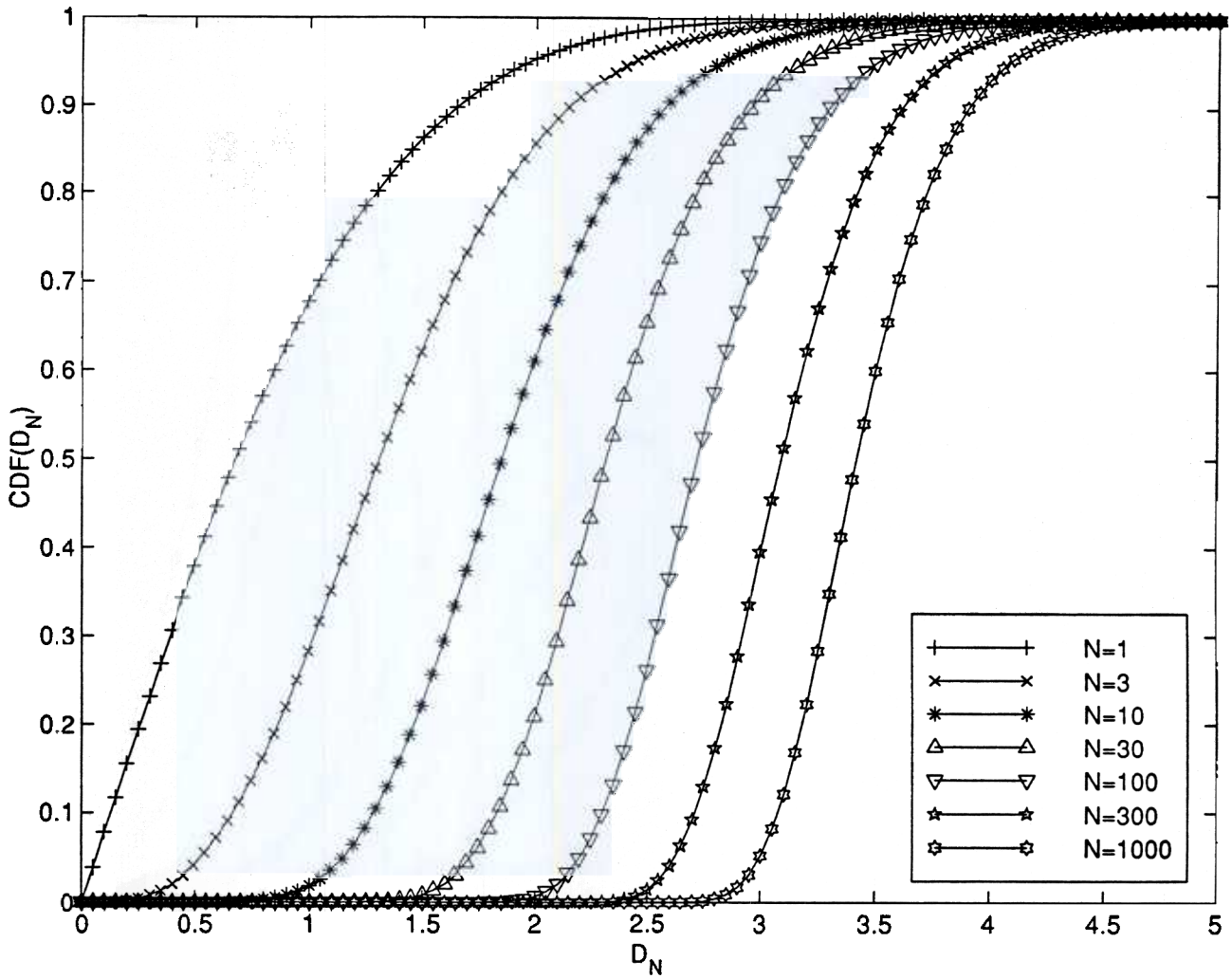


Figure 187: Asymptotic cumulative distribution function $F_{\chi_1(N)}(w_D)$ of max-to-mean ratio of sampled values of $f_{\chi_1}(x)$ for Kholmogorov–Smirnov statistic.

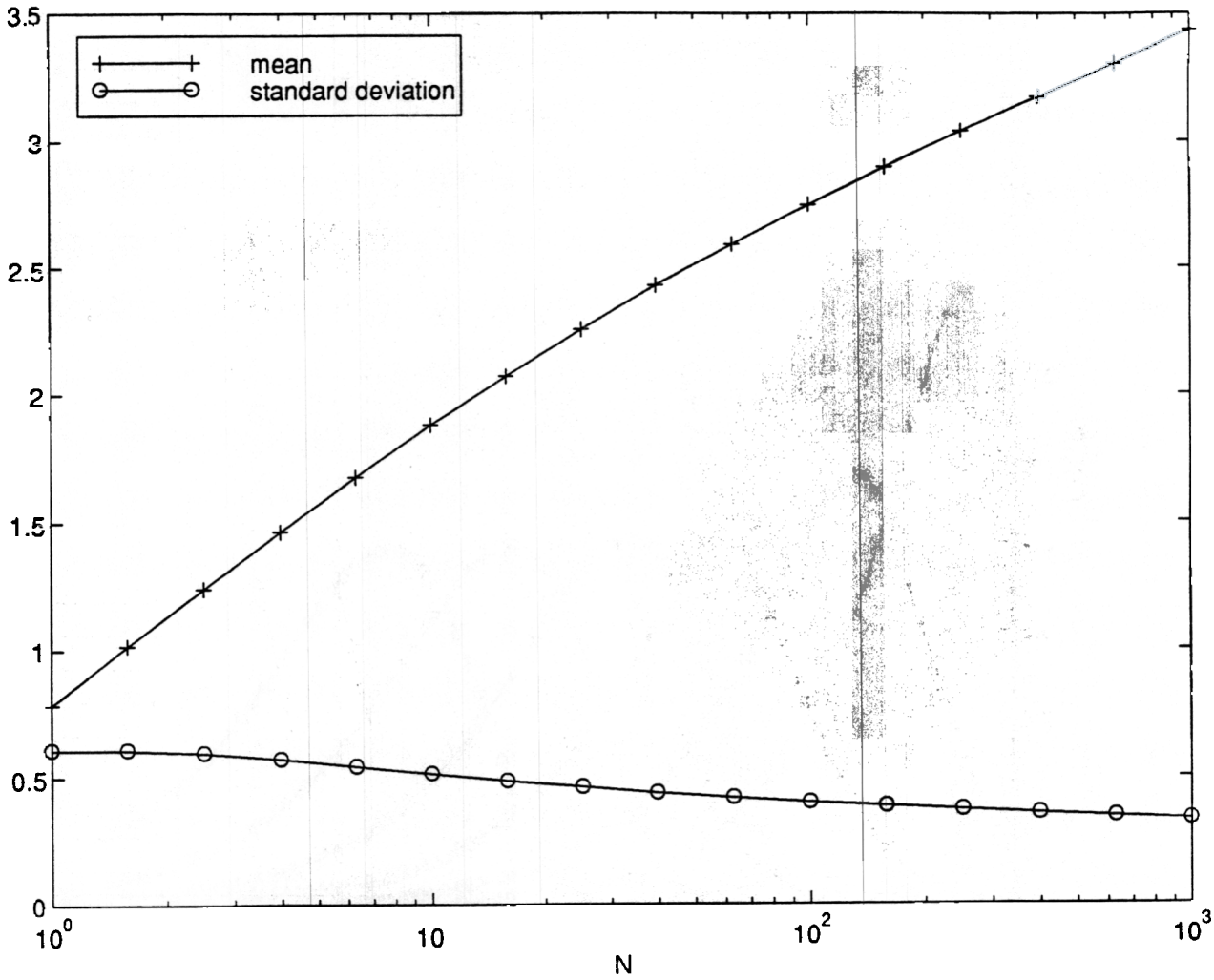


Figure 188: Mean and standard deviation for asymptotic distribution of max-to-mean ratio of sampled values of $f_{\chi_1}(x)$ for Kholmogorov–Smirnov statistic.

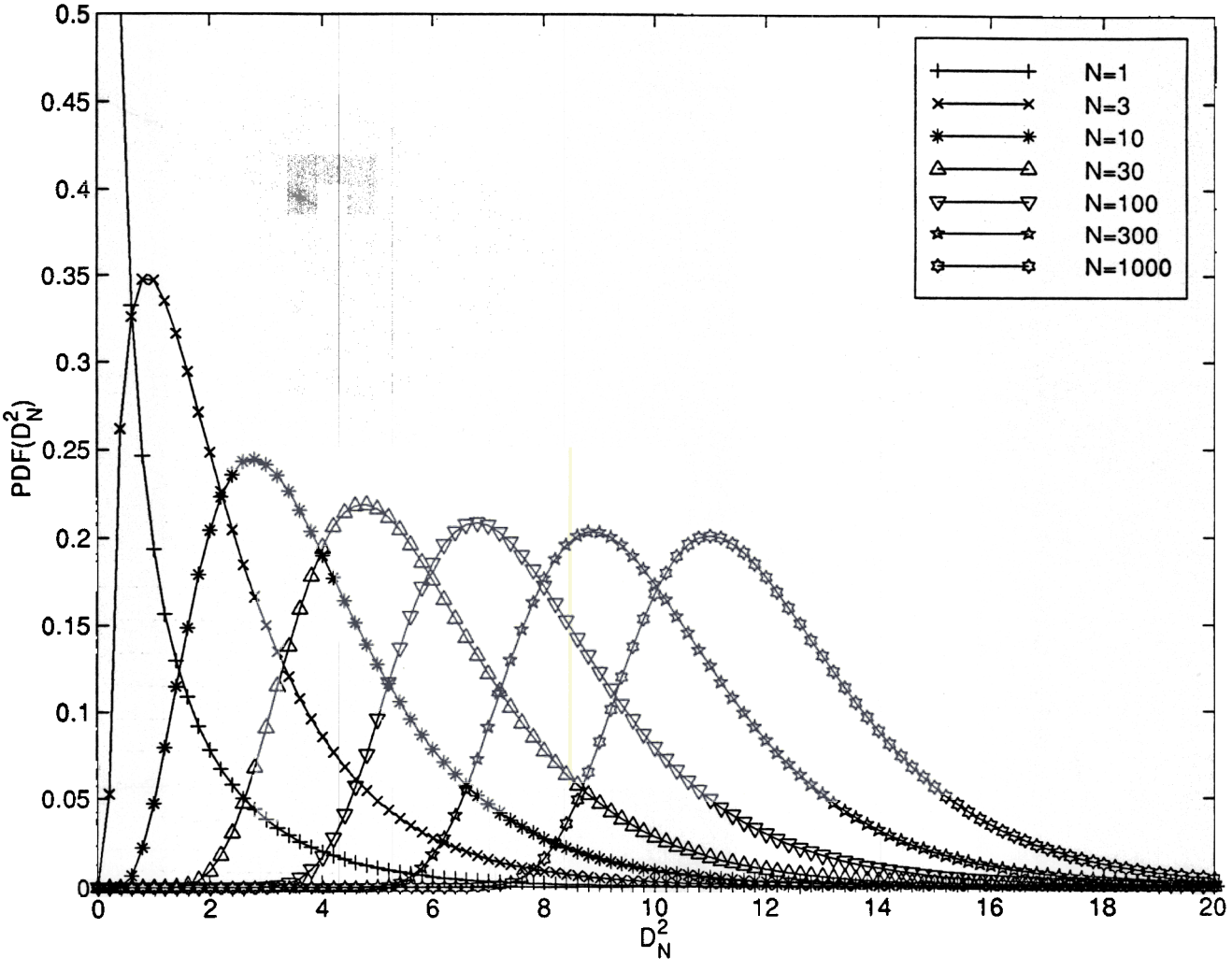


Figure 189: Asymptotic probability density function $f_{\chi^2_1(N)}(w_D)$ of max-to-mean ratio of sampled values of $f_{\chi^2_1}(x)$ for squared Kholmogorov–Smirnov statistic.

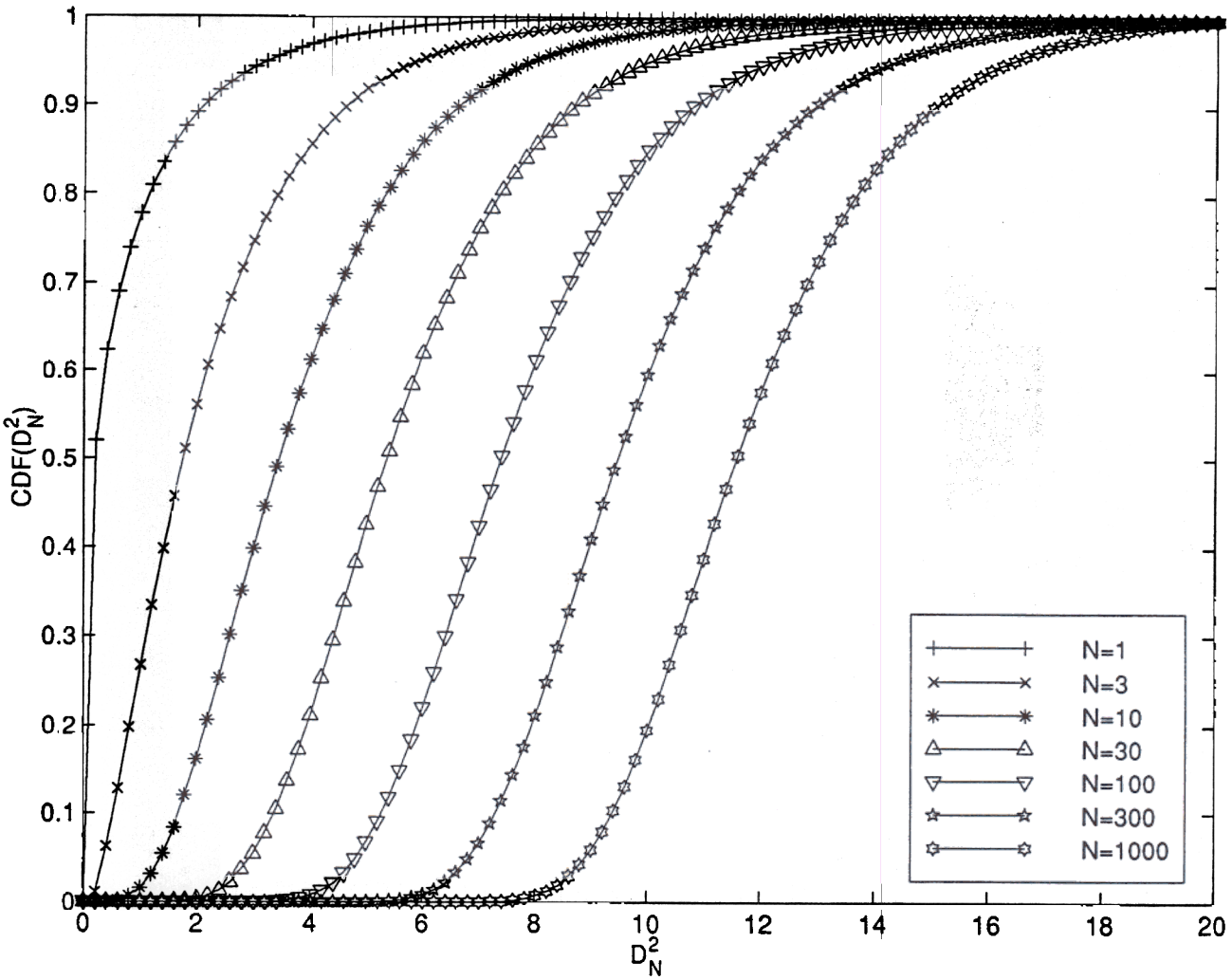


Figure 190: Asymptotic cumulative distribution function $F_{\chi_1^2(N)}(w_D)$ of max-to-mean ratio of sampled values of $f_{\chi_1^2}(x)$ for squared Kholmogorov–Smirnov statistic.

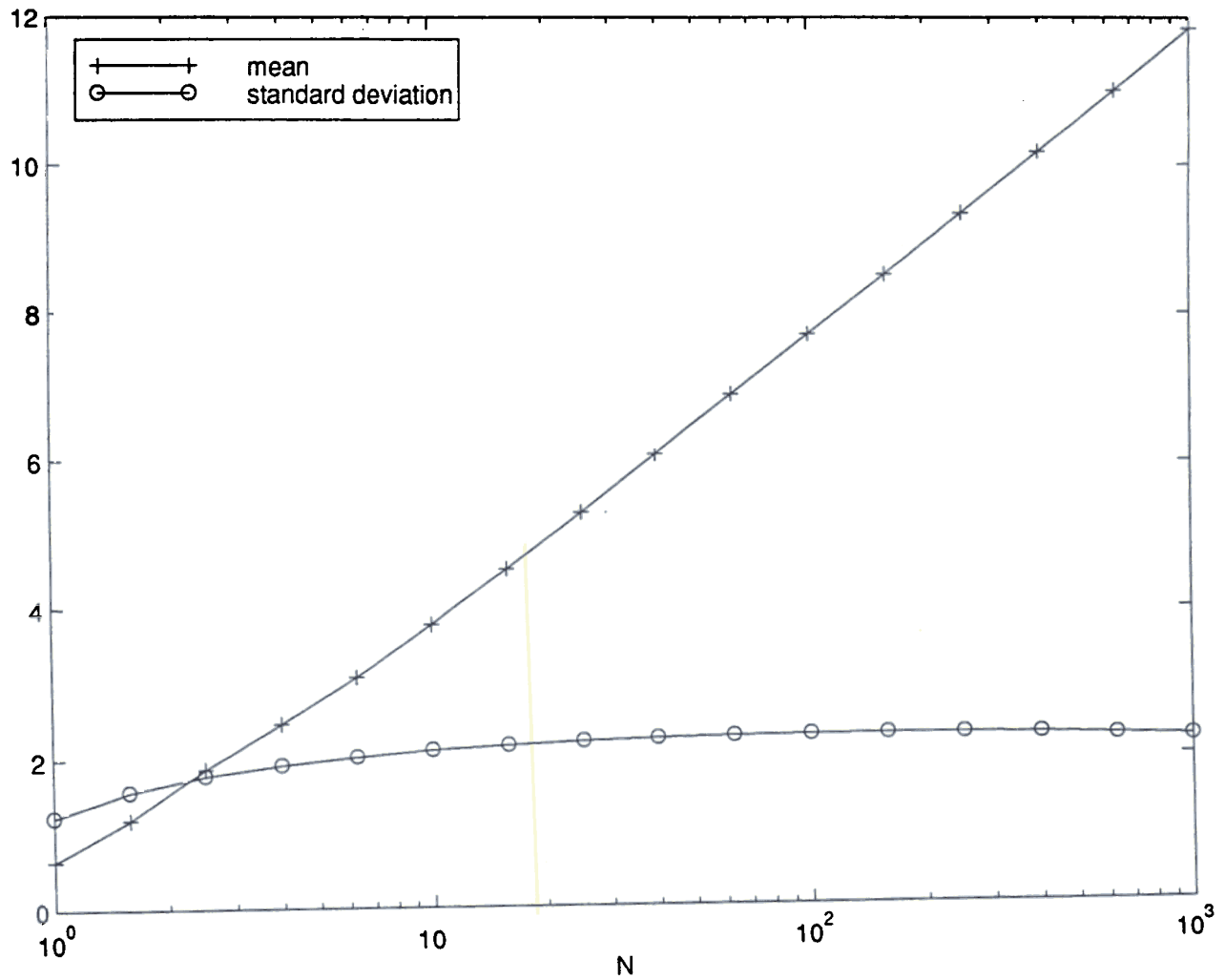


Figure 191: Mean and standard deviation for asymptotic distribution of max-to-mean ratio of sampled values of $f_{\chi^2}(x)$ for squared Kholmogorov–Smirnov statistic.